Volume 1/3

C.E. Coleman

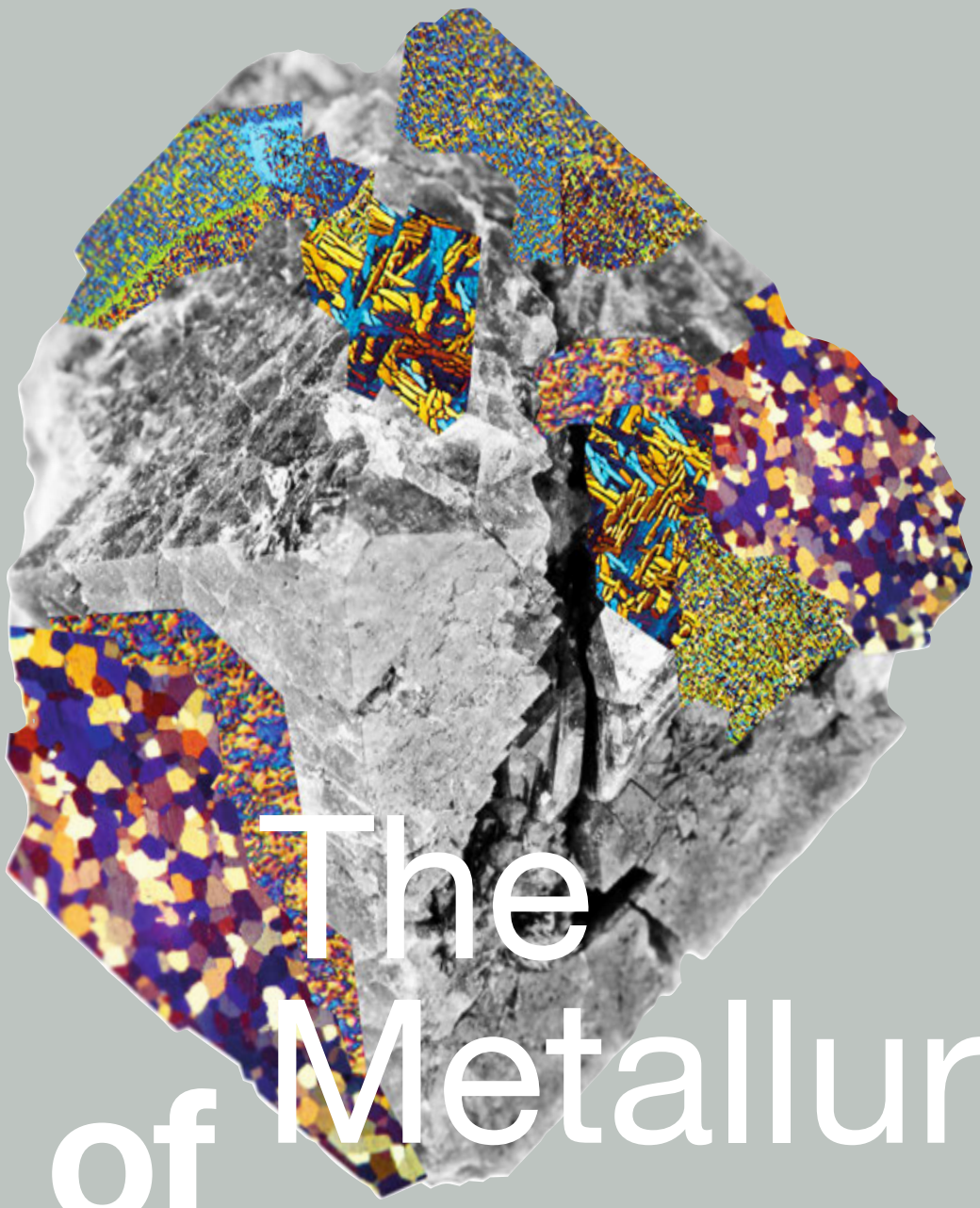

The Metallurgy of Zirconium

IAEA
International Atomic Energy Agency

The Metallurgy of Zirconium

The following States are Members of the International Atomic Energy Agency:

AFGHANISTAN
ALBANIA
ALGERIA
ANGOLA
ANTIGUA AND BARBUDA
ARGENTINA
ARMENIA
AUSTRALIA
AUSTRIA
AZERBAIJAN
BAHAMAS
BAHRAIN
BANGLADESH
BARBADOS
BELARUS
BELGIUM
BELIZE
BENIN
BOLIVIA, PLURINATIONAL STATE OF
BOSNIA AND HERZEGOVINA
BOTSWANA
BRAZIL
BRUNEI DARUSSALAM
BULGARIA
BURKINA FASO
BURUNDI
CAMBODIA
CAMEROON
CANADA
CENTRAL AFRICAN REPUBLIC
CHAD
CHILE
CHINA
COLOMBIA
COMOROS
CONGO
COSTA RICA
CÔTE D'IVOIRE
CROATIA
CUBA
CYPRUS
CZECH REPUBLIC
DEMOCRATIC REPUBLIC OF THE CONGO
DENMARK
DJIBOUTI
DOMINICA
DOMINICAN REPUBLIC
ECUADOR
EGYPT
EL SALVADOR
ERITREA
ESTONIA
ESWATINI
ETHIOPIA
FIJI
FINLAND
FRANCE
GABON
GEORGIA
GERMANY
GHANA
GREECE
GRENADA
GUATEMALA
GUYANA
HAITI
HOLY SEE
HONDURAS
HUNGARY
ICELAND
INDIA
INDONESIA
IRAN, ISLAMIC REPUBLIC OF
IRAQ
IRELAND
ISRAEL
ITALY
JAMAICA
JAPAN
JORDAN
KAZAKHSTAN
KENYA
KOREA, REPUBLIC OF
KUWAIT
KYRGYZSTAN
LAO PEOPLE'S DEMOCRATIC REPUBLIC
LATVIA
LEBANON
LESOTHO
LIBERIA
LIBYA
LIECHTENSTEIN
LITHUANIA
LUXEMBOURG
MADAGASCAR
MALAWI
MALAYSIA
MALI
MALTA
MARSHALL ISLANDS
MAURITANIA
MAURITIUS
MEXICO
MONACO
MONGOLIA
MONTENEGRO
MOROCCO
MOZAMBIQUE
MYANMAR
NAMIBIA
NEPAL
NETHERLANDS
NEW ZEALAND
NICARAGUA
NIGER
NIGERIA
NORTH MACEDONIA
NORWAY
OMAN
PAKISTAN
PALAU
PANAMA
PAPUA NEW GUINEA
PARAGUAY
PERU
PHILIPPINES
POLAND
PORTUGAL
QATAR
REPUBLIC OF MOLDOVA
ROMANIA
RUSSIAN FEDERATION
RWANDA
SAINT KITTS AND NEVIS
SAINT LUCIA
SAINT VINCENT AND THE GRENADINES
SAMOA
SAN MARINO
SAUDI ARABIA
SENEGAL
SERBIA
SEYCHELLES
SIERRA LEONE
SINGAPORE
SLOVAKIA
SLOVENIA
SOUTH AFRICA
SPAIN
SRI LANKA
SUDAN
SWEDEN
SWITZERLAND
SYRIAN ARAB REPUBLIC
TAJIKISTAN
THAILAND
TOGO
TONGA
TRINIDAD AND TOBAGO
TUNISIA
TÜRKİYE
TURKMENISTAN
UGANDA
UKRAINE
UNITED ARAB EMIRATES
UNITED KINGDOM OF GREAT BRITAIN AND NORTHERN IRELAND
UNITED REPUBLIC OF TANZANIA
UNITED STATES OF AMERICA
URUGUAY
UZBEKISTAN
VANUATU
VENEZUELA, BOLIVARIAN REPUBLIC OF
VIET NAM
YEMEN
ZAMBIA
ZIMBABWE

The Agency's Statute was approved on 23 October 1956 by the Conference on the Statute of the IAEA held at United Nations Headquarters, New York; it entered into force on 29 July 1957. The Headquarters of the Agency are situated in Vienna. Its principal objective is "to accelerate and enlarge the contribution of atomic energy to peace, health and prosperity throughout the world''.

The Metallurgy of Zirconium

C.E. Coleman

Volume 1

INTERNATIONAL ATOMIC ENERGY AGENCY
VIENNA, 2022

Marketing and Sales Unit, Publishing Section
International Atomic Energy Agency
Vienna International Centre PO Box 100
1400 Vienna, Austria
fax: +43 1 26007 22529
tel.: +43 1 2600 22417
email: sales.publications@iaea.org
www.iaea.org/publications

Printed by the IAEA in Austria
November 2022
STI/PUB/1943

IAEA Library Cataloguing in Publication Data

Names: International Atomic Energy Agency.
Title: The metallurgy of zirconium / International Atomic Energy Agency.
Description: Vienna : International Atomic Energy Agency, 2022. | Includes bibliographical references.
Identifiers: IAEAL 22-01496 | ISBN 978-92-0-109221-2 (paperback : alk. paper) |
ISBN 978-92-0-109321-9 (pdf) | ISBN 978-92-0-109421-6 (epub)
Subjects: LCSH: Zirconium — Metallurgy. | Zirconium — Properties. | Zirconium — Ductility. | Zirconium alloys.
Classification: UDC 661.883.1 | STI/PUB/1943

FOREWORD

The future of the nuclear industry worldwide depends primarily on the ability of the nuclear community to further improve our understanding of the materials used in the industry. Material science and metallurgy play an important role in reactor performance and safety.

This is the first time in nearly five decades that the International Atomic Energy Agency has gathered and updated information on the scientific and technological application of zirconium in the nuclear industry. The IAEA initiated a comprehensive project on The Metallurgy of Zirconium in 2005, at the request of Member States through the Technical Working Group on Fuel Performance and Technology.

For the greatest convenience of the users of this publication, it has been divided into three volumes. Chapters on fabrication are contained in Volume 1, chapters on the important properties of zirconium relating to its use in nuclear reactors in Volume 2, and information on ductility and fracture is presented in Volume 3.

The contributors to drafting and review were drawn from several countries — Canada, France, Germany, India, the Russian Federation, the United Kingdom and the United States of America. Each chapter was assigned to a leading expert in the field. The publication aims to provide the nuclear industry with a picture of the overall state of development and understanding of zirconium over the years. The first drafts were reviewed by five to seven reviewers, and contributions and appendices from additional authors were added to round out the perspective.

The IAEA wishes to express its gratitude to all the experts who contributed to this publication. Particularly, the IAEA appreciates the support of the main authors of the chapters and C.E. Coleman (Canada), who guided this project to its completion.

The IAEA officer responsible for this publication was M. Veshchunov of the Division of Nuclear Fuel Cycle and Waste Technology.

CONTENTS

Chapter 1

INTRODUCTION

C.E. COLEMAN
Chalk River Laboratories,
Atomic Energy of Canada Limited, Ontario, Canada

1.1. BACKGROUND

Commercial nuclear power is based on the fission of the isotope ^{235}U. In natural ores this isotope constitutes about 0.72% of uranium atoms. The nuclear fission of ^{235}U releases a substantial amount of energy, fast neutrons and new atoms, which are called fission products. In many power reactors, nuclear energy is captured and transported by water as heat and converted to steam to drive turbines to produce electricity. To sustain the nuclear chain reaction, the neutrons must be available for further fission. The efficiency of the fission process is increased by a factor of about 250 if the initial neutron energy of the fast neutrons, averaging about 1 MeV, is reduced to 0.025 eV. This process is called moderation. At this stage the neutrons are called slow or thermal neutrons. To maintain efficiency and minimize the loss of thermal neutrons, structural materials should absorb as few neutrons as possible; in components, the cross-section for the capture of thermal neutrons should be low in both the basic metal and its alloying elements. Zirconium is an example of a suitable basic metal for this application.

Zirconium was first mentioned and named in the scientific literature in 1789 when Klaproth discovered it while analysing the composition of the mineral jargon and could not match it with known elements. In 1824, Berzelius isolated the metal, but a century passed before Van Arkel and De Boer first produced ductile material. Zirconium remained a laboratory curiosity until its true low capture cross-section for thermal neutrons was demonstrated when it was separated from coincidental hafnium (which has a high capture cross-section for thermal neutrons) and Kroll developed a process for producing large amounts of metallic zirconium on an industrial scale, based on his successful process for extracting titanium. Some other metals have lower capture cross-sections for thermal neutrons and other metals and their alloys have greater strength than that of zirconium. When these properties are combined, the choice of zirconium as the base for structural alloys for nuclear applications becomes clear. Table 1.1. shows the relative cross-sections per unit of strength at 573 K (300°C) of alloys of selected metals and thereby demonstrates zirconium's superiority for use in fission nuclear reactors. Tool steels and high strength nickel and titanium alloys have large capture cross-sections while standard aluminium and magnesium alloys have low strengths at 573 K (300°C) because they would be operating at over half the melting point of the pure metal. Beryllium, although attractive because of its low capture cross-section, has severe problems with brittleness and toxicity.

With its good corrosion resistance in hot water and reasonable mechanical properties, zirconium had become by the mid-1950s the metal of choice for protecting nuclear fuel and providing structural support in reactors using water to transport the heat. The maturity of these developments was such that in 1953 a symposium organized by the American Society for Metals was devoted solely to zirconium [1.1]. Miller [1.2] published a monograph summarizing the occurrence, extraction and properties of zirconium, and Lustman and Kerze [1.3] edited a compilation of the work leading to the metal's nuclear uses. In 1964 Douglass first reviewed the physical metallurgy of zirconium and extended this review in 1971 [1.4]. The current publication is intended to further extend this review with more recent data, but for completeness is also a source book for basic information.

TABLE 1.1. COMPARISON OF NEUTRON ECONOMY OF ALLOYS OF COMMON METALS BASED ON STRENGTH

Base metal	Typical alloy	Cross-section for thermal neutrons, for typical alloy (b)	UTS* at 573 K (300°C) for typical alloy (MPa)	Relative cross-section for same design stress	Melting point (K (°C))	573 K (300°C) as homologous temperature
Zirconium	Zr-2.5Nb	0.009	570	1.0	1852 (2125)	0.270
Iron	H11 mod	0.215	1840	7.4	1535 (1808)	0.317
Nickel	Monel K-500	0.369	1000	23.4	1453 (1726)	0.332
Titanium	$Ti_6Al_2Sn_4Zr_2Mo$	0.302	1000	19.1	1660 (1933)	0.296
Aluminium	5154	0.023	80	18.2	660 (933)	0.614
Magnesium	AZ80A	0.0035	75	3.0	649 (922)	0.621
Beryllium	Unalloyed metal	0.001	300	0.21	1278 (1551)	0.369

* Ultimate tensile strength.

Although zirconium is now finding a wide application in the chemical industry and for prosthetics, the largest usage worldwide is in the nuclear industry. The use of zirconium in a nuclear reactor is challenging because its components have to withstand corrosion in water with hydrogen pick-up; multi-axial stresses at high temperatures, often with a temperature gradient; and bombardment with fast neutrons. The crystal structure of common alloys is hexagonal close packed at normal reactor operating temperatures. Most fabrication processes generate a strong crystallographic texture and therefore anisotropy has to be accommodated. Although research and development have added knowledge, since 1970 some of the most important information has been gained from post-irradiation examination of components that have been in service in power reactors. New phenomena have been observed, for example:

— High fluence irradiation has induced shape changes without external stress (called irradiation growth), new phase transformations and new configurations of dislocations.
— Fuel cladding has cracked during power ramps.
— Delayed cracking associated with hydrogen has been implicated in the failures of several types of components.

Failures have led to improvements in design, fabrication and operation. Higher demands on quality and reliability have led to tighter specifications than in the past, requiring improved design, fabrication and alloying. Economic pressures for long duty cycles and higher operating powers and temperatures are pushing the limits of current alloys. Unlike zirconium's sister metal, titanium, alloy development is limited because of constraints on the capture cross-section for thermal neutrons, thus developments over the past 40 years have tended to be small variations based on dilute tin or niobium alloys.

The other big change that has transformed scientific and technological advances since the last major review is the ubiquity of computers. They have been applied in all areas of technology, for example:

— They assist in the control of fabrication so that specifications can be tightened.
— A whole range of analytical tools is now available to investigate microchemistry and microstructure.

- The control and analysis of in situ experiments has been much enhanced so that results and statistics have greater reliability.
- Theoretical calculations, especially finite element analysis and iterations, are readily accomplished.
- The communication and publication of results and ideas are much more rapid and accessible.

To date, the nuclear industry has been very forthcoming in exchanging information. Various national nuclear societies hold regular meetings on nuclear fuel while several specialist conferences on alloys, phase transformations, irradiation, deformation and fracture have included much information on zirconium.

To set the scene, a summary of the basic features of the major designs of nuclear reactors provides the background for the environment that the zirconium alloy components have to withstand. A nuclear reactor produces and controls the release of energy from splitting the atoms of a fissionable element, usually uranium. In a power reactor, the energy released is used as heat to make steam to drive turbines that generate electricity. In a research reactor, the main purpose is to use the production of neutrons for experiments or as a test bed for new components. Nuclear reactors in ships produce steam that drives a turbine directly for propulsion.

There are several types of components common to reactors that involve the use of water:

- Fuel: Pellets of uranium oxide (UO_2) are protected by tubes made from a zirconium alloy to form fuel rods or elements. The rods are arranged into fuel assemblies or bundles in the reactor core. Mixed oxide (MOX) fuel based on both uranium and plutonium is being used in some reactors and is increasingly considered as an option.
- Moderator: This material slows down the fast neutrons released from fission to improve the efficiency of further fission. The moderator can be light water, heavy water or graphite. Light water is more effective than heavy water in slowing neutrons, but it has a higher neutron absorption cross-section. The resulting moderating ratio (slowing power / capture cross-section) is nearly 90 times greater for heavy water than for light water. Graphite has an intermediate moderating ratio that is 2.5 times greater than that of light water.
- Control rods: These components are made with neutron absorbing material such as cadmium, hafnium or boron, and are inserted or withdrawn from the core to control the rate of the reaction or to halt it. Secondary systems involve adding other neutron absorbers to the system, usually as a fluid, to aid fine control or to initiate shutdown.
- Heat-transfer medium (or coolant): Water is circulated through the core to extract the heat.
- Pressure vessel: Either a thick steel vessel contains the reactor core and moderator, or a series of tubes made from a zirconium alloy, penetrating the moderator, hold the fuel and heat transport water.
- Steam generator: The part of the heat transport system where the heat from the reactor is used to make steam for the turbine.
- Containment: The structure around the reactor core that is designed to protect it from outside intrusion and to protect those outside from the effects of ionizing radiation or any malfunction inside. It is typically a concrete and steel structure that is one metre thick.

The various types of reactors use these components differently. When heavy water or graphite is used as the moderator, the fuel may be natural uranium. Natural uranium has the same isotopic composition as when its ore is mined (0.7% ^{235}U, 99.3% ^{238}U). When the moderator is ordinary water, to reach criticality the ^{235}U isotope has to be enriched, with an upper limit set at 5%; such reactors are called light water reactors.

Reactors using pressure vessels need to be shut down for refuelling. Refuelling is done at intervals of 1–2 years, when between a quarter and a third of the fuel assemblies are replaced with fresh ones. Designs that use pressure tubes can be refuelled on-power by disconnecting individual fuel channels from the heat transport system.

1.2. OBJECTIVE

The objective of this publication is to summarize practical experience and the current understanding of phenomena, properties and the development and application of zirconium in the industry,

1.3. SCOPE

1.3.1. Pressurized water reactors

Pressurized water reactors (PWRs) are the most common type of power reactor, with over 200 having been built throughout the world. The design originated in the United States of America in the 1940s as a submarine power plant. The water cooled water moderated power reactor (WWER) is a type of PWR. PWRs use ordinary water for both moderator and heat transport. The design comprises a primary heat transport circuit in which water flows through the core of the reactor under high pressure and a secondary circuit in which steam is generated to drive the turbine. The main features of a PWR are depicted schematically in Fig. 1.1.

A PWR has fuel assemblies of over 200 rods, each about 3.5 m in length, arranged vertically in the core in an open lattice; a large reactor would contain about 150–250 fuel assemblies. The outer surface temperature of the fuel cladding may be about C 623 K (350°) and to ensure the water remains liquid in the reactor core the required pressure is about 15 MPa.

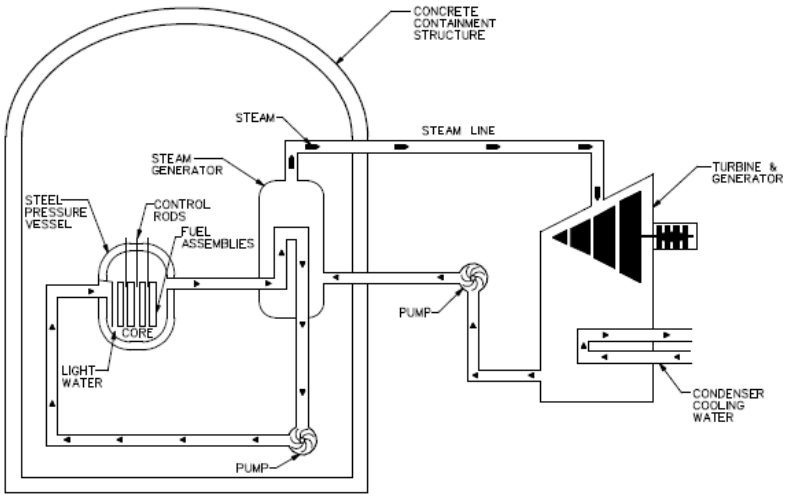

FIG. 1.1. Schematic diagram of a PWR.

1.3.2. Boiling water reactor

The boiling water reactor (BWR) design, although similar to the PWR, contains a single circuit in which the light water is at a pressure of about 7 MPa so that it boils in the core at about 558 K (285°C). The reactor operates with 12–15% of the water in the top part of the core as steam, with subsequent reduced moderating and lower efficiency in this location. The steam passes through steam separators above the core and then directly to the turbines, which are thus part of the reactor circuit. A BWR fuel assembly comprises up to 80 fuel rods, and there are up to 750 assemblies in a reactor core. The main features of a BWR are depicted schematically in Fig. 1.2.

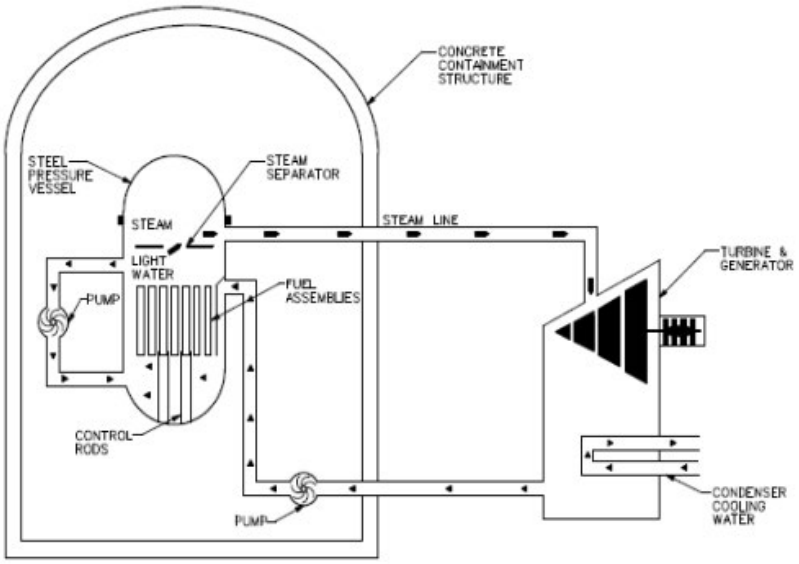

FIG. 1.2. Schematic diagram of a BWR.

1.3.3. Pressurized heavy water reactor

Pressurized heavy water reactors (PHWRs) use heavy water as the coolant and neutron moderator, and may use either natural uranium or very low enriched uranium as fuel, with the latter being much less common. The Canada deuterium uranium (CANDU) reactor is a PHWR that originated in Canada in the 1950s. The fuel is natural uranium and the moderator and heat transport fluid are heavy water. The moderator is held at about 343 K (70°C) in a large tank, called a calandria, penetrated horizontally by up to 480 pairs of concentric tubes forming the fuel channels. The inner tube of the fuel channel, the zirconium alloy pressure tube, is about 6 m long and contains up to 13 fuel bundles and the heat transport fluid, while the outer tube, the zirconium alloy calandria tube, is separated from the hot pressure tube by spacers in the form of garter springs. The calandria tube isolates the hot pressure tube from the cool moderator, insulation being provided by filling the annular space between the two tubes with dry CO_2 at atmospheric pressure. The 500 mm long fuel bundle comprises a number of elements, up to 43. Heat transport is by a flow of heavy water under a pressure up to about 11 MPa with exit temperatures of about 583 K (310°C). As in the PWR, the primary coolant generates steam in a secondary circuit to drive the turbines. The main features of a PHWR are depicted schematically in Fig. 1.3.

Two designs with a direct steam cycle (like a BWR) using pressure tubes in a vertical configuration are the Steam Generating Heavy Water Reactor in the United Kingdom and Fugen in Japan. Heat transport is by light water, and Fugen used MOX fuel. Both reactors have now been retired but they provided valuable technical information from component surveillance.

1.3.4. Light water graphite-moderated reactor

The high-power channel-type reactor, which is abbreviated RBMK for its Russian name reactor bolshoy moshchnosti kanalnyy, was designed in what is now the Russian Federation. It is shown schematically in Fig. 1.4. It is a BWR with over 1600 individual vertical fuel channels, each 8 m long, made from a zirconium alloy. As in a BWR, the heat transport light water is allowed to boil in the core at about 563 K (290°C), because the operating pressure is 7 MPa, and the steam is fed directly into the turbines. The moderator is graphite. The fuel is low enriched uranium oxide, clad in zirconium alloy tubes, made into fuel rods. A set of 18 fuel rods is arranged cylindrically in a carriage to form a fuel assembly 3.5 m long. Two assemblies end-to-end occupy each pressure tube.

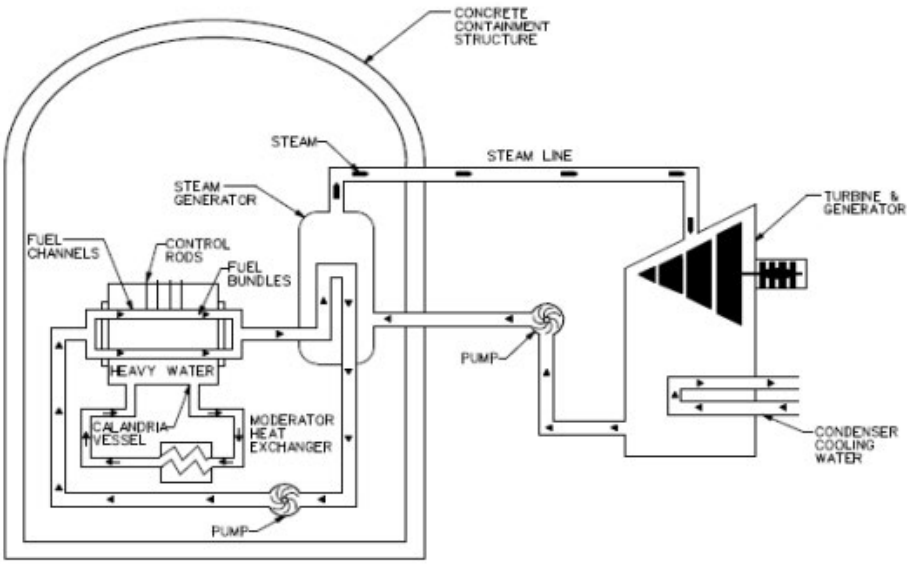

FIG. 1.3. Schematic diagram of a PHWR.

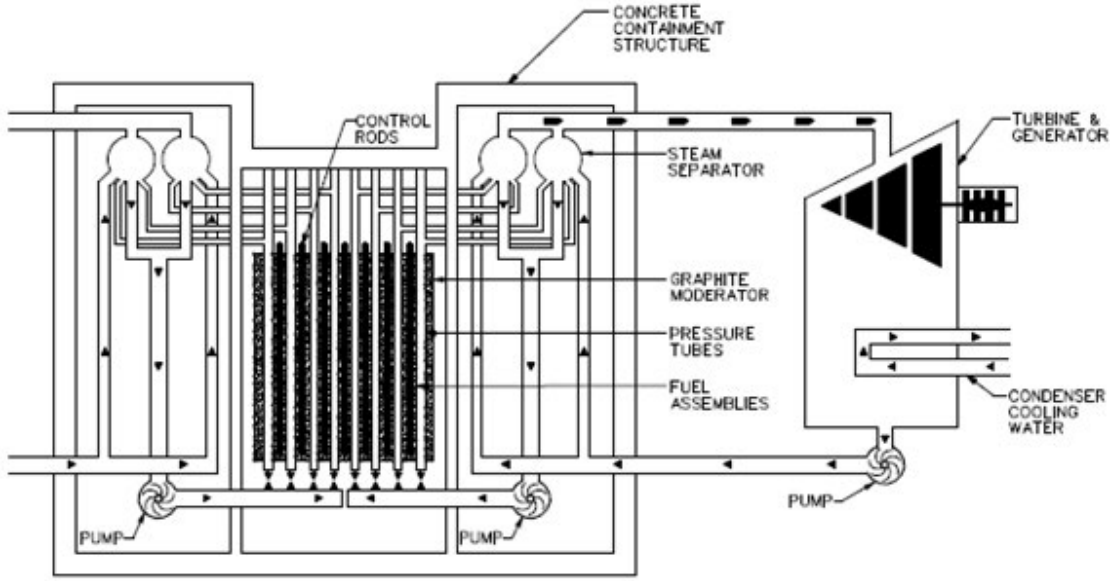

FIG. 1.4. Schematic diagram of a RBMK reactor.

In the USA, the N-Reactor contained horizontal fuel channels that passed through a graphite moderator. The heat transport was by light water. This reactor was retired after a safety evaluation prompted by the Chernobyl accident.

Tables 1.2 and 1.3 summarize typical conditions experienced by zirconium alloy components in various reactors. Much valuable information has been obtained by in situ measurements and from examinations of components both after satisfactory service and after failure. The development of the ability to meet design requirements without failure in these harsh environments and to meet future challenges is the subject of this publication.

1.3.5. Structure

For the greatest convenience of the users of this publication, it has been divided into three volumes. Chapters on fabrication are contained in Volume 1, chapters on the important properties of zirconium relating to its use in nuclear reactors in Volume 2, and information on ductility and fracture in Volume 3.

In Chapter 2, alloy development is summarized. Chapter 3 describes the extraction and consolidation of zirconium. The main features of fabrication, including the formation of crystallographic texture, are outlined in Chapter 4. The consequences of service in a nuclear reactor are then described in Chapter 5, including the production of irradiation damage, in-reactor deformation and corrosion and hydrogen pick-up. Experience with cracking and its mitigation is also discussed.

In Volume 2, a detailed overview of the effects of irradiation on zirconium alloys is provided, including the evolution of the microstructure and subsequent change in properties under various irradiation fluxes obtained in power reactors. In Volume 3, the ductility and fracture of zirconium alloy components during service in a nuclear reactor are described.

TABLE 1.2. DESIGN AND OPERATING DETAILS OF DIFFERENT TYPES OF NUCLEAR FUEL

		PWR	WWER	BWR	CANDU	RBMK
Fuel		UO_2 Enriched 2.25–5.0%, sometimes contains burnable absorbers, e.g. gadolinia, erbia	UO_2 Enriched 3.0–5.0%.	UO_2 Enriched 1.7–5.0%, sometimes contains gadolinia	UO_2 Natural	UO_2 Enriched 1.8–2.6%, sometimes contains erbia
Rods/assembly		176–300	126–312	64–100	28–43	18
Geometry		(14 × 14)–(18 × 18) array	Hexagonal	(8 × 8)–(10 × 10) array	Rings	Rings
Cladding		Zircaloy-4 ZIRLO Zr-1Nb (M5)	Zr-1Nb (E110) E635 Zircaloy-4	Zircaloy-2	Zircaloy-4	Zr-1Nb (E110) E635
Typical dimensions:	Length (m)	3.7–4.4	2.5–3.9	3.8–4.2	0.5	3.5
	Outside diameter (mm)	9.5–11.2	9.1	10.8–12.5	11.5–15.2	13.6
	Wall thickness (mm)	0.6–0.7	0.58–0.65	0.6–0.75	0.4	0.8–0.9
Internal gas		He	Ar and He	He	He	Ar and He
Heat-transport fluid		H_2O	H_2O	H_2O + steam	D_2O	H_2O + steam
Maximum pressure (MPa)		15.5	15.5	7	11	8.2
Maximum clad temp. (K (°C))		350 (623)	350 (623)	320 (593)	330 (603)	325 (598)
Chemistry (pH)		>6.9–7.49(*)	5.7–10.2	5.5*	10.5**	6.5–8
O_2 (ppm)		<1	≤5	300	<10	<20
H_2 (ppm)		3	2.7–5.4	0.003	0.5–1.8	0
B (ppm)		0–1500	0–2160			
Li (ppm)		2	(K+Li+Na) 0.05–0.45 m·mol·L^{-1}	0	0.35–1.4	0
NH_3 (ppm)		0	>5.0	0	0	0
Fast neutron flux (E>1 MeV) × 10^{17} (n·m^{-2}·s^{-1})		3.0	7.0	3.0	8.0	2.4

* At operating temperature.

** D_2O sample measured at 298 K (25°C) with H_2O pH electrode.

TABLE 1.3. DESIGN AND OPERATING DETAILS FOR PRESSURE TUBE REACTORS

	CANDU	Fugen (shut down in 2003)	Steam generating heavy water reactor (retired in 1990)	RBMK	N-reactor (shut down in 1987)
Moderator	Heavy water	Heavy water	Heavy water	Graphite	Graphite
Number of fuel channels	380–480	224	112	1661	1003
Configuration	Horizontal	Vertical	Vertical	Vertical	Horizontal
Material of pressure tube	CW* Zr-2.5Nb (CW Zircaloy-2 in early reactors, heat-treated Zr-2.5Nb in Karachi Nuclear Power Plant)	Heat treated Zr-2.5Nb	CW Zircaloy-2 (Few tubes of Zircaloy-4 and Zr- 2.5Nb)	RBMK 1000 Annealed Zr-2.5Nb RBMK 1500 Quenched and aged Zr-2.5Nb	CW Zircaloy-2
Dimensions: Length (m)	6.0	4.7	4.6	8.0	16.1 (10.6 fuelled section)
Dimensions: Inside diameter (mm)	103	118	130	79.5	68.8
Dimensions: Wall thickness (mm)	4	4.3	5	4.0	6.8
Heat-transport fluid	Heavy water	Light water	Light water	Light water	Light water
Chemistry of heat transport fluid	pH 10.5*** with LiOH	pH 5.5–8.5	pH 7.0	pH 6.5–8.0	pH 9.5–10.4+ with NH4
Maximum pressure (MPa)**	11	7	6.8	8.2	10.7
Maximum temperature [K (°C)]**	295–312 (568–585)	285 (558)	282 (555)	288 (561) (Through-wall temperature gradient 35°C, hotter on outside)	282 (555) (Temperature gradients: azimuthal 17°C, through-wall 25°C hotter on outside)
Max. fast neutron flux (E>1 MeV) × 10^{17} (n·m^{-2}·s^{-1})**	3.7	3.0	2.6	1.2–2.0	2.5
External environment	CO_2	CO_2	CO_2	90% He / 10% N	Moist He
Fuel assemblies/channels	12 or 13	1	1	2	14

* Maxima not in same location in fuel channel.
** D_2O sample measured at 298 K (25°C) with H_2O pH electrode.
\+ At room temperature.
Note: CW — cold worked.

REFERENCES TO CHAPTER 1

[1.1] AMERICAN SOCIETY FOR METALS, Zirconium and Zirconium Alloys: A Symposium, Proc. Symp. Los Angeles, 1953, American Society for Metals, Cleveland, OH (1953).
[1.2] MILLER, G.L., Zirconium, 2nd edn, Butterworths Scientific Publications, London (1957).
[1.3] LUSTMAN, B., KERZE, F. (Eds), The Metallurgy of Zirconium, McGraw-Hill, New York (1955).
[1.4] DOUGLASS, D.L., The Metallurgy of Zirconium, Atom. Energy Rev. **3** 1 (1971) 1–464.

Chapter 2

ALLOY DEVELOPMENT

A.V. NIKULINA†
Bochvar Research Institute of Inorganic Materials,
Moscow, Russian Federation

C. TOFFOLON-MASCLET
Atomic Energy and Alternative Energies Commission,
Gif-sur-Yvette, France

C.E. COLEMAN
Chalk River Laboratories,
Atomic Energy of Canada Limited, Ontario, Canada

2.1. INTRODUCTION

Zirconium alloys have to meet many requirements to provide good service in the conditions that components experience during operation in thermal reactors that use water for heat transport, as described in Chapter 1. The key property of structural materials for fission reactors is their capture cross-section for thermal neutrons; it should be as low as possible to maintain the nuclear chain reaction. The cross-section represents the probability of a reaction between the atomic nucleus of the metal and the impinging particle and has the dimensions of area. The cross-section for a single nucleus is the microscopic cross-section, σ. Since the heavy nuclei have diameters of about 10^{-14} m, it is not surprising that σ for many elements is about 10^{-28} m^2. This number is equal to one 'barn' or 'b'. The macroscopic cross-section, Σ, represents the cross-section of all the nuclei, N, in a standard volume, N m^{-3}; it has the dimensions of a reciprocal length because Σ is equal to σN m^2·m^{-3}. For an element:

$$\Sigma = \sigma \rho N_0 / A \tag{2.1}$$

where
ρ is the mass density of the element;
A is the relative atomic mass;

and N_0 is the Avogadro number.

For an alloy, Σ must be summed for the number of atoms of each element present.

Apart from a low capture cross-section for thermal neutrons, the main requirements are a high corrosion resistance to hot water, great geometrical stability and crack resistance, and that these are all achieved at a reasonable cost. Studying the influence on properties of alloying elements on zirconium through phase diagrams and the effect of microstructure and phase composition has helped the designers to meet these requirements.

Zirconium alloys were developed for use in nuclear reactors by the collective efforts of many scientists in a number of countries. Experimental procedures were developed, including testing in-reactor, and mechanisms that influenced the properties of zirconium alloys were elucidated. The results of these investigations were needed to forecast and improve the in-

reactor service life of components. These methods and the results they obtained formed the foundation for the development and evolution of zirconium alloys. The process is continuing.

2.2. HISTORY OF ALLOY DEVELOPMENT

In the 1940s, at the conceptual stage of thermal reactor development, zirconium did not look promising as a structural material; it was expensive, very little was available and it appeared to have a high σ value of about 6.8 b [2.1]. These measurements also indicated that hafnium had a very high value of σ [2.2]. The small amounts of hafnium that are usually associated with zirconium ores were thought to contribute to its apparent value of σ. Once hafnium could be much reduced, the true value of σ of about 0.18 b was revealed [2.3]; a value of σ of 1.52 b for the isotope ^{91}Zr, which makes up 11.2% of the natural isotopes, contributes most of the value of σ for the element [2.4].

Small quantities of very pure zirconium were made by the van Arkel–de Boer iodide process to make costly 'crystal bar' zirconium. In the United States of America, during the late 1940s and early 1950s, once the useful properties of zirconium for use in the nuclear field had been established, methods of extraction and refinement based on the Kroll process for titanium were developed to produce 'sponge' zirconium. Although sponge zirconium was less pure than crystal bar, the price was reduced by a factor of about 50 and the quantities of metal available for components were increased from a few kilograms to several hundred megagrams. The resulting metal could be formed into various shapes suitable for components and the mechanical properties were acceptable. Later, in what is now the Russian Federation, similar production was in progress by developing the molten salt electrolysis process to make zirconium powder. These processes of refining and forming are described in Chapters 3 and 4.

Unalloyed zirconium exhibited variable corrosion behaviour in water and steam, which stemmed from uncontrolled variations in the concentration of impurities. Zirconium of high purity is corrosion resistant in high temperature water. Impurities such as nitrogen, carbon and aluminium, even in low quantities, degrade the corrosion resistance of zirconium as shown in Figs 2.1 and 2.2 [2.5, 2.6]; see Section 2.7.

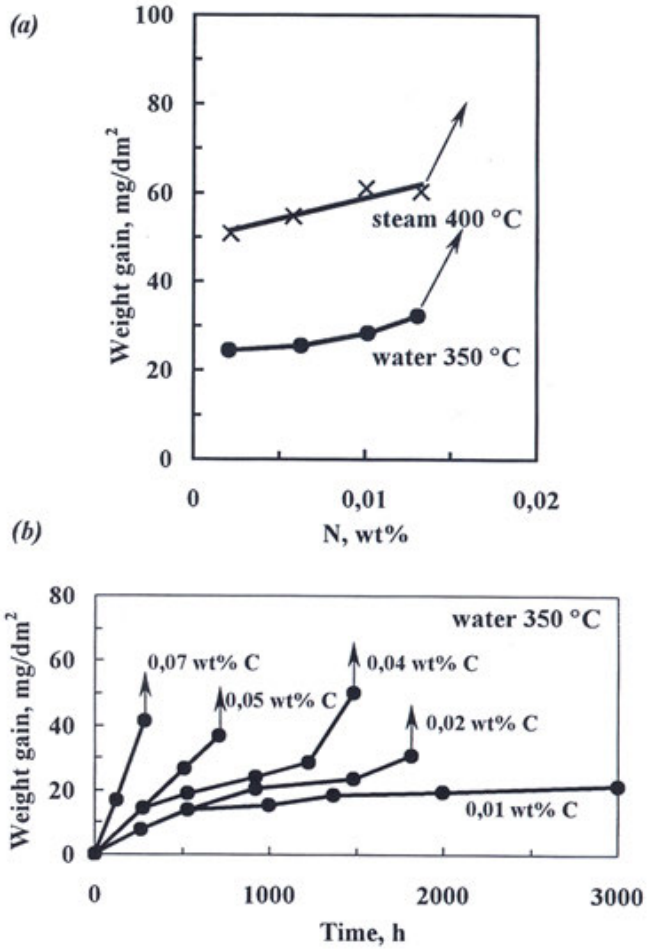

FIG. 2.1. Influence of (a) nitrogen and (b) carbon concentration on the corrosion of zirconium in water and steam [2.5, 2.6].

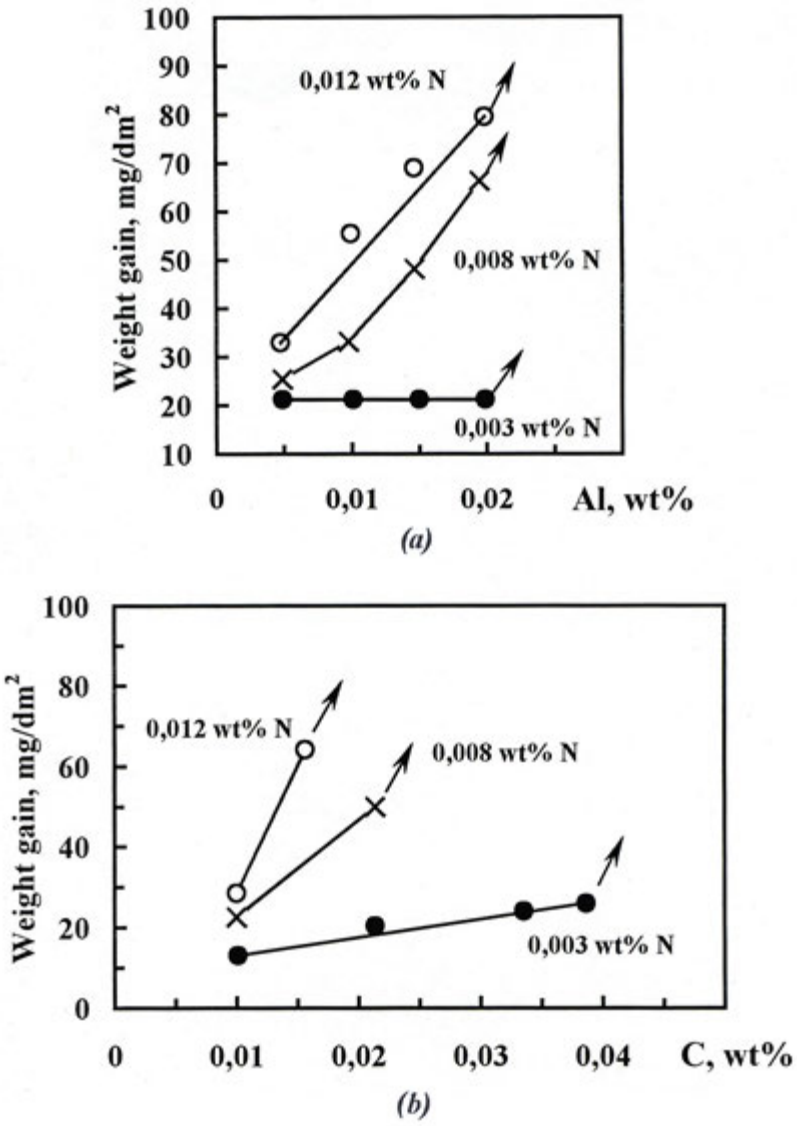

FIG. 2.2. The joint influence of nitrogen, carbon and aluminium impurities on the corrosion of zirconium in water (623 K (350°C), 17 MPa) [2.5, 2.6]: dependence of weight gain on concentration of a) aluminium, and b) carbon, for different concentrations of nitrogen.

The early alloying efforts were focused on maintaining good nuclear properties and ameliorating the deleterious effects of impurities on corrosion resistance. Although tin reduced the corrosion resistance of crystal bar zirconium, it was found to be beneficial for sponge zirconium, overcoming the harmful effects of the impurities. Initially an alloy of 2.5 wt% Sn based on sponge zirconium was recommended. It was called Zircaloy-1. However, its long term corrosion properties were unsatisfactory, and it was abandoned. Tin in the range of 0.5–1.5 wt% introduced into sponge zirconium still improved the corrosion resistance of zirconium and an optimal concentration of tin in the alloy was found that depended on the impurity concentration, specifically, on the concentration of nitrogen (Table 2.1, Fig. 2.3) [2.7, 2.8].

TABLE 2.1. TIN CONCENTRATION NEEDED TO COMPLETELY NEUTRALIZE THE EFFECTS OF DIFFERENT NITROGEN CONCENTRATIONS [2.7, 2.8]

Concentration of tin (wt%)	Concentration of nitrogen (ppm)
0.5	200
1.0	300
2.0	600
2.5	700
3.0	800

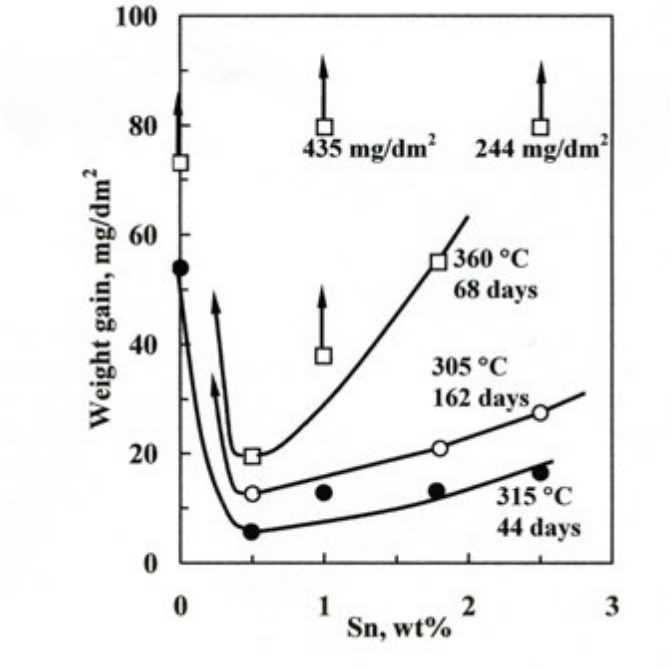

FIG. 2.3. The influence of tin on the corrosion resistance of sponge zirconium in water [2.7, 2.8].

By chance, an ingot was contaminated with stainless steel but showed good corrosion resistance imparted by the additions of iron, nickel and chromium. Purposely adding Fe, Ni and Cr in the quantity of about 0.25 wt% to binary Zr-Sn alloys appreciably increased their corrosion resistance. Additions of Fe and Ni appeared to be more effective than Cr (Fig. 2.4) [2.7, 2.8].

The efficiency of other elements added to binary Zr-Sn alloys to increase corrosion resistance was much lower than Fe, Ni or Cr. This discovery led to the composition of Zircaloy-2. The patent for the alloy [2.9] includes a wide range of compositions but indicates that a suitable alloy contained 1.3–1.6 wt% Sn, 0.09–0.16 wt% Fe, 0.07–0.12 wt% Cr and 0.04–0.08 wt% Ni. The early development of zirconium production and the alloys used as fuel cladding in nuclear submarines were detailed in Ref. [2.10].

Formal presentations of these first results obtained in what is now the Russian Federation and the USA were made at the international conferences on Peaceful Uses of Atomic Energy (Geneva, Switzerland) in 1955 and 1958 [2.8, 2.11–2.16] and at a USAEC-EURATOM symposium (Pleasanton, CA, USA) in 1962 [2.17].

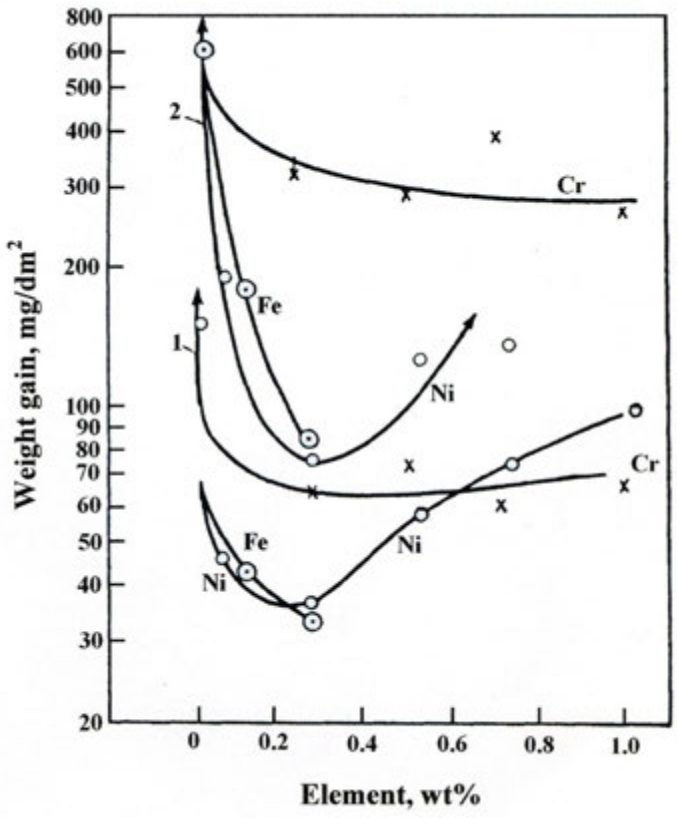

FIG. 2.4. Corrosion in ternary Zr-1.8 % Sn alloy containing Fe, Ni or Cr (the curves marked '2' at the top of the figure indicate steam 673 K (400°C), 10.5 MPa, 68 days; the curves marked '1' at the bottom indicate water 633 K (360°C), 84 days) [2.7, 2.8].

With experience, purity and uniformity gradually improved in the commercial production of zirconium and the need for costly processes for extraction, for example, to obtain crystal bar zirconium, and the need for alloying elements to neutralize the deleterious effects of some impurities could be relaxed. Long term corrosion resistance of tin alloys in some water conditions was found to be inadequate leading to the suggestion that the tin concentration should be lowered while the iron concentration should be increased. The result was Zircaloy-3 containing 0.25 wt% Sn and 0.25 wt% Fe. This alloy did have good corrosion resistance but had low strength, so it too was abandoned.

Hydrogen can be very deleterious to the fracture resistance of zirconium (Chapter 9, Volume 3 of this publication). Hydrogen ingress was promoted by nickel. Zircaloy-2 without Ni was found to have poor corrosion resistance but an alloy with little Ni and increased Fe (to 0.24 wt%) had adequate corrosion resistance and half the hydrogen pick-up (HPU) of Zircaloy-2. This alloy was called Zircaloy-4.

As power reactors, notably the BWR and the pressurized water reactors (PWRs), evolved in the USA, an international effort in studying and improving zirconium alloys commenced. For example, Syre [2.18] and Pickman [2.19] described the European contribution; the development of nuclear power in these countries was of strategic importance because they did not have major oil resources.

Another development in Zircaloy was the fabrication of pressure tubes. The first pressure tube to operate in a reactor core was a loop tube in a research reactor in Canada [2.20]. Zircaloy-2 pressure tubes were specified for the Plutonium Recycling Test Reactor (USA) [2.21], the N-Reactor (USA) [2.22] and the Steam Generating Heavy Water Reactor

(United Kingdom) [2.23] and were also used in early CANDU reactors [2.24–2.26]. Pressure tubes made from Zircaloy-4 operated in the Carolina Virginia Test Reactor (USA) [2.27].

Water cooled water moderated power reactors (WWERs) and boiling water (RBMK) reactors that were under design in the then USSR in the 1950s gave an impetus to study potential zirconium alloys and set up the production of components [2.11]. In the then USSR, zirconium based alloys were originally developed using semicommercially produced pure iodide zirconium and later electrolytic zirconium, with the simultaneous set-up of its commercial production.

The results of the investigations by Ivanov and Grigorovich to study the influence of alloying elements on the tensile properties of zirconium revealed that almost all additives increase its strength and reduce its ductility, the strength becoming higher as the concentration of the alloying elements increases (see Fig. 2.5) [2.14]. The alloying elements Al, Nb, O, Sn and Ti were found to be solid solution strengtheners while Cr, Fe, and Mo, having a low terminal solid solubility in zirconium, formed intermetallic precipitates.

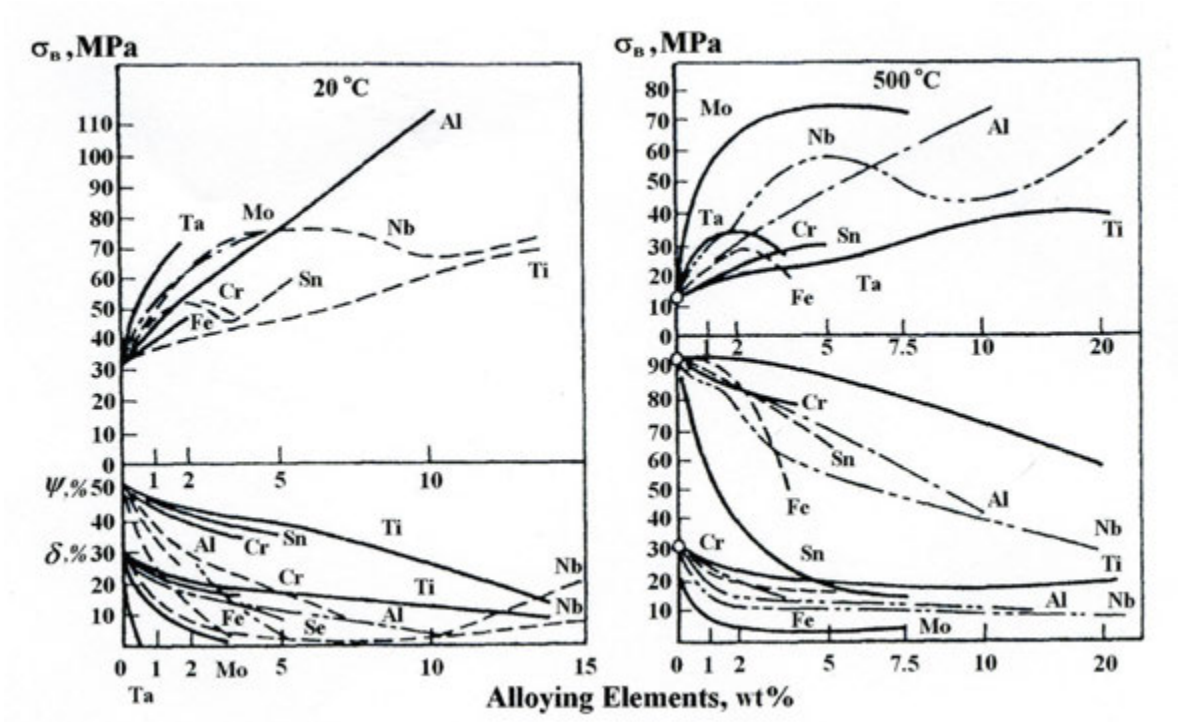

FIG. 2.5. Influence of alloying elements on tensile properties of zirconium [2.14]. σ_B — ultimate tensile strength; ψ — reduction in area; δ — elongation.

Aluminium and titanium when added even in small quantities adversely influenced the corrosion resistance (Table 2.2) [2.5, 2.6]. Less than 0.8 wt% Sn had little effect on the corrosion of iodide zirconium. With an increase of tin concentration, the corrosion of zirconium increased, particularly in steam at 673 K (400°C) and was accompanied by oxide spalling. These results at high temperatures agreed with results obtained in the USA. An addition of niobium also aggravated the corrosion of zirconium; in autoclaves, the resulting oxide was dense but did not spall (see Fig. 2.6) [2.5, 2.6, 2.11]. Of all the elements that were introduced into binary zirconium alloys, only iron added in a wide concentration range did not influence the corrosion of zirconium in water or steam. The uptake of hydrogen released during corrosion was dependent on the alloying element (see Fig. 2.7) [2.5, 2.7]. Niobium, chromium and iron containing Zr alloys showed the least uptake of hydrogen.

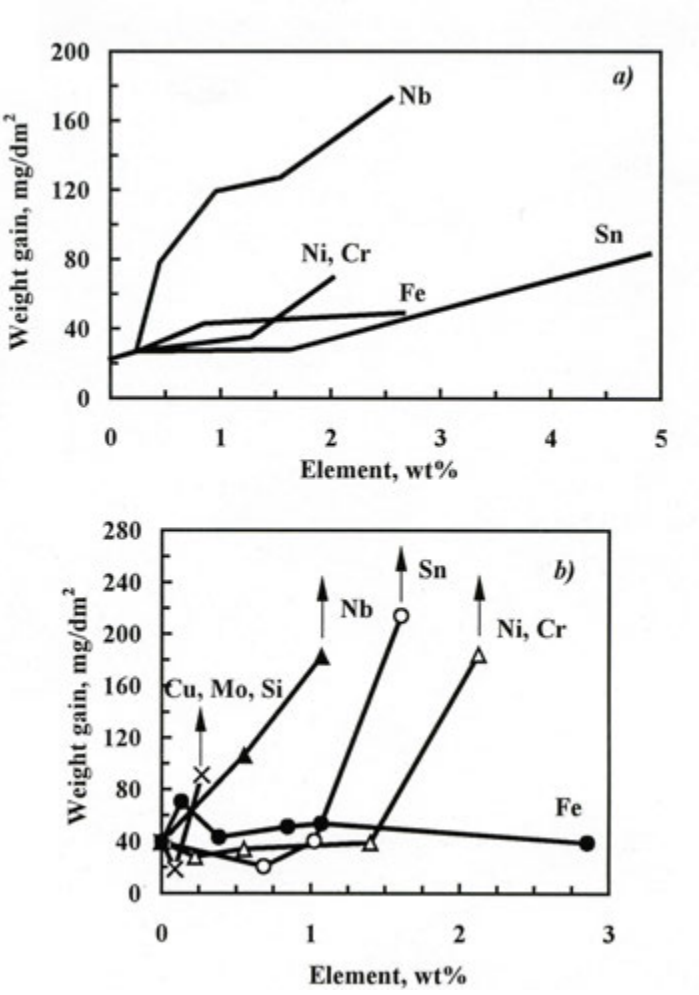

FIG. 2.6. Influence of alloying elements on iodide zirconium corrosion in water 623 K (350°C) (a) and steam 673 K (400°C) (b) for 3000 h [2.6].

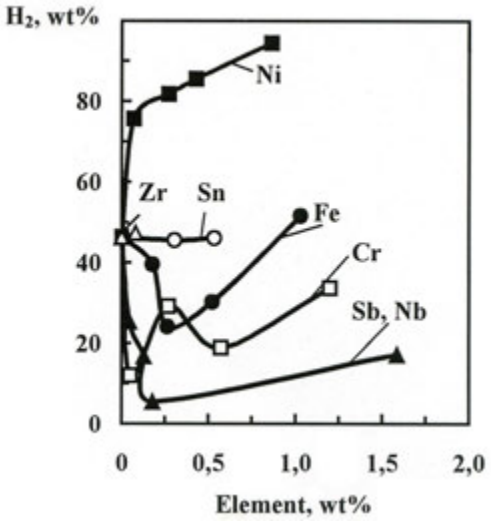

FIG. 2.7. Influence of alloying elements on hydrogen uptake by zirconium during corrosion in water 623 K (350°C) (% of theoretically possible value) [2.7].

TABLE 2.2. INFLUENCE OF TITANIUM AND ALUMINIUM ON ZIRCONIUM CORROSION IN WATER (623 K (350°C), 17 MPa, 1000 H) [2.5, 2.6].

Element	Concentration (wt%)	Weight gain (mg·dm^{-2})
Ti	0.0025	15.0
	0.0035	27.0
	0.010	30.0
	0.060	40.0
	0.11	500.0
	0.19	Oxide spalling
Al	0.005	18.0
	0.020	23.0
	0.050	400.0
	0.10	Oxide spalling

The results of the investigations to study the influence of impurities and alloying elements on the properties of iodide zirconium were used to choose alloys for the first WWER and RBMK nuclear reactors. Taking into account the requirements for the tensile and corrosion resistant properties of components, Ambartsumyan and colleagues recommended alloys containing 1.0 wt% niobium for fuel cladding and 2.5 wt% niobium for pressure tubes [2.11, 2.28–2.30]. These alloys were designated E110 and E125; they remain the basic commercial alloys for the WWER and RBMK cores.

In the 1960s, binary Zr-Nb alloys were also studied in the USA for application in BWRs. The results of corrosion tests on alloys containing up to 4.2 wt% Nb were shown to be sensitive to heat treatment and nitrogen contamination; results in a simulated BWR environment were disappointing and application of these alloys was not recommended for BWRs [2.31, 2.32]. Also in the 1960s, the Zr 2.5 wt% Nb alloy was studied in great detail in Canada [2.33, 2.34] and at the time of writing was used to fabricate pressure tubes for CANDU reactors, replacing Zircaloy-2. In France during the 1990s, a Zr 1.0 wt% Nb alloy M5 was developed for fuel cladding for PWRs [2.35, 2.36].

The results of investigations into the influence exerted by alloying elements and impurities on the properties of zirconium allowed scientists from what is now the Russian Federation to recommend an alloy containing niobium, tin and iron in the ranges of 1.0 wt% Nb, 1.0–1.3 wt% Sn and 0.3–0.5 wt% Fe for further studies and subsequent use [2.37, 2.38]. When creating a multicomponent alloy, the aim is to take advantage of the favourable effects that tin, niobium and iron each have on improving the corrosion resistance in water and steam:

— Niobium enhances resistance to hydrogenation during corrosion and to corrosion under irradiation.
— Tin stabilizes the corrosion resistance of zirconium by reducing its dependence on some deleterious impurities.
— Iron improves the corrosion resistance of zirconium by mitigating its dependence on the temperature of water or steam.

The multicomponent alloy created, which was designated E365, has the favourable properties inherent to the binary Zr-Nb and Zircaloy type alloys but has fewer of their limitations. The advantages of a multicomponent alloy having a composition close to that developed in the Russian Federation were corroborated by investigators from the USA in an alloy containing 1.0 wt% Sn, 1.0 wt% Nb, 0.1 wt% Fe; it was named ZIRLO [2.39–2.41]. The E635 and ZIRLO alloys are employed in the cores of WWERs and PWRs, respectively.

Castaldelli et al. suggested an alloy with a similar composition [2.42]. Other variations on this theme were under development at the time of writing.

In summary, once the true nuclear properties of zirconium were realized and production of large quantities of the metal was possible, alloy development aimed at maintaining the nuclear properties and improving corrosion resistance.

2.3. ZIRCONIUM ALLOYING GUIDELINES

Zirconium components are intended to operate in the core of thermal reactors that use water for heat transport and moderation, primarily PWRs, WWERs, boiling water reactors (BWRs), RBMKs and CANDU reactors. The design of the components, the water chemistry and mechanical loads the components have to withstand are quite different between reactor types but also within the same reactor design. Fuel cladding, seal plugs and spacer grids, guide and shroud tubes, pressure tubes, calandria tubes and sheaths to guide and protect instruments constitute the majority of the components. To operate successfully, the components must be carefully designed, the choice of zirconium alloy must be appropriate and its impurities properly controlled, and the fabrication of the components should be of the highest quality. Reactor operating conditions will determine the alloy and its microstructure, with the latter being controlled by thermomechanical treatments (TMTs) ranging from hot working to cold working and heat treatment.

Guidelines for a successful zirconium alloy for use in thermal reactors should include the following:

(1) Alloying elements should not substantially increase thermal neutron absorption; this condition limits the number of alloying elements for zirconium.
(2) An alloying element should not transmute to isotopes with high capture cross-sections or isotopes that adversely affect important properties, such as corrosion resistance. An alloying element should not contain isotopes that produce long lived radioactive species after irradiation (e.g. cobalt).
(3) Alloying should maintain or minimize the degradation of corrosion resistance of the material in water and steam and maintain or reduce its propensity for hydrogen uptake.
(4) Alloying and trace elements have to maintain or increase tensile strength and retain adequate ductility and resistance to cracking at reactor operating temperatures during neutron irradiation.
(5) Maintaining deformation resistance during irradiation is important, especially for structural components that are required to have lifetimes of several decades, for example, pressure tubes.
(6) The alloy must be amenable to processing and joining, including by welding. (Fabrication into components is described in Chapter 4.)
(7) The alloy should have a reasonable cost for the mass production of components.

Items 1 and 2 refer to all zirconium components that operate in thermal reactor cores. Items 3–6 are interrelated and have to be met during fabrication, and operation of components under fast neutron irradiation at high temperatures and in aggressive environments. Item 7 has to be included in estimates of the unit energy costs for the lifetime of the whole reactor.

Table 2.3 summarizes the effect on the capture cross-section for thermal neutrons, Σ, of zirconium with different alloying elements. These cross-sections are for the addition of 1 wt% of the element using Eq. (2.1); low values are required. ΔE indicates the effect on fuel

and is the quantity of alloying element allowed in cladding made from a binary zirconium alloy at which the fuel needs to be enriched 0.05 wt% ^{235}U to produce the same power as fuel clad with pure zirconium; high values are preferred. With a low neutron capture cross-section, O, Al, Mg, Pb, Si, Sn, Nb and Y are suitable as major alloying elements for zirconium while Hf, Cd, W and Co are immediately disqualified and must be minimized. Other elements with moderate cross-sections can be added in small quantities if they impart desirable properties, for example, Fe, Ni and Cr for corrosion resistance.

TABLE 2.3. THE INFLUENCE OF ALLOYING ELEMENTS ON THERMAL NEUTRON ABSORPTION BY ZIRCONIUM

Element	σ_a (barn)	Σ with 1 wt% alloying element ($cm^2 \cdot cm^{-3}$)	ΔE (wt%)
Zr	0.18	0.0079	—
Al	0.230	0.0081	17.0
Be	0.009	0.0073	100
Co	37	0.060	0.23
Cr	2.9	0.012	2.9
Cu	3.69	0.012	2.9
Fe	2.53	0.011	3.9
Ge	2.35	0.0090	5.2
Hf	105	0.032	0.29
Mg	0.063	0.0060	100
Mo	2.5	0.0094	6.3
Nb	1.1	0.0084	14.1
Ni	4.6	0.014	2.2
O	0.0002	0.0079	100
Pb	0.17	0.0071	100
Sb	5.5	0.0092	3.7
Si	0.13	0.0079	30.2
Sn	0.6	0.0080	25.6
Ta	21.3	0.014	1.4
Te	4.5	0.0088	4.6
Ti	5.8	0.014	1.4
V	5.1	0.014	1.8
W	19.2	0.014	1.8
Y	1.3	0.0082	10.6

* ΔE — the quantity of alloying element in binary Zr alloy at which the nuclear fuel needs to be enriched 0.05 wt% ^{235}U to produce the same power as a fuel clad in pure Zr.

Elements and their quantities intended for alloying that would inhibit the corrosion of zirconium were for the most part chosen empirically, based on the results of autoclave testing without irradiation and on some theoretical views. Zirconium corrodes via anion-vacancy diffusion of oxygen ions through the oxide thickness. At the metal–oxide interface, where the process of film growth starts, the rate controlling step is the high electronic resistivity of the oxide film (see Chapter 8, Volume 2 of this publication). Since most impurities in the oxide result in an increase in electronic conductivity, they all result in at least a small increase in corrosion rate compared with very high purity Zr.

As described in Section 2.1, Sn is useful for suppressing the harmful influence of impurities on corrosion. While weakening the harmful effect of impurities, that of nitrogen in particular, Sn itself promotes the corrosion of zirconium; this degradation may be ameliorated by small additions of other elements, such as Fe, Cr and Ni. However, Ni

increases hydrogen uptake by zirconium during corrosion. Ta and W have high neutron capture cross-sections and are not suitable for zirconium alloying. Thus, only Sn, Nb and Fe can be used with zirconium as major alloying elements and Cr, Ni, V, Cu and Mo as minor alloying elements to provide sufficient corrosion resistance in high temperature water and steam. Autoclave tests of zirconium alloys containing these elements corroborated this conclusion.

Zirconium alloying with the above mentioned elements, in combination with appropriate heat treatment, may endow components with high strength and fracture resistance. This is primarily achieved by using elements with a high solubility in α_{Zr} (Sn and O), those that stabilize the β phase (Nb), elements promoting dispersion strengthening (V, Mo) and elements that form heterogeneous distributions of precipitates in zirconium (Fe, Cr, Ni, Cu). Any trace element present should not embrittle the component.

Since pressure tubes have to retain high pressures, they are designed according to the principles of pressure vessel codes. The design stress is governed by the value of the weakest mechanical property at the operating temperature. Figure 2.8 is a schematic diagram of a design stress for a pressure tube made from a hypothetical zirconium alloy. When operating at temperatures up to about 588 K (315°C), the property determining the design stress is one based on short term tensile strength, usually the ultimate tensile strength (UTS); for example, the design stress should be less than UTS/3, the UTS being measured before reactor operation. At higher temperatures, the property determining the design stress depends on creep; for example, the design stress must be less than the stress to produce a creep rate of 10^{-7}/h. In both temperature regimes, to maintain operational integrity in a neutron flux, limits of deformation are often decisive for determining a component's lifetime.

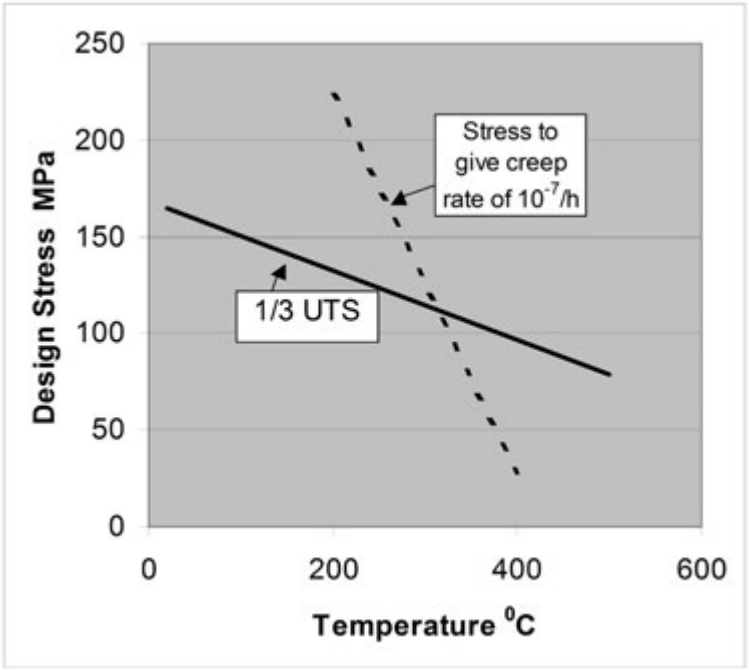

FIG. 2.8. Schematic diagram showing temperature regimes where the design stress of a hypothetical zirconium alloy is controlled by short term and long term mechanical properties.

Components made from zirconium alloys should have a stable microstructure, preferably that of α_{Zr}, and stable dimensions under neutron irradiation. The development of zirconium alloys for long term operation in power reactors is a complicated problem that

requires in-reactor tests, in addition to laboratory investigations. Neutron irradiation changes not only the compositions of the fuel, heat transport system fluid and moderator but also substantially alters the microstructures and properties of zirconium components (see Chapters 6 and 7 in Volume 2 of this publication for detailed discussions on the effects of irradiation). Practical experience from power reactors indicates that the most stable properties in-reactor (regarding deformation, as well as corrosion and tensile properties) are provided by alloys with an equilibrium microstructure that changes only slightly under irradiation.

High strength alloys, having supersaturated solid solution structures that are subject to irradiation induced partial or complete decomposition, may lose their original favourable corrosion and tensile properties. Under irradiation, alloys with a heterogeneous type structure comprising a solid solution and intermetallic particles are capable not only of degrading but also of improving their original properties. These phenomena are explained and governed by the dissolution of intermetallic particles with some of their elements and by changes in the shapes and crystal structure of the particles themselves, for example, amorphization. The same principle of trying to approach equilibrium applies to cold worked (CW) materials that are stress-relief annealed or recrystallized to various degrees.

In summary, some alloying elements are limited by their capture cross-section while others embrittle, promote deformation or induce poor corrosion resistance. Tin, niobium and iron in various combinations have emerged as the most important alloying elements. Unlike its sister element, titanium, many alloying additions in zirconium are limited to a few percent because of their neutron absorption.

2.4. SYSTEMS OF ZIRCONIUM ALLOYS — PHASE DIAGRAMS

2.4.1. Introduction

The alloying of zirconium for use in nuclear technology aims at providing a good performance of fuel assemblies and structural components and requires a versatile approach because of the severe operating conditions that have to be withstood by the components. The performance of components is mostly governed by the chemical composition and microstructure of the material developed during fabrication.

The investigations of the phase diagrams of zirconium with many elements in Mendeleev's periodic table started in the 1920s. The first complete phase diagrams were published in Refs [2.43, 2.44]. The phase diagrams were defined more exactly using zirconium of high purity and improved methods of examination. Lustman and Kerze [2.7], Ivanov et al. [2.45], Douglass [2.46] and Kubaschewski-von Goldbeck [2.47] provided phase diagrams of zirconium with some elements in studies published up to 1976. In the 1980s, scientists from Argentina made a large contribution to these investigations, for example in Refs [2.48–2.51]. Such investigations are continuing, and their results allow reliable determinations of phase diagrams of binary zirconium systems with O, Sn, Nb, Fe, Cr and Ni — the main alloying elements. Some isothermal sections of ternary diagrams have been determined.

2.4.2. Types of phase diagram

Zirconium has an allotropic transformation from a low temperature, hexagonal close packed (HCP) crystal structure, the α phase, to a high temperature body centred cubic (BCC) crystal structure, the β phase. In pure zirconium the α↔β transformation takes place at

1136 K (863°C). The different solubilities of elements in the α phase and β phase allow substantial microstructural variations of the alloys, which influence their properties.

The systems of binary alloys with elements that might be used to alloy zirconium (O, Sn, Nb, Fe, Ni, Cr, Al, Cu, Be, Y, Mo, Gd, V, S), may be present as impurities (C, N, S, Si, Hf, P) or might build up in alloys during operation (H from corrosion or Mo from transmutation) can be subdivided into three types:

(1) Complete solubility in the solid state (Hf).
(2) Expanded α region, with the temperature of α → β transformation greater than for pure zirconium. These elements are α stabilizers: O, Sn, C, N, Al and S.
(3) Expanded β region, with the temperature of α → β transformation lower than for pure zirconium. These elements are β stabilizers: Nb, Fe, Ni, Cr, Cu, Be, Y, Mo, Gd, V, Si and H.

Solid solutions in the α phase can also be classified as substitutional, in which the Zr atoms are replaced by an alloying atom, and interstitial, in which the alloying atoms fit into either octahedral or tetrahedral holes in the HCP lattice. Since nuclear considerations control the concentration of most alloy additions, and the α phase is the preferred phase, the solubility limit of alloying elements in the α phase is of interest. Once the limit has been exceeded, a second phase forms. An estimate of the substitutional solubility limit in α-zirconium can be made using the empirical rules postulated by Hume-Rothery and Raynor [2.52], and modified by Darken and Gurry [2.53]:

— An extensive primary solid solution is hindered when the disparity between the atomic radii, *r*, of the solvent and solute atoms exceeds 15%. The inverse is not necessarily true; other factors may limit solid solubility even when the size factor is favourable.
— When the difference in electronegativity, *X*, of the atoms of the matrix and the alloying element is large, intermetallic compounds tend to form. A difference of about half a unit on the electronegativity scale is often sufficient to limit primary solubility.
— The maximum solubility limit is attained when the valency of the two atoms is the same and when their crystal structure is identical.

Figure 2.9 shows a simultaneous application of the first two rules for zirconium using published values of *r* and *X* [2.54, 2.55]. A large solubility limit would be expected if the solute atom were within the inner ellipse, represented by a 0.2 or less difference in *X* and 7.5% or less difference in *r*. A modest solubility limit would be expected if the solute atom were within the outer ellipse, represented by a 0.4 or less difference in *X* and 15% or less difference in *r*. Outside these ellipses a low solubility limit would be expected. These expectations are mostly fulfilled; Fig. 2.10 is a plot of the maximum solubility limit of elements in zirconium as a function of the deviation from zirconium's position on the *X*-*r* map. Apart from Hf and Ti, which are in the same group as Zr in the periodic table, the remaining elements considered have differences in size factors, electronegativity and crystal structure that promote solubility limits of less than 10 at.%, with most less than 1 at.%. Therefore, second phases will be expected in most alloys.

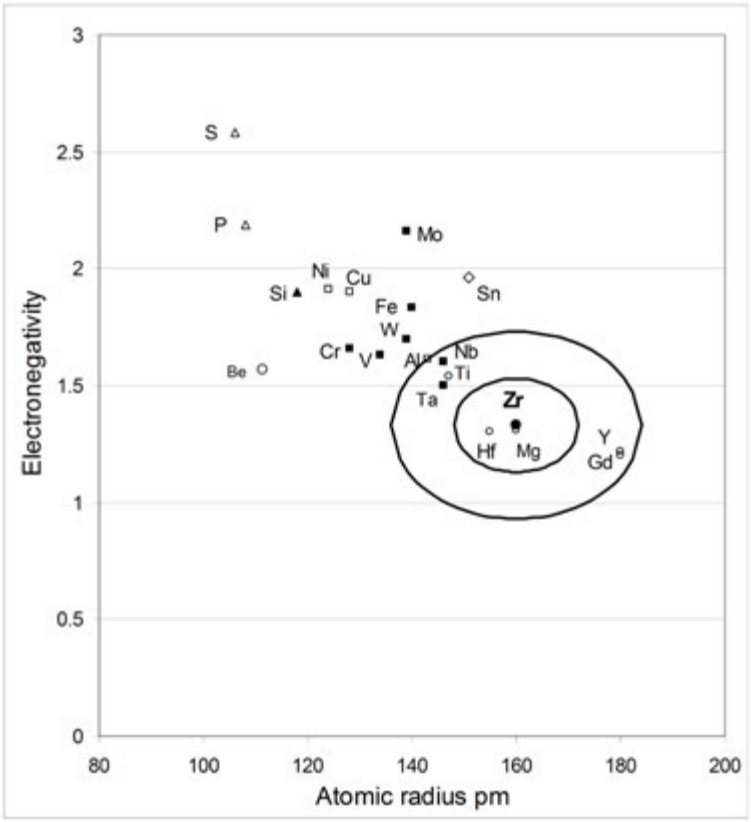

FIG. 2.9. Application of the first two Hume-Rothery rules for the substitutional solubility limit in α-zirconium. The inner ellipse represents a 7.5% difference in r and a 0.2 difference in X. The outer ellipse represents a 15% difference in r and a 0.4 difference in X. Legend: ● — Zr; ○ — hcp; ■ — bcc; □ — fcc; Δ — orthorhombic; ▲ — diamond cubic; ◊ — tetragonal.

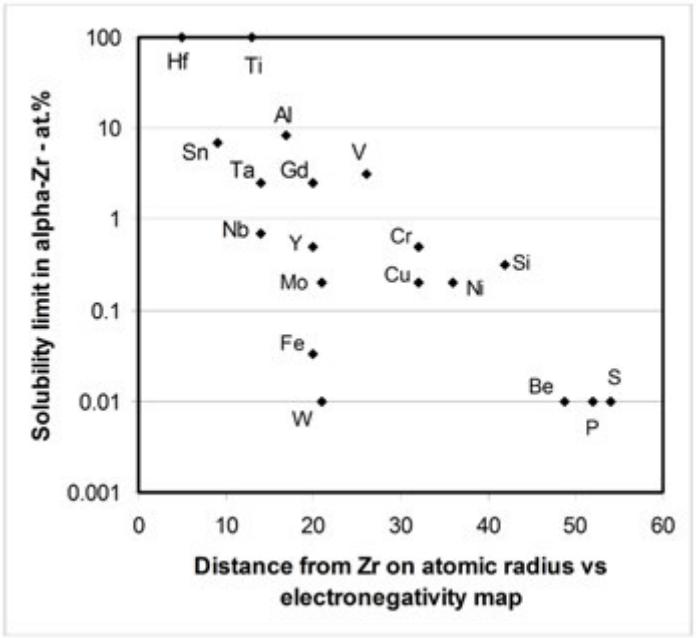

FIG. 2.10. Relationship between the maximum solubility limit of elements in α-zirconium and the deviation from zirconium of the combined effects of size factor and electronegativity plotted in Fig. 2.9.

A more fruitful approach to determining phases in both binary and multicomponent alloy systems is one based on coupling thermochemistry with phase diagram data using computer based methods for the synthesis. This process has been formalized through the computer coupling of phase diagrams and thermochemistry (CALPHAD) method [2.56].

2.4.3. Computational thermodynamics — CALPHAD method

Zirconium industrial alloys are based on multicomponent systems. Experimentally determined phase diagrams are available for binary systems but only partially available for ternary and higher order systems. Since the 1970s, phase diagram determination has evolved thanks to the CALPHAD method and the emergence of computational thermodynamics.

The calculation of a phase diagram is possible when its thermodynamic properties are known: a description of the Gibbs energy of each constitutive phase by a suitable model containing a small number of variable coefficients is needed. The models describing the Gibbs energy involve empirical parameters derived from experimental information or first principle calculations. Once a self-consistent thermodynamic description is obtained, the phase diagram and related thermodynamic properties can be calculated. It is then also possible to extrapolate to multicomponent systems. The first thermodynamic database for Zr alloys, ZIRCOBASE, was created in 1999 using the CALPHAD methodology [2.57]. This version of the thermodynamic database contained 10 elements, 16 binary systems and one ternary system and is frequently updated.

2.4.4. Binary systems of zirconium alloys

In Sections 2.4.4.1–2.4.4.20, both experimentally determined phase diagrams and assessed, optimized and thermodynamically modelled phase diagrams are presented for the important elements for the nuclear applications of zirconium.

2.4.4.1. Zr–O system

Oxygen is an important element for zirconium. The effect of oxygen on zirconium is double faceted. More than a hundred years were spent developing methods of producing ductile zirconium by having a low inventory of interstitial impurities, mainly oxygen. Oxygen is also beneficial and is introduced into zirconium alloys to maintain strength and creep properties without affecting corrosion resistance. Care must be taken to balance each facet since oxygen might enter zirconium during the fabrication of components and during service from interacting with water to form a surface oxide coating.

Data on the Zr–O phase diagram are presented in Refs [2.45, 2.48, 2.58–2.63] and summarized in Fig. 2.11. Additionally, Arroyave et al. describe a thermodynamic model of the Zr–O system in Ref. [2.64].

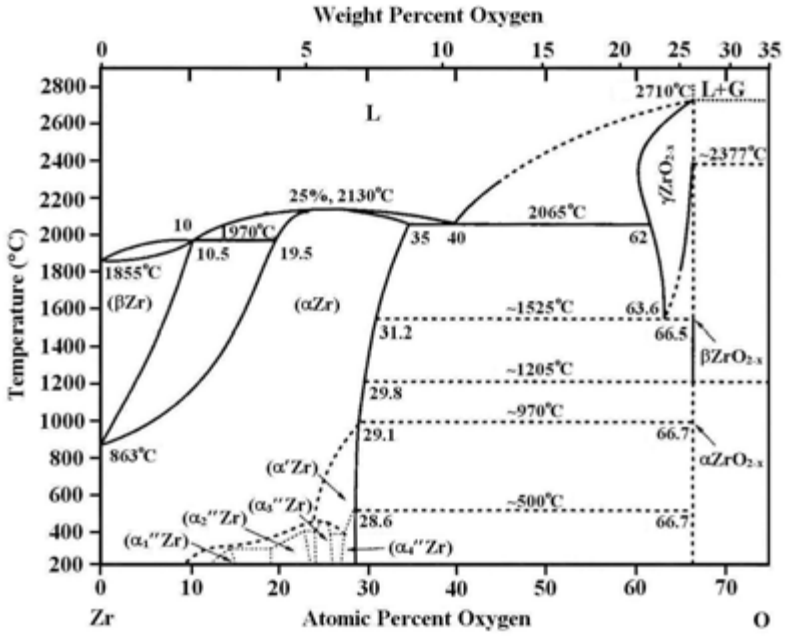

(a)

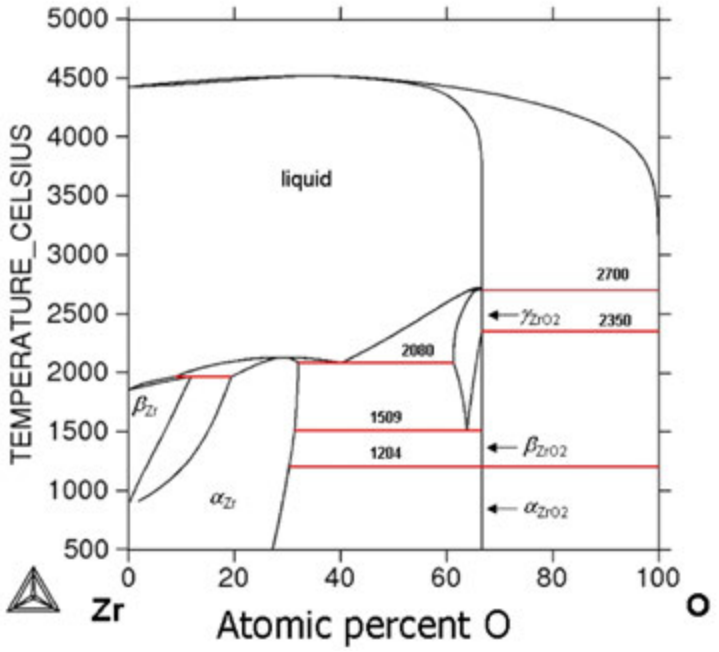

(b)

FIG. 2.11. (a) Zr–O phase diagram (reproduced from Ref. [2.48], with permission of Springer). (b) Zr–O phase diagram [2.60].

Oxygen raises the α → β transformation temperature to the zirconium melting temperature and is an α stabilizer, expanding the α region. The maximum oxygen solubility limit in α_{Zr} is about 35 at.% (8.63 wt%) at 2338 K (2065°C) [2.65] and in β-Zr it is about 10.5 at.% (2.016 wt%) at about 2243 K (1970°C). The oxygen in solid solution in

α-zirconium is interstitial in octahedral sites [2.66]. In the Zr–O system the only available stable oxide is ZrO_2, which has several phase variations. The low temperature monoclinic phase is stable up to about 1478 K (1205°C); at this temperature it transforms to a tetragonal structure that converts to the cubic phase at about 1773 K (1500°C) [2.59]. The monoclinic and tetragonal ZrO_2 phases were considered to be stoichiometric (see Fig. 2.11). Domagala and McPherson [2.44] proved by metallographic observations and X ray analysis that α_{ZrO2} and β_{ZrO2} were non-stoichiometric. Ma et al. [2.67] reassessed the Zr–O binary system to take into account the existence of a homogeneity range for the α_{ZrO2} and β_{ZrO2} phases, resulting in the phase diagram presented in Fig. 2.12.

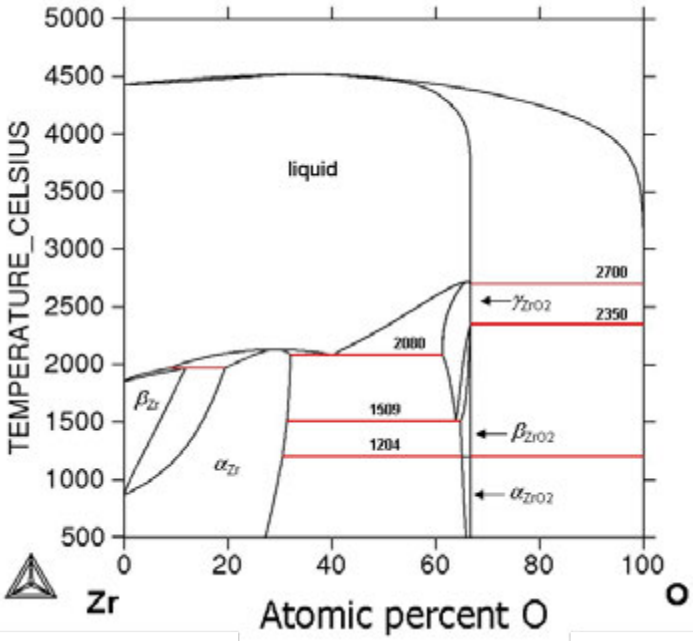

FIG. 2.12. Zr–O phase diagram taking into account the existence of a homogeneity range for the αZrO_2 and βZrO_2 phases (this image was published in Ref. [2.67], copyright Elsevier, 2008).

Impurities stabilize the tetragonal phase while the cubic phase forms in thin coatings at the initial stages of zirconium oxidation by oxygen or air. At about 1243 K (970°C) partially or fully ordered phases of α'_{Zr} or ZrO_x, ZrO_2 and others are formed on the α_{Zr}-substrate. In the technical specifications of zirconium alloys, the amount of oxygen is usually restricted to a range from 800–1600 ppm (0.454–0.905 at.%); all the oxygen will be in solution.

2.4.4.2. Zr–Sn system

As mentioned in Section 2.1 and Section 2.2, tin is an important alloying element for zirconium because it can improve the high temperature aqueous corrosion resistance and strength of sponge zirconium. Tin reduces the temperature of melting. A eutectic reaction exists at about 19 at.% (23.4 wt%) Sn and 1858 K (1585°C). Tin raises the temperature of the $\alpha \leftrightarrow \beta$ transformation of zirconium; it is an α stabilizer. The maximum solubility of Sn in β_{Zr} is about 17 at.% (21 wt%) at 1858 K (1585°C) and in α_{Zr} it is about 7 at.% (8.9 wt%) at 1216 K (943°C). The solubility limit of Sn diminishes with temperature in both β_{Zr} and α_{Zr} [2.45, 2.68–2.72]. When in solution in Zr, Sn is present as a substitutional atom.

The solubility limit of Sn in α_{Zr} has been redetermined using first principle calculations and experimental determinations on Zr–Sn alloys containing less than 100 wt. ppm (0.057 at.%) oxygen [2.73]. These results show that the Sn solubility limit is higher than previously reported (Fig. 2.13).

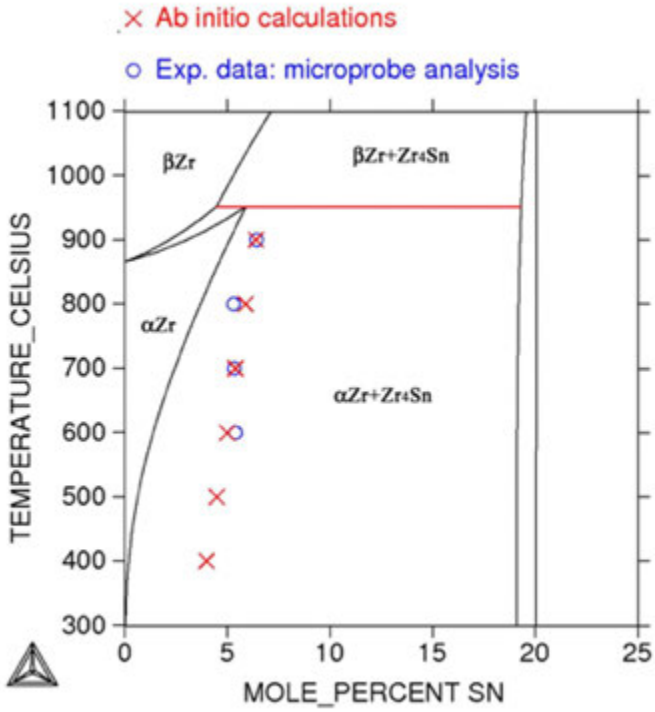

FIG. 2.13. Enlargement of the Zr-rich corner of the assessed Zr–Sn binary system compared with experimental data and first principle calculations (reprinted, with permission, from Ref. [2.73], copyright ASTM International).

In the work performed by Jerlerud-Pérez et al. [2.74], different parts of the Zr–Sn system have been reinvestigated, leading to the phase diagram shown in Fig. 2.14.

In the Zr–Sn system, three intermediate phases exist. The phase Zr_4Sn-A15 is formed via the peritectoid reaction $\beta_{Zr} + \eta \rightarrow Zr_4Sn$-A15 at 1594 K (1321°C) and 20 at.% (24.6 wt%) Sn. The Zr_4Sn compound has the cubic A15 structure, typified by Cr_3Si. Substitution for Zr on the Sn sublattice is responsible for the non-stoichiometry of the Zr_4Sn-A15 phase. This phase is not revealed in the microstructure of Zr in alloys containing <2.0 wt% (1.54 at.%) Sn. An intermediate phase, called η, melts congruently at 2262 K (1989°C). A miscibility gap exists inside the homogeneity domain of the η phase (Zr_5Sn_3-Zr_5Sn_4) from 1273 K (1000°C) down to room temperature. The homogeneity range extends from 35.8–37.5 at.% (42.1–43.8 wt%) Sn on the Zr-rich side and 41.2–44.4 at.% (47.7–51.9 wt%) Sn on the Sn-rich side. A third phase, $ZrSn_2$, is formed by a peritectoid reaction at 1398 (1125°C K) at 66.7 at.% (72.3 wt%) Sn.

For zirconium alloys used in nuclear reactors, the concentration of Sn is usually limited to 2.0 wt% (1.54 at.%); Sn will be in solution. Sn is a basic alloying element in the Zircaloys and is part of the composition of multicomponent alloys such as ZIRLO and E635.

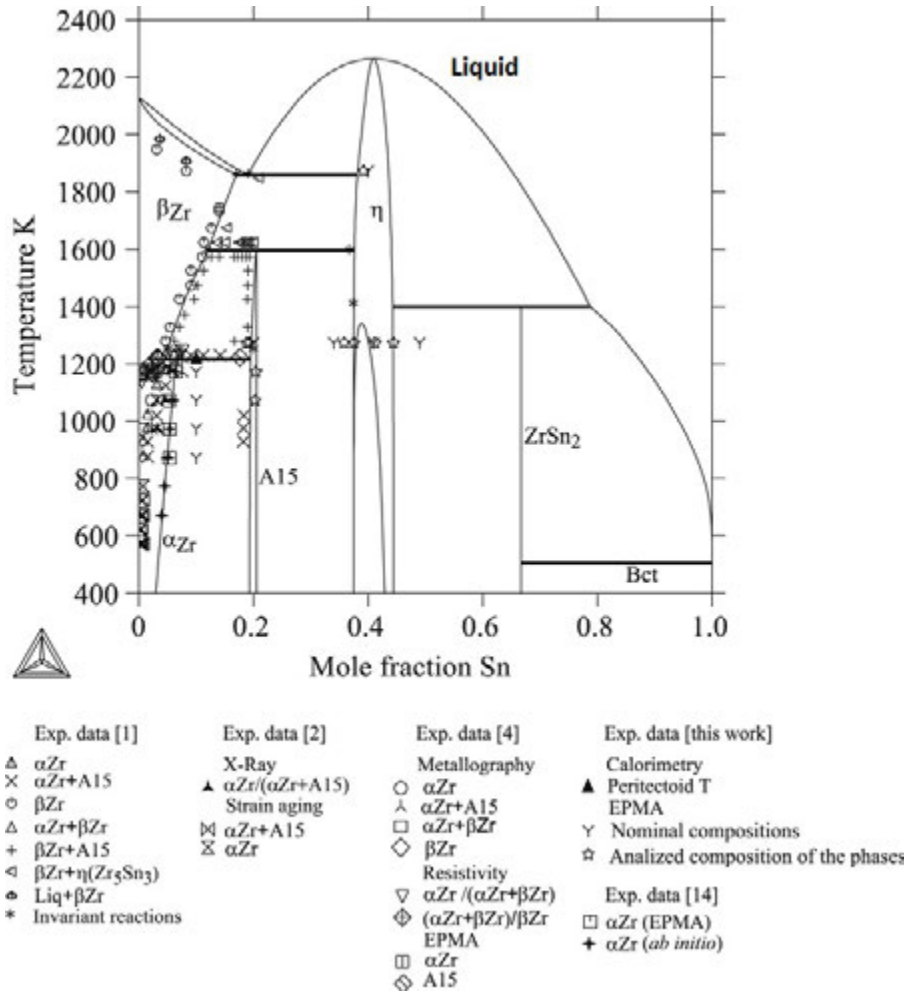

FIG. 2.14. Zr-Sn phase diagram (this image was published in Ref. [2.74], copyright Elsevier, 2008).

2.4.4.3. Zr–Nb system

Niobium added to zirconium improves its strength and resistance to corrosion and hydrogen uptake in high temperature water. The Zr–Nb phase diagram (Fig. 2.15) has been evaluated in Refs [2.45, 2.47, 2.75–2.77] and the stable phases have been thermodynamically analysed [2.78]. Niobium forms a substitutional solid solution with zirconium. At high temperatures, the system demonstrates mutual Nb–Zr solubility both in liquid and solid states. The liquidus has a minimum point at 2013 K (1740°C) at a concentration of 21.7 at.% (22.0 wt%) Nb. At lower temperatures, in the concentration range of about 19–91 at.% (19.3–91.1 wt%) Nb, the solid solution separates into two isomorphic BCC phases, β_{Zr} and β_{Nb}. The critical point of the separation curve is found at 1261 K (988°C) for a niobium composition equal to 60.6 at.% (61.0 wt%).

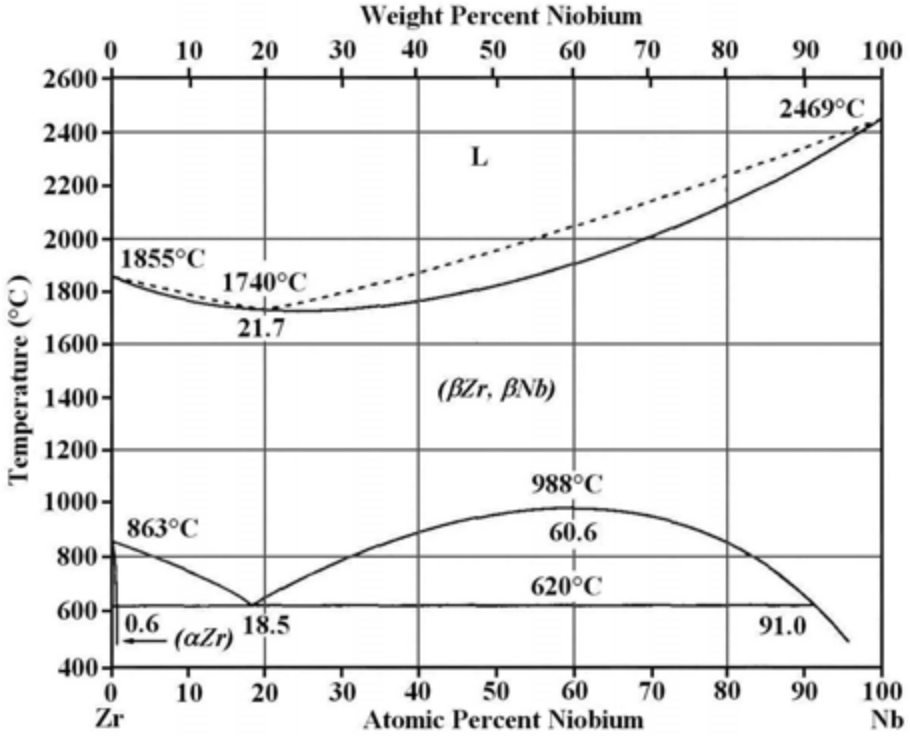

FIG. 2.15. Zr–Nb phase diagram (reproduced from Ref. [2.77] with permission of Springer).

Nb is a β stabilizer. The monotectoid reaction (β_{Zr}, β_{Nb}) → (α_{Zr}) + (β_{Nb}) proceeds at 873–893 K (600–620°C) and at a niobium concentration of about 18.5 at.% (18.8 wt%). The impurity concentration (particularly of O, N and Fe) of alloys strongly affects this reaction temperature and the solubility of Nb in (α_{Zr}), and therefore the values cited by various authors differ perceptibly. For instance, the monotectoid reaction temperature is reported as 893±10 K (620±10°C) [2.45, 2.47, 2.75–2.77], summarized as 883 K (610°C) [2.46], while in Ref. [2.79] 873±5 K (600±5°C) is cited. An even lower value of 858 K (585°C) is reported for Zr–Nb alloys containing 1400 ppm (0.79 at.%) O and 700 ppm (0.11 at.%) Fe [2.80]. The maximum solubility limit of Nb in α_{Zr} is reported to be in the range 0.6–1.1 at.% (0.61 –1.12 wt%). The discrepancy in the terminal solubility of Nb in α_{Zr} is partly caused by oxygen present in alloys and for oxygen concentrations ≥800 ppm (0.45 at.%), Zr–Nb should be viewed as a ternary system.

Oxygen in Zr–Nb alloys substantially alters the location of phase boundaries on the phase diagram of this system, raising the temperature of the $\alpha_{Zr}+\beta_{Nb}\rightarrow\beta_{Zr}$ reaction [2.79]. Because Fe is also a β stabilizer, in Zr–Nb alloys Fe impurities combine with Nb to form precipitates, thus obscuring the determination of the solubility limit of Nb in α_{Zr}. If it is assumed that when all the Fe has been used in the precipitates, the remaining Nb in solution can be used to evaluate the solubility limit, at 848 K (575°C) values of this concentration lie between 0.29 wt% (0.28 at.%) and 0.49 wt% (0.48 at.%) Nb [2.81], while a value as low as 0.2 wt% (0.2 at.%) was reported in Ref. [2.80]. These results suggest that even 'pure' Zr–Nb–alloys should be treated as a quaternary system. The sluggishness of the transformations, because of the low diffusivities of both Zr and Nb atoms in Zr [2.82], also contribute to the apparent discrepancies.

In Zr–Nb alloys metastable phases might form as a result of rapid cooling from the β phase. The formation of the α′, ω and β metastable phases has been established. The formation of a particular phase is related to the Nb concentration of an alloy. The metastable α′ phase is formed by quenching in alloys containing up to 5 at.% (5.1 wt%) Nb. This phase is a supersaturated solid solution of Nb in α_{Zr}. The α′ phase reveals high internal stresses that produce substantial increases in the hardness and strength of the alloys. The α′ phase is similar to the martensite in quenched Fe–C alloys and has an acicular structure.

When quenched from the β phase. the ω phase may form in alloys containing from 5–15 at.% (5.1–15.2 wt%) Nb. The ω phase also forms in alloys containing 1.0 and 2.5 at.% (1.02 and 2.55 wt%) Nb during ageing. The ω phase formation produces a significant increase in strength and a decrease in ductility. In Zr alloys with a Nb concentration ranging from 0.5–2.5 at.% (0.51–2.55 wt%) Nb, the metastable β_{Zr} phase was enriched in Nb precipitate upon cooling after heat treatments in the α + β and β domains, even for slow cooling rates (for example, 0.5°C/min) [2.79].

The latter two transformations of the β phase are summarized in temperature time transformation diagrams [2.83–2.85]. As an example, the transformations possible with approximately the eutectoid composition after cooling from 1123 K (850°C) are illustrated in Fig. 2.16. The lattice parameters of the α′, β and ω phases decline linearly with an increase in Nb concentration, except for a deviation in a_ω below 10.0 at.% Nb (10.2 wt%) [2.86]. The production of β-Nb from the decomposition of the β phase or nucleation and growth from the α phase has been modelled as a competition between the two mechanisms for the available solute [2.87].

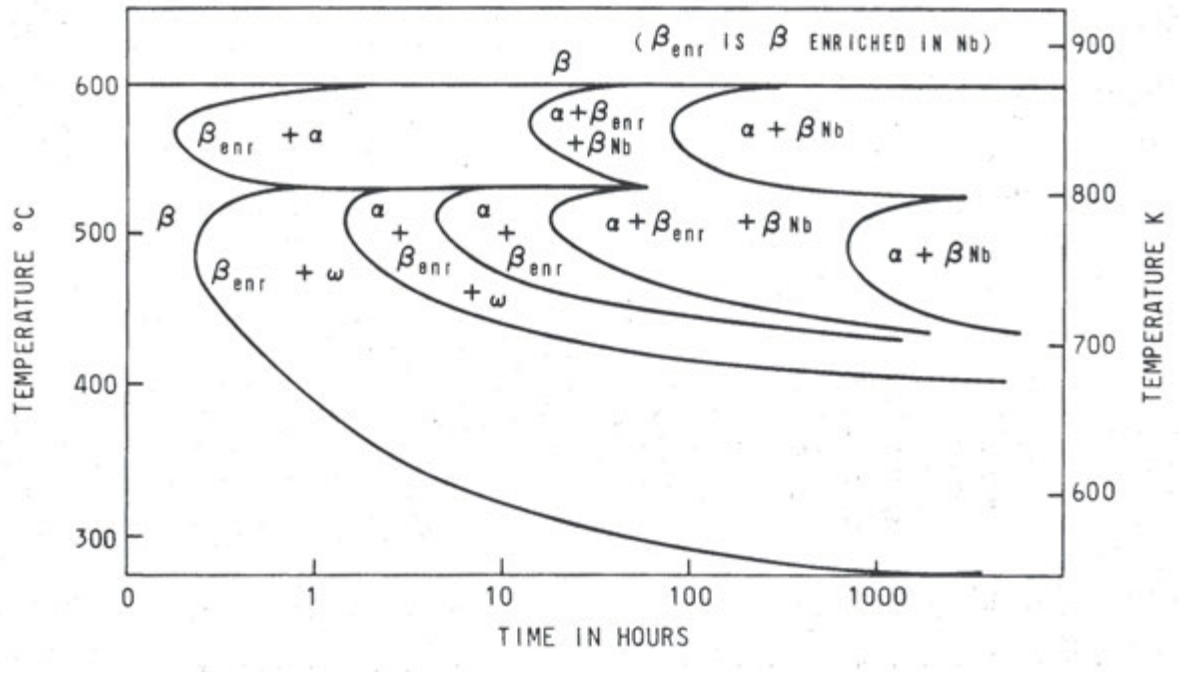

FIG. 2.16. The isothermal transformation behaviour of Zr-19 wt% Nb cooled from 1123 K (850°C) (reproduced from Ref. [2.84] with permission courtesy of AECL, Canada).

For use in nuclear reactors, the niobium concentration of zirconium alloys is usually restricted to 3.0 wt% (2.95 at.%). Niobium is a basic alloying element of E110, M5, E125 and Zr-2.5Nb, and is included in E635 and ZIRLO. It is present in solid solution in the α phase and as part of a second phase.

2.4.4.4. Zr–Fe system

Iron is a valuable element because it favourably affects the resistance of zirconium to corrosion in high temperature water and steam. Investigations into the Zr and Fe system started in 1930. Many experimental studies and assessments have been dedicated to the Zr–Fe binary system; they are sometimes contradictory. Some investigators report the formation of intermediate phases; their quantity, stoichiometry and crystal structures are not always coincident. As a rule, high purity materials were used, and alloys were produced in arc furnaces in argon, in induction furnaces in helium and in electron beam furnaces in vacuum [2.51, 2.88–2.96]. In the experimental study performed by Stein et al. [2.97], a revised version of the Fe–Zr phase diagram was established. Most of these results have been checked and confirmed in Ref. [2.98]; Chatain et al. proposed a thermodynamic reassessment of this system as presented in Fig. 2.17.

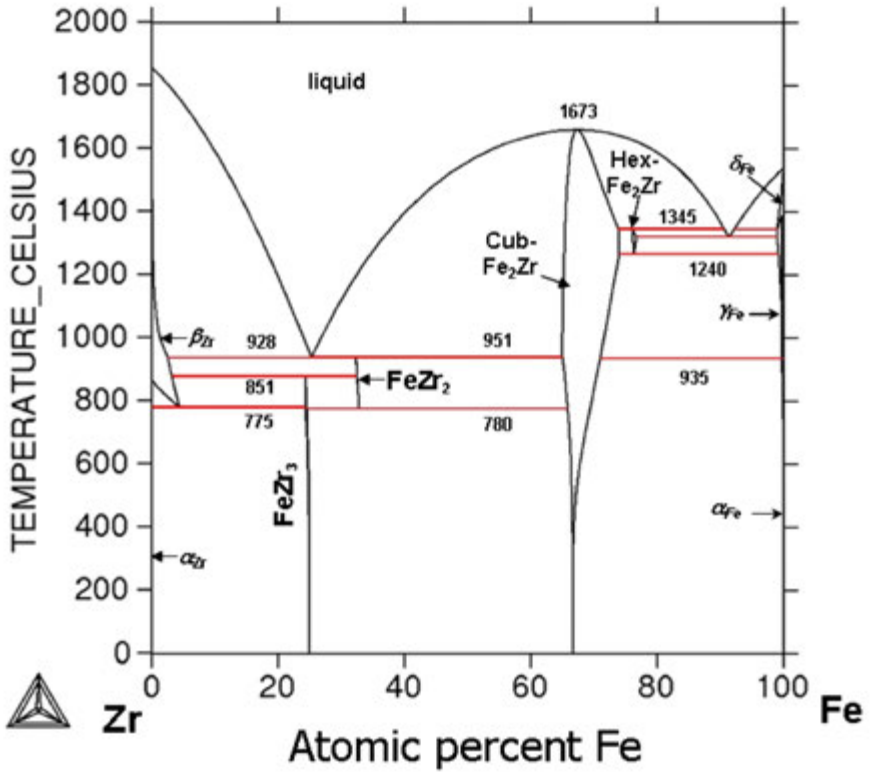

FIG. 2.17. Zr–Fe phase diagram (reproduced from Ref. [2.97] with permission of Springer).

Four intermetallic phases are identified in this system: the cubic C15 and the hexagonal C36 polymorph of the Laves phase Fe_2Zr, and two Zr-rich phases: $FeZr_2$ with a tetragonal structure and $FeZr_3$ with an orthorhombic one. Since it has been demonstrated that the $Fe_{23}Zr_6$

phase is stabilized by O [2.97], it is therefore not considered an equilibrium phase in the system. $FeZr_2$ is a high temperature phase that is stable between 1053 K and 1224 K (780°C and 951°C). Thus, $FeZr_2$ phases found in as-cast samples are metastable. The temperature at which $FeZr_3$ decomposes is 1124 K (851°C), which is lower than some reported temperatures, for example, 1153 K (880°C) [2.89].

The melting temperature of Fe_2Zr is 1946 K (1673°C) and its homogeneity range extends from 68–71 at.% (56.6–60.0 wt%) Fe (Fig. 2.17). Zr_2Fe forms at 1224 K (951°C) via the peritectoid reaction $L + ZrFe_2 \rightarrow Zr_2Fe$. The eutectoid decomposition of this phase takes place at 1053 K (780°C): $Zr_2Fe \rightarrow ZrFe_2 + Zr_3Fe$. The eutectic reaction $L \rightarrow \beta_{Zr} + Zr_2Fe$ proceeds in the Zr-rich part of the phase diagram at 1201 K (928°C). The solubility of Fe in β_{Zr} at the eutectic temperature is 4.8 at.% (3.0 wt%) Fe [2.97]. It diminishes as the temperature decreases.

Iron lowers the temperature of the $\beta_{Zr} \rightarrow \alpha_{Zr}$ transformation. The β_{Zr} base solid solution is subject to the eutectoid decomposition $\beta_{Zr} \rightarrow \alpha_{Zr} + Zr_3Fe$. The eutectoid decomposition proceeds at 1048 K (775°C), although values up to 1073 K (800°C) have been reported [2.99, 2.100]. The eutectoid concentration is about 4.0 at.% (2.5 wt%) Fe. Iron forms a substitutional solid solution with Zr although the maximum solubility limit of Fe in α_{Zr} is very small, between 0.0144–0.033 at.% (0.0088–0.020 wt%). Close to the $\alpha \rightarrow \beta$ transformation temperature, the diffusivity of Fe in Zr is about 10^7 faster than self-diffusion, suggesting diffusion by an interstitial mechanism [2.101].

Iron is a basic alloying element of the Zircaloys and the ZIRLO and E635 alloys. In nuclear reactors, the Fe concentration of zirconium alloys is restricted to < 0.5 wt% (0.81 at.%). It is usually present within intermetallic precipitates.

2.4.4.5. Zr–Ni system

Nickel introduced in specified amounts improves zirconium resistance to corrosion in water and steam. However, nickel promotes HPU in zirconium and its alloys upon interaction with water (Figs 2.6, 2.7). In the Zr–Ni system (Fig. 2.18) eight compounds have been identified [2.45, 2.46, 2.102, 2.103]. Ni_7Zr_2, $Ni_{21}Zr_8$, $Ni_{11}Zr_9$, NiZr and $NiZr_2$ are treated as stoichiometric phases. Experimental results have shown the existence of homogeneity ranges for Ni_5Zr, Ni_3Zr and $Ni_{10}Zr_7$. In Zr-rich alloys containing about 33 at.% (24 wt%) Ni, a single compound exists, Zr_2Ni, with a face centred cubic (FCC) lattice. The experimental peak solubility of Ni in β_{Zr} is 2.92 at.% (1.90 wt%) Ni and the calculated peak solubility is 2.61 at.% (1.70 wt%) Ni. Ni lowers the temperature of the Zr polymorphic transformation and at a temperature of 1100 K (827°C) the eutectoid decomposition proceeds via the reaction $\beta_{Zr} \rightarrow \alpha_{Zr} + Zr_2Ni$. The eutectoid point is at a Ni concentration of 1.8 at.% (1.17 wt%). Ni is soluble in α_{Zr} to less than 0.2 at.% (0.13 wt%) and may be as low as 0.0014 at.% (0.0009 wt%) [2.104]. Ni probably forms a substitutional solid solution but close to the $\alpha \rightarrow \beta$ transformation temperature; the diffusivity of Ni in Zr is about 10^7 faster than self-diffusion, suggesting diffusion by an interstitial mechanism [2.101].

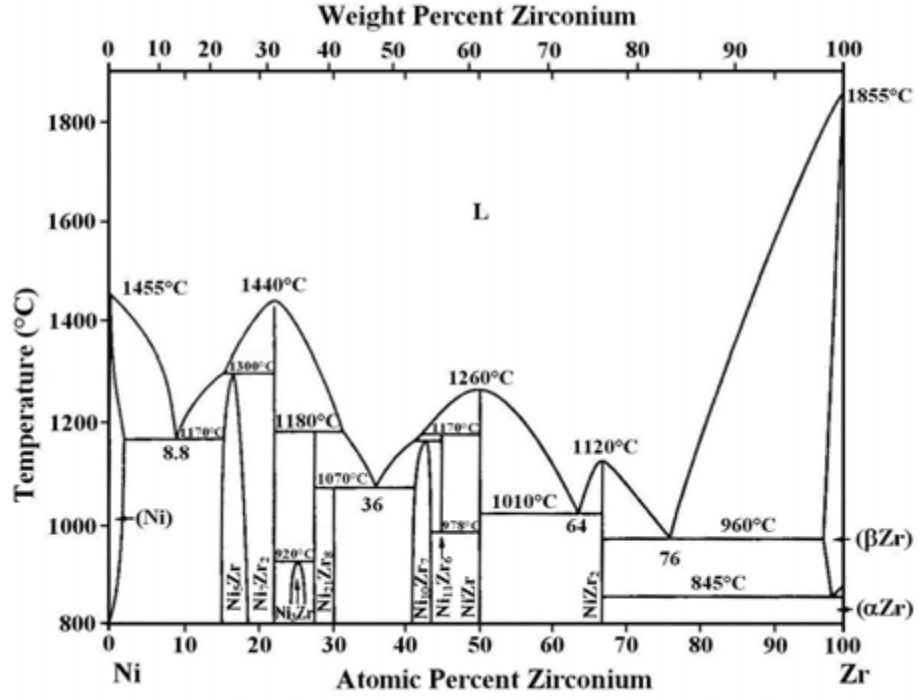

(a)

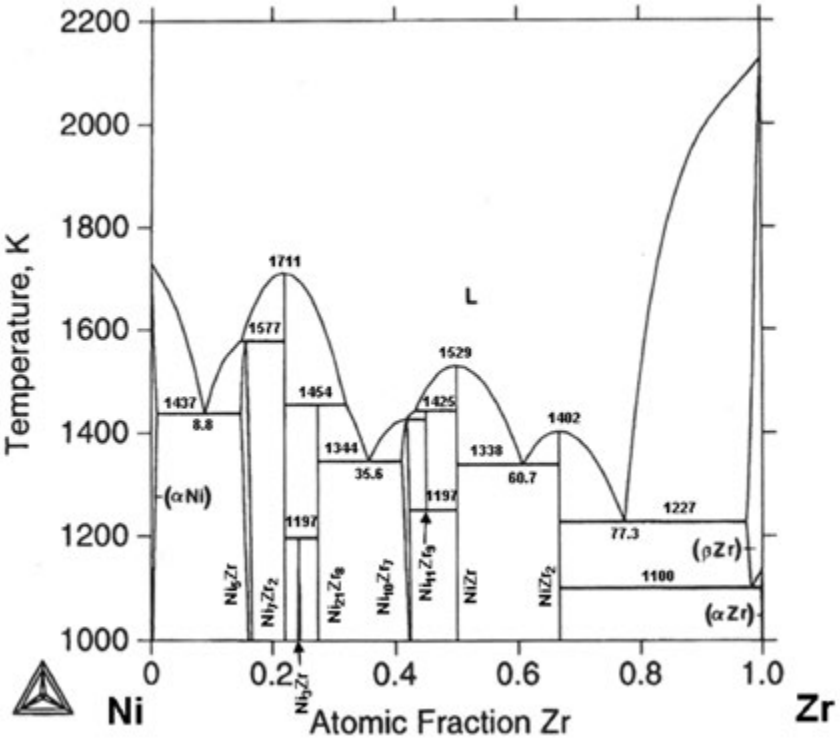

(b)

FIG. 2.18. Two Zr–Ni phase diagrams. (a) A phase diagram originally published in Ref. [2.102]. (b) A phase diagram originally published in Ref. [2.103].

The usual Ni concentration in zirconium alloys intended for use in nuclear reactors is restricted to <0.1 wt% (0.155 at.%). Ni is part of the composition of Zircaloy-2, where it is present in intermetallic precipitates.

2.4.4.6. Zr–Cr system

Chromium added in a small quantity improves zirconium resistance to corrosion and HPU in water and steam (Figs 2.6, 2.7). Many researchers have studied the phase equilibria in the Zr–Cr system and the results are summarized in Fig. 2.19 [2.50, 2.105, 2.106]. The Zr–Cr system is described by a eutectic type phase diagram, with a single intermediate phase $ZrCr_2$ that has three modifications: α_{ZrCr2}, β_{ZrCr2} and γ_{ZrCr2}. The α_{ZrCr2}-phase has a cubic MgCu2-type Laves structure (C15), β_{ZrCr2} has a hexagonal $MgNi_2$-type Laves structure (C36) and γ_{ZrCr2} has a hexagonal $MgZn_2$-type Laves structure (C14). Their homogeneity range extends from 64.1–68.6 at.% (50.4–55.5 wt%) Cr. In this system, two eutectic reactions take place. The first, at 1605 K (1332°C), corresponds to the reaction liquid → β_{Zr} + α_{ZrCr2}. The other, at 1865 K (1592°C), corresponds to the reaction liquid → (Cr) + β_{ZrCr2}. There are also two eutectoid reactions: β_{Zr} → α_{Zr} + α_{ZrCr2} at 1109 K (836°C) and β_{ZrCr2} → (Cr) + α_{ZrCr2} at 1818 K (1545°C) (Fig. 2.19). The maximum solubility of Cr in β-Zr is about 8 at.% (4.7 wt%) at 1605 K (1332°C) and goes down to 1.80 at.% (1.04 wt%) at 1109 K (836°C). The maximum solubility of Cr in α_{Zr} does not exceed 0.5 at.% (0.29 wt%). Cr forms a substitutional solid solution with Zr although, close to the α → β transformation temperature, the diffusivity of Cr in Zr is about 5×10^4 faster than self-diffusion, suggesting diffusion by an interstitial mechanism [2.101]. Quenching may produce metastable phases: HCP α′ martensite in alloys containing <3.3 at.% (1.9 wt%) Cr alloys and the ω phase in alloys with high concentrations of Cr.

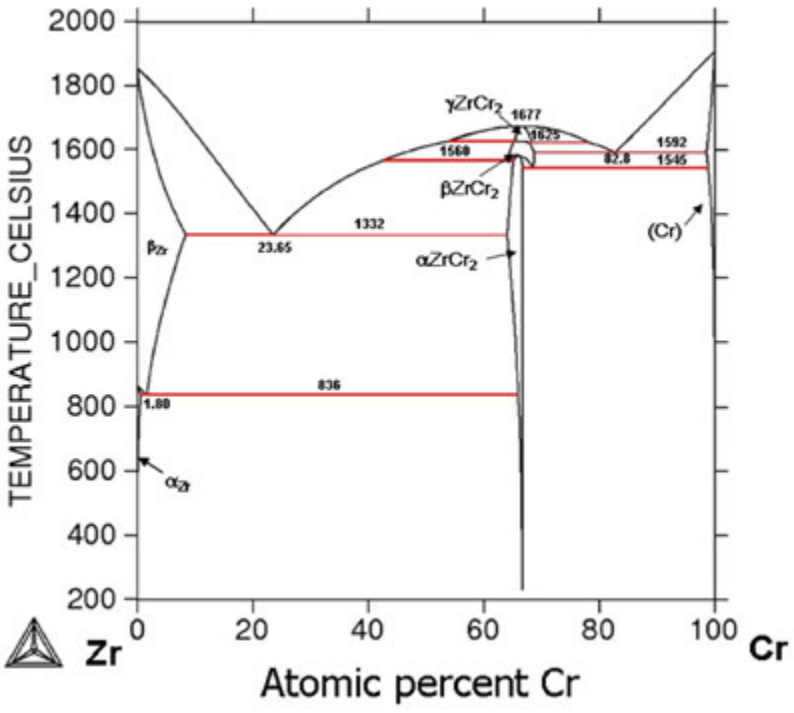

FIG. 2.19. Zr–Cr phase diagram [2.107].

For nuclear applications, Cr is part of the composition of the Zircaloys, where its concentration does not exceed 0.15 wt% (0.26 at.%). It is present in intermetallic precipitates.

2.4.4.7. Zr–C system

Carbon impurities exert an adverse influence on zirconium corrosion in water and steam (Figs 2.1, 2.2) and on fracture properties. Carbon forms interstitial solid solutions with the different phases of zirconium but has very low solubility limits in them: <0.1 at.% (0.014 wt%) in α_{Zr} and 0.7 at.% (0.093 wt%) in β_{Zr}. Carbon raises the $\alpha \rightarrow \beta$ transformation temperature by a small amount and lowers the melting temperature of zirconium. A eutectic reaction exists at a temperature of 2127 K (1854°C) and a carbon concentration of about 0.6 at.% (0.08 wt%) (Fig. 2.20) [2.45, 2.107, 2.108].

The Zr–C system is known to have a single Zr–C compound that has the FCC structure of the NaCl type and a melting temperature of 3693 K (3420°C). ZrC has a homogeneity region that extends from 35.9–49.5 at.% (6.86–11.4 wt%) C. In technical specifications, the tolerable carbon concentration of zirconium alloys is restricted to 270 ppm (0.2 at.%), although some users prefer much lower concentrations.

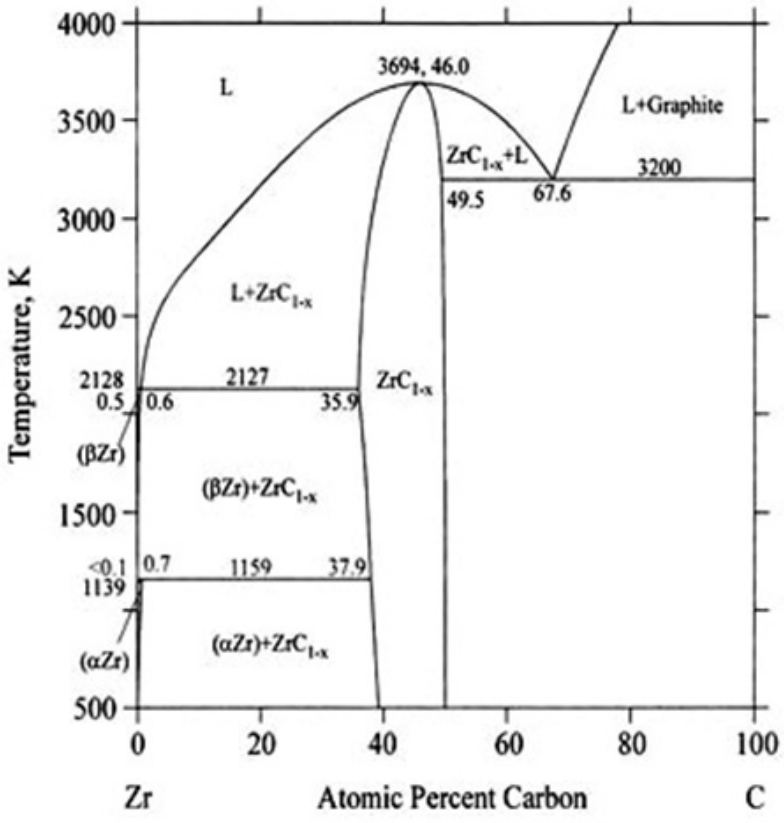

FIG. 2.20. Zr–C phase diagram (this image was published in Ref. [2.108], copyright Elsevier, 1995).

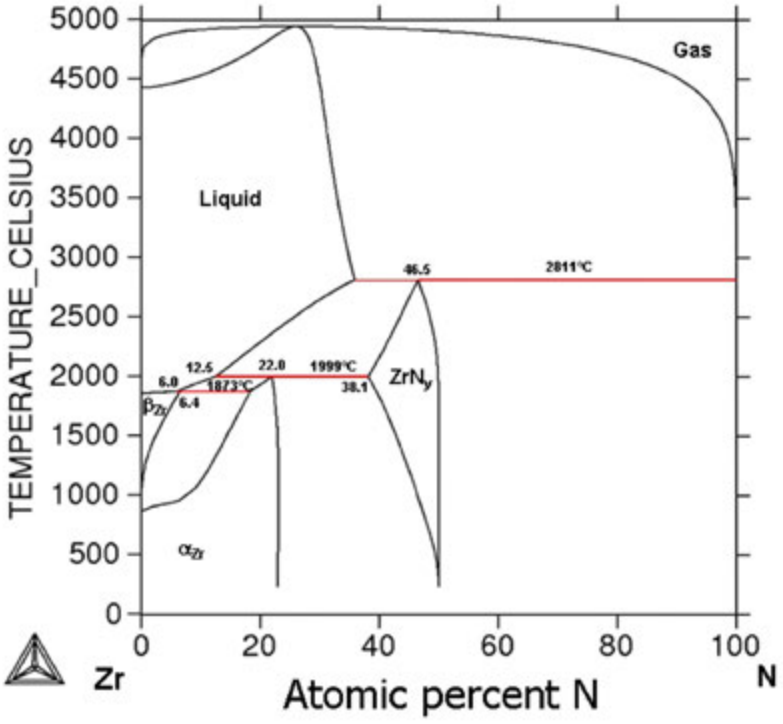

FIG. 2.21. Zr–N phase diagram (this image was published in Ref. [2.109], copyright Elsevier, 2004).

2.4.4.8. Zr–N system

Nitrogen promotes the corrosion of zirconium in water and steam (Figs 2.1, 2.2) and provides much strengthening [2.66]. Nitrogen increases the temperatures of Zr melting and polymorphic transformation and forms interstitial solid solutions with zirconium. Nitrogen is an α stabilizer. The maximum limits of nitrogen solubility in the α and β phases of zirconium are, respectively, 22 at.% (4.16 wt%) at 2272 K (1999°C) and 6.4 at.% (1.04 wt%) at 2146 K (1873°C) (Fig. 2.21). The only chemical compound in the system is zirconium nitride, denoted ZrN_y. Its homogeneity range extends from 38–47 at.% (8.6–12 wt%) N, and its melting temperature is 3084 K (2811°C) [2.45, 2.109, 2.110].

In typical technical specifications for zirconium alloys, the nitrogen concentration is restricted to 80 ppm (0.052 at.%), where it will be present in solid solution.

2.4.4.9. Zr–Al system

Aluminium strengthens zirconium but impairs its corrosion resistance in water (Fig. 2.2). Aluminium increases the temperature of the (α → β) transformation of zirconium and is an α stabilizer. Several experimental studies have been performed on this system [2.111–2.115]. A thermodynamic assessment, mainly based on these experimental data, has been performed [2.116], and the resulting phase diagram is presented in Fig. 2.22. Aluminium forms substitutional solid solutions with α and β zirconium. A peritectoid transformation $\beta_{Zr} + Zr_3Al \rightarrow \alpha_{Zr}$ proceeds at 1183 K (910°C) for an Al concentration of 8.2 at.% (2.57 wt%). As the temperature is lowered, the terminal solubility of Al in α_{Zr} diminishes; at about 873 K

(600°C) it is 1.5 at.% (0.45 wt%) Al. The maximum solubility in β_{Zr} is about 25 at.% (8.98 wt%) Al.

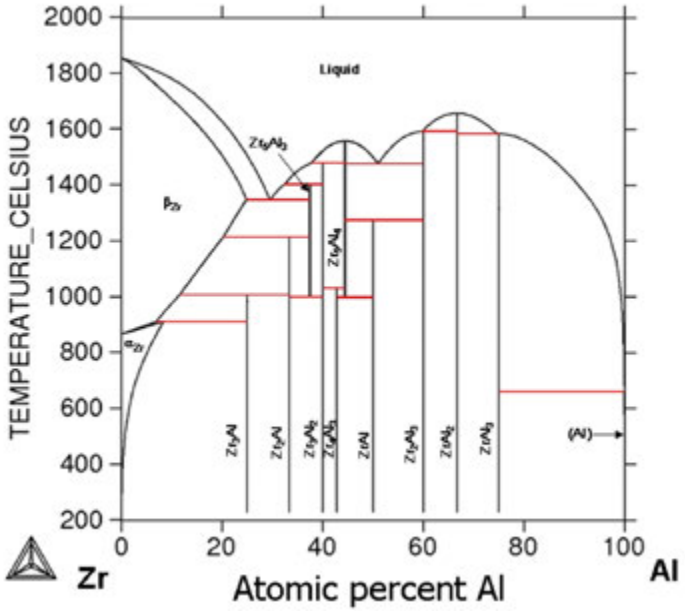

FIG. 2.22. Zr–Al phase diagram (reproduced from Ref. [2.116], with permission of Springer).

Ten compounds are formed in the Zr–Al system. The most zirconium enriched compounds, Zr_3Al, Zr_2Al and ZrAl, form in the solid state as a result of peritectoid transformations at 1292 K, 1487 K, and 1548 K (1019°C, 1214°C and 1275°C), respectively [2.45, 2.117]. Zr_3Al and Zr_2Al have hexagonal structures while ZrAl is orthorhombic.

In Canada, an alloy was based on the ordered compound Zr_3Al with the aim of producing a material with high strength and low deformation [2.118]. In standard alloys for use in water reactors Al is an impurity and its concentration is specified as less than 75 ppm (0.025 at.%).

2.4.4.10. Zr–H system

Hydrogen is very important for zirconium since hydrides can embrittle components (Chapter 9, Volume 3 of this publication) and a huge effort has been expended in measuring the solubility limit of hydrogen in the α phase of α and (α + β) alloys and its consequences below 673 K (400°C).

The Zr–H phase diagram is of the eutectoid type at the Zr-rich end [2.45, 2.119]. A thermodynamic model of this system based on experimental data is summarized in Fig. 2.23 [2.57]. Hydrogen forms interstitial solid solutions in zirconium; in the α phase the hydrogen resides in tetrahedral sites. The maximum solubility limit of hydrogen in α_{Zr} is 5.93 at.% (0.0691 wt%) but less than 0.56 at.% (0.0062 wt%) at 573 K (300°C). The eutectoid reaction proceeds at 823 K (550°C) at a hydrogen concentration of about 32.0 at.% (0.513 wt%). The solubility of hydrogen in β_{Zr} is 53 at.% (1.22 wt%) H at 1140 K (867°C). Two hydride phases exist in the hydrogen concentration range of 60–67 at.% (1.62–2.18 wt%): δ-phase with an FCC lattice and ε phase with a face centred tetragonal lattice (c/a < 1). Above about 1073 K (800°C) the single hydride phase is δ_{ZrH2}. The results

of microstructural examinations suggest that the tetragonal crystal lattice ε phase of hydride forms via a pseudomartensitic transformation of the cubic phase or by twinning. At low hydrogen concentrations, a tetragonal γ phase (c/a > 1), ZrH, has been observed. Its appearance is promoted by high purity and rapid cooling rates; it has also been observed during transformation of the δ phase at low temperatures in Zr-2.5Nb. Lanzani and Ruch [2.120] have summarized the various apparently contradictory results on the occurrence of γ and δ hydrides. A transient hydride phase has been reported that may be a precursor to γ or δ hydrides [2.121]. This metastable phase is called ζ hydride; it has a composition of $ZrH_{0.25\text{-}0.5}$ and an HCP structure.

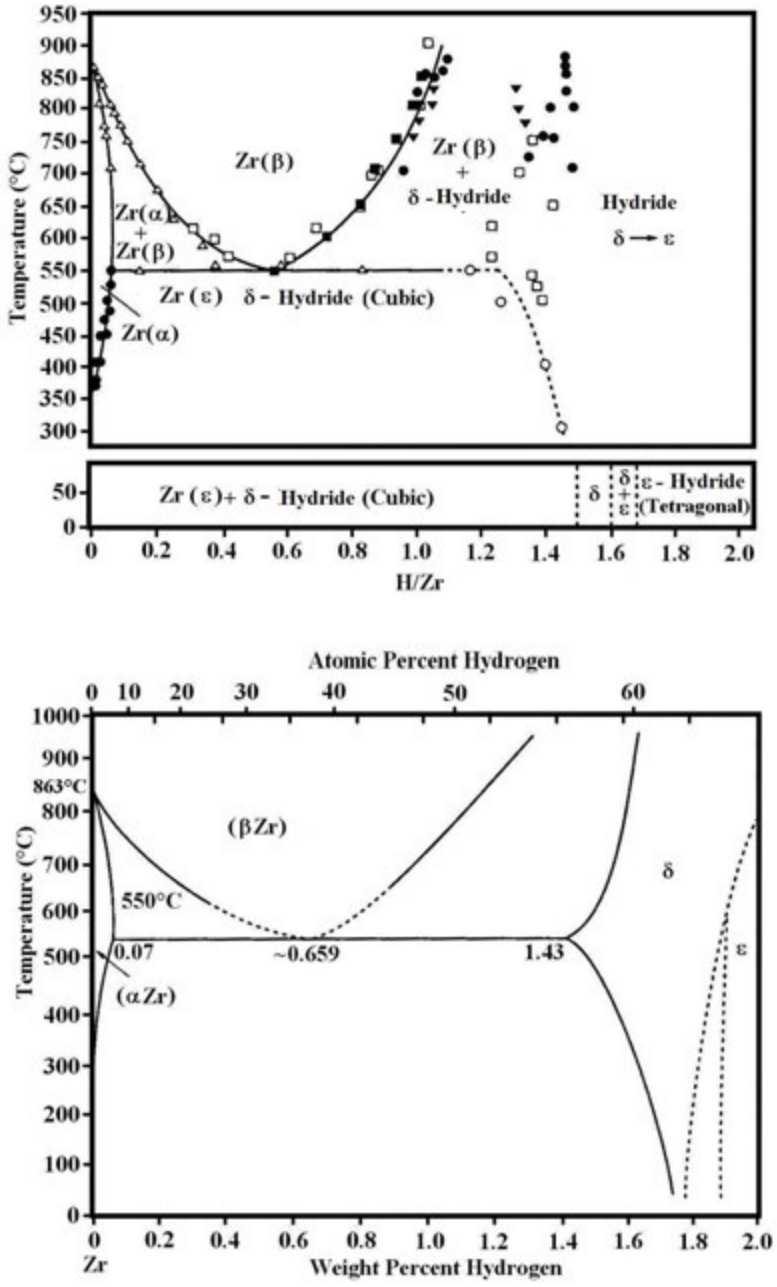

FIG. 2.23. (a) Zr–H phase diagram (reproduced from Ref. [2.119], with permission of Springer).

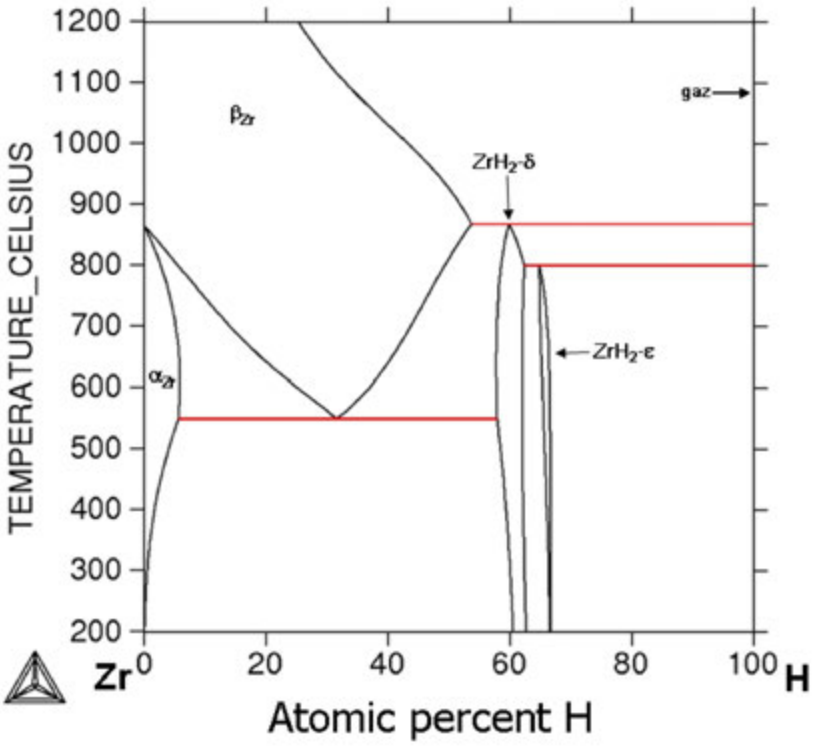

FIG. 2.23. (b) Zr-H phase diagram (this image was published in Ref. [2.57], copyright Elsevier, 1999).

Hydrides are being developed as potential energy vectors and moderators in nuclear reactors and are a transient part of some fabrication processes [2.122]. For finished nuclear components made from a zirconium alloy, the hydrogen concentration is restricted to 25 ppm (0.23 at.%) before loading into a reactor. In some components, for example, pressure tubes, the allowable initial concentration is lower, 5 ppm (0.05 at.%); even at this low concentration, hydrides will be present in components at room temperature.

2.4.4.11. Zr–S system

Sulphur is present in zirconium as an impurity. Researchers in France have reported [2.123] that sulphur has a favourable influence on the creep resistance of the M5 alloy for S concentrations not higher than 20 wt.ppm (0.0057 at.%) (see Section. 2.5.2.2, Fig. 2.74). This value corresponds to the S solubility limit in α_{Zr} confirming that the effect of S on creep strength results from solid solution hardening. The Zr–S phase diagram has not been fully constructed. Some sulphides have been identified, but their numbers and compositions are uncertain. The phase diagram is schematically shown in Fig. 2.24 [2.123–2.151]. The solubility limit of sulphur in β_{Zr} is higher than in α_{Zr}, but has not been precisely determined. The availability of sulphur rich compounds with homogeneity regions, for example, ZrS_3 and ZrS_2, has been ascertained. Charquet [2.123] has identified Zr_9S_2 sulphides with a tetragonal structure in crystal bar Zr. In the analogous Ti–S system, the high Ti sulphide is Ti_6S [2.125].

Apart from its presence in the M5 alloy and some heats of Zircaloy-4, S is not considered in technical specifications. Sulphur has been implicated in examples of hot shortness and cracking during cold work in experimental alloys containing up to 150 ppm (0.043 at.%) S. Since S may be present in recycled materials and some users wish it to be absent, care is taken to keep its concentration in ingots to <10 ppm (0.0028 at.%) [2.126].

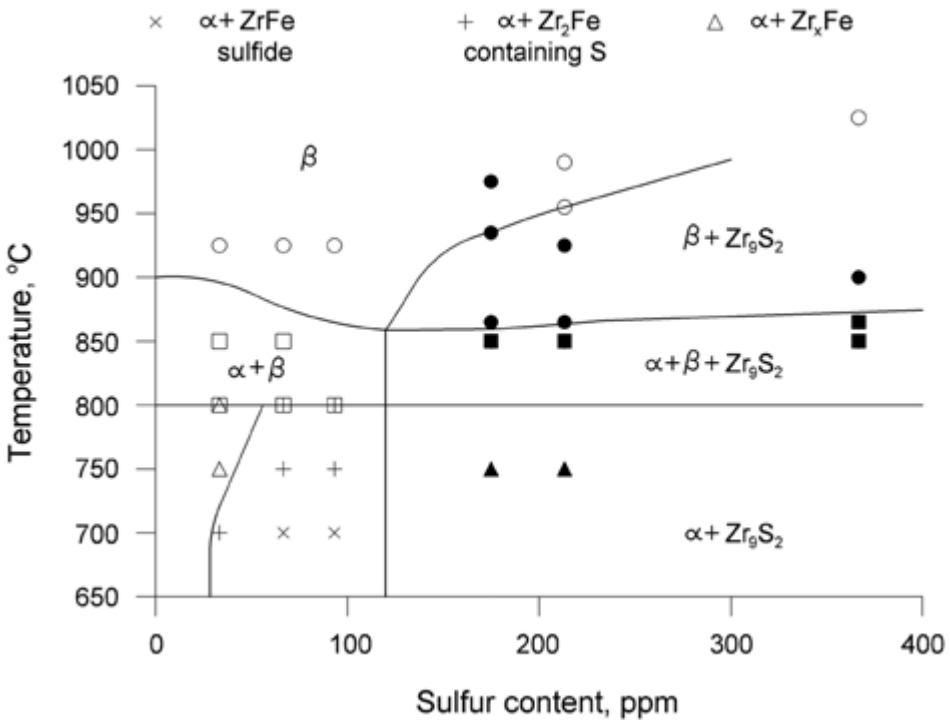

(a)

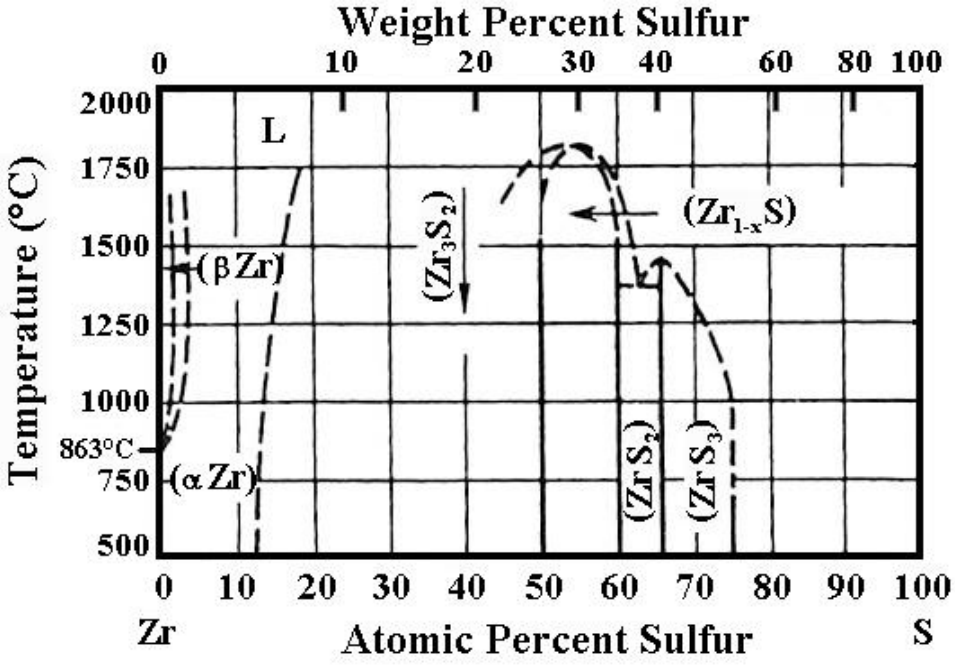

(b)

FIG. 2.24. (a) Zr-S phase diagram (this image was published in Ref. [2.123], copyright Elsevier, 2002). (b) Zr-S phase diagram [2.124].

2.4.4.12. Zr–Si system

Silicon is present in zirconium as an impurity; in small quantities it might be used to alloy zirconium (Fig. 2.6) although the intermetallic particles are brittle. A thermodynamic assessment, based on the available experimental data in the literature, has been performed [2.127]. The Zr–Si system features seven intermetallic compounds (Fig. 2.25) [2.45, 2.127, 2.128]. The most Zr-rich compound is Zr_3Si, which forms by a peritectic reaction at about 1927 K (1654°C). The maximum silicon solubility limit in β_{Zr} at 1814 K (1541°C) is ≤ 0.2 wt% (0.65 at.%). The silicon solubility limit in α_{Zr} at 1138 K (865°C) does not exceed 0.1 wt% (0.32 at.%). There are two eutectics in the system: one of them is formed by zirconium with Zr_3Si at 8.8 at.% (2.9 wt%)Si at 1814 K (1541°C), while the other is formed by silicon with $ZrSi_2$ at 90.7 at.% (75 wt%) Si at 1634 K (1361°C). In nuclear components, the concentration of Si zirconium alloys is usually specified to be <120 ppm (0.039 at.%).

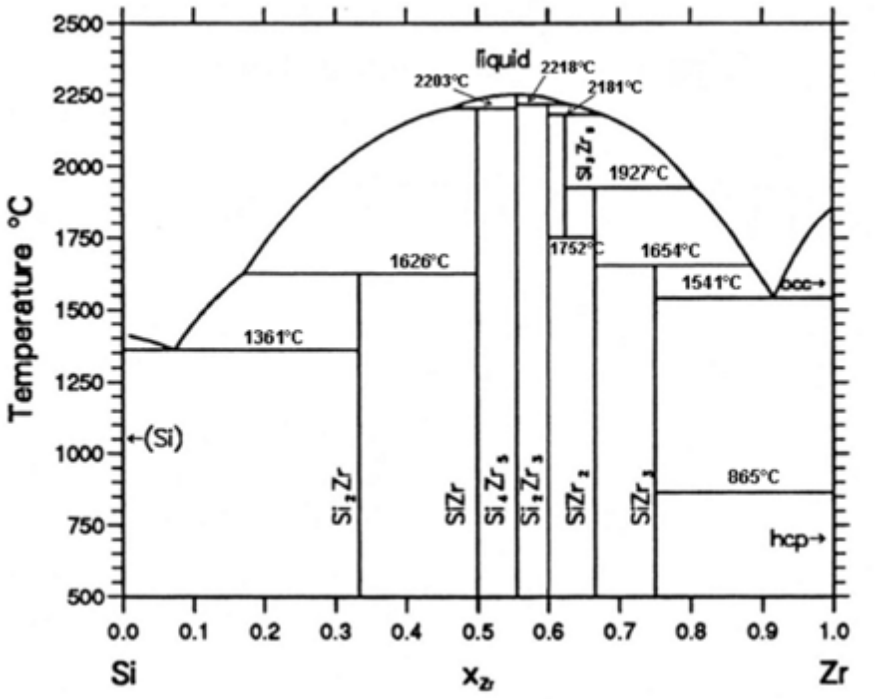

FIG. 2.25. Zr–Si phase diagram (this image was published in Ref. [2.127], copyright Elsevier, 1994).

2.4.4.13. Zr–Cu system

Copper might be present in zirconium as an impurity and could be used in a small quantity as an additive to zirconium to raise its corrosion resistance in steam (Fig. 2.6). A thermodynamic description of this system has been performed [2.129] (Fig. 2.26). Six intermediate compounds are identified in the system [2.45, 2.130–2.135]. The compound with the highest zirconium concentration is Zr_2Cu (25.83 wt% Cu), which has a tetragonal

crystal structure. Between Zr_2Cu and β_{Zr}, a eutectic reaction is available at a temperature of about 1279 K (997°C) and 30.0 at.% (23.0 wt%) Cu. The maximum solubility limit of copper in β_{Zr} at the eutectic temperature is about 5.3 at.% (3.75 wt%). Copper lowers the temperature of the $\alpha \rightarrow \beta_{Zr}$ transformation. The eutectoid reaction $\beta_{Zr} \rightarrow Zr_2Cu + \alpha_{Zr}$ proceeds at 1089 K (816°C) for a Cu concentration of 2.2 at.% (1.54 wt%). At this temperature, the solubility limit of copper in α_{Zr} is <0.2 at.% (0.14 wt%).

In most technical specifications, the concentration of copper is restricted to <50 ppm (0.007 at.%).

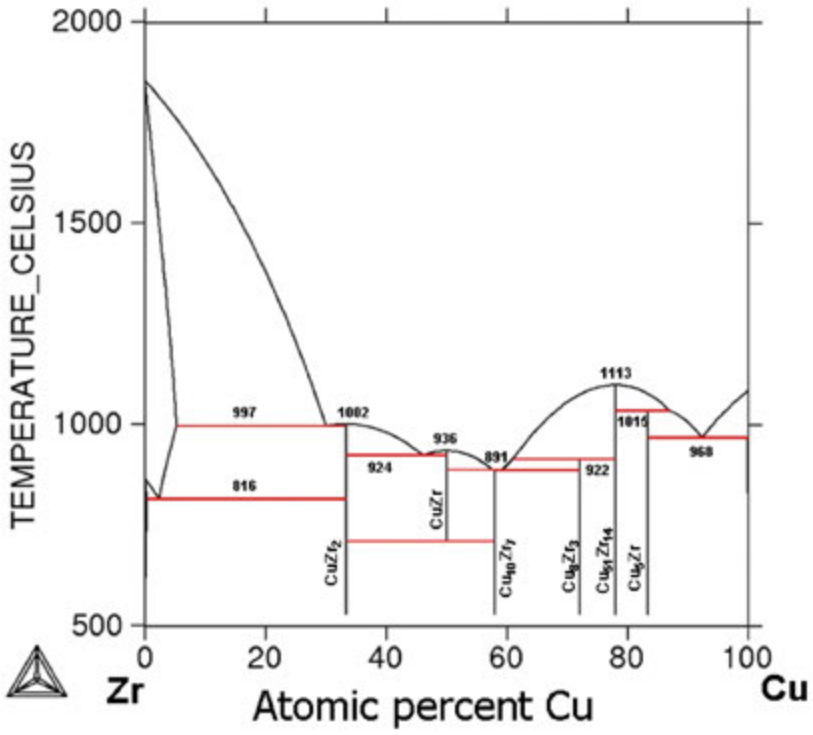

FIG. 2.26. Zr–Cu phase diagram (reproduced from Ref. [2.129], with permission of Springer).

2.4.4.14. Zr–Hf system

Hafnium is a critical element for zirconium. These elements are found together in nature but, because Hf has a large capture cross-section for thermal neutrons, for nuclear applications they have to be separated, as described in Chapter 3. The Zr–Hf phase diagram is illustrated in Fig. 2.27 [2.49]. Zr and Hf are completely soluble in the liquid state and form continuous solid solutions in the α and β phases.

In technical specifications, the concentration of hafnium is restricted to 100 ppm (0.005 at.%) with enriched fuel, but lowered to 50 ppm (0.0026 at.%) with natural UO_2.

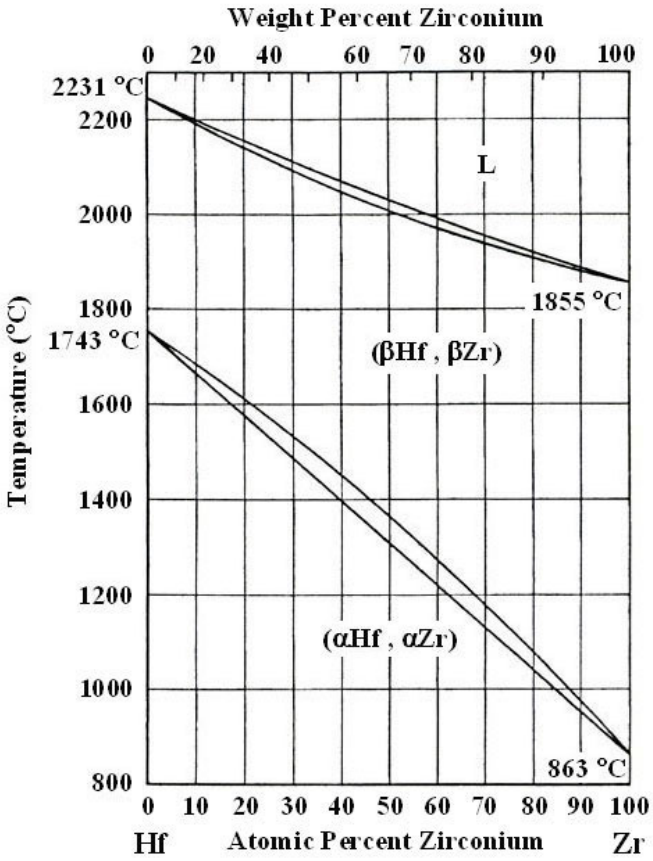

FIG. 2.27. Zr–Hf phase diagram (reproduced from Ref. [2.49], with permission of Springer).

2.4.4.15. Zr–Be system

Okamoto et al. [2.136] have critically assessed the Zr–Be phase diagram based mainly on experimental work found in the literature and their own thermodynamic modelling. A thermodynamic analysis has been performed by combining the thermodynamic properties based on ab initio energetic calculations with the available experimental data on the phase boundaries of this system [2.137] (Fig. 2.28). Four intermetallic compounds are identified in this system: $ZrBe_2$, $ZrBe_5$, Zr_2Be_{17} and $ZrBe_{13}$.

The compound with the highest zirconium concentration is $ZrBe_2$ (16.5 wt% (66.6 at.%) Be), which has a hexagonal crystal structure. Between $ZrBe_2$ and β_{Zr}, a eutectic reaction is available at a temperature of about 1243 K (970°C) and 35.0 at.% (5.1 wt%) Be. The maximum solubility limit of beryllium in β_{Zr} at the eutectic temperature is about 4.0 at.% (3.75 wt%). Beryllium lowers the temperature of the $\alpha \rightarrow \beta_{Zr}$ transformation. The eutectoid reaction $\beta_{Zr} \rightarrow ZrBe_2+\alpha_{Zr}$ proceeds at 1073 K (800°C) with a Be concentration of 2.0 at.% (0.2 wt%). At this temperature, the solubility limit of Be in α_{Zr} is < 0.1 at.% (0.01 wt%). An alloy with the eutectic composition Zr-5.1 wt% Be is used to braze attachments onto CANDU fuel elements [2.138]. Otherwise, Be does not feature in technical specifications.

(a)

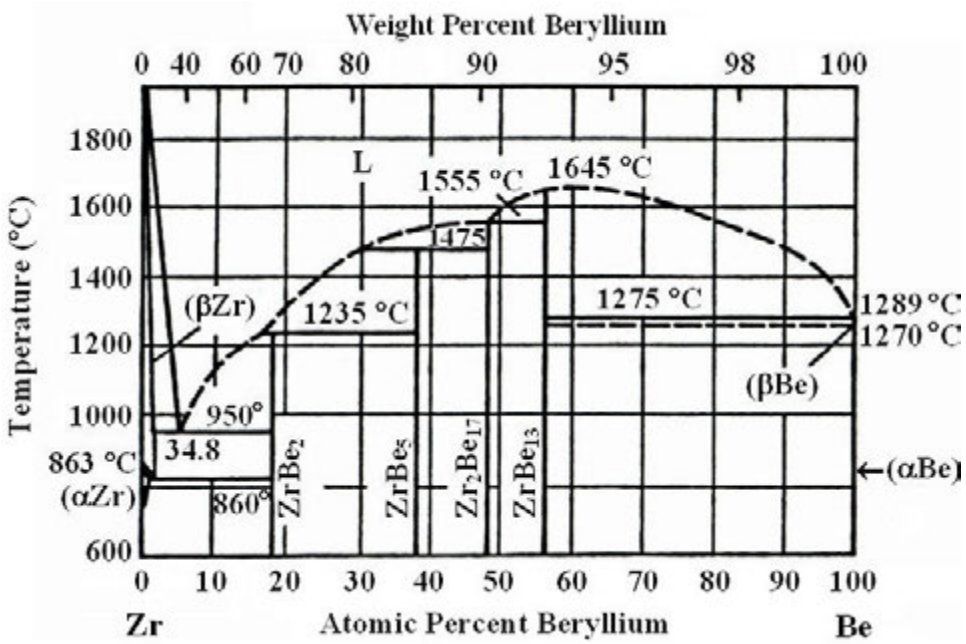

(b)

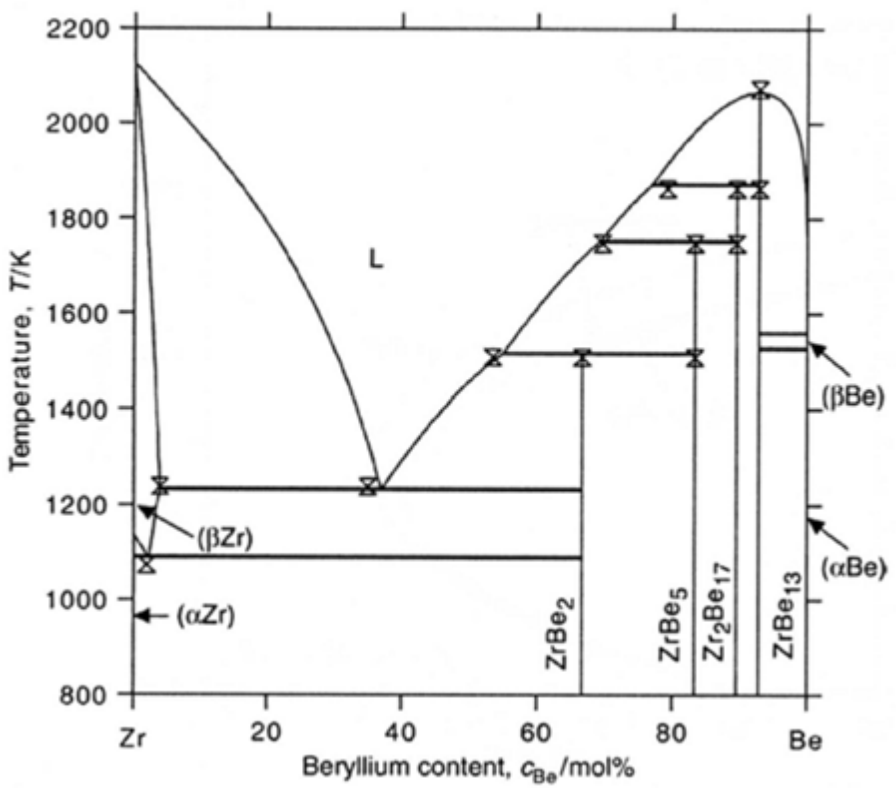

FIG. 2.28 (a) Zr–Be phase diagram (this image was published in Ref. [2.136], copyright Elsevier, 1990). (b) Zr–Be phase diagram (this image was published in Ref. [2.137], copyright Elsevier, 2006).

2.4.4.16. Zr–Y system

The Zr–Y phase diagram contains a eutectic reaction at 1636 K (1363°C) at 40.4 at.% (39.8 wt%) Y, as shown in Fig. 2.29 [2.69, 2.139]. The maximum solubility limit of yttrium in β_{Zr} at the eutectic temperature is about 3.9 at.% (3.8 wt%). Yttrium raises the temperature of the $\alpha \rightarrow \beta$ transformation of zirconium to the peritectoid reaction temperature 1159 K (886°C). The maximum solubility of yttrium in α_{Zr} is around 1 at.% (1 wt%). Quenching from the liquid state leads to metastable solid solutions with the HCP crystal lattice. Small quantities of yttrium increase the corrosion resistance and tensile strength of zirconium. Attempts have been made to exploit the high stability of yttrium hydride to limit the mobility of hydrogen in Zr-2.5Nb. An alloy containing 1.4–1.7 at.% (1.36–1.66 wt%) was effective in reducing hydride cracking but its corrosion resistance was very poor, its toughness was low and solid solution strengthening from oxygen was much reduced because of additional gettering by the yttrium [2.140, 2.141]. Dispersions of yttria have been proposed for strengthening at 773 K (500°C) but the benefits appeared marginal [2.142, 2.143] and the idea has not been pursued. For standard alloys, Y is not considered in technical specifications.

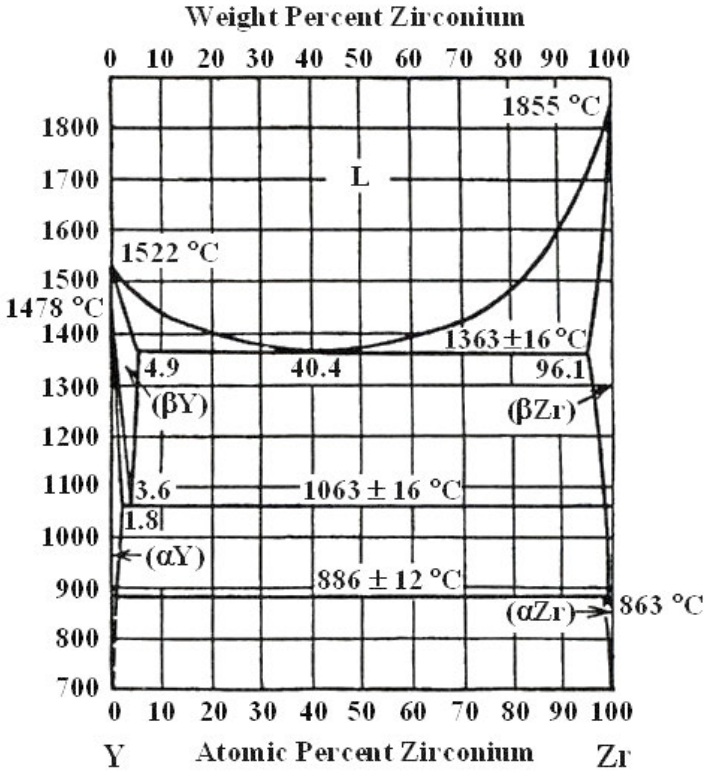

FIG. 2.29. Zr–Y phase diagram [2.139].

2.4.4.17. Zr–P system

No Zr–P phase diagram has been constructed, but six zirconium phosphides have been identified. P_2Zr decomposes into P vapour and α_{ZrP} on heating at around 1123 K (850°C) in vacuum [2.109, 2.144]. Additionally, α_{ZrP} and β_{ZrP} contain between 47.0 and 49.7 at.% (23.1–25.1 wt%) P [2.45]. The $\alpha_{ZrP} \rightarrow \beta_{ZrP}$ transformation is not only temperature but also pressure dependent. When heated in vacuum to 1798 K (1525°C), β_{Zr} loses some phosphorus

and transforms into α_{ZrP}. Its retransformation is only feasible at lower temperatures and given an excess pressure of phosphorus. The analogous system in titanium has a eutectic reaction with Ti_3P and very little solid solubility in either β- or α-Ti [2.145].

Phosphorus can be present in zirconium as an impurity. Little is known of the influence exerted by phosphorus on the corrosion of zirconium. In small quantities, P embrittles zirconium. Institutional specifications for nuclear components do not mention P, but some users specify a limit of 10 ppm (0.0029 at.%) while in practice producers limit phosphorus concentration to 6 ppm (0.0018 at.%).

2.4.4.18. Zr–Mo system

The corrosion resistance of dilute Mo alloys could be made superior to that of Zircaloy-4 once an optimum heat treatment was applied [2.146]. The mechanical properties and resistance to corrosion of Zr-1.2 wt% Sn containing different amounts of Mo have been studied [2.147]. The addition of Mo in Zr-Nb-Sn alloys improves their mechanical properties and restrains abnormal grain growth during exposure of this material to high temperatures [2.147, 2.148].

Jerlerud-Pérez and Sundman [2.149] carried out a thermodynamic assessment of this system based on available experimental data on the phase diagram and estimated enthalpy values of the intermetallic compound, as shown in Fig. 2.30. Molybdenum is a β_{Zr} stabilizer. One intermediate phase is reported in this system: Mo_2Zr, with a Laves-C15 cubic type structure. There are three invariant reactions in this system. The eutectic, involving β_{Zr} and Mo_2Zr, takes place at about 1825 K (1552°C) at 28.6 at.% (29.6 wt%) Mo, and the eutectoid $\beta_{Zr} \rightarrow \alpha_{Zr} + Mo_2Zr$ at 1050 K (777°C) at 4.3 at.% (4.5 wt%). The maximum solubility limit of Mo in β_{Zr} and α_{Zr} are respectively equal to 21 at.% (21.9 wt%) Mo and 0.2 at.% (0.21 wt%) Mo.

Although molybdenum may be beneficial for zirconium alloys, the technical specification in current commercial alloys limits the concentration of Mo to 50 ppm (0.0048 wt%).

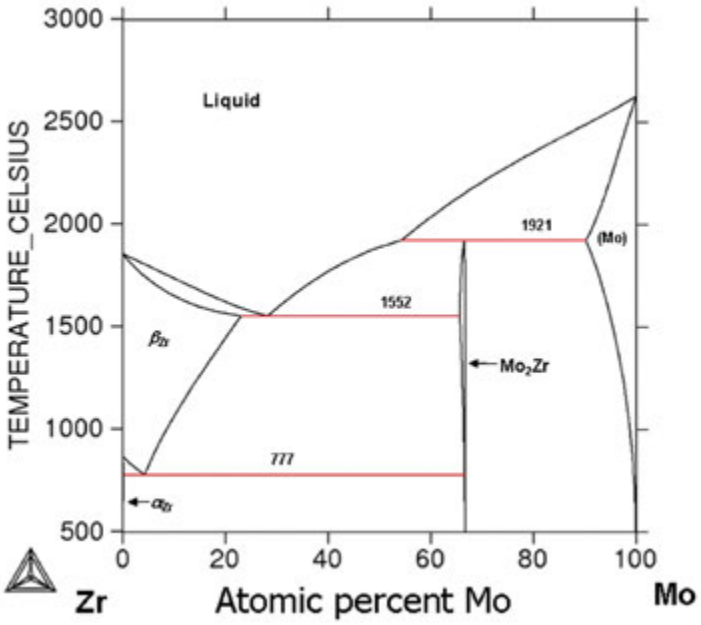

FIG. 2.30. Zr–Mo phase diagram (this image was published in Ref. [2.149], copyright Elsevier, 2003).

2.4.4.19. Zr–Gd system

A thermodynamic assessment of this system is described in Ref. [2.150] and shown in Fig. 2.31. The Zr–Gd phase diagram contains a eutectic reaction with no intermediate phases. It is constituted by the following terminal phases: α_{Gd} and α_{Zr}, with HCP structure, and β_{Gd} and β_{Zr}, with BCC structure. The eutectic reaction liquid → α_{Gd} + β_{Zr} proceeds at 1486 K (1213°C) at a Gd concentration of about 87 at.% (92 wt%). The maximum solubility limit of Gd in β_{Zr} is about 7 at.% (11.5 wt%). A peritectoid reaction proceeds at 1162 K (889°C) at a Gd concentration of 2.5 at.% (4.2 wt%), which is also the maximum solubility limit of Gd in α_{Zr}.

Gadolinium has a very high thermal neutron capture cross-section (σ = 49 000 b for Gd^{157}) and fast burn-out rate, and is of interest in nuclear reactors as a burnable poison for short lived cores or low burnup application in longer lived cores [2.151]. For standard alloys, Gd is not considered in technical specifications but is assumed to be very low.

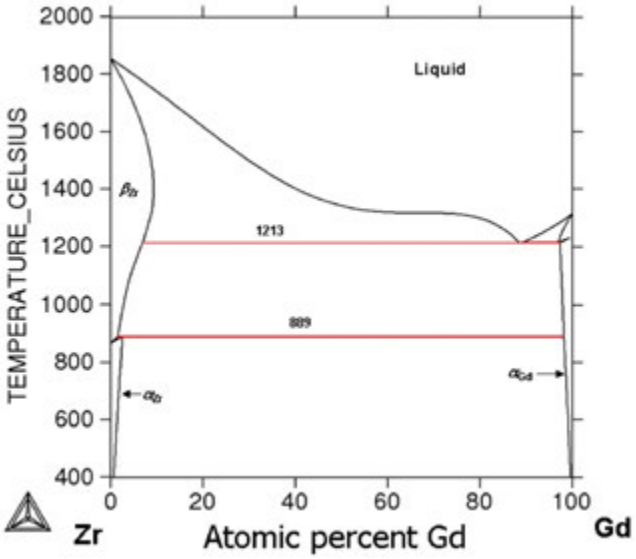

FIG. 2.31. Zr–Gd phase diagram (reproduced from Ref. [2.150] with permission of Springer).

2.4.4.20. Zr-V system

Adding V to zirconium [2.146] and Zircaloy-4 [2.152] can improve corrosion resistance. The improvement in mechanical properties and resistance to corrosion of Zr-1.2 wt% Sn containing different amounts of V have been studied by Jago et al. [2.147].

A thermodynamic assessment of this system was performed [2.153] (Fig. 2.32). One intermediate compound exists in this system: V_2Zr, with a Laves-C15 cubic type structure. Three invariant reactions proceed in this system: a peritectic reaction L + β_V → V_2Zr at 1586 K (1313°C), a eutectic reaction L → V_2Zr + β_{Zr} at 1525 K (1252°C) at 43 at.% (29.6 wt%) V, and a eutectoid reaction β_{Zr} → V_2Zr+α_{Zr} at 1046 K (773°C) at 8.6 at.% (5.0 wt%). The maximum solubility limit of V in β_{Zr} is about 17 at.% (10.3 wt%) and 3.1 at.% (1.76 wt%) in α_{Zr}.

The institutional technical specifications do not include limits on V but some users require the concentration of V to be < 50 ppm (0.009 at.%).

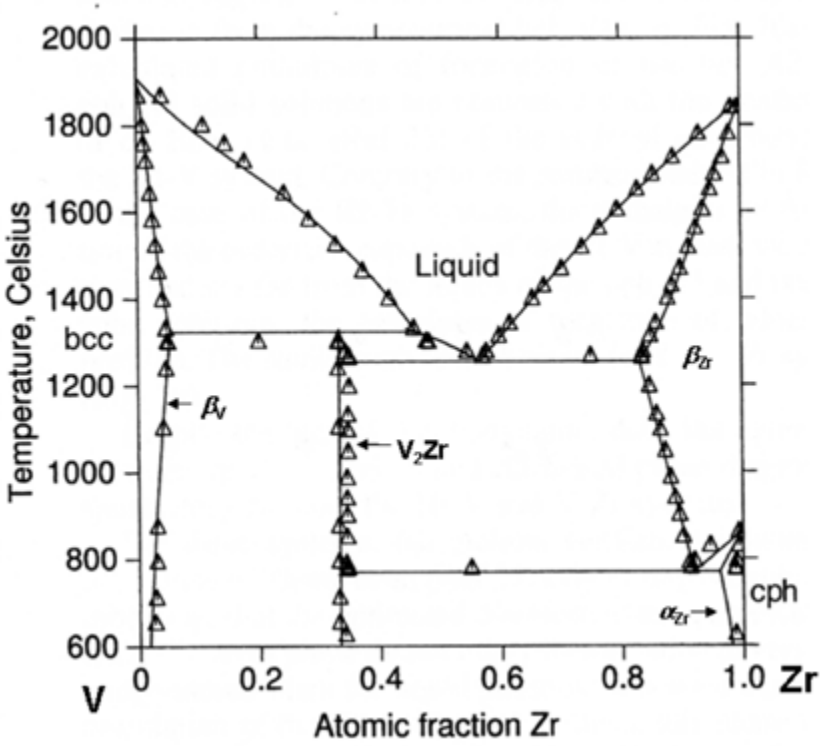

FIG. 2.32. Zr–V phase diagram (reproduced from Ref. [2.153], with permission of Springer).

2.4.5. Ternary systems of zirconium alloys

2.4.5.1. Zr–Nb–Sn system

In the Zr–Nb–Sn system the zirconium-rich corner has been investigated up to 30 at.% Nb and 10 at.% Sn (29.5 wt% Nb, 12.6 wt% Sn). The isothermal sections of the zirconium corner have been constructed at 1213 K, 1123 K, 998 K and 773 K (940°C, 850°C, 725°C and 500°C) (Fig. 2.33) [2.14].

The β stabilizing effect of Nb in the system is higher than the α stabilizing effect of tin. Peritectoid reactions proceed in the system [2.45]:

$$\beta_1 + Nb_3Sn \leftrightarrow \beta_2 + Zr_4Sn, \text{ terminating at 923 K (650°C)} \quad (2.2)$$

$$\beta_3 + Zr_4Sn \leftrightarrow \alpha + \beta, \text{ terminating at 893 K (620°C)} \quad (2.3)$$

At 1323 K (1050°C) in the zirconium corner there is a β solid solution region (up to 7 at.% Sn (8.9 wt%)) along the Zr–Sn side and up to 2.5 at.% (3.2 wt%) Sn at 30 at.% (30.2 wt%) Nb that borders the regions of $\beta+Zr_4Sn$ and $\beta+Nb_3Sn$.

After quenching from 773 K (500°C) in the zirconium corner, a region of the α solid solution (a little more than 1 at.% Nb+Sn) is located contiguous to the regions $\beta + Zr_4Sn$ and $\alpha + \beta_{Nb}$ (the niobium base solid solution). This ternary system forms the basis for the alloys E365 and ZIRLO.

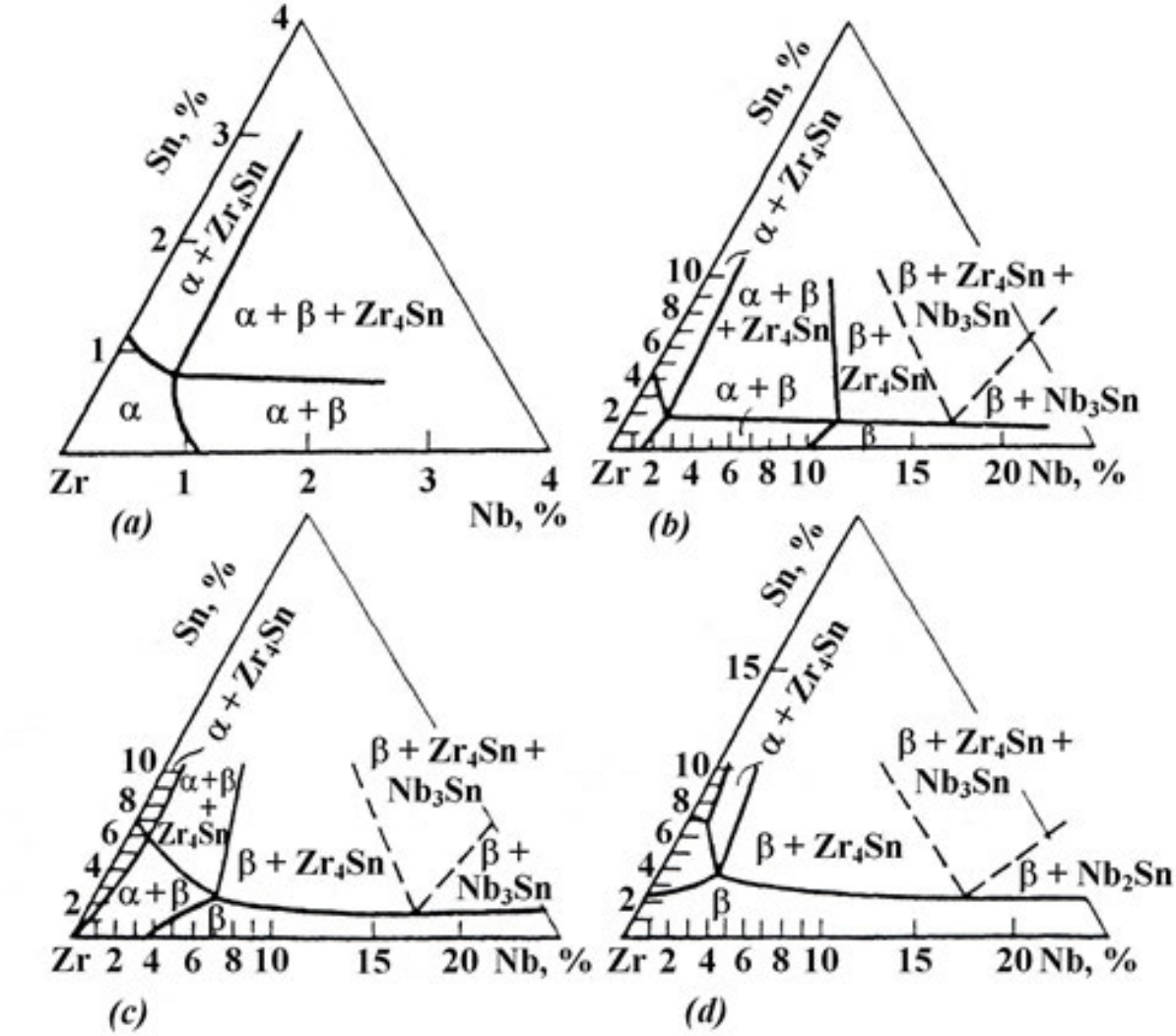

FIG. 2.33. Isothermal section of the Zr–Sn–Nb system after thermal anneal at (a) 773 K (500°C); (b) 998 K (725°C); (c) 1123 K (850°C); and (d) 1213 K (940°C) [2.14].

2.4.5.2. Zr–Sn–Fe system

Figure 2.34 illustrates isothermal sections of the Zr–Sn–Fe system at 1073 K and 1173 K (800°C and 900°C) [2.45]. The phase diagram is complicated, particularly on the Zr–Sn side. Four non-variant reactions are observable in the zirconium corner of the ternary system:

$$L \rightarrow \beta + \theta + ZrFe_2 \ (1203\ K\ (930°C)\ ) \quad (2.4)$$

$$\beta + Zr_4Sn \rightarrow \alpha + Zr_4Sn_3 \text{ and } \beta + Zr_5Sn_3 \rightarrow \alpha + \theta \quad (2.5)$$

(the above reactions proceed in succession between 1253 K and 1173 K (980°C and 900°C)).

$$\beta + \theta \rightarrow ZrFe_2 \ (1063-1073\ K\ (790-800°C\ )) \quad (2.6)$$

Nieva and Arias [2.154] have studied this system experimentally and confirmed the existence of two ternary intermetallic phases named θ and N and characterized a third called X phase. They proposed two partial isothermal sections at 1073 K and 1173 K (800°C and 900°C), shown in Figs 2.35 and 2.36. They report that Zr_2Sn and Zr_5Sn_3 phases have a low solubility limit of Fe and that Zr_3Fe and Zr_2Fe show a low solubility limit of Sn. In contrast, a moderate solubility limit of Fe in the Zr_5Sn_4 phase and Sn in the $ZrFe_2$ was measured. This system is important for the Zircaloys.

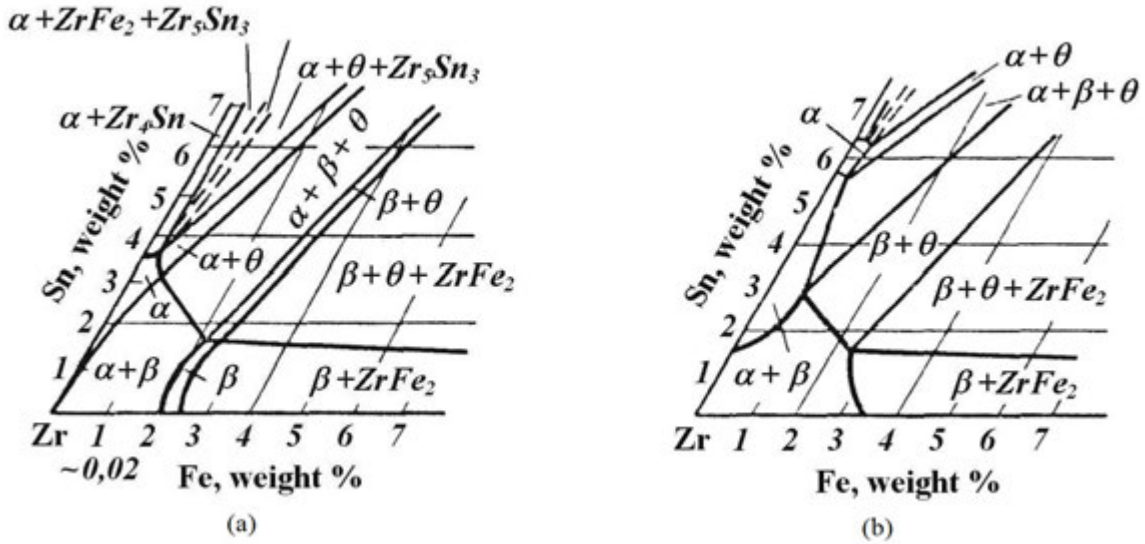

FIG. 2.34. Isothermal section in the zirconium part of Zr–Sn–Fe system after thermal anneal at (a) 1073 K (800°C) and (b) 1173 K (900°C) [2.45].

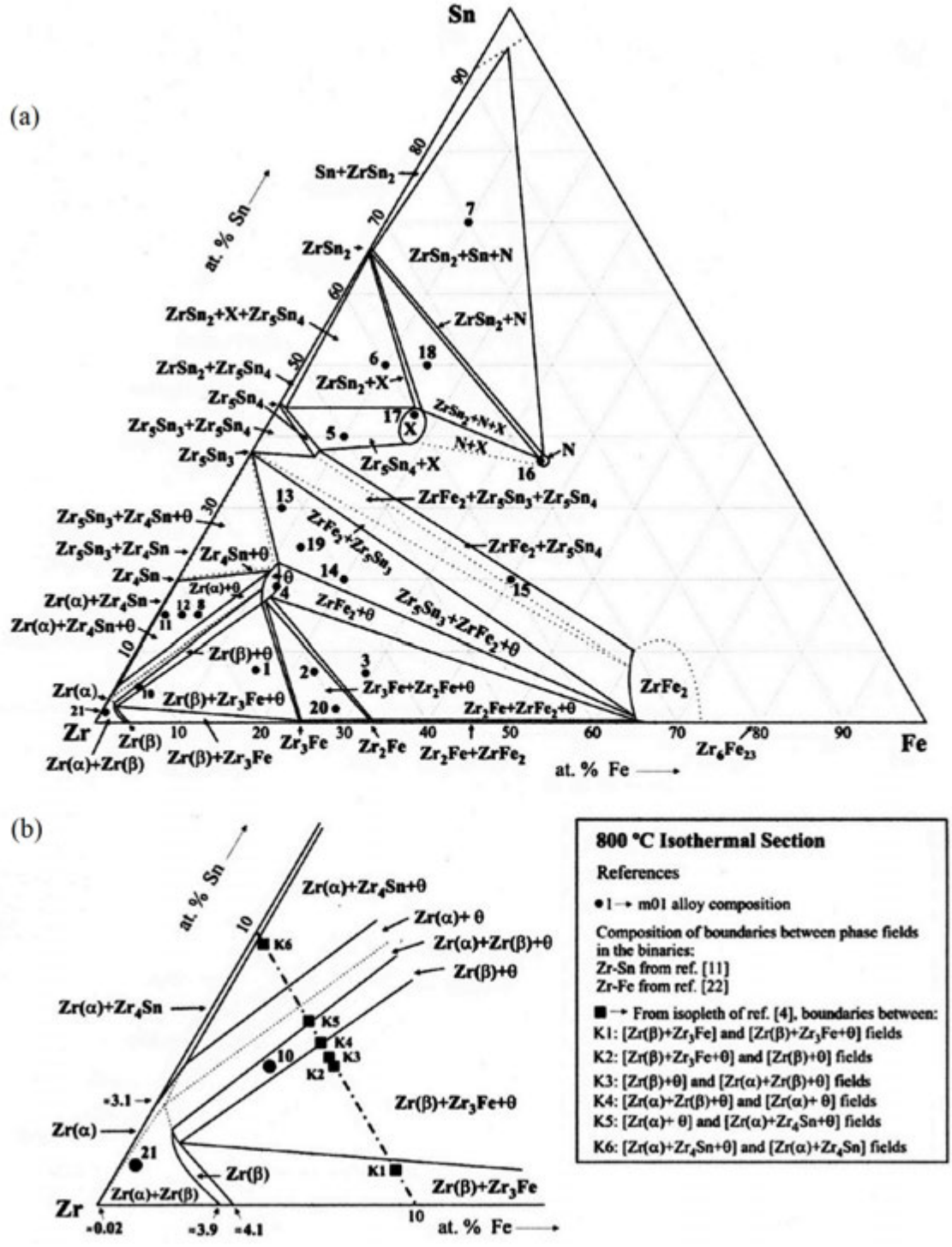

FIG. 2.35. Isothermal section of the Zr–Sn-Fe system in the Zr-rich part at 1073 K (800°C) (this image was published in Ref. [2.154], copyright Elsevier, 2006).

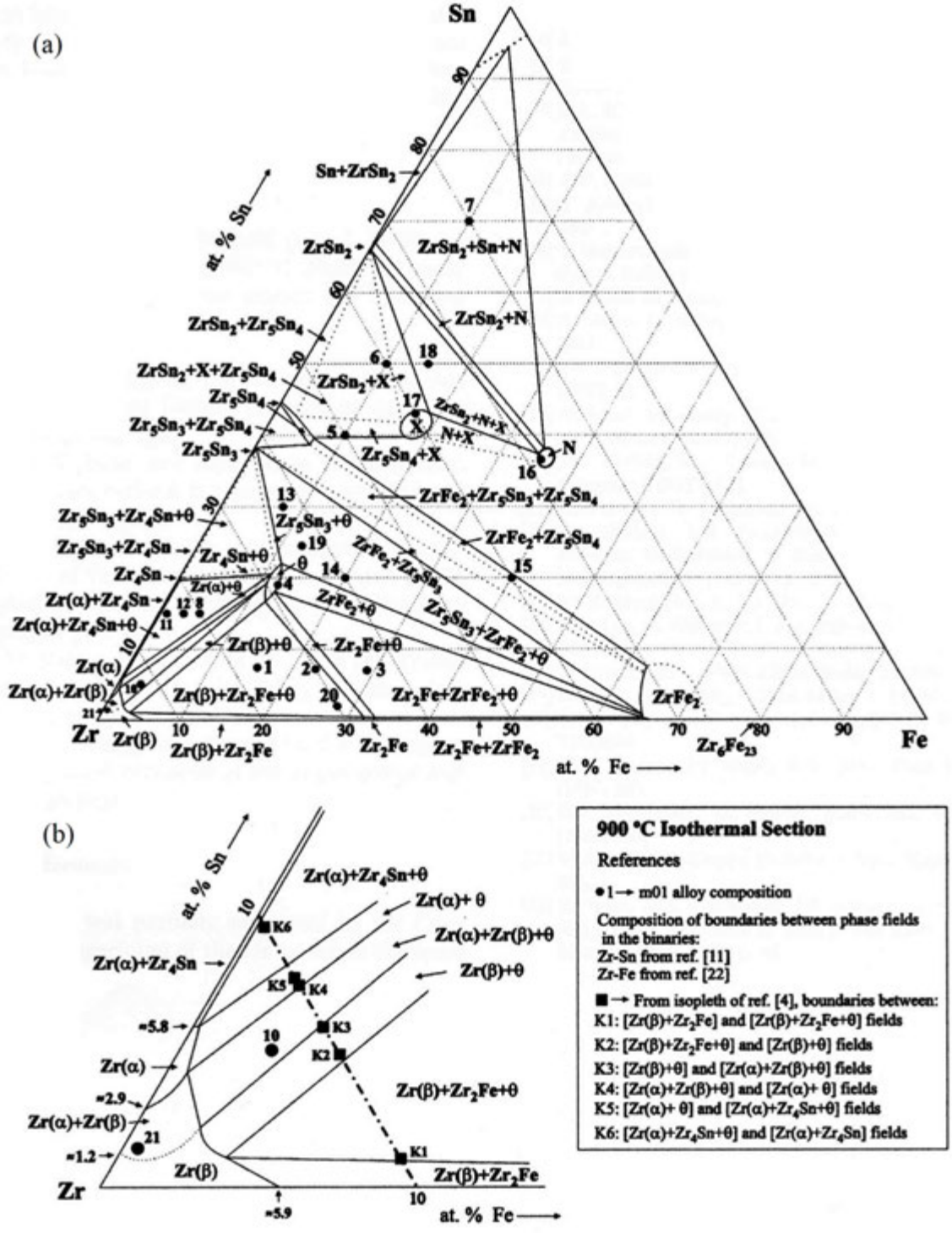

FIG. 2.36. Isothermal section of the Zr–Sn–Fe system in the Zr-rich part at 1173 K (900°C) (this image was published in Ref. [2.154], copyright Elsevier, 2006).

2.4.5.3. Zr–Nb–Fe system

The first results of isothermal sections in the Zr–Nb–Fe system were published in Ref. [2.155]. One intermetallic phase (ZrNbFe) was established experimentally. At the same time there were indications of the existence of the Laves phases (Fe_2Nb, Fe_2Zr), $Fe_{23}Zr_6$ and

β_{Zr} in the system. The recent evolution of zirconium alloys containing Nb and Fe gave an impetus to studying the ternary ZrNbFe system [2.79, 2.156, 2.157].

The results of investigations by Russian and French scientists [2.79, 2.156, 2.157] of the isothermal sections of this system were similar (Figs 2.37, 2.38). Aside from the α_{Zr} and β_{Nb} solid solutions, two intermetallic phases (ZrNbFe) that differ in their crystal lattices and concentrations of zirconium and niobium are present in the system: $Zr(Nb,Fe)_2$ with an HCP lattice (35 at.% Zr, 35 at.% Nb, 30 at.% Fe); $(Zr,Nb)_2Fe$ with an FCC lattice (60 at.% Zr, 10 at.% Nb, 30 at.% Fe). The existence of a homogeneity range for these two phases was also demonstrated [2.158]. The phase $(Zr,Nb)_2Fe$ exists in the temperature range 973–1023 K (700–750°C) while $Zr(Nb,Fe)_2$ forms from 923 to 1073 K (650 to 800°C) [2.79]. The alloys investigated in Refs [2.79, 2.157] differed in their concentration of oxygen: 700–800 ppm (about 0.40–0.45 at.%) in Ref. [2.157] and 1000–2800 ppm (about 0.57–1.58 at.%) in Ref. [2.79]. The two ternary intermetallic phases have been confirmed experimentally [2.158, 2.159]. The authors proposed two experimental isothermal sections at 1073 K and 1173 K (800°C and 900°C), showing the homogeneity ranges of these ternary phases (Figs 2.39, 2.40).

Thermodynamic assessments of this system have also been performed [2.73, 2.160], which are in good agreement (Figs 2.41, 2.42), except that Ref. [2.73] took into account the updated version of the Zr–Fe system [2.97]. This system is relevant for the E110, M5, E125 and Zr-2.5Nb alloys.

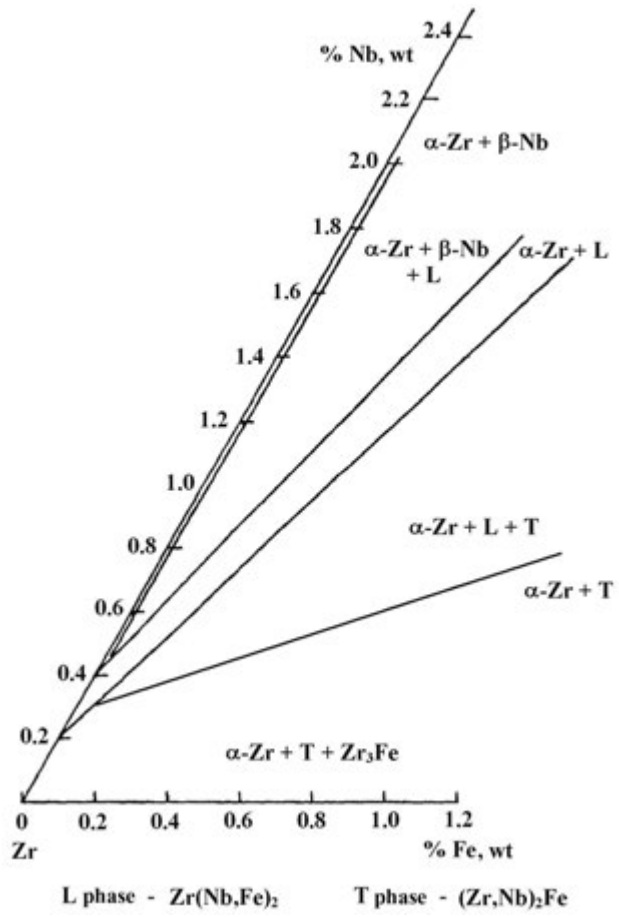

FIG. 2.37. Zirconium angle of ternary Zr–Nb–Fe system (thermal anneal at 772 K (500°C)) [2.157].

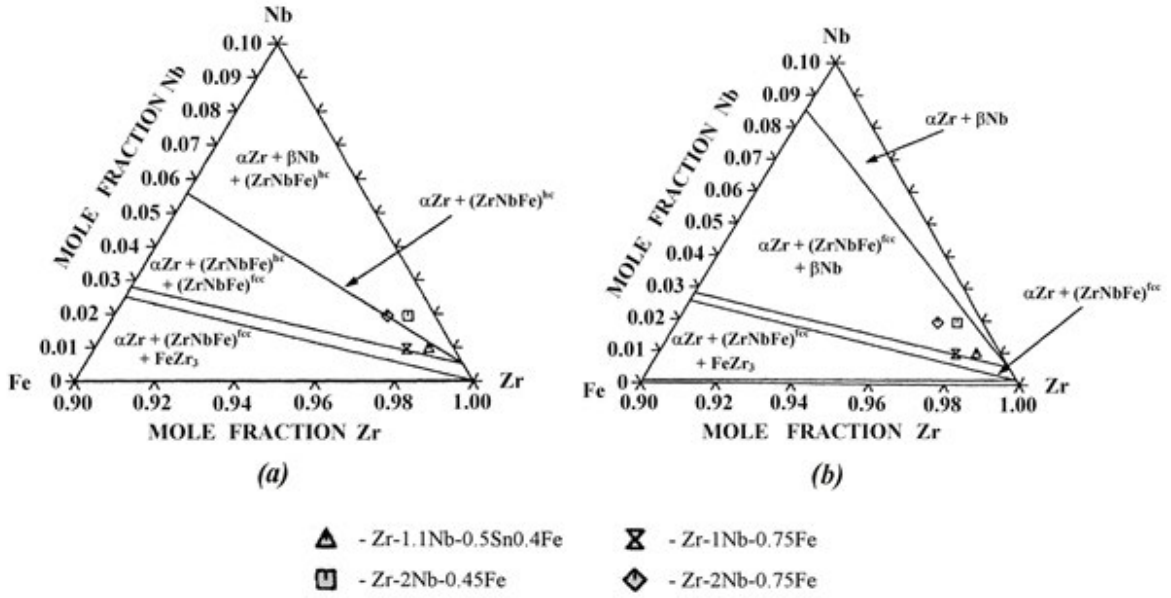

FIG. 2.38. Zirconium angle of ternary Zr–Nb–Fe system (thermal anneal at (a) 843 K (570°C) and (b) 953 K (680°C) (reprinted, with permission, from Ref. [2.79], copyright ASTM International).

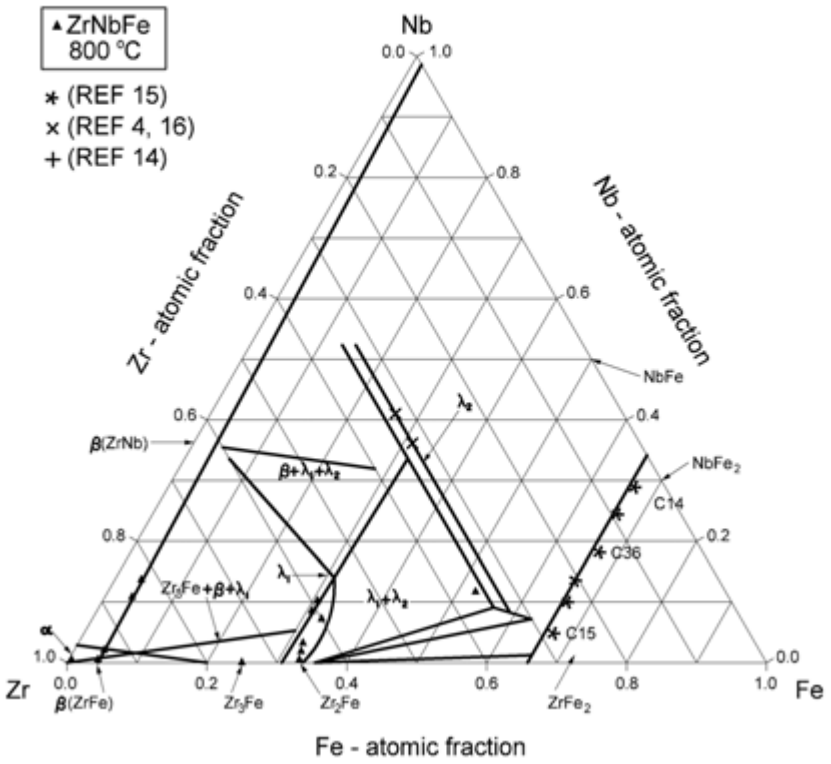

FIG. 2.39. Zr–Nb–Fe ternary system: Isothermal section determined experimentally at 1073 K (800°C) (this image was published in Ref. [2.158], copyright Elsevier, 2002).

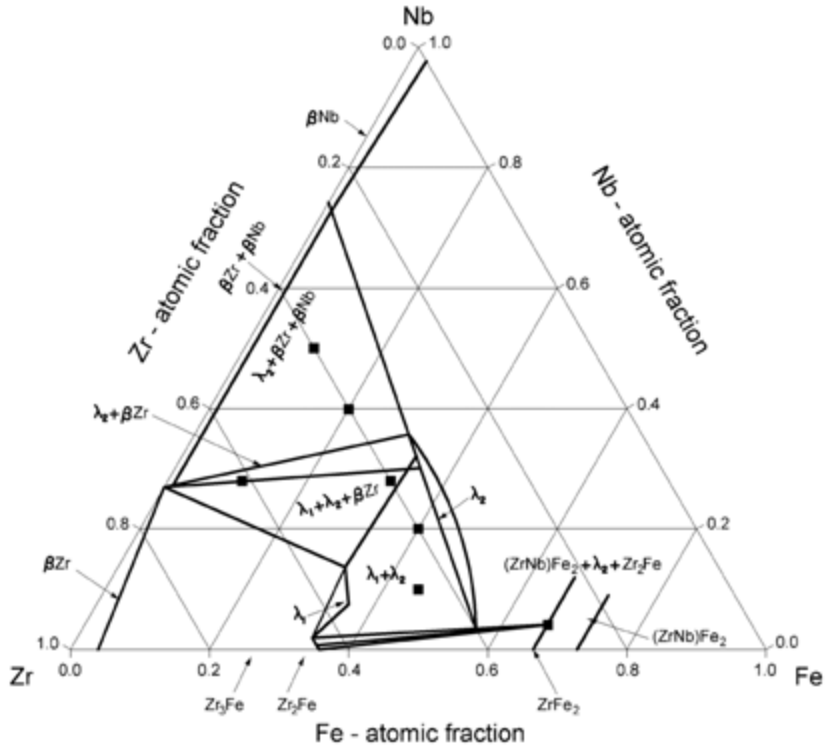

FIG. 2.40. Zr–Nb–Fe ternary system: Isothermal section determined experimentally at 1173 K (900°C) (this image was published in Ref. [2.159], copyright Elsevier, 2007).

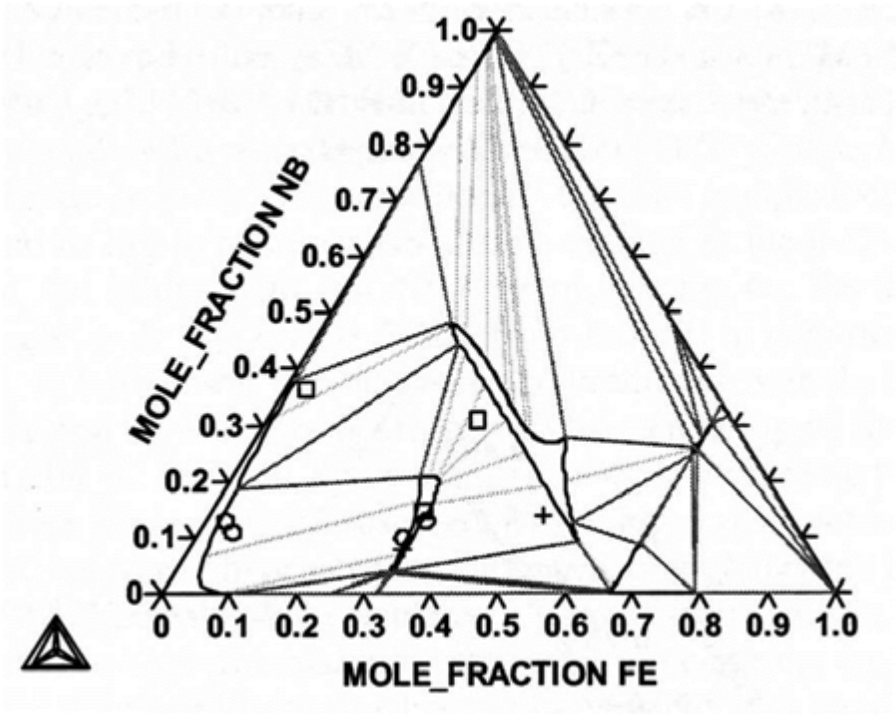

FIG. 2.41. Calculated isothermal section of the Zr–Nb–Fe ternary system at 1173 K (900°C) [2.160].

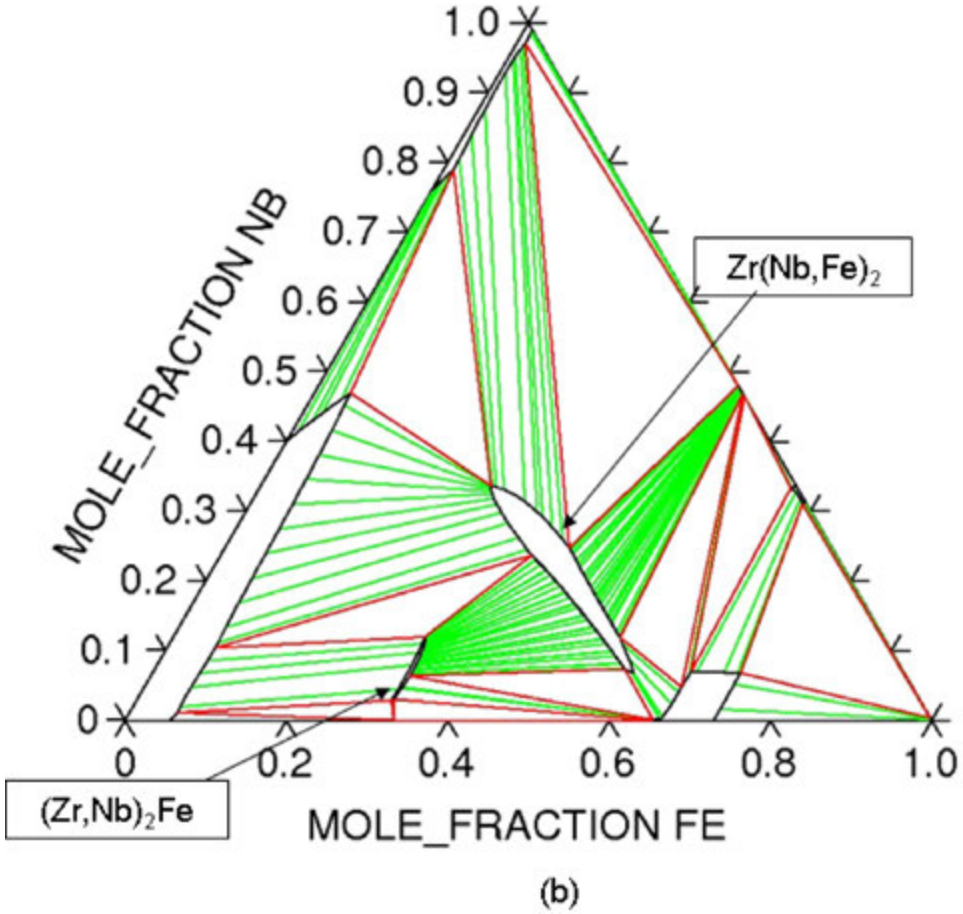

FIG. 2.42. Calculated isothermal section of the Zr–Nb–Fe ternary system at 1173 K (900°C) (reprinted, with permission, from Ref. [2.73], copyright ASTM International).

2.4.5.4. Zr–Fe–Cr system

An experimental study and a thermodynamic assessment of this system have been performed [2.161], which reported the presence of $Zr(Fe,Cr)_2$ phases that can have the Laves C14 or Laves C15 crystallographic structures and focused on the Zr-rich part of the system. The authors obtained good agreement comparing experimental data, included in the optimization process, with the corresponding calculated ternary sections at 973 K, 1073 K and 1148 K (700°C, 800°C and 875°C) in Fig. 2.43, and at 873 K and 1023 K (600°C and 750°C) in Fig. 2.44. An alloy of composition Zr-1.2 wt% Cr-0.1 wt% Fe was proposed for high temperature service.

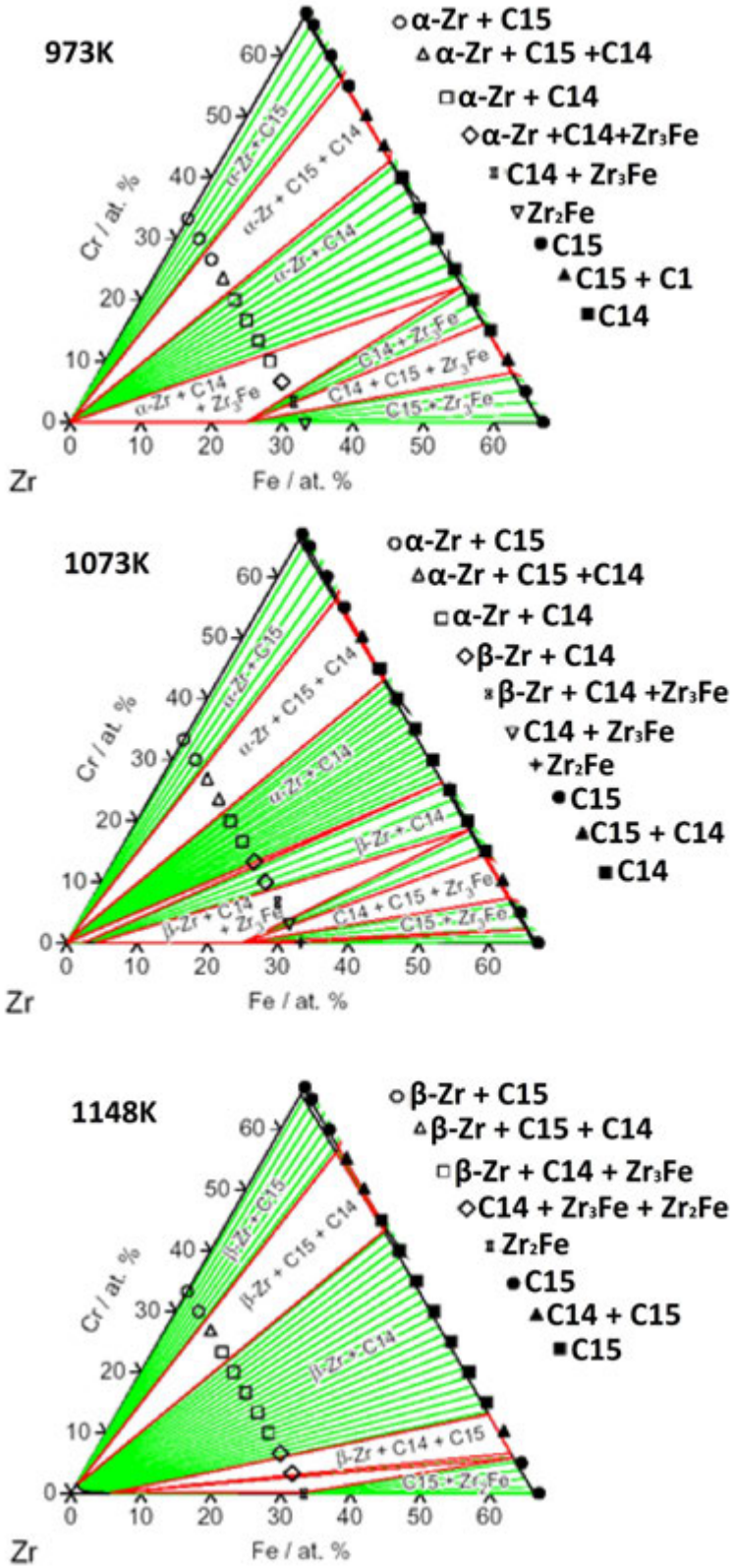

FIG. 2.43. Zr–Fe–Cr system: Three isothermal sections at 973 K (700°C), 1073 K (800°C) and 1148 K (875°C) comparing experimental data from the literature and calculated results (reprinted, with permission, from Ref. [2.161], copyright ASTM International).

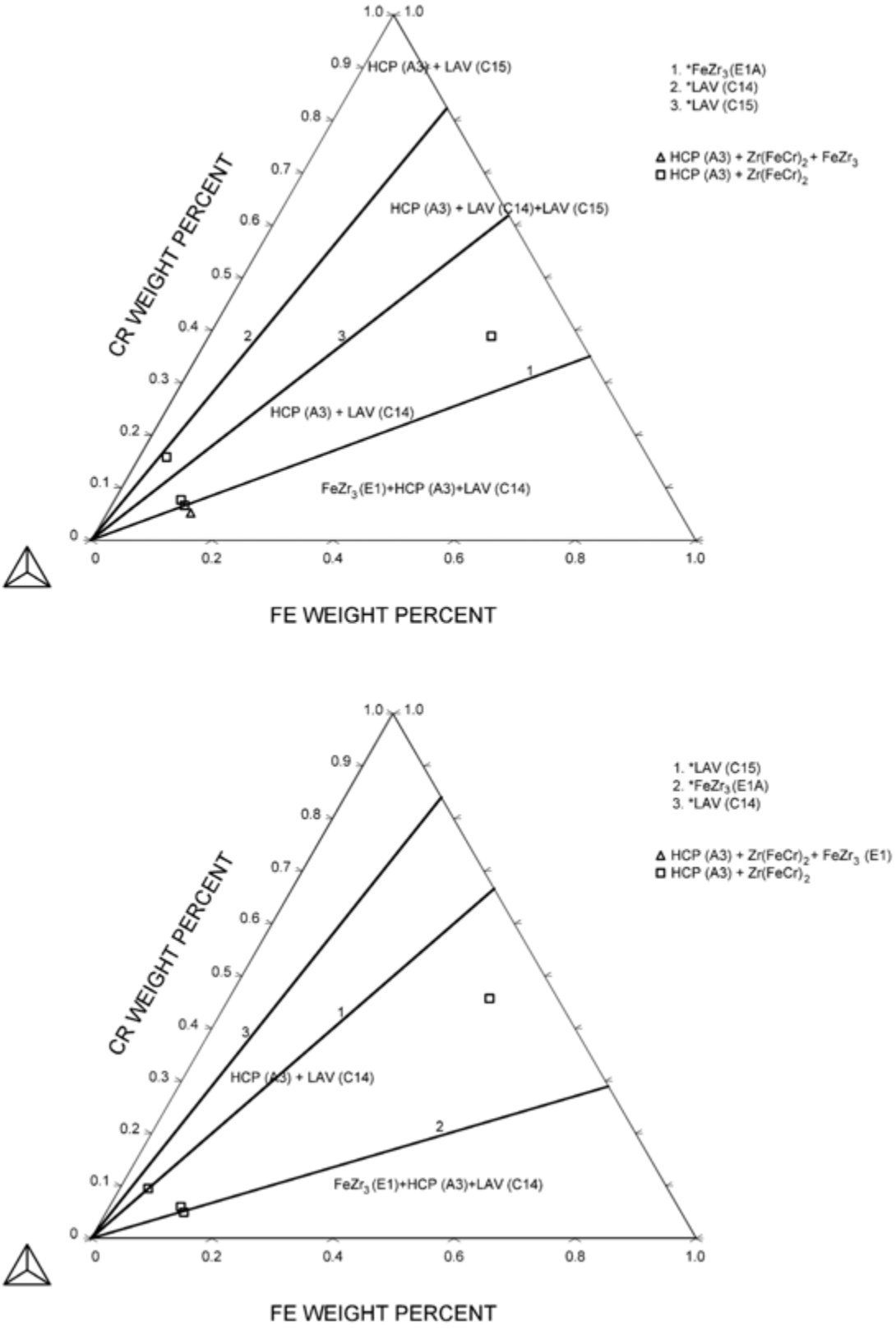

FIG. 2.44. Enlargement of the isothermal sections of the Zr–Fe–Cr system at 873 K (600°C) (top) and 1023 K (750°C) (bottom) (reprinted, with permission, from Ref. [2.161], copyright ASTM International).

2.4.5.5. Zr–Fe–Ni system

A calculated isothermal section at 1000 K (1273°C) and an isoplethal section at 75 at.% Fe are presented in Fig. 2.45, based on a thermodynamic assessment of this system [2.161]. The interaction between Fe and Ni is assumed to be ideal, since no experimental data are available. The phases $Zr_2(Fe, Ni)$ and $Zr_3(Fe, Ni)$ are reported.

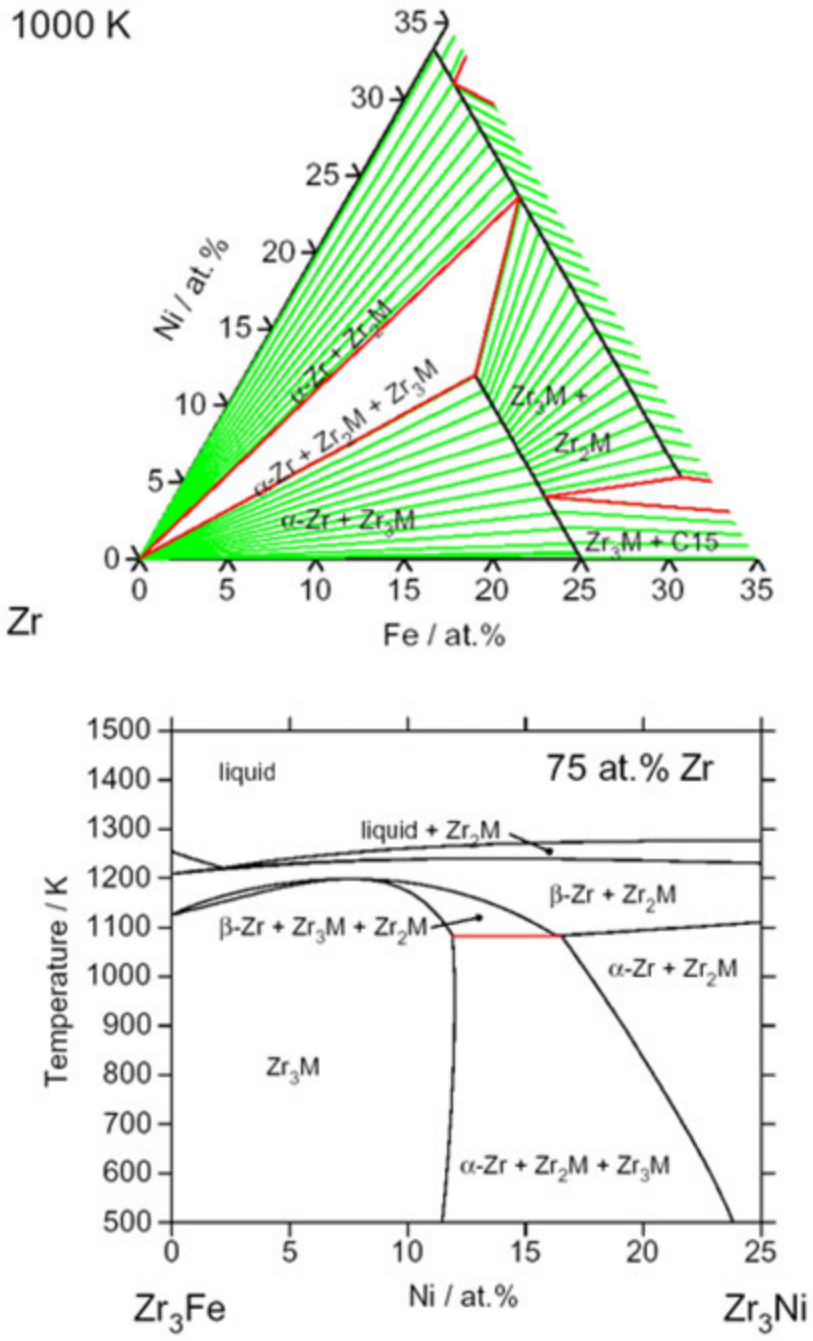

FIG. 2.45. Zr–Fe–Ni system: calculated isothermal section at 1000 K (727°C) and isoplethal section at 75% at.% Fe (reprinted, with permission, from Ref. [2.161], copyright ASTM International).

2.4.5.6. Zr–Ni–Cr system

An experimental investigation and a thermodynamic assessment of this system was performed [2.161]. Four experimental alloys were fabricated and annealed at 873 K and 1023 K (600°C and 750°C). Iron was present as an impurity in the experimental alloys resulting in two intermetallic phases, $Zr(Fe,Cr)_2$ and $Zr_2(Fe,Ni)$. The thermodynamic assessment of this system is mainly based on the experimental work reported in Ref. [2.162]. An isothermal section obtained at 1273 K (1000°C) is presented in Fig. 2.46. Two ternary intermetallic phases are described: a Laves phase C15, originating from the binary system Cr–Zr, which changes to C14 as the Ni concentration increases.

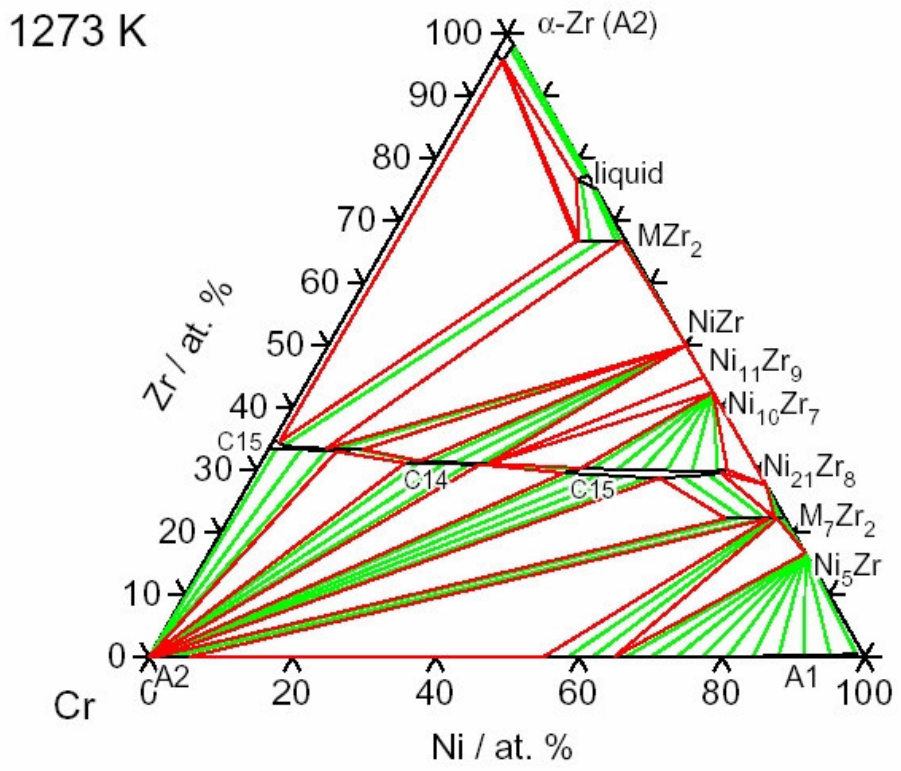

FIG. 2.46. Zr–Cr–Ni system calculated isothermal section at 1273 K (1000°C) (reproduced from Ref. [2.162], with permission of Springer).

2.4.5.7. Zr–Nb–O system

A thermodynamic assessment of this system has been performed [2.163] based on experimental data available in the literature. This is a combination of the three binary systems: Zr–O, Nb–O and Zr–Nb. There is no ternary intermetallic phase in this system. Calculated isothermal sections at 1273 K and 1773 K (1000°C and 1500°C) are presented in Figs 2.47 and 2.48. This system is relevant to Zr-Nb alloys because in practice they may contain close to 1 at.% (1660 ppm) oxygen.

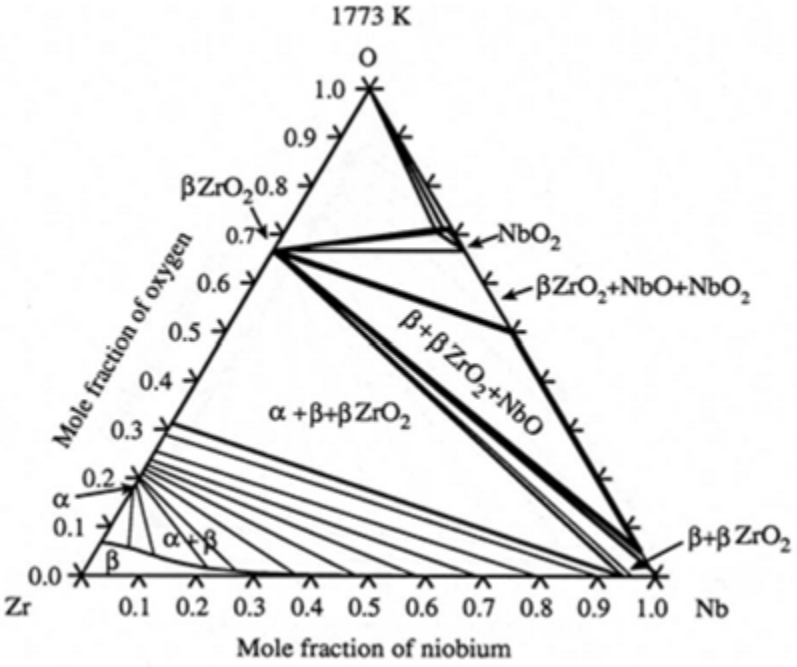

FIG. 2.47. Zr–Nb–O system: Calculated isothermal section at 1773 K (1500°C) (this image was published in Ref. [2.163], copyright Elsevier, 2007).

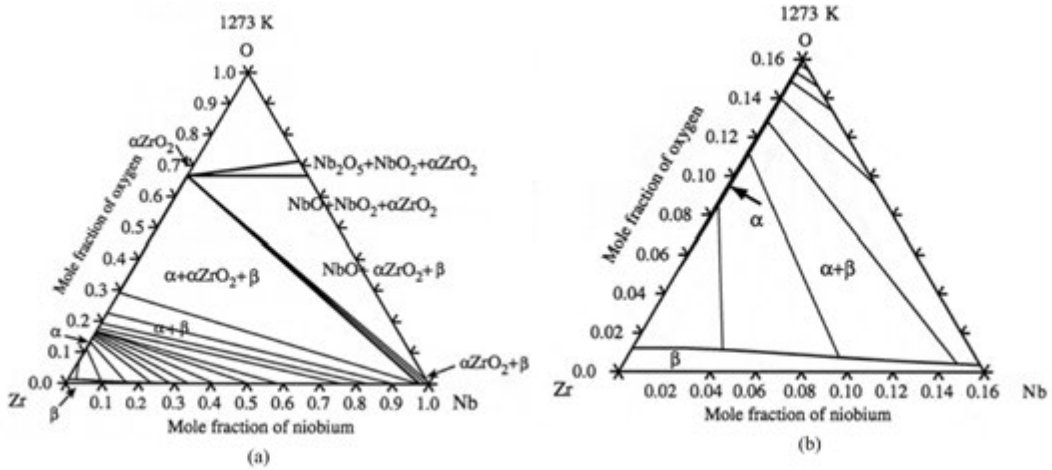

FIG. 2.48. Zr–Nb–O system calculated isothermal section (a) at 1273 K (1000°C) and (b) enlargement (this image was published in Ref. [2.163], copyright Elsevier, 2007).

2.4.5.8. Zr–Sn–O system

An experimental study of the Zr-rich part of the Zr–Sn–O system was carried out [2.164]. Eight experimental alloys were fabricated and annealed at 1323 K and 1573 K (1050°C and 1300°C), then the microstructure was characterized using different devices (light microscopy, X ray diffraction, electron microprobe). Figures 2.49 and 2.50 present isothermal sections at 1323 K and 1573 K (1050°C and 1300°C) deduced in Ref. [2.164] from their experimental results. These authors have shown that the Sn solubility limit in α_{Zr} was lower than 7 at.% (8.9 wt%) at 1323 K and 1573 K (1050°C and 1300°C). The study of this system is relevant to the behaviour at high temperatures of alloys containing Sn.

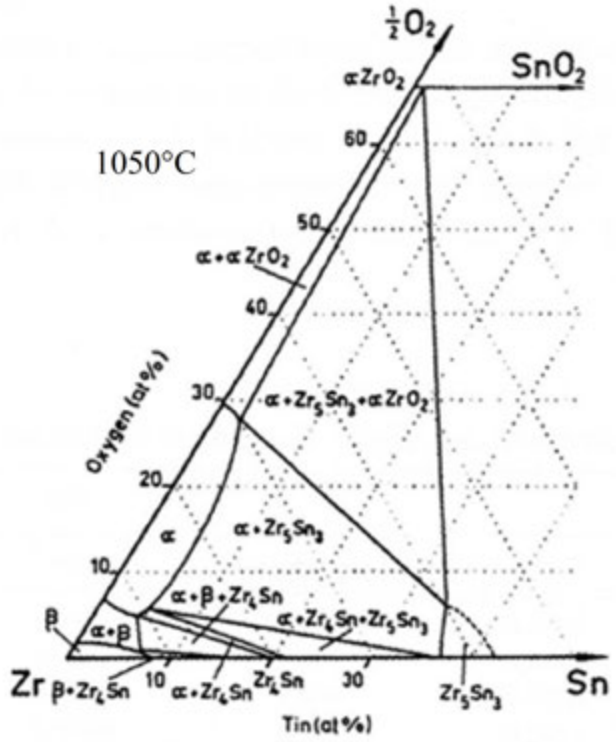

FIG. 2.49. Zr–Sn–O system: Experimental isothermal section at 1323 K (1050°C) (this image was published in Ref. [2.164], copyright Elsevier, 1999).

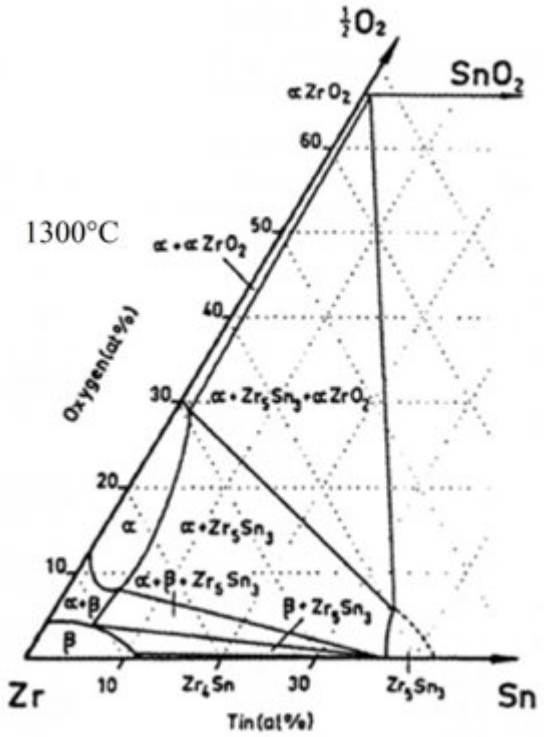

FIG. 2.50. Zr–Sn–O system: Experimental isothermal section at 1573 K (1300°C) (this image was published in Ref. [2.164], copyright Elsevier, 1999).

2.4.5.9. Zr–O–H system

An experimental thermodynamic study of the Zr–O–H system was performed [2.165]. The authors show that hydrogen solubility in the HCP α phase first increases with oxygen concentration and then decreases at higher oxygen contents. The H solubility in $\beta_{Zr(O)}$ first decreases with oxygen and then increases slightly. The H solubilities in the ZrO_2 were found to be from 10^{-5}–10^{-4} $mol_H \cdot mol_{oxide}^{-1}$) and to decrease with increasing temperature. The authors also proposed an experimental isothermal section at 973 K (700°C) (Fig. 2.51).

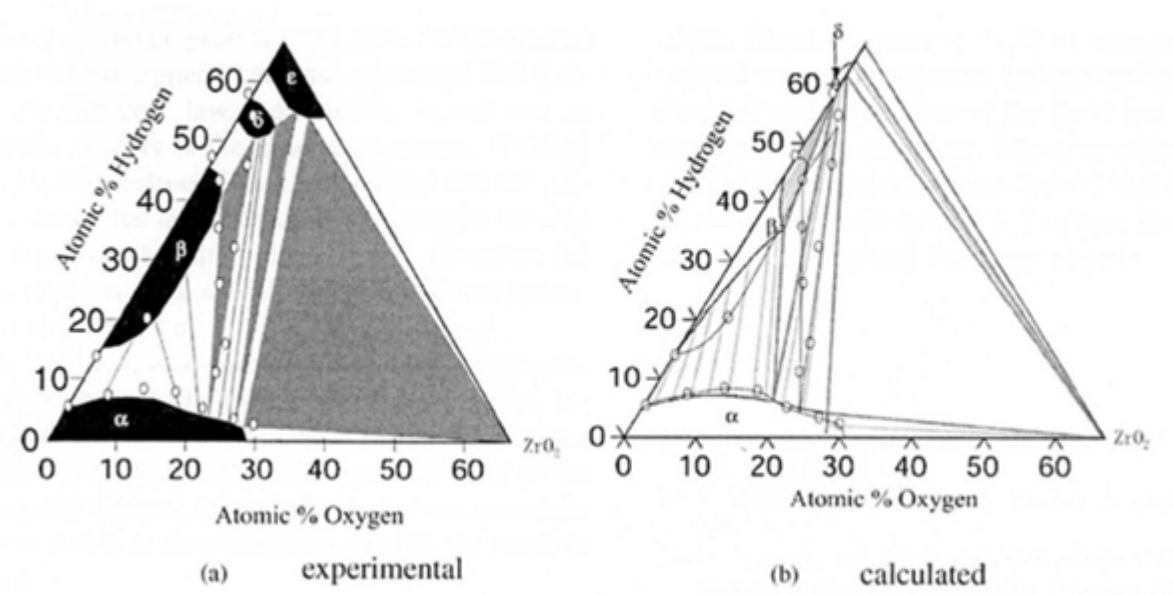

FIG. 2.51. Zr–O–H system: (a) experimental and (b) calculated isothermal sections at 973 K (700°C) (this image was published in Ref. [2.165], copyright Elsevier, 1999).

These experimental data were very useful for thermodynamic assessments of this system using the CALPHAD method [2.166]. A calculated isothermal section at 973 K (700°C) is shown in Fig. 2.51. The authors show that an increase of oxygen concentration in Zr greatly shifts the α/(α + β) phase boundary but has only a small effect on the α/(α + δ) phase boundary. This system is important when dealing with corrosion and hypothetical accident conditions.

2.4.5.10. Zr–Mo–Fe system

Many experimental studies have been performed on this system. These data were taken into account by Ref. [2.167] in a thermodynamic modelling of this system. Figure 2.52 presents a calculated isothermal section at 1173 K (900°C). Three ternary compounds are represented: two ternary Laves phases, C14 and C15, and a ternary phase named τ, treated as a stoichiometric compound. At 1173 K (900°C), a continuous single phase field connects the C14 Laves phase $Fe_2(Mo,Zr)$ and the λ phase $(Fe,Mo)_2Zr$. The τ phase is predicted to be stable at temperatures 1173 (≤900°C K). The C14 Laves phase exists in the ternary system at temperatures greater than 1173 K (900°C) and its congruent melting point lies between

2193 K and 2223 K (1920°C and 1950°C) for an approximate composition of 33.3 at.% (36.3 wt%) Zr, 40 at.% (45.9 wt%) Mo and 26.7 at.% (17.8 wt%) Fe.

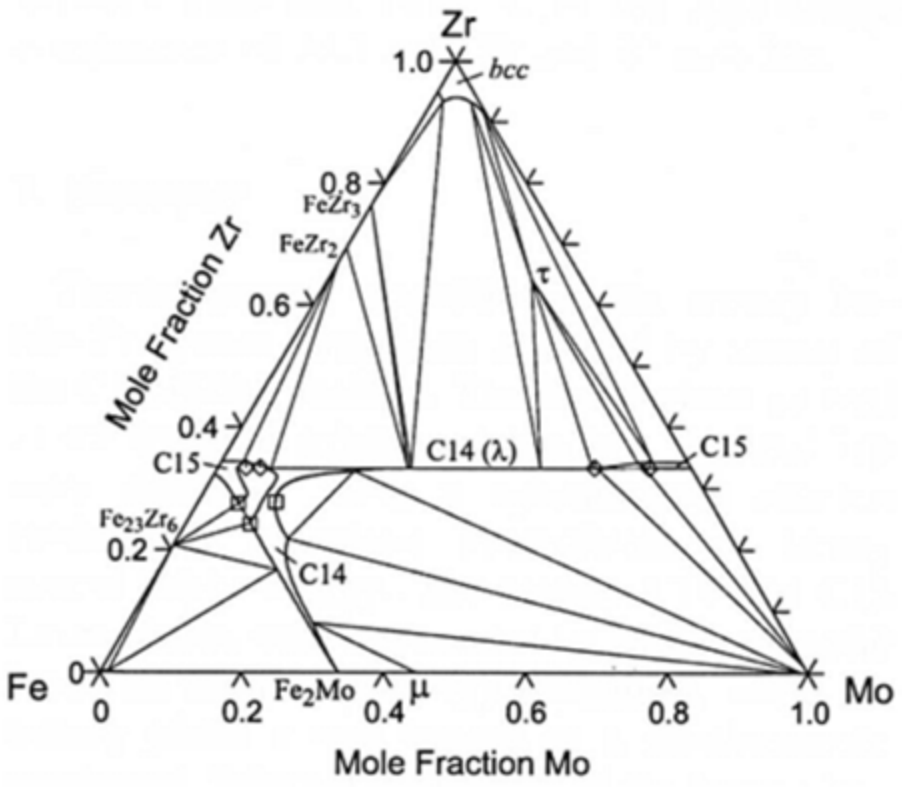

FIG. 2.52. Zr–Fe–Mo system: Calculated isothermal section at 1173 K (900°C) compared with experimental data (this image was published in Ref. [2.167], copyright Elsevier, 2002).

2.4.5.11. Zr–Nb–Cu system

The zirconium corner of the Zr–Nb–Cu system was studied in the three sections of Nb:Cu equal to 4:1, 1:1 and 1:4 from 1–25 at.% Nb+Cu. The isothermal sections for temperatures from 873 to 1573 K (600 to 1300°C), the polythermal sections and the projection of the phase diagram of the zirconium corner of the Zr–Nb–Cu system were constructed [2.168]. The maximum solubility limits of niobium and copper in β-Zr at 1203–1233 K (930–960°C) vary within 5–16 at.% from the Nb:Cu section equal to 1:4 to section 4:1. The maximum solubility limits of Nb and Cu in α-Zr are less than 1 wt% (Fig. 2.53). The authors [2.168] demonstrated experimentally that the Nb-Zr_2Cu section is quasi-binary of the eutectic type. The eutectic point corresponds to the composition 63.6 wt% Zr + 21.6 wt% Nb + 14.8 wt% Cu (60 at.% Zr + 20 at.% Nb + 20 at.% Cu).

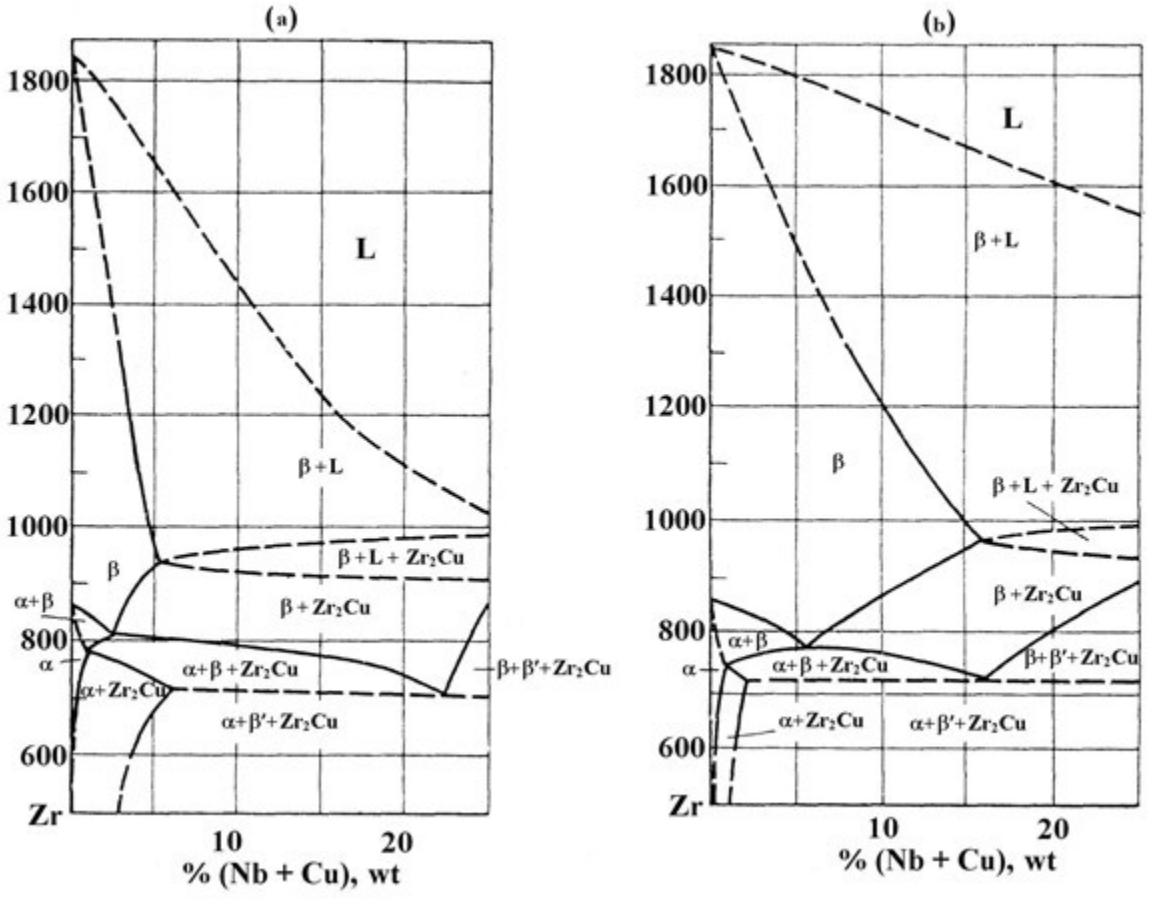

FIG. 2.53. Polythermal sections of the zirconium angle of the Zr–Nb–Cu system. (a) Nb: Cu = 4:1; (b) Nb: Cu = 1:4 [2.168].

The alloy Zr-2.5 wt% Nb-0.5 wt% Cu (Zr-2.45 at.% Nb-0.72 at.% Cu) has good corrosion resistance in air and CO_2 and is used for spacers to separate the pressure tubes from the calandria tubes in some CANDU reactors [2.33, 2.169]. Quenching this material from the (α + β) phase region and subsequent ageing provide the alloy with adequate ductility and higher strength compared with the Zr-2.5Nb alloy.

2.4.6. Quaternary systems of zirconium alloys

Phase diagrams of quaternary zirconium systems containing elements of commercial or promising alloys have been studied to a very limited extent. Some data on the structures of the zirconium-rich corners of the Zr–Nb–Sn–Fe and Zr–Fe–Cr–Ni systems are reported in Refs [2.79, 2.161, 2.170, 2.171]. Several quaternary Zr systems are described in Ref. [2.45] but their compositions are not of direct interest for use in the zirconium alloys already developed or currently under development for water cooled reactor cores.

In summary, the most important binary phase diagrams are well understood, ternaries less so while the development of quaternaries, which represent practical alloys, is still rudimentary. The development of computational thermodynamics should be helpful in elucidating these more complicated systems.

2.5. COMMERCIAL ALLOYS

The main zirconium alloys used commercially as structural components in the cores of water and BWRs (PWR, WWER, BWR, RBMK) are:

— Zircaloy-4 and Zircaloy-2;
— Binary Zr-1Nb alloys (E110 and M5);
— Binary Zr-2.5Nb alloy;
— Multicomponent zirconium alloys with additions of Sn, Nb and Fe (E635 and ZIRLO alloys).

The composition and structure of these alloys are subject to constant modification because of changing requirements for materials intended for increasingly onerous in-pile conditions of operation. They are summarized in Table 2.4. This section briefly sketches these developments and subsequent properties.

TABLE 2.4. ALLOYING COMPOSITIONS OF COMMERCIAL ZIRCONIUM ALLOYS

Alloy name	Concentration (wt%)					
	Sn	Fe	Ni	Nb	Cr	O
Zircaloy-2	1.2–1.7	0.07–0.20	0.03–0.08	—	0.05–0.15	0.09–0.16
Zircaloy-4	1.2–1.7	0.18–0.24	—	—	0.07–0.13	0.09–0.16
E110	—	—	—	0.9–1.1	—	0.06
M5	—	—	—	0.8–1.2	—	0.125
E125	—	—	—	2.4–2.7	—	0.05
Zr-2.5 Nb	—	—	—	2.4–2.8	—	0.125
E635	1.1–1.3	0.3–0.45	—	0.69–1.10	—	0.08
ZIRLO	1.0–1.1	0.09–0.10	—	1.0–1.2	—	0.125

2.5.1. Zircaloy-2 and Zircaloy-4

Zircaloy-2 and Zircaloy-4, included in Table 2.5 [2.172], have been the main materials for fuel cladding and other structural components for many years. In the 1990s, Zircaloy-4 started to be replaced by ZIRLO and Zr-1Nb in PWRs. The long term operation of Zircaloys in various power reactors has provided much information on their behaviour, particularly, their property dependence on metallurgical factors and parameters of operation. These continuing investigations are leading to their further improvement and evolution of the alloys.

TABLE 2.5. ASTM STANDARD B353 [2.172] FOR ALLOYING ELEMENTS IN THE ZIRCALOYS

Alloying elements (wt%) *	Zircaloy-2	Zircaloy-4
Sn	1.20–1.70	1.20–1.70
Fe	0.07–0.20	0.18–0.24
Cr	0.05–0.15	0.07–0.13
Ni	0.03–0.08	—
O	0.09–0.16	0.09–0.16
Fe+Cr+Ni	0.18–0.38	—
Fe+Cr	—	0.28–0.37

*: The conventional concentration of oxygen is usually 1000–1400 ppm and is stipulated by the customer.

Zircaloy-2 is primarily used as fuel cladding in BWRs that feature high oxygen and low hydrogen contents of the heat transport fluids. In PWRs, the heat transport fluid has low oxygen and higher hydrogen contents and the fuel cladding and other structural components are primarily fabricated from Zircaloy-4 [2.173–2.175]. Zircaloy-2 and Zircaloy-4 fuel

cladding, particularly in PWRs, pick up a noticeable quantity of hydrogen, up to 500 ppm and higher, from corrosion. In BWRs, at high heat fluxes the fuel cladding may suffer localized corrosion, called nodular corrosion [2.175].

The corrosion resistance of Zircaloy claddings is strongly dependent on the concentration of tin, and the size and number density of intermetallic precipitates in the tube microstructure. The results of studying those dependencies allowed the optimization of the alloy compositions and the processes used to fabricate cladding tubes. For example, the concentration of tin reduced within the specifications from 1.5 wt% to 1.2–1.3 wt% resulted in in-pile corrosion that was lower by a factor of two (Fig. 2.54) [2.176]. The lower tin concentration of Zircaloy-4 in combination with an upgraded process of tube fabrication led to the OPTIN alloy with higher corrosion resistance than that of Zircaloy-4 and an alloy with a low tin concentration, as shown in Fig. 2.55 [2.177]. In contrast to increasing the tin concentration, increasing the iron concentration of Zircaloy to the specified maximum value also promoted lower corrosion (Fig. 2.56) [2.175, 2.178].

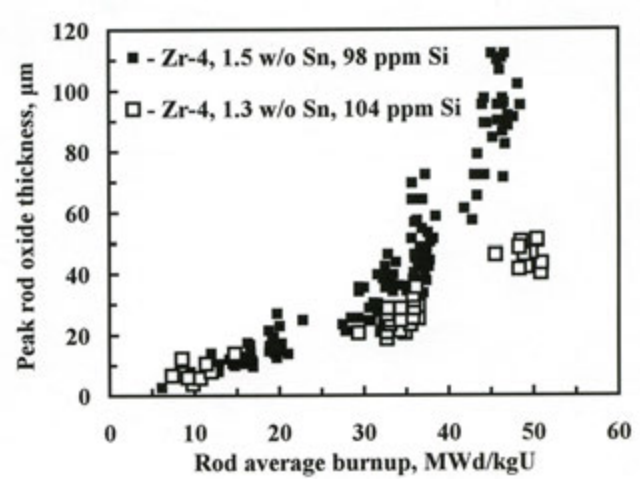

FIG. 2.54. Peak measured oxide thickness versus rod average burnup for Zircaloy-4 after 3 cycles of operation in-reactor [2.176].

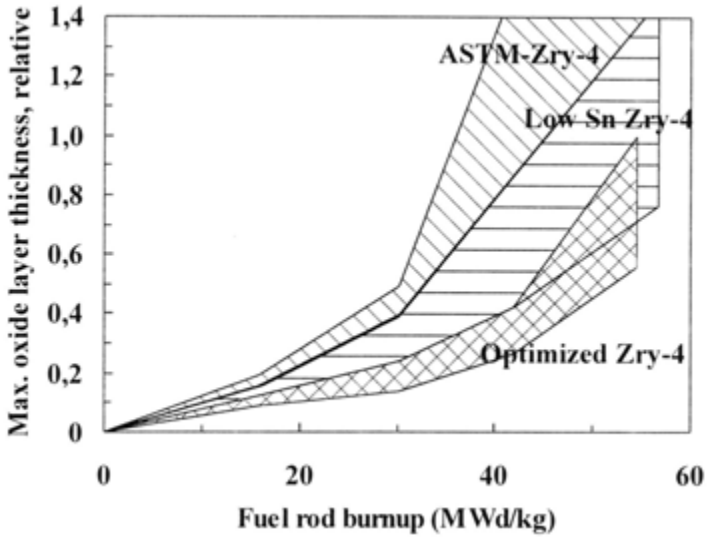

FIG. 2.55. Maximum oxide coat thickness on fuel claddings of standard and optimized Zircaloy-4 [2.177].

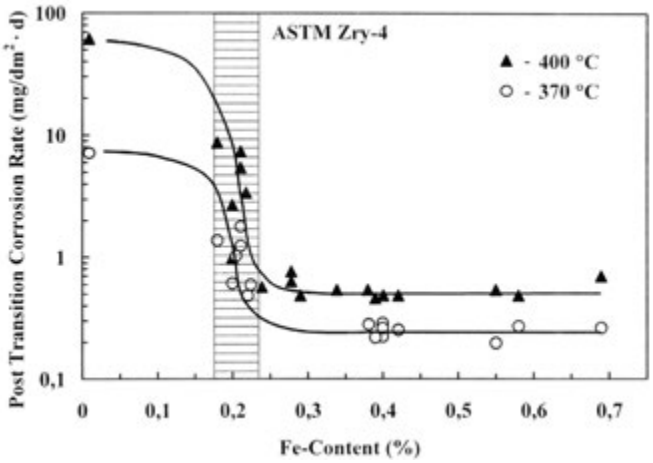

FIG. 2.56. Influence of Fe on corrosion in laboratory autoclave testing (reprinted, with permission, from Ref. [2.175], copyright ASTM International).

Since the in-pile corrosion resistance of zirconium has priority over other properties for fuel cladding, the quest for higher corrosion resistance of Zircaloy components in the face of extended fuel burnup has given rise to studies aimed at optimizing not only the compositions of Zircaloys but also their microstructures.

Metallurgical factors play an important part in the production and properties of Zircaloy cladding tubes. Their individual effects manifest themselves differently in the properties of Zircaloy-2 and Zircaloy-4 [2.175, 2.179]. Zircaloy-2 cladding tubes intended for BWR fuels are used with a recrystallized, equiaxed grain structure. Zircaloy-4 tubes for PWR fuels are usually used after a stress-relief anneal, which provides elongated, distorted grains that have the needed high strength. The high resistances to corrosion, irradiation induced growth and creep with a full anneal are depicted in Figs 2.57 and 2.58 [2.174, 2.175, 2.179]. The Zircaloy microstructure comprises an α solid solution and intermetallic particles. The particle morphology strongly affects all the properties of Zircaloys. In Zircaloy-4 the particles are primarily of the $Zr(Fe,Cr)_2$-type Laves phase. In Zircaloy-2, aside from $Zr(Fe,Cr)_2$, particles of the $Zr_2(Fe,Ni)$ phase exist. In other alloys of the Zircaloy type at the Fe/Cr ratio >4, Zr_3Fe precipitates are also available. With an increase in the particle diameters from 0.05–0.1 μm or higher, the in-pile corrosion of Zircaloy cladding diminishes appreciably. Nodular corrosion may occur in BWR cladding with a further increase in the particle diameters above about 0.15 μm (Fig. 2.59) [2.175].

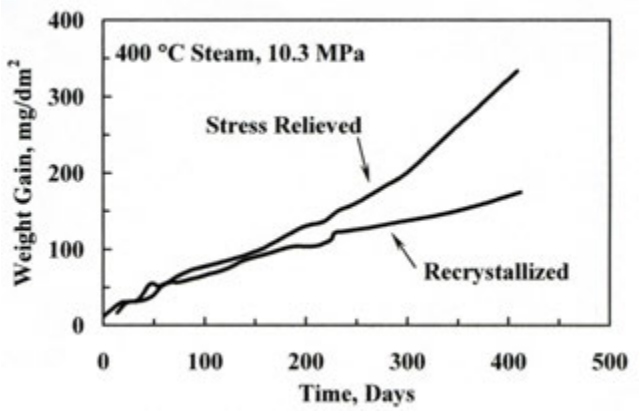

FIG. 2.57. Comparison of stress-relieved and recrystallized Zircaloy-4 tubing tested in 673 K (400°C) steam [2.174].

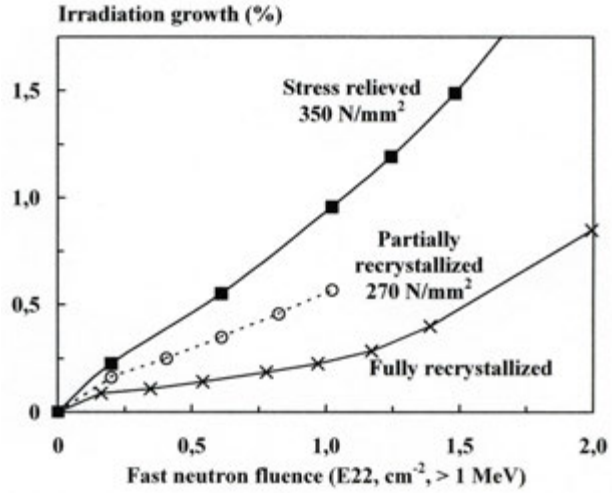

FIG. 2.58. Irradiation growth of Zircaloy samples at 573 K (300°C) (reprinted, with permission, from Ref. [2.175], copyright ASTM International).

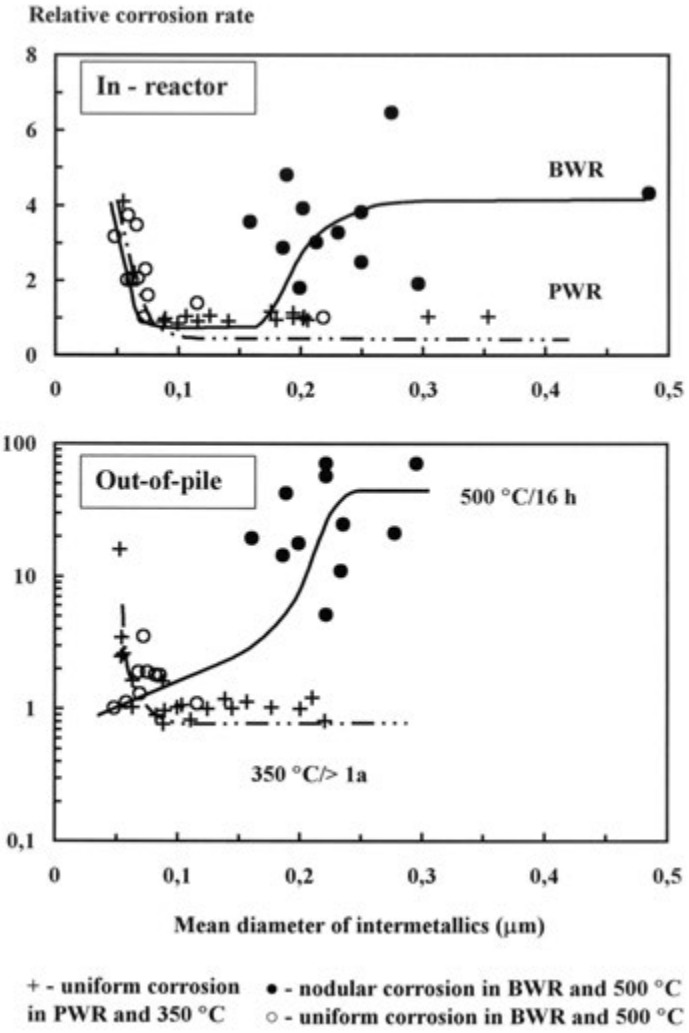

FIG. 2.59. Corrosion of Zircaloy as a function of size of intermetallic particles (reprinted, with permission, from Ref. [2.175], copyright ASTM International).

The optimum second phase particle sizes and number density in Zircaloy cladding are different for PWRs and BWRs. The tube production process, often using an annealing parameter A to control particle growth, can regulate the size of second phase particles. The parameter A is normalized time calculated from different anneal durations and temperatures of individual process operations in the fabrication. The annealing parameter is:

$$A = \sum_i t_i \exp(-Q/\mathrm{R}\,T_i) \tag{2.7}$$

where

t_i is the time in h of annealing step i;
T_i is the temperature in K;
Q/R is the activation temperature, usually taken to be 40 000 K;

and R is the gas constant.

The influence of the A parameter on the strength and corrosion of Zircaloy tubing is illustrated in Figs 2.60 and 2.61 [2.175, 2.179, 2.180]. The sample weight gain versus parameter A value correlates with hydrogen uptake. To attain high resistance to uniform corrosion in PWR, the parameter A has to be in the range of (1.5–6.0) × 10^{-19} h. In BWRs, the cladding has to be highly resistant to nodular and extensive uniform corrosion after high fuel burnups. To meet this requirement, the parameter A value for the Zircaloy type cladding in BWRs has to be in the range (0.5–1.5) × 10^{-18} h [2.181].

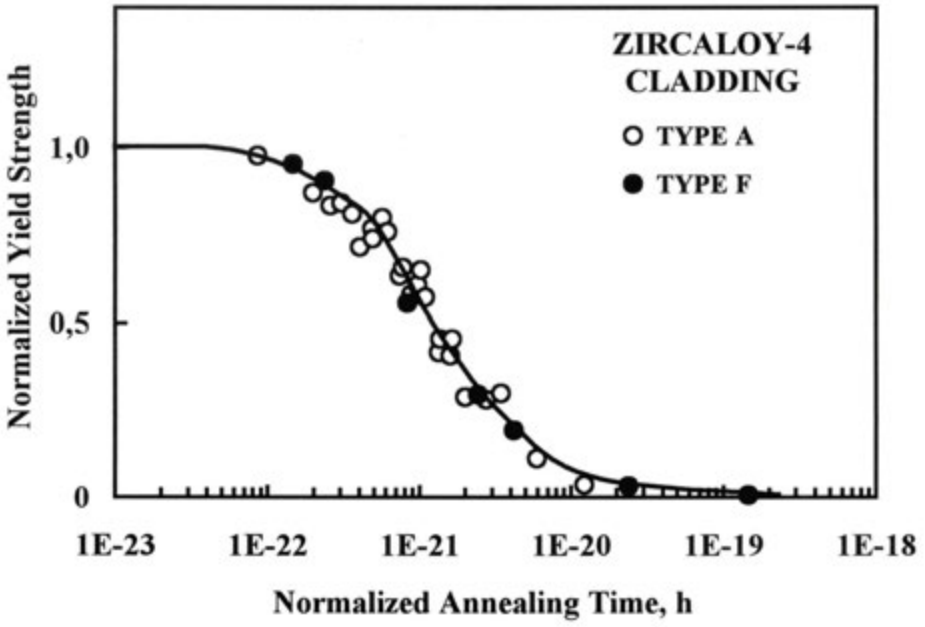

FIG. 2.60. Correlation between normalized unirradiated yield strength of Zircaloy at 673 K (400°C) and normalized annealing (reprinted, with permission, from Ref. [2.180], copyright ASTM International).

During the fabrication of components, Zircaloy may be cooled rapidly from the β phase, for example, before extrusion, at the final dimensions [2.182], or during welding or brazing. The resulting microstructure consists of a Thomson-Widmanstätten structure within prior β grains. The latter can appear in two variations: packets of parallel platelets of α phase

having similar orientation or a basketweave structure in which the α platelets are randomized. The basketweave microstructure is much preferred because it confers uniform mechanical properties. Trace elements that are retained as precipitates [2.183] or aggregates in the β phase, or that precipitate ahead of the β → α transformation [2.184], provide nucleation sites for α grains during rapid cooling and therefore care has to be taken to prevent their concentration from becoming too low. Candidate elements are C [2.183, 2.185], Si [2.184, 2.186], P [2.186–2.188] and Cl [2.184]. Of these elements, Cl appears to be the most effective in promoting basketweave microstructures whereas C, Si and P have to be present in concentrations that are harmful for other properties.

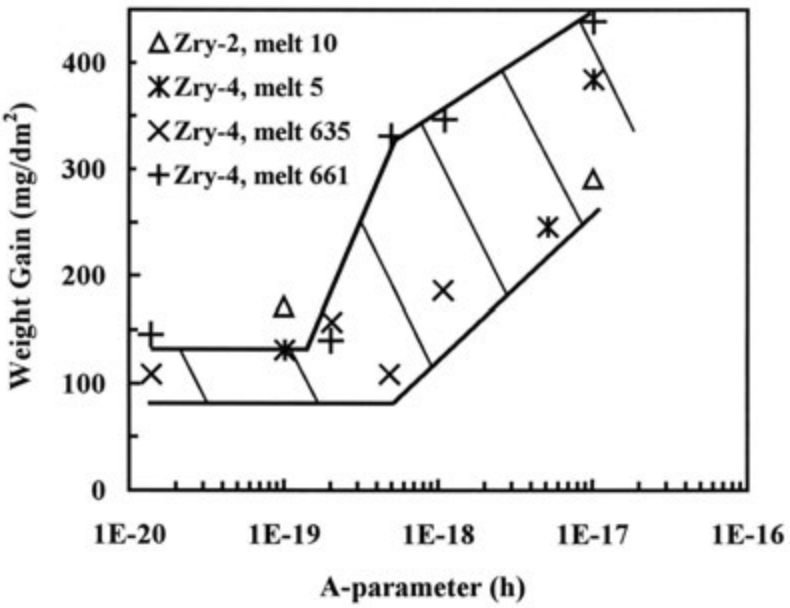

FIG. 2.61. Corrosion of Zircaloy-2 and Zircaloy-4 in a BWR after 1372 equivalent full power days (neutron fluence about 9×10^{25} n/m^2 (E > 1 MeV)) versus the A parameter [2.179].

Other properties have to be considered. For example, the tensile properties of unirradiated CW Zircaloy cladding tubes depend on the annealing temperature, as shown in Table 2.6 and Fig. 2.62 [2.174, 2.188]. The major metallurgy factors and the levels to which they influence the properties of the Zircaloys are summarized in Tables 2.7–2.9 [2.175].

TABLE 2.6. TENSILE PROPERTIES OF ZIRCALOY-2 AND ZIRCALOY-4 TUBES [2.188]

Cladding type	Final anneal (°C)	Recrystallization (%)	Room temperature			385°C		
			$\sigma_{0.2}$ (MPa)	σ_u (MPa)	Elong. (%) (50 mm)	$\sigma_{0.2}$ (MPa)	σ_u (MPa)	Elong. (%) (50 mm)
Zircaloy-4 (SR*)	486°C 3.5 h	4	576	775	18	358	452	20
Zircaloy-2 (SR)	486°C 3.5 h	12	567	769	16	354	458	20
Zircaloy-2 (PR**)	502°C 3.5 h	49	458	648	23	239	345	29
Zircaloy-2 (PR)	502°C 3.5 h	100	376	547	30	148	254	43

* SR — stress-relieved.
** PR — partially recrystallized.

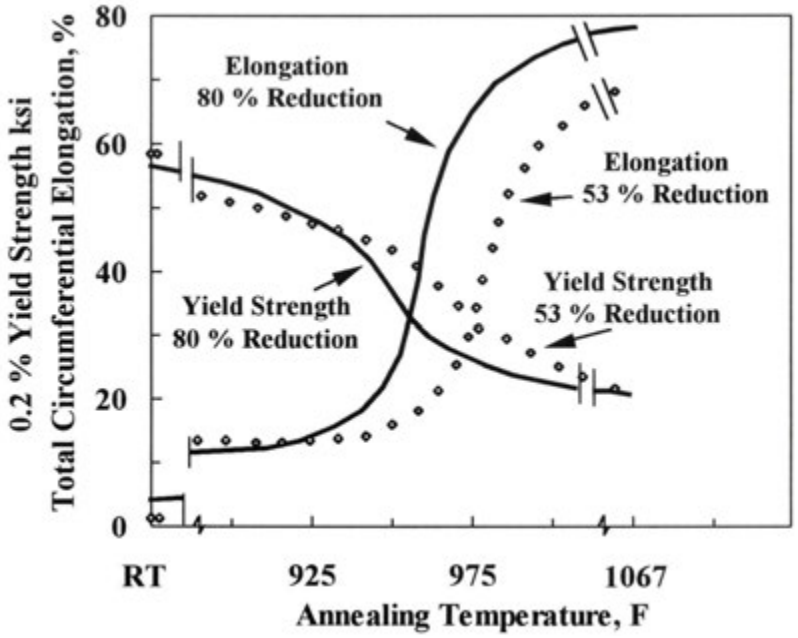

FIG. 2.62. Effect of final anneal temperature on tensile properties of Zircaloy tubing [2.174].

TABLE 2.7. INFLUENCE OF ALLOYING ELEMENTS ON CORROSION RESISTANCE OF Zr [2.175]

Alloying element	BWR	PWR	In water out of pile	In steam ≥ 500°C
Sn	Favourable	Unfavourable	Unfavourable	Unfavourable
Fe	Weakly favourable	Favourable	Favourable	Favourable
Cr	Weakly favourable	Favourable	No effect	Favourable
O	Unfavourable	No effect	No effect	Weakly favourable
Si	Favourable	Weakly favourable	Weakly favourable	No effect
C	No effect	Weakly favourable	Weakly favourable	No effect

TABLE 2.8. EFFECT OF MATERIAL PARAMETERS ON IN-PILE CREEP RATE [2.175]

Material parameter	Effect	Notes
Grain size (increase)	Strong (decrease)	Only at <2 μm at >320°C
Cold work and recrystallization degree (decrease)	Strong (increase)	At recrystallization degree of 0–60%
Tin content (decrease)	Strong (increase)	
Niobium content (decrease)	Moderate (increase)	At 0–0.5%
Oxygen content (decrease)	Moderate (increase)	

TABLE 2.9. MATERIAL PARAMETERS INFLUENCING IRRADIATION GROWTH [2.175]

Material parameter	Effect	Notes
Texture (increase)	Strong (decrease)	Only at grain size of <2 μm
Grain size (decrease)	Strong (decrease)	At recrystallization degree of 0–60%
Cold work and recrystallization degree (increase)	Strong (decrease)	
Tin concentration (decrease)	Strong (decrease)	
Carbon concentration (decrease)	Moderate (decrease)	At >100 ppm

Some modifications of Zircaloy that have been suggested are:

— PCA-Zircaloy: upgraded Zircaloy-4 containing substantially reduced quantities of C, Si, P and N [2.189–2.191];
— OPTIN: Zircaloy-4 of low Sn and high Fe concentration produced by the optimized tube fabrication process [2.177, 2.192];
— BETACLAD: β quenched outer surfaces of tubes [2.174].

A second option for improvement is to make the tube in layers, usually by co-extrusion. The two main applications are tubing with high corrosion resistance and tubing to mitigate pellet–clad interactions. For the former, an inner component made from Zircaloy-4 provides good mechanical properties while a thinner, outer layer is made from a zirconium alloy with excellent corrosion resistance. Such tubes are called duplex cladding [2.175, 2.178]. Several choices of alloy for the outer layer have been explored. One approach is to use a Zircaloy type alloy but with a Sn concentration slightly lower and Fe and Cr concentrations higher than allowed by the specification [2.178, 2.193]. Another approach is to use an outer layer quite different from Zircaloy-4, for example, an alloy such as Zircaloy-3 or Zr-2.5Nb [2.194]. Both types of duplex cladding are reported to have better corrosion resistance than standard Zircaloy-4. For the second application, to increase the tolerance to pellet–clad interaction in BWRs, a thin layer of pure zirconium is placed on the inside surface to guard against stress corrosion cracking from fission products during power ramps [2.195]. An additional layer could be added to the inside surface to retard post-failure local hydriding; this further layer is made from corrosion resistant Zircaloy-2 [2.196]. An alternative approach is to make the liner of a Zr-0.25 wt% Sn-Fe alloy to deal with both problems [2.197]. To minimize pellet–clad interactions in CANDU fuel, a thin graphite coating is placed on the inside surface of the cladding [2.198].

Pressure tubes made from Zircaloy-2 have given good service for several years. The tubes were used in the CW and stress relieved condition. Their biggest drawbacks were their low strength and absorption of large amounts of hydrogen — for example, over 150 ppm after 10 years operation in the N-Reactor [2.199] and Pickering 1 and 2 [2.200]. Zr-2.5Nb, which absorbs much less hydrogen and is stronger when it has a similar microstructure to Zircaloy-2, was chosen for tube replacement and for new CANDU reactors. The higher strength allowed the wall thickness of the tubes to be reduced from about 5 mm to about 4 mm, thus reducing the amount of neutron absorbing material.

2.5.2. Binary Zr-1Nb alloys (E110, M5)

2.5.2.1. E110 alloy

The binary Zr-1 wt%Nb alloy[1] developed in what is now the Russian Federation has been widely used since the 1960s as fuel cladding in WWERs and RBMKs. Under WWER conditions, the E110 alloy cladding tubes feature a high resistance to corrosion together with the formation of very thin oxides and a low hydrogen uptake. After 4–6 year cycles of operation in WWER reactors to a fuel burnup of 55–66 MWd/kgU, the thickness of oxide coating on cladding is < 15 μm and the hydrogen concentration of cladding is < 100 ppm (0.9 at.%) [2.201, 2.202]. Similar results are obtained with experimental fuels that have operated in reactor loops to reach a burnup of 93 MWd/kgU [2.203]. In boiling RBMK reactors, fuel rods clad in E110 alloy have been in operation for 3–4 year cycles to a burnup of about 24 MWd/kgU. Some parts of the oxidized cladding outer surface reveal nodules that have no impact on the reliability of fuels under those operating conditions.

TABLE 2.10. CHEMICAL COMPOSITION OF E110 ALLOY [2.204]

Chemical element	Composition		Chemical element	Composition	
	Tolerable concentration (ppm, wt)	Typical concentration (ppm, wt)		Tolerable concentration (ppm, wt)	Typical concentration (ppm, wt)
	Alloying element [wt%]				
Nb	0.9–1.1	0.95–1.1			
	Impurity			Impurity	
O	1000	500–700	B	5	<0.4
Si	200	46–90	Mo	50	<30
Al	80	<30	K	40	<30
Ni	200	<30–39	Li	2	<2
Cu	50	<10	Cr	200	<30
Be	30	<30	F	30	<30
Ca	300	<100	Cl	30	<7
Mn	20	<3	N	60	<30–40
Ti	50	<30	C	200	<40–70
Pb	50	<50	H	15	4–7
Hf	500 (100)	300–400 (≤80)	Fe	500	140
Cd	3	<0.3	Sn	500	<100

E110 is produced from a mixture of electrolytic powder and iodide zirconium. The impurity content of the alloy is specified by the requirements for the alloy and is limited by well-established processes for fabricating the alloy and components (Table 2.10) [2.204]. This is based on studies of the interrelationship between composition and microstructure, and the properties of semi-finished and finished tubes. Since Zr-Nb alloys have unlimited solubility of niobium in β-Zr, the dissolution mechanism during cooling may result in the formation of metastable phases that influence the properties of components [2.204, 2.205]. The rate of heating and cooling for heat treatments and their duration at temperature and

[1] The value of Nb concentration in Zr-Nb alloys will be expressed only in wt%, in line with the specifications and values usually reported. Numerically, at.% can be taken as the same number as wt% since the atomic weights of Zr and Nb are within 1.8% of each other and the specifications allow a range of values.

amounts of hot work were chosen based on the interrelationship between corrosion and the tensile properties of E110 and its metastable phases (β_{Zr}, α′, ω) and decomposition (Figs 2.63–2.65) [2.45, 2.204, 2.205]. E110 cladding tubes for WWER and RBMK fuels are used with a recrystallized microstructure, featuring fine α grains containing β_{Nb} phase particles (Nb ≥ 85%). This structure promotes the highest resistances to corrosion and creep, as well as providing ductility and crack resistance during operation (Table 2.11) [2.204]. The above mentioned microstructure of tubes is produced by annealing at 833–853 K (560–580°C) after cold reduction greater than 50% [2.205].

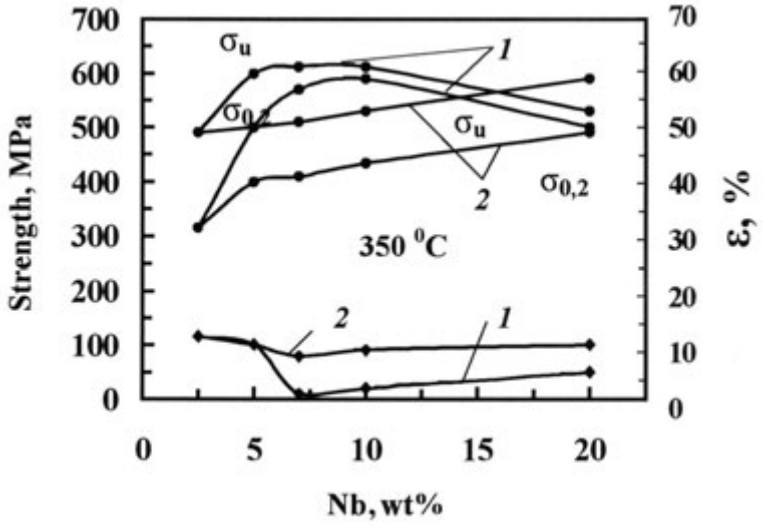

FIG. 2.63. Influence of niobium concentration on the tensile properties of Zr-Nb alloys. Legend: 1 — quenching from 1223 K (950°C); 2 — quenching from 1223 K (950°C), ageing at 773 K (500°C), 24 h (reprinted, with permission, from Ref. [2.204], copyright ASTM International).

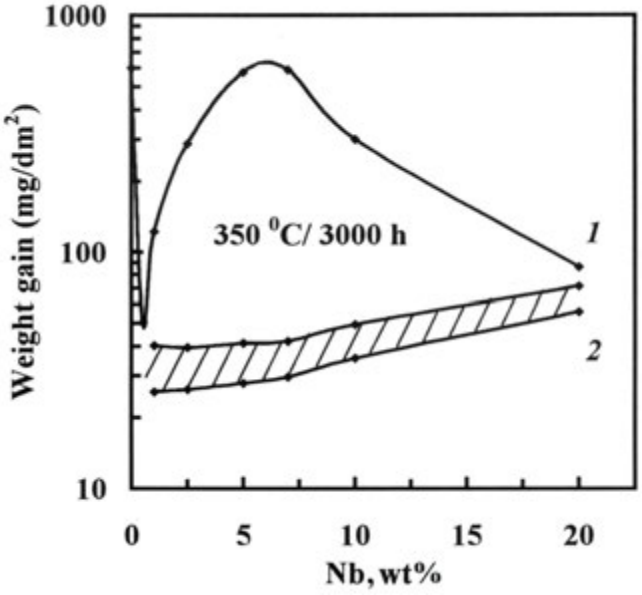

FIG. 2.64. Influence of niobium concentration on aqueous corrosion of zirconium in water (623 K (350°C), 3000 h). Legend: 1 — quenching from 1223 K (950°C) into water; 2 — quenching from 1223 K (950°C) into water, ageing at 773 K (500°C), 24 h (reprinted, with permission, from Ref. [2.204], copyright ASTM International).

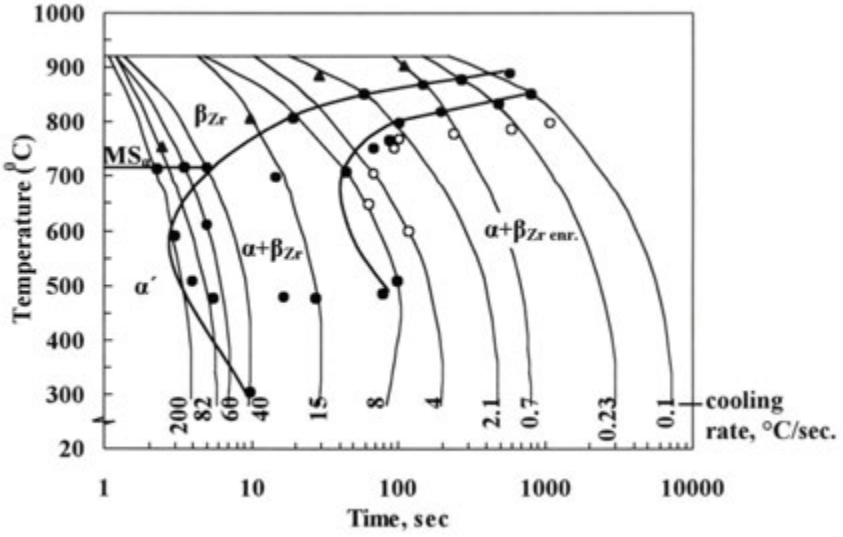

FIG. 2.65. Time–temperature–transformation diagram of Zr-1Nb alloy upon continuous cooling (reprinted, with permission, from Ref. [2.204], copyright ASTM International).

TABLE 2.11. INFLUENCE OF RECRYSTALLIZATION DEGREE ON E110 ALLOY CLADDING TUBES PROPERTIES [2.204]

Recrystallization degree (%)	Elongation in tension δ (%) (20°C)		Creep rate (ε_ϕ) (400°C/100 MPa) (10^{-4}%·h^{-1})	Cyclic (5.4 s^{-1}) Alternate loading at (350°C) cycles before fracture
	Axial	Transverse (ring)		
Cold work	15–18	8–11	60–70	150–160
10	20–24	14–18	50–55	—
30	24–30	20–24	40–45	—
60	26–32	23–27	30–34	190–200
90	36–40	26–30	9–10	470–480
100	37–41	27–31	8–9	490–500

Table 2.12 [2.205] summarizes the initial tensile properties of E110 cladding tubes; the increase in strength and reduction in ductility when fuel cladding is irradiated are illustrated in Fig. 2.66 [2.204]. Similar changes of the tensile properties of the E110 cladding tubes are produced by an increase in oxygen concentration. Also, as the concentration of oxygen increases from 600 ppm to 1300 ppm (0.34–0.74 at.%), the creep resistance of the tubes becomes almost two times higher (Table 2.13) [2.203–2.208]. The presence of β_{Zr} phase in the microstructure of tubes is not desirable because it reduces corrosion resistance, although it increases creep strength (Fig. 2.67) [2.204–2.208].

TABLE 2.12. TENSILE PROPERTIES OF E110 ALLOY CLADDING TUBES
(*diameter 9.13 × 7.73 mm* [2.205])

Testing direction	20°C			360°C		
	σ_u (MPa)	$\sigma_{0.2}$ (MPa)	δ (%)	σ_u (MPa)	$\sigma_{0.2}$ (MPa)	δ (%)
Axial	400–420	240–270	48–49	200–230	90–120	52–56
Transverse	360–380	320–340	35–38	190–210	130–160	38–43

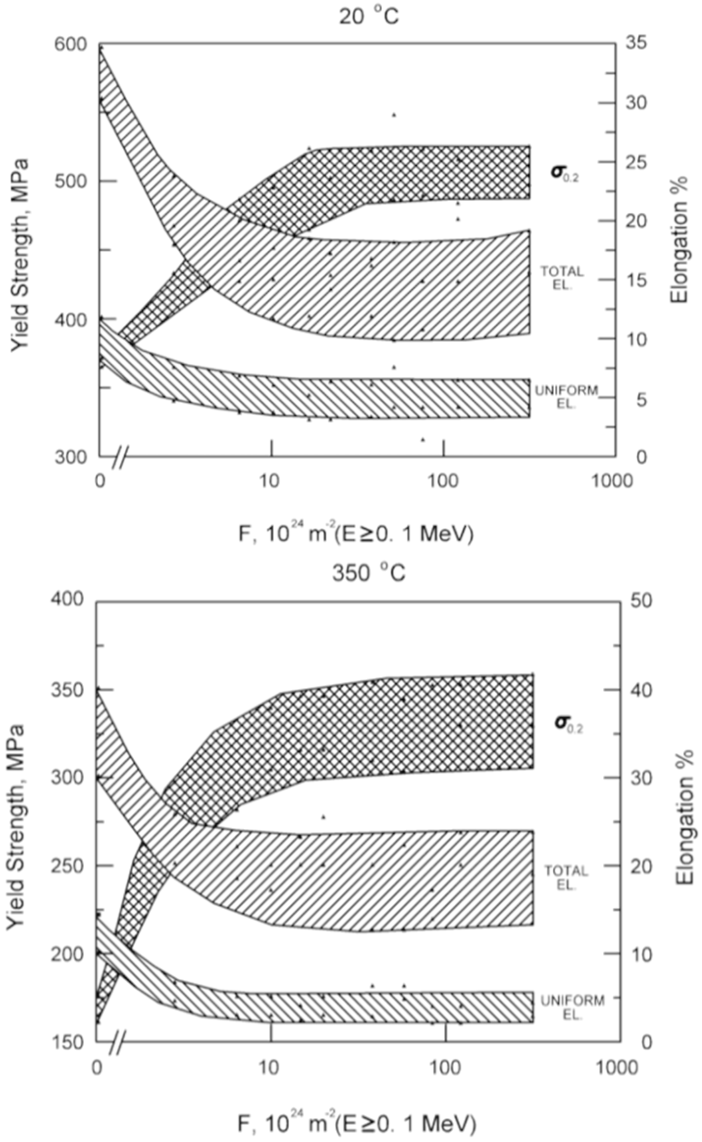

FIG. 2.66. Tensile properties of E110 alloy claddings of WWER-1000 irradiated fuels (reprinted, with permission, from Ref. [2.204], copyright ASTM International).

TABLE 2.13. EFFECT OF OXYGEN CONCENTRATION ON E110 ALLOY CLADDING TUBE PROPERTIES [2.204]

Oxygen concentration (ppm)	Fluence ($E \geq 0.1$ MeV) (m^{-2})	Tensile properties				Creep rate (tangential) (ε_{ϕ}) (350°C/100 MPa) ($10^{-4}\%\cdot h^{-1}$)
		20°C		350°C		
		$\sigma_{0.2}$ (MPa)	δ (%)	$\sigma_{0.2}$ (MPa)	δ (%)	
600–800	0	360–380	32–35	160–180	36–40	1.14–1.36
	3×10^{26}	500–530	16–19	330–360	19–24	1.2–1.4
1300	0	490–510	28–31	180–200	32–36	0.62–0.75
	3×10^{26}	660–680	12–15	360–380	16–21	0.7–0.8
1600	0	510–530	26–30	200–220	31–35	0.43–0.56
	3×10^{26}	670–690	10–13	380–400	15–19	0.5–0.6

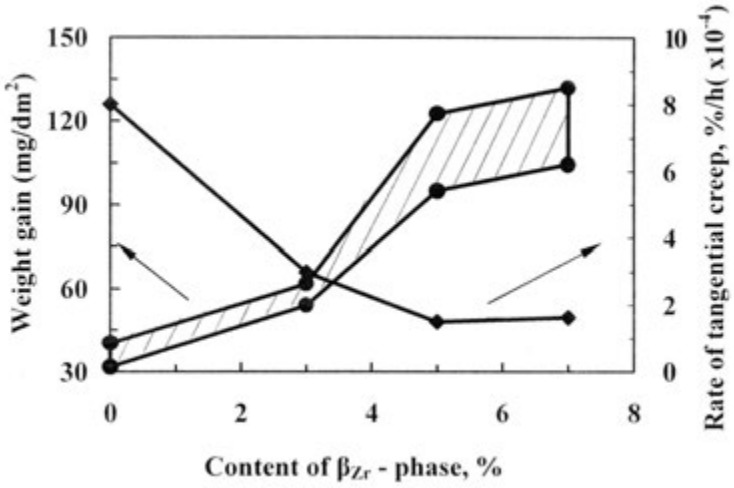

FIG. 2.67. Influence of β_{Zr} phase content on properties of recrystallized E110 alloy cladding tubes (out-reactor creep at 673 K (400°C)/100 MPa, aqueous corrosion at 623 K (350°C)/3 000 h) (reprinted, with permission, from Ref. [2.204], copyright ASTM International).

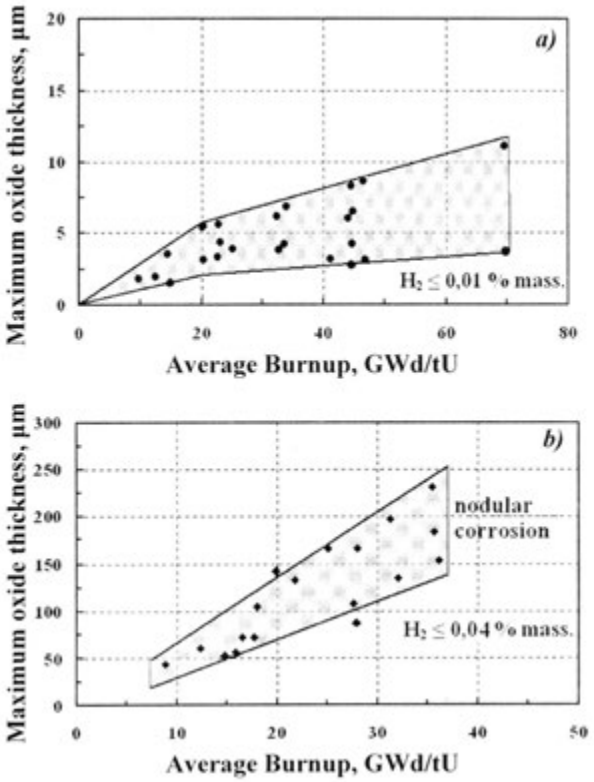

FIG. 2.68. Corrosion of E110 alloy claddings of fuel under conditions typical of (a) WWER and (b) RBMK [2.209]. The hydrogen concentration in the cladding is given on the bottom right of the figures.

In 1980, a modified version of E110 (E110K) containing 900–1300 ppm (0.51–0.74 at.%) oxygen was developed and produced commercially [2.205]. Under the conditions specific for the water chemistry of WWER (pressurized water containing

ammonia, boron and ≤0.005 ppm oxygen), E110 has a high resistance to corrosion [2.201, 2.202, 2.209, 2.210]. A higher oxygen concentration (>0.005 ppm) in the heat transport water and surface or bulk boiling aggravate the corrosion of E110 cladding [2.204, 2.209]. Along with a uniform thin oxide coat, nodules of a white loose oxide evolve; their quantity and depth increase with fuel burnup, as seen in Fig. 2.68 [2.209]. To enhance the resistance of fuel cladding to corrosion and increase creep strength under boiling conditions, a modified E110 alloy, called E110M, was designed that contains about 1250 ppm (0.02 at.%) iron and 1250 ppm (0.71 at.%) oxygen (Figs 2.69, 2.70, Table 2.14) [2.211]. For the E110M alloy, under autoclave conditions, corrosion resistance is a little higher and creep resistance during irradiation is almost doubled compared with the original version of E110 [2.211]. E110 alloy is sensitive to the lithium concentration of water, which is demonstrated by the aggravated corrosion and hydriding of the cladding tubes when 70 ppm of lithium is present (Fig. 2.70(d)).

TABLE 2.14. CREEP STRAIN OF CLADDING TUBES [2.211]

(Tube diameter variation under internal pressure (%), σ = 100 MPa)

Alloy	No irradiation (T = 400°C, 3000 h)	Under irradiation (T = 330°C, fluence = 10^{26} m^{-2})
E110	4.9	0.37
E110K	3.5	0.20
E110M	3.9	0.20

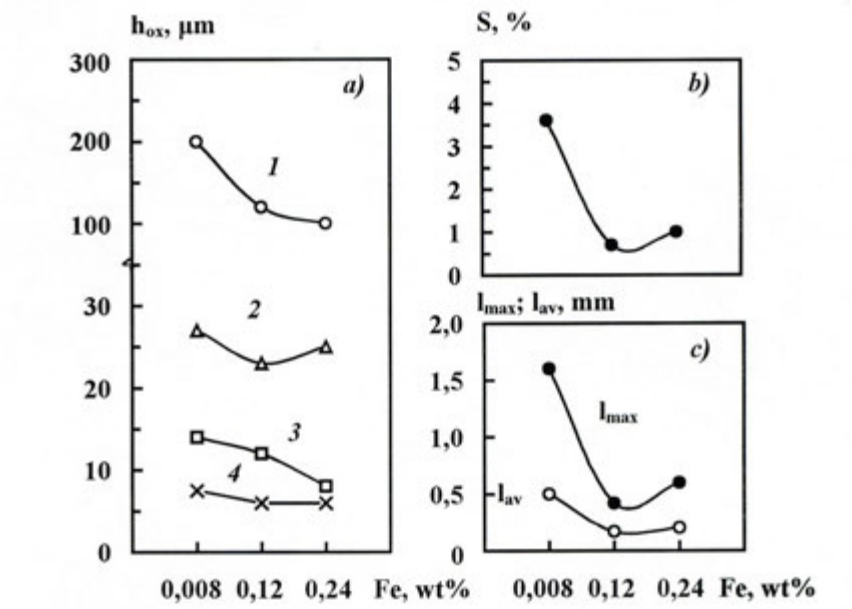

FIG. 2.69. (a) Oxide coat thickness (h_{ox}), formed in autoclave tests for corrosion in water (1, 3, 4) and steam (2) and (b) nodular corrosion characteristics vs (c) iron concentration of E110 alloy. Legend: 1 — 633 K (360°C), 150 days, 70 ppm Li;2 — 673 K (400°C), 600 days; 3 — 633 K (360°C), 150 days, 300 ppm O; 4 — 633 K (360°C), 600 days; l_{max} and l_{av} — maximum and average sizes of nodules; S — specific surface [2.211].

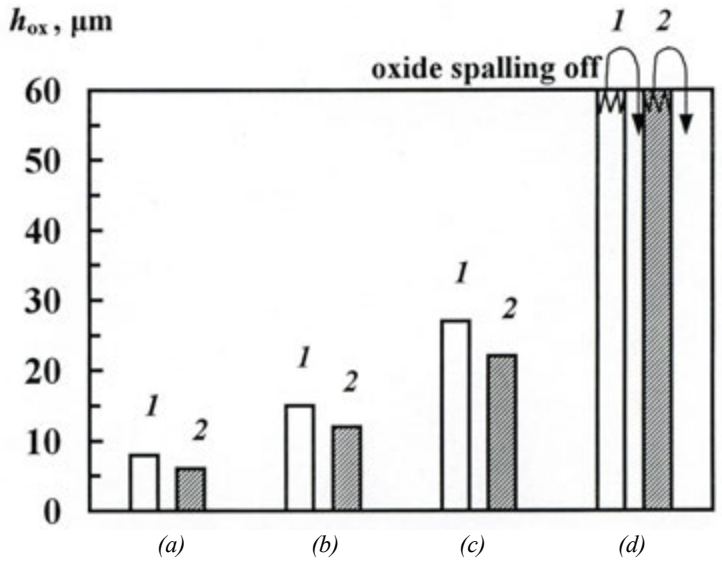

FIG. 2.70. Thickness of oxide coats on E110 (1) and E110M (2) tubes:(a): water at 633 K (360°C), 600 days; (b): water at 633 K (360°C), 600 days, 300 ppm O; (c): steam at 673 K (400°C), 600 days; (d): water at 633 K (360°C), 300 days, 70 ppm Li [2.211].

2.5.2.2. M5 alloy

The M5 alloy was developed in France in the 1990s. It is based on sponge zirconium and, like E110, contains nominally 1.0 wt% niobium as the main alloying element, with deliberate additions of oxygen between 900 and 1800 ppm (0.51–1.02 at.%). It is considered to be a ternary Zr-Nb-O alloy (Table 2.15) [2.212–2.215]. The M5 alloy is mainly used as a cladding material for fuels and for other structural components in PWRs [2.212, 2.214, 2.215].

TABLE 2.15. CHEMICAL COMPOSITION OF M5 ALLOY [2.214]

Element		Concentration (ppm)
Alloying element	Nb	0.80–1.20 (wt%)
	O	900–1800
Impurity range	Fe	150–600
	C	25–120
	S	0–35

The process of fabricating M5 cladding tubes is traditional and is similar to that used for other zirconium alloys. The cladding tubes are produced via multiple steps of cold pilgering to intermediate and final sizes followed by anneals at a temperature below 873 K (600°C), which promotes recrystallization [2.215].

The microstructure of the recrystallized M5 cladding tubes consists of equiaxed α grains, 3–5 μm in diameter, within which are β_{Nb} phase particles about 50 nm in size containing 85–90% Nb, and a small quantity of coarse (100–200 nm) particles of

$Zr(Nb, Fe, Cr)_2$ type intermetallics with a hexagonal crystal structure. The particles are composed of 41±4% Nb and 18±3% Fe + Cr [2.215, 2.216]. The iron and chromium in the intermetallic particles are likely explained by their presence as impurities in zirconium sponge.

The tensile properties of M5 cladding tubes before and after service in PWRs are tabulated in Table 2.16 [2.213, 2.214], indicating an increase in strength and reduction of ductility after irradiation. Under PWR conditions, the M5 cladding and guide thimble tubes that have operated for 3 or 4 cycles to reach burnups up to about 56 MWd/kgU have thin oxides, <20 μm thick, and low hydrogen uptake (<100 ppm (0.9 at.%)).

The corrosion resistance of M5 alloy is much superior to that of Zircaloy-4 under PWR conditions (Figs 2.71, 2.72) [2.214–2.216]. The creep resistance of recrystallized M5 tubes is similar to that of recrystallized Zircaloy-4 (Fig. 2.73) [2.214].

TABLE 2.16. TENSILE PROPERTIES OF M5 ALLOY CLADDING TUBES (AXIAL) [2.213, 2.214]

No irradiation				Irradiation in PWR					
				1 cycle (10 MW·d·kg^{-1} U)			3 cycles (38 MW·d·kg^{-1} U)		
T (°C)	σ_u (MPa)	$\sigma_{0.2}$ (MPa)	δ_{tot} (%)	σ_u (MPa)	$\sigma_{0.2}$ (MPa)	δ_{tot} (%)	σ_u (MPa)	$\sigma_{0.2}$ (MPa)	δ_{tot} (%)
20	479	316	36	681	582	9.3	715	635	6.0
350	250	130	40	470	429	12.4	474	428	9.7

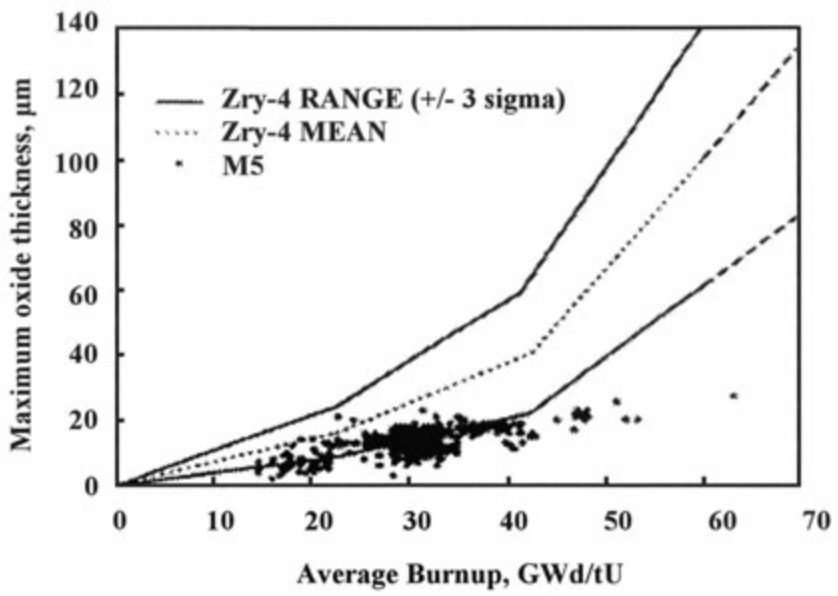

FIG. 2.71. Thickness of oxide coats on M5 and Zircaloy-4 fuel cladding [2.214, 2.216].

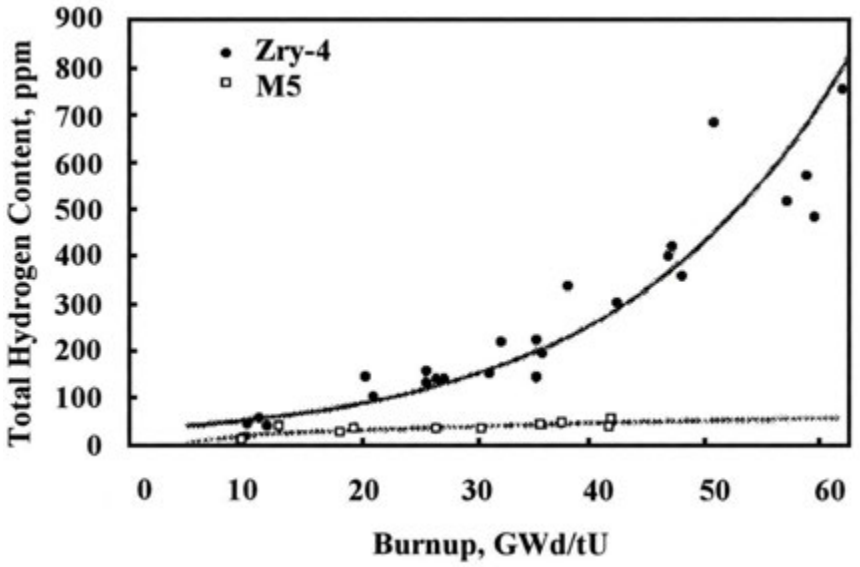

FIG. 2.72. Hydrogen concentration of M5 and Zircaloy-4 fuel cladding versus fuel burnup [2.214, 2.216].

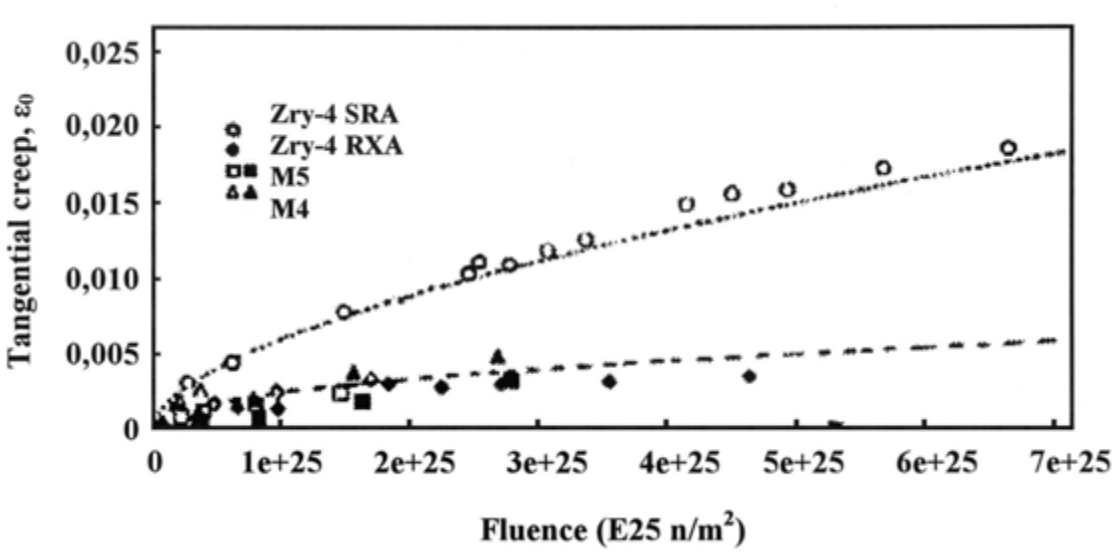

FIG. 2.73. Tangential creep of M5 and Zircaloy-4 cladding tubes [2.214].

During optimization of M5 alloy, the importance of the final annealing and the concentration of oxygen, sulphur and intermetallics for corrosion and tensile properties of the cladding tubes was demonstrated [2.214, 2.217]. In M5 alloy a special emphasis is placed on sulphur because it reduces cladding tube creep. With concentrations of sulphur between 20 and 40 ppm (0.0057–0.011 at.%) and oxygen between 1000 and 1500 ppm (0.57–0.85 at.%), the thermal creep of the M5 alloy tubes is lowered by a factor of about five and the benefit is still discernible during irradiation, as shown in Fig. 2.74 [2.214, 2.217]. According to the patent, "the sulphur concentration of the alloy should be between 8–30 ppm (0.0022–0.0086 at.%)" [2.212].

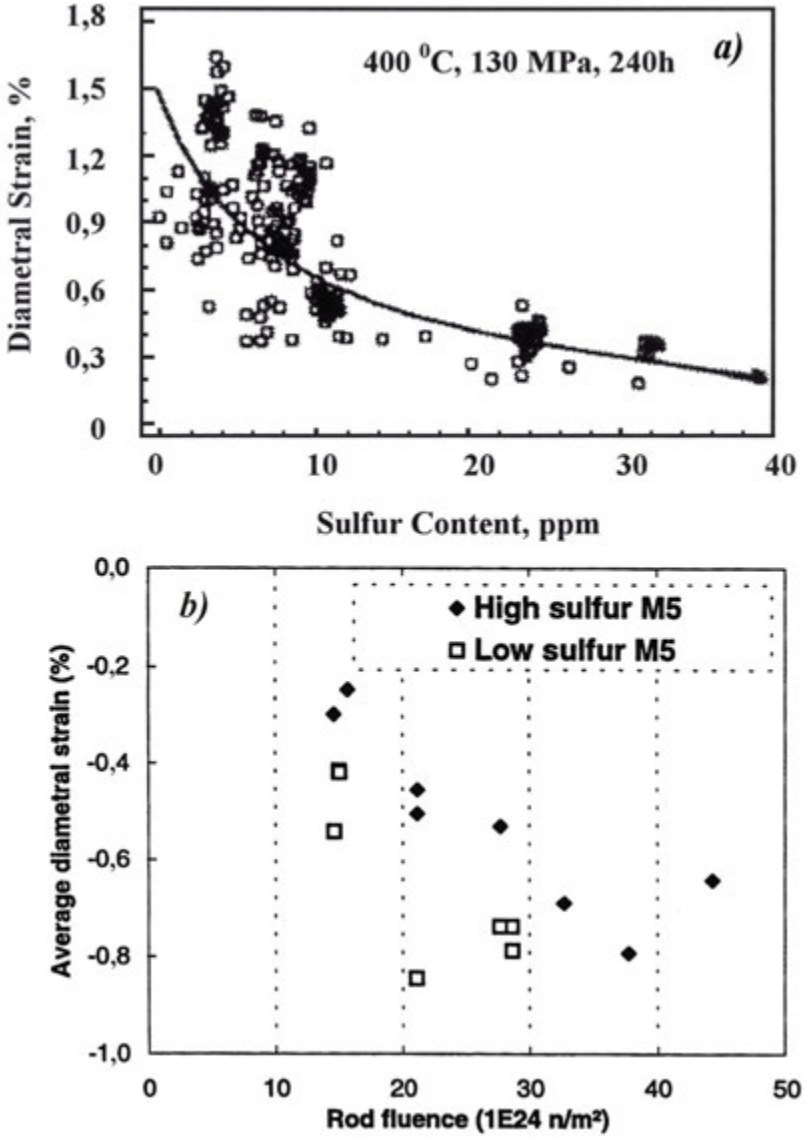

FIG. 2.74. Influence of sulphur concentration on creep of M5 cladding tubes (a) before irradiation [2.214]; (b) for M5 fuel roads (reproduced from Ref. [2.217] with permission of the Institute for Energy Technology).

2.5.3. Alloys of Zr–Nb–Sn–Fe system (ZIRLO, E635)

The American alloy ZIRLO and the Russian alloy E635 have both been developed with a view to extend fuel burnup in PWRs and WWERs. The application of these alloys with high corrosion resistance and dimensional stability for average burnups > 60 MWd/kgU should result in lower fuel cycle costs and maintenance, and lower irradiation doses to plant operators than with earlier fuels.

2.5.3.1. ZIRLO alloy

ZIRLO is a multicomponent alloy, containing tin, niobium, iron and oxygen (Table 2.17), used for PWR fuel cladding and fuel assembly components such as grids, guide thimbles and instrumented tubes. [2.39, 2.41, 2.218].

TABLE 2.17. NOMINAL CHEMICAL COMPOSITION OF ZIRLO [2.39, 2.41, 2.218]

Alloying element	Concentration (wt%)	Impurity element	Concentration (ppm)
Nb	1.0	Cr	≈80
Sn	1.0	C	60–80
Fe	0.10	Si	<40
O	0.09–0.12	Al	22–30

Testing demonstration fuel rods clad in ZIRLO began in the 1980s and tests of fuel assemblies in commercial PWRs commenced in 1991. The results demonstrated the good performance of ZIRLO components. In comparison with Zircaloy-4, ZIRLO provided:

— Reduced oxidation of components;
— Lower hydrogen uptake with subsequent lower embrittlement of components;
— Lower irradiation induced growth and creep leading to enhanced geometrical stability of fuel cladding and assemblies [2.218].

ZIRLO cladding tubes are fabricated from triple melted ingots of sponge zirconium. They are subjected to β treatments, extrusion, cold pilgering and recrystallization vacuum anneals within 853–873 K (580–600°C) for 4 hours. The final anneal of ZIRLO is carried out at a low temperature that provides a partially recrystallized state [2.40, 2.219]. The microstructure of these cladding tubes consists of α grains containing particles < 80 nm in diameter of two types:

— Zr and Nb (β_{Nb} phase);
— Zr, Fe and Nb $(Zr, Nb)_2Fe$.

In uniaxial tension tests on the tubes, the tensile properties of ZIRLO cladding tubes are similar to those of Zircaloy-4 (Table 2.18) [2.219]. Compared with Zircaloy-4, ZIRLO components have a higher corrosion resistance in water at about 633 K (360°C), particularly in water containing high concentrations of lithium, as shown in Figs 2.75 and 2.76 [2.219]. This good corrosion resistance of ZIRLO is preserved to high fuel burnups (Table 2.19, Fig. 2.77). The oxide thickness on ZIRLO cladding does not exceed 40 μm at a fuel burnup of up to 55 MWd/kgU. Also, during in-pile corrosion, ZIRLO cladding has a similar HPU to Zircaloy-4 (Table 2.20) [2.220].

TABLE 2.18. TENSILE PROPERTIES OF CLADDING TUBES [2.219]

Properties	Material		
	ZIRLO	CON Zircaloy-4	IMP Zircaloy-4
Room temperature:			
$\sigma_{0.2}$ (MPa)	421	450	407
σ_{u} (MPa)	560	578	545
Elongation δ_{tot} (%)	16.5	15.0	18.3
T = 385°C			
$\sigma_{0.2}$ (MPa)	280	268	243
σ_{u} (MPa)	340	323	303
Elongation δ_{tot} (%)	15.0	18.5	18.5

Note: CON — conventional Zircaloy; IMP — improved Zircaloy.

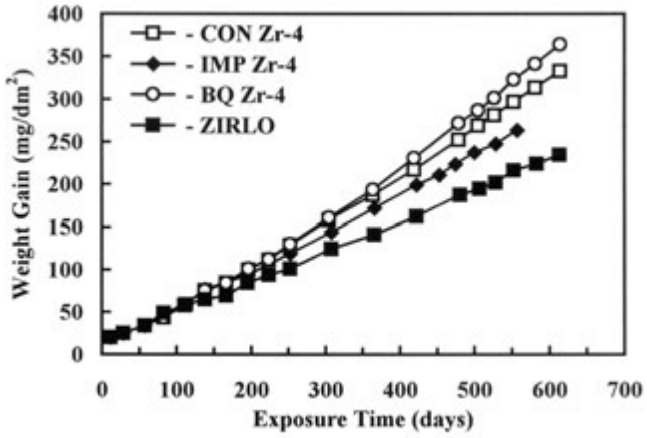

FIG. 2.75. Corrosion of tubes in autoclaves containing pure water at 633 K (360°C). Legend: CON — conventional, IMP — improved, BQ — beta — treated (reprinted, with permission, from Ref. [2.219], copyright ASTM International).

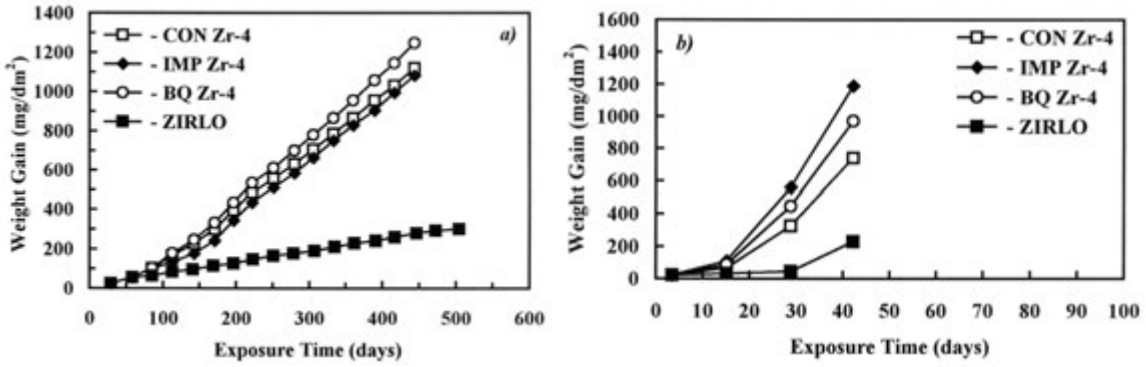

FIG. 2.76. Corrosion of tubes in autoclaves containing water with (a) 70 ppm and (b) 210 ppm lithium at 633 K (360°C) (reprinted, with permission, from Ref. [2.219], copyright ASTM International).

TABLE 2.19. CORROSION OF FUEL CLADDING IN NORTH ANNA REACTOR *(burnup > 38 MWd/kgU) [2.219]*

Material	Average thickness of oxide coat (two cycles)	Percentage of CON Zircaloy-4
	μm	%
CON Zircaloy-4	53.8	100
IMP Zircaloy-4	40.5	75
ZIRLO	15.1	28

Note: CON — conventional Zircaloy; IMP — improved Zircaloy.

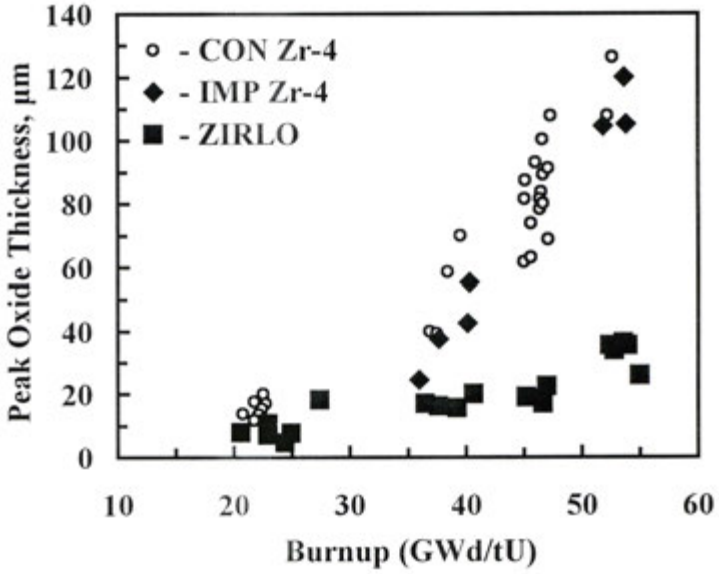

FIG. 2.77. In-pile corrosion of three types of cladding (reprinted, with permission, from Ref. [2.218], copyright 1997, American Nuclear Society, La Grange Park, Illinois).

TABLE 2.20. OXIDE THICKNESS AND HYDROGEN CONCENTRATION DURING CORROSION OF FUEL CLADDING [2.220]

Alloy	Oxide thickness (μm)	H_2 concentration (ppm)	% of theoretical concentration
ZIRLO Burnup = 44.8 MWd/kgU	5	24	9.9
	12	87	14.6
	16	120	15.6
	25	240	19.7
	32	165	10.5
IMP [improved] Zircaloy-4 Burnup = 46.7 MWd/kgU	5	32	12.9
	20	180	18.9
	25	210	17.5
	69	620	17.4

The corrosion resistance of ZIRLO tubes is governed by the tin concentration of the alloy (the patent tolerates a range 0.7–1.5 wt% (0.54–1.16 at.%) Sn [2.39]. As the tin concentration of the alloy is reduced from 1.1–1.2 wt% (0.85–0.92 at.%) to 0.95 wt% (0.73 at.%), the in-pile corrosion resistance of claddings becomes almost two times higher (Fig. 2.78) [2.221]. Further reductions of Sn to 0.75 wt% (0.58 at.%) improve in-reactor corrosion resistance by up to 30% up to burnups of 52 MW d/kgU. A minimum concentration of Sn (probably between 0.5 wt% (0.38 at.%) and 0.3 wt% (0.23 at.%)) is required to avoid accelerated corrosion when Li is present in the water. The controlling processing variable for good corrosion resistance appeared to be one hour at temperatures ≥ 823 K (550°C) after final CW that resulted in the refinement of second phase particles [2.222].

In-pile, the structural elements of a fuel assembly (ZIRLO cladding, grids and guide thimbles) show high dimensional stability (Figs 2.79–2.81) [2.219, 2.220]. For example, in the temperature range 565–605 K (292–332°C) to a neutron fluence of about 9×10^{25} n·m^{-2} (E > 1 MeV), guide tubes and grids made from ZIRLO grew by 0.08% whereas those made from Zircaloy-4 grew by 0.34%, a difference of over a factor of four [2.219].

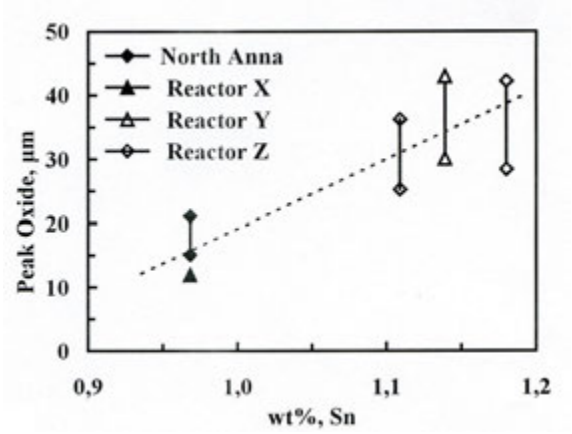

FIG. 2.78. Maximum thickness of oxide on ZIRLO claddings of fuel rods versus concentration of tin (reprinted, with permission, from Ref. [2.221], copyright ASTM International).

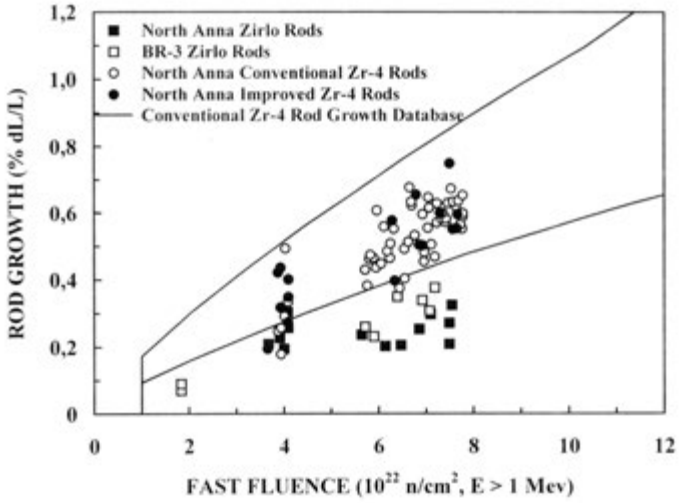

FIG. 2.79. Growth of fuel rods clad in ZIRLO and Zircaloy-4 (reprinted, with permission, from Ref. [2.219], copyright ASTM International).

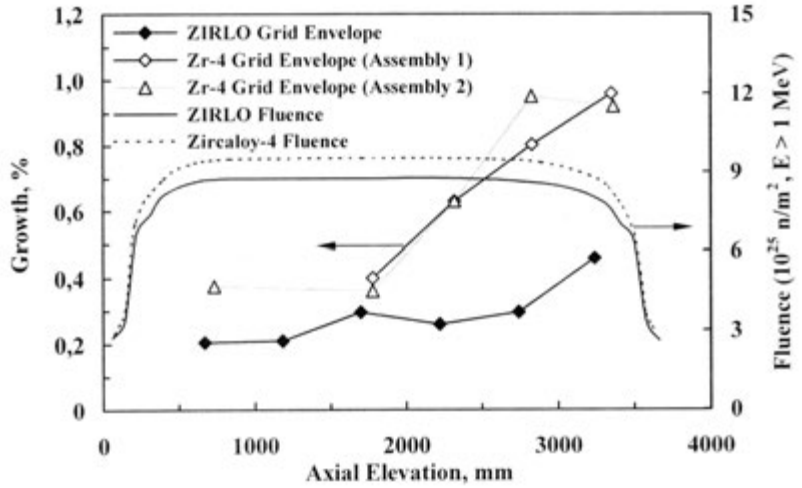

FIG. 2.80. Dimensional changes of ZIRLO and Zircaloy-4 (Wolf Creek) structural components as a function of fuel assembly elevation (reprinted, with permission, from Ref. [2.220], copyright ASTM International).

ZIRLO fuel rods and assemblies are in operation in many PWRs. The results of their operation attest to the good properties of the alloy, permitting a high fuel burnup to 75 MW d/kgU in PWRs [2.223].

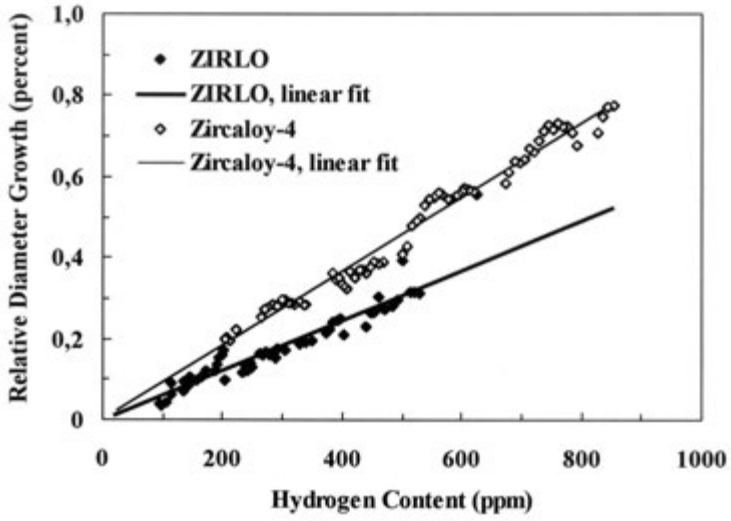

FIG. 2.81. Relative diameter changes in guide tubes as a function of hydrogen concentration (reprinted, with permission, from Ref. [2.224], copyright ASTM International).

2.5.3.2. E635 alloy

The chemical composition of the E635 alloy, shown in Table 2.21, is similar to that of ZIRLO, except for its slightly higher iron concentration and typically lower oxygen concentration. E635 is intended for use in fuel cladding and other structural components of fuel assemblies used in PWRs and BWRs. This alloy is highly resistant to corrosion, HPU, irradiation creep and growth. It features high strength and ductility after irradiation. Its good properties make it a promising structural material that is capable of withstanding extended fuel burnup and corresponding long operation in WWERs and RBMKs. As a structural material, the properties of E635 are superior to those of E110 alloy and Zircaloy [2.225–2.227].

TABLE 2.21. CHEMICAL COMPOSITION OF E635 ALLOY [2.225]

	Tolerable concentration	Typical concentration
Alloying element (wt%):		
Niobium	0.9–1.1	0.95–1.05
Tin	1.1–1.4	1.20–1.30
Iron	0.3–0.5	0.34–0.40
Impurity (ppm)		
Oxygen	500–1200	500–700
Carbon	200	50–100
Silicon	200	50–100
Nitrogen	60	30–60

As with E110, E635 is produced from a mixture of electrolytic powder and iodide zirconium. The basic stages of fabrication are similar to those of other zirconium alloys and involve β quenching, hot working and multiple cold rollings with anneals at the intermediate and finishing stages at about 873 K (600°C) [2.225].

The microstructure of components fabricated from the E635 alloy consists of grains of α solid solution and a fine dispersion of intermetallic particles of composition $Zr(Nb,Fe)_2$ and $(Zr,Nb)_2Fe$ (Table 2.22) [2.225, 2.226, 2.228]. After irradiation, the Laves phase, $Zr(Nb,Fe)_2$, becomes depleted in Fe and transforms from HCP to BCC, while the $(Zr,Nb)_2Fe$ precipitates are unaltered except for a redistribution of Nb on their surface. No amorphization was observed [2.229].

TABLE 2.22. MICROSTRUCTURE CHARACTERISTICS OF E635 ALLOY CLADDING TUBES [2.225, 2.226, 2.228]

Characteristics	Average value
Average grain size (μm)	3.0–4.5
Average particle size (nm)	100
Particle number density (cm^{-3})	$(2–4) \times 10^{13}$
Particle composition (at.%) $Zr(Nb,Fe)_2$ – HCP: a = 0.53 nm, c = 0.85 nm	Zr-35, Nb-35, Fe-30
$(Zr,Nb)_2Fe$ – FCC: a = 1.21 nm	Zr-60, Nb-10, Fe-30
Texture parameters	f_r=0.57–0.61, f_t=0.28–0.32, f_l=0.07–0.11

Fuel components are either fully or partially recrystallized and show a high resistance to corrosion under WWER and RBMK conditions. After a fuel burnup in WWER of 55–60 MWd/kgU, the oxide thickness on E635 fuel cladding is in the range 40–50 μm, about five times higher than on E110 fuel cladding. Under conditions of surface and bulk boiling in RBMKs, E635 components corrode to form uniform, dense oxides without nodular corrosion and with low HPU, and are superior to E110 components (Fig. 2.82) [2.211, 2.225, 2.230]. Their corrosion resistance is independent of the amount of recrystallization (Fig. 2.83) [2.226, 2.228]. The highest corrosion resistance is demonstrated by cladding tubes in which the A parameter of the annealing is between 10^{-18} and 10^{-19} h. The microstructure of these tubes contains particles of 85–92 nm in size with a number density of $(2–4) \times 10^{19}$ m^{-3} [2.227]. The E635 alloy is weakly sensitive to the lithium concentration of water and in this respect it is far superior to binary Zr-Nb alloys and Zircaloy-4 (Fig. 2.84) [2.226, 2.228]; this property of the alloy makes it promising for PWRs.

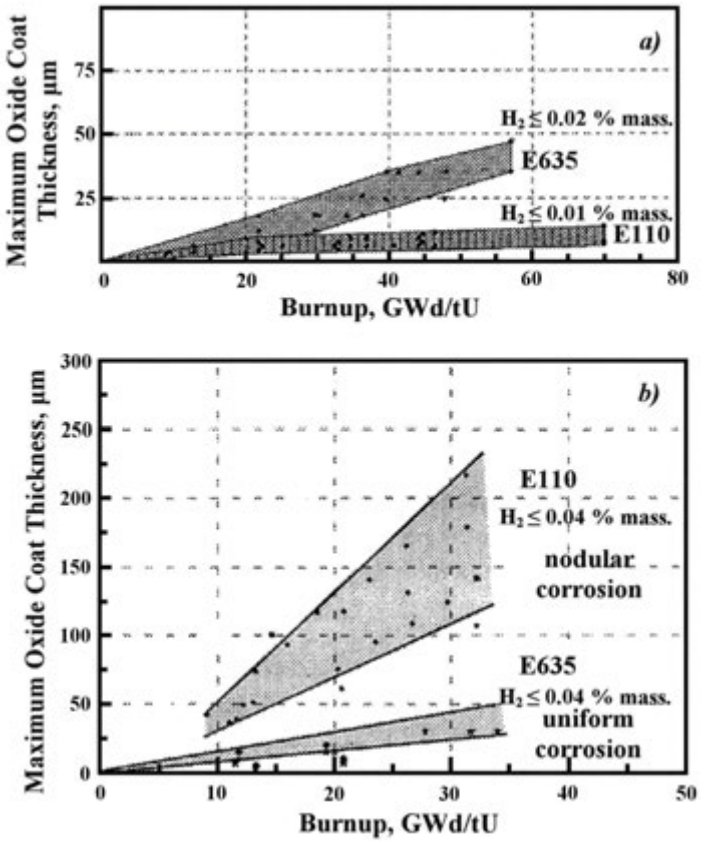

FIG. 2.82. Maximum oxide coat thickness on fuel cladding versus burnup under conditions specific to (a) WWERs and (b) RBMKs [2.211].

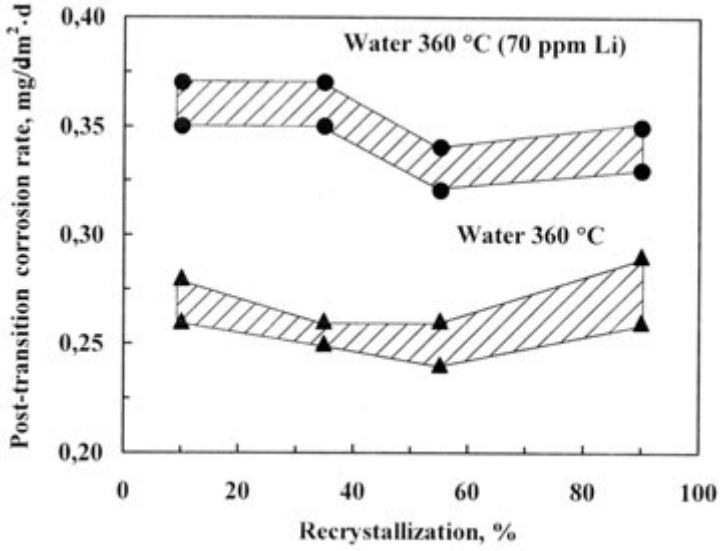

FIG. 2.83. Influence of amount of recrystallization in E635 alloy tubes on the post-transition corrosion rate [2.226, 2.228].

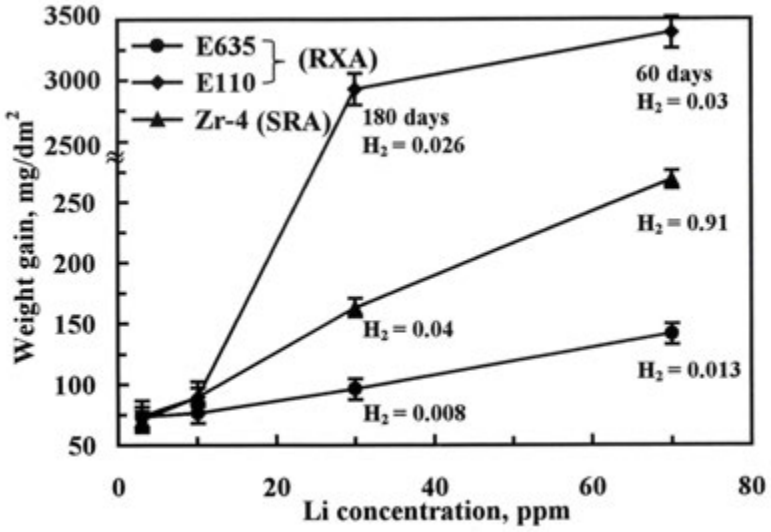

FIG. 2.84. Corrosion of alloys in autoclaves containing water with Li additives [2.226, 2.228].

Typical tensile properties of recrystallized E635 cladding are summarized in Table 2.23 [2.225]. Under neutron irradiation, E635 alloy components strengthen while retaining ductility (Fig. 2.85) [2.225, 2.226]. The most important feature of E635 products is their high resistance to thermal and irradiation induced creep and growth (Fig. 2.86) [2.225]. Compared with E110 and Zircaloy, the irradiation growth of E635 does not appear to depend on CW or the state of recrystallization (Fig. 2.87) [2.206, 2.227]. This feature of the alloy allows its application for components that are highly loaded and have to be dimensionally stable [2.156]. At an expanded scale, the highest resistance to irradiation growth is demonstrated by fully recrystallized E635 (Fig. 2.88) [2.228]. The role of Fe is to suppress the formation of <c> dislocations and reduce growth. Concentrations of > 0.35 wt% (0.57 at.%) Fe provide good protection from breakaway growth [2.156]. The high resistance of the E635 alloy to creep and growth under irradiation and good corrosion resistance was corroborated by observations on guide thimbles in WWER-1000 and pressure tubes in boiling RBMK [2.231, 2.232].

TABLE 2.23. TENSILE PROPERTIES OF E635 ALLOY TUBES [2.225]

Test T (°C)	Tension			Rupture under internal pressure	
	σ_u (MPa)	$\sigma_{0.2}$ (MPa)	δ (%)	σ_u (MPa)	δ (%)
Room temp.	480	300	33	600	45
300	280	160	38	340	50
400	250	150	35	—	—

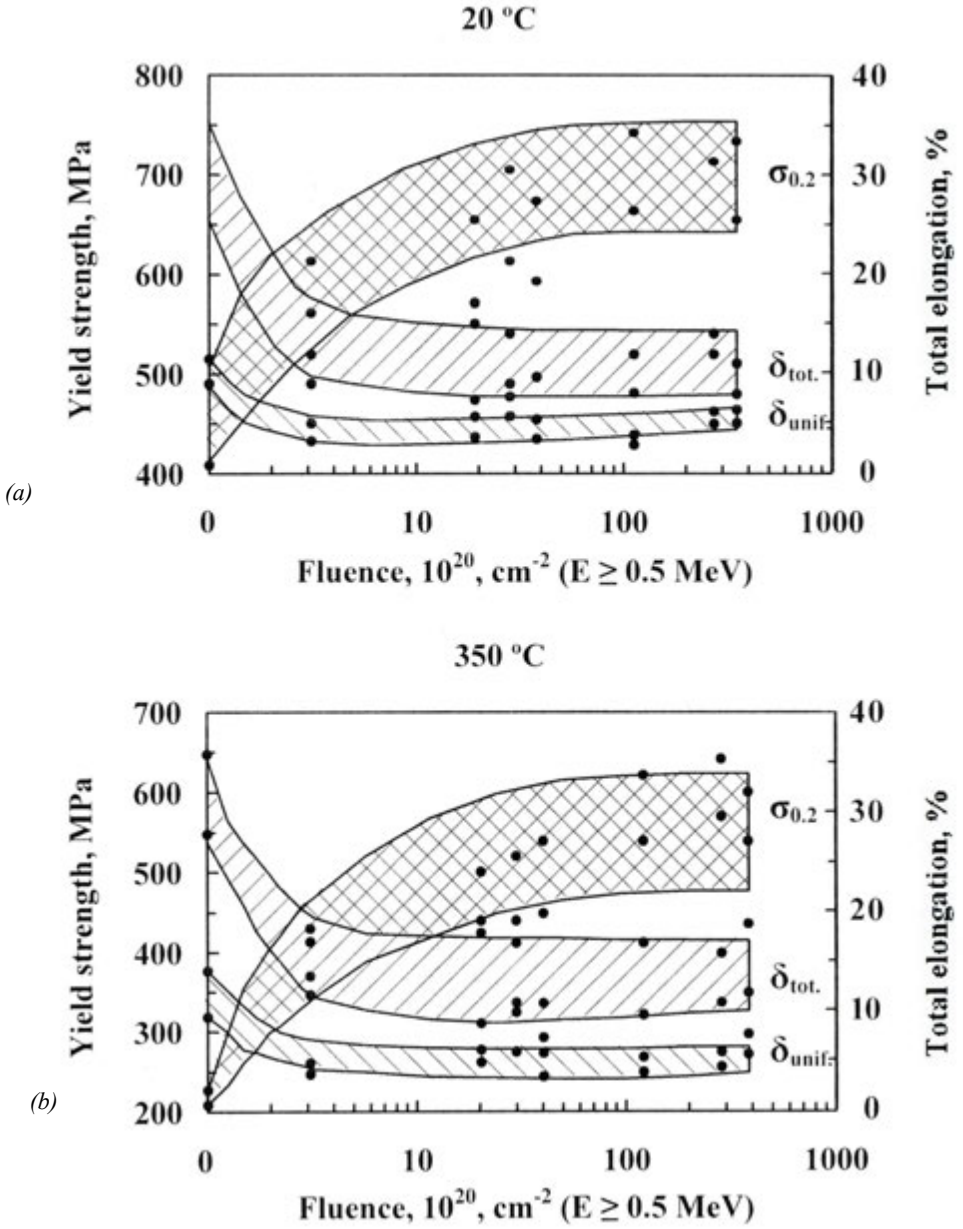

FIG. 2.85. Tensile properties of E635 cladding samples unloaded from reactor at 293 K (20°C) (a) and 623 K (350°C) (b) (reprinted, with permission, from Ref. [2.225], copyright ASTM International).

(a)

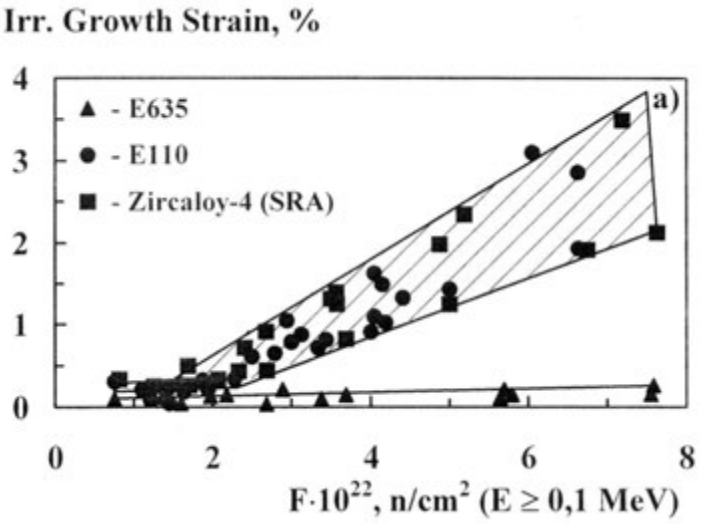

(b)

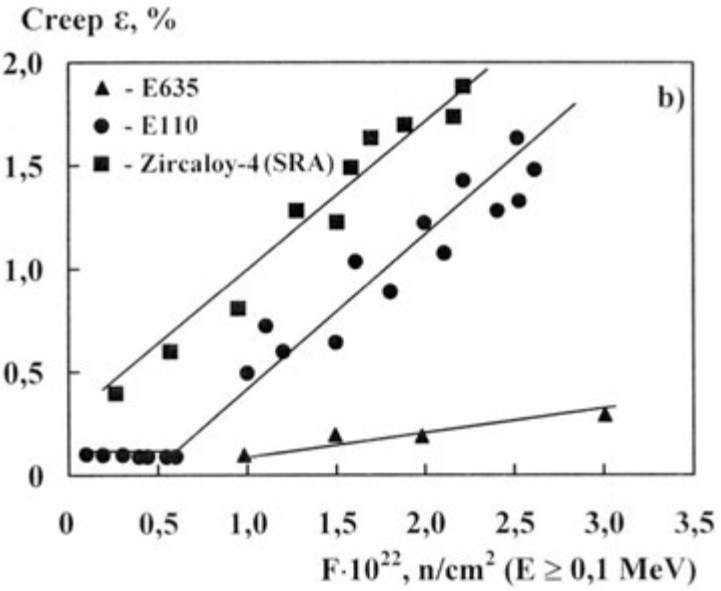

FIG. 2.86. Influence of neutron irradiation at 603 K to 623 K (330°C to 350°C) on (a) irradiation growth strain, and (b) creep (σ = 100 MPa, 8500 h) of tubes (reprinted, with permission, from Ref. [2.225], copyright ASTM International).

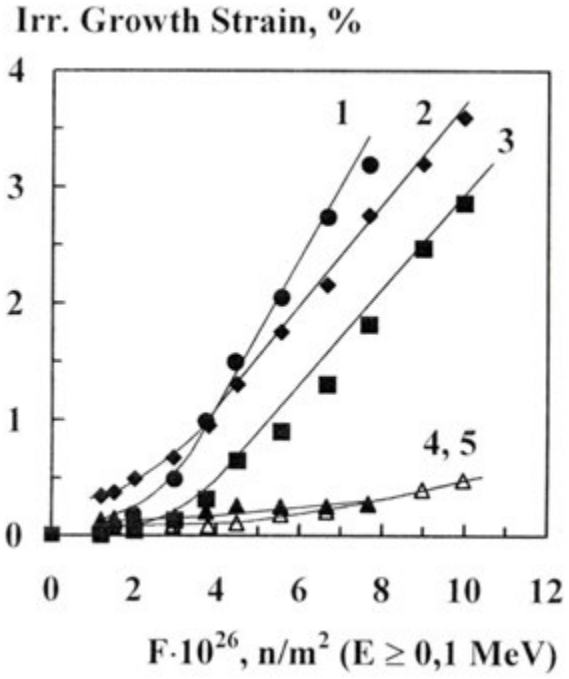

FIG. 2.87. Irradiation growth of (1) fully recrystallized E110; (2) CW Zr; (3) fully recrystallized E125; (4) CW E635; and (5) fully recrystallized E635 [2.206, 2.227].

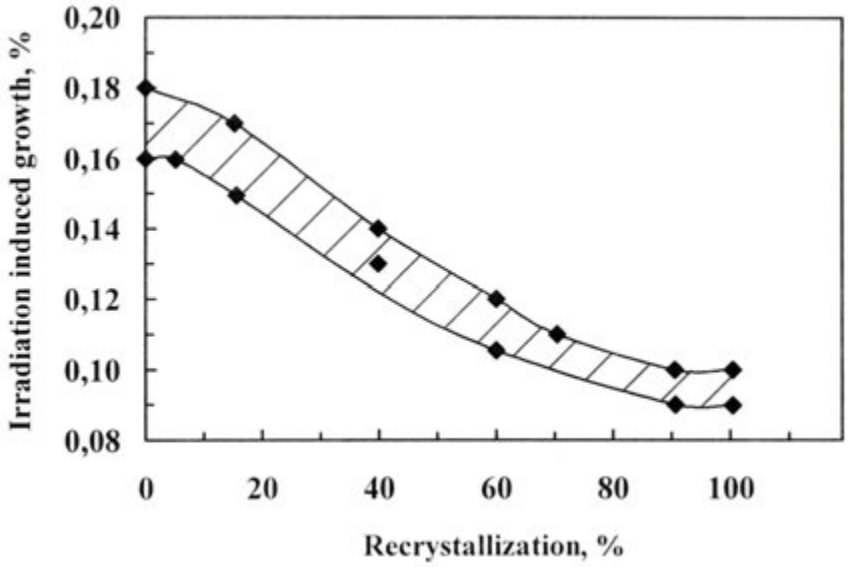

FIG. 2.88. Influence of amount of recrystallization on irradiation induced growth of E635 alloy tubes (T_{irr} = 628 K to 638 K (355°C to 365°C), $\Phi = 3\times10^{26}$ n/m^2, $E \geq 0.1$ MeV) [2.228].

Using the E635 alloy as a base, a modified alloy E635M has been designed, the tin and niobium concentrations of which were reduced to 0.70–0.90 wt% (0.54–0.69 at.% Sn, 0.69–0.89 at.% Nb) with the aim of diminishing the thickness of the oxide to that of E110 alloy on fuel cladding under WWER conditions (Fig. 2.89) [2.233]. E635M alloy preserves the high resistance to creep and growth and is suitable for fuel cladding and fuel assembly components of WWERs and PWRs aiming to reach high fuel burnup [2.233].

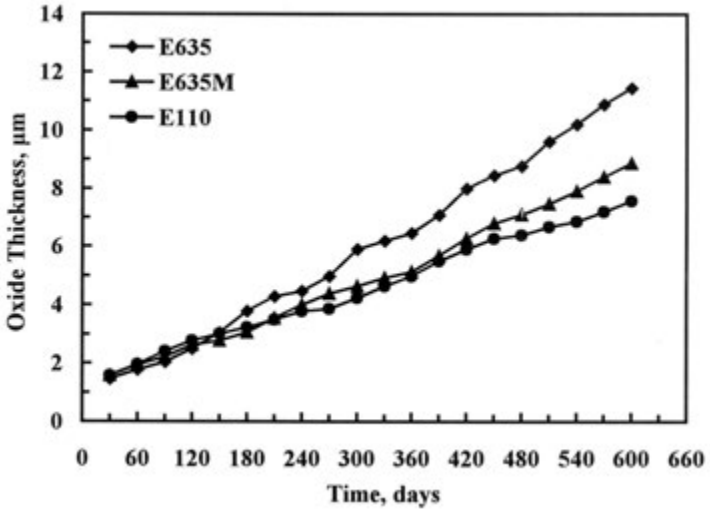

FIG. 2.89. Corrosion of alloys in pure water autoclaves (633 K (360°C), 18.6 MPa) [2.233].

2.5.4. Zr-2.5Nb alloy

The binary Zr-2.5 wt% Nb alloy was developed in the then USSR for pressure tubes in RBMKs, for fuel assembly shrouds of WWER-440s [2.205] and, later, in Canada for pressure tubes in CANDU reactors [2.234]. This alloy remains the chosen material for pressure tubes. Compared with fuel cladding, pressure tubes of RBMK and CANDU are large: 4–8 m in length, 80–110 mm in diameter, d, and about 4 mm in wall thickness, t. Under reactor operating conditions, the pressure, P, of the heat transport water imposes tensile hoop stresses in the range 80–160 MPa, based on $Pd/2t$.

The main requirements for pressure tubes are dimensional stability, low rates of corrosion (oxidation and hydrogen uptake) and high resistance to cracking to ensure structural integrity for in-reactor operation of up to 30 years.

In the Russian Federation, Zr-2.5Nb alloy is called E125. Pressure tubes are fabricated from a mixture of electrolytic powder and iodide zirconium (Table 2.24) [2.205, 2.235, 2.236]. The operating conditions of pressure tubes in RBMK-1500s are more onerous than those in RBMK-1000s (Table 2.25) [2.237].

TABLE 2.24. CHEMICAL COMPOSITION OF E125 ALLOY USED FOR RBMK PRESSURE TUBES [2.236, 2.237]

Element	Required concentration	Typical concentration
Alloying element (wt%):		
Niobium	2.4–2.7	2.5–2.6
Impurity maximum (ppm):		
Iron	500	300–500
Copper	50	10–30
Nickel	60	30–40
Oxygen	1000	400–700
Carbon	200	30–70
Silicon	200	20–80
Aluminium	80	30–40

TABLE 2.25. OPERATING CONDITIONS OF PRESSURE TUBES IN RBMK-1500s AND RBMK-1000s

Parameters	RBMK-1000	RBMK-1500
Average temperature of tube wall (K (°C))	304 (577)	314 (587)
Hoop stress (MPa)	86	93.6
Fast neutron flux ($n \cdot m^{-2} \cdot s^{-1}$)	1.65×10^{17}	2.56×10^{17}

Consequently, the microstructure and properties of the tubes are different. For RBMK-1000s, the tubes are cold rolled (total reduction of 40–50%) and annealed at 803-813 K (530–540°C), which produces a partially recrystallized microstructure (CW-A). For RBMK-1500, the tubes are subjected to TMTs involving heating in the (α + β) region followed by quenching in water (TMT-1) or an inert gas (TMT-2), CW (10–15%) and a final α anneal [2.237, 2.238]. The microstructure of TMT-1 tubes consists of a martensite α Zr phase and 10–20 vol.% of a non-transformed α phase. After TMT-2, the tube microstructure consists of transformed lamellar Thomson-Widmanstätten α grains and a small quantity of non-transformed α phase grains. The texture parameters of those tubes are also different from CW-A; the values are related to the volume fraction of the residual α phase (Table 2.26) [2.205, 2.235, 2.239].

TABLE 2.26. TEXTURE PARAMETERS OF E125 ALLOY TUBES [2.235, 2.239]

Tube treatment conditions	f_T	f_R	f_Z
Anneal (550°C)	0.4–0.5	0.4–0.5	0.06–0.09
TMT-1, TMT-2	0.3–0.4	0.3–0.4	0.24–0.25

TABLE 2.27. TENSILE PROPERTIES OF E125 ALLOY PRESSURE TUBES (AXIAL DIRECTION) [2.235]

Tube condition	Testing temperature of 20°C			Testing temperature of 350°C		
	σ_u (MPa)	$\sigma_{0.2}$ (MPa)	δ (%)	σ_u(MPa)	$\sigma_{0.2}$(MPa)	δ (%)
Anneal 550°C-5h	510–560	320–370	24.0–30.0	340–340	190–230	28–34
TMT-1	645–725	510–635	18.5–22.5	450–520	375–440	16.0–21.0
TMT-2	475–550	350–415	20.0–28.0	290–360	205–280	18.5–27.0

The microstructure and texture of E125 alloy tubes are responsible for their strength, creep resistance (Tables 2.27 and 2.28) [2.235–2.237] and corrosion response (Fig. 2.90) [2.235]. Thermomechanically treated tubes have higher strength and creep resistance but lower corrosion resistance than annealed tubes. These properties depend on the metastable β-Zr phase and the extent of its decomposition.

TABLE 2.28. CREEP RATE OF E125 ALLOY PRESSURE TUBES [2.236, 2.237]

Tube condition	ε (%·h^{-1}) (3500C/100 MPa)	ε (%·h^{-1}) (3500C/100 MPa)	
	Axial loading	Axial loading	Tangential loading
Anneal	$(2.7–4.2) \times 10^{-5}$	$(1.0–3.1) \times 10^{-4}$	$(1.6–3.1) \times 10^{-4}$
TMT-1	$(2.0–2.5) \times 10^{-5}$	$(3.1–7.0) \times 10^{-5}$	$(3.0–6.5) \times 10^{-5}$
TMT-2	$(2.0–2.5) \times 10^{-5}$	$(5.7–8.2) \times 10^{-5}$	$(3.4–4.1) \times 10^{-5}$

(a)

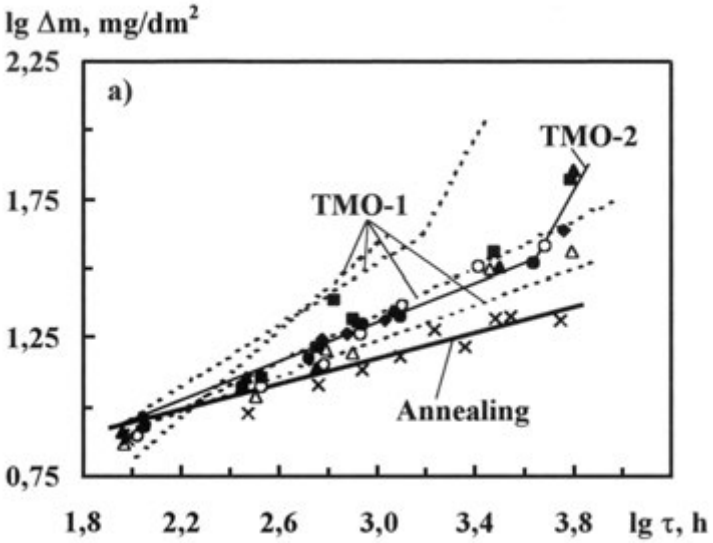

(b)

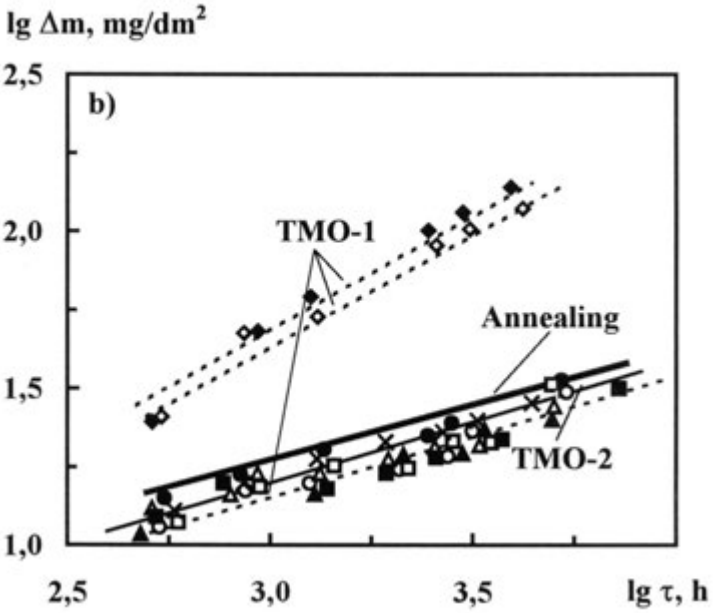

FIG. 2.90. Corrosion of E125 alloy tubes in (a) water containing 0.1 to 0.3 mg/kg oxygen at 583 K (310°C) and (b) in mixed gases (90 % He + 10 % N) at 623 K (350°C) [2.235].

The Zr-2.5Nb alloy used for CANDU pressure tubes is made from zirconium sponge. The chemical composition of the alloy is summarized in Table 2.29 [2.234, 2.240]. The corrosion resistance of the tubes is not a critical factor for their operation but the pick-up of hydrogen as a result of the corrosion is very important for fracture properties (Chapter 9, Volume 3 of this publication). Unlike with RBMKs, the design hoop stress for CANDU pressure tubes is up to 160 MPa so their strength must be high (at 573 K (300°C) and the UTS in the axial direction has to be > 480 MPa, Table 2.30) [2.235, 2.241].

To meet this requirement and provide high resistance to creep and corrosion, the tube fabrication process consists of deforming ingots by forging in the temperature range of the β and (α + β) phases and subsequently extruding in the (α + β) phase. In the final stage, the tube extrusion is cold drawn by a 25–30% reduction followed by heat treatment in an autoclave at 673 K (400°C) for 24 hours (CW) [2.234, 2.240]. The microstructure and crystallographic texture are formed during extrusion. The microstructure of the tubes consists of elongated α grains separated by β phase interlayers whose initial Zr/Nb ratio of 4:1 decreases during final heat treatment and subsequent reactor operation. The texture contains a high concentration of basal poles in the tangential direction [2.234, 2.242].

TABLE 2.29. CHEMICAL COMPOSITION OF Zr-2.5Nb ALLOY FOR CANDU PRESSURE TUBES [2.234, 2.240]

Element	Specified concentration (until 1994)	Specified concentration (after 1994)
Alloying element:		
Niobium	2.4–2.8 (wt%)	2.5–2.8 (wt%)
Oxygen	900–1300 (ppm)	1000–1300 (ppm)
	Impurity maximum (ppm)	
Carbon	270	125
Chromium	200	100
Chlorine	—	1
Hydrogen	25	5
Iron	1500	650
Nickel	70	35
Nitrogen	65	65
Phosphorus	—	10
Silicon	120	100

TABLE 2.30. TENSILE PROPERTIES OF CANDU CW Zr-2.5Nb PRESSURE TUBES AT 300°C (AD) [2.234, 2.241]

Property	Specified value	Typical value
Yield strength (MPa)	>330	330–380
UTS (MPa)	>480	489–531
Elongation (%)	>12	14–16

The microstructure in combination with the tangential type of the texture provides the CANDU pressure tubes with high hoop strength and diametral creep resistance. The fracture toughness of this material was highly variable until the role of trace elements was recognized [2.243] and controlled [2.240, 2.241]. These pressure tubes remain susceptible to delayed hydride cracking, thus great attention is paid to keeping hydrogen concentrations low and defects absent. In Zr-2.5Nb alloy pressure tubes, strength is one of the governing factors determining delayed hydride cracking velocity, as shown in Fig. 2.91, and, to a lesser extent, fracture toughness [2.244].

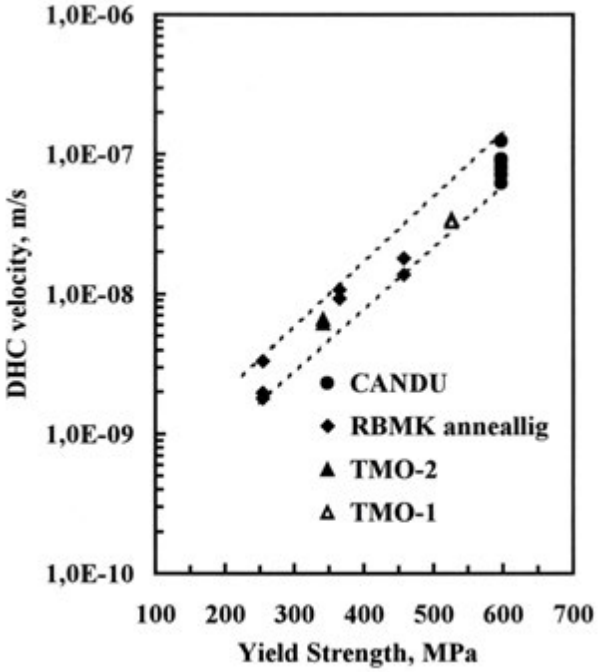

FIG. 2.91. Delayed hydride cracking velocity versus yield strength of CANDU and RBMK pressure tubes (523 K (250°C)), transverse direction) [2.244].

CANDU pressure tubes made from electrolytic powder provided the opportunity to compare their properties with those generated by the RBMK fabrication routes [2.245], Table 2.31. The strength effect on delayed hydride cracking velocity and the good resistance to creep at a higher hoop stress in CANDU were confirmed. With TMT-2 processing, the large grain size and Thomson-Widmanstätten distribution of the α grains are speculated to be responsible for the high fracture toughness after irradiation and resistance to in-reactor creep.

TABLE 2.31. COMPARISON OF PROPERTIES OF Zr-2.5Nb PRESSURE TUBES AFTER FOUR DIFFERENT FABRICATION ROUTES [2.245]

Material	UTS at 300°C, transverse direction, fluence $>10^{25}$ n·m^{-2} (MPa)	Delayed hydride cracking velocity at 250°C, axial crack, unirradiated ($\times 10^{-8}$ m/s)	Crack growth resistance at 250–300°C, axial crack, fluence $>10^{25}$ n·m^{-2} (MPa)	Diametral creep rate in power reactors ($\times 10^{-28}$ m^2·n^{-1})
CW-A	540	0.24	–	2.0
TMT-1	665	3.3	144	1.1
TMT-2	584	0.63	230	0.4
CW	826*	8.1	120	1.3**

* Tested at 250°C.
** Hoop stress 130 MPa.

A treatment similar to TMT-1 was used for the pressure tubes in the Karachi Nuclear Power Plant [2.246] and Fugen [2.247] and for a single tube in the Nuclear Power Demonstration reactor [2.248]. Surveillance on tubes and specimens removed from these

reactors showed that their corrosion resistance was good, and compared with CW tubes, they elongated more slowly, and their mechanical properties had similar responses to irradiation.

In an effort to reduce the elongation of CANDU pressure tubes, three variations of post-extrusion forming were explored under a programme called TG3 [2.249]:

— Route 1: 40% CW and stress-relieved at 773 K (500°C);
— Route 2: 20% CW, anneal at 923 K (650°C), 20% CW;
— Route 3: anneal at 973 K (700°C), CW 40%, stress-relieved at 748 K (475°C).

Examination of pilot tubes in service in a power reactor showed that only Route 1 reduced elongation, but that this came at the expense of increased diametral creep [2.250]. Pressure tubes using the main features of TG3 Route 2 are fabricated in India for use in CANDU type reactors [2.251, 2.252].

Zr-2.5Nb pressure tubes for Advanced CANDU reactors are to be fabricated by the CW process [2.253] The wall thickness will be 6.5 mm to enhance safety and reduce deformation driven by a pressure of around 12 MPa and a maximum temperature of 591 K (318°C).

In summary, with experience and a drive for efficiency and higher burnups, the basic commercial alloys have been improved and replaced. This process will continue. The importance of microstructure for determining properties has highlighted not only the role of chemical composition but has led to changes in philosophies of fabrication from one of expediency to one of strict control at each step in the process. The details of fabrication and in-reactor properties briefly mentioned here will be much expanded in the following chapters.

2.6. ALLOYS UNDER DEVELOPMENT

Improvement of zirconium cladding corrosion resistance is required to accommodate increasing fuel burnup (above 60 MWd/kgU), extending the time between fuel reloads and raising the temperature of the heat transport water in PWRs, WWERs and BWRs. As summarized above, ZIRLO [2.222], E110 and E635 [2.211], and M5 [2.217] are already being modified to improve their properties. Other alloys are being examined and tested in a large international development effort. Table 2.32 summarizes representative compositions of these alloys. They are mostly based on multicomponent alloying with Sn, Nb and Fe; Cr, Mo, Te, V and Cu have been added to some alloys. Testing in research and power reactors is in progress.

Using standard and optimized Zircaloy-2 and Zircaloy-4 as controls, the multicomponent new developed alloy (NDA) and Mitsubishi developed alloy (MDA) are being tested in Japanese PWRs and BWRs to evaluate their corrosion resistance [2.254–2.258]. Alloys containing Sn, Nb and Mo or Te were also tested [2.259]. Data on the superiority of the NDA and MDA over commercial alloys for conditions of extended fuel burnup have not yet been demonstrated. Alloys based on Nb, called J-alloys, are showing good corrosion resistance up to 68 MWd/kg [2.260].

A series of multicomponent alloys based on low concentrations of tin, M2, M3 and M4, are being tested in France. Compared with M5, the advantages of these alloys for fuel cladding are not yet apparent [2.212, 2.214, 2.261]. Increasing the iron concentration in M5 improves corrosion resistance without negatively affecting other properties [2.262].

Similar multicomponent alloys developed in the USA and designated ‘A’, ‘C’ and ‘E’ also show promise. Alloy ‘A’, when compared with optimized Zircaloy-4, demonstrates

noticeably lower corrosion (by almost a factor of two) to a fuel burnup of 69 MWd/kgU, and about 30% lower irradiation growth at a neutron fluence of 1.5×10^{26} n·m^{-2} [2.192].

TABLE 2.32. COMPOSITION OF ZIRCONIUM ALLOYS UNDER DEVELOPMENT

Alloy (Country)	Concentration (wt%)*						
	Sn	Nb	Fe	Cr	Ni	V	Cu
MDA (Japan)	0.8	0.5	0.2	0.1	—	—	—
NDA (Japan)	1.0	0.1	0.27	0.16	0.01	—	—
J1 (Japan)	—	1.8	—	—	—	—	—
J2 (Japan)	—	1.6	—	0.1	—	—	—
J3 (Japan)	—	2.5	—	—	—	—	—
M2 (France)	0.5	—	0.20	0.10	—	—	—
M3 (France)	0.50	0.50	0.25	—	—	—	—
M4 (France)	0.50	—	0.60	—	—	0.3	—
M5+Fe (France)	—	1.0	0.1	—	—	—	—
Q alloy (France)	0.25	1.0	0.35	—	—	—	—
Optimized ZIRLO (USA)	0.67	1.0	0.1	—	—	—	—
A (USA)	0.50	0.30	0.35	0.25			
C (USA)	0.40	—	0.50	0.24	—	—	—
E (USA)	0.70	0.40	0.45	0.24	0.03	—	—
AXIOM X1 (USA)	0.3	0.7–1.0	0.05	—	—	0.2	0.12
AXIOM X2 (USA)	—	1.0	0.06	—	—	—	—
AXIOM X3 (USA)	—	1.0	0.06	0.25	0.05	—	0.1
AXIOM X4 (USA)	0.3	0.7	0.35	0.25	—	—	—
HANA-3 (Rep. of Korea)	0.4	1.5	0.1	—	—	—	0.1
HANA-4 (Rep. of Korea)	0.4	1.5	0.2	0.1	—	—	—
HANA-6 (Rep. of Korea)	—	1.1	—	—	—	—	0.05
BWR 1 (Germany)	1.3	—	0.3	—	—	—	
BWR 2 (Germany)	1.0	3	—	—	—	—	—
PWR (Germany)	0–1.8	0.2–1.0	0.15–0.5	0.05–0.3	—	0.05–0.3	—

* Nominal oxygen concentration of alloys is 900–1250 ppm.

It should be noted that when the composition of Alloy A is described in atomic percent, Fe has the greatest concentration of the alloying elements: Sn 0.38 at.%, Fe 0.57 at.%, Cr 0.44 at.%, Nb 0.29 at.%. Another series of alloys called AXIOM is based on Zr-Nb [2.263–2.266]. The composition of ZIRLO is also being optimized by lowering the concentration of tin to reduce uniform corrosion [2.265, 2.267, 2.268].

A series of Nb containing alloys called HANA (the name derives from high performance alloy for nuclear application) are being explored in the Republic of Korea [2.269–2.272]. HANA-3 and HANA-4 are similar to ZIRLO and E635 but with the addition of a small amount of Cu (HANA-3) or Cr (HANA-4), while HANA-6 is similar to E110 and M5 except for the addition of a small amount of Cu. In out-reactor tests in pure water at 633 K (360°C) HANA-4 and HANA-6 both corrode more slowly than Zircaloy–4, with HANA-6 being better than HANA-4 [2.2721]. Both alloys benefited from a low temperature final anneal. The Cu is thought to be included in precipitates of β-Nb rather than as Zr_2Cu. In an irradiation to 12 MWd/kgU using all three alloys, HANA-4 had the lowest corrosion and creep-down, its values being about half those of Zircaloy-4 [2.269].

Alloy developments in Germany for BWRs and PWRs are summarized in Refs [2.273–2.275]. For BWRs the aim was to exploit irradiation resistant SPPs of either Zr_3Fe or β-Nb. A wide range of alloys and fabrication routes were studied for PWRs. The corrosion rate of Zr-Sn-(Fe, Cr, V) alloys decreases with the reduction of the concentration of Sn and the increasing of the concentration of Fe+Cr+V up to about 0.6 wt%. The addition of Nb compensates for the amount of Fe+Cr+V needed to reduce corrosion, but only up to Sn concentrations of 0.4 wt%. Although some correlation between in-reactor and out-reactor behaviour was observed, for reliable and predictable performance in a power reactor, in-reactor testing was shown to be necessary.

In summary, although many valuable insights have been gained with the current programmes of alloy development, not all the proposed alloys and their various fabrication routes have reached commercial maturity.

2.7. ZIRCONIUM ALLOYS NOT USED COMMERCIALLY

Other alloys have been examined but not used in power reactors. Some alloys aspired to surpass the properties of the Zircaloys and binary niobium alloys while a second type was aimed at reactors operating at high temperatures where Zircaloy and Zr-Nb alloys failed to provide the required properties. The main reasons for these alloys not being used were that:

— The new alloys were not superior to Zircaloy or Zr-Nb alloys.
— The new alloys were difficult to process.
— The novel reactor design for which the alloys were intended was cancelled.

The alloys examined included: Ozhennite, Scanuk, Excel, Zr_3Al and alloys of the Zr-Cr–Fe and Zr–Fe–Cu systems. The compositions of the alloys and their properties in comparison with Zircaloys and Zr-Nb alloys are summarized in Table 2.33.

TABLE 2.33. ZIRCONIUM ALLOYS NOT USED IN POWER REACTORS

Name and composition of alloy (wt%)	Reason not used	Country
Ozhennite-0.5 (Zr-0.2Sn-0.1Fe-0.1Ni-0.1Nb)	Corrosion resistance was no better than Zircaloy and Zr-Nb alloys.	Russian Federation
Scanuk (Zr-(0.5-1) Nb-(0-0.5) Cr-(0-0.3) Mo-0.04Fe-0.06Sn)	Corrosion and tensile properties similar to those of Zircaloy.	UK and Scandinavia
Excel (Zr-3.5Sn-0.8Mo-0.8Nb)	High strength and creep resistance. Low corrosion resistance and high HPU in water.	Canada
Zr_3Al (ordered solid solution, 7–9.5%Al)	High strength. Inadequate processability. Poor response to irradiation.	Canada
Valloy (Zr-1.2Cr-0.1Fe)	High corrosion resistance to steam, $T \geq 400$°C. Aqueous corrosion and mechanical properties similar to Zircaloy and binary Zr-Nb alloys.	USA
Zr-1.2Cu-0.28Fe	Corrosion resistance to water inferior to that of Zircaloys and Nb containing alloys. Corrosion resistance in steam at >400°C is a little superior.	Canada
Zr-1.0Fe-1.0Cr-0.4W	Corrosion resistant to water and steam at >400°C. Strength and creep resistance are a little lower than those of Zircaloy and Zr-1Nb alloy.	Russian Federation
Zr-1.0Fe-1.0Cu-0.4W	Corrosion resistant in steam at about 500°C. Corrosion resistance to water is inferior to that of Zircaloy and Nb containing alloys.	Russian Federation

The multicomponent alloy Ozhennite-0.5 [2.11] has potential for operating in water and organic coolants at around 673 K (400°C) and above. In out-reactor tests it was shown to have superior corrosion and HPU properties to Zircaloy-4 and Zr-2.5Nb in steam at 673 K and 773 K (400°C and 500°C) and was recommended for trial fuel cladding and pressure tubes for an organically cooled reactor [2.276]. Under irradiation in organic coolant at 623–673 K (350–400°C) the superiority of Ozhennite-0.5 disappeared [2.277] Examination of a pressure tube made from Ozhennite-0.5, after nearly 21 000 h irradiation at 648–673 K (375–400°C) and a maximum neutron flux of 2.4×10^{17} n·m^{-2}·s^{-1}, showed that the oxidation was not excessive, and the maximum thickness 20 μm, but the HPU was high, with a maximum concentration of 400 ppm (3.5 at.%). The tensile strength was only modestly increased because the irradiation damage was annealed out rapidly at the operating temperatures [2.278]. The reactor design was abandoned, and this alloy development ceased.

Scanuk alloys were intended for fuel cladding in superheated steam. They are based on 0.5–1 wt%Nb. Compared with Zircaloy, these alloys had superior corrosion resistance at 773 K (500°C) but did not demonstrate any large advantages in their corrosion and mechanical properties over Zircaloy at temperatures around 573 K (300°C); the alloy Zr-1Nb-0.5Cr appeared the most promising [2.279]. Reactor development has not proceeded and the incentive for further studies on these alloys has disappeared.

Excel alloy was originally intended to provide high strength for pressure tubes for CANDU type reactors operating at 723 K (450°C). The main strengthening agents were to be solutes and precipitates and any loss in corrosion protection was to be recovered by cladding the tube with a weaker but corrosion resistant material [2.280]. Scoping trials with various compositions [2.281, 2.282] led to the alloy Zr-3.5Sn-0.8Mo-0.8Nb, called Excel. Subsequently, the focus reverted to improving in-reactor creep properties at about 570 K (300°C). The strength of the alloy is sufficient that it can be used in the annealed condition; in this condition its in-reactor creep is less than half that of CW Zr-2.5Nb. Pick-up of hydrogen is greater and oxide thicknesses are about twice those of Zr-2.5Nb; if necessary, an extra corrosion allowance could be applied [2.283]. Rates of delayed hydride cracking are up to ten times faster than in Zr-2.5Nb [2.284]. These latter three properties have postponed the application of this alloy in power reactors.

The alloy based on the Zr_3Al ordered FCC phase containing 8.6 wt% (24.3 at.%) Al was thought to provide improved in-reactor creep strength. The hypothesis was that some long range order would reduce diffusion rates of vacancies produced by irradiation, increase the recombination of vacancies and interstitials and thus reduce the rate of dislocation climb, a possible rate controlling step in in-reactor creep. Also, some disorder from irradiation could impede dislocation glide, a possible strain producing step after the climb [2.285]. Although great care had to be taken in heat treatment to avoid brittleness, early results of properties of Zr_3Al showed promise [2.286, 2.287]. However, after neutron irradiation to a fluence of 2.3×10^{25} n·m^{-2} (E > 1 MeV), the alloy became disordered and amorphous, lost all ductility and had the fracture toughness of glass [2.288]. Thus the development programme was terminated.

The multicomponent alloys containing Cr, Fe, Cu and W were corrosion resistant in steam at >673 K (400°C) and were intended for fuel cladding in BWRs with superheated steam. These alloys surpassed both Zircaloy and Zr-Nb alloys in terms of corrosion out-reactor in steam at 673 K (400°C) and higher. The reactors for which these alloys were intended were not built and using these alloys for current operating temperatures was not pursued because their corrosion in water was similar or greater, and their strength and creep resistance were similar or lower than those of Zircaloy and Nb alloys [2.289–2.294].

In summary, the last two sections have illustrated the difficulties of improving zirconium alloys because of the constraints imposed by nuclear considerations, the necessity for extensive in-reactor testing and the high standard set by the original alloys, Zircaloy and dilute Zr-Nb alloys.

2.8. CONTROL OF IMPURITIES IN ZIRCONIUM ALLOYS

Impurities in zirconium alloys originate from the initial ores and from processing. The majority of impurities degrade the properties and characteristics of materials. Their concentrations are limited by adherence to standards and specifications. These restrictions are set to preserve a low neutron capture cross-section and provide high corrosion resistance, good processability and high crack resistance during working as well as during reactor operation. Some trace elements are remarkably effective in controlling properties and only a few atoms are required to do so.

Cd, B, Hf and Co are elements that increase neutron capture cross-section and must be minimized.

The influence of impurities on Zr corrosion was recognized in the first few years of the development of corrosion resistant alloys. N, Al, Ti and C impurities are most harmful for corrosion of zirconium (Figs 2.1, 2.2). Synergies between elements can alleviate some deleterious consequences. For example, in Zr-2.5Nb, iron interacts with carbon to reduce the corrosion rate and HPU with minimum values being achieved with additions of about 1000 ppm (0.16 at.%) Fe [2.295].

C, H, Si, Cl, P, F and O impurities decrease the ductility of zirconium and its alloys, thus, degrading processability and crack resistance as seen, for example, in Figs 2.92–2.94:

- Hydrogen is particularly dangerous because even at any reasonably low concentration it is always present as brittle hydrides at room temperature. Delayed hydride cracking has been demonstrated with concentrations as low as 2 ppm (0.018 at.%); only 2 out of every 10 000 atoms were hydrogen [2.296].
- A concentration of chlorine as low as 2 ppm (0.0005 at.%), that is, 5 atoms out of every 1 000 000 atoms, can reduce the crack growth resistance of Zr-2.5Nb by a factor of two [2.243]. The Cl segregates in association with C to form planes of weakness in a highly anisotropic microstructure. The concentration of Cl can be reduced to innocuous amounts by multiple melting. Small concentrations of Cl are useful in Zircaloy-2 or Zircaloy-4 for promoting a basketweave microstructure after rapid cooling so for some alloys a small inventory of Cl is beneficial [2.184].
- In the earliest development of zirconium, high oxygen concentrations produced embrittlement. Vacuum processing for the parts of the fabrication that require very high temperatures eliminated this problem. Oxygen is often considered an alloying element at concentrations between 800 and 1600 ppm (0.45–0.91 at.%) to provide strengthening.

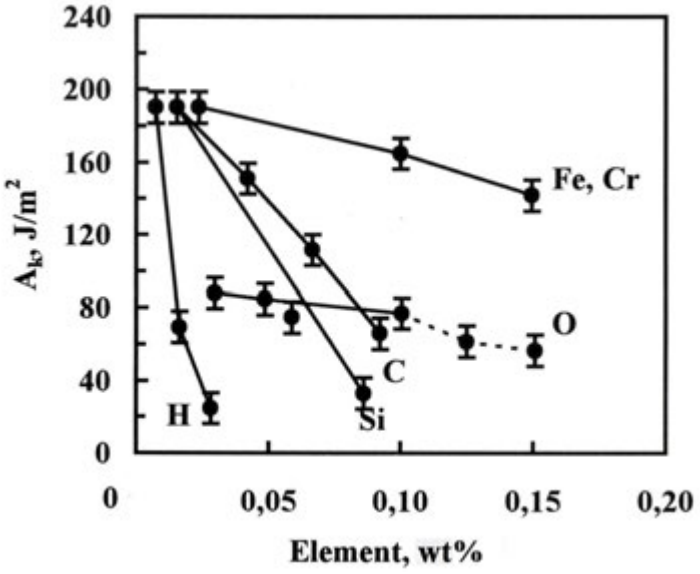

FIG. 2.92. Influence of impurity concentration on the impact toughness of Zr-1%Nb alloy [2.205].

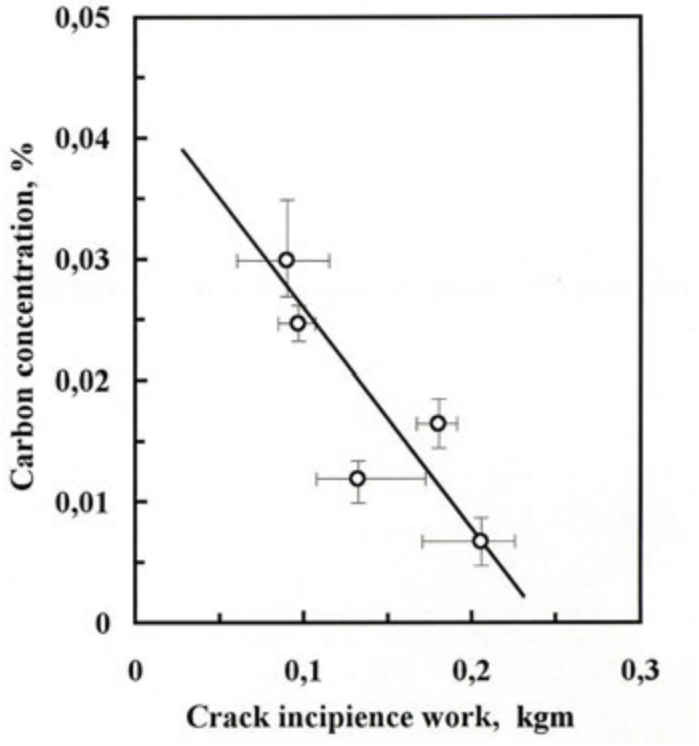

FIG. 2.93. Influence of carbon concentration on crack nucleation strain in Zr-2.5Nb alloy [2.206].

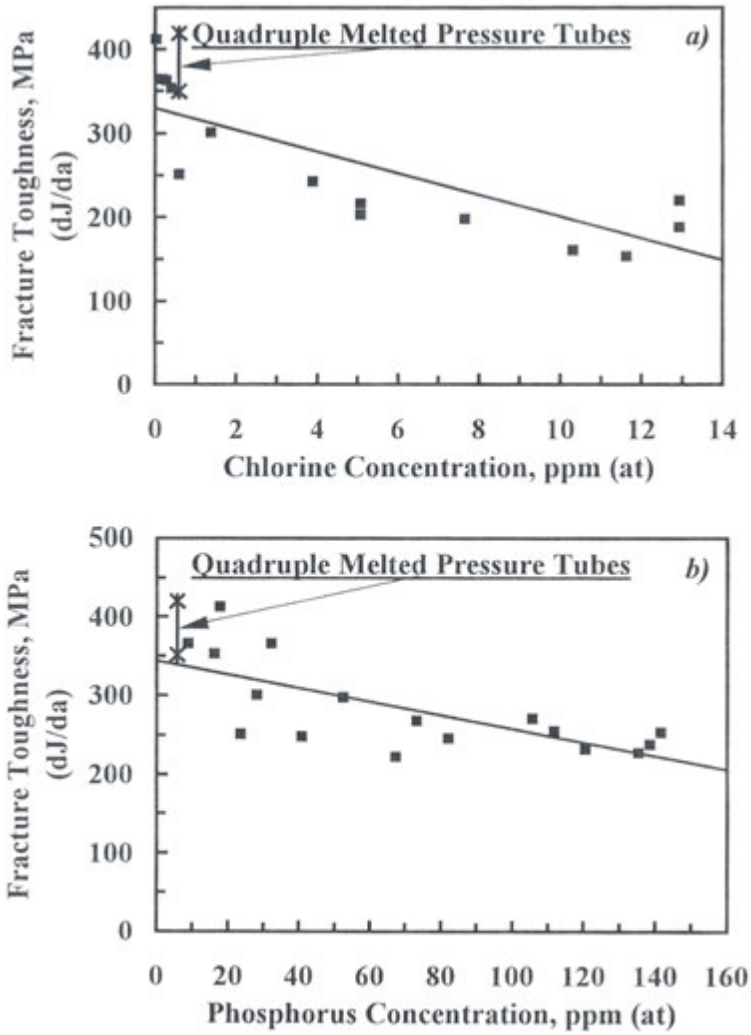

FIG. 2.94. Fracture toughness of pressure tubes as a function of chlorine (a) (with phosphorus concentrations of <30 ppm (at) [100 ppm (wt)]) and phosphorus (b) concentration (with chlorine concentrations <1 ppm (at) [0.4 ppm (wt)]) (reproduced from [2.243] with permission courtesy of AECL, Canada).

Traces of Na, Mg, Cl, K, Ca, Al, Si and F have been shown to promote oxidation and hydrogen absorption in Zr-1Nb in steam at 1373 K (1100°C) [2.211].

As well as having a favourable effect on the corrosion of zirconium, minor additions of Fe can aid deformation resistance. For example, 0.35 wt% (0.57 at.%) Fe postpones breakaway growth in E635 alloy to beyond 8×10^{26} n·m^{-2} (E > 0.1 Mev) [2.157]. A small concentration of S slows creep; 25 ppm (0.007 at.%) — that is, 7 atoms out of every 100 000 atoms — is enough to reduce the creep of Zr-1Nb by a factor of 3 at 673 K (400°C) [2.297]. Strengthening by similar small concentrations of S and P has been observed at room temperature [2.298, 2.299]. The mechanism for this strengthening is either one of sulphur segregation to dislocation cores, slowing their movement without changing the basic mechanism [2.297] or one where the sulphur atoms pin the dislocations and effectively shorten their length [2.298]; P is postulated to strengthen by the latter mechanism.

In summary, small amounts of impurity elements can make a large difference to some properties of zirconium alloys and their control or exploitation can be very important. Control is exercised through specifications. Table 2.34 [2.172] provides examples of specifications for the impurity concentrations allowed by the nuclear industry for zirconium and alloys.

TABLE 2.34. CONCENTRATION OF IMPURITIES ALLOWED BY ASTM STANDARD B353 [2.172] FOR ZIRCONIUM AND SOME ALLOYS USED IN THE NUCLEAR INDUSTRY

Element	Pure Zr	Zircaloy-2	Zircaloy-4 Impurity max (ppm)	E125 (2.4–2.8%Nb)	Zr-2.5Nb (2.5–2.8%Nb)
			Impurity, max [ppm]:		
Al	75	75	75	75	75
B	0.5	0.5	0.5	0.5	0.5
Cd	0.5	0.5	0.5	0.5	0.5
C	270	270	270	270	150
Cr	200	—	—	200	200
Co	20	20	20	20	20
Cu	50	50	50	50	50
Hf	100	100	100	100	100
H	25	25	25	25	25
Fe	1500	—	—	1500	650
Mg	20	20	20	20	20
Mn	50	50	50	50	50
Mo	50	50	50	50	50
Ni	70	—	70	70	35
N	80	80	80	80	65
Pb	—	—	—	—	50
Si	120	120	120	120	120
Sn	50	—	—	50	100
Ta	—	—	—	—	100
Ti	50	50	50	50	50
U	3.5	3.5	3.5	3.5	3.5
V	—	—	—	—	50
W	100	100	100	100	100

2.9. CONCLUSION

Development of a new alloy takes several years. Unless reliable and relevant accelerated test methods and confident extrapolations from short duration experiments can be developed for corrosion and creep evaluation, these tests will always require much time. In-reactor experience, especially in a working component, is vital to provide confidence in performance. Again, such irradiations and subsequent examination, testing and evaluation can take many months. When developing new zirconium materials, Zircaloy was commonly used as a standard material for comparison. As the newer commercial alloys based on Zr-1Nb and Zr-1Sn-1Nb-(0.1–0.5) Fe become firmly established and gain experience, they then should become the standard against which any new alloys are compared.

REFERENCES TO CHAPTER 2

[2.1] HAVERS, W.W., WU, C.S., RAINWATER, L.J., MEAKER, C.L., Slow neutron velocity spectrometer studies. II. Au, In, Ta, W, Pt, Zr, Phys. Rev. **71** (1947) 165–173.

[2.2] ROSS, M., STORY, J.S., Slow neutron absorption cross sections of the elements, Rep. Prog. Phys. **12** (1948–49) 291–304.

[2.3] POMERANCE, H., Thermal neutron capture cross sections, Phys. Rev. **83** (1951) 641–645.

[2.4] POMERANCE, H., Thermal neutron capture cross sections, Phys. Rev. **88** (1952) 412–413.

[2.5] ZAIMOVSKY, A.S., NIKULINA, A.V., "Effects of impurities and alloying elements on zirconium resistance to high-temperature water," Proc. Conf. on Use of Zirconium Alloys in Nuclear Reactors (Zirconium 66), Mariánské Lázně (1966) 183–195.

[2.6] ZAIMOVSKY, A.S., NIKULINA, A.V., RESHETNIKOV, N.G., Zirconium Alloys in Nuclear Power, Atomizdat, Moscow (1981) (in Russian).

[2.7] LUSTMAN, B., KERZE, F. (Eds), The Metallurgy of Zirconium, McGraw-Hill, New York (1955).

[2.8] THOMAS, D.E., "Aqueous corrosion of zirconium and its alloys at elevated temperatures," Int. Conf. on Peaceful Uses of Atomic Energy, Geneva, 1955, United Nations, New York (1955) Paper N537.

[2.9] THOMAS, D.E., GOLDMAN, K.M., GORDON, R.B., JOHNSON, W.A., Zirconium Alloys, US Patent 2 772 964, Dec. 1956.

[2.10] RICKOVER, H.G., GEIGER, L.D., LUSTMAN, B., History of the Development of Zirconium Alloys for Use in Nuclear Reactors, Rep. TID-26740, US Energy Research and Development Administration, Washington, DC (1975).

[2.11] AMBARTSUMYAN, R.S., et al., "Mechanical properties and corrosion resistance of zirconium and its alloys in water, steam and gases at elevated temperatures", 2nd Int. Conf. on Peaceful Uses of Atomic Energy, Geneva, 1958, Vol. 5, United Nations, New York (1958) Paper N2044, 12–33.

[2.12] ADAMSON, G.M., BETTERTON, J.O., FRYE, J.H., PICKLESIMER, M.L., "Recent advances in the metallurgy of zirconium and titanium alloys of special interest in reactor technology", 2nd Int. Conf. on Peaceful Uses of Atomic Energy, Geneva, 1958, Vol.5, United Nations, New York (1958) Paper 1993, 33–11.

[2.13] KISELEV, A.A., et al., "Some problems in working zirconium and its alloys", 2nd Int. Conf. on Peaceful Uses of Atomic Energy, Geneva, 1958, Vol. 5, United Nations, New York (1958) Paper 2049, 52–59.

[2.14] IVANOV, O.S., GRIGOROVICH, V.K., "Structure and properties of zirconium alloys", 2nd Int. Conf. on Peaceful Uses of Atomic Energy, Geneva, 1958, Vol. 5, United Nations, New York (1958) Paper 2046, 34–51.

[2.15] EMELYANOV, V.S., GODIN, Y.G., EVSTYUKHIN, A.I., "Mechanical properties of zirconium binary and ternary alloys with tantalum and niobium at room and elevated temperatures", 2nd Int. Conf. on Peaceful Uses of Atomic Energy, Geneva, 1958, Vol. 5, United Nations, New York (1958) Paper 2055, 69–74.

[2.16] GLATTER, J., et al., "The manufacture of PWR blanket fuel elements containing high density uranium dioxide", 2nd Int. Conf. on Peaceful Uses of Atomic Energy, Geneva, 1958, Vol. 6, United Nations, New York (1958) Paper 2, 630–644.

[2.17] KASS, S., "The development of the Zircaloys", Proc. USAEC symp. on Zirconium alloy development, GEAP-4089 (KLEPFER, H.H., Ed.) (1962) Paper 1–1, 1–44.

[2.18] SYRE, R.P., "Zirconium activities in Europe: 1945–1984", Zirconium in the Nuclear Industry: Seventh International Symposium, Proc. ASTM STP 939, Strasbourg, 1985 (ADAMSON, R.B., VAN SWAM, L.F.P., Eds), ASTM International, West Conshohocken, PA (1987) 35–46.

[2.19] PICKMAN, D.O., "Zirconium alloy performance in LWRs: A review of UK and Scandinavian experience," Zirconium in the Nuclear Industry: Tenth International Symposium, Proc. ASTM STP 1245, Baltimore, 1993 (GARDE, A.M., BRADLEY, E.R., Eds), Proc. ASTM International, West Conshohocken, PA (1994) 19–32.

[2.20] LIEBERMAN, R.M., "The Zircaloy-2 in-pile tube for the NRX central thimble", Westinghouse Rep. WAPD-TM-51, Bettis Plant, Pittsburgh, PA (1957).

[2.21] FOX, J.C., JOHNSON, D.E., "Design basis for PRTR process tubes", Hanford Rep. HW-50337, Hanford Atomic Products Operation, Richland, WA (1957).

[2.22] AUNGST, R.C., CURTISS, D.H., "Procurement of Zircaloy-2 process tubes for N-reactor, General Electric Corporation", Hanford Labs, Report No. HW-80566, Hanford Labs, Richland, WA (1964).

[2.23] WATKINS, B., COCKADAY, R.E., Development of zirconium alloy pressure tubes for Winfrith Heath Steam Generating Heavy Water Reactors, Institution Mech. Eng. **180** Part 3D (1965–66) 53–63.

[2.24] KRENZ, F.H., BIEFER, G.J., GRAHAM, N.A., "Chalk River experience with Zircaloy-2 and Aluminum-Nickel-Iron alloys in high-temperature water," 2nd Int. Conf. on Peaceful Uses of Atomic Energy, Geneva, 1955, United Nations, New York (1958) Paper 194.

[2.25] THOMAS, W.R., "The development of zirconium alloys for pressure tubes in water-cooled power reactors", Proc. USAEC symp. on Zirconium alloy development, GEAP-4089 (KLEPFER, H.H., Ed.) (1962) Paper 2–0, 2–11.

[2.26] THOMAS, W.R., et al., "Irradiation experience with Zircaloy-2", 3rd Int. Conf. Peaceful Uses of Atomic Energy, Geneva, 1964, United Nations, New York (1965) Paper P/21.
[2.27] LANDERMAN, E., et al., "Summary report of the CVTR Zircaloy-4 pressure tube fabrication development and mechanical properties", CVNA-141, Carolinas Virginia Nuclear Power Associates, Charlotte, NC (1962).
[2.28] AMAEV, A.D., et al., "Influence of some factors on hydriding and the variation of properties of a zirconium alloy containing one per cent niobium used for fuel element canning in water cooled power reactors", 3rd Int. Conf. Peaceful Uses of Atomic Energy, Geneva, 1964, Vol. 9, United Nations, New York (1965) Paper 342, 492–501.
[2.29] AMAEV, A.D., et al., "Test and investigation of lead FA with sintered UO_2 fuel rods clad in Zr-1%Nb alloy at maximum burnup of 68 000 MWd/kgU", Conf. on the Use of Zirconium Alloys in Nuclear Reactors, Mariánské Lázně, 1966, House of Technics, Škoda, Plzeň (1966) 143–157.
[2.30] AMAEV, A.D., et al., "Some results of MR loop testing pilot fuel rods clad in Zr-Alloys," Proc. Conf. on the Use of Zirconium Alloys in Nuclear Reactors, Mariánské Lázně, 1968, House of Technics, Škoda, Plzeň (1968) 37–67.
[2.31] KLEPFER, H.H., Zirconium-niobium binary alloys for BWR service — Part I — Corrosion resistance, J. Nucl. Mater. **9** (1963) 65–76.
[2.32] KLEPFER, H.H., Zirconium-niobium binary alloys for BWR service Part II — Corrosion hydrogen embrittlement, J. Nucl. Mater. **9** (1963) 77–84.
[2.33] ELLS, C.E., DALGAARD, S.B., EVANS, W., THOMAS, W.R., "Development of Zirconium-Niobium alloys", 3rd Int. Conf. Peaceful Uses of Atomic Energy, Geneva, 1964, United Nations, New York (1965).
[2.34] ELLS, C.E., FIDLERIS, V., Effect of neutron irradiation on tensile properties of the zirconium-2.5% niobium alloy, J. Electrochem. Tech. **4** (1966) 268–274.
[2.35] MARDON, J.P., CARQUET, D., SENEVAT, J., "Development of new zirconium alloys for PWR fuel rod cladding", Int. Topical Mtg on LWR Fuel Performance, Palm Beach, 1994, American Nuclear Society, La Grange Park, IL (1994) 643–649.
[2.36] MARDON, J.P., SEVENAT, J., CHARQUET, D., Method for Producing a Tube for a Nuclear Fuel Assembly and the Tubes Produced Thereby, European Patent EP0720177A1, filed Dec. 1996, granted Apr. 1998, available on-line.
[2.37] AMAEV, A.D., et al., "Corrosion of zirconium alloys in boiling water under irradiation", 4th Int. Conf. on Peaceful Uses of Atomic Energy, Geneva, 1971, Vol. 10, United Nations, New York (1971) Paper 428, 537–548.
[2.38] NIKULINA, A.V., et al., Zirconium-based Material, Article Made of the Said Material for Use in the Active Zones of Atomic Reactors, and a Process for Obtaining Such Articles, European Patent EP 0643144131, filed Jul. 1993, granted Dec. 1997, US patent 5560790A, filed Jul. 1993, granted Oct. 1993, available on-line.
[2.39] FOSTER, J.P., COMSTOCK, R.J., WORCESTER, S.A., SABOL, G.P., ZIRLO Material for LWR Applications, US Patent 5112573, granted May 1992, available on-line.
[2.40] SABOL, G.P., KILP, G.R., BALFOUR, M.G., ROBERTS, E., "Development of a cladding alloy for high burnup", Zirconium in the Nuclear Industry: Eighth International Symposium, Proc. ASTM STP 1023, San Diego, 1988 (VAN SWAM, L.F.P., EUCKEN, C.M., Eds), ASTM International, West Conshohocken, PA (1989) 227–244.
[2.41] SABOL, G.P., "ZIRLO™ — An alloy development success", Zirconium in the Nuclear Industry: Fourteenth International Symposium, Proc. ASTM STP 1467, Stockholm, 2004 (RUDLING, P., KAMMENZIND, B., Eds), ASTM International, West Conshohocken, PA (2006) 3–24.
[2.42] CASTALDELLI, L., FIZZOTTI, C., LUNDE, L., "Long-term test results of promising new zirconium alloys", Zirconium in the Nuclear Industry: Fifth International Symposium, Proc. ASTM STP 754, Boston, 1980 (FRANKLIN, D.G., Ed.), ASTM International, West Conshohocken, PA (1982) 105–126.
[2.43] HANSEN, M., ANDERKO, K., Constitution of Binary Alloys, McGraw-Hill, New York (1958).
[2.44] DOMAGALA, R.F., McPHERSON, D.J., System zirconium-oxygen, Trans. AIME **200** (1954) 238–246.
[2.45] IVANOV, O.S., ADAMOVA, A.S., TARARAEVA, E.M., TREGUOBOV, I.A., Structure of Zirconium Alloys, Nauka, Moscow (1973) (in Russian).
[2.46] DOUGLASS, D.L., The Metallurgy of Zirconium, Atom. Energy Rev. **3** 1 (1971) 1–464.
[2.47] KUBASCHEWSKI-VON GOLDBECK, O., Phase diagrams, zirconium: Physico-chemical properties of its compounds and alloys, Atom. Energy Rev. **6** (1976) 67–139.
[2.48] ABRIATA, J.P., GARCES, J., VERSACI, R., The O-Zr (oxygen-zirconium) system, Bull. Alloy Phase Diagrams **7** (1986) 116–124.
[2.49] ABRIATA, J.P., BOLCICH, J.C., PERETTI, H.A., The Hf-Zr (hafnium-zirconium) system, Bull. Alloy Phase Diagrams **3** (1982) 29–34.
[2.50] ARIAS, D., ABRIATA, J.P., The Cr-Zr (chromium-zirconium) system, Bull. Alloy Phase Diagrams **7** (1986) 237–244.
[2.51] ARIAS, D., ABRIATA, J.P., The Fe-Zr (iron-zirconium) system, Bull. Alloy Phase Diagrams **9** (1988) 597–604.

[2.52] HUME-ROTHERY, W., RAYNOR, G.V., The Structure of Metals and Alloys, Institute of Metals, London (1962).
[2.53] DARKEN, L.S., GURRY, R.W., "The influence of chemical factors on the extent of primary solid solution", Physical Chemistry of Metals, McGraw-Hill, New York (1953) 79–90.
[2.54] DEAN, J.A. (Ed.), Lange's Handbook of Chemistry, 15th edn, McGraw-Hill Handbooks, New York (1999).
[2.55] LIDE, D.R. (Ed.), Handbook of Chemistry and Physics, Taylor and Francis, Boca Raton (2005–2006).
[2.56] KAUFMAN, L., Foreword, CALPHAD **1** 1 (1977) 1–6.
[2.57] DUPIN, N., et al., Thermodynamic database for zirconium alloys, J. Nucl. Mater. **275** (1999) 287–295.
[2.58] TSUJI, T., AMAYA, M., Study on order-disorder transition of Zr-O alloys by heat capacity measurement, J. Nucl. Mater. **223** (1995) 33–39.
[2.59] HAYWARD, P.J., GEORGE, I.M., Determination of the β/β+γ eutectoid transition in ZrO_{2-x} at variable heating/cooling rates, J. Nucl. Mater. **265** (1999) 60–68.
[2.60] LIANG, P., et al., Thermodynamic assessment of the Zr-O binary system, Z. Metallkd. **92** 7 (2001) 747–756.
[2.61] WANG, C., ZINKEVICH, M., ALDINGER, F., On the thermodynamic modeling of the Zr-O system, CALPHAD **28** (2004) 281–292.
[2.62] HORZ, G., HAMMEL, M., KANBACH, H., Electrical resistivity of β-zirconium-oxygen solid solutions as a function of oxygen concentration and temperature, J. Nucl. Mater. **55** (1975) 291–298.
[2.63] LYAKISHEV, N.P. (Ed.), "O-Zr", Phase Diagrams of Binary Metallic Systems: A Handbook, Vol. 3, Mashinostroenie, Moscow (2001) 724–726 (in Russian).
[2.64] ARROYAVE, R., KAUFMAN, L., EAGAR, T.W., Thermodynamic modeling of the Zr-O system, CALPHAD **26** (2002) 95–118.
[2.65] ACKERMANN, R.J., GARG, S.P., RAUH, E.G., High-temperature phase diagram for the system Zr-O, J. Amer. Ceram. Soc. **60** (1977) 341–345.
[2.66] TYSON, W.R., Strengthening of HCP Zr, Ti and Hf by interstitial solute — A review, Can. Metall. Q. **6** (1968) 301–332.
[2.67] MA, X., TOFFOLON-MASCLET, C., GUILBERT, T., HAMON, D., BRACHET, J.C., Oxidation kinetics and oxygen diffusion in low-tin Zircaloy-4 up to 1523 K, J. Nucl. Mater. **377** (2008) 359–369.
[2.68] ABRIATA, J.P., BOLCICH, J.C., ARIAS, D., The Sn-Zr (tin-zirconium) system, Bull. Alloy Phase Diagrams **4** (1983) 147–154.
[2.69] LYAKISHEV, N.P. (Ed.), "Y-Zr", Phase Diagrams of Binary Metallic Systems: A Handbook, Vol. 3, Book 2, Mashinostroenie, Moscow (1996) 431–432 (in Russian).
[2.70] ARIAS, D., ROBERTI, L., The solubility of tin in α and β zirconium below 1000°C, J. Nucl. Mater. **118** (1983) 143–149.
[2.71] ABRIATA, J.P., BOLCICH, J.C., ARIAS, D., "Sn-Zr (tin-zirconium)", Binary Alloy Phase Diagrams, 2nd edn (MASSALSKI, T.B., Ed.), Vol. 3 (1990) 3416–3419.
[2.72] KWON, Y.-U., CORBETT, J.D., The zirconium–tin system, with particular attention to the Zr_5Sn_3–Zr_5Sn_4 region and Zr_4Sn, Chem. Mater. **2** (1990) 27–33.
[2.73] TOFFOLON-MASCLET, C., et al., Contribution of thermodynamic calculations to metallurgical studies of multi-component zirconium based alloys, J. ASTM Int. **5** (2008) Paper JAI101122.
[2.74] JERLERUD-PÉREZ, R., et al., The Zr-Sn binary system: New experimental results and thermodynamic assessment, CALPHAD **32** (2008) 593–601.
[2.75] LYAKISHEV, N.P. (Ed.), "Nb-Zr", Phase Diagrams of Binary Metallic Systems: A Handbook, Vol. 3, Book 1, Mashinostroenie, Moscow (2001) 570–571 (in Russian).
[2.76] FLEWITT, P.E.J., A re-assessment of the monotectoid loop (β-Nb + β-Zr) in the niobium-zirconium system, J. App. Crystallog. **5** (1972) 423–425.
[2.77] ABRIATA, J.P., BOLCICH, J.C., The Nb-Zr system, Bull. Alloy Phase Diagrams **3** 1 (1982) 34–44.
[2.78] GUILLERMET, A.F., Thermodynamic analysis of the stable phases in the Zr-Nb system and calculation of the phase diagram, Z. Metallkd. **82** (1991) 478–487.
[2.79] TOFFOLON, C., et al., "Experimental study and preliminary thermodynamic calculations of the pseudoternary Zr-Nb-Fe-(O, Sn) system", Zirconium in the Nuclear Industry: Thirteenth International Symposium, Proc. ASTM STP 1423, Annecy, 2001 (MOAN, G.D., RUDLING, P., Eds), ASTM International, West Conshohocken, PA (2002) 361–381.
[2.80] KIM, H.-G., PARK, J.-Y., JEONG, Y.-H., Phase boundary of the Zr-rich region in commercial grade Zr-Nb alloys, J. Nucl. Mater. **347** (2005) 140–150.
[2.81] WOO, O.T., GRIFFITHS, M., The role of Fe on the solubility of Nb in α-Zr, J. Nucl. Mater. **384** (2009) 77–80.
[2.82] HOOD, G.M., ZOU, H., SCHULTZ, R.J., MATSUURA, N., Nb Diffusion in Single-crystal α-Zr, AECL Report RC-1674, Atomic Energy of Canada Limited, Chalk River, ON (1996).
[2.83] HEHEMANN, R.F., Transformations in zirconium-niobium alloys, Can. Metall. Q. **11** (1972) 201–211.
[2.84] CHEADLE, B.A., ALDRIDGE, S.A., The transformation and age-hardening behaviour of Zr-19 wt%Nb, J. Nucl. Mater. **47** (1973) 255–258.
[2.85] GRIFFITHS, M., WINEGAR, J.E., BUYERS, A., The transformation behaviour of the β-phase in Zr-2.5Nb pressure tubes, J. Nucl. Mater. **383** (2008) 28–33.

[2.86] BENITES, G.M., FERNANDEZ GUILLERMET, A., CUELLO, G.J., CAMPO, J., Structural properties of metastable phases in Zr-Nb alloys I. Neutron diffraction study and analysis of lattice parameters, J. Alloys Compd **299** (2000) 183–188.
[2.87] ROBSON, J.D., Modelling precipitation in zirconium niobium alloys, J. Nucl. Mater. **377** (2008) 415–422.
[2.88] LYAKISHEV, N.P. (Ed.), "Fe-Zr", Phase Diagrams of Binary Metallic Systems: A Handbook, Vol. 2, Mashinostroenie, Moscow (1997) 586–591 (in Russian).
[2.89] KUBASCHEWSKI, O., Iron-binary Phase Diagrams, Springer, Berlin (1982) 175–78.
[2.90] ALEKSEEVA, Z.M., KOROTKOV, N.V., The Zr-Fe phase diagram, Russ. Metall. **4** (1989) 197–203 (in Russian).
[2.91] ARIAS, D., et al., "Fe-Zr" Phase Diagrams of Binary Iron Alloys (OKAMOTO, H., Ed.), ASM International, Materials Park, OH (1993) 467–472.
[2.92] OKAMOTO, H., Fe-Zr (iron-zirconium), J. Phase Equilibria **18** (1997) 316.
[2.93] PELTON, A., LEIBOWITZ, L., BLOMQUIST, R.A., Thermodynamic analysis of phase equilibria in the iron-zirconium system, J. Nucl. Mater. **201** (1993) 218–224.
[2.94] SERVANT, C., GUENEAU, C., ANSARA, I., Experimental and thermodynamic assessment of the Fe-Zr system, J. Alloys Compd **220** (1995) 19–26.
[2.95] GRANOVSKY, M.S., ARIAS, D., Intermetallic phases in the iron-rich region of the Zr-Fe phase diagram, J. Nucl. Mater. **229** (1996) 29–35.
[2.96] JIANG, M., OIKAWA, K., IKESHOJI, T., WULFF, L., ISHIDA, K., Thermodynamic calculations of Fe-Zr and Fe-Zr-C systems, J. Phase Equilibria **22** (2001) 406–417.
[2.97] STEIN, F., SAUTHOFF, G., PLAM, M., Experimental determination of intermetallic phases: Phase equilibria and invariant reaction temperatures in the Fe-Zr system, J. Phase Equilibria **23** (2002) 480–494.
[2.98] CHATAIN, S., LAROUSSE, B., MAILLAULT, C., GUÉNEAU, C., CHATILLON, C., Thermodynamic activity measurements of iron in Fe–Zr alloys by high temperature mass spectrometry, J. Alloys Compd. **457** (2008) 157–163.
[2.99] BORRELLY, R., MERLE, P., ADAMI, L., Study of the solubility of iron in zirconium by thermoelectric power measurements, J. Nucl. Mater. **170** (1990) 147–156.
[2.100] ZOU, H., HOOD, G.M., ROY, J.A., SCHULTZ, R.J., JACKMAN, J.A., The solid solubility of Fe in α-Zr: A secondary ion mass spectrometry study, J. Nucl. Mater. **210** (1994) 239–243.
[2.101] HOOD, G.M., SCHULTZ, R.J., Tracer diffusion in α-Zr, Acta Met. **22** (1974) 459–464.
[2.102] LYAKISHEV, N.P. (Ed.), "Ni-Zr", Phase Diagrams of Binary Metallic Systems: A Handbook, Vol. 3 book 1, Mashinostroenie, Moscow (2001) 672–675 (in Russian).
[2.103] GHOSH, G., Thermodynamics and kinetics of stable and metastable phases in the Ni-Zr system, J. Mater. Res. **9** (1994) 598–161.
[2.104] ZOU, H., HOOD, G.M., NAKAJIMA, H., ROY, J.A., SCHULTZ, R.J., "The solid solubility of Ni and Co in α-Zr: A secondary ion mass spectrometry study", Report No. AECL-11211, Atomic Energy of Canada Limited, Chalk River, ON (1995).
[2.105] LYAKISHEV, N.P. (Ed.), "Cr-Zr", Phase Diagrams of Binary Metallic Systems; A Handbook, Vol. 2, Mashinostroenie, Moscow (1997) 204–206 (in Russian).
[2.106] ZENG KEJUN, HÄMÄLÄINEN, M., LILIUS, K., Thermodynamic modeling of the Laves phases in the Cr-Zr System, CALPHAD **17** (1993) 101–107.
[2.107] LYAKISHEV, N.P. (Ed.), "C-Zr", Phase Diagrams of Binary Metallic Systems: A Handbook, Vol. 1, Mashinostroenie, Moscow (1996) 783–784 (in Russian).
[2.108] FERNÁNDEZ GUILLERMET, A., Analysis of thermochemical properties and phase stability in the zirconium-carbon system, J. Alloys Compd. **217** (1995) 69–89.
[2.109] MA, X., LI, C., BAI, K., WU, P., ZHANG, W., Thermodynamic assessment of the Zr-N system, J. Alloys Compd. **373** (2004) 194–201.
[2.110] LYAKISHEV, N.P. (Ed.), "N-Zr", Phase Diagrams of Binary Metallic Systems: A Handbook, Vol. 3 book 1, Mashinostroenie, Moscow (2001) 499–500 (in Russian).
[2.111] McPHERSON, D.J., HANSEN, M., The system zirconium-aluminum, Trans. ASM **46** (1954) 354–374.
[2.112] TIWARI, S.N., TANGRI, K., The solid solubility of aluminium in α-zirconium, J. Nucl. Mater. **34** (1970) 92–96.
[2.113] SCHULSON, E.M., McCOLL, D.H., LING, V.C., "Refinement of the Zr/Zr_2Al duplex structure in Zr-7.6–9.0 wt percent Al ingots". Report No. AECL-5176, Atomic Energy of Canada Limited, Chalk River, ON (1975).
[2.114] KEMATICK, R.J., FRANZEN, H.F., Thermal study of the zirconium-aluminum system, J. Solid State Chem. **54** (1984) 226–234.
[2.115] PERUZZI, A., Reinvestigation of the Zr-rich end of the Zr-Al equilibrium phase diagram, J. Nucl. Mater. **186** (1992) 89–99.
[2.116] WANG, T., JIN, Z., ZHAO, J.-C., Thermodynamic assessment of the Al-Zr binary system, J. Phase Equilibria **22** (2001) 544–551.
[2.117] LYAKISHEV, N.P. (Ed.), "Al-Zr", Phase Diagrams of Binary Metallic Systems: A Handbook, Vol. 1, Mashinostroenie, Moscow (1996) 242–244 and 623–625 (in Russian).

[2.118] SCHULSON, E.M., A short review of the physical metallurgy of ordered Zr_3Al: Science and engineering, Report No. AECL-5843, Atomic Energy of Canada Limited, Chalk River, ON (1977).
[2.119] ZUZEK, E., ABRIATA, J.P., SAN-MARTIN, A., MANCHESTER, F.D., The H-Zr (hydrogen-zirconium) system, Bull. Alloy Phase Diagrams **11** (1990) 385–395.
[2.120] LANZANI, L., RUCH, M., Comments on the stability of zirconium hydride phases in Zircaloy, J. Nucl. Mater. **324** (2004) 165–176.
[2.121] ZHAO, Z., et al., Characterization of zirconium hydrides and phase field approach to a mesoscopic-scale modeling of their precipitation, J. ASTM Int. **5** (2008) Paper JAI101161.
[2.122] HAYGARTH, J.C., GRAHAM, R.A., "Zirconium and hafnium", Review of Extraction Processes, Properties and Applications of Reactive Metals (MISHRA, B., Ed.), The Minerals, Metals and Materials Society, Pittsburgh, PA (1999) 1–71.
[2.123] CHARQUET, D., Phase constitution and steam corrosion resistance of binary Zr-S alloys, J. Nucl. Mater. **304** (2002) 246–248.
[2.124] LYAKISHEV, N.P. (Ed.), "S-Zr", Phase Diagrams of Binary Metallic Systems: A Handbook, Vol. 3, Book 2, Mashinostroenie, Moscow (2000) 227–229 (in Russian).
[2.125] MURRAY, J.L., "S-Ti (Sulfur-titanium)", Binary Alloy Phase Diagrams, 2nd edn, Vol. 3 (MASSALSKI, T.B., Ed.), (1990) 3286–3288.
[2.126] GRAHAM, R.A. (ATI Wah Chang), Private communication, 2008.
[2.127] GUÉNEAU, C., SERVANT, C., ANSARA, I., DUPIN, N., Thermodynamic assessment of the Si-Zr System, CALPHAD **18** (1994) 319–327.
[2.128] LYAKISHEV, N.P. (Ed.), "Si-Zr", Phase Diagrams of Binary Metallic Systems: A Handbook, Vol. 3 book 2, Mashinostroenie, Moscow (2000) 306–309 (in Russian).
[2.129] ZENG, K.J., HÄMÄLÄINEN, M., LUKAS, H.L., A new thermodynamic description of the Cu-Zr System, J. Phase Equilibria **15** (1994) 577–586.
[2.130] LYAKISHEV, N.P. (Ed.), "Cu-Zr", Phase Diagrams of Binary Metallic Systems: A Handbook, Vol. 2, Mashinostroenie, Moscow (1997) 356–361 (in Russian).
[2.131] MASSALSKI, T., MURRAY, J.L., BENNETT, L.H., BAKER, H. (Eds), Binary Alloy Phase Diagrams, Vol. 1, ASM International, Materials Park, OH (1986) 982.
[2.132] GLIMOIS, J.L., FOREY, P., FERON, J.L., Études structurales et physiques d'alliages riches en cuivre dans le systeme Cu-Zr, J. Less-Common Met. **113** (1985) 213–224.
[2.133] LOU, M. Y.-W., GRANT, N.J., Identification of Cu_5Zr phase in Cu-Zr alloys, Metall. Trans. A **15** (1984) 1491–1493.
[2.134] ARIAS, D., ABRIATA, J.P., Cu-Zr (Copper-Zirconium), Bull. Alloy Phase Diagrams **11** 5 (1990) 452–459.
[2.135] VITEK, J.M., Electron microprobe investigation of the intermediate phases in the Cu-Zr system, Z. Metallkd. **67** (1970) 559–563.
[2.136] OKAMOTO, H., TANNER, L.E., ABRIATA, J.P., "Be-Zr (Beryllium-zirconium)", Binary Alloy Phase Diagrams, 2nd edn, Vol. 1 (MASSALSKI, T.B., Ed.), ASM International, Materials Park, OH (1990) 716–718.
[2.137] TOKUNAGA, T., OHTANI, H., HASEBE, M., Thermodynamic analysis of the Zr-Be system using thermochemical properties based on ab initio calculations, CALPHAD **30** (2006) 201–208.
[2.138] BATES, K.T., "Brazing of Zircaloy in nuclear fuel", paper presented at NUCLEX '66 Int. Industries Fair and Technical Mtgs, Basel, Switzerland, 1966.
[2.139] PALENZONA, A., CIRAFICI, S., "Y-Zr (Yttrium-zirconium)", Binary Alloy Phase Diagrams, 2nd edn, Vol. 3 (MASSALSKI, T.B., Ed.), ASM International, Materials Park, OH (1990) 3535–3539.
[2.140] COLEMAN, C.E., SAGAT, S., AMOUZOUVI, K.F., "Control of microstructure to increase the tolerance of zirconium alloys to hydride cracking", paper presented at 26th Ann. Conf. of Metallurgists, Canadian Institute of Mining and Metallurgy, Winnipeg, MAN, 1987.
[2.141] AMOUZOUVI, K.F., et al., The effect of the addition of 1.7 at.% yttrium on the mechanical properties of Zr-2.5Nb alloy, Scripta Met. Mat. **25** (1991) 1155–1160.
[2.142] REZEK, J., CHILDS, B.G., Structure and properties of yttria-zirconium dispersions, J. Nucl. Mater. **26** (1968) 285–299.
[2.143] PARSONS, P.O., ADOLPH, E., Zirconium alloys dispersion strengthened with yttria, Can. Metall. Q. **11** (1972) 223–235.
[2.144] IRANI, K.S., GINGERICH, K.A., Structural transformation of zirconium phosphide, J. Phys. Chem. Solids **24** (1963) 1153–1158.
[2.145] MURRAY J.L., P-Ti (Phosphorus-titanium), Binary Alloy Phase Diagrams, 2nd edn, Vol. 3 (MASSALSKI, T.B., Ed.), ASM International, Materials Park, OH (1990) 2989–2991.
[2.146] SABOL, G.P., COMSTOCK, R.J., NAYAK, U.P., "Effect of dilute alloy additions of molybdenum, niobium and vanadium on zirconium corrosion", Zirconium in the Nuclear Industry: Twelfth International Symposium, Proc. ASTM STP 1354, Toronto, 1998 (SABOL, G.P., MOAN, G.D., Eds), ASTM International, West Conshohocken, PA (2000) 525–544.
[2.147] JAGO, G., et al., "Metallurgy and mechanical tensile properties of Zr-1.2Sn-(Fe,V,Mo) alloys", poster presented at Zirconium in the Nuclear Industry: 12th Int. Symp., Toronto, 1998.

[2.148] CHUN, Y.B., HWANG, S.K., KIM, M.H., KWUN, S.I., KIM, Y.S., Effect of Mo on recrystallization characteristics of Zr-Nb-(Sn)-Mo experimental alloys, J. Nucl. Mater. **265** (1999) 28–37.
[2.149] JERLERUD-PÉREZ, R., SUNDMAN, B., Thermodynamic assessment of the Mo-Zr binary phase diagram, CALPHAD **27** (2003) 253–262.
[2.150] ZINKEVICH, M., MATTERN, N., SEIFERT, H.J., Thermodynamic assessment of Gd-Zr and Gd-Mo Systems, J. Phase Equilibria **22** (2001) 43–50.
[2.151] ANDERSON, W.K., THEILACKER, J.S. (Eds), Neutron Absorber Materials for Reactor Control, US Govt Printing Office, Washington, DC (1962) 538.
[2.152] ISOBE, T., MATSUO, Y., "Development of highly corrosion resistant zirconium-base alloys", Zirconium in the Nuclear Industry: Ninth International Symposium, Proc. ASTM STP 1132, Kobe, 1990 (EUCKEN, C.M., GARDE, A.M., Eds), ASTM International, West Conshohocken, PA (1991) 346–367.
[2.153] SERVANT, C., Thermodynamic assessments of the phase diagrams of the hafnium-vanadium and vanadium-zirconium systems, J. Phase Equilibria and Diffusion **26** (2005) 39–49.
[2.154] NIEVA, N., ARIAS, D., Experimental partial phase diagram of the Zr-Sn-Fe system, J. Nucl. Mater. **359** (2006) 29–40.
[2.155] KOROTKOVA, N.V., ALEKSEEVA, Z.M., Topology of the Zr-Nb-Fe phase diagram in the range 500–800°C, Russ. Metall. (Metally) **3** (1989) 198–204.
[2.156] SHISHOV, V.N., et al., "Influence of Zirconium alloy chemical composition on microstructure formation and irradiation induced growth", Zirconium in the Nuclear Industry: Thirteenth International Symposium, Proc. ASTM STP 1423, Annecy, 2001 (MOAN, G.D., RUDLING, P., Eds), ASTM International, West Conshohocken, PA (2002) 758–778.
[2.157] SHISHOV, V.N., et al., "Influence of structure-phase state of Nb containing Zr alloys on irradiation growth strain", Zirconium in the Nuclear Industry: Fourteenth International Symposium, Proc. ASTM STP 1467, Stockholm, 2004 (RUDLING, P., KAMMENZIND, B., Eds), ASTM International, West Conshohocken, PA (2006) 666–685.
[2.158] GRANOVSKY, M.S., CANAY, M., LENA, E., ARIAS, D., Experimental investigation of the Zr corner of the ternary Zr-Nb-Fe phase diagram, J. Nucl. Mater. **302** (2002) 1–8.
[2.159] RAMOS, C., SARAGOVI, C., GRANOVSKY, M.S., Some new experimental results on the Zr-Nb-Fe system, J. Nucl. Mater. **366** (2007) 198–205.
[2.160] JERLERUD-PÉREZ, R., Thermodynamic Database for Zirconium Alloys, PhD Thesis, Royal Institute of Technology, Stockholm, Sweden (2006).
[2.161] BARBERIS, P., DUPIN, N., LEMAIGNAN, C., PASTUREL, A., GRANGE, J.M., "Microstructure and phase control in Zr-Fe-Cr-Ni alloys: Thermodynamic and kinetic aspects", Zirconium in the Nuclear Industry: Fourteenth International Symposium, Proc. ASTM STP 1467, Stockholm, 2004 (RUDLING, P., KAMMENZIND, B., Eds), ASTM International, West Conshohocken, PA (2006) 129–156.
[2.162] ANSARA, I., DUPIN, N., JOUBERT, J.M., LATROCHE, M., PERCHERON-GUEGAN, A., Thermodynamic study of the Cr-Ni-Zr system, J. Phase Equilibria **19** (1998) 6–10.
[2.163] JERLERUD-PÉREZ, R., MASSIH, A.R., Thermodynamic evaluation of the Nb-O-Zr system, J. Nucl. Mater **360** (2007) 242–254.
[2.164] ARICÒ, S.F., GRIBAUDO, L.M., The α-Zr phase field in the Zr-Sn-O system, Scripta Mat. **41** (1999) 159–165.
[2.165] MIYAKE, M., UNO, M., YAMANAKA, S., On the zirconium-oxygen-hydrogen ternary system, J. Nucl. Mater **270** (1999) 233–241.
[2.166] SETOYAMA, D, YAMANAKA, S., Phase diagram of Zr-O-H ternary system, J. Alloys Compd **370** (2004) 144–148.
[2.167] ZINKEVICH, M., MATTERN, N., Thermodynamic modelling of the Fe-Mo-Zr system, Acta Mater. **50** (2002) 3373–3383.
[2.168] KUDRYAVTSEV, D.L, TARARAEVA, E.M., "The zirconium corner of the zirconium-copper-niobium phase diagram", Fiziko-khimiya splavov tsirkoniya, Nauka, Moscow (1968) 169–175 (in Russian).
[2.169] ELLS, C.E., "Deformation of irradiated zirconium-niobium alloys", Zirconium in Nuclear Applications, ASTM STP 551 (SCHEMEL, J.H., ROSENBAUM, H.S., Eds), ASTM International, West Conshohocken, PA (1974) 311–327.
[2.170] CANAY, M., DANON, C.A., ARIAS, D., Phase transition temperature in the Zr-rich corner of Zr-Nb-Sn-Fe alloys, J. Nucl. Mater. **280** (2000) 365–371.
[2.171] NIKULINA, A.V., et al., Irradiation-induced microstructural changes in Zr-1%Sn-1% Nb-0.4% Fe, J. Nucl. Mater. **238** (1996) 205–210.
[2.172] ASTM INTERNATIONAL, Standard Specification for Wrought Zirconium and Zirconium Alloy Seamless and Welded Tubes for Nuclear Service (Except Nuclear Fuel Cladding), ASTM B353-12(2017), ASTM International, West Conshohocken, PA (2017).
[2.173] COX, B., "Oxidation of zirconium and its alloys", Advances in Corrosion Science and Technology, Vol. 5 (FONTANA, M.G., STAEHLE, R.W., Eds), Plenum Press, New York (1976) p. 173.
[2.174] SCHEMEL, J., "Zirconium alloy fuel clad tubing", Engineering Guide, Sandvik Special Metal, Kennewick, WA (1989).

[2.175] GARZAROLLI, F., STEHLE, H., STEINBERG, E., "Behaviour and properties of Zircaloys in power reactors: A short review of pertinent aspects in LWR fuel", Zirconium in the Nuclear Industry: Eleventh International Symposium, Proc. ASTM STP 1295, Garmisch-Partenkirchen, 1995 (BRADLEY, E.R., SABOL, G.P., Eds), ASTM International, West Conshohocken, PA (1996) 12–32.

[2.176] LIMBACK, M., KRAMMEN, M.A., RUDLING, P., PATI, S.R., GARDE, A.M., "Corrosion and hydriding performance of Zircaloy-2 and Zircaloy-4 cladding materials in PWRs", Int. Topical Mtg on Light Water Reactor Fuel Performance, Avignon, 1991, American Nuclear Society, La Grange Park, IL (1994) 286–295.

[2.177] PATI, S.P., JOUDAIN, P., SMITH, G.P., GARDE, A.M., HALLSTADIUS, L., "Performance of standard and advanced fuel rod cladding for high burnup applications in PWRs", Proc. Int. Topical Mtg on Light Water Reactor Fuel Performance, American Nuclear Society, La Grange Park, IL (1997) 413–420.

[2.178] SEIBOLD, A., GARZAROLLI, F., STEINBERG, E., "Optimized Zry-4 with enhanced Fe and Cr content and DUPLEX cladding: The answer to corrosion on PWR", Int. KTG/ENS Topical Mtg on Nuclear Fuel, TopFuel 95, Würzburg, Germany, 1995 (1995) 117–120.

[2.179] GARZAROLLI, F., HOLZER, R., Waterside corrosion performance of light water power reactor fuel, Nucl. Energy **31** (1992) 65–86.

[2.180] GARDE, A.M., SMERD, P.G., GARZAROLLI, F., MANZEL, R., "Influence of metallurgical condition on the in-reactor dimensional changes of Zircaloy fuel rods", Zirconium in the Nuclear Industry: Sixth International Symposium, Proc. ASTM STP 824, Vancouver, 1982 (FRANKLIN, D.G., ADAMSON, R.B., Eds), ASTM International, West Conshohocken, PA (1984) 289–305.

[2.181] RUHMANN, H., MANZEL, R., SELL, H.J., CHARQUET, D., "In-BWR and out-of-pile nodular corrosion behavior of Zr-2/4 type melts with varying Fe, Cr, and Ni content and varying process history", Zirconium in the Nuclear Industry: Eleventh International Symposium, Proc. ASTM STP 1295, Garmisch-Partenkirchen 1995, (BRADLEY, E.R., SABOL, G.P., Eds), ASTM International, West Conshohocken, PA (1996) 865–883.

[2.182] DAHLBÄCK, M., et al., The effect of beta-quenching in final dimension on the irradiation growth of tubes and channels, J. ASTM Int. **2** (2005) JAI12337.

[2.183] ÖKVIST, G., KÄLLSTRÖM, K., The effect of zirconium carbide on the β→α transformation structure in Zircaloy, J. Nucl. Mater. **35** (1970) 316–321.

[2.184] CHARQUET, D., ALHERITIERE, E., "Influence of impurities and temperature on the microstructure of Zircaloy-2 and Zircaloy-4 after the beta→alpha phase transformation", Zirconium in the Nuclear Industry: Seventh International Symposium, Proc. ASTM STP 939, Strasbourg, 1985 (ADAMSON, R.B., VAN SWAM, L.F.P., Eds), ASTM International, West Conshohocken, PA (1987) 284–291.

[2.185] FONG, W.L., NORTHWOOD, D.O., Microstructure-impurity content relationships in Zircaloy-4 nuclear fuel sheathing, Microstruct. Sci. **10** (1982) 123–130.

[2.186] HOLT, R.A., The beta to alpha phase transformation in Zircaloy-4, J. Nucl. Mater. **35** (1970) 322–334.

[2.187] QUACH, V., NORTHWOOD, D.O., Influence of the phosphorus impurity content on the microstructure of Zircaloy-4 air cooled from the high temperature beta phase region, Metallography **17** (1984) 191–201.

[2.188] LIMBACK, M., ANDERSSON, T., "A model for analysis of the effect of final annealing on the in- and out-of-reactor creep behaviour of Zircaloy cladding", Zirconium in the Nuclear Industry: Eleventh International Symposium, Proc. ASTM STP 1295, Garmisch-Partenkirchen, 1995 (BRADLEY, E.R., SABOL, G.P., Eds), ASTM International, West Conshohocken, PA (1996) 448–468.

[2.189] FUCHS, H.P., et al., "Cladding and structural materials development for the advanced Siemens PWR fuel FOCUS", Proc. ANS-ENS Int. Topical Mtg on LWR Fuel Performance, Avignon, 1991, American Nuclear Society, La Grange Park, IL (1991) 682–690.

[2.190] VAN SWAM, L.F., GARZAROLLI, F., STEINBERG, E., "Advanced PWR cladding", Proc. Int. Topical Mtg on LWR Fuel Performance, West Palm Beach, 1994, American Nuclear Society, La Grange Park, IL (1994) 303–308.

[2.191] WEIDINGER, H.G., LETTAU, H., "Advanced material and fabrication technology for LWR fuel", IAEA Int. Symp. on Improvements in Water Reactor Fuel Technology and Utilization, Stockholm, 1986, IAEA, Vienna (1987) 451–467.

[2.192] GARDE, A.M., SMITH, G.P., PIREK, R.C., "In-PWR irradiation performance of dilute tin-zirconium advanced alloys", Zirconium in the Nuclear Industry: Thirteenth International Symposium, Proc. ASTM STP 1423, Annecy, 2001 (MOAN, G.D., RUDLING, P., Eds), ASTM International, West Conshohocken, PA (2002) 490–506.

[2.193] ARBORELIUS, J., et al., The effect of duplex cladding outer component tin content on corrosion, hydrogen pick-up, and hydride distribution at very high burn-up, J. ASTM International **2** (2005) Paper JAI12411.

[2.194] BESCH, O.A., YAGNIK, S.K., WOODS, K.N., EUCKEN, C.M., BRADLEY, E.R., "Corrosion behavior of duplex and reference cladding in NPP Grohnde", Zirconium in the Nuclear Industry: Eleventh International Symposium, Proc. ASTM STP 1295, Garmisch-Partenkirchen, 1995 (BRADLEY, E.R., SABOL, G.P., Eds), ASTM International, West Conshohocken, PA (1996) 805–824.

[2.195] ARMIJO, J.S., COFFIN, L.F., ROSENBAUM, H.S., "Development of zirconium-barrier fuel cladding", Zirconium in the Nuclear Industry: Tenth International Symposium, Proc. ASTM STP 1245, Baltimore, 1993 (GARDE, A.M., BRADLEY, E.R., Eds), ASTM International, West Conshohocken, PA (1994) 3–18.

[2.196] WILLIAMS, C.D., et al., "Zircaloy-2 lined zirconium barrier fuel cladding", Zirconium in the Nuclear Industry: Eleventh International Symposium, Proc. ASTM STP 1295, Garmisch-Partenkirchen, 1995 (BRADLEY, E.R., SABOL, G.P., Eds), ASTM International, West Conshohocken, PA (1996) 676–694.

[2.197] DAHLBÄCK, M., et al., The effect of liner component iron content on cladding corrosion, hydriding, and PCI resistance, J. ASTM Int. **2** (2005) JAI12444.

[2.198] BAIN, A.S., WOOD, J.C., COLEMAN, C.E., "Fuel designs to eliminate defects on power increases", Proc. Int. Conf. on Nuclear Fuel Performance, London, 1973, Proc. British Nuclear Energy Society, London (1974) 56.1–56.5.

[2.199] LANNING, D.D., JOHNSON, A.B., TRIMBLE, D.J., BOYD, S.M., "Corrosion and hydriding of N-reactor pressure tubes", Zirconium in the Nuclear Industry: Eighth International Symposium, Proc. ASTM STP 1023, San Diego, 1988 (VAN SWAM, L.F.P., EUCKEN, C.M., Eds), ASTM International, West Conshohocken, PA (1989) 3–19.

[2.200] URBANIC, V.F., COX, B., Long-term corrosion and deuteriding behaviour of Zircaloy-2 under irradiation, Can. Metall. Q. **24** (1985) 189–196.

[2.201] SMIRNOV, A., et al, "Results of post-irradiation examination to validate WWER-440 and WWER-1000 fuel efficiency at high burn-ups", Proc. Int. Conf. on WWER Fuel Performance, Modelling and Experimental Support, Bulgarian Academy of Sciences, Sofia (2002) 63–82.

[2.202] MOLCHANOV, V.L., "Perspective decisions of WWER nuclear fuel: Implementation at Russian NPPs", Proc. 4th Int. Conf. on WWER Fuel Performance, Modelling and Experimental Support, Bulgarian Academy of Sciences, Sofia (2002) 25–36.

[2.203] CHANTOIN, P., et al., "Results of post-irradiation examination to validate WWER-440 and WWER-1000 fuel efficiency at high burnups", Proc. 4th Int. Conf. on WWER Fuel Performance, Modelling and Experimental Support, Bulgarian Academy of Sciences, Sofia (2002).

[2.204] SHEBALDOV, P.V., et al., "E110 alloy cladding tube properties and their interrelation with alloy structure-phase condition and impurity content", Zirconium in the Nuclear Industry: Twelfth International Symposium, Proc. ASTM STP 1354, Toronto, 1998 (SABOL, G.P., MOAN, G.D., Eds), ASTM International, West Conshohocken, PA (2000) 545–559.

[2.205] ZAIMOVSKY, A.S., NIKULINA, A.V., RESHETNIKOV, N.G., Zirconium Alloys in Nuclear Power, Energoatomizdat, Moscow (1994) (in Russian).

[2.206] ZAVIALOV, A.R., et al., "Effect of zirconium alloy chemical composition and microstructure on creep strength", Proc. Int. Conf. on Physical Metallurgy of Reactor Materials, Alushta, USSR, 1978, Nauka i Tekhnika, Moscow (1978) 153–173 (in Russian).

[2.207] NIKULINA, A.V., et al., "Metallurgical factors defining materials science", Proc. Int. Conf. on Reactor Material Science, Alushta, USSR, 1990, Vol. 4, Fiziko-Tekhnicheskij Institut, Kharkov (1990) 40–46 (in Russian).

[2.208] KOBYLYANSKY, G.P., NOVOSELOV, A.E., "Irradiation resistance of Zr and alloys on its base", Handbook Data on Reactor Materials Science, Research Institute of Atomic Reactors, Dimitrovgrad (1996) (in Russian).

[2.209] NIKULINA, A.V., et al., "Zirconium-Niobium alloys for use as components of WWER reactor cores", Proc. Int. Symp. Fontevraud 5: Contribution of Materials Investigation to the Resolution of Problems Encountered in Pressurized Water Reactors, French Nuclear Society, Paris (2002) 505–515 (in Russian).

[2.210] SOLONIN, M.I., et al., "State of the art and prospects of work evolution in Russia on fuel rod materials for water cooled reactors", Proc. 5th Int. Conf. on Reactor Materials Science, Dimitrovgrad, 1988, Vol. 1, Research Institute of Atomic Reactors, Dimitrovgrad (1988) 3–32 (in Russian).

[2.211] NIKULINA, A.V., Zirconium alloys in nuclear power engineering, Metal Science and Heat Treatment **46** (2004) 458–462.

[2.212] REBEYROLLE, V., CHARQUET, D., Zirconium Base Alloy, Resistant Against Creep and Against Corrosion by Water and Steam, Manufacturing Process and Application in a Nuclear Reactor, European Patent EP0802264A1, filed Oct 1997, available on-line.

[2.213] MARDON, J.P., GARNER, G., BESLU, P., CHARQUET, D., SENEVAT, J., "Update on the development of advanced zirconium alloys for PWR fuel rod cladding," Proc. Int. Topical Mtg on LWR Fuel Performance, Portland, American Nuclear Society, La Grange Park, IL (1997) 405–412.

[2.214] MARDON, J.P., et al., "The M5 fuel rod cladding", TopFuel '99. LWR Nuclear Fuel Highlights at the Beginning of the Third Millennium, Avignon, France, 1999 (1999) 407–414.

[2.215] MARDON, J.P., CHARQUET, D., SENEVAT, J., "Influence of composition and fabrication process on out-of-pile and in-pile properties of M5 alloy", Zirconium in the Nuclear Industry: Twelfth International Symposium, Proc. ASTM STP 1354, Toronto, 1998 (MOAN, G.D., SABOL, G.P., Eds), ASTM International, West Conshohocken, PA (2000) 505–524.

[2.216] GARNER, G.L., BOSHERS, J.A., WILSE, J.T., "The performance of zirconium alloy cladding and structural components in high duty U.S. pressurized water reactors", Proc. Int. Symp. Fontevraud, Vol. 5, French Nuclear Society, Paris (2002) 489.

[2.217] REBEYROLLE, V., MARDON, J.P., CHARQUET, D., SENEVAT, J., "Corrosion and creep properties of M5 alloy: Optimization and validation under irradiation", Proc. Enlarged Halden Group Mtg on High Burn-up Fuel Performance, Safety and Reliability and Degradation of In-core Materials and Water

Chemistry Effects and Man-machine System Research, Loen, Norway, Institutt for Energiteknikk, Halden, Norway (1999) HPR-351-V2.

[2.218] WESTINGHOUSE ELECTRIC CORPORATION NUCLEAR MANUFACTURING DIVISION, Optimized ZIRLO™ High-performance Fuel Cladding Material, https://westinghousenuclear.com/Portals/0/Operating%20Plant%20Services/Fuel/Fuel%20Products/NF-FE-0046%20Optimized%20ZIRLO%20HP%20Fuel%20Clad%20Mtl.pdf

[2.219] SABOL, G.P., COMSTOCK, R.J., WEINER, R.A., LAROUERE, P., STANUTZ, R.N., "In-reactor corrosion performance of ZIRLO™ and Zircaloy-4", Zirconium in the Nuclear Industry: Tenth International Symposium, Proc. ASTM STP 1245, Baltimore, 1993 (GARDE, A.M., BRADLEY, E.R., Eds), ASTM International, West Conshohocken, PA (1994) 724–744.

[2.220] SABOL, G.P., COMSTOCK, R.J., SCHOENBERGER, G., KUNISHI, H., NUHFERM, D.L., "In-reactor fuel cladding corrosion performance at higher burn-ups and higher coolant temperatures", Proc. ANS Int. Topical Mtg on LWR Fuel Performance, Portland, 1997, American Nuclear Society, La Grange Park, IL (1997) 397–404.

[2.221] COMSTOCK, R.J., SCHOENBERGER, G., SABOL, G.P., "Influence of processing variables and alloys chemistry on the corrosion behavior of ZIRLO™ nuclear fuel cladding", Zirconium in the Nuclear Industry: Eleventh International Symposium, Proc. ASTM STP 1295, Garmisch-Partenkirchen, 1995 (BRADLEY, E.R., SABOL, G.P., Eds), ASTM International, West Conshohocken, PA (1996) 710–725.

[2.222] YUEH, H.K., et al., Improved ZIRLO™ cladding performance through chemistry and process modifications, J. ASTM Int. **2** (2005) Paper JAI12344.

[2.223] WILSON, H.W., ESPOSITO, V.J., SABOL, G.P., Westinghouse high-burnup experience, Trans. ANS **77** (1997) 67–68.

[2.224] KING, S.J., et al., "Impact of hydrogen on dimensional stability of ZIRLO™ fuel assemblies", Zirconium in the Nuclear Industry: Thirteenth International Symposium, Proc. ASTM STP 1423, Annecy, 2001 (MOAN, G.D., RUDLING, P., Eds), ASTM International, West Conshohocken, PA (2002) 471–489.

[2.225] NIKULINA, A.V., et al., "Zirconium alloy E635 as a material for fuel rod cladding and other components of WWER and RBMK cores", Zirconium in the Nuclear Industry: Eleventh International Symposium, Proc. ASTM STP 1295, Garmisch-Partenkirchen, 1995 (BRADLEY, E.R., SABOL, G.P., Eds), ASTM International, West Conshohocken, PA (1996) 785–804.

[2.226] SOLONIN, M.I., et al., "Zirconium alloy for fuel assemblies of new generation WWER", Int. Topical Mtg TopFuel '99, Proc. SFEN/ENS conf., Avignon, 1999, French Nuclear Society, Paris (1999) 165–177.

[2.227] NIKULINA, A.V., Zr-Nb alloys for core components of pressurized water reactors, Metalloved. i Termicheskaya Obrab. Met. **8** (2003) 7–13 (in Russian).

[2.228] NIKULINA, A.V., et al., Zirconium alloy E635 as a material for fuel rod cladding and other components of VVER and RBMK cores, Zirconium in the Nuclear Industry: Eleventh International Symposium, Proc. ASTM STP 1295, Garmisch-Partenkirchen, 1995 (BRADLEY, E.R., SABOL, G.P., Eds), ASTM International, West Conshohocken, PA (1996) 785–804.

[2.229] SHISHEV, V.N., et al., Structure-phase state, corrosion and irradiation properties of Zr-Nb-Fe-Sn system alloys, J. ASTM Int. **5** (2008) Paper JAI101127.

[2.230] KON'KOV, V.F., NIKULINA, A.V., SHISHOV, V.N., KHOKHUNOVA, T.N., NOVOSELOV, A.E., "Factors affecting out-of- and in-reactor corrosion of Zr claddings of fuel rods", Water Chemistry and Corrosion Control of Cladding and Primary Circuit Components, IAEA-TECDOC-1128, IAEA, Vienna (1999) 103–113.

[2.231] NIKULINA, A.V., et al., "Zr-1Sn-1Nb-0.5Fe alloy for technologic channel tubes of RBMK type reactors", Vopr. At. Nauki Tekh. **2** 36 (1990) 58–66 (in Russian).

[2.232] AVERIN, S.A., et al., "Evolution of dislocation and precipitate structure in Zr alloys under long-term irradiation", Zirconium in the Nuclear Industry: Twelfth International Symposium, Proc. ASTM STP 1354, Toronto, 1998 (MOAN, G.D., SABOL, G.P., Eds), ASTM International, West Conshohocken, PA (2000) 105–121.

[2.233] NIKULINA, A.V., "State of the art and prospects of zirconium material evolution for fuel rod claddings and other components of WWER type reactors in Russia", EUROMAT-96 Topical Conf. on Materials and Nuclear Power, Bournemouth, UK, Institute of Materials, London (1996) 157–169.

[2.234] CHEADLE, B.A., COLEMAN, C.E., LICHT, H., CANDU-PHW pressure tubes, their manufacture, inspection and properties, Nucl. Tech. **57** (1982) 413–425.

[2.235] NIKULINA, A.V., et al., "Technology of Zr-2.5Nb alloy channel tubes installed in RBMK". Vopr. At. Nauki Tekh. **2** 36 (1990) 46–58 (in Russian).

[2.236] NIKULINA, A.V., et al., "Results of investigations into stabilizing structure and properties of cold worked Zr-2.5Nb channel tubes", Vopr. At. Nauki Tekh. **1** 48 (1993) 3–12 (in Russian).

[2.237] PLATONOV, P.A., et al., Creep of Zr-2.5Nb alloy technologic channels in RBMK, Vopr. At. Nauki Tekh. **2** 36 (1990) 22–33 (in Russian).

[2.238] GRIGORIEV, V.M., et al., Feasibility analysis of improving serviceability of Zr-2.5Nb pressure tubes for RBMK reactors, Vopr. At. Nauki Tekh. **2** 36 (1990) 54–58 (in Russian).

[2.239] NIKULIN, S.A., et al., Influence of heat-treatment on tensile properties and fracture toughness of Zr-2.5%Nb technologic channel tubes, Vopr. At. Nauki Tekh. **2** 36 (1990) 67–73 (in Russian).

[2.240] THEAKER, J.R., et al., “Fabrication of Zr-2.5Nb pressure tubes to minimize the harmful effects of trace elements”, Zirconium in the Nuclear Industry: Tenth International Symposium, Proc. ASTM STP 1245, Baltimore, 1993 (GARDE, A.M., BRADLEY, E.R., Eds), ASTM International, West Conshohocken, PA (1994) 221–242.

[2.241] COLEMAN, C.E., CHEADLE, B.A., CANN, C.D., THEAKER, J.R., “Development of pressure tubes with service life greater than 30 years”, Zirconium in the Nuclear Industry: Eleventh International Symposium, Proc. ASTM STP 1295, Garmisch-Partenkirchen, 1995 (BRADLEY, E.R., SABOL, G.P., Eds), ASTM International, West Conshohocken, PA (1996) 884–898.

[2.242] CHOUBEY, R., ALDRIDGE, S.A., THEAKER, J.R., CANN, C.D., COLEMAN, C.E., “Effects of extrusion billet preheating microstructure and properties of Zr-2.5Nb pressure tube material”, Zirconium in the Nuclear Industry: Eleventh International Symposium, Proc. ASTM STP 1295, Garmisch-Partenkirchen, 1995 (BRADLEY, E.R., SABOL, G.P., Eds), ASTM International, West Conshohocken, PA (1996) 657–675.

[2.243] AITCHISON, I., DAVIES, P.H., Role of microsegregation in fracture of cold-worked Zr-2.5Nb pressure tubes, J. Nucl. Mater. **203** (1993) 206–220.

[2.244] MARKELOV, V.A., et al., Fracture toughness and delayed hydride cracking velocity of zirconium alloy pressure tubes for channel type reactors, Vopr. At. Nauki Tekh. **1** 61 (2003) 39–56 (in Russian).

[2.245] COLEMAN, C., et al., Mechanical properties of Zr–2.5Nb pressure tubes made from electrolytic powder, J. ASTM International **4** (2007) Paper JAI101111.

[2.246] CHEADLE, B.A., CELOVSKY, A., GHAFOOR, M., BUTT, W., “Assessment of the integrity of KANUPP fuel channels”, Report No. AECL-11710, Atomic Energy of Canada Limited, Chalk River, ON (1996).

[2.247] KOIKE, M.H., AKIYAMA, T., NAGAMATSU, K., SHIBAHARA, I., “Change of mechanical properties by irradiation and evaluation of the heat–treated Zr–2.5Nb pressure tube”, Zirconium in the Nuclear Industry: Tenth International Symposium, Proc. ASTM STP 1245, Baltimore, 1993 (GARDE, A.M., BRADLEY, E.R., Eds), ASTM International, West Conshohocken, PA (1994) 183–201.

[2.248] CHOW, C.K., et al., “Properties of an irradiated heat-treated Zr-2.5Nb pressure tube removed from the NPD reactor”, Zirconium in the Nuclear Industry: Eleventh International Symposium, Proc. ASTM STP 1295, Garmisch-Partenkirchen, 1995 (BRADLEY, E.R., SABOL, G.P., Eds), ASTM International, West Conshohocken, PA (1996) 469–491.

[2.249] FLECK, R.G., PRICE, E.G., CHEADLE, B.A., “Pressure tube development for CANDU reactors”, Zirconium in the Nuclear Industry: Sixth International Symposium, Proc. ASTM STP 824, Vancouver, 1982 (FRANKLIN, D.G., ADAMSON, R.B., Eds), ASTM International, West Conshohocken, PA (1984) 88–105.

[2.250] BICKEL, G.A., GRIFFITHS, M., Manufacturing variability and deformation for Zr-2.5Nb pressure tubes, J. Nucl. Mater. **383** (2008) 9–13.

[2.251] SRIVASTAVA, D., DEY, G.K., BANERJEE, S., Evolution of microstructure during fabrication of Zr-2.5Nb alloy pressure tubes, Met. Mat. Trans. A **26** (1995) 2707–2718.

[2.252] GANGULY, C., “Advances in zirconium technology for nuclear reactor application,” Proc. Symp. Zirconium-2002, Mumbai, 2002 (DE, P.K., Ed.), Bhabha Atomic Research Centre, Mumbai (2002) 1–27.

[2.253] MILLARD, J.W.F., DIMITROV, L., BAJWA, D., “ACR-1000 fuel channel developments”, Advances in Nuclear Materials: Processing, Performance and Phenomena, Mumbai, 2006, Elsevier, Amsterdam (2006).

[2.254] ISHIMOTO, S., et al., “Development of new Zirconium alloys for ultra-high burn-up fuel”, Proc. Int. Topical Mtg LWR Fuel Performance, Park City, 2000, American Nuclear Society, La Grange Park, IL (2000) 499–510.

[2.255] NANIKAWA, S., et al., “Correlation between characteristics of oxide films formed on Zr alloys in BWRs and corrosion performance”, Zirconium in the Nuclear Industry: Twelfth International Symposium, Proc. ASTM STP 1354, Toronto, 1998 (MOAN, G.D., SABOL, G.P., Eds), ASTM International, West Conshohocken, PA (2000) 815–834.

[2.256] ANADA, H., et al., “Out-of-pile corrosion behavior and corrosion mechanism of NDA for high burn-up fuel of PWR”, Proc. Int. Topical Mtg LWR Fuel Performance, Park City, 2000, American Nuclear Society, La Grange Park, IL (2000) 445–456.

[2.257] YAMATE, K., et al., “Burnup extension of Japanese PWR fuels”, Proc. Int. Topical Mtg LWR Fuel Performance, Portland, 1997, American Nuclear Society, La Grange Park, IL (1997) 318–325.

[2.258] KIDO, T., SENDA, Y., TUKUTA, Y., HAYASHI, H., MURAI, K., “Quantitative assessment of irradiation effect on creep and corrosion properties of Zr-base alloys”, Zirconium in the Nuclear Industry: Thirteenth International Symposium, Proc. ASTM STP 1423, Annecy, 2001 (MOAN, G.D., RUDLING, P., Eds), ASTM International, West Conshohocken, PA (2002) 780–795.

[2.259] ETOH, Y., et al., “Development of new Zirconium alloys for BWR”, Zirconium in the Nuclear Industry: Eleventh International Symposium, Proc. ASTM STP 1295, Garmisch-Partenkirchen, 1995 (BRADLEY, E.R., SABOL, G.P., Eds), ASTM International, West Conshohocken, PA (1996) 825–849.

[2.260] YOSHINO, A., ONO, S., KIDO, T., ONOOKA, H., “Irradiation behavior of J-Alloy"T"M at high burnup”, Water Reactor Fuel Performance Meeting/TopFuel/LWR Fuel Performance Meeting, Sendai, 2014, Atomic Energy Society of Japan, Tokyo (2014) Paper 100153.

[2.261] GAILLAC, A., LEMAIGNAN, C., BARBERIS, P., Damage build-up in zirconium alloys during mechanical processing: Application to cold pilgering, J. ASTM Int. **8** (2011) Paper ID JAI103026.
[2.262] KACZOROWSKI, D., MARDON, J.P., BARBERIS, P., HOFFMANN, P.B., STEVENS, J., "Impact of iron in M5™", Zirconium in the Nuclear Industry: Seventeenth International Symposium, Proc. ASTM STP 1543, Hyderabad, 2013 (COMSTOCK, R., BARBERIS, P., Eds), ASTM International, West Conshohocken, PA (2015) 159–183.
[2.263] GARDE, A.M., et al., Advanced zirconium alloy for PWR application, J. ASTM Int. **7** (2010) Paper ID JAI103030.
[2.264] PAN, G., et al., "Advanced material for PWR applications: AXIOM™ cladding", Water Reactor Fuel Performance Meeting/TopFuel/LWR Fuel Performance, Orlando, 2010, American Nuclear Society, La Grange Park, IL (2010) Paper 0074.
[2.265] ROMERO, J., et al., "Evolution of Westinghouse fuel cladding", Water Reactor Fuel Performance Meeting/TopFuel/LWR Fuel Performance Meeting, Sendai, 2014, Atomic Energy Society of Japan, Tokyo (2014) Paper 100019.
[2.266] GARDE, A.M., PAN, G., MUELLER, A.J., HALLSTADIUS, L., "Oxide surface peeling of advanced zirconium alloy cladding after high burnup irradiation in pressurized water reactors", Zirconium in the Nuclear Industry: Seventeenth International Symposium, Proc. ASTM STP 1543, Hyderabad, 2013 (COMSTOCK, R., BARBERIS, P., Eds), ASTM International, West Conshohocken, PA (2015) 673–692.
[2.267] PAN, G. GARDE, A.M., ATWOOD, A.R., KÄLLSTRÖM, R., JÄDERNÄS, D., "High burnup Optimized ZIRLO™ cladding performance", TopFuel 2013: LWR Fuel Performance Meeting, Charlotte, 2013, American Nuclear Society, La Grange Park, IL (2013) Paper 8427.
[2.268] PAN, G., GARDE, A.M., ATWOOD, A.R., "Performance and property evaluation of high-burnup optimised ZIRLO™ cladding", Zirconium in the Nuclear Industry: Seventeenth International Symposium, Proc. ASTM STP 1543, Hyderabad, 2013 (COMSTOCK, R., BARBERIS, P., Eds), ASTM International, West Conshohocken, PA (2015) 607–627.
[2.269] JEONG, Y.K., et al., Out-of-pile and in-pile performance of advanced zirconium alloys (HANA) for high burn-up fuel, J. Nucl. Sci. Technol. **43** (2006) 977–983.
[2.270] PARK, J.-Y., CHOI, B.-K., YOO, S.J., JEONG, Y.H., Corrosion behavior and oxide properties of Zr-1.1 wt%Nb-0.05 wt%Cu alloy, J. Nucl. Mater. **359** (2006) 59–68.
[2.271] PARK, J.-Y., YOO, S.J., CHOI, B.-K., JEONG, Y.H., Corrosion and oxide characteristics of Zr-1.5Nb-0.4Sn-0.2Fe-0.1Cr alloys in 360°C pure water and LiOH solution, J. Nucl. Mater. **373** (2008) 343–350.
[2.272] PARK, J.-Y., CHOI, B.-K., YOO, S.J., JEONG, Y.H., Corrosion and oxide properties of HANA alloys, J. ASTM International **5** (2008) Paper JAI101129.
[2.273] CURTIS, R.E., DRESSLER, G., "Effect of thermomechanical processing and heat treatment on the properties of Zr-3Nb-1Sn strip and tubing", Proc. Int. Symp. on Zirconium in Nuclear Applications, ASTM STP 551, Portland, 1973 (SCHEMEL, J.H., ROSENBAUM, H.S., Eds), ASTM International, West Conshohocken, PA (1974) 104–128.
[2.274] GARZAROLLI, F., RUHMANN, H., VAN SWAM, L., "Alternative Zr alloys with irradiation resistant precipitates for high burnup BWR application", Zirconium in the Nuclear Industry: Thirteenth International Symposium, Proc. ASTM STP 1423, Annecy, 2001 (MOAN, G.D., RUDLING, P., Eds), ASTM International, West Conshohocken, PA (2002) 119–132.
[2.275] SEIBOLD, A., GARZAROLLI, F., "Influence of composition and condition on in-PWR behaviour of Zr-Sn-Nb-Fe-Cr-V alloys," Zirconium in the Nuclear Industry: Thirteenth International Symposium, Proc. ASTM STP 1423, Annecy, 2001 (MOAN, G.D., RUDLING, P., Eds), ASTM International, West Conshohocken, PA (2002) 743–757.
[2.276] BOULTON, J., WRIGHT, M.G., "Ozhennite 0.5 — Its potential and development", Applications-related Phenomena in Zirconium and Its Alloys, ASTM STP 458 (BAROCH, E.F., Ed.), ASTM International, West Conshohocken, PA (1969) 325–337.
[2.277] BOULTON, J., Behaviour of zirconium alloys in organic coolants, Can. Metall. Q. **11** (1972) 1–5.
[2.278] BRADY, G.R., "Post-irradiation examination of cold-reduced Ozhennite-0.5 pressure tubes irradiated at 400°C in the WR-1 reactor", Report No. WNRE-502, Atomic Energy of Canada Limited, Chalk River, ON (1981).
[2.279] TYZACK, C., et al., SCANUK: A collaborative programme to develop new zirconium cladding alloys, J. Nucl. Mater **66** (1977) 163–186.
[2.280] WILLIAMS, C.D., Development potential of zirconium alloys for high-temperature applications, Reactor Tech. **13** (1970) 147–169.
[2.281] WILLIAMS, C.D., ELLS, C.E., DIXON, P.R., Development of high strength alloys, Can. Metall. Q. **11** (1972) 257–271.
[2.282] IBRAHIM, E.F., PRICE, E.G., WYSIEKIERSKI, A.G., Creep and stress-rupture of high strength zirconium alloys, Can. Metall. Q. **11** (1972) 273–283.
[2.283] CHEADLE, B.A., HOLT, R.A., FIDLERIS, V., CAUSEY, A.R., URBANIC, V.F., "High-strength, creep resistant EXCEL pressure tubes", Zirconium in the Nuclear Industry: Fifth International Conference, Proc.

ASTM STP 754, Boston, 1980 (FRANKLIN, D.G., Ed.), ASTM International, West Conshohocken, PA (1982) 193–207.

[2.284] ELLS, C.E., COLEMAN, C.E., CHEADLE, B.A., SAGAT, S., RODGERS, D.K., The behaviour of hydrogen in Excel alloy, J. Alloys Compd. **231** (1995) 785–791.

[2.285] SCHULSON, E.M., Order strengthening as a method for reducing irradiation creep: A hypothesis, J. Nucl. Mater. **66** (1977) 322–324.

[2.286] CAUSEY, A.R., FIDLERIS, V., ROSINGER, H.E., SCHULSON, E.M., URBANIC, V.F., "Irradiation response of the ordered phase Zr_3Al", Zirconium in the Nuclear Industry: Third International Conference, Proc. ASTM STP 633, Quebec City, 1976 (LOWE, A.L., PARRY, G.W., Eds), ASTM International, West Conshohocken, PA (1977) 437–454.

[2.287] SCHULSON, E.M., CAMERON, D.J., High strength corrosion-resistant zirconium aluminum alloys, CA patent document 988748/A/., 25 pp., available from Supply and Services Canada, Publishing Center, Ottawa, 11 May 1976.

[2.288] ROSINGER, H.E., Effect of fast neutron irradiation on the properties of Zr3Al-based alloys, J. Nucl. Mater. **95** (1980) 171–180.

[2.289] KLEPFER, H.H., MEHNER, A.D., Specific Zirconium Alloy Design Program, General Electric Report No. GEAP-10044, General Electric, San Jose, CA (1969).

[2.290] SLATTERY, G.F., Mechanical properties and structure of as-received, heat-treated and hydrided Zr-1.5 wt% Cr-0.1 wt% Fe alloy tubing, Can. Metall. Q. **11** (1972) 237–248.

[2.291] NORTHWOOD, D.O., BAHEN, L.E., Correlation of Microstructure and Corrosion Performance of Zr-1.15 % Cu-0.1% Fe in Water and Steam, Report No. AECL-5019, Atomic Energy of Canada Limited, Chalk River, ON (1975).

[2.292] HOLT, R.A., ELDER, F.G., The Effect of Microstructure and Lattice Strain on the Corrosion Resistance and Mechanical Properties of β-quenched Zr-1.14 wt% Cr-0.1 wt% Fe, Report No. AECL-4586, Atomic Energy of Canada Limited, Chalk River, ON (1974).

[2.293] ZAIMOVSKY, A.S., "Zirconium alloys in atomic power engineering", Proc. Int. Conf. on Reactor Materials Science, Alushta, USSR, 1978, Vol. 5, Nauka i Tekhnika, Moscow (1978) 132–145 (in Russian).

[2.294] NIKULINA, A.V., PEREGUD, M.M., SHAMARDIN, V.K., KOBYLYANSKIJ, G.P., "Metallurgical factors determining zirconium irradiation behaviour", Proc. Int. Conf. on Radiation Materials Science, Alushta, USSR, 1990, Vol. 4, Kharkov Institute of Physics and Technology, Kharkov, USSR (1990) 40–46 (in Russian).

[2.295] PLOC, R.A., "The effect of minor alloying elements on oxidation and hydrogen pick-up in Zr-2.5Nb", Zirconium in the Nuclear Industry: Thirteenth International Symposium, Proc. ASTM STP 1423, Annecy, 2001 (MOAN, G.D., RUDLING, P., Eds), ASTM International, West Conshohocken, PA (2002) 297–312.

[2.296] COLEMAN, C.E., AMBLER, J.F.R., Measurement of effective solvus temperature of hydrogen in Zr-2.5 wt% Nb using acoustic emission, Can. Metall. Q. **17** (1978) 81–84.

[2.297] FERRER, F., et al., "The effect of small concentrations of sulfur on the plasticity of zirconium alloys at intermediate temperatures," Zirconium in the Nuclear Industry: Thirteenth International Symposium, Proc. ASTM STP 1423, Annecy, 2001 (MOAN, G.D., RUDLING, P., Eds), ASTM International, West Conshohocken, PA (2002) 863–887.

[2.298] CHANG, K.I., HONG, S.I., Effect of sulphur on the strengthening of a Zr-Nb alloy, J. Nucl. Mater. **373** (2008) 16–21.

[2.299] CHOI, Y.C., KO, S., CHANG, K.I., CHO, N.C., HONG, S.I., Effect of phosphorus on the mechanical behavior of a Zr-Nb alloy, J. Nucl. Mater. **383** (2009) 270–273.

Chapter 3

FROM SAND TO INGOT — EXTRACTION AND CONSOLIDATION OF ZIRCONIUM

R.A. GRAHAM, J.C. HAYGARTH
Teledyne Wah Chang,
Albany, OR, USA

3.1. INTRODUCTION

This chapter describes the various schemes for taking zirconium ores and reducing them to metal. The chapter starts with a review of the different ore types and availability. Discussions follow on unlocking the ore from mineral by-products, the separation of hafnium from zirconium, the reduction of zirconium metal and the purification of zirconium. A description of alloying and melting schemes to consolidate the metal into ingots is given below.

3.2. ZIRCONIUM ORE

Because of their chemical similarity, zirconium and hafnium are always found together in nature, although in widely differing proportions. Erlank et al. [3.1] list 38 zirconium minerals, of which 27 are silicates, 9 are oxides, 1 is a carbonate and 1 a sulphate.

For zircon from metamorphic rocks, Erlank et al. [3.2] cite studies showing hafnium mass concentrations of 1.47–3.70% in altered alkali rocks, higher than the value for corresponding unaltered rocks. In altered sub-alkali rocks, the value was higher still at 5.88–8.33%. The reason for this difference is thought to be the preferential removal of zirconium during alteration; zircons in hydrothermally deposited veins have low Hf:Zr values, in the range of 0.53–2.08%.

Zirconium and hafnium are almost exclusively obtained from zircon, $ZrSiO_4$, and baddeleyite, ZrO_2. According to Erlank [3.1], zircon is the most common zirconium silicate and is found in nearly all rock types. Baddeleyite occurs in association with pyrochlore and apatite in carbonatite ore bodies [3.3].

Hafnium mass concentrations are around 2–2.5% in ores exploited for zirconium used in nuclear reactors.

3.2.1. Abundance of zirconium ore in the earth's crust

Erlank et al. [3.4] cite several estimates each for average igneous, metamorphic and sedimentary rocks and select 190 ppm for the abundance of zirconium in the continental crust. Using this value and 2.5% as the average mass percentage of hafnium relative to zirconium in the continental crust, the same authors [3.5] arrive at 4.8 ppm for the continental crustal abundance of hafnium. These authors also suggest abundances of 100 ppm for zirconium and 2.8 ppm hafnium in the oceanic crust [3.4, 3.5].

By contrast, the 2010 edition of the Handbook of Chemistry and Physics [3.6] gives 165 ppm and 3 ppm for the respective crustal abundances of zirconium and hafnium. This concentration makes zirconium more prevalent than many well-known metals such as Cd, CO, Cr, Cu, Pb, Sn, Ni and Zn.

3.2.2. Deposits and mining

The only commercially important zirconium and hafnium minerals are zircon (zirconium silicate, $ZrSiO_4$) and baddeleyite (zirconium oxide, ZrO_2). Zircon is by far the more important, accounting for about 98% of the zirconium and hafnium mined in 1997 [3.7].

Almost all the zircon mined commercially comes from beach and dune deposits, the largest of which are found in the Murray Basin of Australia and in Western Australia, north of Perth; Richards Bay in the Republic of South Africa; along the Trail Ridge in Florida, USA; Ukraine; Tamil Nadu and Kerala states in India; and Sri Lanka.

Most zircon is mined as a co-product of titanium ores, ilmenite and rutile. The sand deposits are mined using dredges or with front-end loaders after removal of overburden. Sand typically contains about 5% heavy minerals, of which only one tenth or less is zircon. The bulk of the mineralization is made up of ilmenite, monazite and garnet, all of which have higher magnetic susceptibilities than zircon, and rutile and leucoxene, which are titanium minerals that are not magnetic, but are electrically conductive.

Debris is screened out, the ore is hydrated and then subjected to gravity separation techniques using devices such as spirals and Reichert cones. The wet concentrate may be subjected to magnetic separation before drying, after which a combination of magnetic and electrostatic treatments segregates it into separate minerals.

Zircon, a non-conducting, non-magnetic mineral is often given further gravity as well as magnetic and electrostatic treatments to remove impurities such as monazite, which contributes thorium; xenotime, which contributes phosphorus; and kyanite and sillimanite, which contribute aluminium. Woodcock [3.8] has edited a collection of papers that describe in detail the recovery of zircon and other minerals from Australian sands. The major zirconium producers intentionally select sand based on the ease with which impurities such as P, Al, U and Th can be removed during subsequent processing.

Baddeleyite (zirconium oxide) is produced commercially at two locations, Phalaborwa in South Africa and the Kola Peninsula in the Russian Federation. Baddeleyite represents less than 2% of the ore converted into zirconium metal.

3.2.3. Ore production and reserves

The worldwide production of zirconium ore concentrates (both zircon and baddeleyite) is slightly over one million tonnes per year (value for 2001) [3.9]. Of this amount, only about 1% goes into metal production. Most of the zirconium ores are used for ceramic glaze opacifiers, refractories and moulds for making sand castings, glass additions and abrasives. Figure 3.1 shows the utilization of zircon as a percentage by category.

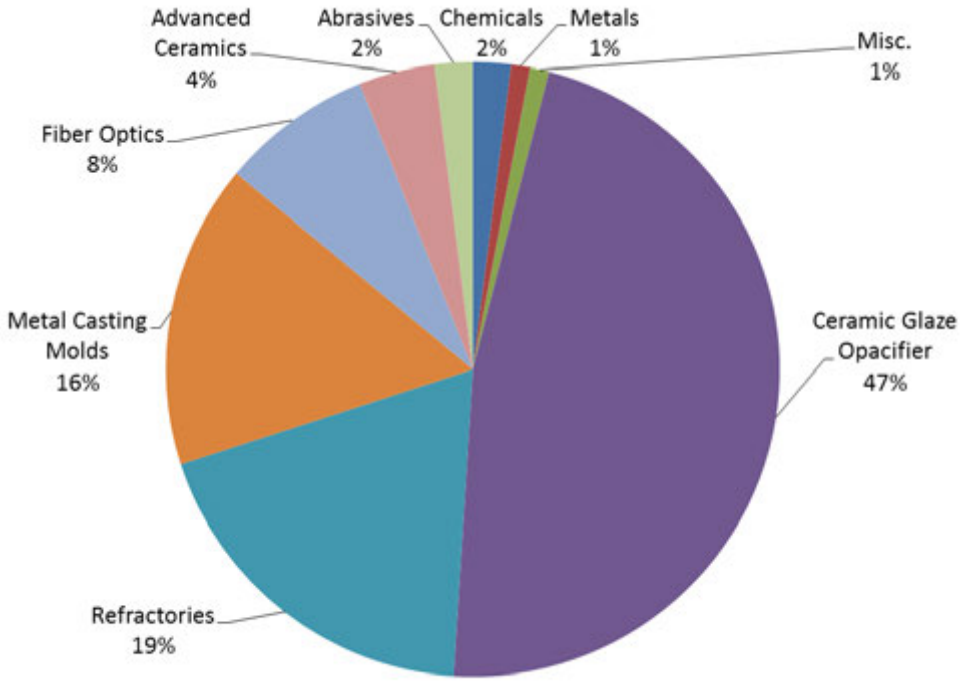

FIG. 3.1. Uses of zircon as a percentage by category.

Hedrick [3.10] gives the reserve and reserve base for zirconium expressed in terms of the oxides. Reserves are defined as currently proven ore bodies, and the reserve base is an estimated value of the total ore body. These values are given in Table 3.1. Exploration and development are in progress in Australia, Canada, India, Kenya, South Africa, Ukraine and the United States of America.

TABLE 3.1. RESERVE AND RESERVE BASE FOR ZIRCONIUM AND HAFNIUM BY COUNTRY

Country	ZrO_2 ($\times 10^6$ tonnes)	
	Reserve	Base
Australia	9.1	29.8
Brazil	0.4	0.4
China	0.5	1.0
India	3.4	3.8
South Africa	14.3	14.3
Ukraine	4.0	6.0
USA	3.4	5.3
All others	0.9	4.1
Total	36	65

Figure 3.2 shows the distribution of zircon reserves as a percentage by country, while Fig. 3.3 shows the zircon reserve base (the totality of identified zircon) in a similar fashion. Figure 3.4 shows zircon mine production by country as a percentage, where the total worldwide production in 2001 was 1.04 million tonnes [3.9].

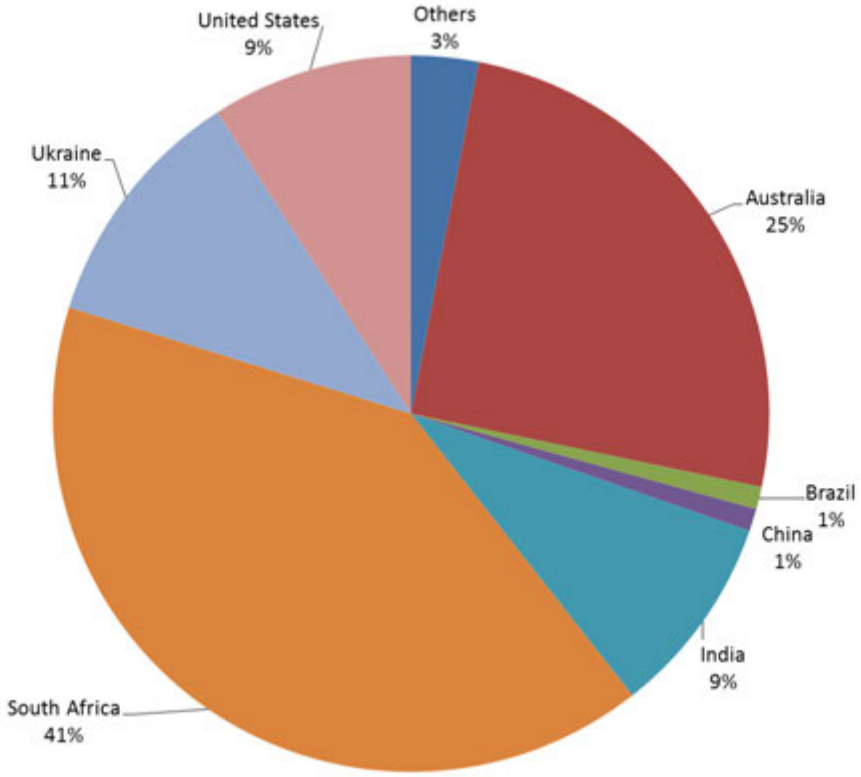

FIG. 3.2. World reserves of zircon as a percentage by country.

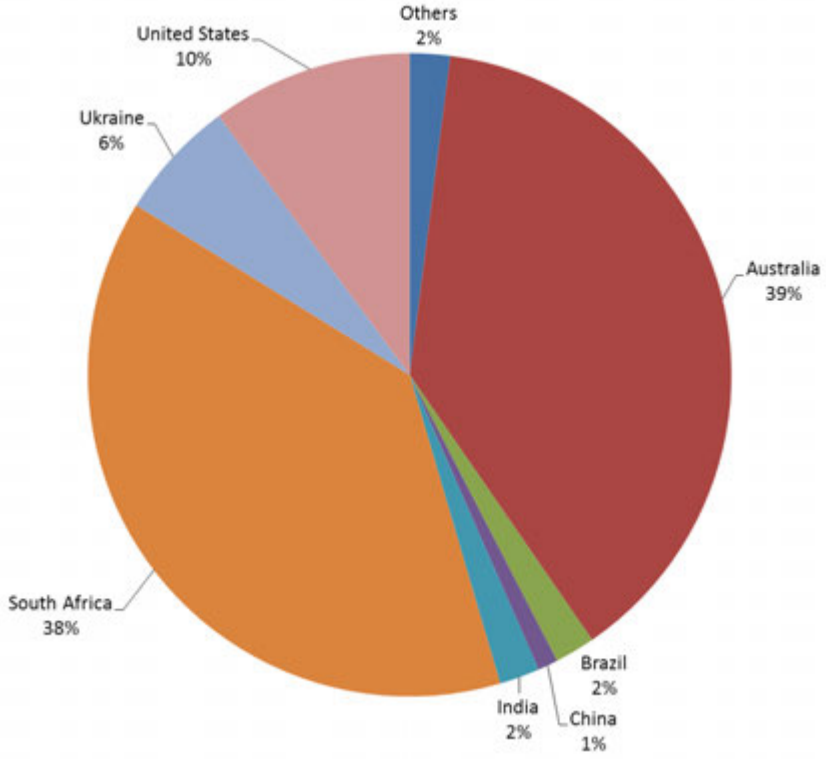

FIG. 3.3. World reserve base of zircon as a percentage by country.

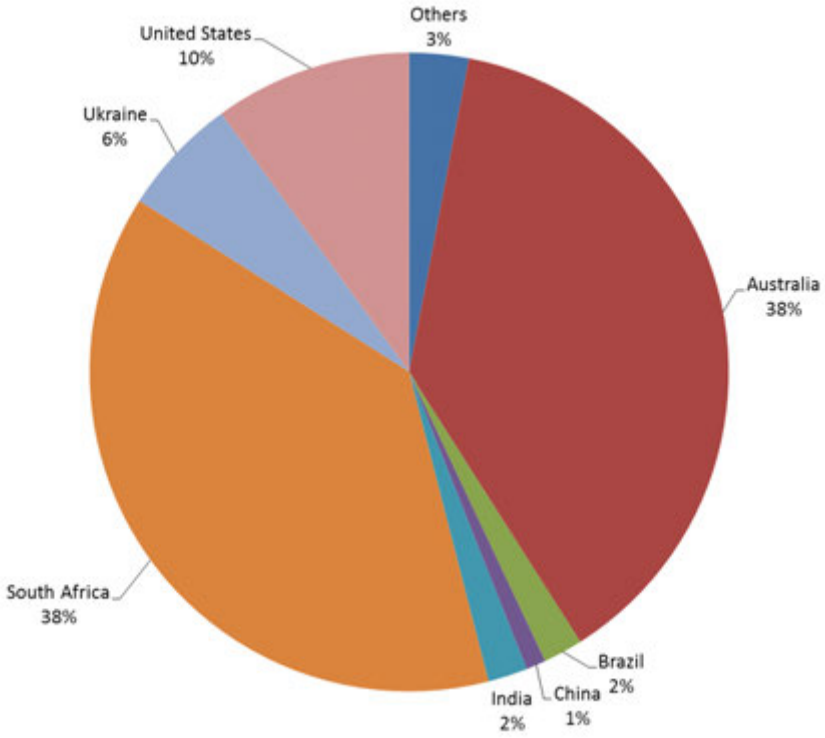

FIG. 3.4. World mine production of zircon as a percentage by country.

3.2.4. Production of reactor grade zirconium

Broad overviews of the chemical processes of zirconium extraction from zircon and baddeleyite include Lustman and Kerze [3.7], Haygarth and Graham [3.9], Ganguly [3.11], Stephens [3.12], Nielsen et al. [3.13], Zelikman et al. [3.14], Skaggs et al. [3.15], and Mallikarjunan and Sehra [3.16].

Zircon is a highly refractory mineral, and the ore is decomposed only with strong reagents and high temperatures. There are three basic operations in processing zircon to make reactor grade zirconium. The first of these involves decomposition of the ore to remove the silica fraction. Next, for neutron economy, the hafnium has to be stripped from the zirconium. Finally, the separated zirconium compound must undergo reduction to obtain metallic sponge or crystals (in the form of powder). Each of these three processes will be treated in detail in separate sections (Sections 3.3–3.5). Current commercial practices will be described first, followed by alternative processes that have been proposed or actually tried.

3.3. DECOMPOSITION OF ZIRCONIUM ORES

The primary objective of decomposition is to remove the silica fraction. However, there are other ‘problematic’ elements that also need to be minimized. Removal and safe disposal of the naturally occurring radioactive elements, uranium and thorium, and their decay products is mandatory. Commercially available zircon usually contains less than a total of 500 ppm (U + Th).

Ore-unlocking processes that have been used, or are currently being used in production, include carbothermic reduction, alkali fusion, fluorosilicate fusion and carbochlorination.

3.3.1. Carbothermic reduction

The process of carbothermic reduction preceded direct carbochlorination and is in effect an intermediate step whereby zirconium carbide or carbonitride is first produced, and then chlorinated [3.7]. The stated advantage was that a large portion of the silicon present was eliminated during the carbide formation step. The elimination of the silicon as the monoxide requires very high temperatures; an arc furnace was incorporated to utilize this principle.

The zirconium ore was mixed with the appropriate amount of coke, placed in a vertical iron cylinder and the central region subjected to a 50 V direct current (DC) arc. The reacted mass was allowed to cool, then removed, separated from the unreacted charge and crushed to powder. This product was called zirconium carbonitride, since it contained nitrogen and also oxygen from air occluded in the charge. It can be roasted in air, to convert it to a crude zirconium oxide, or chlorinated to zirconium tetrachloride.

The reaction is roughly:

$$\mathrm{ZrSiO_4 + 4C \rightarrow Zr(C,N,O) + SiO + 3CO\ (2775\ K\ (2500°C)\ in\ an\ electric\ arc)} \tag{3.1}$$

The reaction is run with a deficiency of carbon to convert silica to silicon monoxide and preclude making silicon carbide. If more coke is added, more silicon is retained as the carbide in the fused ingot. Some carbon used in the reaction comes from the graphite electrode.

The SiO was evolved during carbothermic reduction as a product volatile at reaction temperature and was released to the atmosphere. A cloud of SiO_2 particles would have to be captured, scrubbed and disposed with current environmental considerations, and this cleaning would raise costs considerably. The process recovered about 92% of the zirconium as carbide, for an energy expenditure of about 8–11 kWh/kg carbide. The product composition typically was about 88% Zr, 8% C, 2% Si and up to 2% N. About 1.4 tonnes were made per run. Although cheap and easy, the process was abandoned in the USA because of the availability of zirconium tetrachloride at lower price as a by-product of the direct chlorination of zircon, which was done at the time to produce silicon tetrachloride. Subsequent chlorination of the carbonitride takes place according to the following reactions:

$$\mathrm{ZrC + 2Cl_2 \rightarrow ZrCl_4 + C} \tag{3.2}$$

$$\mathrm{ZrN + 2CL_2 \rightarrow ZrCL_4 + 1/2\ N_2} \tag{3.3}$$

Chlorination is accomplished in a shaft type chlorinator. A coke bed is laid over a graphite distributor plate. The coke bed is initially heated by hot air, and the bed is covered with a 50 mm layer of carbonitride. Once started, chlorination proceeds spontaneously. Intensive chlorination starts at about 675 K (400°C). The tetrachloride vapours are released from the top of the furnace and condensed in a nickel condenser maintained at about 425 K (150°C).

This process has the advantage of conducting the chlorination reaction at lower temperatures than direct carbochlorination. It was used in the early zirconium extraction schemes in the USA but is no longer being used primarily because the poor economics of a

two-step process, chlorine-resistant materials and better construction led to the modern fluidized bed chlorinators currently in use. The Islamic Republic of Iran has used the carbothermic reduction process in their zirconium production plant [3.17].

3.3.2. Alkali fusion

Roasting with sodium hydroxide, sodium carbonate or calcium oxide can be used to decompose zircon, leaving the zirconium in a form that can be converted to a water soluble compound. The process is described in Refs [3.7, 3.18] and in greatest detail by Zelikman et al. [3.14].

The zirconium and silicon compounds formed depend on the alkali used, the initial ratio of alkali to zircon, and the temperature required to effect reaction depends on the alkali chosen. In the case of calcium oxide, the addition of calcium or alkali metal chlorides lowers the reaction temperature from 1673–1773 K (1400–1500°C) to 1273–1373 K (1000–1100°C) [3.14]. In practice, reaction with CaO is used when the direct recovery of zirconia is the goal. Reactions between zircon and sodium hydroxide, sodium carbonate and lime are:

$$ZrSiO_4 + 4NaOH \rightarrow Na_2ZrO_3 + Na_2SiO_3 + 2H_2O \left(873\ K\ (600°C)\right) \quad (3.4)$$

$$ZrSiO_4 + 2Na_2CO_3 \rightarrow Na_2ZrO_3 + Na_2SiO_3 + 2CO_2 \left(1273\ K\ (1000°C)\right) \quad (3.5)$$

$$ZrSiO_4 + 3CaO \rightarrow CaZrO_3 + Ca_2SiO_4 \left(1373\ K\ (1100°C)\right) \quad (3.6)$$

In caustic fusion, sodium hydroxide is added at 50% excess to ensure quantitative decomposition of the zircon. Fusion is carried out in iron crucibles or cast iron vessels. The melt is poured into water in a thin jet to form small granules. An exhaust hood is fitted over the crucible to evacuate the sodium hydroxide aerosol that is formed. Titanium impurities react to yield sodium titanate. Iron and aluminium are present in the melt as sodium ferrite and aluminate. The advantage of sodium hydroxide fusion is the low operating temperature and a fairly high output rate. A disadvantage is the rapid corrosion of the iron vessels by the alkaline melt.

Leaching can be done with either water or hydrochloric or sulphuric acids. Water leaching is carried out in iron tanks fitted with stirrers in two stages with intermediate decantation. During leaching with water, most of the silicon is absorbed into solution as sodium silicate. In the second stage of leaching, the partial hydrolysis of sodium silicate also takes place. Sodium titanate remains in the residue together with the zirconium, while sodium aluminate passes into solution. The iron is decomposed back into ferrite. The approximate composition of the residue is 80–84% ZrO_2, 8–12% SiO_2 and 4–6% Na_2O. Also present is residual sodium silicate, sodium zirconate, silicic acid and sodium zirconosilicate. The residue is then acid leached.

Finally, the hydrated zirconia can be dissolved in hydrochloric acid to yield a solution of zirconium oxychloride, from which zirconium oxychloride crystals, $ZrOCl_2 \cdot 8H_2O$, may be recovered. It may also be dissolved in sulphuric acid to produce zirconium acid sulphate. MacDonald et al. [3.19] describe the fusion of zircon with sodium hydroxide followed by leaching the frit so formed with water to remove soluble sodium silicate, then with sulphuric acid to recover zirconium as the soluble acid sulphate.

In sintering with lime, the interaction between zircon and lime only becomes noticeable at 1673–1773 K (1400–1500°C). Addition of calcium chloride lowers the reaction

temperature to 1273–1373 K (1000–1100°C), because of the formation of an intermediate liquid phase ($CaCl_2$ melts at 1043 K (775°C)) and the possibility that the reaction is catalytically accelerated owing to chlorination taking place from the calcium chloride. The amount of lime is 100–150% of the stoichiometric amount required, while the amount of calcium chloride is about 20% (by weight) of the lime charge. The sintering is carried out in a rotary furnace at a very slow rate, taking 8–10 hours. The degree of decomposition reaches 90–94%.

Decomposition of zircon by sintering with lime and calcium chloride has advantages over caustic fusion, including less costly reagents, and the ability to utilize large industrial furnaces. Hydrochloric or sulphuric acids are used to leach the sintered mass. This process is currently in use by the Nuclear Fuel Complex (NFC), India [3.11].

3.3.3. Fluorosilicate fusion

A mixture of potassium hexafluorosilicate and zircon can be roasted at 953 K (680°C) to yield the water soluble potassium hexafluorozirconate and insoluble silica. The process was patented by Kawecki [3.20] and is described in detail in Ref. [3.14] and by Sajin and Pepelyaeva [3.21]. The reaction proceeds according to:

$$ZrSiO_4 + K_2SiF_6 \rightarrow K_2ZrF_6 + 2SiO_2 \left(923–973\ K\ (650–700°C)\right) \quad (3.7)$$

The Chepetsky Mechanical Plant in Glazov, Russian Federation, uses this process. It is stated in Ref. [3.14] that Russian Federation practice is to add potassium chloride to intensify the degree of decomposition. Potassium hexafluorosilicate is added at 50% excess over the stoichiometric requirement. The reaction is carried out in a molten state of charge in a furnace.

The potassium hexafluorozirconate is crushed and then leached with a 1% HCl at 360 K (90°C) for 1.5–2 hours. After leaching, the solution is subjected to precipitation and filtration. The solution is allowed to clear while standing, keeping the temperature greater than 350 K (80°C), and then transported to the crystallizer.

The solubility of K_2ZrF_6 increases sharply with increasing temperature, and as a result the solution may crystallize 75–90% of the zirconium present. This feature allows the separation of zirconium and hafnium by means of fractional crystallization; see Section 3.4.1. Ammonium hydroxide is added to precipitate the residual zirconium ions as zirconium hydroxide, which is returned to the furnace for another fusion. Leaching and crystallization are carried out in stainless steel vessels.

Crystals prepared by fluorosilicate fusion from zircon ore bodies located in the Azov alkaline massif area of Ukraine contain about 32% Zr + Hf, 27% K, 40% F, 0.045% Fe, 0.04% Ti and 0.07% Si.

3.3.4. Carbochlorination

The first chlorination step is known in the industry as ‘sand chlorination’. Both zircon and baddeleyite can be reacted with carbon, usually as petroleum coke and chlorine, to give zirconium tetrachloride, as described by Spink and Jonasson [3.22], and Stephens [3.12]. Zircon requires reaction near 1373 K (1100°C) and yields silicon tetrachloride as a by-product. Baddeleyite reacts at the significantly lower temperature of 1173 K (900°C). In the carbochlorination process, only the constituents of zircon and baddeleyite (and impurities in the petroleum coke) that form chlorides volatile below about 973–1073 K (700°C–800°C)

leave the chlorinator; the chlorides of scandium, yttrium, lead, radium, thorium and the lanthanides remain in the chlorinator residue, which comprises mostly zircon and coke that have not reacted. The only radioactive element that remains with the zirconium tetrachloride is uranium.

Chlorinators are typically of a fluidized bed design using chlorine as the fluidizing medium. Chlorinators are heated by use of electrothermal fluidized beds, induction heating or resistance heating. Chlorine efficiencies (stoichiometric utilization) are typically 98% or better [3.13].

The chlorination of zircon at high temperature is according to the following reaction:

$$ZrSiO_4 + 4C + 4\,Cl_2 \rightarrow ZrCl_4 + SiCl_4 + 4CO\ \left(1373\ K\ (1100°C)\right) \quad (3.8)$$

In practice, some carbon dioxide is also formed, especially in the chlorination of baddeleyite, which is done at 1175 K (900°C). The chlorination also produces some sulphur chlorides from sulphur in the coke. If moist air is admitted to the process or contacts the product gas, traces of perchlorodisiloxane (with a normal boiling point near 409 K (136°C)) can contaminate the zirconium tetrachloride and also the silicon tetrachloride.

Zirconium tetrachloride, with a triple point at 710 K (437°C) and a sublimation temperature of 604 K (331°C), has no liquid phase at atmospheric pressure. The product gases are first cooled to below 475 K (200°C) to selectively condense zirconium tetrachloride. The silicon tetrachloride is subsequently condensed as a liquid in a quench condenser whereby the warm gases are scrubbed in a counter current fashion with liquid silicon tetrachloride at 250 K (−20°C). The so-called 'siltet', ($SiCl_4$), is purified by stripping and further distillation, and sold as a by-product.

The 'sand' chlorination process is currently practised by Wah Chang (USA), CEZUS (France) and Western Zirconium (USA).

3.3.5. Alternate processing

An alternate process whereby zircon sand is passed through a plasma arc furnace at flame temperatures of about 11 000 K (10 727°C) has been described in Ref. [3.23]. Scammon gives details of the equipment in his patent [3.24] and of the process in Scammon et al. [3.25]. The process decomposes the ore into essentially zirconia and silica. The silica is retained in the solid phase as a highly reactive amorphous form that can be leached with 50% sodium hydroxide at 413 K (140°C). The zirconia is in the form of porous spheres. With appropriate leaching a zirconia purity concentration of 99% can be reached. This material would be suitable for subsequent chlorination.

In summary, several methods are available and in current use for the initial separation of zirconium-rich material from the ore. This material provides the feed to separate the hafnium from the zirconium.

3.4. SEPARATION OF ZIRCONIUM AND HAFNIUM

Zircon naturally contains about 2–2.5 wt% (1–1.3 at.%) hafnium. About 99.5% of the hafnium has to be removed, typically to less than 100 ppm (0.005 at.%), for nuclear reactor grade materials. Pure zirconium has a low absorption cross-section for thermal neutrons, σ_a, of about 0.18 b while hafnium's cross-section is 105 b. ASTM specifications for nuclear applications require a hafnium concentration of less than 100 ppm (0.005 at.%) [3.16].

Separation processes that have been used in industrial settings include fractional crystallization, methyl isobutyl ketone-thiocyanate (MIBK) and tributyl phosphate (TBP) solvent extraction, and extractive distillation. These processes are described first, followed by some alternative separation processes that have not been used on an industrial scale.

3.4.1. Fractional crystallization

Fractional crystallization of potassium fluorozirconate–potassium fluorohafnate mixtures was the first separation method used by Hevesy [3.26]. The Chepetsky Mechanical Plant in Glazov, Russian Federation, now uses it, as described in Ref. [3.14]. The process takes up to 18 stages to approach 100 ppm (0.005 at.%) hafnium in the zirconium, using starting material containing 1.8% (0.93 at.%) hafnium; it is routinely operated to reach 300–500 ppm (0.015–0.026 at.%) hafnium, but can be extended to <50 ppm (0.0026 at.%). The reduction process used at the plant allows for a further separation, as described later.

The principle for separation is that molar solubility in water for K_2HfF_6 is about 1.5 that for K_2ZrF_6. As a result, fractional crystallization concentrates hafnium salts in the mother liquor. The $K_2(Zr,Hf)F_6$ crystals are initially dissolved in water at about 363 K (90°C). Each succeeding fraction of the crystals is dissolved in the mother liquor of the preceding crystallization. The concentration is about 140 g/L. The solutions are cooled to 278 K (15°C). The solubility of K_2ZrF_6 at that temperature is about 16.3 g/L. The crystals formed are allowed to settle, the mother liquor is decanted, the mother liquor from the preceding stage is poured on the crystals and the next crystallization stage is performed. The separation process recovers about 80% of the zirconium input and yields a 6% hafnium concentrate [3.14].

3.4.2. Solvent extraction processes

Two processes are known to be in commercial operation today, and both are described in detail in Refs [3.9, 3.11, 3.14].

3.4.2.1. MIBK-thiocyanate process

The MIBK process was developed by Union Carbide at Y-12 National Security Complex in Oak Ridge, Tennessee, USA. It was based on the discovery that hafnium thiocyanate is absorbed by MIBK and, being lighter than the aqueous phase, it rises to the top in separation columns. This discovery was reported by Fischer and Chalybaeus [3.27]. This process is used by Wah Chang in Albany, OR and by Western Zirconium, in Ogden, UT, both in the USA. It was used formerly by the Carborundum Company and by Amax Specialty Metals in the USA, by CEZUS in France and by Toyo Zirconium in Japan. The process also was operated at pilot scale by Magnesium Elektron on behalf of the UK Atomic Energy Authority, as described by Foley [3.28].

This process starts with zirconyl chloride solution from the hydrolysis of zirconium tetrachloride, at about 1 molar metal concentration and total acidity adjusted to about 3.8 N with ammonia. It is freed of ferric ion by scrubbing with MIBK, then ammonium thiocyanate is added to form thiocyanate complexes of zirconium and hafnium, and the solution is contacted in a continuous counter current mode with MIBK containing some thiocyanic acid.

The process is performed in packed columns and uses about 10–15 stages of separation, including extraction and stripping. The zirconium stays in the aqueous phase. The aqueous raffinate (the portion left over after the hafnium has been extracted by the MIBK solvent) is

scrubbed with pure ketone to remove the thiocyanic acid. The separation factor[2], *S*, is a measure of the efficiency of the ability of the solvent to separate and carry away the hafnium from the zirconium in the aqueous phase.

The raffinate is diluted to a zirconium concentration of about 12 g/L, and is treated with sulphuric acid to precipitate the zirconium as a complex sulphate, $Zr_5O_8(SO_4)_2 \cdot x(H_2O)$. The precipitated sulphate is filtered, washed and re-pulped with ammonia to convert the zirconium to the hydrate. The hydrate is re-filtered to remove sulphate ions, washed and then calcined to the oxide. Alternatively, the sulphate may be calcined directly to the oxide. Removal of uranium from this solution can be done as described by Ref. [3.29], after which the solution is treated to recover ammonia then adjusted, the pH is neutralized and the solution is discharged to waste water.

The hafnium is extracted to the less dense organic phase, from which it is stripped by 5 N sulphuric acid and precipitated as hydrated oxide by neutralization with ammonia. The process is capable of producing zirconium with less than 25 ppm (0.0013 at.%) hafnium, while producing hafnium with well under 1 wt% (1.94 at.%) zirconium [3.9].

For the preparation of the metals, the oxide is converted to the tetrachloride by carbochlorination in a fluidized bed reactor. A minority of the oxides produced is sold to users of the pure oxides.

Chiang et al. [3.30] have also suggested the process as a means of separating zirconium isotopes. Zirconium-90 has σ_a = 0.011 b and a naturally occurring abundance of about 51.5 at.%. Zironium-91 to ^{96}Zr comprise the other isotopes, and they have higher values of σ_a such that zirconium with all isotopes has a cross-section of about 0.18 b. Zirconium-90 accumulates preferentially to the aqueous phase of the thiocyanate process. Unfortunately, the separation factor is quite low, being 1.007 (the separation factor for hafnium from zirconium is about 1.2). This value of *S* means that to enrich ^{90}Zr from 51.5 at. % up to 90 at.% would take about 370 stages of separation, or a factor of 30 times more than those required to separate hafnium from zirconium. Building and operating a plant with this many stages of extraction, exchange and stripping would be extremely costly and very difficult to operate.

3.4.2.2. TBP-nitric acid process

The TBP-nitric acid process was developed by Iowa State University in the USA. The process was used by Eldorado Corporation, Port Hope, Canada, but abandoned because of economics. It was used by the now closed Pridneprovsky Chemical Plant, in the city now known as Kamianske, Ukraine, where the recovered nitrates were converted to other zirconium and hafnium compounds, including tetrafluorides. The process is currently used by NFC, Hyderabad, India. The principle is analogous to the MIBK process.

The process starts with frit from the alkali cracking of zircon or from hydrated zirconium-hafnium oxide precipitated with aqueous ammonia from the hafnium-enriched product of the recrystallization process. This frit is leached with nitric acid to produce zirconyl nitrate solution with free nitric acid. This solution is then contacted with TBP dissolved in a hydrocarbon

[2] The separation factor, *S*, is the ratio of the distribution factors for zirconium and hafnium. The distribution factor is defined as the ratio of the concentrations of an element in the organic and aqueous phases. The subscripts ‘o’ and ‘a’ are used to refer to the organic and aqueous phases, $D_{Zr} = (Zr)_o/(Zr)_a$, $D_{Hf} = (Hf)_o/(Hf)_a$, and $\underline{S} = D_{Hf}/D_{Zr}$.

solvent in counter current mode, and the zirconium is extracted in the organic phase while the hafnium remains in the aqueous phase.

The separation factor decreases from 12 to 4 as the nitric acid concentration of the feed solution is increased from 6 N to 9 N. The extraction is best carried out with high separation coefficients from solutions containing 5–6 N HNO_3. The TBP solvent has a high density and viscosity and is usually mixed with inert diluents such as kerosene or n-heptane (C_7H_{16}). The extraction can be carried out in columns or in extractors of the mixer-settler type. Feed solutions contain about 125 g/L ZrO_2. The zirconium and the nitric acid are re-extracted from the organic phase with water. Both metal product streams are distilled to recover free nitric acid, and neutralized to precipitate the hydrates, which are then calcined to the oxides. The extraction also separates impurities such as Al, Ca, Fe, Mg, Si and Ti.

While the TBP-nitric acid process is capable of producing zirconium with less than 100 ppm (0.005 at.%) of hafnium, the production of hafnium with a low concentration of zirconium is reported to be difficult. For example, Cox's flow sheet shows a residual zirconium concentration of 24 wt% in the hafnium. Descriptions of the process are given by Cox et al. [3.31], by Ganguly [3.11], and by Zelikman et al. [3.14].

3.4.3. Extractive distillation process

This process relies on the higher vapour pressure of $HfCl_4$ in a recirculating column of molten salt solvent, the temperature of which is maintained to retain $ZrCl_4$, while the $HfCl_4$ exits as a vapour phase. Exploiting this effect saves process steps, avoids consumption of process chemicals and generates far less volume of waste products than the other processes. It is described by Besson et al., the inventors, in their patent [3.32], by Tricot [3.33] and by Skaggs et al. [3.15], and is in commercial operation by CEZUS in Jarrie, France.

It is not possible to separate the tetrachlorides by direct distillation at atmospheric pressures because the sublimation temperature is 592 K (319°C) for $HfCl_4$ and 604 K (331°C) for $ZrCl_4$, much too close for an industrial process to operate reliably. In a clever twist, the tetrachloride mixture from the chlorination is sublimed and fed as vapour at atmospheric pressure into a 50 m vertical distillation column down which flows a molten mixture of aluminium chloride and potassium chloride at a temperature of close to 625 K (350°C) in a molar ratio maintained in the range 1.04–1.10.

Both zirconium and hafnium chlorides dissolve, but hafnium tetrachloride has a higher vapour pressure and a mixture of tetrachlorides enriched in hafnium is condensed from the vapour emerging from the top of the column. The zirconium tetrachloride partitions to the liquid phase and is recovered from the salt removed from the bottom of the column by stripping with nitrogen at about 775 K (500°C), typically with a hafnium concentration of under 50 ppm.

Figure 3.5 is a schematic diagram of CEZUS' extractive distillation process [3.32]. The unseparated tetrachloride is supplied by the sublimer to the distillation column containing the molten salts. A pump recirculates the solvent down the column, through a boiler, an exhaustion column, a reservoir, an absorber/condenser, and back to the distillation column. Zirconium and hafnium tetrachloride vapours saturate the solvent recirculated to the absorber/condenser, which is cooled to about 623 K (350°C). The boiler temperature is maintained at about 770 K (500°C) so that the solvent leaving the boiler via the valve contains only a few percent of $ZrCl_4$. The zirconium tetrachloride is stripped from the solvent by a nitrogen stream that is recycled by a booster pump. The nitrogen entrained $ZrCl_4$ is condensed in the lower condenser. Hafnium-rich $ZrCl_4$ is produced by the absorber/condenser and is condensed in the upper condenser, which is vented at atmospheric pressure.

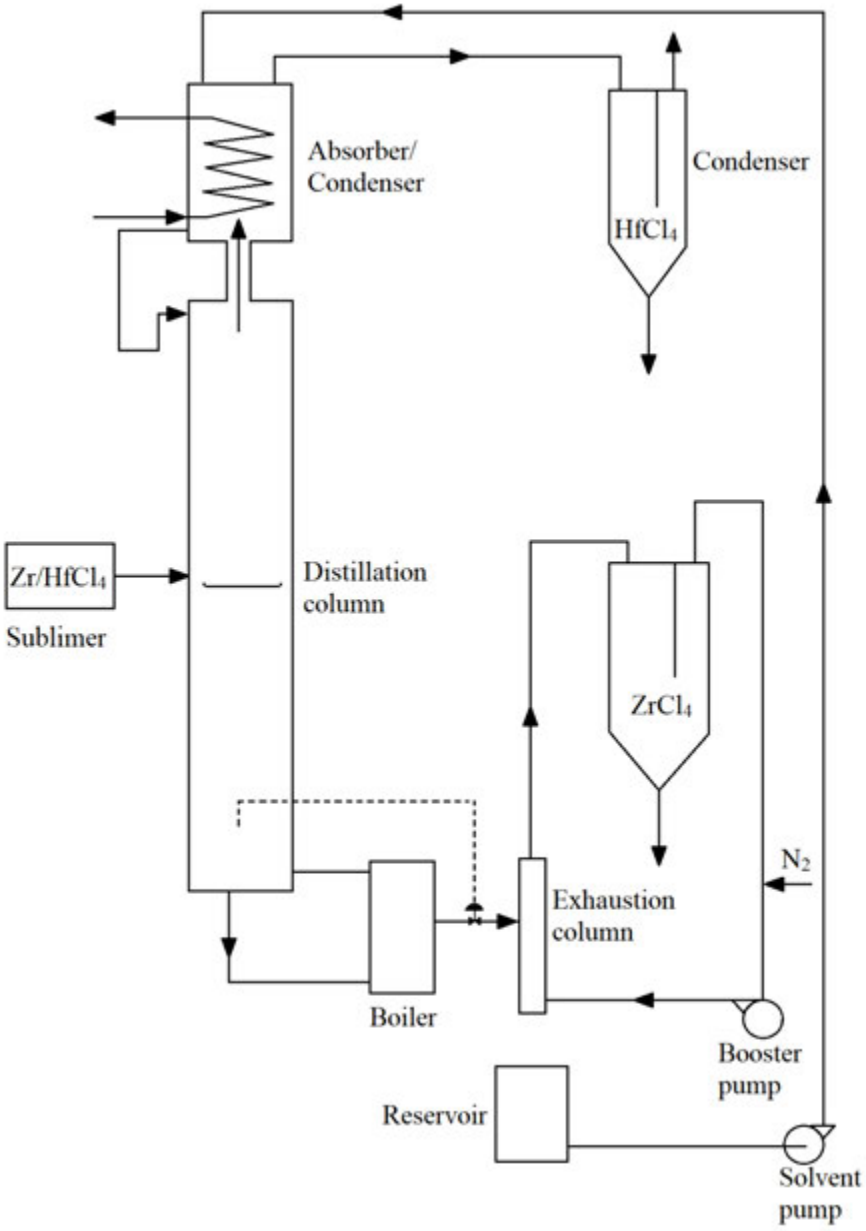

FIG. 3.5. CEZUS extractive distillation process.

There is no need to re-chlorinate a separated oxide product as there is with aqueous separation techniques; the tetrachloride vapours can be fed directly to the reduction stage.

The hafnium-rich condensate produced in normal operation appears from Ref. [3.32] to require further processing before it can serve as a source of hafnium low in zirconium, and so could be saved for campaigns to produce purer hafnium. This process, with its minimal reagent consumption and small waste stream production, as well as its elimination of process steps, is the most significant advance in Zr/Hf separation technology since the widespread adoption of the MIBK process.

3.4.4. Alternative separation processes

These processes can be divided into anhydrous processes and aqueous processes. Anhydrous processing has the allure of being able to separate the tetrachlorides or tetrafluorides and then passing them on directly to Kroll or electrolytic reduction. Aqueous processing

requires additional steps, including roasting and re-chlorination of a precipitated hydrate before reduction.

3.4.4.1. Anhydrous processes

Work in this area up to 1983 is described by Skaggs et al. [3.15] and up to 1986 by Mallikarjunan and Sehra [3.16]. Skaggs et al. group the processes according to whether they depend on the relative volatility of given Zr and Hf compounds or whether they utilize differences in chemical reactivity. In practice, most work on anhydrous separation has been confined to the tetrachlorides and compounds that can be prepared from them inexpensively, and to sodium and potassium fluorohafnates and fluorozirconates.

Three groups of methods, two of which are intended to operate at near atmospheric pressure, depend on differences in volatility of the tetrachlorides and are listed in Ref. [3.15].

The first group, characterized as thin film sublimation, attempts to use the fact that solid $HfCl_4$ is about 1.9 times more volatile than solid $ZrCl_4$ from 425 to 625 K (150 to 350°C). A sublimation column operates at atmospheric pressure, in which the solid tetrachlorides are mechanically transferred down the column while the gas phase flowed upwards. The concept was explored by Plucknett [3.34], who attempted to separate zirconium and hafnium tetrachlorides in a plate-type column with mechanical transfer of the solids down the column. Separation was not achieved because the gas phase only contacted the surface of the solids and diffusion within the solids was too slow to effect separation.

Jacque and Dumez [3.35] tried the opposite case in which stationary solids were contacted by an inert gas as a carrier for the volatilized tetrachlorides. Temperatures on a 2 m high column were 575–675 K (300–400°C) at the bottom, decreasing to 425–500 K (150–230°C) at the top. By repeating the batch process several times, a hafnium concentration as low as 250 ppm (0.013 at.%) was produced.

The second group takes advantage of the difference in volatility of the two tetrachlorides when dissolved in certain molten salt mixtures. This concept of extractive distillation from molten salts has received considerable attention, and Ref. [3.15] cites the pioneering efforts of groups led by Spink [3.36] and by Dutrizac and Flengas [3.37–3.39]. Spink utilized a feed mixture of 63 mol% tetrachlorides, 29 mol% KCl and 8 mol% NaCl. This mixture is a ternary eutectic with a melting point of 491 K (218°C). The crude feed and eutectic solution are fed, mid length, into a distillation column operating between 600 K (330°C) at the top and 675 K (400°C) at the bottom. The size of the column was based on 50 theoretical plates that correspond to a relative volatility of 1.7 for the tetrachlorides. In practice, 60–70 plates may be required.

Reflux of the $HfCl_4$-rich overhead vapour stream and recycle of the stripped $ZrCl_4$-rich salt bottoms are included in the scheme. Removal of the product tetrachloride from the overhead and bottom streams is a major problem in molten salt distillation and Spink concluded [3.36] that a combination of high temperature and vacuum was necessary to completely remove the $ZrCl_4$ from the salt bottoms because of the high stabilities of K_2ZrCl_6 and Na_2ZrCl_6.

Besson's process for CEZUS is similar to the Spink process, but with two important improvements. Besson uses $AlCl_3$ instead of NaCl, which likely unlocks the $ZrCl_6^{2-}$ ion and increases the activity of $ZrCl_4$. This technique permits the $ZrCl_4^-$ ion to be more easily stripped out of the solvent salt by a nitrogen stream and condensed. Besson reports [3.32] that at 773 K (500°C) and 1.7 kPa, the residual $ZrCl_4$ was reduced to 0.6 g/100 g $KAlCl_4$.

The third group seeks to exploit the difference in volatility of the two chlorides in the liquid state utilizing a high pressure liquid-vapour distillation process. Table 3.2, taken from Denisova et al. [3.40], gives parameters for the triple and critical points of the two tetrachlorides.

Triple point is where the liquid, solid and vapour phases coexist. The critical point is the point of termination of a phase equilibrium curve, which separates the two distinct phases of gas and liquid.

TABLE 3.2. TRIPLE POINT AND CRITICAL POINT PARAMETERS FOR ZIRCONIUM AND HAFNIUM TETRACHLORIDES [3.40]

Tetrachloride	Triple point (K)	Triple point (MPa)	Critical point (K)	Critical point (MPa)	Critical vol. ($cm^3 \cdot mol^{-1}$)
$ZrCl_4$	710.2	2.236	778.2	5.766	319.3
$HfCl_4$	705.2	4.501	722.4	5.776	303.6

A separation process using distillation of the liquid chlorides would need to operate in the temperature range 705–778 K (430–505°C) and at pressures ranging from about 4 MPa to about 6 MPa. These conditions, and the reactivity of the tetrachlorides and accompanying impurities are very demanding of construction materials; nevertheless [3.15] cites successful demonstration of the process by Bromberg [3.41] and by Ishizuka [3.42]. The expense of the equipment and the inconvenience of the process probably account for its lack of commercial application. Further, production of pure hafnium tetrachloride would be difficult because of the small temperature difference between the triple and critical points.

The chemical stability of corresponding zirconium and hafnium compounds differ slightly, with hafnium usually the more stable, and these differences have been exploited in several separation schemes.

Since the reaction:

$$ZrO_2 + HfCl_4 \rightarrow ZrCl_4 + HfO_2 \quad (3.9)$$

is favoured, Chandler [3.43] suggested passing the mixed tetrachloride from zircon chlorination over a bed of the mixed oxides. He achieved removal of about 66% of the hafnium at 1223 K (950°C).

Sixteen or seventeen stages of separation would be required to achieve less than 100 ppm hafnium reliably in the final product.

Berl [3.44] attempted to use the exothermic reaction of zirconium tetrachloride with oxygen to precipitate zirconia from gaseous mixtures of the tetrachlorides. The reaction for $ZrCl_4$ with oxygen proceeds much more rapidly than does the reaction with $HfCl_4$.

The reactions include:

$$ZrCl_4 + O_2 \rightarrow ZrO_2 + 2Cl_2 \quad (3.10)$$

$$HfCl_4 + O_2 \rightarrow HfO_2 + 2Cl_2 \quad (3.11)$$

ZrO_2 preferentially builds up in the solid phase and $HfCl_4$ enriches in the gas phase. $HfCl_4$ is then separated from the chlorine by selective condensation at 273–573 K (0–300°C). Berl suggested conducting the reaction above 873 K (600°C) in a fluidized bed of pure zirconium oxide, which may provide a catalytic substrate.

A separation scheme has been proposed based on the higher stability of hafnium trichloride compared with zirconium trichloride. The process, patented by Newnham [3.45, 3.46], is described in some detail in Refs [3.15, 3.16].

The process is based on the fact that when the mixed tetrachlorides are heated with a reducing agent, in one case $ZrCl_2$, and in another, Zr, the $ZrCl_4$ is preferentially reduced to $ZrCl_3$ and $HfCl_4$ is not affected. Separation is achieved by sublimation of the $HfCl_4$, leaving non-volatile $ZrCl_3$. The $ZrCl_3$ is then converted to the tetrachloride by disproportionation. The reactions proceed according to:

$$ZrCl_4(g) + HfCl_4(g) + ZrCl_2 \rightarrow 2ZrCl_3(s) + HfCl_4(g) \quad (3.12)$$

$$2\,ZrCl_3 \rightarrow ZrCl_2(s) + ZrCl_4(g) \quad (3.13)$$

and

$$HfCl_4(g) + 3ZrCl_4 + Zr(s) \rightarrow 4ZrCl_3(s) + HfCl_4(g) \;\; (643\ K\ (370°C)) \quad (3.14)$$

$$2ZrCl_3\ (s) \rightarrow ZrCl_2(s) + ZrCl_4(g) \;\; \left(473\ K\ (200°C)\right) \quad (3.15)$$

Despite extensive investigation and investment, the process has never been operated commercially. Kirihara et al. have patented an electrolytic adaptation of the process [3.47].

Megy proposed a reductive separation [3.48, 3.49]. This process relies on the considerable lowering of the activity of zirconium compared with hafnium on dissolution in liquid zinc. The process feed was a molten mixture of sodium hexafluorozirconate and hafnate (prepared from sodium hexafluorosilicate and zircon) that was contacted with liquid zinc containing aluminium.

The reaction:

$$3Na_2(Zr, Hf)F_6 + 4Al(Zn) \rightarrow Zr(Zn) + 2Na_3Al_2F_9 \quad (3.16)$$

takes place with a strong preference for zirconium over hafnium. As a result, only two stages of counter current contact between the salt and molten metal phases produce zirconium with a hafnium concentration of less than 100 ppm (0.005 at.%). Process economics partially depended upon the prospects of sale of the sodium aluminium fluoride produced (called pseudocryolite) to the aluminium industry. Unfortunately, the demand for pseudocryolite dropped as the aluminium industry curtailed its fluoride discharge. Additionally, the container materials are subject to severe attack by molten zinc and molten fluoride. The process was found to be of limited interest because of the severe economic penalties.

For details on other processes for separation under anhydrous conditions, the reader is referred to Refs [3.15, 3.16], where processes based on preferential decomposition of salts and on electrolytic methods are discussed.

3.4.4.2. Processes based on aqueous solutions

A third type of solvent extraction, the amine sulphate process, uses a zirconium-hafnium feed in about 2 N sulphuric acid and a tertiary amine (dissolved in kerosene) as an extractant. MacDonald [3.50] describes details of the amine sulphate system. The system consists of an aqueous feed solution containing zirconyl-hafnyl sulphate in dilute sulphuric acid, and a water immiscible organic phase containing 10% Alamine 336 and 5% decanol in kerosene.

The aqueous feed solution enters the first extraction stage while lean, neutralized Alamine 336 enters the last extraction stage. Dilute sulphuric acid enters at the first scrubber stage. In each scrubber and extractor stage, both zirconium and hafnium are distributed between the aqueous and organic phases. In this system, zirconium is in the organic phase. There is also a distribution of the H_2SO_4 between phases; in the last extraction stage, uptake of H_2SO_4 by the incoming neutral organic phase is substantial.

In the stripper stages, zirconium is removed from the loaded organic phase, producing an aqueous strip liquor low in hafnium. The organic solution is restored to a lean and neutralized condition in the regenerator stages.

According to Nielsen et al. [3.13], Nippon Mining has used a trioctylamine-sulphate system commercially, as described by Takahashi et al. [3.51]. Ganguly [3.11] mentions that a pilot plant has been successfully operated at the NFC, Hyderabad, using the amine sulphate process.

Chromatography using a suitable ion exchange resin has been proposed as a continuous process for the separation of zirconium and hafnium on a commercial scale. The process and a continuous chromatograph are described by Byers et al. [3.52]. Others have patented its use for the chemical separation of zirconium isotopes; see, for example, Snyder et al. [3.53].

Means of improving the separations process based on the fractional crystallization of mixtures of potassium hexafluorozirconate and hexafluorohafnate have been proposed [3.9]. This separation is possible because potassium hexafluorohafnate (K_2HfF_6) can be almost quantitatively converted to potassium pentafluorohafnate ($KHfF_5$) by addition of a 5–10 fold excess of $NaZrF_5$ (with respect to K_2HfF_6 in the mixture). The pentafluoro salts differ in crystal structure from the hexafluoro salts, and do not form solid solutions with them. Thus, the pentafluorohafnate stays in solution when the hexafluoro salts crystallize, and the latter contain much less hafnium than in the original process. Hafnium concentrations of about 2% in the feed can be reduced to around 40 ppm (0.002 at.%) in the product in mere 3–4 recrystallizations, compared with over twenty for the original process. This process appears to be viable but would need further review from an environmental emissions standpoint.

In summary, several processes for separating zirconium from hafnium are available and in commercial operation. Other proposed processes have not been exploited either because of inefficiencies, practical difficulties caused by materials degradation or environmental issues. The product containing a low concentration of hafnium is now ready for reduction to metal.

3.5. REDUCTION TO THE METAL

Gases such as oxygen and nitrogen dissolve into interstitial locations in the zirconium crystal lattice. Excessive quantities of these gases have detrimental effects on the final properties of zirconium metal. As a result, the starting materials for reduction have to be reasonably free of these contaminants, and due care must be exercised when storing and transporting the tetrachlorides prior to reduction. All subsequent high temperature processing has to be accomplished under strict controls for atmospheric impurities, whether that is by inert atmosphere processing or vacuum processing.

As for separation processes, the reduction processes known to be in commercial operation will be described first, followed by an outline of processes that have been developed as intended improvements on the existing processes. Reduction processes generally produce two product forms, either sponge or metallic powder.

3.5.1. Reduction of the metal tetrachlorides with magnesium

The Kroll reduction process, named after its inventor[3] [3.54], is the most widely used of the three commercial reduction processes. It is in use by CEZUS, Wah Chang, Western Zirconium and NFC, Hyderabad. The Chepetsky Mechanical Plant has commissioned a Kroll reduction process. Chlorinating the pure metal oxide obtained from the solvent extraction separation process produces the tetrachloride, except in CEZUS' case, where hafnium-free zirconium tetrachloride is obtained directly from the separation process. The reaction is carried out in a fluidized bed chlorinator according to:

$$ZrO_2 + 2Cl_2 + 2C \rightarrow ZrCl_4 + 2CO \text{ (1123 K (850°C))} \quad (3.17)$$

[3] Further details on the life and scientific works of W.J. Kroll can be found in Ref. [3.55].

This reaction is similar to zircon sand chlorination except that gross impurities like the silica fraction have been previously removed. The reductant is liquid magnesium and the process proceeds according to:

$$2Mg + ZrCl_4 \rightarrow Zr\ (sponge) + 2MgCl_2 \ \ (near\ 1000\ K\ (726°C)) \qquad (3.18)$$

An early version of the process on a large scale is described in Ref. [3.7], where the zirconium tetrachloride is purified by sublimation in hydrogen to form and leave behind the less volatile lower chlorides of impurity elements such as iron, then condensed in the upper chamber of a cylindrical reactor, the lower part of which contains magnesium ingots in about 20% excess over the amount required by Eq. (3.18). Before the reduction is started, the vessel is evacuated and back filled with argon or helium. The lower part is heated to melt the magnesium, and then the upper part is heated to sublime the tetrachloride so it can react with the magnesium.

A contemporary version of the reduction retort is shown in Fig. 3.6. The whole vessel is of mild steel. The upper part, or retort, is charged with zirconium tetrachloride and the lower part, or crucible, is equipped, according to Ganguly [3.11] and Nielsen [3.13], with a stainless steel sheet liner and charged with fresh or recycled magnesium ingots. The two parts are then welded together making a vacuum tight joint, and the retort evacuated and back filled with helium as before.

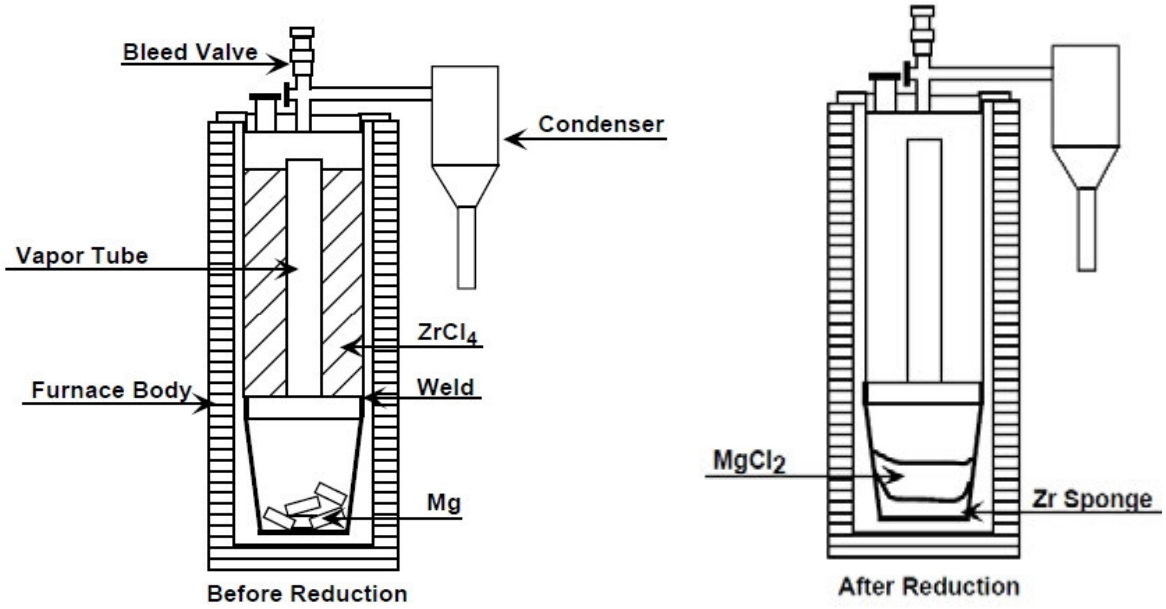

FIG. 3.6. Kroll reduction vessels, before and after the reduction run has been completed.

The retort is placed in a furnace with zone heaters. The magnesium is brought up to the melting temperature first, and then heat is applied to the upper half of the vessel to sublime the tetrachloride. The tetrachloride travels down the central transport tube and the tetrachloride vapours react with the molten magnesium.

While it is thermodynamically possible to reduce $ZrCl_4$ with either sodium or calcium, the preferred method is to use magnesium. Both sodium and calcium have a more negative free energy of formation than magnesium, as is shown in the Ellingham plot, after Sommers [3.56], in Fig. 3.7. Even with magnesium, the rate of reduction has to be controlled by the rate of sublimation of the tetrachloride to prevent the reaction products from overheating and adversely reacting with the crucible. The reaction would be much more vigorous with sodium or calcium. Hunter [3.57], developed a sodium reduction process that was carried out in a high

pressure bomb at 1123 K (850°C). The size of the reduction reaction was limited by the pressure capability of the reaction vessel. Additionally, magnesium has handling advantages in that it will not burn on exposure to air or form explosive hydrogen when wet. See Section 3.5.2 for a further discussion of calcium reduction.

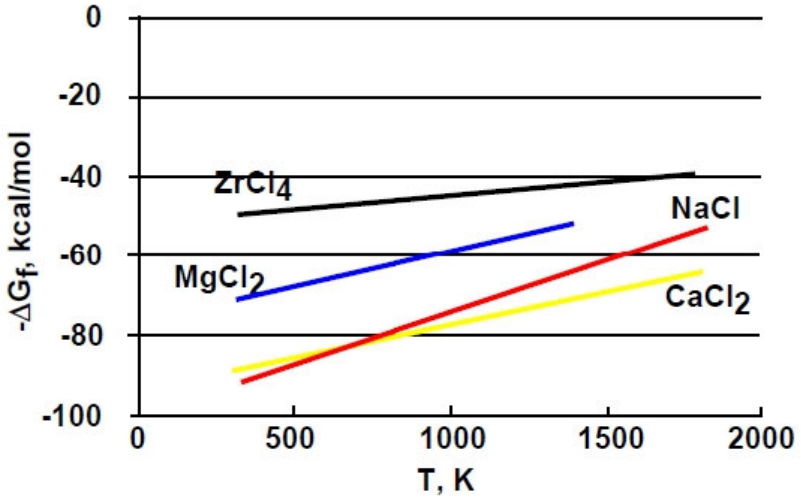

FIG. 3.7. Gibb's free energy of formation as a function of temperature for some chlorides.

After the tetrachloride is consumed, the vessel is removed from the furnace and allowed to cool, and then it is cut open at the weld. The liner and its contents are removed from the crucible, and the liner is peeled away to reveal a lower layer comprising the zirconium product called 'sponge', excess magnesium and an upper layer of magnesium chloride. The two layers are separated at the interface, and the metal layer, a cake about 1.2–1.5 m diameter by 0.4 m high, is stacked with several others in the upper chamber of a vacuum still, as shown in Fig. 3.8.

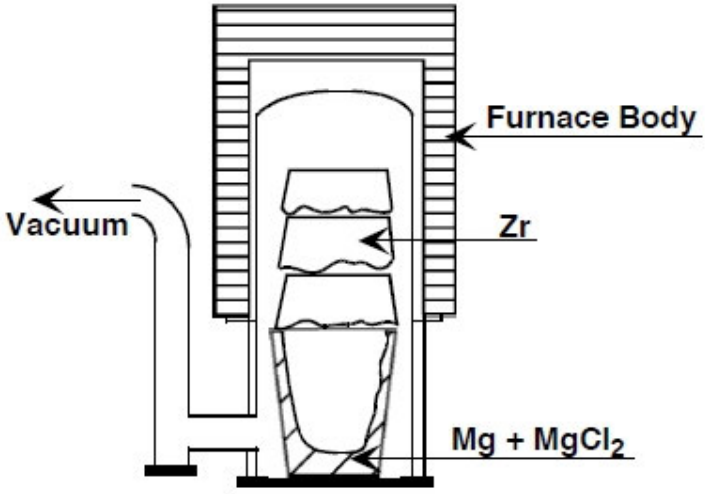

FIG. 3.8. Distillation furnace showing the product of several reduction runs being vacuum distilled.

The zirconium sponge is placed in a furnace, evacuated and back filled with argon several times, and then it is evacuated with a dynamic vacuum. As related by Nielsen [3.13], the upper part containing the cakes is heated to about 1253 K (980°C) so that the excess magnesium melts and magnesium chloride evaporates from the metal cakes and condenses lower on the walls of the furnace. The molten magnesium and condensed chloride vapours flow to a collection can

in the bottom section and are kept molten so that they can separate into two layers. The zirconium in the cake sinters and hardens somewhat during the final stages of distillation. The sponge is removed after cooling and is broken into lumps that are further milled to chunks with a maximum dimension of about 25 mm and below, then chemically analysed, blended with product from other runs, inspected and sent to the melt shop, or for a minority of the material, for further purification by Van Arkel–de Boer processing or by electron beam purification. Mechanical blending is used to make the large batch sizes required to feed the vacuum arc melting process, and it also promotes homogeneous sponge chemistry.

The magnesium chloride by-product from the reduction, and that separated from the magnesium recovered in the vacuum distillation, is crushed and sealed in barrels for sale. The recovered magnesium is reused. Titanium producers routinely recycle their $MgCl_2$ in large electrolytic reduction cells to generate fresh Mg and Cl_2 for the process. In principle this recycling can also be done with the $MgCl_2$ that comes from zirconium reduction.

There have been several attempts to modify and improve the Kroll process, of which one of the most notable was the continuous reactor of Dunham and Toomey [3.58] and Doyle [3.59], which reacts sodium or magnesium or a mixture thereof and zirconium tetrachloride in a vertical, cylindrical reactor such that the zirconium collects at the bottom and is periodically compacted with a hydraulic ram and pushed out the bottom as a compacted mass suitable for arc melting. The by-product of one or more chlorides are removed near the top of the cylinder as a melt. The ramming action squeezes out chlorides trapped in the sponge and helps densify it. Though having the advantages of a continuous process, the concept was never adopted commercially.

A technical difficulty, yet to be resolved, was that the residual chloride content of the sponge was sufficiently high that it interfered with vacuum arc melting during the first melt due to excess gas loading in the furnace.

3.5.2. Reduction of the metal tetrafluorides with calcium

The reduction of the metal tetrafluorides with calcium is essentially a thermite reaction. The zirconium tetrafluoride is first sublimed in vacuum near 1123 K (850°C) and recovered with an oxygen concentration under 0.1 wt% (0.6 at.%). Next it is mixed with calcium and with the oxides of any desired alloying elements then placed in a crucible so that it can be induction heated [3.14]. The reaction starts on heating, proceeds exothermically and produces a mass of metal that consolidates below a layer of by-product calcium fluoride. Electron beam melting can purify the metal. The now closed Prydneprovsky Chemical Plant in the city now known as Kamianskoe, Ukraine, operated this process.

3.5.3. Electrolytic reduction

Ogarev et al. [3.60] developed the electro-winning of zirconium as now practiced at the Chepetsky Mechanical Plant in the Russian Federation. The process is described in some detail by Barishnikov et al. [3.61] and in Ref. [3.14], which cites work showing that electrolysis favours the deposition of zirconium over hafnium. Under certain conditions, the hafnium concentration of the deposited zirconium is less than one tenth that of the electrolyte [3.62]. This purification would supplement achieving lower hafnium concentrations for the relatively impure zirconium (300–500 ppm Hf concentration) produced by the fractional crystallization process. The product of this process is zirconium powder in the form of very fine crystals.

Electrolysis uses an electrolyte containing potassium hexafluorozirconate, potassium chloride and potassium fluoride. The composition in mass percent is given by Refs [3.14, 3.61] as 25–30% K_2ZrF_6, 70–75% KCl. The ranges of optimum temperature and current density are 1023–1073 K (750–800°C), 3.5–4 $A \cdot cm^{-2}$ according to Ref. [3.61].

The cell operates at a potential of 10–20 V. Joule heating is used to maintain the cell temperature. The cathodic reaction involved in the electrolysis is:

$$ZrF_6^{2-} \leftrightarrow Zr^{4+} + 6F^- \tag{3.19}$$

$$Zr^{4+} + 4e^- \rightarrow Zr \tag{3.20}$$

Fluoride ions are discharged at the anode. The elemental fluorine reacts immediately with the chloride ions; thus, chlorine is evolved at the anode. The anodic reaction is:

$$4F^- + 4KCl - 4e^- \rightarrow 4KF + 2Cl_2 \tag{3.21}$$

Thus, potassium fluoride gradually accumulates in the bath. The bath also works with NaCl substituting for the KCl; however, the solubility of KF in water is higher than for NaF, thereby facilitating the separation of the electrolyte and the zirconium powder.

The cathode is periodically withdrawn, and the deposit scraped off into a receiver. The whole electrolysis and product recovery operation is done in an argon atmosphere. The product consists of about 25–30% zirconium by mass, although a product higher in metal is described by Ref. [3.61] as being produced when the original mixture is forced through a die while the salt is still molten. Current efficiency is quoted as 60–80% by Ref. [3.59] and 60–65% by Ref. [3.14]. When cool, the product is crushed and leached with water to yield a coarse metal powder consisting of particles ranging from 0.1 mm to a 0.5 mm maximum dimension. The particles appear crystalline under moderate magnification. The purity of the nuclear grade product, except for the hafnium concentration, is similar to Kroll process sponge.

The process is conducted in a graphite lined vessel that can serve as the anode, or in a vessel protected by a skull of frozen electrolyte in which a graphite anode is used. The cathode may be steel, molybdenum or graphite. Elaborate diagrams of several designs are shown in Refs [3.14, 3.61].

Until resistive heating takes over, the salt baths are supplementarily heated with graphite electrodes using AC current.

A simple picture of the process is that zirconium crystals are deposited at the cathode, while chlorine is evolved at the anode. The electrolyte is replenished with additions of potassium chloride and hexafluorozirconate, and it is replaced periodically so the accumulated potassium fluoride could be recovered. This description is complicated by the fact that the carbon of the anode participates in the anode reaction, and that along with chlorine, carbon tetrafluoride and chlorofluorocarbons are evolved.

The overall reaction is approximated by:

$$7K_2ZrF_6 + 16KCl + 4C \rightarrow 7\,Zr + 6\,Cl_2 + 30KF + 4CF_3Cl \tag{3.22}$$

Ogarev et al. [3.63] state that for the conditions quoted above, the anode gases contain, by volume, 55–60% chlorine and 45–60% freons. In turn, the freons comprise, by volume, 35–37% CF_4, 40–44% CF_3Cl, 12–16% CF_2Cl_2 and 8–11% $CFCl_5$. The production of chlorofluorocarbons has been reported as an anode product of electrolysis with carbon anodes of melts containing mixtures of potassium chloride, potassium fluoride and potassium hexafluorosilicate [3.64], and melts of alkali metal chloride-fluoride mixtures [3.65], so the phenomenon is not unique to zirconium systems.

The chlorofluorocarbons are at least sequestered during the operation of the cell as it is hermetically sealed. Care has to be exercised to ensure complete capture of these chlorinated fluorocarbons any time the electrolytic cell has to be breached to atmosphere.

3.5.4. Alternative reduction processes

3.5.4.1. Reductive extraction

The reductive extraction process of Megy [3.66] combines the separation of zirconium and hafnium with reduction to metal, and so is also a novel reduction process.

The process utilizes Al as the reductant dissolved in molten zinc as a solvent. If aluminium is used in a straightforward Kroll type reaction with the tetrachloride, the end result is a zirconium/aluminium sponge alloy that consists of a number of brittle intermetallics.

The molten zinc/zinc phase is contacted with a fused salt phase that contains the zirconium salt to be reduced. The aluminium is transported from the molten metal phase to the fused salt phase, replacing zirconium in the salt, while zirconium is transported from the fused salt phase to the molten metal phase. The fused salt phase and the molten metal phase are separated.

After the separation, the zirconium is present as a liquid alloy with zinc containing up to 10% Zr. The zinc is removed by distillation and reused, and the zirconium recovered as a porous solid that can be compacted and arc melted in the same way as Kroll process sponge. This process is covered in more detail in Section 3.4.4.

3.5.4.2. Continuous aerosol reduction

Leland [3.67, 3.68] disclosed a novel method to produce zirconium and other reactive metals continuously by mixing an atomized spray of molten reductant with the metal chloride vapour. The exothermic reaction produces solid particles of the product metal and molten droplets of the by-product reductant chloride. The intent was to collect the product in an inductively heated molten pool, and continuously withdraw it as an ingot, while collecting and withdrawing the molten by-product separately. A similar concept, using the reductant metal as vapour instead of an aerosol, was described by Ogasawara [3.69], who demonstrated titanium ingot production as well as the reduction concept.

3.5.4.3. Reduction with solid metal reductant

Becker and Careatti [3.70] patented a reduction process to produce fine zirconium powder. It uses magnesium to reduce zirconium tetrachloride dissolved in a molten salt at temperatures below the melting point of magnesium.

The salt consists of 40–50 mol% KCl, 40–50 mol% NaCl, and about 10 mol% $ZrCl_4$. Gaseous $ZrCl_4$ and solid magnesium powder are both fed continuously to a lower portion of the bath, while the bath is agitated. Excess salt produced by the reaction is removed together with zirconium powder. The salt bath is maintained at a temperature of about 900 K (627°C), less than the melting point of pure magnesium, which is 923 K (650°C). The process is intended to operate continuously, and incorporates an electrolysis step to recover magnesium, and chlorine that is used to produce more zirconium tetrachloride.

3.5.4.4. Direct electrolytic reduction

Fray et al. [3.71] have developed a process for the direct electrolytic reduction of TiO_2. The process should work for any of the Group 4 metals. The process utilizes an electrolyte of pure $CaCl_2$. Sintered pellets of metal oxide become the cathode. The anode is graphite. Electrolyte temperatures are about 1123 K (850°C). The process works at a potential of about 3 V. Small pellets of metal oxide have a wire embedded in them. The reaction requires that oxygen diffuse out of the metal oxide and be reduced to its metallic state. A possible limitation

may be the reaction kinetics involving the diffusion of oxygen out of the oxide. This potential problem can be mitigated to some extent by sintering the metal oxides into a wafer-like configuration; such a scheme needs a full scale demonstration to evaluate economic feasibility. As an example, the sintered oxide in a broken-up sheet form could be contacted by a metal gridwork to form the cathode side of the cell. These oxide 'sheets' would be continuously fed into the apparatus, reduced and then removed as the metal.

3.5.4.5. Hafnium reduction

While this chapter has concentrated on the extraction and reduction of zirconium, hafnium has significant applications as a neutron absorber for control rod elements and follows very similar processing to zirconium with a few exceptions. These exceptions are the result of hafnium's intolerance to interstitial impurities such as oxygen and nitrogen.

Following liquid phase extraction using MIBK, the hafnium bearing stream is treated with sulphuric acid to form a hydrous hafnium sulphate and is then precipitated as a hydroxide by the addition of ammonia. The precipitate is then roasted to the oxide at about 1275 K (1000°C). Like zirconium, the hafnium is then chlorinated a second time, and the $HfCl_4$ is subjected to a Kroll type reduction with magnesium as the reductant. For economic reasons, the scale of these operations is much smaller than for zirconium because the starting zircon sand contains so little hafnium. A vacuum distillation at 1175–1275 K (900–1000°C) removes excess magnesium and $MgCl_2$ from the reduced hafnium regulus.

At this point the sponge is crushed, and it generally has impurities of oxygen in the 500–1000 ppm (0.55–1.1 at.%) range. Where zirconium remains ductile at oxygen concentrations of 1000–1500 ppm (0.57–0.85 at.%), hafnium would be severely embrittled, particularly for any operations that require cold deformation. The final operation, prior to melting, is to purify the hafnium sponge to less than 100 ppm (0.11 at.%) oxygen concentration using the Van Arkel–de Boer iodide transport process, described in Section 3.6.1.

CEZUS' extractive distillation process yields $HfCl_4$ directly. Rather than reducing to sponge and purifying by the Van Arkel–de Boer process, the metal is reduced by direct electrolysis in molten salt and then purified by electron beam melting. The $HfCl_4$ is introduced to a molten bath of purified salts of NaCl, KCl and a small amount of NaF. The salt bath is operated at a temperature of 1023–1123 K (750–850°C) and results in crystals or flakes of electrolytic hafnium. The hafnium crystals are reported by Tricot [3.33] to contain an oxygen concentration of about 500 ppm (0.55 at.%). Electron beam (EB) melting is used to volatilize and remove elements such as Al, Cr, Cu, Fe, Sn, Mn and V. With slow EB melting, Tricot states it is possible to obtain an oxygen concentration of less than 400 ppm (0.44 at.%).

3.6. PURIFICATION PROCESSES

The concentration of most trace elements in sponge and powder is generally fixed at the reduction stage. The chemical separation process fixes hafnium concentrations. Aluminium, carbon, silicon, iron, chromium, nickel, phosphorous, uranium, thorium, oxygen and nitrogen are fixed unless additional purification techniques are employed.

Two purification processes are described below. The oldest technique, the Van Arkel–de Boer iodide transport process, yields material with very low interstitial concentrations. It is common to achieve <50 ppm (<0.03 at.%) oxygen concentration in the output material, called, 'crystal bar'. The second technique is EB drip melting. This process is primarily used to remove high vapour pressure species elements such as aluminium, iron, manganese and copper from reactive metals.

3.6.1. Iodide transport process

Zirconium (or hafnium) with the highest purity is usually produced by the iodide crystal bar process utilizing the principle of the thermal dissociation of zirconium iodide. The process as now practised is largely attributed to the Dutch scientists, Van Arkel and de Boer, who applied the process to zirconium in 1925. Van Arkel later worked with Fast in the 1930s to develop an improved commercial version of the process.

Details of the process as operated in the 1950s for zirconium production are given by Ref. [3.7]. Rolsten [3.72] repeats much of the detail of Ref. [3.7] and adds a short section on hafnium. He also gives an outline of attempts to understand the process quantitatively. McDonald and Stephenson [3.73] describe the use of the process for depositing coatings of zirconium and hafnium and other metals. A short description of the process appears in the book of Powell et al. [3.74]. Lamaze and Charquet [3.75] describe a recent approach to improving the process for hafnium. Baryshnikov et al. [3.61] give a detailed description of the theory and practice of the process.

The principle of the process when used for refining zirconium or hafnium is to form the tetraiodide using an iodine vapour at a low temperature, and to decompose the tetraiodide to metal and iodine at a high temperature. This process is traditionally performed in a sealed Inconel vessel where the outside is uniformly heated (for example, by a circulating salt bath).

The metal to be refined is usually in the form of sponge and is pressed into rings that fit the inside diameter of the vessel. The inside surface of the rings is retained with a perforated molybdenum screen. One or more hairpin shaped loops of high purity wire drawn from the metal to be refined are suspended from the lid of the vessel, as shown in Fig. 3.9.

These hairpins are inboard of the peripherally placed sponge. (In the case of furnaces used at the Chepetsky Mechanical Plant, the compacted electrolytic powder is in the centre of the vessel and several crystal bar hairpins are suspended around the periphery of the zirconium.) The vessel is evacuated and back filled with argon several times, then, after the last evacuation, iodine is admitted so that the operating pressure is several hundred Pa. The wire, which starts at about 2.5 mm diameter, is heated resistively and grows to a diameter of 50 mm over about 15 days.

The overall reactions for the process are:

for (523–573 K (250–300°C)) or (743–823 K (470–550°C)), $Zr + 2I_2 \rightarrow ZrI_4$ (3.23)

and for (1573–1673 K (1300–1400°C)), $ZrI_4 \rightarrow 2I_2 + Zr$ (3.24)

The reason for two temperature ranges for iodide formation is that between about 575 K (300°C) and 743 K (470°C), the tetraiodide reacts with zirconium to form mostly the low volatility tri-iodide, according to:

$3ZrI_4 + Zr \rightarrow 4ZrI_3$ ((573–743 K (300–400°C)) (3.25)

The vapour pressure of the ZrI_4 increases above 723 K (450°C) because of the disproportionation of the lower iodides. Thus, if the low purity metal is held in the intermediate temperature range, very little tetraiodide is evolved, and the growth rate of the refined metal drops [3.14]. The optimal tetraiodide formation temperature for hafnium is near 673 K (400°C).

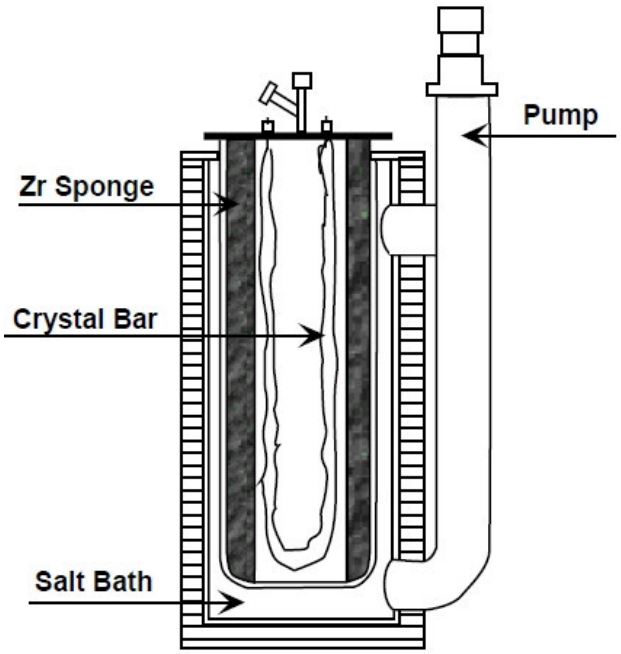

FIG. 3.9. Layout of a typical iodide transport purification cell.

The process effectively removes impurities, such as carbon, nitrogen and oxygen, which do not form iodides under the operating conditions and metals that form relatively non-volatile iodides under the chosen iodizing conditions, such as copper, chromium, cobalt and magnesium. The process is less successful in removing those elements that form volatile iodides, notably iron, which usually occurs in the product near 150–250 ppm (0.025–0.04 at.%). Likewise, titanium and hafnium transport with the zirconium iodide and are not removed. Table 3.3 shows the transfer of impurities in the iodide process after Lustman and Kerze [3.7].

TABLE 3.3. TRANSFER OF IMPURITIES IN THE IODIDE PROCESS

after Lustman and Kerze [3.7]

Element	Feed (ppm)	Crystal bar (ppm)	Transfer coefficient[a]
Ni	1600	10	0.006
Cr	1000	20	0.02
N	1100	3–82	0.003–0.075
C	2900	60–310	0.02–0.11
Si	1100	130	0.12
Fe	1200	280–390	0.23–0.33
Al	1100	700–800	0.64–0.73
Ti	—	—	1
Hf	—	—	1

[a] Fraction of the impurity in the feed carried over to the crystal bar.

3.6.2. EB melting

EB melting is used to purify and consolidate zirconium and hafnium [3.33, 3.76]. In one method, multiple electron guns with several hundred kilowatts of power are focused on a rotating electrode. The energy of the EB superheats the metal at the tip of the electrode and causes it to drip into a cylindrical, water cooled, copper crucible located immediately below the electrode. The EB extends past the electrode and also impinges on the top of the molten pool. Typically, the electron guns are tilted towards the axis of the electrode and cause the electrode to melt into the shape of a sharpened pencil.

Mechanical devices lower the electrode as it is consumed and withdraw the ingot from the bottom of the crucible. The length of ingot is limited by the size of the starting electrode and the vertical distance the ingot can be withdrawn.

A vacuum with a pressure of about 10^{-3} Pa is established inside the furnace chamber. The combination of vacuum and superheated metal causes metallic elements with high vapour pressure such as iron, chromium, nickel and tin to be swept away from the pool. Typically, these elements condense on the colder walls of the furnace, or on specially installed condensation screens or traps.

Purity is a function of melting rate, vacuum level, superheat of the melt pool and the number of repetitive melting steps employed. Typically, only a single EB melt is used for zirconium.

The resulting product can be used as-cast, or it can undergo one or more vacuum arc melts to further refine the as-cast grain structure and blend the purified metal with other input stocks such as sponge and alloy additions or recycle compacts. EB melting can be combined with the iodide transport process to produce extremely refined (and extremely expensive) zirconium approaching 99.9995 wt% purity.

3.7. ZIRCONIUM EXTRACTION FLOWSHEETS

Flowsheets of four of the current commercial processes are presented in Figs 3.10–3.13. These include flowsheets for Wah Chang, NFC, CEZUS and Chepetsky Mechanical Plant. Each of the process flows is different. They are intended to be instructional in the degree of latitude that can be exercised to produce the same end-product, zirconium metal. The main processing steps are compared and summarized in Table 3.4.

TABLE 3.4. MAIN PROCESSING STEPS FOR CONVERSION OF ZIRCON SAND TO METALLIC ZIRCONIUM

	NFC	Chepetsky Mechanical Plant	Wah Chang	CEZUS
Ore decomposition	Caustic fusion	Fluorosilicate fusion	Carbochlorination	Carbochlorination
Separation	TBP-nitric	Fractional crystallization	MIBK	Extractive distillation
Reduction	Kroll	Electrolytic	Kroll	Kroll
Distillation	Vacuum	–	Vacuum	Vacuum
Purification	–	Crystal bar	Crystal bar/EB	Crystal bar/EB

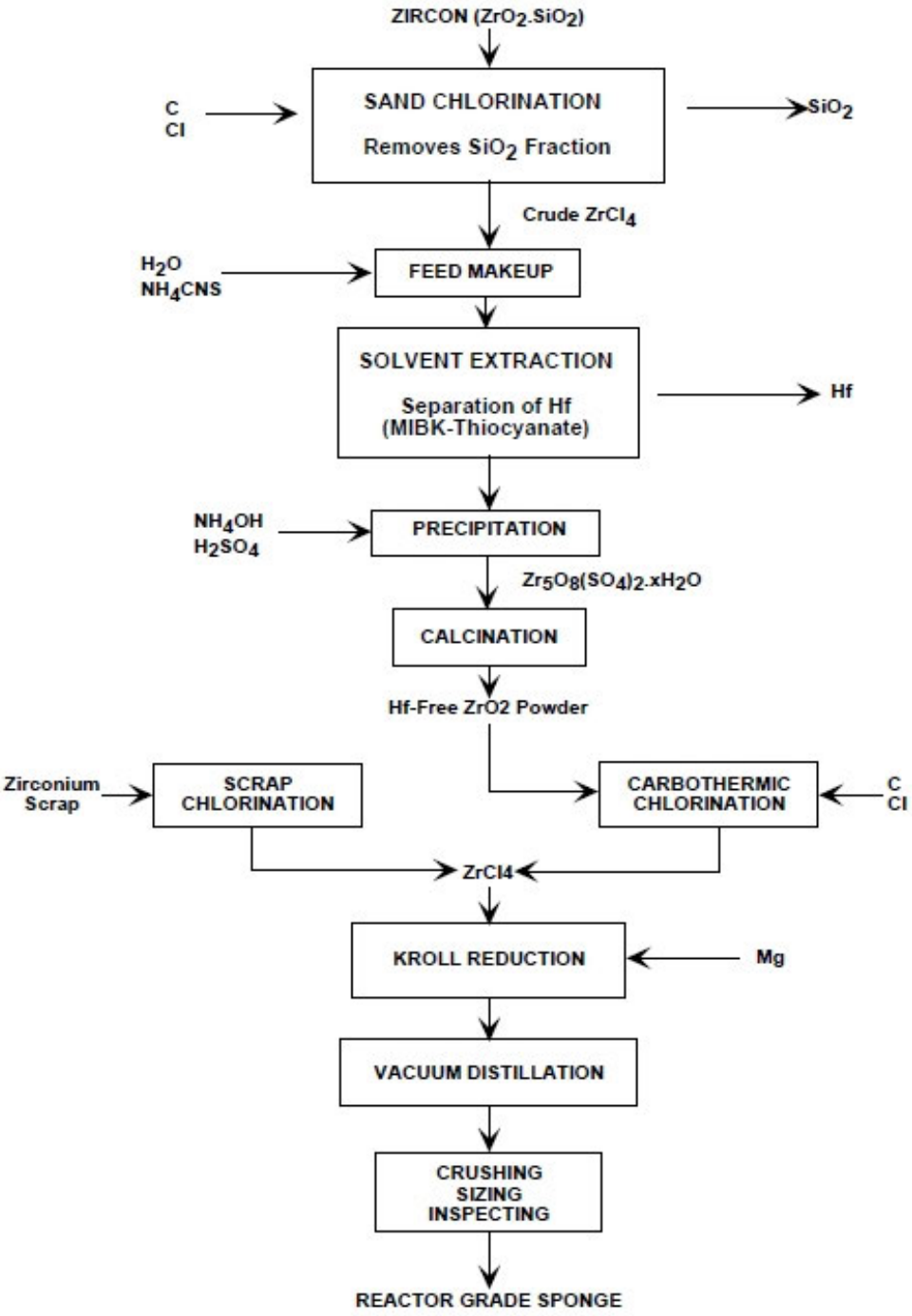

FIG. 3.10. Flow sheet for production of nuclear grade sponge at Wah Chang, USA.

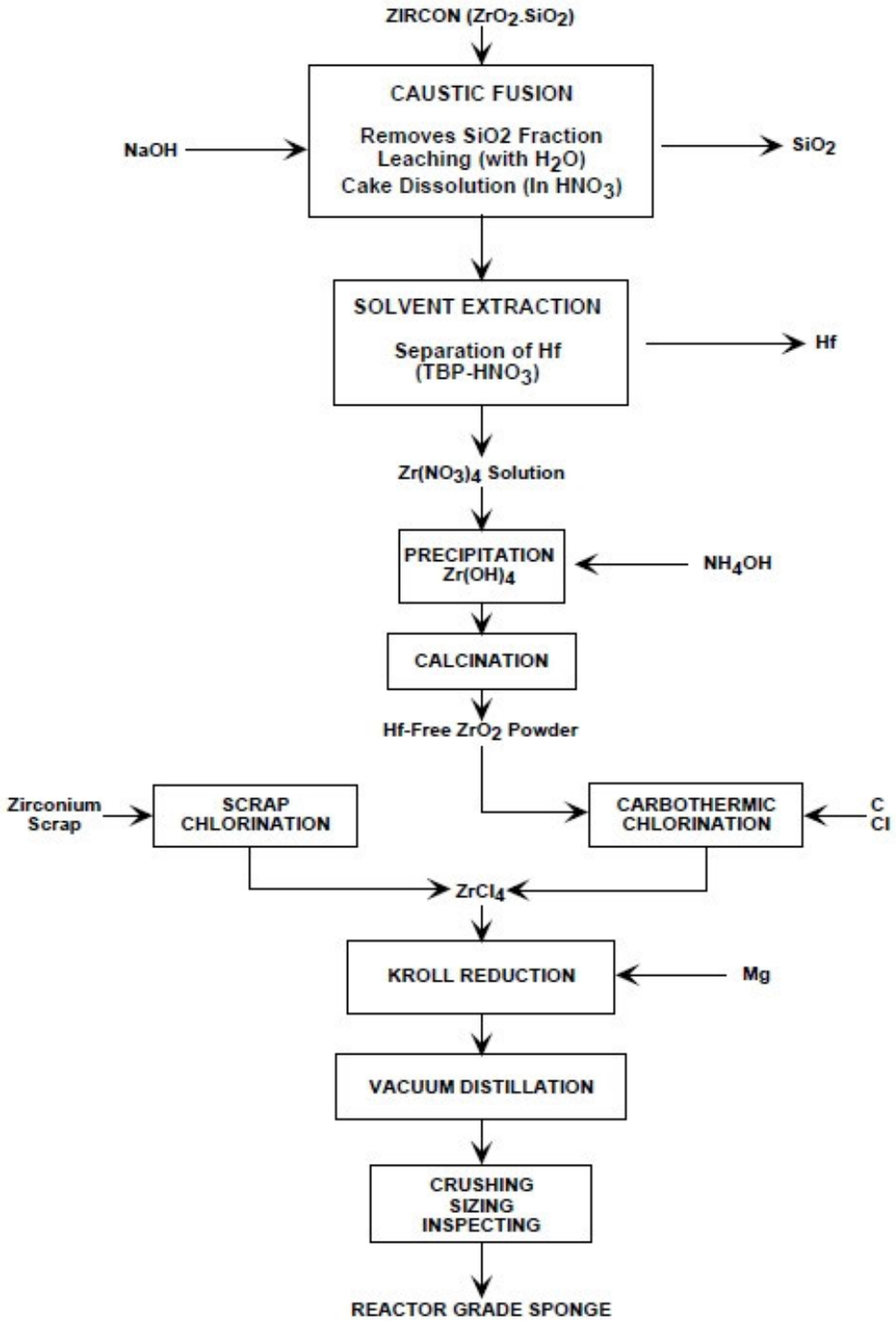

FIG. 3.11. Flow sheet for production of nuclear grade sponge at NFC, India.

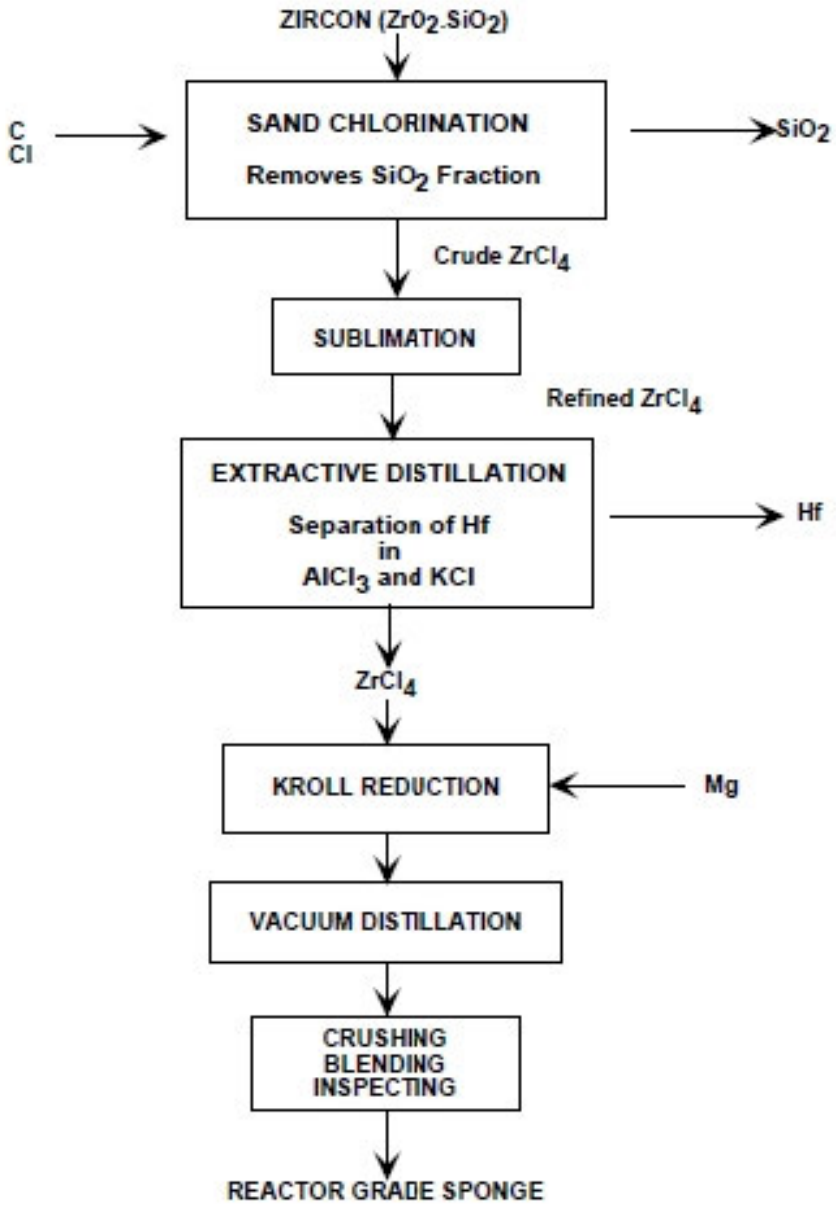

FIG. 3.12. Flow sheet for production of nuclear grade sponge at CEZUS, France.

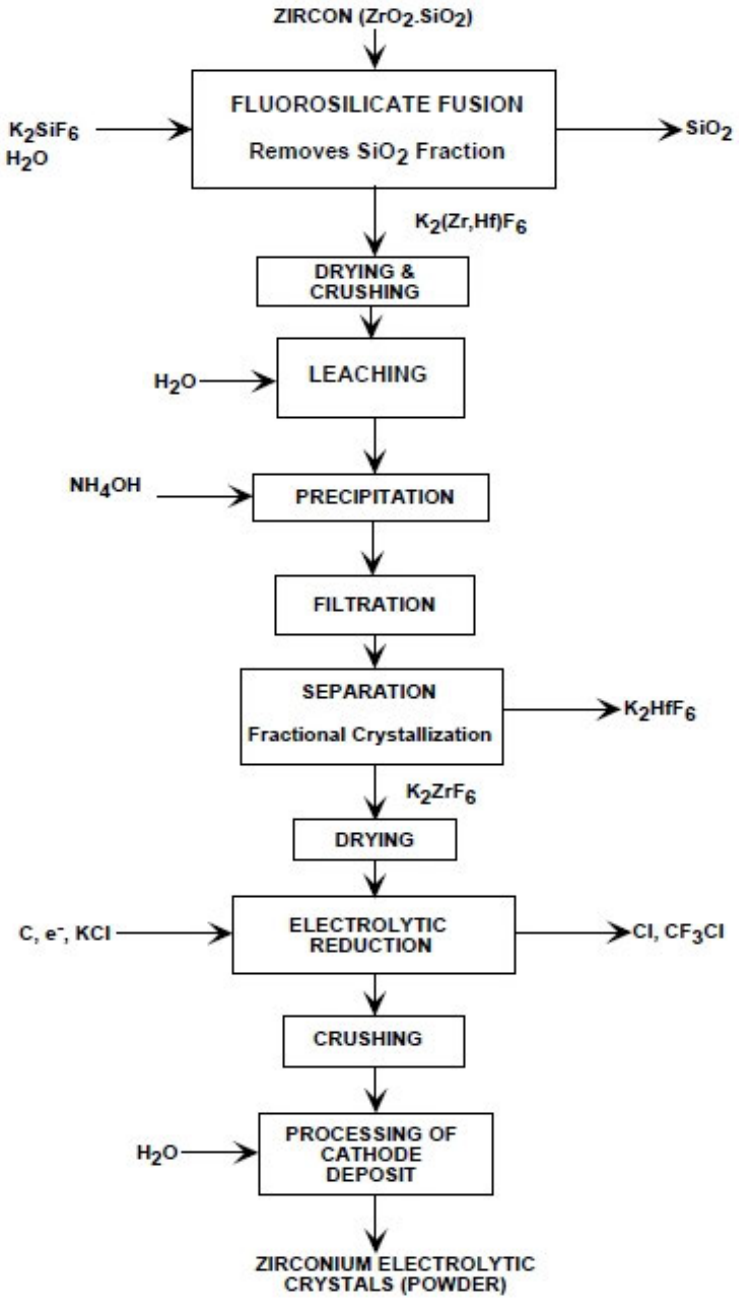

FIG. 3.13. Flow sheet for production of nuclear grade powder at Chepetsky Mechanical Plant, Russian Federation.

3.8. MELTING

Zirconium sponge or powder is the major input material for the fabrication of the zirconium alloy components required for nuclear reactors. Zirconium sponge or electrolytic processed powder is mixed with alloying elements in the required proportions and then consolidated into ingot form by vacuum arc re-melting (VAR). Double melting is the minimum practice for all zirconium based alloys, but for better homogeneity, to reduce surface and subsurface defects, and to remove critical gaseous impurities, triple or quadruple melting is also carried out. Arc melted ingots are then subjected to various fabrication processes such as

forging, extrusion, rolling, pilgering and drawing, to obtain different shapes of zirconium alloy components, as discussed in Chapter 4. Specific references to VAR of zirconium and its alloys are sparse. A good overview of VAR is provided by Child and Oldfield [3.77]. General references to VAR melting reactive metals are included in Refs [3.78–3.84].

3.8.1. Preparation of electrodes for VAR

The melting process used for zirconium is consumable vacuum arc melting, in which an arc is struck between consumable electrodes made out of material to be melted and the copper crucible. The consumable electrode melts owing to the intense heat of the arc and metal droplets drip off into the molten pool contained in the copper crucible, thereby forming an ingot. The consumable electrode preparation is done either by compaction of sponge or powder briquettes followed by EB welding. Scrap or revert can also be welded together to make a VAR electrode. Additionally, scrap can be processed by introduction to a plasma arc furnace, as practised by NFC. A typical flow sheet for making zirconium alloy is provided in Fig. 3.14.

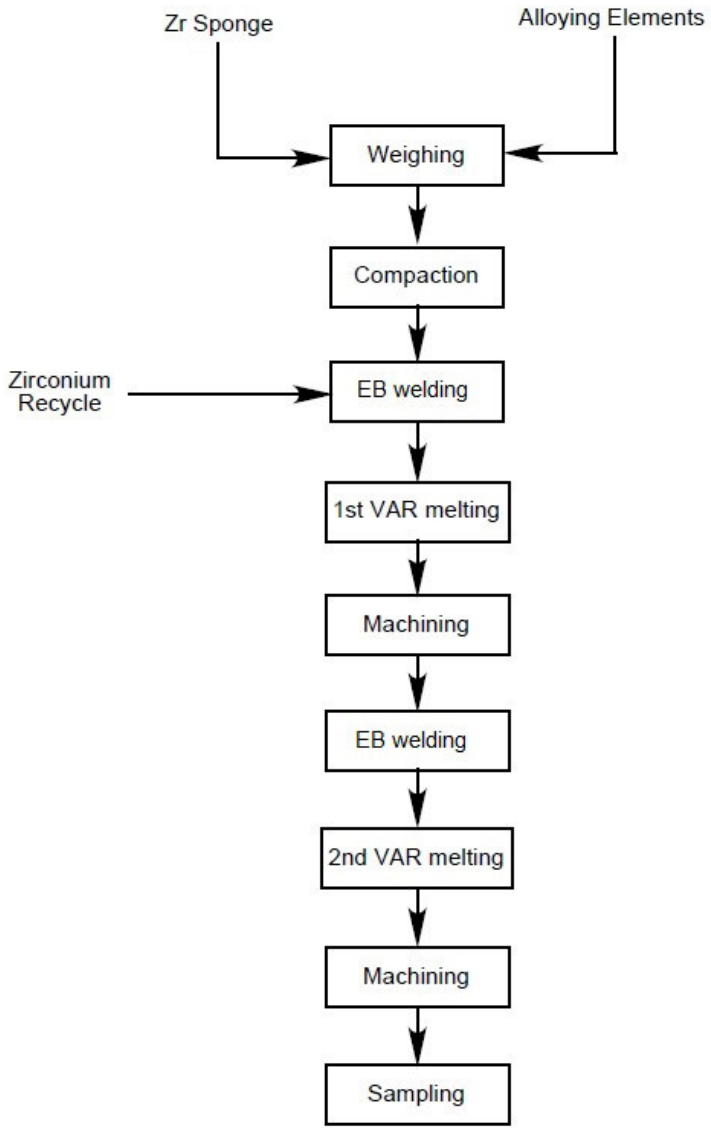

FIG. 3.14. Flow sheet for ingot production.

Weighed sponge along with pre-weighed and packaged alloying elements are poured into a die cavity and compacted to either cylindrical or semioctagonal shaped logs. The compaction pressure is such that the compact has adequate strength for handling, and density adequate to carry electrical current during melting. Cylindrical compacts are preferred over polygonal compact assemblies to avoid side arcing from the vertices during melting operation. Compaction pressures of the order of 400–600 MPa (40–60 kg/mm^2) are required depending on the size. Hydraulic presses with a capacity of 1000–5000 tonnes are used. A compact density of about 80% of the theoretical density is sufficient to achieve efficient melting.

EB welding, plasma arc welding and gas metal arc welding techniques are used for welding compacts. The compacted briquettes are assembled together in a fixture and loaded in a welding furnace. After evacuation, the first melt electrode is welded. Deep penetration welds are used to weld the compacts together. The weld strength has to be sufficient to support the complete weight of the electrode and the weld width should be sufficient to allow enough current to pass during melting.

The consumable electrode for double arc melting is similarly welded out of first melted ingots, by welding around the circumference at the junction of two ingots. These ingots may be inverted to provide better homogeneity. Additional melts (as in triple or quadruple melted ingots) are handled in a similar fashion. A typical first melt electrode has a diameter of 400 mm. This electrode would be melted into a 500 mm first melt ingot, subsequently to a 585 mm second melt ingot, and finally to a 675–700 mm final ingot. This ingot may weigh approximately 8 t.

Chepetsky Mechanical Plant compacts electrolytic powder into right circular cylinders. These compacts are welded together by EB welding to form an electrode. Rods of crystal bar zirconium (Van Arkel–de Boer processed material with a higher purity) are welded on the outside of the compacts to provide a blended electrode that meets chemistry requirements. This technique is used to offset the high interstitial impurity concentration of the electrolytically produced powder.

3.8.2. Vacuum arc melting

Two major variations of the basic arc melting process can be considered for the melting of reactive metals such as zirconium. These include non-consumable electrode melting and consumable electrode melting.

3.8.2.1. Non-consumable electrode melting

The electrode used in this case is usually made of thoriated tungsten, graphite or some metal carbides having high melting temperatures. Water cooled metal crucibles are mostly used. This process has certain inherent disadvantages. These include the possibility of contaminating the melt by the electrode and the necessity of using a controlled atmosphere instead of a vacuum. Further disadvantages include low melting rates, limitations on the size of the ingots and difficulty in achieving complete homogeneity. This process was abandoned as soon as consumable vacuum arc melting was developed.

3.8.2.2. Consumable electrode arc melting

The use of consumable electrodes eliminates most of the disadvantages of non-consumable electrode melting. The electrode contains no metals other than the one to be melted (except for the inherent impurities) and therefore contamination of the ingot is eliminated. The melting can be carried out under vacuum, thus avoiding the use of an inert gas atmosphere. The pick-up up of harmful gases is thereby minimized.

The consumable electrode allows for a controlled feed rate and high melting rates because heat losses are low. The electrical efficiency of the furnace is high. By combining melting with casting, ingot defects, such as centre porosity and segregation, are minimized. Effective degassing during melting may increase purity.

A consumable electrode has some disadvantages. The preparation of electrodes requires an expensive hydraulic press and the handling of many compacts. The re-melting of scrap is difficult owing to its unsuitability for incorporation into consumable electrodes. Use of a cold crucible produces ingots that often have very coarse columnar grain structure.

With large grain size, and small grain surface per unit volume, the impurities with low solubility limits in the solid metal may concentrate at the grain boundaries during solidification. Depending on the kind of intergranular constituent, these impurities may induce brittleness.

For several high melting point metals, the vapour pressure of their monoxides is higher by many orders of magnitude than that of the metal itself. In such cases, de-oxidation via the vapour phase may take place even at a low oxygen concentration. With the usual arc melting conditions, it is very difficult to remove either nitrogen or oxygen from zirconium. Thus, it is mandatory to start with the lowest interstitial concentration material for melting, since no attempt is made to reduce further the oxygen and nitrogen concentration during arc melting operations. Hydrogen can be removed during arc melting because of the favourable conditions that exist for the decomposition of hydride.

Vacuum arc melting furnaces have either one melting station and two cooling positions for the crucibles, or a single melting and cooling position, Fig. 3.15. For furnaces with two cooling positions, after the completion of the melting operation, the crucible assembly can be sealed off by means of an isolating valve and can be detached from the furnace without waiting for the ingot to cool to room temperature. The next melting operation can be carried out after assembling the crucible with the electrode and evacuating the furnace. Melting time for one electrode will depend on the electrode weight. After sufficient cooling, the ingots are removed from the crucibles.

The bulk of the volatile impurities will be removed during the first melt. The impurities become concentrated on the ingot surface due to volatilization. These impurities can be removed by scalping, or by pressure washing the surface of the ingot.

Double melting is used to achieve homogeneity and reduce subsurface defects. The primary melted electrode is re-melted into a larger diameter crucible. Multiple primary melted electrodes may be assembled and welded together. The second melting is carried out with more precise control to avoid defects in the melted ingots. The current is reduced at the end of the melting, in an operation known as hot topping. Melt rates of 10–50 kg/min are quite common depending on the diameter of the electrode.

Triple melting is employed to minimize the occurrence of nitrides, and to permit the casting of massive ingots. Nitrides are usually substoichiometric with a melting point that varies with nitrogen concentration. Irrespective of stoichiometry, they will melt at a higher temperature than the melting point of zirconium. The additional molten pool residence time afforded by triple melting helps dissolve nitrogen-rich particles.

The ingots are cooled under vacuum or inert gas, such as argon or helium, after the completion of the melting and are stripped from the copper crucible. Helium helps reduce the cooling time owing to its superior thermal conductivity.

The ingot is machined and samples from several places of the ingot are taken in the form of turnings or solids for chemical and spectroscopic analysis and gas analysis. Hardness may be measured at various places on the surface of the ingot. The ingot is also tested ultrasonically to ascertain the integrity of the material and to locate any shrinkage cavity or piping-type defects.

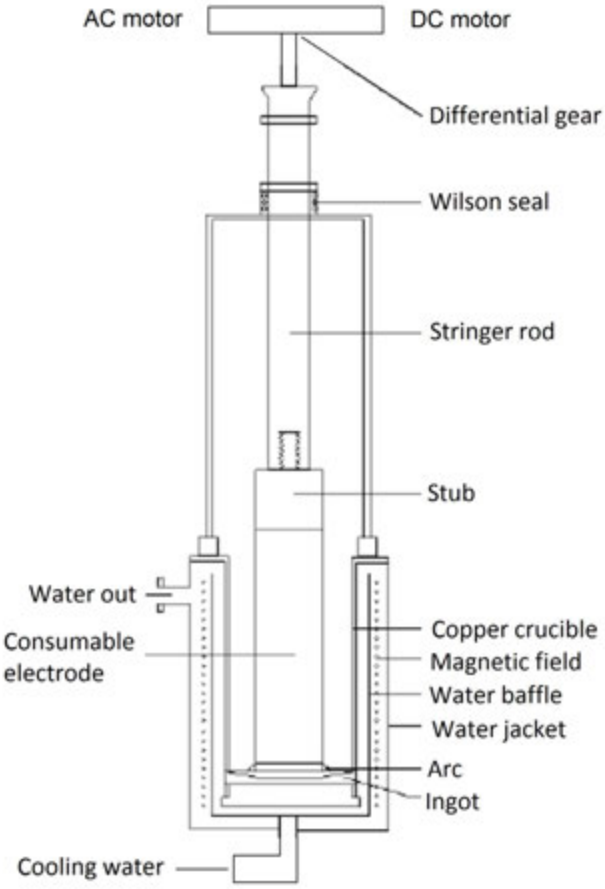

FIG. 3.15. Schematic diagram of a VAR furnace.

Safety is of the utmost concern during VAR processing. If insufficient cooling is provided and the copper crucible is breached, molten metal has the opportunity to react directly with the cooling water. A hydrogen explosion created when the molten zirconium is oxidized by the steam, thereby liberating hydrogen, may follow an immediate steam explosion. Evans and McLaughlin [3.85] conducted a thermodynamic investigation into reactive metal melting furnace explosions and concluded that, while titanium has a higher likelihood of creating a steam/hydrogen explosion than zirconium, this reaction cannot be ruled out for zirconium.

3.8.3. Melting parameters

Initially high melting power is avoided until a molten pool has been established to avoid damaging the bottom of the crucible. The melting power is then raised to a higher value than is intended for the main melting period to offset the chill effect of the crucible base. As ingot build-up proceeds, the cooling effect from the base is reduced to negligible proportions. The melting power is reduced to avoid the formation of a molten pool that is too deep. The power level is maintained constant over the major portion of the ingot until the end of the melt. The power is reduced during the final melting stage to minimize shrinkage in the top of the ingot.

The choice of melting current is a compromise. For high productivity, it should be as high as possible to minimize furnace time. Metallurgical requirements demand a low melting power to maintain a shallow molten pool and minimize segregation effects. A simple relation

may specify the current requirements for large ingots. The current must be held proportional to the ingot's cross-sectional area to maintain a constant power per unit area of ingot, and therefore the current should be controlled in proportion to the (diameter)^2.

Arc voltage is maintained constant, thus the melt rate of material from the electrode is proportional to current and may conveniently be expressed in terms of weight per kiloampere·minute (k_1). Some typical values are shown in Table 3.5. These factors are used to estimate total melting times and are of particular value in the calculation of hot topping schedules, by indicating the amount of electrode remaining and hence the point at which hot topping should be commenced.

TABLE 3.5. TYPICAL VALUES FOR SPECIFIC MELT RATES

Material	(kg·kA^{-1}·min)
Iron and nickel based alloys	0.565–0.70
Niobium and molybdenum alloys	0.255–0.32
Titanium (sponge)	0.53
Titanium (re-melt)	0.55
Copper	0.7
Zirconium	0.4–0.5

A large annulus between the electrode and the crucible wall allowing good gas egress is desirable for purification, but a large gap may result in inadequate filling of the molten pool leading to a poor ingot surface. The clearance between electrode and crucible must be larger than the arc gap between the two surfaces to minimize unwanted side arcs; a value of 15–30 mm is normal.

The actual power required to arc melt depends directly on the melting point, the specific heat, the heat of fusion and the thermal conductivity of the metal or alloy under consideration. The data in Table 3.6 present typical power requirements necessary to successfully arc melt zirconium ingots of various diameters.

TABLE 3.6. VAR APPLIED ELECTRODE CURRENT AS A FUNCTION OF ELECTRODE DIAMETER

Element	Melting point (K)	Typical arc melting voltages (V)	DC electrode negative, kA for millimetres of electrode diameter						
Zirconium	2145	28–38	mm	200	250	380	508	585	685
			kA	5	6	11	17	24	35

The melt profile is selected to maintain a constant melt rate and uniform molten pool depth, Fig. 3.16. Such a profile will result in uniform composition, grain size and grain orientation along the length of the ingot, and helps to ensure uniform properties in the final product. There has been substantial modelling of the arc plasma behaviour during VAR melting, including studies directly related to zirconium alloys [3.86–3.88].

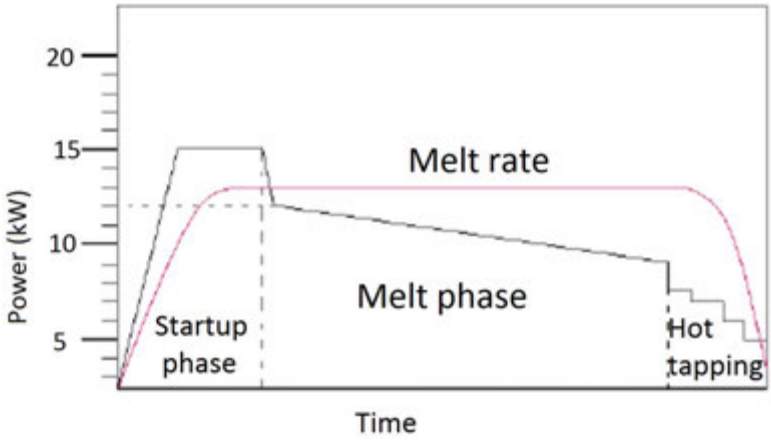

FIG. 3.16. Typical melt profile for zirconium melting.

3.8.4. Purification by vacuum arc re-melting

Electrodes made from sponge and powder de-gas before melting (i.e. in the heated portions of the electrode adjacent to the arc). With solid electrodes, degassing occurs primarily in the arc zone and takes place on the face of the electrode, the surface of the molten pool and to a lesser extent during the passage of the metal from the electrode to the pool in the form of droplets.

The effectiveness of the process in removing volatile impurities depends on the pressure and temperature in the arc and on the residence time in the molten state. The residence time is dependent to a certain extent on the melting current, but melt diameter is the major factor influencing the time exposed to vacuum. An improved refining condition can be expected as the ingot diameter increases. The process of VAR liberates volatile components, primarily chlorine, hydrogen and magnesium.

Factors such as the number of successive melts, the vacuum pumping capacity and the electrode to crucible annulus (which controls vacuum diffusion) all exert an influence on the amount of volatile material removed from the final ingot. A high amount of volatile material is liberated during the first melt. During primary melting, the volatile material contributes to a high vapour pressure in the vacuum system and limits the removal of volatile material. Subsequent melts are much less ‘gaseous’ and can further reduce chlorine and magnesium concentrations.

3.8.4.1. Removal of volatile impurities

Hydrogen can be removed during arc melting by exposing molten metal to a vacuum for extended periods. Oil ejector diffusion pumps have better pumping efficiency for hydrogen than mechanical blower pumps. Figure 3.17 demonstrates the reduction in hydrogen possible with multiple VAR melts.

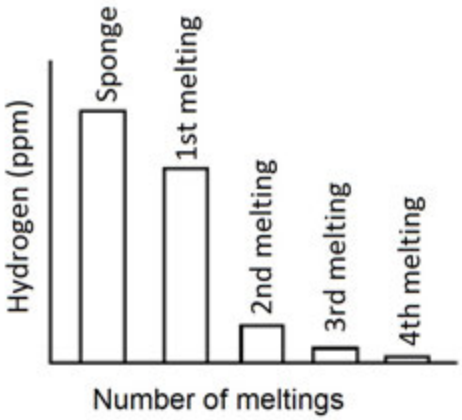

FIG. 3.17. Reduction of hydrogen with multiple meltings.

Chlorine is an important element because it reduces the fracture toughness of Zr-2.5Nb pressure tubes, and it promotes formation of a basket weave microstructure during the α to β transformation, especially for the Zircaloys. If sufficient chlorine is not available to form nucleation sites, the α platelets nucleate on the β grain boundaries since these are the only heterogeneous structures available. Depending on crystallographic orientation, certain β grains can be filled where the 'feathers' of the α platelets nucleating off the β grain boundaries rapidly consume the entire β grain with long parallel platelet colonies [3.89].

Chlorine and magnesium come from the Kroll reduction process. A study was performed on Zr-2.5Nb to determine how much chlorine was liberated after each melt. Starting with a sponge chlorine concentration of about 150 ppm, the first melt reduced the chlorine concentration to between 5 and 10 ppm. The second melt dropped the chlorine concentration to less than 5 ppm. The third melt decreased the chlorine concentration to less than 1 ppm, and after the fourth melt the chlorine concentration was less than 0.5 ppm [3.90].

3.8.4.2. Removal of nitrides

Melting also promotes the dissolution of nitrogen-rich particles that may be incorporated in recycled materials, or from sponge that has locally overheated from friction burns during crushing. A true stoichiometric nitride contains about 14 wt% (50 at.%) nitrogen. Most nitrogen-rich particles contain substantially less nitrogen concentration at about 1–5 wt% (3.6–17.9 at.%). Nitrogen increases the melting point. A stoichiometric nitride has a melting point of about 3775 K (3500°C).

Nitrides and nitrogen-rich particles are quite refractory and are difficult to dissolve. There is never enough superheat on the pool to directly melt a nitride. Nitrides have to dissolve by diffusion of the nitrogen into the molten pool. This decomposition necessitates having sufficient time for diffusion to occur. In the early days of manufacturing zirconium alloys, a small double melted ingot was the norm. As manufacturers recognized the issues associated with nitrides, they employed a triple melting practice and used larger ingots to increase molten pool residence times sufficiently to dissolve nitrogen-rich particles.

This practice has eliminated the carryover of nitrogen-rich particles and parallel practices established by aerospace industries in melting titanium alloy ingots for rotating engine components [3.91]. The presence of nitrogen-rich inclusions (Type II, hard alpha particles in

aerospace parlance) in titanium compressor rotors has been known to cause catastrophic failures in these rotating parts. During in-reactor service, nitrides in zirconium accelerate corrosion associated with the very high local nitrogen concentration of the inclusion.

3.8.4.3. Removal of high density inclusions

High density inclusions normally come from some type of tungsten carbide cutting tool that has chipped off during a machining operation and is inadvertently recycled. These particles can be eliminated in several ways. A high cobalt binder content generally allows tungsten carbide tooling to dissolve at the molten pool temperatures of zirconium alloy (roughly 2175 K (1900°C)). Since the cobalt binders are paramagnetic, a powerful electromagnet can be used to sweep machined chips for tungsten carbide particles as part of a chip cleaning procedure prior to their being compacted to make recycling ingots. Recycled components can be radiographed for high density inclusions. If inclusions are found, they are removed by machining them out of the recycled material.

3.9. TECHNIQUES FOR RECLAMATION OF ZIRCONIUM SCRAP

During the fabrication of zirconium alloy components, scrap is generated at different stages of operation. This scrap is preferably recycled by melting rather than reclaiming it farther back in the process as a cost control measure. Depending on the product, the yield of useful product can be in the range of 60–75%.

The bulk of scrap generated can be classified into two major categories:

(1) Light scrap generated in machining operations that produce turnings, shredded cladding tubes or spacer strip skeletons and punching accounts for about 30% of the total and is generally contaminated with oxygen, nitrogen and carbon.
(2) Massive scrap, for example, in the form of slab and billet bloom ends, trepan cores from the production of extrusion billets for tubing and rejected pieces accounts for nearly 70% of the total scrap.

Recycling these scrap pieces in their metallic state is preferred because this material contains much added value. Some scrap is too contaminated or too susceptible to ignition to be cleaned and degreased prior to being re-melted, but still contains value. It is usually too hazardous to be dumped in a landfill. This scrap must be recycled farther back in the process, either by oxidation or chlorination processes.

3.9.1. Oxidation of scrap

Scrap of either low value, such as grinding fines, and scrap with a configuration unsuitable for re-melting, can be treated by oxidation with air in a suitably designed and operated rotary kiln. The product is metal oxide, and its quality determines the subsequent processing. If it is sufficiently pure, it can be returned to the process stream in a plant using ore and oxide chlorination as feed supplement at either process stage. If it is too impure, it can be sent to a landfill.

3.9.2. Chlorination of scrap

Forming volatile chlorides can be done easily in molten salt that contains a chlorination catalyst such as iron chloride or copper chloride. In most cases, chloride can be recovered that

is suitable for recycle to the extraction circuit, either as feed to the zirconium-hafnium separation process or directly to the reduction step.

The reprocessing of off-grade mill scrap is converted into sponge by direct chlorination in water cooled, packed-bed reactors, then mixed along with normal chlorinated zirconium oxide for further reduction and vacuum distillation.

3.9.3. Recycle of metallic solids by melting

Clean metallic recycle material can take on various physical forms, including bulk solids, small solids and chips [3.92, 3.93]. These pieces can be made into electrodes that can be re-melted into recycle ingots.

In one scheme, bulk solids are welded together to form an electrode and are melted into a cylindrical ingot. The ingot is sampled for composition and then sawed into solid compacts approximately the dimensions of the starting sponge compacts. Chips are degreased by washing, dried and then compacted using a hydraulic press, welded into an electrode and melted into a recycle ingot. Recycle billets are sawed from the ingots and may receive special testing such as radiography, as described in Chapter 3.8.4.3, to determine that no unwanted inclusions are present.

Recycled material is consumed along with fresh sponge in the manufacture of subsequent first melt electrodes. Recycled material may be introduced from the recycle ingots to the first melt electrode, or as the direct addition of well-characterized solids to a second melt electrode. The ratio of recycle to sponge may vary from 20–65%, but a steady recycle percentage might be 35–45% based on average product yields.

Cleanliness and appropriate grading of recycled material is crucial. Contaminants that find their way back into recycle include oxides, nitrides and carbonaceous materials. If several grades are processed through the same fabrication equipment, care has to be taken to identify and segregate each of the various grades. For example, a small quantity of Zr-2.5Nb can easily contaminate a Zircaloy-2 grade ingot where niobium is not permitted. Recycled material with high concentrations of impurities can often be blended with sponge to deliver a final product that meets the specification for chemical analysis.

Several vacuum arc re-melt electrode configurations are used. Primary melt electrodes may consist of 100% sponge and alloy input, or a combination of sponge and solid recycled material input. Methods for adding recycled material vary.

Billets of compressed sponge and recycled material are interspersed to promote mixing of sponge and recycled metal during subsequent VAR melting. The billets are welded circumferentially to each other. In some cases, longitudinal stripes are made down the length axis of the outside surface of the electrode to promote good electrical conductivity through the sponge compacts.

A novel approach by Western Zirconium employs a central slab-shaped ‘spar’ that is an ingot of recycled material that has been forged to a slab, and hot rolled to constant thickness. This recycled material spar forms the central section of the electrode. The spar has multiple purposes, including being the method for adding recycled material, providing mechanical strength for the overall electrode, providing a good means of electrical conductivity from the top to bottom of the electrode and providing a convenient method to weld sponge compacts together. The sponge compacts are shaped in a semi-circle or D shape. These compacts are lined up on either side of the spar and an EB welder is used to make four longitudinal welds at the root of the sponge compacts adjacent to the spar [3.94].

3.9.4. Consolidation of chemically acceptable scrap by plasma melting

Plasma arc melting may be used to consolidate scrap, combining the intense heat from a plasma torch with a water cooled hearth. Plasma torches can operate in a vacuum, as described here, or in a partial pressure inert atmosphere. Scrap is re-melted by a hot hollow cathode discharge technique. Another advantage of this technique is the feasibility of producing a suitable consumable electrode for re-melting to the final ingot by vacuum arc melting.

A schematic diagram of the plasma melting furnace is illustrated in Fig. 3.18. The chamber is evacuated to about 10^{-1} Pa, and the hollow cathode and anode (work piece to be heated) are placed opposite each other. A DC power source provides the primary power. A high frequency starter current maintains the arc, much like in gas-tungsten arc welding (GTAW) (discussed further in Chapter 4). A very small amount of plasma source gas (generally argon) is introduced in the cathode and ionized by the high frequency electric field thus closing the circuit. This technique results in the formation of low-pressure gas plasma, which consists of positive ions, electrons and neutral gas molecules.

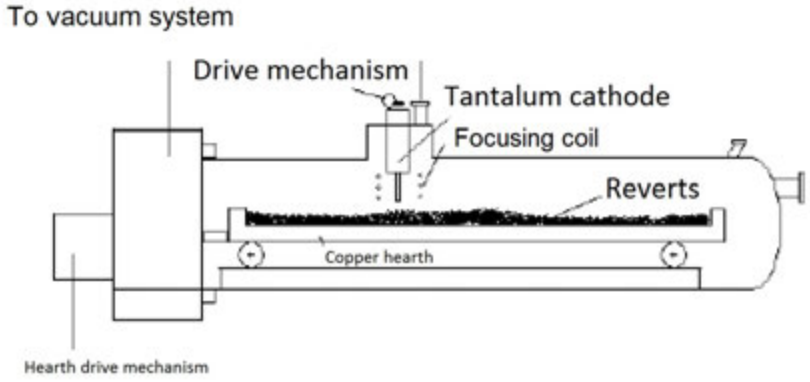

FIG. 3.18. Schematic diagram of plasma melting furnace.

The positive ions raise the temperature of the cathode by bombarding its inner surface to about 2300–2400 K (2025–2125°C) and raising the temperature to above the threshold value for the generation of thermal electrons. With the emission of thermions, the electron density around the cathode increases rapidly. At this stage, two sources of electrons (i.e. from the plasma in the hollow cathode and from the cathode inner surface) come into effect. These electrons pass though the plasma and reach the work piece because of the potential difference, thereby heating the anode surface.

The equipment comprises a horizontal cylindrical steel chamber connected to a high vacuum pumping system capable of generating a vacuum of 7×10^{-3} Pa in the main chamber and of 10^{-1} Pa in the scrap-charging chamber. The main chamber carries a water cooled copper hearth for loading massive scrap. The plasma gun is mounted on the top of the chamber.

The scrap to be melted has to undergo a considerable amount of cleaning, such as cutting, sand blasting, pickling and degreasing before it is suitable for re-melting.

To yield the best combination for loading in the furnace, another important aspect for re-melting is the segregation and sorting out of the various types and sizes of scrap. NFC currently uses this process. It is also a well-accepted method in the titanium processing industry.

3.10. MELTING DEFECTS

The partition of the total electrical power between the anode and cathode, which is dissipated in the arc melting process, differs from one metal to another and depends on the melting current. The fill ratio, which is defined as the ratio between the cross-section of the electrode to that of the crucible, governs the melt rate of the electrode once a power setting has been chosen. Usually this setting is chosen so that the liquid metal fills the cold crucible just to the edge. Use of lower power results in a rough ingot surface full of 'cold shuts', and power in excess of this results in high melt rates and an excessively deep molten pool, which in turn causes coarsening of the ingot macrostructure.

In the final melting, a hot topping practice is used to draw the internal shrinkage cavity close to the top of the ingot. Hot topping consists of reduced power melting, which permits feeding molten metal to the bottom of the shrinkage cavity before it has an opportunity to freeze. A melt interruption (loss of power or vacuum) on a final melt before hot topping commences results in excessively deep shrinkage cavities or 'piping' that has to be managed by any one of several removal processes — re-melting the ingot, cutting off the ingot top containing the shrinkage cavity or subsequent removal at some intermediate processing stage.

In the VAR process, limited molten pool depth maintained by melt rate control results in avoidance of gross segregation of alloying elements. Segregation is defined as the difference in chemical composition between two remote parts of the same ingot. The very high thermal gradients existing in the molten pool (from the opposing effects of the arc power supplied at the surface of the melt and the rapid cooling from the base and sides of the water cooled crucible) favour columnar crystallization in the ingot. At the base of the ingot, crystal growth is vertical from the rapid chill effect. As the ingot builds up, the cooling effect from the base is minimized and radial columnar grains dominate the cast structure, with crystal growth following the direction of heat flow and normal to the solidification front. Columnar crystal growth is promoted because the material has high purity and few nucleation sites.

The following processes of redistribution of impurities take place in VAR melted ingots:

(a) The impurities, which are vaporized from the melt in the form of condensable metals or compounds such as oxides, condense on the cold crucible wall at some distance above the arc zone. As the crucible is filled with metal, these deposited impurities are exposed to intense arc heat and are re-vapourized and subsequently condensed further on the crucible wall. This mechanism leads to the progressive concentration of impurities in the upper portion of the ingot. This phenomenon is more prominent in the ingot melted first as it contains more volatile impurities. To achieve homogeneity in a double melted ingot, the upper portion of the first melted ingot is inverted during the second melting operation.
(b) The annular gap between the electrode and the crucible presents a restriction on the transport of gaseous and volatile impurities to the vacuum pumping system. As melting progresses, the distance between the melting and the pump is reduced and hence offers less resistance to pumping impurities. This shortening of the vacuum path leads to more pure material at the top of the ingot for some gaseous impurities. Inversion of the electrode from one melt to the next helps to address the issues raised in (a) and (b).
(c) The volatile impurities released during arc melting cause disturbances in the arc plasma, which leads to power gradients to the molten pool. These gradients lead to surface defects, such as surface roughness and cold shuts, which are especially noticeable on the sidewalls of single melt ingots.
(d) During the starting of the melting, degassing the cold copper crucible, the electrode and the furnace chamber interior will take place. When the arc is struck, molten metal formed during the initial meltdown acts as a getter, increasing the gaseous impurity content in the

bottom portion of the ingot. At the same time, the bottom portion of the ingot is not fully melted due to a cold crucible, greater heat loss from the bottom of the crucible and less power availability. This problem is recognized and dealt with later in the fabrication process. The bottom of the ingot is cut off before forging begins, and that portion of the forging that represents the non-consolidated bottom is ultrasonically tested and cut off before further processing is permitted.

The removal of impurities is controlled by residence time, power and vacuum. A limitation of the arc melting operation is that as the power is increased, the melt rate also increases correspondingly, reducing the residence time and exposure to the vacuum.

There is always a skin effect on VAR melted ingots, and zirconium alloys are no different in this regard. This results in a localized segregation of elements near the surface of the ingot. During sampling, the sample volume needs to come from some distance under the skin of the ingot to get an accurate analytical value. This is particularly true for oxygen and iron. Oxygen concentration is high in this skin layer and iron concentration is generally low. The skin layer is removed during subsequent processing (it sloughs off as oxide during air heating for hot working operations, or it is removed by abrasive or chemical conditioning) and therefore is not representative of the final product. This effect occurs because the skin layer is the first metal to freeze and transform from the β phase to the α phase. As oxygen is an α phase stabilizer, it concentrates in the skin layer.

A condition known as ‘glow discharge’ can occur when the vacuum is impaired and the annulus between the electrode and crucible is small. This condition can lead to local overheating of the copper crucible and deposition of copper on the sidewall of the ingot. The sidewall takes on a coppery appearance. This contamination is generally associated with the surface and may be removed by machine scalping. The machining takes place on the ingot sidewall before it is used as an electrode in a subsequent melt. Otherwise, the copper will be distributed in the molten pool and it would be impossible to remove without excising that portion of the ingot.

In summary, the product of the reduction processes is compacted and melted in a vacuum to produce ingots. The chemical composition of the last ingot is the final composition of the material. Other than the opportunity for subsequent hydrogen pick-up and diffusion, all the other elemental concentrations in the finished product remain as they existed in the final ingot. The metal is now ready to be made into components for nuclear reactors.

REFERENCES TO CHAPTER 3

[3.1] ERLANK, A.J., et al., Abundance in Rock-Forming Minerals, Phase Equilibria, Zirconium Minerals “Section 40-D”, Handbook of Geochemistry, Vol. II4 (WEDEPOHL, K.H., Ed.), Springer, Heidelberg, Germany (1978).

[3.2] ERLANK, A.J., et al., Abundance in Rock-Forming Minerals, Phase Equilibria, Hafnium Minerals “Section 72-D”, Handbook of Geochemistry, Vol. II/5 (WEDEPOHL, K.H., Ed.), Springer, Heidelberg, Germany (1978).

[3.3] VLASOV, K.A., “Geochemistry and mineralogy of rare elements and Genetic Types of Their Deposits; Volume 2: Mineralogy of Rare Elements”, Israel Program for Scientific Translations, Jerusalem (1966).

[3.4] ERLANK, A.J., et al., Abundance in Common Igneous Rock Types; Crustal Abundance (Zirconium) “Section 40-E, Handbook of Geochemistry, Vol. II/4 (WEDEPOHL, K.H., Ed.), Springer, Heidelberg, Germany (1978).

[3.5] ERLANK, A.J., et al., Abundance in Common Igneous Rocks; Crustal Abundance (Hafnium) “Section 72-E”, Handbook of Geochemistry, Vol. II/5 (WEDEPOHL, K.H., Ed.), Springer, Heidelberg, Germany (1978).

[3.6] LIDE, D.R. (Ed.), “Section 14”, CRC Handbook of Chemistry and Physics, 90th edn, CRC Press, Boca Raton, FL (2010) 14–17.

[3.7] LUSTMAN, B., KERZE, F., The Metallurgy of Zirconium, McGraw-Hill, New York (1955).

[3.8] WOODCOCK, J.T. (Ed.), “Chapter 18”, Mining and Metallurgical Practices in Australasia: The Sir Maurice Mawby Memorial Volume, Monograph Series No. 10, The Australasian Institute of Mining and Metallurgy, Victoria (1980).

[3.9] HAYGARTH, J.C., GRAHAM, R.A., Zirconium and Hafnium, Review of Extraction, Processing, Properties and Applications of Reactive Metals (MISHRA, B., Ed.), TMS (2001) 1–71.

[3.10] HEDRICK, J.B., Zirconium and Hafnium, US Geological Survey Minerals Yearbook, Reston, VA (1999).

[3.11] GANGULY, C., "Advances in zirconium technology for nuclear reactor application", Proc. Symp. Zirconium 2002 (ZIRC-2002), Bhabha Atomic Research Centre, Mumbai (2002) 1–27.
[3.12] STEPHENS, W.W., "Extractive metallurgy of zirconium — 1945–the present", Zirconium in the Nuclear Industry: Sixth International Symposium, Proc. ASTM STP-824, Vancouver, 1982 (FRANKLIN, D.G., ADAMSON, R.B., Eds), ASTM International, West Conshohocken, PA (1984) 5–36.
[3.13] NIELSEN, R.H., SCHLEWITZ, J.H., NIELSEN, H., "Zirconium and zirconium compounds", Kirk-Othmer Encyclopedia of Chemical Technology, 3rd edn, Vol. 24, John Wiley, New York (1984) 863–902.
[3.14] ZELIKMAN, A.N., KREIN, O.E., SAMSONOV, G.V., "Chapter V", Metallurgy of Rare Metals, 2nd edn, Israel Program for Scientific Translations, Jerusalem (1964) 213–257 (in Russian).
[3.15] SKAGGS, R.L., ROGERS, D.T., HUNTER, D.B., Review of Anhydrous Zirconium-Hafnium Separation Techniques, US Bureau of Mines Information Circular IC 8963, Albany, OR (1984).
[3.16] MALLIKARJUNAN, R., SEHRA, J.C., Pyrometallurgical processes for the separation of hafnium from zirconium, Bull. Mater. Sci. **12** 3 (1989) 407–434.
[3.17] GHANNADI-MARAGHEH, M., "Iranian nuclear fuel cycle experience", Proc. World Nuclear Association Annual Symposium 2003, World Nuclear Association, London (2003) Session V, 1–23.
[3.18] FARNSWORTH, F., JONES, S.L., McALPINE, I., "The production, properties and uses of zirconium chemicals", Specialty Inorganic Chemicals, Special Publication No. 40 (THOMPSON, R., Ed.), The Royal Society of Chemistry, London (1981) 248–284.
[3.19] MacDONALD, D.J., GUIDOTTI, R.A., HENRY, J.G., "Method of producing zirconyl sulfate solution from zircon sand", RI 8718, US Bureau of Mines Report of Investigations, Washington, DC (1982).
[3.20] KAWECKI, H.C., Production of Alkali Fluotitanates and Fluozirconates, US Patent 2 653 855, May 25, 1953, filed May 25, 1951.
[3.21] SAJIN, N.P., PEPELYAEVA, E.A., "Separation of hafnium from zirconium and production of pure zirconium dioxide", Proc. Inter. Conf. on Peaceful Uses of Atomic Energy, Geneva, 1955, Vol. 8, United Nations, New York (1958) 559–562.
[3.22] SPINK, D.R., JONASSON, K.A., "Separation of $HfCl_4$ and $ZrCl_4$ by fractional distillation", Extractive Metallurgy of Refractory Metals (SOHN, H.Y., CARLSON, O.N., SMITH, J.T., Eds), The Metallurgical Society of AIME, Warrendale, PA (1981) 297–314.
[3.23] THORPE, M.L., Jr., WILKS, P.H., Electric arc furnace turns zircon sand to zirconia, Chem. Eng. **8** (1971) 117–119.
[3.24] SCAMMON, L.W., Jr., Material Treatment Apparatus, US Patent 3 661 764 A, May 1972, filed Nov. 1969; available on-line.
[3.25] SCAMMON, L.W., Jr., GRANT, C.L., WILKS, P.H., Processing of Silicate Ores and Product Thereof, US Patent 3 749 763, May 1974, filed Dec. 1973, available on-line.
[3.26] HEVESY, G., The discovery and properties of hafnium, Chem. Rev. **2** (1925) 1–41.
[3.27] FISCHER, W., CHALYBAEUS, W., ZUMBUSCH, M., Über die Trennung anorganischer Stoffgemische durch Verteilung zwischen zwei Lösungsmitteln, 4. Die präparative Gewinnung reiner Hafniumverbindungen durch Verteilung, Z. Anorg. Allg. Chem. **255** (1948) 277–286.
[3.28] FOLEY, E., "The production of reactor grade ZrO_2 and HfO_2", Extractive Metallurgy of Refractory Metals (SOHN, H.Y., CARLSON, O.N., SMITH, J.T., Eds), The Metallurgical Society of AIME, Warrendale, PA (1981) 341–358.
[3.29] ASH, K., et al., Zirconium-Hafnium Separation and Purification Process Using Vapors, US Patent 5 160 482, Mar. 1992, filed Feb. 1989, available on-line.
[3.30] CHIANG, P.T., LAHODA, E.J., BURGMAN, H.A., Process for Separating Zirconium Isotopes, US Patent 4 584 183, Apr. 1986, filed Dec. 1983, available on-line.
[3.31] COX, R.P., PETERSON, H.C., BEYER, G.H., Separating hafnium from zirconium, Ind. Eng. Chem. **50** (1958) 141–144.
[3.32] BESSON, P., et al., Process for the Separation of Zirconium and Hafnium Tetrachlorides from Mixtures Thereof, US Patent 4 021 531, May 1977, filed Apr. 1976, available on-line.
[3.33] TRICOT, R., The metallurgy and functional properties of hafnium, J. Nucl. Mater. **189** 3 (1992) 277–288.
[3.34] PLUCKNETT, W.K., Separation of Zirconium and Hafnium Halides, US Patent 2 816 814, Dec. 1957, filed Aug. 1953, available on-line.
[3.35] JACQUE, L., DUMEZ, P., Continuous fractional sublimation without reflux and its use in the separation of zirconium and hafnium, Chim. Ind., Genie Chim. **97** (1967) 1677.
[3.36] SPINK, D.R., Separation of Zirconium and Hafnium, US Patent 3 966 458, Jun. 1976, filed Sep. 1974, available on-line.
[3.37] DUTRIZAC, J.E., FLENGAS, S.N., "Pressure-temperature measurements on alkali and alkaline earth complex chlorides of zirconium and hafnium", Proc. Advanced Extractive Metallurgy Symposium, Institution of Mining and Metallurgy, London (1968) 572–599.
[3.38] DUTRIZAC, J.E., FLENGAS, S.N., Separation of Zirconium and Hafnium, Canadian Patent 863 258, Feb. 1971.
[3.39] FLENGAS, S.N., DUTRIZAC, J.E., A new process for separating zirconium from hafnium, Metall. Trans. B **8** (1977) 377–385.
[3.40] DENISOVA, N.D., et al., Boundary liquid-vapor curve and saturated vapor pressure of zirconium and hafnium tetrachlorides, Russ. J. Phys. Chem. **41** (1967) 30–33 (in Russian).
[3.41] BROMBERG, M.L., Purification of Zirconium Tetrachloride by Fractional Distillation, US Patent 2 852 446, September 16, 1958, filed December 7, 1956.

[3.42] ISHIZUKA, H., Separation of Zirconium and Hafnium Tetrachlorides, Japan Patent, Japan Kokai 76, 65, 093 (1976).
[3.43] CHANDLER, H.W., Method of Separating Hafnium from Zirconium, US Patent 3 276 862, October 4, 1966, filed October 24, 1962.
[3.44] BERL, L., Process for the Separation of Zirconium and Hafnium Values, US Patent 3 012 850, December 12, 1961, filed November 15, 1957.
[3.45] NEWNHAM, I.E., Process for Removal of Hafnium from Zirconium-containing Material, US Patent 2 791 485, May 7, 1957, filed June 8, 1953.
[3.46] NEWNHAM, I.E., Method of purifying Zirconium Tetrahalide, US Patent 2 916 350, December 8, 1959, filed February 19, 1957.
[3.47] KIRIHARA, T., et al., Process for Separation of Hafnium Tetrachloride from Zirconium Tetrachloride, US Patent 5 009 751, April 23, 1991, filed January 5, 1989.
[3.48] MEGY, J.A., Method of Separating Hafnium from Zirconium, US Patent 4 072 506, Feb. 1978, filed Oct. 1975, available on-line.
[3.49] MEGY, J.A., FREUND, H., Separating zirconium and hafnium in a molten salt–molten zinc system, Metall. Trans. B **10** (1979) 413–421.
[3.50] MacDONALD, D.J., Computer simulation of zirconium hafnium separation by counter current extraction, Sep. Sci. Technol. **16** (1981) 1355–1371.
[3.51] TAKAHASHI, M., MIYAZAKI, H., KATON, Y., "New solvent extraction process for zirconium and hafnium", Zirconium in the Nuclear Industry: Sixth International Symposium, ASTM STP 824, Vancouver, 1982 (FRANKLIN, D.G., ADAMSON, R.B., Eds), ASTM International, West Conshohocken, PA (1984) 45–56.
[3.52] BYERS, C.H., et al., Zirconium and Hafnium Separation in Chloride Solutions Using Continuous Ion Exchange Chromatography, US Patent 5 762 890, Jun. 1998, filed Oct. 1996, available on-line.
[3.53] SNYDER, T.S., et al., Continuous Anion Exchange Chromatography for Separation of Zirconium Isotopes, US Patent 5 174 971, Dec.1992, filed Oct. 1990, available on-line.
[3.54] SCHLECHTEN, A.W., KROLL, W.J., YERKES, L.A., Apparatus for Refining Metals, US Patent 2 482 127, September 20, 1949, filed August 7, 1946.
[3.55] FOUNDATION NICOLAS LANNERS, William J. Kroll, A Luxembourg Scientist, Foundation Nicolas Lanners, Luxembourg (1998).
[3.56] SOMMERS, J., ATI Wah Chang, personal communication, 2005.
[3.57] HUNTER, M.A., Metallurgy of the rare metals, J. Met. 5 (1953) 130–137.
[3.58] DUNHAM, W.W., TOOMEY, R.D., Ram reactor provides continuous zirconium production, J. Met. **11** (1959) 438–440.
[3.59] DOYLE, G.W., Method for Producing Zirconium Metal, US Patent 2 942 969, June 28, 1960, filed July 19, 1956.
[3.60] OGAREV, A.N., et al., "Preparation of ductile zirconium by fused salt electrolysis", Proc. 2nd Int. Conf. on the Peaceful Uses of Atomic Energy, Vol. 4, United Nations, New York (1958) 280–285.
[3.61] BARYSHNIKOV, N.V., et al., Metallurgy of Zirconium and Hafnium, Metallurgiya, Moscow (1979) (in Russian).
[3.62] KAPLAN, G.E., SILINA, G.F., OSTROUSHKO, Y.I., Electrolysis in the Metallurgy of Rare Metals, Metallurgizdat, Moscow (1963) 21 (in Russian).
[3.63] OGAREV, A.N. et al., "On processes taking place on graphite anodes in fluoride-chloride melts in metal production", Thermodynamics and Electrochemistry of Molten Salts, Kiev (1982) 98–99 (in Russian).
[3.64] ADRIENKO, A.A., DELIMARSKII, Y.K., CHERNOV, R.V., Gas-chromatographic study of the composition of anodic products of the electrolysis of the melt potassium chloride–potassium fluoride–potassium hexafluorosilicate, Ukr. Khim. Zh. **50** (1984) 1175–1180 (in Russian).
[3.65] TITARENKO, V.I., KANASHIN, Y., "Polarization of graphite electrodes in chloride-fluoride electrodes of alkali metals", All-Union Institute of Scientific and Technical Information (VINITI), VINITI 1901–76 (1976) 1–11 (in Russian).
[3.66] MEGY, J.A., Method of Reducing Zirconium, US Patent 4 127 409, Nov. 1978, filed May 1976, available on-line.
[3.67] LELAND, J.D., "Titanium by aerosol reduction", Final Report from the Titanium Industry Workshop, Welches, OR, 1997, ASME Research Report CRTD Vol. 46, American Society of Mechanical Engineers, Washington, DC (1997) 264–277.
[3.68] LELAND, J.D., Economically producing reactive metals by aerosol reduction, J. Met. **48** 10 (1996) 52–55.
[3.69] OGASAWARA, T., "Development of titanium reduction process", Final Report from the Titanium Industry Workshop, Welches, 1997, ASME Research Report CRTD Vol. 46, American Society of Mechanical Engineers, Washington, DC (1997) 278–292.
[3.70] BECKER, A.J., CAREATTI, R., Continuous Production of Finely Divided Zirconium Powder, US Patent 4 285 724, Aug. 1981, filed Nov. 1979, available on-line.
[3.71] FRAY, D., FARTHING, T., CHEN, Z., Removal of Oxygen from Metal Oxides and Solid Solutions by Electrolysis in a Fused Salt, World Patent WO 99/64638, Dec. 1999, filed Jun. 1999, available on-line.
[3.72] ROLSTEN, R.F., Iodide Metals and Metal Iodides, Wiley, New York (1961) 41–77.
[3.73] McDONALD, H.O., STEPHENSON, J.B., Chemical Vapor Deposition of Group IVB, VB and VIB Elements: A Literature Review, US Bureau of Mines Information Circular 8794, US Department of the Interior, Washington, DC (1979).
[3.74] POWELL, C.F., OXLEY, J.H., BLOCHER, J.M., Vapor Deposition, Wiley, New York (1966), 299–300, 328–330.

[3.75] LAMAZE, A.P., CHARQUET, D., “Development of hafnium tetrachloride electrolysis”, Refractory Metals: Extraction, Processing and Applications, Proc. Symp. New Orleans, 1991 (LIDDELL, K.C., SADOWAY, D.R., BAUTISTA, R.G., Eds), The Metals, Minerals and Materials Society, Warrendale, PA (1990) 231–254.

[3.76] ARZHAKOVA, V.M., et al., “Electron beam melting and casting of zirconium and titanium alloys”, Proc. Conf. Electron Beam Melting and Refining State of the Art, Reno, 1994 (BAKISH, R., Ed.), Bakish Materials Corporation, Englewood, NJ (1994) 276.

[3.77] CHILD, H.C., OLDFIELD, G.E., “Vacuum arc melting,” Vacuum Metallurgy (WINKLER, O., BAKISH, R., Eds), Elsevier, Amsterdam (1971) 553–593.

[3.78] BEALL, R.A., et. al., Cold-mold Arc Melting and Casting, Bulletin 646, US Bureau of Mines, Washington, DC (1968).

[3.79] WOOD, F.W., BEALL, R.A., Studies of High-Current Metallic Arcs, Bulletin 625, US Bureau of Mines, Washington, DC (1965).

[3.80] JOHNSTON, J.H., “Consumable electrode arc melting of non-refractory metals”, Vacuum Metallurgy (BUNSHAH, R.F., Ed.), Reinhold, New York (1958) 153–161.

[3.81] NOESEN, S.J., PARKE, R.M., “Consumable electrode arc melting of refractory metals”, Vacuum Metallurgy (BUNSHAH, R.F., Ed.), Reinhold, New York (1958) 162–171.

[3.82] BOXMAN, R.L., MARTIN, P.J., SANDERS, D.M. (Eds), Handbook of Vacuum Arc Science and Technology, Noyes, Park Ridge, NJ (1995).

[3.83] SURI, A.K., GUPTA, C.K., Melt refining of special metals and alloys, Indian Foundry J. **39** (1993) 15–27.

[3.84] MITCHELL, A., “The production of high-quality materials by vacuum melting processes,” Proc. 10th Int. Conf. on Vacuum Metallurgy, Beijing, 1990, Vol. 1, Special Melting (JIE, F., Ed.), Metallurgical Industry Press, Beijing (1990) 1–16.

[3.85] EVANS, S.C., McLAUGHLIN, D.F., A thermodynamic investigation into reactive-metal melting-furnace explosions, J. Met. **57** 10 (2005) 49–52.

[3.86] CHAPELLE, P., et al., An experimental study of the electric arc during vacuum arc melting, High Temp. Mater. Process. **4** (2000) 493–506.

[3.87] CHAPELLE, P., et al., Modelling of the arc plasma behaviour in the VAR process, J. Mater. Sci. **39** (2004) 7145–7152.

[3.88] ZANNER, F.J., BERTRAM, L.A., “Vacuum arc remelting — An overview,” Proc. 8th Int. Conf. on Vacuum Arc Metallurgy, Linz 1985, Interco International, Linz, Austria (1985) 30–71.

[3.89] CHARQUET, D., ALHERITIERE, E., “Influence of impurities and temperature on the microstructure of Zircaloy-2 and Zircaloy-4 after the beta to alpha phase transformation”, Zirconium in the Nuclear Industry: Seventh International Symposium, Proc. ASTM STP 939, Strasbourg, 1985 (ADAMSON, R.B., VAN SWAM, L.F.P., Eds), ASTM International, West Conshohocken, PA (1987) 284–291.

[3.90] THEAKER, J.R., et al., “Fabrication of Zr-2.5Nb pressure tubes to minimize the harmful effects of trace elements”, Zirconium in the Nuclear Industry: Tenth International Symposium, Proc. ASTM STP 1245, Baltimore, 1993 (GARDE, A.M., BRADLEY, E.R., Eds), ASTM International, West Conshohocken, PA (1994) 221-241.

[3.91] VAN DEN AYVLE, J.A., BROOKS, J.A., POWELL, A.C., Reducing defects in remelting processes for high-performance alloys, J. Met. **50** (1998) 22–25.

[3.92] WEBSTER, R.T., Zirconium and Hafnium, ASM Handbook, Vol. 2, 10th edn, American Society for Metals, Metals Park, OH (1990) 661–669.

[3.93] SCHEMEL, J.H., Zirconium Alloy Fuel Clad Tubing Engineering Guide, 1st edn, Sandvik Special Metals Corporation, Kennewick, WA (1989) 88–90.

[3.94] WEBER, S., Spar Type Consumable Electrodes for Vacuum Arc Melting of Zirconium or Titanium Alloys, US Patent 4 539 688, Mar. 1985, filed Oct. 1983, available on-line.

Chapter 4

FABRICATION OF ZIRCONIUM — FROM INGOT TO COMPONENT

R.A. GRAHAM
Teledyne Wah Chang,
Albany, OR, USA

C.E. COLEMAN
Chalk River Laboratories,
Atomic Energy of Canada Limited, Ontario, Canada

With N. Saibaba, J. Smith, O.T. Woo, G.J.C. Carpenter, D. Harvey, J. Tosdale, G. Beck, D. Legg, R. Sutherlin, M. Halfman and B. Webb

4.1. INTRODUCTION

Chapter 3 describes unlocking zirconium from the ore, separating the hafnium fraction, reducing to metal and finally alloying and consolidating into an ingot.

This chapter discusses the fabrication of zirconium mill products and reactor components made from zirconium ingots. Topics include primary and secondary fabrication operations as well as inspection activities such as non-destructive testing and chemical analysis.

Primary fabrication operations consist of hot deformation processing as well as cold working and various heat treatment schemes. The initial studies on zirconium and its alloys were reported in Lustman and Kerze [4.1] and Miller [4.2].

Secondary fabrication techniques such as conditioning, stamping and forming, welding and joining, and machining are reviewed. Finally, a description is provided for the fabrication of reactor mill products such as tube reduced extrusions (TREX), spacer strips, bar stock and wire as well as components fabricated from mill products, including cladding, spacer grids, channel boxes for boiling water reactors (BWRs), pressure tubes and calandria tubes for pressurized heavy water reactors (PHWRs) and fuel assemblies.

The quality aspects and the testing that ensures conformance to international standards of acceptability are explained. Included are non-destructive testing, mechanical property and hardness testing, corrosion testing, metallographic examination, microanalytical techniques and analytical testing for chemical composition.

While a thorough recitation of fabrication techniques could be the basis for an entire publication, the list of references on each topic will provide the reader with much further insight into details not presented in this chapter.

4.2. HOT DEFORMATION

Hot deformation is used to refine the as-cast microstructure of zirconium alloy ingots and to achieve shape control. This dual function requires balancing processing conditions to achieve an intermediate shape and size while reducing grain size and improving microstructural homogeneity. Ingot grain structure consists of either a basket weave or parallel α platelet structure contained in a network of prior β grain boundaries. Figure 4.1 illustrates a typical as-cast microstructure.

The prior beta grains exist as a columnar structure near the surface of the ingot, changing to a relatively equiaxed structure near the centre of the ingot.

The thermal heat flow of vacuum arc cast ingots is generally radially outward. The strong radial heat gradient contributes to columnar grains. This wide variation in structure must be converted to a more uniform, equiaxed, microstructure throughout the volume of the metal.

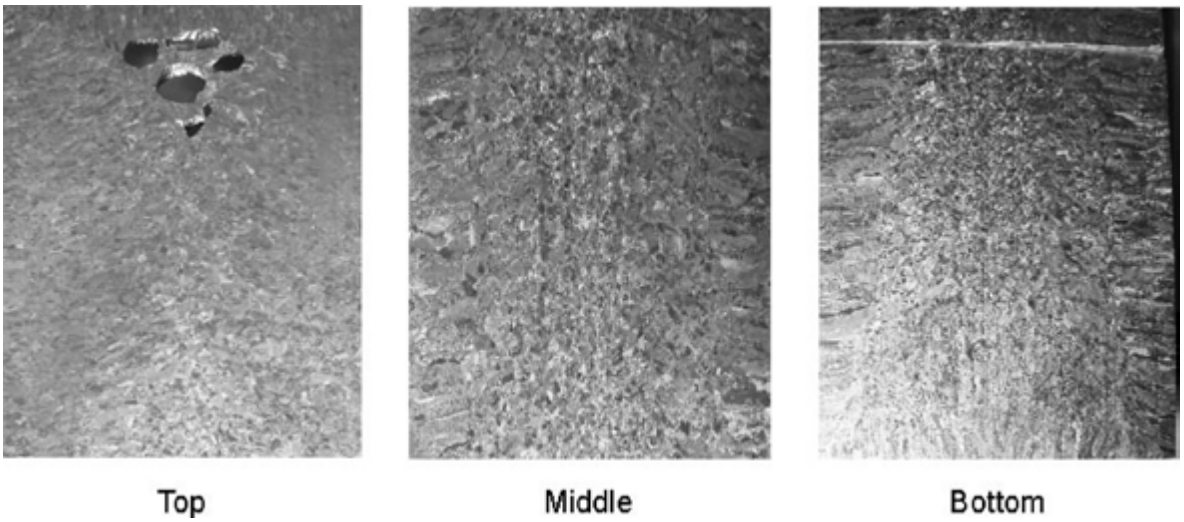

FIG. 4.1. As-cast microstructure. Longitudinal mid-diameter slices from a 585 mm ingot. Shrink pipe formation can be seen in the top slice. Columnar grain structure surrounds the periphery of the ingot, consistent with heat flow during cooling. Slow cooled areas near the centre of the ingot form an equiaxed grain structure.

Among all the thermomechanical processing methods, the ingot (bulk) metal working stage is considered to be of primary importance for two reasons. First, in this stage, major microstructural changes occur, and these have a profound influence on the subsequent processing steps. Second, in view of the large tonnage of material being processed by bulk metalworking, any improvement in processing techniques has a multiplying effect on overall productivity in manufacturing.

The ultimate objective is to manufacture components with controlled microstructure and properties, without macrostructural or microstructural defects, on a repeatable basis in a manufacturing environment. Modelling techniques are employed to arrive at optimum processing conditions, thereby controlling the microstructure in the component. This modelling permits the engineer to design optimum tooling or preform geometry without resorting to shop floor trials and to obtain the limits for the design of control systems for the fabrication process, as reported in Prasad and Seshachrayulu [4.3].

4.2.1. Workability

The measure of how easily a material can be shaped into a new form is known as workability. It is a crucial parameter and involves other terms such as formability (applied to sheet metal working), extrudability, rollability and forgeability. Many elements influence workability, including the stress state in the deformation zone, the strain and strain rate, the temperature applied and the microstructure of the material. Workability consists of two individual aspects, intrinsic workability and state of stress (SOS).

Below the $\alpha \rightarrow \beta$ phase transformation temperature, zirconium alloys have a predominantly hexagonal closed packed (HCP) crystal structure. The HCP structure has limited slip systems and is anisotropic. As a result, the preferred SOS is hydrostatic compressive. This SOS holds true for dual phase alloy systems containing beta phase (as $\alpha + \beta$) because the beta phase is cubic with higher symmetry and more slip systems. The

tensile components of the stress tensor tend to induce void nucleation and lead to excessive thinning during pure tensile stretching. SOS workability depends upon the geometry of the deformation zone in which the work piece is subjected to a three dimensional stress state. This stress state is represented as a stress tensor with nine components or six independent components of which three shear stress components contribute to the plastic flow of the material while the hydrostatic components control the workability; see Dieter [4.4].

For example, if the hydrostatic components are tensile, weak interfaces in the material will open up and cause internal fractures. Therefore, for good SOS workability the hydrostatic components should be compressive. The SOS is controlled by the nature of the applied stress and the geometry of the deformation zone, both of which are different for different metal working processes. The SOS workability is thus specific to the mechanical working process and is independent of the material behaviour.

Initial microstructure is a result of strain rate, the temperature applied and the total strain in processing as well as the history of processing and alloy chemistry; all these factors affect the intrinsic workability [4.5].

The flow stress variations with temperature, strain rate and strain are implicitly embedded in the workability response of the material. The imposed process parameters result in clear material response, while mechanisms and microstructural changes take place in the material, which necessitates characterization. For instance, some conditions such as localized or unstable flow may result in microstructural damage [4.5].

4.2.2. Hot deformation mechanisms

The microstructural changes described in Sections 4.2.2.1–4.2.2.6 may occur in zirconium metal and alloys during hot deformation.

4.2.2.1. Dynamic recrystallization

The nucleation and growth processes result in deformation, which occurs during the process of recrystallization [4.5]. New nucleation points are constantly being formed by the applied strain. In dynamic recrystallization (DRX), there is sufficient heat to drive recrystallization during deformation, even as new grain nucleating sites are forming. Static recrystallization differs from DRX in the sense that "DRX characteristics are decided by the rate of nucleation versus rate of growth under given imposed conditions of temperature and strain rate. In static recrystallization on the other hand, a fixed amount of stored energy (dependent on cold work) is released by thermally activated dislocation recovery and grain boundary migration and may be termed a kinetic process" [4.5].

Owing to DRX's good workability and stable flow, it is an important process in the hot deformation of zirconium and works by continuously softening it while refining the as-cast microstructure. For instance, to make a wrought (equiaxed α or $\alpha + \beta$) microstructure, the as-cast microstructure is broken down by DRX [4.5].

Figure 4.2 shows a typical microstructure. The dynamic recrystallization domain generally occurs in the temperature range of 1003–1153 K (730–870°C) and at intermediate strain rates of 0.1–1 s^{-1} for zirconium alloys.

Owing to DRX's ability to optimize control and hot workability of the microstructure, it is a 'safe' domain for bulk metalworking [4.5]. Conventional open die press forging is typically carried out in the strain rate–temperature domain of dynamic recrystallization.

4.2.2.2. Dynamic recovery

As described in Ref. [4.5],

> "Thermal recovery of dislocations due to their climb causes dynamic recovery that occurs in the range of 450–650°C (723–923 K) for most zirconium alloys. The dynamically recovered microstructure has well defined subgrains with interiors containing few dislocations. Dynamic recovery causes work hardening of the material, the rate of which is lower than that obtained in cold working."

Warm extrusion and warm strip rolling exploit dynamic recovery.

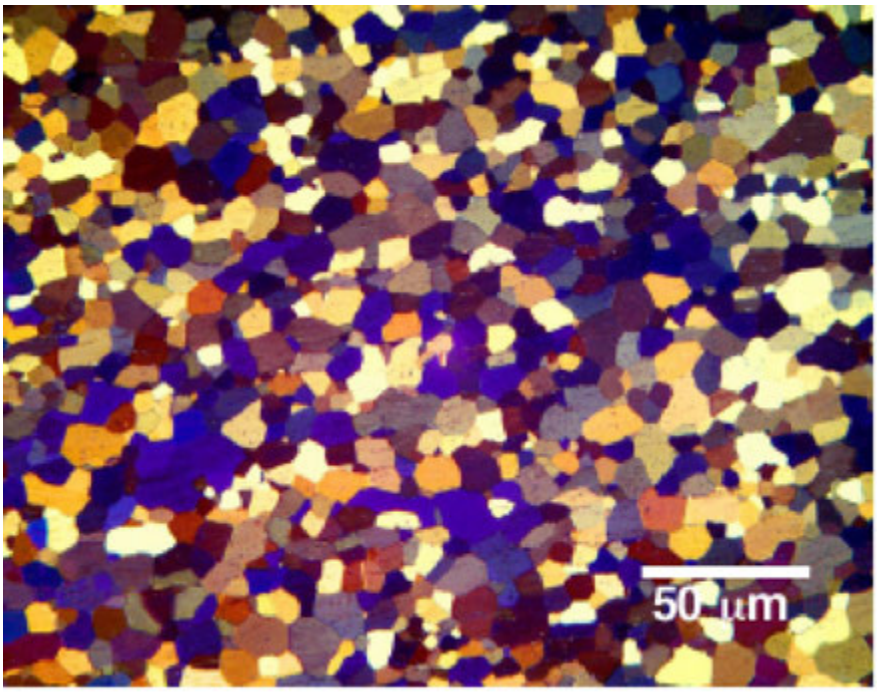

FIG. 4.2. Wrought microstructure of Zircaloy.

4.2.2.3. Wedge cracking

As described in Ref. [4.5],

> "Under conditions of low strain rate and high temperature (0.001 s^{-1}, and 950°C) where grain boundary sliding occurs under shear stress, wedge cracks may be produced at grain boundary triple points to relieve the stress concentration. Wedge cracking is reduced by increasing the strain rate, or by decreasing the hot working temperature, or by decreasing both parameters."

Wedge cracking is undesirable. It has been observed during press forging of high strength zirconium alloys, for example, Zircaloy, and is shown in Fig. 4.3.

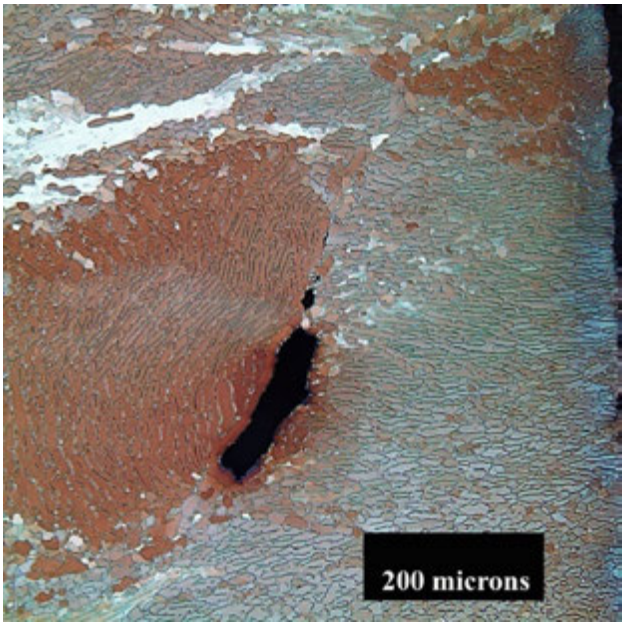

FIG. 4.3. Wedge cracking or strain induced porosity.

4.2.2.4. Porosity formation

Porosity formation is described in Ref. [4.5]. If the soft matrix contains hard inclusions, cracking and debonding result owing to deformation as a result of plastic flow of the matrix whereas no deformation takes place in the hard particles. This results in particle cracking or interface separation owing to large stress accumulation, which further leads to cavity formation, resulting in microstructural damage and finally in ductile fracture.

Zirconium nitrides (ZrN) are associated with porosity formation after hot working operations, such as plate or bar rolling. Figure 4.4 shows a nitrogen-rich particle surrounded by porosity.

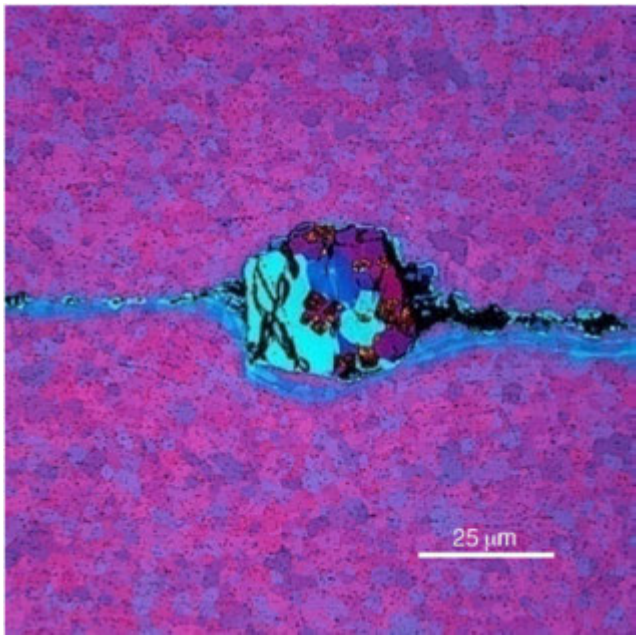

FIG. 4.4. Void with nitride particle.

Independent of the presence of hard, second phase particles, porosity may also form as the result of non-uniform strain gradients across the work piece. Porosity is often observed in rotary forged or rotary swaged products, especially near the centreline of the work piece. These types of forging operations induce a high strain rate and work hardening on the surface of the work piece. This hardening prevents deformation from reaching the central core of the work piece. The outer fibres elongate more rapidly than the core fibres. Hydrostatic compressive stresses are set up in the outer fibres and tensile stresses are set up in the inner fibres. The tensile stresses may be enough to nucleate cavities that then coalesce to form porosity. Figure 4.5 is a macrograph of porosity formation in barstock. From this example it can be seen that the SOS can be complex and non-uniform during the processing of zirconium.

4.2.2.5. Intercrystalline cracking

As stated in Ref. [4.5], "The propagation of cracks along the grain boundaries during deformation may occur when low melting compounds are formed due to segregation of certain alloying additions."

Chapter 2 has noted that low melting eutectics of iron (at 1201 K (928°C)), chromium (at 1605 K (1332°C)) and nickel (at 1227 K (954°C) can form and may lead to this kind of behaviour. Figure 4.6 displays iron segregation that led to cracking during subsequent forming operations. Large, rounded intermetallic inclusions of iron-rich ($ZrFe_2$) particles aligned near the surface of this plate. During bending the plate cracked, and from this photograph it is clear that the initiation site was the iron-rich particles. These particles segregated and aligned between the alpha platelets during extensive processing in the ($\alpha + \beta$) phase. During subsequent processing in the α phase, the aligned particles did not redistribute homogeneously because the temperature was too low for extensive Fe diffusion. The particles remain aligned as if they were still between the initial alpha platelets.

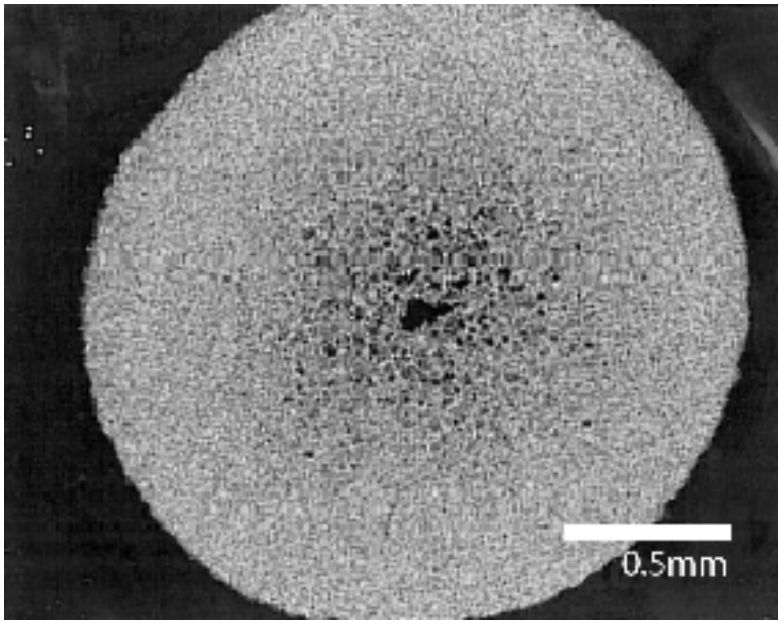

FIG. 4.5. Porosity formulation in barstock.

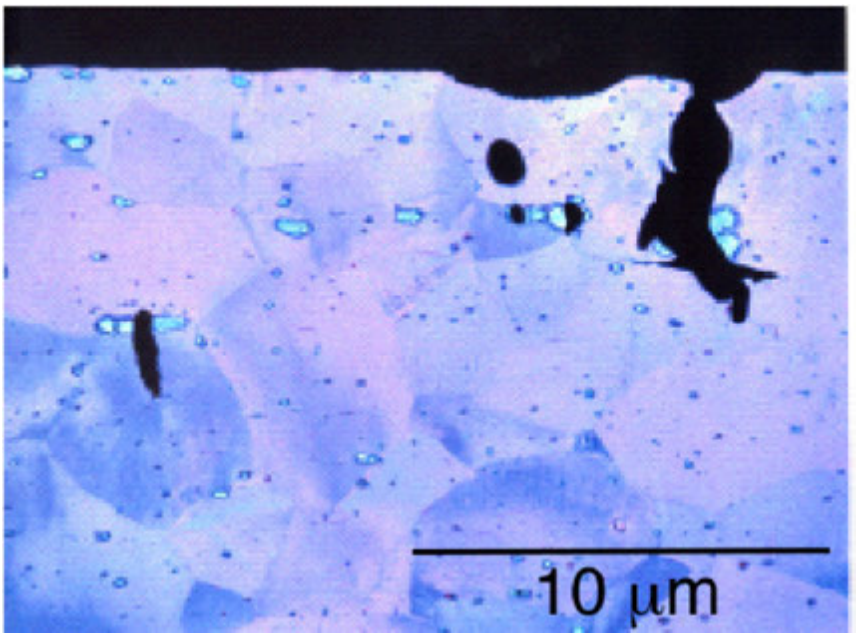

FIG. 4.6. Iron segregation: Large, rounded intermetallic inclusions of iron-rich ($ZrFe_2$) particles are aligned near the surface of this plate.

4.2.2.6. Flow instability processes

One of the most common flow instabilities is the formation of adiabatic shear bands. At high strain rates, heat is generated. Strain softening arising during high temperature deformation becomes unstable so that small deviations in the flow accelerate, increasing the plastic work and heat generation locally, softening the material still further, and eventually lowering the ability of the material to transmit the shear stresses, thus forming an adiabatic shear band.

Phase transformation, recrystallization or cracking along the macroscopic shear planes may be exhibited by adiabatic shear bands. In addition to the deformation characteristics, the physical properties of the material such as conductivity and specific heat determine the intensity of these processes [4.5].

Relative to zirconium alloys, titanium alloys have low specific heat and poor thermal conductivity and are much more sensitive to adiabatic shear band formation than zirconium alloys, even though the two metals are considered sister elements.

Flow localization is the second common flow instability manifestation in the microstructure [4.5], which is often seen to be associated with surface cracks in cold reduced strip materials. The crack propagates along the 45° principal stress directions associated with cold rolling, (the crack is oriented transverse to the rolling direction and is tilted 45° in the rolling direction) and a highly localized shear deformation is often seen coming off the tip of the crack. Flow localization usually indicates excessive strain buildup without some form of softening heat treatment such as stress relieving or recrystallization annealing.

From this discussion, it can be seen that dynamic recrystallization and recovery are beneficial mechanisms for refining the microstructure. Wedge cracking, porosity formation, intercrystalline cracking and flow instabilities are to be avoided.

4.2.3. Process maps

Process maps provide a useful guide in designing the hot working processes. The process parameters are controlled to be in 'safe' processing domains or at least away from the undesirable regions. A compilation of process maps (including for α and β zirconium, Zircaloy-2, Zr-2.5Nb and Zr-2.5Nb-0.5Cu) and the details of the theory of dynamic material model are provided in Prasad and Sasidhara's Hot Working Guide [4.5].

As described in Ref. [4.5], a process map is "a representation of the response of a material, in terms of microstructural mechanisms, to the imposed process parameters and consists of a superimposition of a power dissipation map and an instability map" (to be defined below).

A process map is generated using values of flow stress as a function of temperature and strain rate over a wide range. These values are best obtained using a hot compression test. Such a map for metallic materials exhibits safe domains for processing in terms of a combination of temperature and strain rate and will also contain regimes of flow instabilities and cracking that should be avoided.

The non-linear dynamics of a dissipative system are analysed considering a work piece deformed at high temperature as a dissipater of power. A constitutive equation describes the manner in which the power is converted at any instant into two forms: thermal and microstructural. The instantaneous power dissipated consists of two complimentary parts: *G* content, representing the temperature rise due to internal friction; and *J* co-content, representing the dissipation through metallurgical processes such as subgrain formation and creation of grain boundaries. The factor that partitions power between *G* and *J* is the strain rate sensitivity, m, of the flow stress, σ. The J co-content is given by $J = \sigma\dot{\varepsilon}m/(m+1)$ where $\dot{\varepsilon}$ = strain rate. For an ideal dissipater, $m = 1$ and $J = J_{max} = \sigma\dot{\varepsilon}/2$. The efficiency of power dissipation of a non-linear dissipater may be expressed as a dimensionless parameter, $\eta = J/J_{max} = 2m/(m+1)$. The variation of η with temperature and strain rate represents the characteristics of power dissipation through microstructural changes in the work piece material.

The power dissipation map is presented as a topographic display of the power dissipation factor. The abscissa axis represents temperature and the ordinate axis represents strain rate. The variation of efficiency of power dissipation, η, with temperature and strain rate, constitutes a power dissipation map, which exhibits domains such as dynamic recrystallization and dynamic recovery.

The flow instability parameter is microstructure related and is a function of strain rate and strain rate sensitivity. The flow instability parameter is given by $\xi(\dot{\varepsilon}) = \{\partial \ln[m/(m+1)] / \partial \ln \dot{\varepsilon}\} + m\xi(\dot{\varepsilon})$ and is calculated and also plotted as a function of temperature and strain rate. The regime where it is negative will produce flow instabilities. Such a plot is called an instability map. The physical meaning of the above instability criterion is that if the system is not able to generate entropy at a rate that at least matches the imposed deformation rate, the system will localize the flow and cause flow instability. Entropy is used in the statistical mechanical sense, whereby the increase in entropy relates to an increase in the randomness of the microcrystalline state through the introduction of the twins and dislocations needed to accommodate the external forces of deformation. When these microcrystalline 'defects' (defects in the sense that they reduce repetitive order in the crystal structure and result in increased entropy in the system) cannot be formed at a sufficiently fast rate, localized friction effects start to dominate. This creates bands or zones of higher temperature and concomitant

lower flow stress, and results in flow localizations or instabilities such as the adiabatic shear bands discussed in Section 4.2.2.6.

The instability map may be superimposed on the power dissipation map to obtain a processing map. The dynamic recrystallization domain generally occurs in the temperature range of 1003–1153 K (730–870°C) and at intermediate strain rates 0.1–1 s^{-1} for zirconium alloys. The maximum efficiency of dissipation is about 30–35% within safe domains for materials like zirconium. This energy dissipation factor is that portion of the total work on the object that is being spent on metallurgical refinement.

The super plasticity and wedge cracking domains occur at temperatures in the range of 1173–1473 K (900–1200°C) and strain rates lower than 0.01 s^{-1}. Both processes are characterized by a high efficiency of power dissipation (>60%) and a steep rise of efficiency with a decrease in strain rate. Wedge cracking may be identified by microscopic observation at the grain boundary triple points, particularly in the area of the material where a tensile component of stress occurs.

In the laboratory, manifestations of flow instabilities are easily identified by microscopic examination of deformed specimens. The adiabatic shear bands occur at an angle of 45° with respect to the applied stress axis and under intense conditions; there could be cracking along these bands. Bands due to flow localization occur at an angle of about 35° and exhibit inhomogeneous deformation.

To optimize intrinsic workability and controlling microstructure, the domain of DRX is used for the bulk metal working of zirconium and the temperature and strain rate corresponding to the peak efficiency in this domain are chosen as the optimum processing parameters. The temperature and strain rate ranges for this domain are the processing limits on the basis of which the controls may be set. To obtain a fine grain size in the component at the finishing stages of the operation, lower temperatures of the domain may be chosen at the strain rate corresponding to the peak efficiency. The process is safe if the temperature and strain rate ranges do not enter the instability or cracking regimes of the maps at any stage of operation.

4.2.3.1. Examples of processing maps for zirconium alloys

Figure 4.7 presents a processing map developed by Chakravartty et al. [4.6] for Zircaloy-2 at a strain of 0.5. The prior history for the material was as-extruded and cold drawn rods that were β quenched from 1315 K (1040°C).

The processing map in Fig. 4.7 exhibits three different safe domains:

(1) A domain occurs in the temperature range 1000–1145 K (730–870°C) and strain rate range 0.01–0.2 s^{-1}. This domain represents a dynamic recrystallization mechanism. A typical microstructure of a specimen deformed at 1073 K (800°C) and 0.1 s^{-1} is shown in Fig. 4.8. These conditions are considered optimum for forging Zircaloy-2.

(2) A domain occurring at 923 K (650°C) and 0.001 s^{-1} with a peak efficiency of about 35% represents a region of dynamic recovery; the microstructure tends to consist of low angle grain boundaries.

(3) The domain occurring at 1223 K (950°C) and 0.001 s^{-1} has a peak efficiency (68%). The equiaxed grain structure after deformation and high elongation suggests superplastic deformation.

The dotted shaded region (upper part of Fig. 4.7) corresponds to flow instability and is to be avoided.

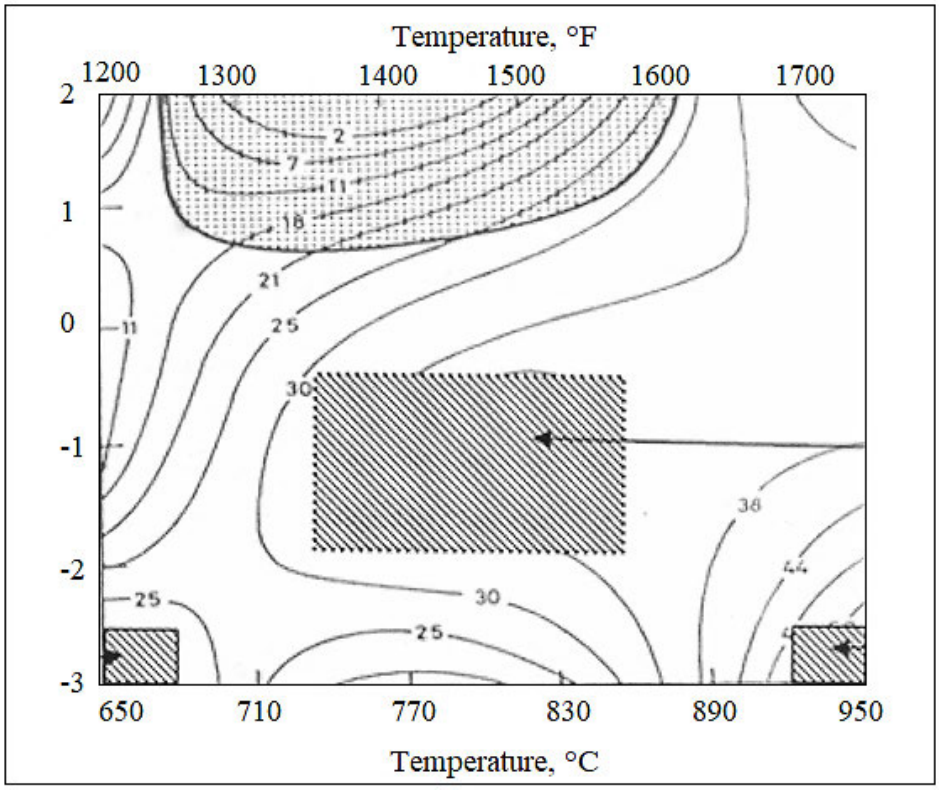

FIG. 4.7. Processing map of Zircaloy-2 at a strain of 0.5. Contour numbers represent efficiency of power dissipation as a percentage. Shaded areas represent regions of microstructural instability [4.6].

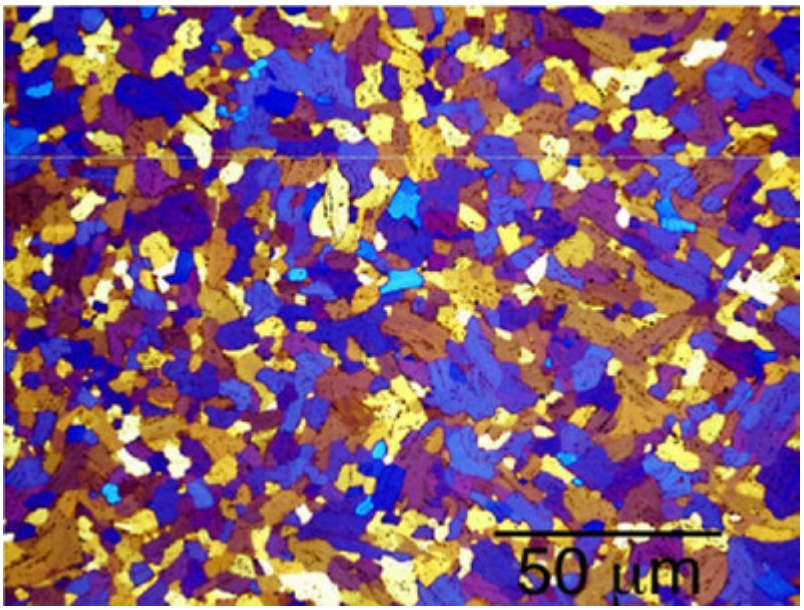

FIG. 4.8. Microstructure of Zircaloy-2 forged at 1073 K (800°C).

Figure 4.9 shows a processing map for Zr-2.5Nb at a strain of 0.4. The prior history of the material was extrusion followed by water quenching from 1273 K (1000°C) after soaking for 30 minutes in the β phase.

The processing map in Fig. 4.9 exhibits a single domain with a peak efficiency of about 50% occurring in the (α + β) phase at about 1043 K (770°C) and 0.001 s^{-1}. This regime is identified to represent the dynamic recrystallization of the acicular β quenched structure consisting of the conversion of platelets of α phase to a more equiaxed structure due to grain rotation and subsequent recrystallization. This type of DRX is strain dependent and shows flow softening. The tensile ductility in this domain is very high and the resulting grain sizes are very small.

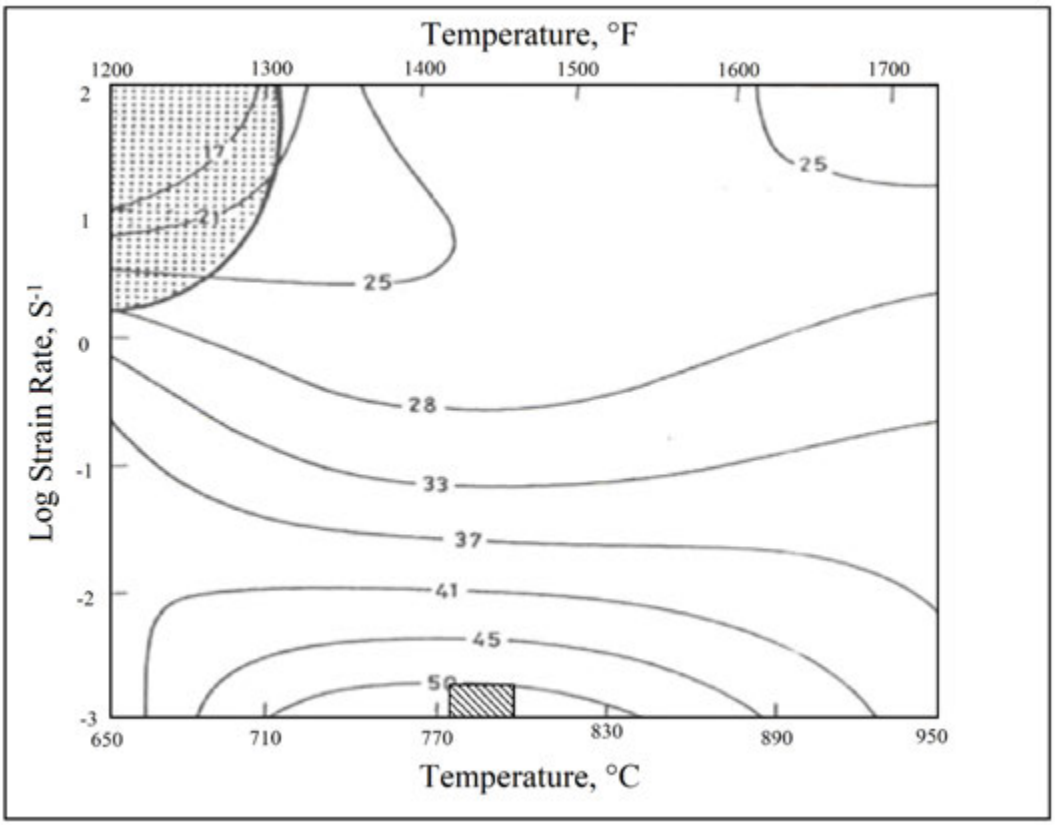

FIG. 4.9. Processing map for Zr-2.5Nb (β quenched) at a strain of 0.4. Contour numbers represent the efficiency of power dissipation. The shaded region corresponds to flow instability [4.5]. (Reprinted with the permission of ASM International. All rights reserved.)

4.3. HOT WORKING PROCESSES USED FOR ZIRCONIUM

Conventionally, hot working processes such as forging, rolling and extrusion are used in the first step of converting a cast ingot into a wrought product. The strain in hot working is large, ε = 2–4. Hot working is usually carried out at temperatures above 0.6 T_m (where T_m = the melting temperature), and at strain rates in the range of 0.5–500 s^{-1}. For zirconium alloys, this temperature is in the all β phase. Hot working refines the microstructure and controls the primary shape of the work piece. A concise summary of zirconium alloy hot working practices is provided in Ref. [4.7].

4.3.1. Press forging

Press forging is often the first hot working operation performed on zirconium alloy ingots. Press forging has two functions: the first being the metallurgical refinement of the as-cast grain structure, and the second being shape control. Figure 4.10 provides a schematic diagram of press forging.

Preheating for press forging is done in gas or electric fired furnaces. If gas furnaces are used, care must be taken to ensure that a slightly oxidizing flame atmosphere is used. If the atmosphere is reducing, there will be too much accumulation of hydrogen from the combustion products. Likewise, before loading material into the furnaces, it must be dry to avoid forming steam, which could dissociate and lead to excessive hydrogen pick-up.

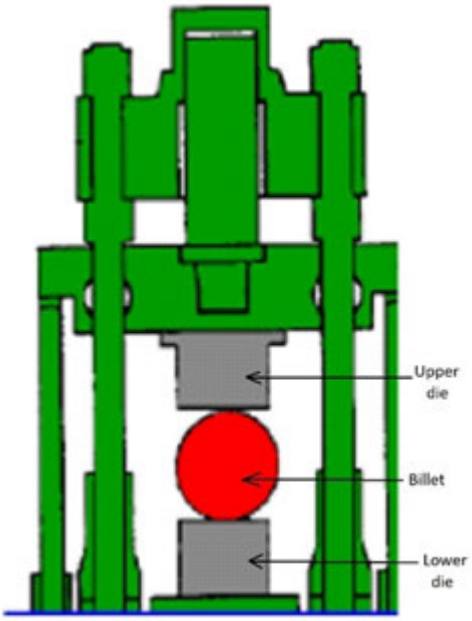

FIG. 4.10. Press forge (schematic).

The preheating must allow adequate time to heat up the centre of the ingot, and some soaking time for the ingot to come to thermal equilibrium. A glass coating can be used to prevent excessive oxidation of the ingot surface, which comes to temperature quickly and therefore experiences a long time-at-temperature. A rule of thumb for heat-up allowance is that zirconium alloys require about a minute per millimetre of cross-sectional diameter or thickness; an ingot with a diameter between 585 and 660 mm has to be heated for about 10 h. Ingots are usually preheated into the temperature range of the β phase.

The forging equipment usually consists of an open die, hydraulic energized forge. These forges can be either of a four post design with the hydraulic cylinder mounted on the top of the press, or a two post pull down design where the cylinder is located below grade. Manipulators are provided on either side of the dies to handle the material and present it to the press. Manipulators may be either rail bound or free roaming, or a combination of each. Generally, manipulators are provided on both sides of the forge, but in some cases a single manipulator is all that is used.

Press forging is a slow strain rate operation (e.g. ~ 0.01 s^{-1}). As ingots are preheated into the all beta range, they cool during subsequent forging, and much of the forging is accomplished through the $\beta \rightarrow \alpha$ transformation. This condition corresponds to the regime of dynamic recrystallization as shown in the processing map in Fig. 4.7. Most forging is done by drawing out the work piece in a lengthwise fashion. The ingot is side-forged and reduced in cross-sectional area. Typically, reductions are limited to about 30% per press pass [4.4].

The manipulators are used to maintain the shape of the piece as it is being drawn to size. Round ingots generally remain an axisymmetric shape for making round billets for bar or extrusion billets. The ingot is forged into a rough octagon, and then into a multisided polygon. Saddle dies or swaging dies can be used to finish billets to a true cylinder. An ingot with a diameter of 660 mm may be forged to a range of smaller sizes, but a convenient stopping point for subsequent quenching or further forging is a 350 mm diameter. The total area reduction is approximately 70% in this example.

During the early stages of forging, a single manipulator is sufficient to handle the ingot. As the ingot elongates, both manipulators are required owing to the length and tipping moment created. When the forged billets become too long, a shearing apparatus consisting of a wedge-shaped blade can be installed in lieu of the upper die, and the forging is sheared into two parts by the shear blade. The manipulators rotate the billet as the shear blade takes successively deeper bites into the billet. The sheared excess material is placed back in the furnace for reheating, while the remaining work piece continues to be forged to a smaller cross-section.

Slabs are ‘blocked’ first, down to a square shape, and are then spread to a rectangular shape for subsequent hot rolling to make hotbands for strip and sheet. Thus, a 660 mm diameter ingot may be forged to a slab with dimensions of 100–125 mm thickness by 500–1000 mm width × length.

Parts being forged require periodic reheating if they are cooled below about 973 K (700°C). In reality, flow stresses become greater than the pressing forces of many forges and loading capacity becomes the limiting factor during forging. If the material becomes too cold there is a danger of cracking, especially at edges and corners that have two to four surfaces exposed for radiant heat loss.

The forge dies have to have appropriate widths and radiuses on the sides of the die. The manipulators have to have the proper index spacing so that there is some overlap of each forward traverse onto the dies. If the manipulators push material forward without regard to overlap, a rough surface with peaks will result. The peaks will cool quickly, and subsequent forging will press these cooled and hardened peaks into the surface, forming laps and folds. The depth of forge bite must not exceed the height of the radius on the forging dies. To do so leads to high, localized strains that can induce wedge cracking.

Since much of the ingot breakdown forging is conducted through the transus regime, there is a considerable amount of segregation of alloying elements. The alpha stabilizers, such as oxygen, nitrogen and tin, will partition to the alpha phase, and beta stabilizers such as iron, chromium, nickel and niobium will partition to the beta phase. This segregation is eliminated by the addition of a recrystallization anneal in the β phase followed by water-cooling, or ‘beta quench’ as it is known. By reheating into the beta range, all the alloying elements are dissolved and short range diffusion processes even out spatial distributions of these elements. Quenching in water is a method of retaining the spatial uniformity of the alloying elements. Beta quenching also refines second phase particle size. Any subsequent forging must be done in the all-alpha temperature range (or $(\alpha + \beta)$ range for two phase alloys such as Zr-2.5Nb) to prevent re-segregating the alloying components.

4.3.2. Rotary forging and hot swaging

In many cases, press forging is the only method of performing primary breakdown of the material, and extrusion billets for cladding, for example, are press forged directly. An elegant method of finishing billets for extrusion or bar rolling is to employ a rotary forge. Rotary forges consist of four opposing hammers or dies that are mechanically reciprocated in a radial fashion to the billet being forged. There are two rail bound manipulators that handle the material and feed it through the hammers. The rotary forge excels in forging axisymmetrical shapes such as cylinders, hollow cylinders, cones, stepped cylinders and even round cornered squares. Rotary forges were first developed to forge large, fixed position gun barrels. The forging action is rapid with several hundred strokes per minute. Figure 4.11 shows, schematically, the operation of a rotary forge.

In practice, the rotary forge is used to reduce a large polygonal press forging into a billet suitable for extrusion or bar rolling. A typical machine can handle an input size of 380 mm diameter and reduce that down to 65 mm diameter with appropriate die changes. This deformation represents a 95% reduction in area. The rotary forge can work with a broad range of temperatures, but for zirconium alloys it is usually limited to forging in the α or (α + β) phase range.

The manipulators advance the material through the hammers as well as rotate the material with every stroke. The manipulators are closely coupled, electronically, to the motion of the hammers and rotation is effected with the hammers open. Rotation stops as the hammers close down on the forged work piece. Large machines can hold a tolerance to ± 0.5 mm on a piece of about 200 mm in diameter. By fixing the manipulators from rotating (longitudinal translation only) it is possible to forge a near square shape with rounded corners.

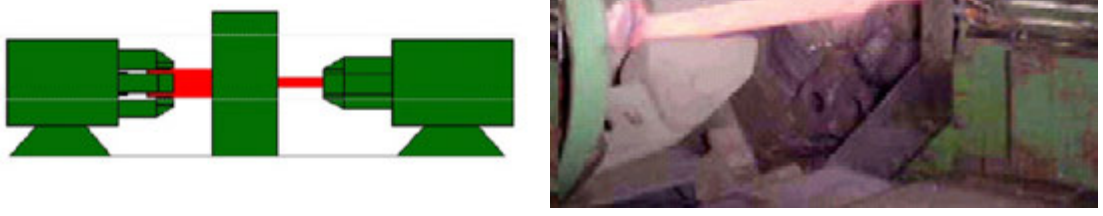

(a) (b)

FIG. 4.11. Rotary forge schematic (a) and (b) view of manipulator feeding billet into the reciprocating dies.

Rotary forges are used primarily for shape control. They are not as effective as press forges for refining grain structure because they tend to operate at higher strain rates and lower temperatures, outside the strain rate–temperature space that promotes dynamic recrystallization. Dies have to be designed to impart strain energy all the way to the centre of the billet. If not, the billet is worked excessively on the surface and this leads to end related defects known as ‘end suck’, and potentially to strain induced porosity near the centre of the work piece. Strain induced porosity is the result of the central portion of the billet being

placed in tension as it elongates to keep pace with the outside fibres elongating under radial compressive strains (Section 4.2.2.4).

Modern rotary forges utilize programmable logic controllers; variables such as feed rate, pass schedules (reduction per pass) and manipulator coordination are automated. Manipulators can operate singly or in tandem to control the motion of the billet through the dies. Cooling tables are generally provided at the exit of the rotary forge to allow the freshly forged billet an opportunity to cool down prior to handling it.

Hot swaging machines are synonymous with rotary forges, only they are smaller machines. The input size of the hot swage might be 65 mm diameter with a capability of going to 18 mm diameter as a finished size. This deformation is a 90% reduction in area. These machines are often set up with in-line furnaces on either side of the forging block. The manipulators are fixed (non-rail-bound) and the spindles are hollow permitting the forging to pass through the fixed manipulator. The four opposing hammers are arranged like the rotary forge. The in-line furnaces are necessary because these small diameter bars do not have sufficient mass to retain heat. Hot swaging is used to reduce large bars to a small diameter appropriate for end cap bar stock and for wire drawing.

4.3.3. Hot rolling and hot bar rolling

Hot rolling of plates, hotband and bars are very similar processes except for the shape of the item being rolled. Hot mills are classified by the number of rolls used and by whether the mill is set up for continuous rolling or piece rolling. Items such as plates are generally rolled on four-high reversing mills. These mills have two small diameter work rolls, backed up by two large diameter rolls to prevent deflection of the work rolls. These mills operate in a reversing fashion with each pass through the mill resulting in a reduction of area and lengthening of the slab. Slabs can be either straight rolled, or cross-rolled to spread the plates out to a wider finished shape. These mills input slabs in the 100–150 mm thick range and can roll down to a thickness of 4 mm. This deformation represents an area reduction of about 95%.

Reversible hot finishing mills, such as Steckel mills, are used to roll continuous hotband coils. In this arrangement, a slab is preheated by the use of induction coils or pusher-type hearth furnaces, and the slab is fed to a four-high roughing mill that reduces it to a thickness of about 16 mm. This resulting ‘transfer bar’ is then hot transferred through a flying shear that crops off the lead and tail end blooms (these bloom ends elongate to form rounded or fingernail shaped ends and need to be trimmed before the subsequent rolling operations start). The transfer bar is then fed to the Steckel mill, which is a reversing four-high mill (two work rolls, with two large diameter backup rolls) with two coilers on either side of the mill. The coiler drums are housed in furnace boxes that maintain temperature to the hotband as it is being reduced.

As the transfer bar enters the Steckel mill, a first pass is taken and a diverter skid plate directs the nose end of the transfer bar up into the coiler. The mill is then reversed and the tail end of the hotband now becomes the lead end and it too is diverted to a hot box. The material is passed back and forth for five or seven passes (depending on the end thickness required) with a reduction in area of about 5% per pass. At the conclusion of the last pass, the material is released to an upcoiler where it forms a coil of up to 120 m in length.

Another type of hot mill is the continuous mill, with roll stands most often in a four-high configuration. This high production-rate mill typically has four or five roll stands in tandem. Each roll stand makes a reduction on the metal and as the metal passes through each

roll stand it becomes thinner and elongates. These mills are generally fed slabs that have been rough rolled on a reversing mill to get a slab with the shape required to roll efficiently.

Hotband can also be hot rolled on two- or four-high reversing mills in shorter lengths without coiling. The metal can be reheated as required. Area reductions of about 10–20% per pass are used, with total area reductions being about 75%. Individual strips may be up to 10 m long. From this description, it is seen that the continuous rolled hotband coils enjoy some advantages over piece-rolled hotband, in that much longer lengths are produced from one slab, and the gauge control, shape control and thermomechanical properties can be much more uniform.

Hot mills operate at high enough strain rates that the most efficient metallurgical refinement does not occur (compared with press forging). The caveat to this statement is where hot rolling is combined with reheats where recrystallization can take place.

Bars can be hot rolled in an analogous manner to continuous hot rolling of sheet. In this concept, a large diameter bar of about 150 mm diameter is preheated with induction or air atmosphere gas-fired furnaces. The bar is fed into a multistand bar rolling mill. These mills can be of the Danieli-type, with a pair of upper and lower rolls that have grooves machined into the circumference of the rolls to accommodate the bars, or they can be of the Kocks-type mill where three grooved rolls are situated at 120° intervals around the periphery of the bar.

In a Danieli mill, the first stand converts the bar into a flattened oval shaped cross-section and even-numbered stands convert it back into a round. These mills have from 8–16 stands, always an even number, as odd-numbered stands make an oval shape and even-numbered stands convert it back to a round. A 16-stand mill can convert a 300 kg, 150 mm diameter bar to 15 mm diameter wire in less than five minutes. This deformation represents a reduction in area of 90%. Large, water-cooled coilers are available at the exit end of the mill to coil the wire as it exits the last stand. These mills can also roll straight lengths and include flying shears to crop bars to a uniform length upon exiting the mill. Large diameter structural bars are made by opening up the small diameter finishing stands and only using the larger diameter starting and intermediate stands.

Kocks mills are more amenable to hot rolling zirconium alloys because they maintain axisymmetric shapes during rolling. The Kocks mill has stands that alternately roll the bar from a hexagonal shape to a round shape, back and forth, as it is being reduced in area. This format results in less folding and lapping of the surfaces than occurs with the extreme shape changes that occur in a Danieli-type mill.

Defects that are common with hot rolling include rolled-in debris such as oxide particles, rolled-in laps and seams, and overheating by adiabatic work into the beta temperature range. Rolled-in debris can be minimized by induction heating (which reduces oxide scale on the surface of the slab because heating times are short), by blowing off loose oxide particles prior to hot rolling and by thoroughly cleaning the mill rolls and conveyor rolls prior to use.

Overheating can be controlled by a combination of preheat temperature control, strain rate control, the amount of reduction per pass and by intentional delays built into the process to allow the heated metal to cool to a lower temperature. Generally, hot rolling produces sound structures in the interior of the piece being rolled. There is little concern for porosity or internal voids formed during hot rolling.

4.3.4. Indirect extrusion and expansion

The process of indirect extrusion is utilized to produce hollow shells and billets from solid billets or disks. The hollow shells are then extruded to form blanks. A billet is placed in a cavity (i.e. a close-ended container) and then an extrusion press ram pushes a punch into the raw material, as shown in Fig. 4.12 [4.8]. While the punch moves forward, the wall of the product can move backwards, escaping through the annular gap between the punch and the container. Obviously, with all the sliding surfaces, a significant amount of friction exists. Lubricants are utilized to reduce this friction. Lubricants can consist of copper metal or graphite-bearing glasses. Because the wall of the tube thus produced moves backwards in the direction opposite to that of the forward motion of the tool, the process is sometimes also called back-extrusion.

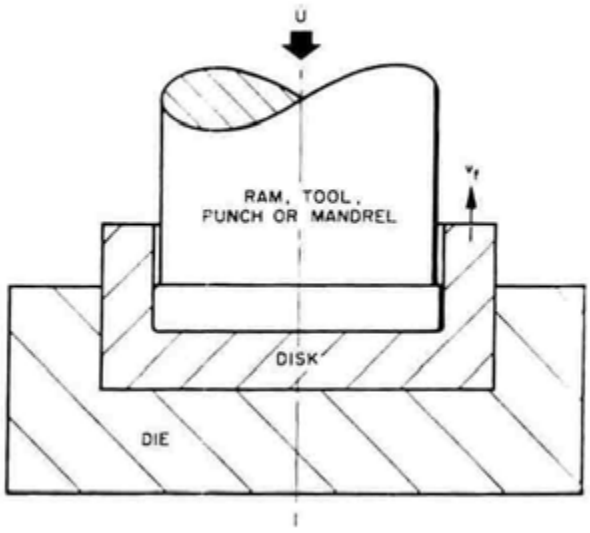

FIG. 4.12. Schematic diagram of indirect extrusion (reprinted with permission from Ref. [4.8], copyright ASM International).

In the indirect extrusion of thick wall tubes of Zircaloy, it is sufficient to place a copper disc between the billet and the extrusion stem to obtain a smooth internal surface.

The process shown in Fig. 4.13 [4.8] is termed expansion, since a pilot hole is drilled through the billet and the expanding tip expands the hole to near final size. The expansion process is frequently used to give large amounts of deformation in high strength material such as zirconium alloys, titanium alloys, stainless steels and superalloys. A closely related process is piercing, whereby the piercing tip is thrust through the metal without the pilot hole. Expansion is preferred over piercing because the bore diameter can be made larger with less force, and better concentricity can be held. The expanding tip follows the pilot hole. The expanded inside surface also has a better surface finish than a pierced billet.

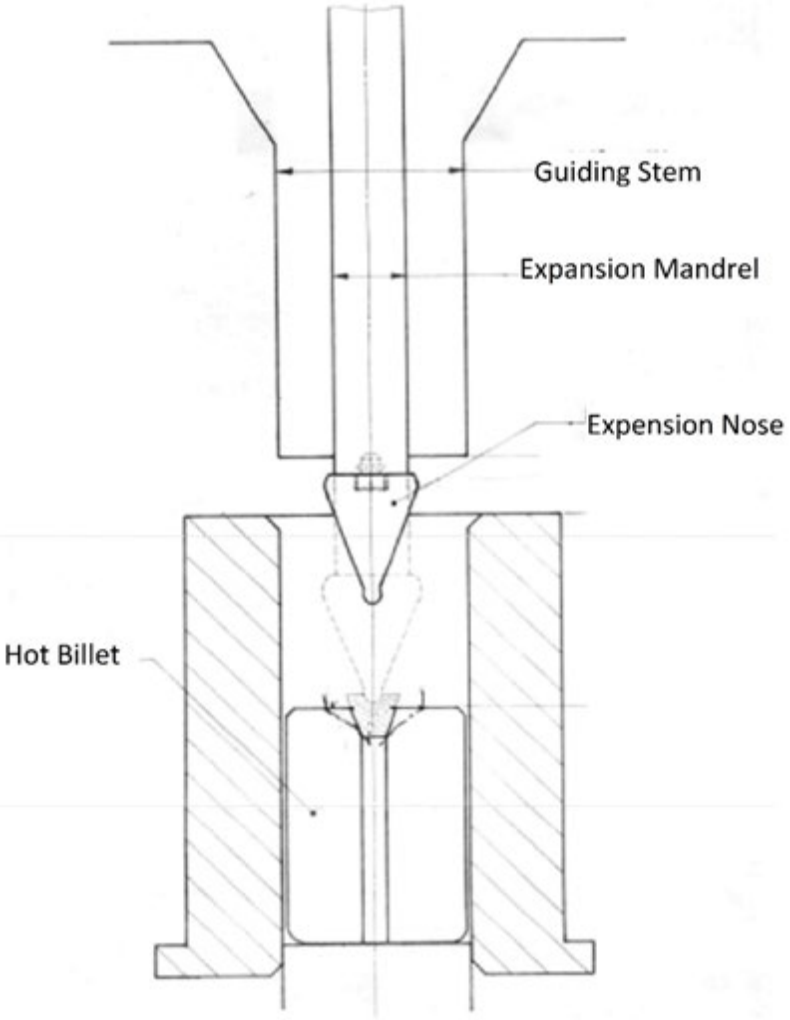

FIG. 4.13. Expansion process [4.8].

The two common defects that limit the extent to which indirect extrusion can be used are the fishskin defect in the interior of the tube and the cavitation defect at the outside bottom. In addition to these, eccentricity and galling are also observed at times.

The fishskin rupture in the interior (Fig. 4.14 [4.8]) is most prevalent during the early stages of indirect extrusion and for heavy wall thicknesses. Cavitation, shown in Fig. 4.15 [4.8], takes place at the end of the stroke and limits the permissible penetration, thus forcing the designer to leave a heavy-gauge bottom on the closed-end cup of the indirect extrusion.

When fishskin occurs in the interior, it originates at the corner of the ram and penetrates deeply into the tube. Observation of fishskin at the end of the stroke reveals that whenever there is a tendency for this defect to occur, there is also a tendency for cavitation to appear.

Eccentricity may occur owing to misalignment of the bottom surface of the punch with the die; consequently, uniform wall thickness of the product is not obtained. Inhomogeneous heating can exacerbate the eccentricity. Eccentricity can be prevented by using a punch recessed on the front face, and by providing for uniform heating of the billet before expansion.

FIG. 4.14. Fishskin defect. The defect started at the interior of this tube and telegraphed to the outside (reprinted with permission from Ref. [4.8], copyright ASM International).

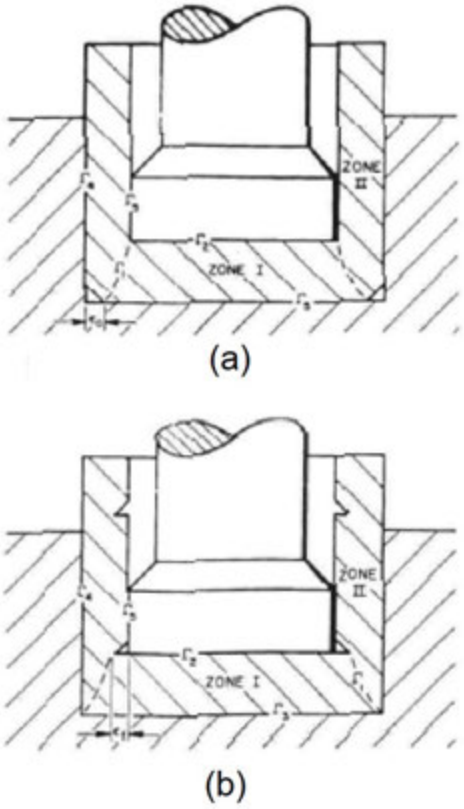

FIG. 4.15. Fishskin and cavitation during final stage of indirect extrusion: (a) Representation of flow with cavitation; (b) Representation of flow with fishskin. It should be noted that fishskin starts at the corner of the ram on the inside of the workpiece and then telegraphs to the outside (reprinted with permission from Ref. [4.8], copyright ASM International).

Galling is a defect in which the tool leaves deep grooves in the product. Galling may be observed on both inner and outer cylindrical surfaces of the product. The effect of eccentricity and improper lubrication causes this defect. An adequate layer of lubricant must be applied to all surfaces, including the lead end of the billet, the outside of the billet and between the mandrel and the inside of the billet. When long tubes are to be produced, the surface stretches and the film of lubricant may break open under high pressure resulting in deep scratches and galling. Therefore, the lubricant has to be ensured to be present until the end of the stroke. Various schemes are employed to lubricate the punch. A common technique is to place a matt of fibreglass on the top of the billet prior to back-extrusion. The glass melts under the combination of heat and pressure and supplies lubrication for the whole process.

4.3.5. Direct extrusion of zirconium alloys

Working at high temperatures results in a lowering of the energy required to deform the metal and an increased ability to flow without cracking. The rapid diffusion at hot working temperatures aids in decreasing the chemical inhomogeneities of the cast ingot structure. Small internal voids and porosity are eliminated by diffusion, welding these cavities together, and the coarse columnar grains of the casting are broken down and refined

into smaller equiaxed recrystallized grains. The changes in the metallurgical structure as a result of hot working lead to an increase in ductility and toughness over those of the as-cast state.

Hot working has certain disadvantages. Because high temperatures are usually involved, surface reactions between the metal and the furnace atmosphere become a problem. Ordinarily, hot working is done in air, oxidation results, and a considerable amount of metal may be lost. Reactive metals such as zirconium and titanium are severely embrittled by large concentrations of oxygen, hydrogen and nitrogen and therefore they must be hot worked in an inert atmosphere or protected from the air by a suitable barrier.

Although the β phase has the best hot working properties because the flow stress of β zirconium is low, and dynamic recrystallization is possible, extrusion temperatures of 973–1073 K (700–800°C) are preferred because gas (light element) pick-up is much reduced.

The structure and properties of hot worked metals are generally not so uniform over the cross-section as they are in metals that have been cold worked and annealed. Since the deformation is always greater in the surface layers, the metal will have a finer recrystallized grain size in this region and because the interior cools off more slowly than the external surfaces, grain growth can occur in the centre of large size pieces.

Zirconium, like titanium, welds very easily to the tooling during deformation and good lubrication is always required. One method of lubrication is extrusion in a skirt or can. The extrusion billets are usually surrounded with a sheath of copper or brass, sometimes with an intermediate layer of iron or soft steel sheet, and heated in a flame or electric resistance furnace. The sheathing hinders or prevents gas absorption and long lengths can be extruded with a good surface finish when conical dies ($2\alpha = 90–140^{o}$, where α is the included angle of the entry cone to the die) and additional lubrication such as oil or water-based graphite are used. The sheath is removed from the extruded product either mechanically or by dissolving in nitric acid.

Another method of lubrication is to initially heat the zirconium billets in a salt bath and then coat them with a glass film. Temperatures of 1273–1373 K (1000–1100°C) are used for this method. This method of billet heating can detract from the surface quality of the product because of the detrimental effect of the salt.

The high temperature flow stress of most zirconium alloys is relatively low and not very strain rate dependent; consequently, a wide range of extrusion speeds can be used. The lower speed limit is slow, approximately 1.5 m/min exit speed, because there is only a slight danger that the billet will stick. The upper limit for the exit speed is taken to be approximately 60 m/min. Much extrusion of zirconium alloys takes place in the dynamic recovery regime and well away from the region of flow instability characterized by adiabatic shear band formation. For example, the extrusion temperature for Zircaloy is 923–1023 K (650–750°C) and for Zr-2.5Nb it is 1053–1093 K (780–820°C), both at strain rates between 10^{-1} and 10^{-3} s^{-1}; see Figs 4.7 and 4.9.

Tubes can be produced by direct extrusion by attaching a mandrel to the end of the ram. The clearance between the mandrel and the die wall determines the wall thickness of the tube. Tubes are produced either by starting with a hollow billet or by a two step extrusion operation in which a solid billet is first pierced and then extruded. Figure 4.16 shows a schematic diagram of the direct extrusion process used to produce tubing [4.4].

The principal variables that influence the force required to cause extrusion are:

— The type of extrusion (direct versus indirect);
— The extrusion ratio;

— The working temperature;
— The preheat time;
— The extrusion rate;
— The frictional conditions at the die and container wall.

In Fig. 4.17 [4.4], the extrusion pressure is plotted against ram travel for direct and indirect extrusion. Extrusion pressure is the extrusion force divided by the cross-sectional area of the billet. The rapid rise in pressure during the start of ram travel is due to the initial compression of the billet to fill the extrusion container. For direct extrusion, the metal begins to flow through the die at the maximum value of pressure, the breakthrough pressure. As the billet extrudes through the die, the pressure required to maintain flow progressively decreases with decreasing length of the billet in the container. For indirect extrusion, there is no relative motion between the billet and the container wall. Therefore, after the initial compression the extrusion pressure is approximately constant with increasing ram travel and represents the stress required to deform the metal through the die.

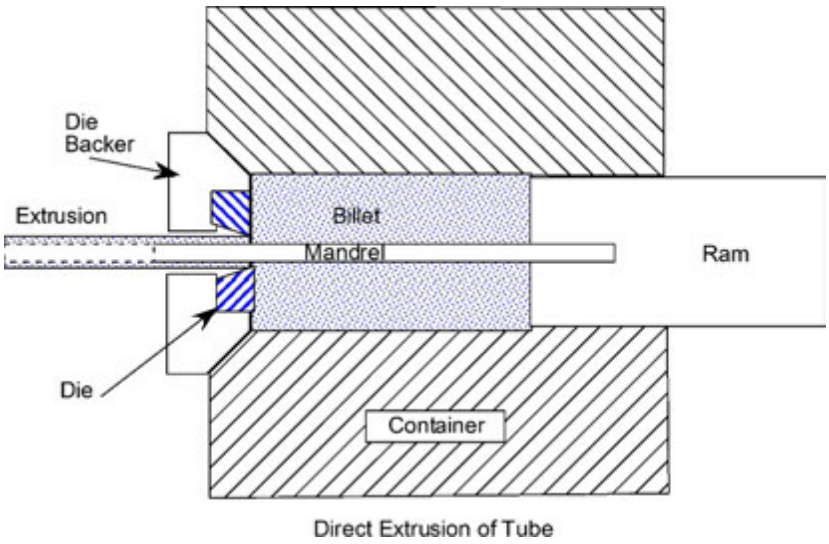

FIG. 4.16. Direct extrusion of tubing [4.4].

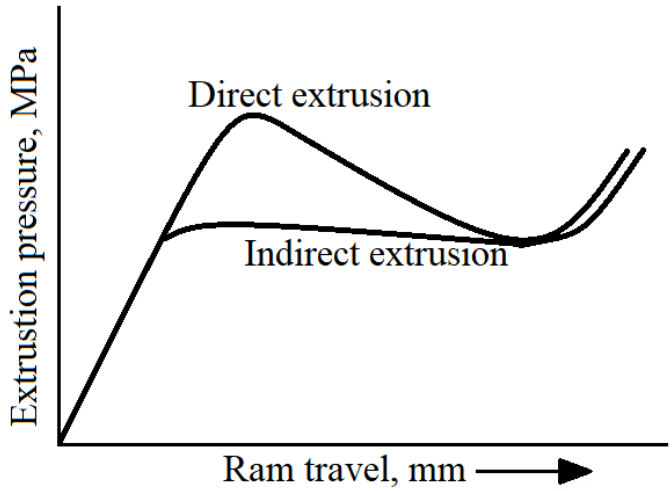

FIG. 4.17. Extrusion pressure versus ram [4.4].

The extrusion ratio, R, is the ratio of the initial cross-sectional area of the billet, A_0, to the final cross-sectional area after extrusion, A_f:

$$R = A_0/A_f \tag{4.1}$$

The extrusion pressure, P, is directly related to the natural logarithm of the extrusion ratio, so that the extrusion force may be expressed as:

$$P = \mathrm{K}A_0 \ln(A_0/A_f) \tag{4.2}$$

where K is the extrusion constant, an overall factor that accounts for the flow stress, friction and inhomogeneous deformation for a given material.

Figure 4.18 [4.4] shows the characteristic types of deformation in extrusion.

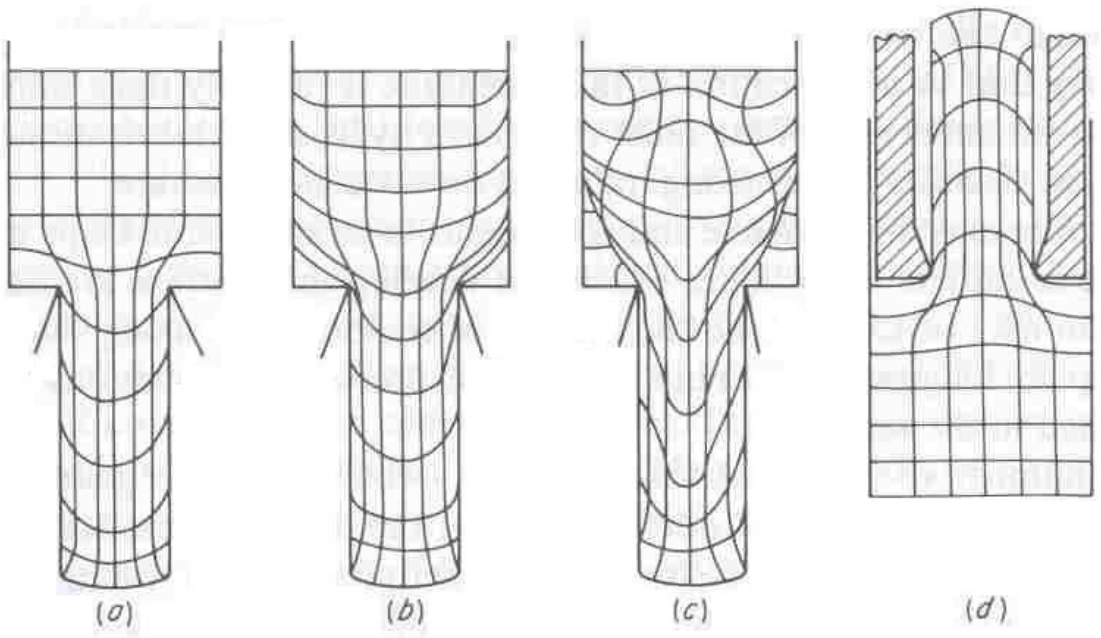

FIG. 4.18. Deformation types in extrusion [4.4].

Figure 4.18 (a) and (b) are indicative of low container wall friction with a well lubricated billet. Deformation of the billet is uniform until close to the die entrance. Figure 4.18 (b) shows the increased wall thickness distorting the grid pattern. If the billet surface in contact with the cold container wall is chilled, the container–billet interface friction will further increase and the grid pattern will be severely distorted, as shown in Fig. 4.18 (c). Figure 4.18 (d) shows the flow pattern resulting from indirect extrusion [4.4].

There are a few extrusion defects that must be avoided. Because of the inhomogeneous deformation in the direct extrusion of a billet, the centre of the billet moves faster than the periphery. As a result, the dead metal zone extends down along the outer surface of the billet. After about two thirds of the billet is extruded, the outer surface of the billet moves towards

the centre and extrudes through the die near the axis of the rod. Since the surface of the billet often contains an oxidized skin, this type of flow results in internal oxide stringers. This defect can be considered to be an internal pipe. On a transverse section through the extrusion, this defect will appear as an annular ring of oxide. The tendency towards the formation of this extrusion defect increases as the container wall friction becomes greater. If a heated billet is placed in a cooler extrusion container, the outer layers of the billet will be chilled and the flow resistance of this region will increase. There will be a tendency for the central part of the billet to extrude before the surface skin, and the tendency for the formation of the extrusion defect is increased. Hence, it is essential to keep the container in a preheated condition.

Zirconium alloy billets extruded with copper or brass cladding normally do not exhibit a very smooth surface finish after the removal of cladding. This poor surface finish is due to the difference in relative flow stresses of the zirconium alloy and clad material at extrusion temperature. The quantity of graphite lubrication applied on the container and the dies must be optimized to prevent any lubrication failure on the zirconium alloy billets during extrusion. Lubrication failure during early stages leads to the pick-up of metal over the die surface, which leads to deep scoring marks — galling — on the outer surface of the extruded tubes.

Extrusion temperature and preheat soak time of billets can have a measurable effect on the microstructural and mechanical properties of finished zirconium alloy tubes. Such a study on two phase Zr-2.5Nb pressure tubes for PHWRs has been made [4.9]. The β quenched billets from a quadruple melted ingot were extruded in the (α + β) phase at 1053 K, 1088 K and 1123 K (780°C, 815°C and 850°C) with varying preheat soak times of 15–300 minutes. The billets were extruded maintaining an extrusion ratio of 10.5:1 and a ram speed of 0.01 m/s. The extruded hollows were finished by cold drawing (with 28% area reduction) and then stress relieved at 673 K (400°C) for 24 h. The tensile properties were found to vary with the preheat temperature and soak time, as shown in Fig. 4.19. The tubes with 1053 K (780°C) preheat have a very fine and uniform α grain structure, giving high strength and fracture toughness, as shown in Fig. 4.20, at all soak times. The opposite was true for the 1123 K (850°C) soaks; the α grain structure was coarse and inhomogeneous, and materials tended to be less strong and less tough. Figure 4.21 shows scanning electron microscope (SEM) micrographs of extruded hollows under two extreme conditions of preheat temperature and soak times. The extrusion constant, k, of the alloy is controlled by the flow stress of each phase, α and β, and their volume fraction, which changes at differing preheat temperatures. As the preheat temperature is increased the volume fraction of the α phase, V_{α}, decreases rapidly as shown in Fig. 4.22. The flow stress for the BCC β phase is significantly lower than for the α phase material, which results in a very rapid decrease in the extrusion pressure as the temperature increases within the two phase field (Fig. 4.23). The decrease in extrusion pressure with increasing preheat soak time can be attributed to the increase in grain size.

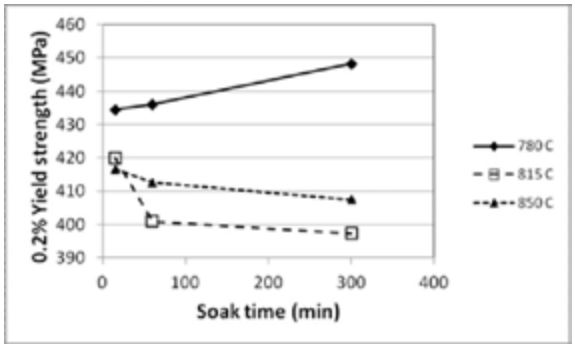

(a)

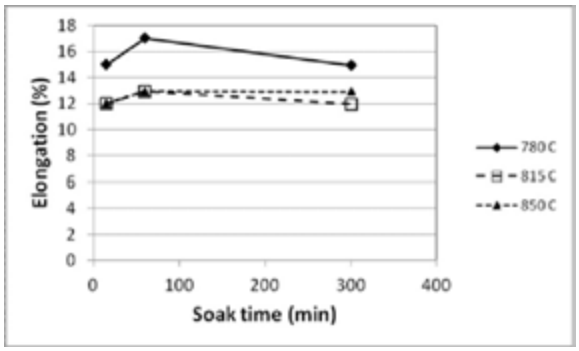

(b)

FIG. 4.19. Effects of billet preheat temperature and soak time on the longitudinal tensile properties of Zr-2.5Nb (front ends) tested at 300°C, that is on: (a) yield strength; (b) % elongation, (reproduced from Ref. [4.9] with permission courtesy of AECL, Canada).

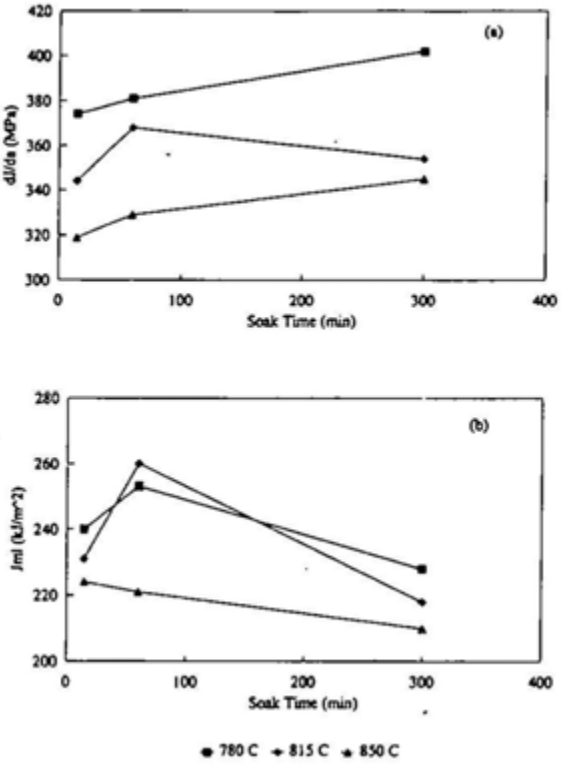

FIG. 4.20. Effects of billet preheat temperature and soak time on the fracture toughness properties of Zr-2.5Nb pressure tubes tested at 250°C (reproduced from Ref. [4.9] with permission courtesy of AECL, Canada).

A process known as coextrusion is used to produce BWR liner tubes to mitigate the effects of pellet–clad interactions (see Chapter 9, Volume 3 of this publication). In this process an inner, pure or nearly pure zirconium liner tube is fixed inside an outer billet, typically made from Zircaloy-2. The pure zirconium tube is extruded from a billet and is machined to mate with a large diameter hole machined in the outer Zircaloy-2 billet. The mating surfaces are cleaned, and the liner tube is electron beam welded to each end of the billet under a vacuum. The assembled billet is lubricated, heated and direct extruded. During the extrusion process, there is sufficient temperature, pressure and time to metallurgically bond the pure zirconium liner to the outer tube of Zircaloy-2. Figure 4.24 is a photomicrograph of the bond between the pure zirconium liner and the outer Zircaloy-2 tube. Other liner materials, such as zirconium with additions of tin or iron, are extruded in a similar fashion.

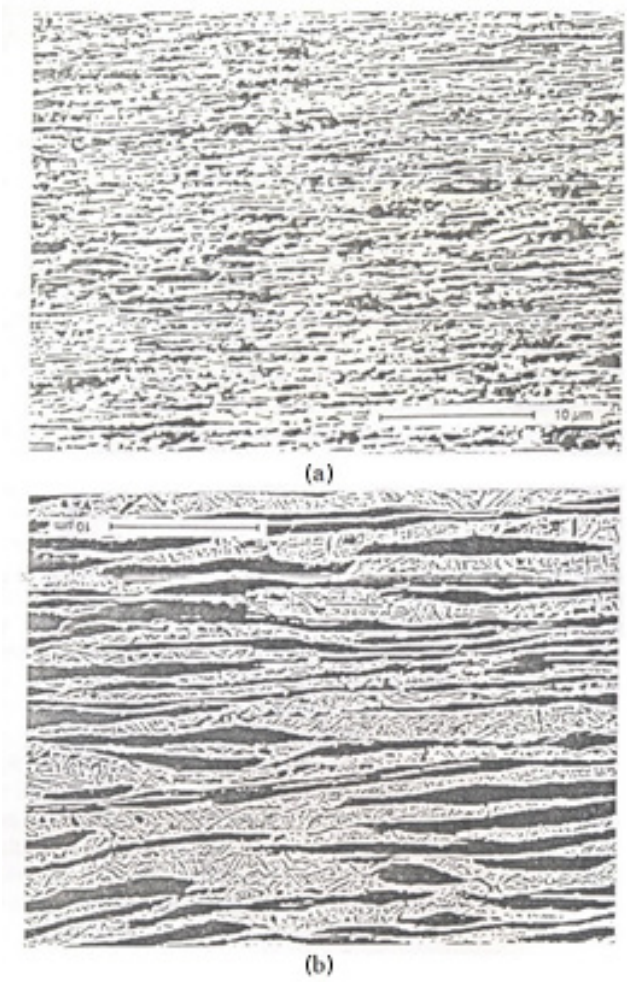

FIG. 4.21. SEM micrographs of extruded tube hollows under two extreme preheat temperatures and soak times: (a) 780°C/15 min, showing fine and uniform elongated α grains (dark phase) with a thin β filament at grain boundaries; and (b) 850°C/300 min, showing regions of Thomson-Widmanstätten α plate structure between the elongated primary α grains (dark phase). (Reproduced from Ref. [4.9] with permission courtesy of AECL, Canada.)

To improve corrosion resistance but maintain strength, an outer layer of zirconium with a low tin concentration and an inner billet of Zircaloy-4 is co-extruded into fuel cladding used in some PWRs (see Section 4.11.1.1 on PWR cladding).

In summary, the hot working of zirconium alloys is used to reduce the dimensions of an ingot towards those required to make components and to homogenize and refine the microstructure. Processing maps provide a guide to the selection of the range of temperatures and strain rates during hot working of any given alloy system. To minimize defects, attention has to be paid to the processing history of the material, temperature and preheat soaking time, material transfer time to the work site, amount and rate of working, and the condition of lubrication.

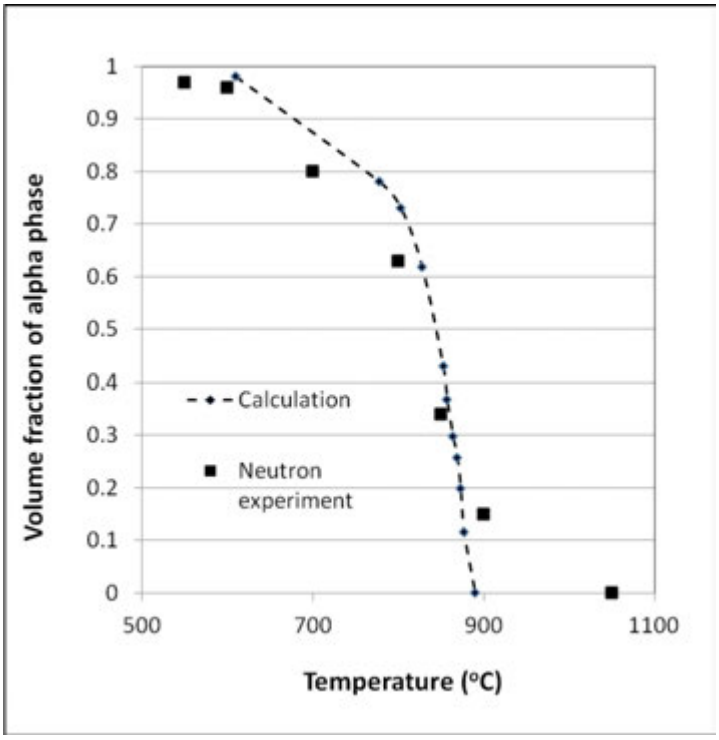

FIG. 4.22. Calculated and measured volume fractions of α at different temperatures in the (α + β) temperature range for Zr-2.5Nb alloy; based on Ref. [4.9].

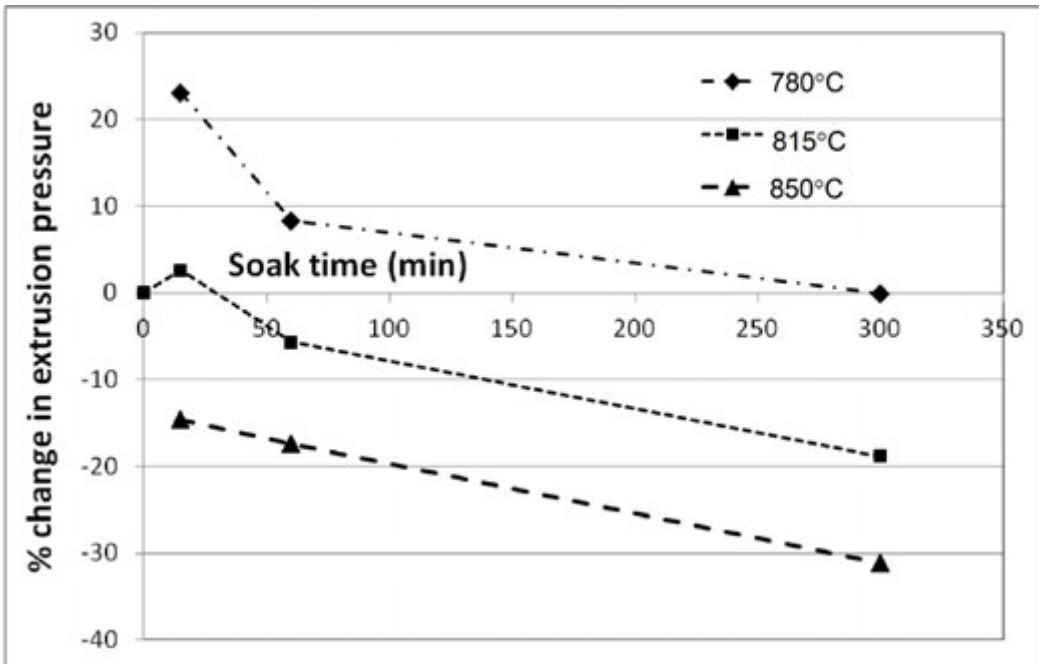

FIG. 4.23. Relative (%) changes in the extrusion pressure for various preheat temperatures and soak times; based on Ref. [4.9].

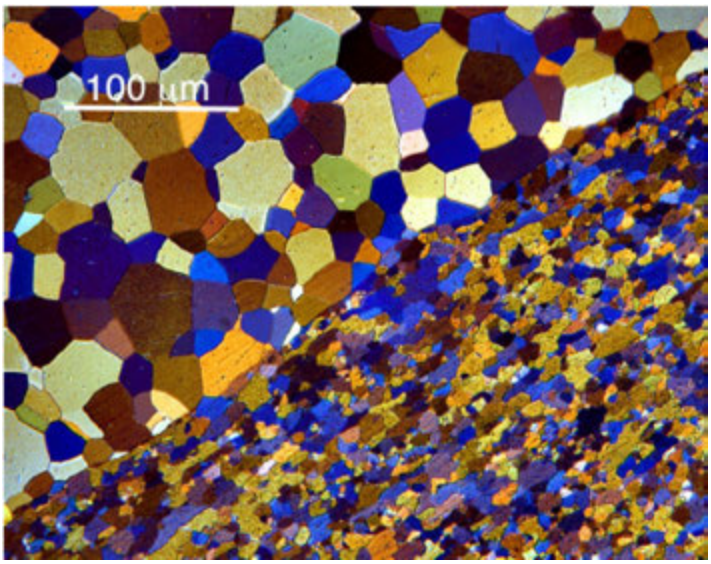

FIG. 4.24. Coextrusion. The large grains are pure zirconium and the small grains are Zircaloy-2. The solid state bond zone runs from the lower left to upper right of the photomicrograph.

4.4. COLD WORKING

Cold working processes are used to further define the shape and refine the metallurgical characteristics of zirconium mill products. Cold rolling improves dimensional and surface finish attributes, and, in conjunction with intermediate and final annealing, creates a refined grain structure [4.4, 4.10]. Cold working operations include pilgering for reducing the diameter and wall thickness of tubing, cold rolling of sheet and strip, swaging bar, drawing of tubes, bar and wire, and various special cold forming operations such as roll extrusion and flow forming.

4.4.1. Pilgering

Pilgering is a cold working operation where the outside diameter, inside diameter and wall thickness of tubes are simultaneously reduced over the working length under a pair of dies with almost semicircular tapered grooves cut on them. The grooves on the dies are precisely cut according to an engineered design and the groove shape provides for the reduction of the outside diameter from the incoming tube shell to the finished tube. A tapered mandrel, matching the contour of the dies, is placed centrally between the grooves, which in turn determines the wall thickness of the reduced tube along the working length. Large amounts of cold work can be imparted in the process of cold pilgering owing to the application of biaxial compressive stresses. During pilgering, the ring dies rotate backward and forward and reduce the tube, analogous to a rolling pin preparing pastry. At the end of each stroke, the work piece advances and rotates. The forming process often requires more than ten small steps of feeding and rotation to attain the full reduction in area, and it is the large number of small steps that ensures a constant wall thickness and homogeneous microstructure. For zirconium alloys, pilgering is the main process used for fuel cladding and some pressure and calandria tubes, indicating its flexibility and range of application.

The pilgering operation has several advantages for cold working seamless zirconium alloy tubes. Pilgering improves the dimensional tolerances of the extrusion to a great extent. Internal material defects are reduced owing to the application of high compressive stresses

during pilgering, whereas defects are elongated and are likely to be magnified in processes such as drawing. There is very little loss of material in the process. Pilgering results in excellent surface finish on the inside and outside surfaces. The material is homogeneous and possesses a uniform microstructure. The process is ideally suited for the cold working of zirconium alloys as the crystallographic texture in the finished product can be controlled by varying the ratio of wall thinning to diameter reduction. A very large reduction in area (RA) of 70% or more is achievable by pilgering. RAs are higher than those that can be achieved for cold rolling sheet materials because of the applied stress state and the axisymmetrical shape of the product being reduced.

Figures 4.25 [4.7], 4.26 and 4.27 show schematic examples of a two-roll mill with full ring dies, a two-roll mill with half ring dies and a three roll mill of the high pressure tube reducer type.

The Q factor is defined as the ratio of percentage wall thickness reduction to percentage diameter reduction, and influences the final crystallographic texture of the finished product. It is generally necessary to maintain a high Q (not less than 1.05), particularly during the final cold pilger pass in the fabrication of anisotropic materials such as zirconium and titanium alloys. In all cases, $Q > 1$ is beneficial to reduce the propensity for inside surface cracking.

The Q factor is calculated from the initial and final dimensions of the tube for each rolling stage. When the tube is produced by several stages of cold pilgering, the overall Q factor value bears no relation to the individual Q factors. Similarly, if the working length is divided into a number of intervals and the incremental Q values, Q_i, are calculated for each interval, these values are not constant and vary depending on the tool curvature. Q_i is calculated from the changes in diameter and wall thickness that occur in small intervals along the working length. The pattern of incremental Q factors along the reduction zone was found to have a large effect on the crystallographic texture according to Cook et al. [4.11].

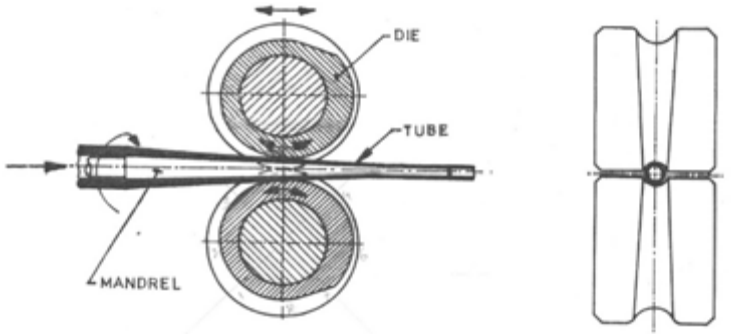

FIG. 4.25. Pilgering: two-roll mill (full ring dies) (reprinted with permission from Ref. [4.7], copyright ASTM International).

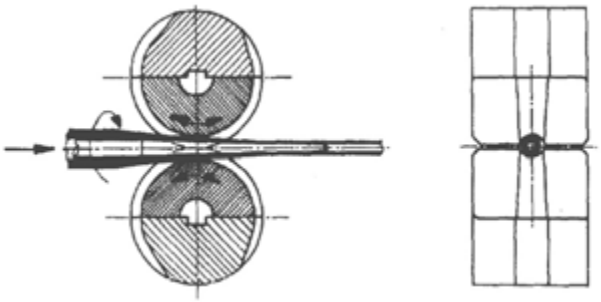

FIG. 4.26. Pilgering: two-roll mill (half ring dies).

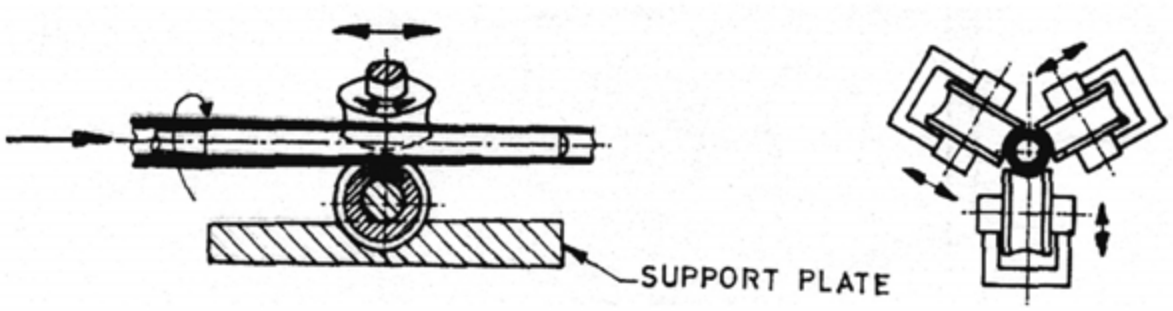

FIG. 4.27. Pilgering: three-roller mills (high pressure tube reducer type).

The process of pilgering is illustrated in Fig. 4.28 [4.11], which illustrates the reduced tube and the mandrel. The incremental ratio Q_i is defined as:

$$Q_i = \frac{\text{Incremental true strain in radial direction } (\mathrm{E'r})}{\text{Incremental true strain in circumferential direction } (\mathrm{E'c})}, \tag{4.3}$$

$$\text{i.e. } Q_i = \frac{\ln(W_x/W'_x)}{\ln(MD_x/MD'_x)} \tag{4.4}$$

where W_x and W'_x are wall thickness values at an increment apart, and MD_x, MD'_x are the corresponding mean diameters.

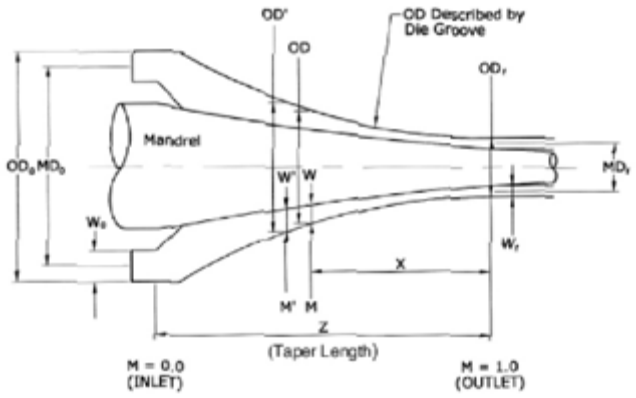

FIG. 4.28. Pilgering process (reprinted with permission from Ref. [4.11], copyright ASTM International).

A higher radial texture component is produced when the Q_i is increased over the working length, which in turn depends on the mandrel geometry. The fraction of radial poles, f_r, was increased both by the RA during the pilgering pass and with the Q value increase in the final pass of cold pilgering, as reported by Vaibhaw et al. [4.12].

Hydrides can reduce the ductility of zirconium. In tubes, hydrides normal to their platelets in the radial direction (circumferential hydrides) have little effect on ductility whereas hydrides normal to their platelets in the hoop direction (radial hydrides) are not desirable because their orientation, combined with a hoop stress, may induce failure by cracking. Hydride platelets precipitate normal to the platelets parallel to the direction of deformation. Thus, after much compressive deformation, as in pilgering, initial hydrides are circumferential. Under a tensile stress, hydrides may reorient so the plate that is normal to

the hydride is parallel with the stress. Thus, a hoop stress could induce radial hydrides. Texture plays an important role in the stress reorientation of hydrides. Radial basal poles result in circumferential hydrides and tangential basal poles result in radial hydrides. Pilgering schedules are designed with high Q ratios and the tooling is designed to develop a predominant radial texture in the clad tubes; see Schemel and McKenzie [4.13]. This texture protects against the formation of radial hydrides and will ensure tangential hydrides in the tubes and prevent possible rupture.

High Q factors can considerably enhance the creep resistance and transverse ductility of the pilgered tubes. The design of tooling and selection of rolling schedules, starting from the hot extruded blanks to the finished size passing through a series of cold reduction steps, plays a key role in the texture of the finished product. Hence, the mechanical and physical properties of zirconium alloy tubes are strongly influenced by crystallographic anisotropy formed during the pilgering process, according to Konishi et al. [4.14].

The reduction profile of the tooling along the working length as reported by Nagai et al. [4.15] also plays a crucial role in determining the crystallographic texture. The reduction in diameter from the incoming tube to the finished size can be obtained in a linear or parabolic fashion. A die design with an initial steep parabolic curve provides large amounts of wall reduction at the start of the working length.

Parabolic die grooves are illustrated in Fig. 4.29 [4.15]. As the curves straighten towards the latter half of the working length, dimensional tolerances that result are better than those that result from a straight taper. This design also reduces the amount of side relief required in the die grooves. While the tool costs are higher with a parabolic rather than linear profile, the texture in the tubes can be better controlled.

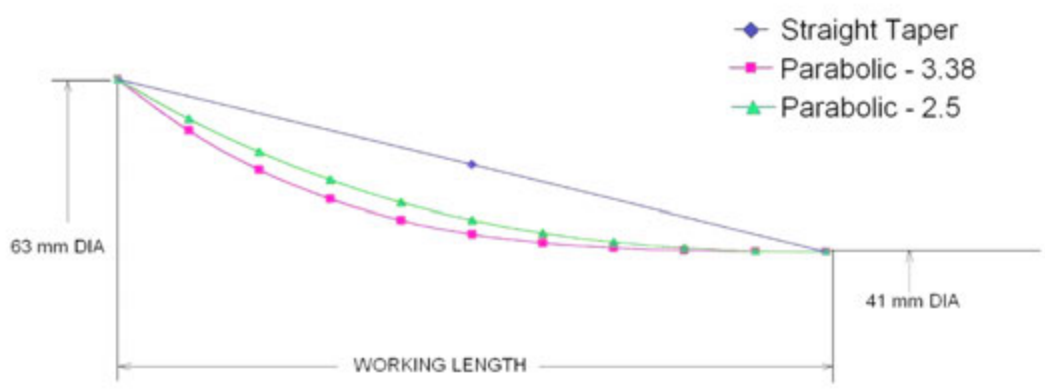

FIG. 4.29. Straight versus parabolic tapers over the working length of a pilger die (reprinted with permission from Ref. [4.15], copyright ASTM International).

Side relief in the die grooves is a departure from the circularity of the die groove itself. The groove has a cross-sectional shape that approximates an ellipse (where the major axis is across the horizontal centre of the tube). The die groove is not truly semicircular in cross-section. The groove is ground to provide extra side clearance at the periphery of the die (i.e. the groove is wider at the periphery of the die than for a true semicircle). This side relief is necessary to prevent a ‘scrubbing’ motion at the edges of the groove as the die rolls down the tube and helps prevent excessive pick-up and galling from the friction of the sidewall of the die rolling down the tube.

Lubrication is another important variable in pilgering. Lubricants for the outside surface of the work piece can be divided into two categories. The lubricant most often used is a water-emulsified animal-fat-based lubricant containing fatty acids, stearic acid and fatty esters. This lubricant is sprayed onto the outside of the tube and is used to both lubricate and carry away heat generated by the high reductions. Another outer lubricant that has been used with some success is a highly chlorinated oil-based lubricant. This lubricant is somewhat more difficult to clean off the finished tube, but it has higher lubricity and the advantage that it can operate with higher temperatures than water-based lubricants. Higher temperatures can promote additional ductility in the tubing with the potential for higher reductions with fewer surface related defects.

Lubricants for the inside surface of the work piece have much heavier viscosity (grease consistency) than outside lubricants and are injected by a pumping system through the mandrel support rod. These lubricants contain chlorinated paraffin, colloidal clay, emulsifier, fatty acids and water.

4.4.2. Wire drawing

Drawing is a process in which the shape and the cross-sectional area of the work piece are reduced by pulling through a die. It is suitable for long products with constant cross-sections requiring an excellent surface finish and closely controlled dimensions. Drawing is done on a machine called a draw bench. The final dimensions and resultant cross-sectional area are a function of the die geometry. Drawing is a cold working operation usually conducted at room temperature using a number of dies with diminishing diameters located in series. Tubes, rods and wires can be produced by drawing; see Schemel [4.7].

In spite of the tendency of zirconium to gall and work-harden, it has good hot and cold formability. However, the drawing of zirconium and its alloys requires careful development of tooling. A tooling design that eliminates severe or abrupt section changes and that allows generous radii is essential. The die design should also allow for the spring back tendency of zirconium and its alloys. Figure 4.30 [4.16] shows the configuration of a die for rod or wire drawing.

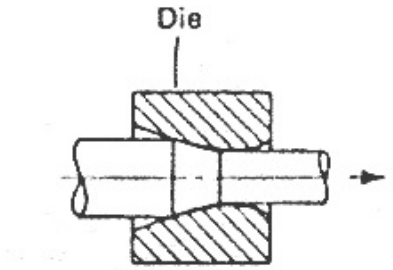

FIG. 4.30. Rod and wire drawing [4.16].

The most important and elementary consideration in drawing is that the pulling force, or drawing stress, should not exceed the strength of the material being drawn to avoid unstable deformation and fracture. This factor limits the amount of RA possible in one pass; the limit for zirconium is about 16% RA per pass. Usually, many reductions are required to achieve the desired final dimensions. To produce nuclear fuel cladding, drawing is not competitive with cold pilgering in which very high RAs are achievable.

Drawing reduction and the die approach angle are the most important parameters in the drawing process. Most aspects of drawing, such as friction, redundant work of deformation and heat generation during drawing, can be explained in terms of these two basic parameters.

In wire drawing, the section is usually round, although other shapes can be drawn. The supporting equipment used ensures that the feedstock can be uncoiled easily, and the drawn wire can be rewound. This process usually enables the production of wires without severe limitation on their length. The drawing of wires is carried out in several passes with intermediate annealing steps.

Intermediate annealing is carried out in the temperature range of 973–1123 K (700–850°C). To eliminate galling, zirconium alloys can be sheathed in copper or steel during drawing. This sheathing material is removed after drawing by dissolution in acid. Chemical conversion coatings are also used directly on the zirconium wire in conjunction with solid (powder based) lubricants to eliminate the requirement for sheathing [4.16].

Material flow occurs only within a limited domain among all possible combinations of die angle, reduction and friction values. In Fig. 4.31 [4.16], the upper part represents sound flow diagrammatically along with two other common modes of flow: dead zone formation and shaving. Dead zone formation occurs when a material is drawn through dies of high cone angle and shears within itself to develop a dead metal zone that no longer takes part in the flow but adheres to the die, forming a die-like channel through which the incoming material passes in a still-converging mode of flow. Shaving develops when the dead zone material does not adhere to the die but starts to move backwards, peeling off as in a metal cutting operation; the core of the billet deforms less, or may no longer deform at all and moves through the die with essentially no change in diameter and with an exit velocity the same as the entrance velocity.

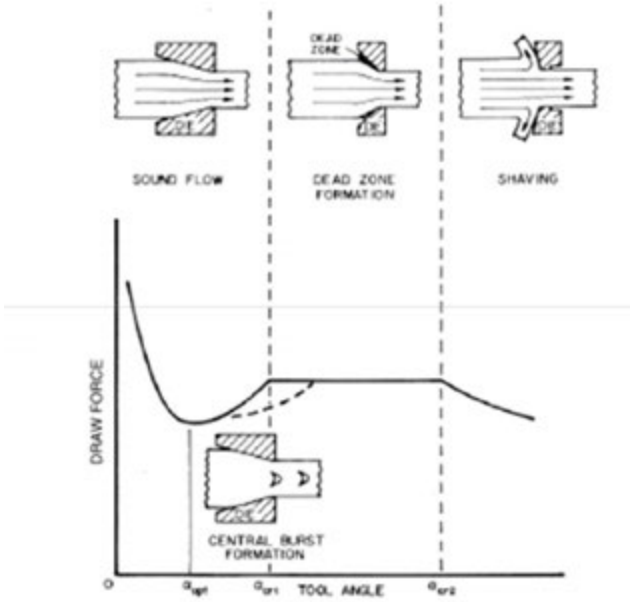

FIG. 4.31. Schematic illustration of the effect of tool angle and mode of flow (including central burst) on drawing [4.16].

A typical defect, although an infrequent one, is the central burst defect. While central burst does not occur often, it is of great concern because it occurs internally. The voids are in the interior of the product, where they may not be readily detected, but they may then cause unexpected failures in service. These types of defects are associated with small reductions and moderate die angles. Their occurrence will be noted when the material is processed

subsequent to previous severe cold work. Figure 4.31 shows how central burst depends on the tool angle and mode of flow.

Galling of the outer surface is primarily a lubrication defect. The high pressure and sliding friction inherent in wire drawing can easily lead to surface galling defects. Factors that influence galling include lubrication type, amount and method of application, die angles and the surface finish of the entry and throat areas of the die.

4.4.3. Tube drawing

Drawing of tubes can be broadly divided into drawing without a mandrel (free sinking) and drawing with a plug or mandrel. Drawing with a plug or mandrel can be accomplished by drawing with a moving mandrel, drawing with a fixed mandrel or drawing with a floating plug. Figure 4.32 [4.17] shows tube drawing with a fixed mandrel.

When a tube is pulled through a converging conical die to decrease its outer diameter without internal tooling, the process is called tube sinking or free tube drawing. It can be performed on a draw bench to form straight tubes of a finite length. Unfortunately, HCP metals such as zirconium do not respond well to drawing in a free sinking mode. The inside surfaces tend to wrinkle and continued drawing leads to longitudinal cracking on the inside wall.

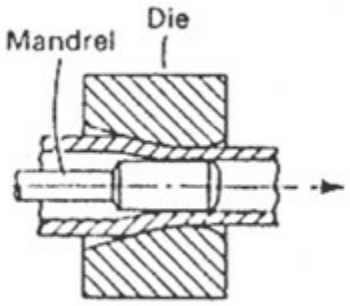

FIG. 4.32. Tube drawing [4.17].

The use of a mandrel improves both inner surface finish and dimensional control. The choice of the diameter of the mandrel is critical for successful tube drawing.

A long mandrel of hard metal can be drawn with the tube through the die. This mandrel is called a moving mandrel. Both inner and outer diameters of the tube are reduced, and the wall thickness is controlled through the gap between the die and the mandrel, while causing tube elongation. Both emerging tube and mandrel move at the same speed, minimizing mandrel to work piece interface friction that manifests itself as heat. The removal of the mandrel from the product may pose problems. The process is done on a draw bench and limited to a finite tube length dictated by the equipment. Figure 4.33 [4.17] is a schematic diagram of tube drawing with a moving mandrel.

Drawing using a fixed mandrel (or plug drawing) is designed to eliminate the problems of removal of the tube from the mandrel and is shown in Fig. 4.34 [4.17]. The cylindrical mandrel is fixed in position relative to the die and is stationary. Friction losses between mandrel and tube are high. The length of tube and mandrel may be limited further because the elastic extension of the mandrel may create chatter problems.

The mandrel is tipped with a conical converging plug. The function of the plug is to squeeze the tube during its converging flow, before it reaches the exit of the die. The mandrel is used to determine the proper axial position for the plug. However, with proper design the tension on the mandrel is minimal or non-existent for floating plugs. While dimensional control and surface finish are good, only tubes of finite lengths can be produced.

The floating plug is a natural extension of the fixed mandrel with a conical plug. It is clamped in axial position at its extreme left and is pulled in tension caused by friction drag from the deforming tube. In fixed plug drawing, the plug is pulled forward by friction drag. The axial component of the pressure between the plug and the tube along the conical surface acts to oppose the friction drag. The tension in the mandrel is balanced between the friction drag force and the axial component of the interface pressure between the plug and the tube.

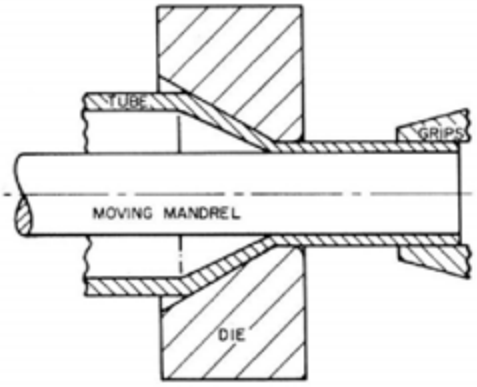

FIG. 4.33. Tube drawing with moving mandrel [4.17].

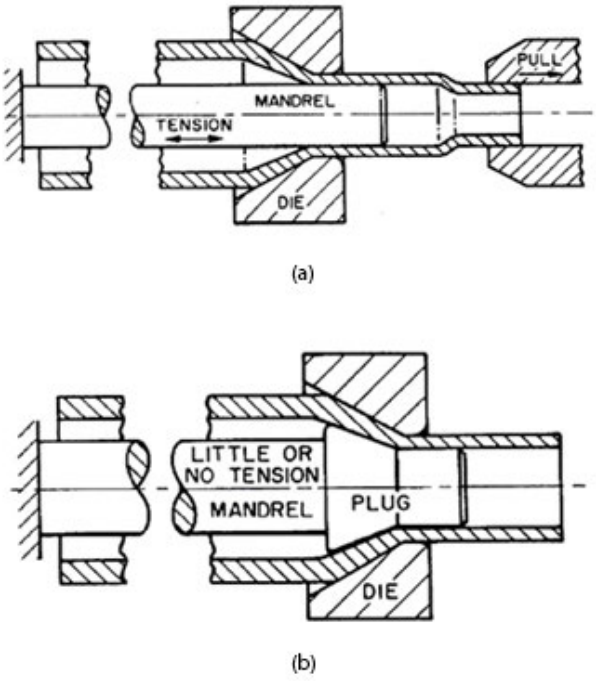

FIG. 4.34. Tube drawing with (a) a fixed cylindrical mandrel and (b) a fixed plug [4.17].

The art of the design and use of a floating plug is to maintain the delicate balance between the axial component of pressure and friction drag that will result in zero total axial force and no tension on the mandrel [4.17]. The plug–tube interface pressure over the conical portion of the plug results in a force, *P*, while the interfacial friction forces are *F1* and *F2* over the conical and cylindrical surfaces of the plug, respectively. The smaller diameter portion of the plug, the 'nib', controls the inner diameter of the tube. Occasionally, mainly in small diameter heavy wall tubes, the nib is not cylindrical, but conical. When the plug is properly designed, the following balance prevails:

$$P \sin \alpha_{\mathrm{p}} - \left(F_1 \cos \alpha_{\mathrm{p}} + F_2\right) = 0 \tag{4.5}$$

where

P is the pressure over conical portion of the plug;
F_1 is the interfacial friction force over the conical surface;
F_2 is the interfacial friction force over the cylindrical surface;

and α_{p} is the entry angle of the plug.

Floating plug drawing, shown in Fig. 4.35 [4.17], has several advantages over a fixed mandrel, including the ability to continuously draw at a high rate of production with a high degree of inner surface quality. Floating plug drawing permits the precise control of the inner diameter and better material utilization. It is the preferred method for drawing small diameter zirconium tubing.

Commercial practice for lubricating zirconium involves a fluoride phosphate conversion coating that is applied by immersion in an aqueous solution containing hydrofluoric and orthophosphoric acid. The lubricants for these conversion coatings are soaps (such as lithium stearate), greases, oils or emulsions. For uncoated zirconium wires and tubes, a mixture of insoluble stearates and extreme pressure additives with a high MoS_2 content are generally used.

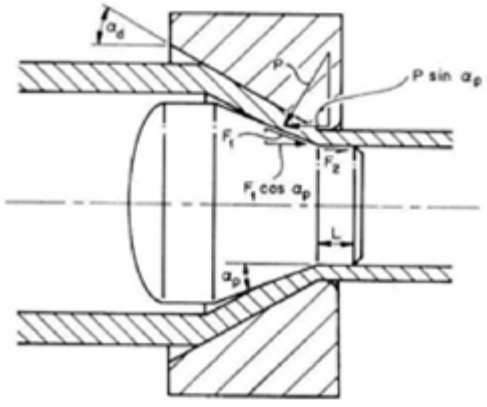

FIG. 4.35. Tube drawing with a floating plug [4.17].

Defects formed during tube drawing consist primarily of surface defects. These can include galling and microcracking. Galling is controlled by appropriate lubrication of the tube in contact with the plug and die. Microcracking can also be controlled by adequate

lubrication, and by maintaining a smooth surface on the inside and outside surfaces. The purpose of the conversion coating is to enhance the adhesion of the lubricant, and it is important that this function be maintained to provide gall-free surfaces.

4.4.4. Swaging

Swaging is a mechanical deformation technique for reducing or shaping the cross-section of rods or tubes by means of repeated impacts or blows. It reduces the diameter and tapers (or points) round bars (or tubes) by external hammering. If a shaped mandrel is inserted into a tube before swaging, the metal can be collapsed around it to simultaneously shape and size both the interior and exterior of a product.

Swaging is performed by a rotary machine, as shown in Fig. 4.36 [4.18]. High speed rotation of the spindle forces the backer blocks outwards where they encounter opposing rollers that are mounted in a massive machine housing. To pass beneath these rollers, the dies must be squeezed tightly together. Once cleared, the dies can again separate and the cycle repeats. The motion is sustained by using an external motor connected to a large flywheel.

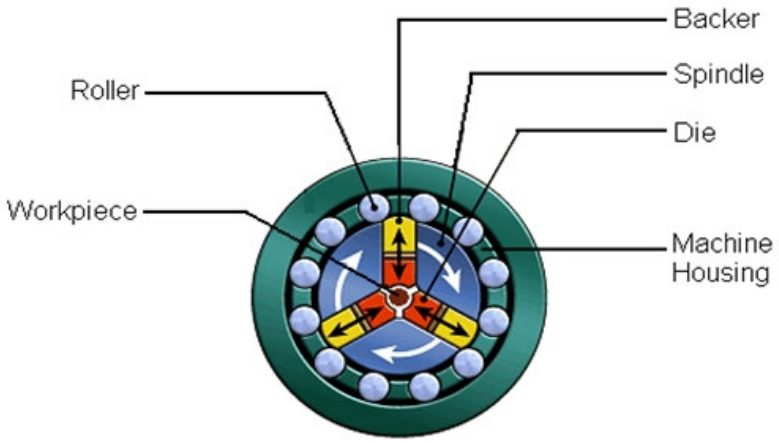

FIG. 4.36. Schematic diagram of swaging [4.18].

The work piece (e.g. rod, tube) is inserted between the dies and is advanced during the periods of die separation. The repeated closures squeeze the work piece from a variety of angles around the periphery, reducing the diameter and increasing the length. Zircaloy is swaged to produce rods that are then cut to make end plugs for fuel elements of light water reactor (LWR) and PHWR fuel bundles.

Defects formed during swaging consist of two categories: (1) internal voids at the ends of the swaged rod; and (2) a chopped-up surface from contact with the dies. During swaging, the outside fibres are compressed more than the inside fibres putting the outer fibres into compression and the inner fibres into tension. The resulting tensile force at mid-diameter can lead to the nucleation of voids and the formation of a central burst of honeycomb-type defects. Since these defects mostly occur near the free-ends of the bar, the most expedient measure is to cut off the ends that contain the defects. The chopped-up surface can be mitigated by a combination of die design (primarily die angle) and lowering the reduction ratio achieved during swaging.

4.4.5. Roll extrusion

Roll extrusion was developed for the manufacture of tubes with a large ratio of diameter to wall thickness. This process imparts high strength and fine grain size to roll extruded tubes. Roll extrusion has been used for the trial production of thin walled seamless calandria tubes in CANDU reactors, as presented by Theaker and Coleman [4.19]. There are two types of roll extrusion methods, external roll extrusion and internal roll extrusion.

In external roll extrusion, the hollow is placed over a mandrel. Two annular die rings are brought into position on the hollow. The mandrel and hollow are rotated while the die rings progress axially through a series of passes. Wall thickness and outer diameter are simultaneously reduced while the length of the work piece increases. The internal diameter remains constant in this process, as shown in Fig. 4.37 [4.20].

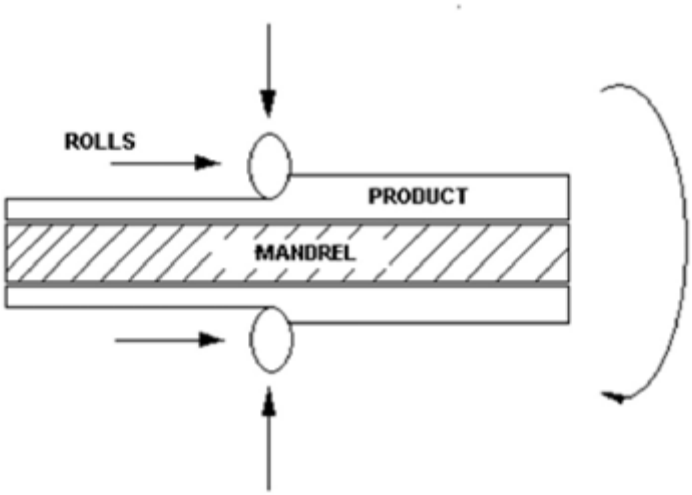

FIG. 4.37. Schematic diagram of external roll extrusion (reproduced from Ref. [4.20] with permission courtesy of AECL, Canada).

In internal roll extrusion the starting hollow, often after external roll extrusion, is placed inside a one-piece, cylindrical die ring. The rollers inside the starting hollow are displaced radially outward until they bite into the inside diameter of the hollow surface by a controlled amount. The hollow outside diameter remains constant while the wall thickness decreases and both the internal diameter and length increase, as shown in Fig. 4.38 [4.20]. In both of the above processes, intermediate annealing has to be carried out owing to the cold work induced into the material during roll extrusion. Surface tears during internal roll extrusion can be eliminated by careful surface preparation, including sufficient lubrication, and by specifying the reduction rates.

Roll extrusion is a suitable process for making seamless calandria tubes from Zircaloy. The tubes so produced have a strong radial texture that gives them high biaxial strength. The internal diameter can be varied by suitable oscillation of the position of the dies to produce ridges of various depths, lands and spacings. Such ridges provide flexibility in reactor design, for example, to mitigate loss-of-coolant accidents.

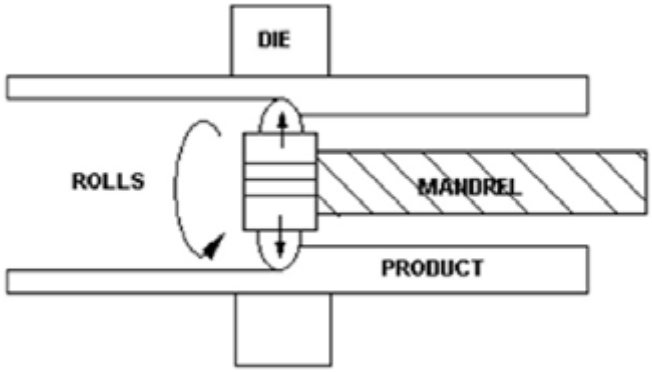

FIG. 4.38. Schematic diagram of internal roll extrusion (reproduced from Ref. [4.20] with permission courtesy of AECL, Canada.

4.4.6. Flow forming

Flow forming is a cold forming process of manufacturing dimensionally precise, axially symmetrical, hollow components of cylindrical, conical or ogival shapes. Flow forming can also be used to produce seamless zirconium tubes and pipes with a cold worked surface finish and high radial texture [4.21].

The headstock provides the rotational drive to the internal mandrel for the component to be flow formed. The tailstock applies the necessary force for clamping the component to the mandrel in the case of a closed or semi-closed cylinder (forward flow forming) and, in the instance of an open-ended tube (reverse flow forming), the tailstock can be swung out of the machine centreline to allow an unobstructed path to the component being flow formed.

Flow forming is performed by the application of uniform compression to the outside surface of a cylindrical component using a combined axial–radial force from three numerically controlled rollers, as shown in Fig. 4.39 [4.21]. The metal is compressed and plastically deformed and made to flow in the axial direction onto a rotating mandrel. The increase in the length of the work piece is directly proportional to the percentage of wall reduction. With a uniform wall thickness, the finished or starting length can be calculated using the following formula:

$$L_0 = L_1 \frac{S_1(d_1+S_1)}{S_0\,(d_1+S_0)} \tag{4.6}$$

where

L_0 is the preform length;
L_1 is the workplace length;
S_0 is the starting wall thickness;
S_1 is the final wall thickness;

and d_1 is the internal diameter.

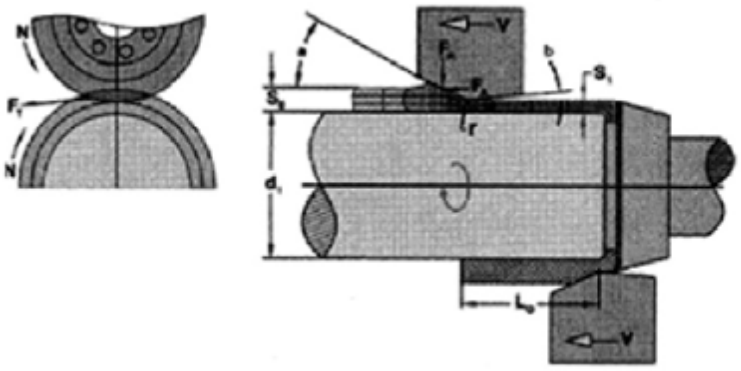

FIG. 4.39. Schematic diagram of flow forming [4.21].

Although the maximum reduction is dependent on the formability of the material, reductions between 75% and 90% are achievable before intermediate annealing is necessary. Depending on the amount of reduction required, one or more passes may be given. Typically, the preform can be flow formed with an elongation of four to six times the input billet length before a need for intermediate annealing of the metal is required.

Even with extensive lubrication, there is substantial adiabatic heating at the point of contact for the rollers. Zirconium and zirconium alloys exhibit additional deformation modes at temperatures as low as 150 K above room temperature. This undoubtedly helps the zirconium to deform. Since almost all of the deformation is in a wall thinning mode, the resulting basal pole [0002] texture is highly oriented in the radial direction.

In flow forming, it is essential to properly control the flow of material in the axial direction. The internal mandrel and the three rollers are made from hardened tool steel (above 60Rc), with a fine surface finish to minimize friction. The positions of the three rolls are staggered axially and each has a different geometry depending on its role in the process, as shown in Fig. 4.40 [4.21].

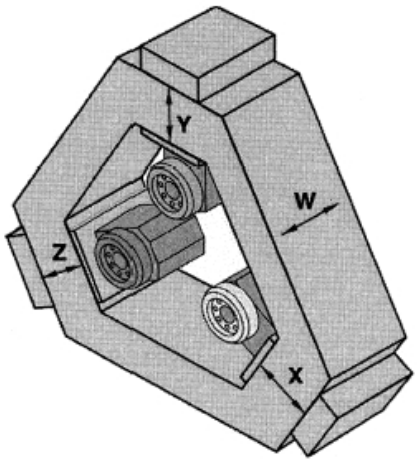

FIG. 4.40. Flow forming roll assembly [4.21].

Based on the direction of material flow relative to the direction of roll movement, flow forming is classified as forward flow forming or as reverse flow forming, as described by Fonte and Tosdale [4.22].

Forward flow forming is employed when the component to be flow formed has one closed or semiclosed end. The bottom of the preform rests against and rotates with the mandrel. As rollers are fed along the axial direction, the material being flow formed moves in the same direction. The maximum length of a component achievable by forward flow forming is limited by the longitudinal stroke of the equipment being used.

Reverse flow forming is used for manufacturing tubular components. The preform is placed on a mandrel and pushed to the headstock end against a 'toothed' driving ring. The preform (and mandrel) are rotated and the rollers move over the preform towards the headstock. As the preform's wall thickness is reduced, it elongates over the mandrel and moves in an axial direction, opposite that of the rollers. The percentage of wall reduction and the starting length of the preform govern the maximum length achievable by reverse flow forming.

The grain structure of a flow formed component is flattened and elongated in the axial direction, with a minor amount of spiral formation that can be controlled by the proper choice of operating parameters. The controlled mechanical deformation of the work piece results in strain hardening (cold working) of the base metal, increasing tensile strength and hardness throughout the flow formed area.

The process is ideal for producing large diameter, thin walled tubes that are difficult to pilger. Flow forming has several advantages over seam welded tubes, the fabrication route for most calandria tubes, including the obvious ability to produce highly accurate net shapes without welds. The process has a high degree of accuracy in the dimensional control of diameters, wall thickness, roundness, eccentricity and straightness. Its mechanical properties are good as the high degree of deformation produces a very small grain size — about 15 μm. Surface finishes down to 0.2 micrometers arithmetic average amplitude can be achieved. The process can also produce tubes with varying wall thickness, tapers and radii on the outside surface of the tube.

The most common defect associated with flow forming is transverse cracking on the outer surface. This cracking can occur when the reduction in wall thickness that has taken place is too great, or when the forming roll is an improper shape. Another, more minor defect is a slight surface ripple that appears on the outside surface. These minor defects can be easily removed by a belt sanding or polishing operation. The surface ripple can be minimized by using appropriate reductions in wall thickness, slowing down the helix pitch or advance of the rollers, and by controlling the roller shape.

4.4.7. Cold rolling

Cold rolling is used to reduce strip and sheet thickness below that achievable by hot rolling, and to improve surface finish and gauge or thickness control. Zirconium and most of its alloys can be readily cold rolled. The RA can range from 20% up to 50%. For alloyed zirconium, reductions of 30% to 40% are generally employed. The area reduction has to be sufficiently large to avoid critical grain growth during heat treatment (Section 4.6.2.1) and remain below a regime where work hardening can lead to cracking.

Zirconium strip and sheet can be cold rolled in a number of different ways. For the most part, cold rolling is conducted in a uniaxial orientation — as contrasted with cross-rolling in longitudinal and transverse orientations. Cold rolling can be performed in coil

format or in flat-rolled sheet format. Further, coil-to-coil rolling can be conducted on simple reversing mills, or on more complex cluster mills of the Sendzimir type. Sendzimir mills (also known as Z-mills) are a special form of cluster mill that contain small diameter work rolls backed up by successively larger rolls. A mill capable of rolling strip 0.3 meters wide has work rolls that are about 12 mm in diameter. These pencil-thin rolls would easily deflect without adequate backup. In one configuration, there are ten rolls above the strip pass line and ten rolls below the strip pass line — in other words, there is a work roll and nine backup rolls on either side of the pass line. A second feature of a Sendzimir mill is that the coilers are capable of pulling about 60% of the yield strength of the strip in tension. The combination of a small diameter work roll and coil tension permits very thin foils to be rolled, down to about 20 μm thickness.

Reversing mills are usually configured in 'four-high' format. This means there are two small diameter work rolls that contact the work piece, backed up by two larger diameter rolls. The backup rolls are used to apply the rolling force to the work rolls, and to stop the work rolls from bending around the width of the strip. If the rolls bend excessively, a transverse 'crown' is rolled into the strip, whereby the edges are thinner than the mid-width position. These mills are capable of cold rolling strip over a range from 5 mm thick hotband down to about 0.5 mm finished thickness.

As zirconium is rolled it work-hardens. It can be stress relief annealed at 773–823 K (500–550°C) or fully annealed at 923–1023 K (650–750°C). The annealing strategy depends on the alloy. In the case of niobium-bearing alloys, the best corrosion resistance is maintained by annealing below 873 K (600°C). Thus, the strategy is to cold roll with about 35–40% area reductions, clean the rolling oils off the strip and then either continuous inert gas anneal or vacuum anneal coils or flat sheets. This cycle is repeated to achieve the final strip thickness.

Defects on cold rolled strip are primarily surface related. Inadequate surface conditioning of hotband can leave small pockets of surface oxides from the heating prior to hot rolling (see Section 4.9). These oxide pockets are brittle, and cracks can form in them. These cracks are oriented transverse to the rolling direction, are thumbnail shaped and are slanted at about 45° along the principal stress planes.

Imperfections in the rolls will leave a repetitive pattern equal to the circumference of the work rolls. These imperfections usually take on the appearance of small raised areas when the roll surface has a dent in it. These dents are caused by pieces of hard debris that get between the rolls and the work piece. The source of this debris is pieces broken from the edge of the strip. To remove this source of debris and help prevent this type of defect, the strip is edge-trimmed or slit back in width to prevent the overrolled edges from cracking and slivering.

Shape issues manifest themselves in more dramatic ways. 'Oil canning' is created when the centre of the sheet is elongated more than the edges with the result that the strip puckers up in the centre of the width during cold rolling. The strip is said to have a loose middle and tight edges. This defect is created when excessive crown from the hotband is eliminated by cold rolling. Convex shaped work rolls will tend to thin the centre-width of the strip, and this central portion will elongate more than the edges. The central material, restrained by the edges, has nowhere to go, and it will gather or pucker forming 'oil can'.

If the strip has a wedge shape across the width (thick on one edge, thin on the other), rolling out the wedge will create a camber. The thicker edge has to be rolled more than the thinner edge and this elongates the thicker edge more than the opposite side. This extra elongation causes the material to take on camber down the length of the strip.

4.5. SECONDARY FORMING OPERATIONS

Secondary forming operations do not reduce the thickness of the material to any significant degree. They may change the shape of an object such as during blanking, stamping raised features or bending operations.

4.5.1. Coining

Coining is when metal is squeezed between the surfaces of a die and takes on any surface pattern. This process may result from an intentional act or an unintentional one. When intentionally performed, the coining die consists of a punch and die, which are engraved with the necessary details required on both sides of the final object. Coining is essentially a cold forging operation except for the fact that the flow of the material occurs mostly in the outside layers of the work piece and not in the entire volume [4.17, 4.23, 4.24].

A work piece is placed in a confined die. A movable punch is located within the die. The action of this punch cold works the material and can form intricate features. Pressures as high as 1375 MPa are required to generate the very fine features that are normally desired in coining.

Unintentional coining can often occur as the result of worn or misaligned tooling. This defect is seen in zirconium alloys during the formation of complex spacer strip features. As strip is drawn down between the punch and die, it is trapped just by the punch below the entry to the die. As the forming progresses, the strip can no longer flow down into the die and localized stretching and thinning occurs. The strip fails in tension, creating localized cracks. Close examination of the metal features often shows the point of entrapment. If die clearances are inadequate because the strip is too thick, failures may occur in various locations. If the tooling is misaligned or otherwise worn, the cracking will likely occur on the same feature over repeated parts.

4.5.2. Press brake forming

Press brake forming is a process in which the work piece is placed over an open die and pressed down into the die by a punch that is actuated by the ram portion of a machine called a press brake, as described by Semiatin [4.25]. The process is most widely used for the forming of long, narrow parts that are not adaptable to press forming and for applications in which production quantities are too small to warrant the tooling cost for contour roll forming. Calandria tubes, which are extremely thin walled tubes, are conventionally produced by cold rolling sheets, shaping them into cylinders by press brake forming and welding them along the longitudinal seam.

In press-break forming, when a bend is made, tensile strains occur in the outer fibres, and compressive strains in the inner fibres; both decrease in magnitude towards the neutral axis. The applied forces create a strain gradient across the thickness of the work piece in the area of die contact.

The sheet is cut to the required dimensions and the edges are milled in a planer milling machine. The edges are deburred after milling. Markings are made on the ends of the sheet to denote the positions where the die has to be pressed. These markings are aligned with the longitudinal axis of the die each time the sheet is pressed. The markings should be as close as feasible to ensure a uniform circumference, free of flat areas, in the tube.

A strip of spring steel is placed on a urethane block and the zirconium alloy sheet is placed on this strip. Pressing it between the circular die and the strip of spring steel forms the

tube. The optimum tube diameter to die diameter ratio is about 9:5. For cold forming zirconium tubes, a minimum bend radius of three times the wall thickness is advisable [4.26].

After completing half the sheet, it is taken out, reversed and the other side is formed. Once the entire sheet has been formed, it is tungsten inert gas welded along the gap between the two edges, with or without filler metal, in an argon/helium atmosphere (or a suitable combination of these gases). The seam thus formed is then bead-rolled to give a uniform and smooth outer surface. The tubes are then finished in several ways, including a light draw pass to improve geometry, and belt polishing the outer surface. The finished tubes may be annealed to remove the residual stresses induced by the cold forming and welding.

Figure 4.41 [4.26] illustrates how sheet material can be press brake formed into a tube.

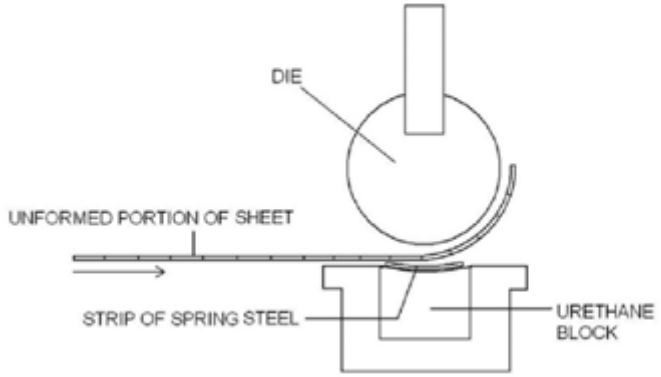

FIG. 4.41. Press brake forming of sheet to make a tubular shape [4.26].

4.5.3. Blanking

Blanking is a process of cutting features out of a flat sheet of metal. Both outside perimeters and interior cut-outs are formed by blanking dies. The process is analogous to shearing. Upper and lower dies are machined to cut out the desired shape. The shapes can be quite complex, for example, PWR interior grid straps, where interior 'windows' are blanked out, along with narrow slots that permit the grids to be assembled 'egg-crate' style. The exterior perimeter is blanked at the same time. Upper and lower dies must align very closely with a small amount of 'draft' or relief cut into the dies to provide clearance as the dies are meshed together. The gap between the female and male dies must be closely controlled to limit the amount of burr that forms on the part, and this gap is dependent on the thickness of the material being blanked as well as its yield strength.

4.5.4. Bending

One example of bending Zircaloy is in forming the four 90° corners of BWR channel boxes, described in Section 4.12.2. In addition, bending is part of the deformation in many other forming operations such as making complicated PWR spacer grids, described in Section 4.12.1.

Bending zirconium and zirconium alloys is readily accomplished. The bend radius, R, is the radius of curvature on the concave or inside of the bend. During bending, the outer fibres of the sheet are stretched and the inner fibres are compressed. A neutral axis runs

through the mid-thickness of the sheet during elastic bending, but as the bending becomes plastic, the neutral axis moves closer to the inside surface of the bend. The plastic strain is in proportion to the distance from the neutral axis, so the outer fibres are stretched more than the inner fibres are contracted. Consequently, there must be a corresponding decrease in thickness (in the radial direction) at the bend to preserve the constancy of volume. The smaller the bend radius, the thinner the material becomes on bending.

For a given bending operation and material, the bend radius cannot be smaller than a minimum value, or the metal will crack parallel to the bend axis on the outer tensile surface. In bending narrow strips (bend axis transverse to the long direction) the cracking will generally occur near the edges because the biaxiality is low at the centre of the strip [4.4]. The minimum bend radius without cracking is usually expressed in multiples of sheet thickness, *T*. Thin sheets of Zircaloy, such as for spacer strips, can be bent to a tight bend radius. For example, 0.5 mm strip may be capable of bending to 1.75*T* or 2*T*. For Zircaloy sheet of 1–3 mm thick, a good figure for the minimum bend radius is 3*T*. Zircaloy plate from 12 mm up to 25 mm thick will require a minimum bend radius of 5*T*.

The value of the critical radius is reduced by precise dimensional control of the tooling, decreasing friction by assuring smooth surfaces of the strip and the tooling and sometimes by introducing friction reducing adhesive films applied to the surface of the strip, reducing the yield strength by lowering the strain rate, and increasing the temperature of the material being bent. Thick plates usually require some heating to form bends without cracks. Heating can be performed either by hand torch (with an oxidizing flame) or in furnaces. Heating in the range of 673–773 K (400–500°C) is appropriate.

Zr-2.5Nb generally has an as good if not smaller minimum bend radius than Zircaloy in thin (<1 mm) strips. This good behaviour is caused by the much finer grain size of Zr-2.5Nb strip and sheet; 1 mm thick Zircaloy sheet and strip would be expected to have a grain size between ASTM 9 and 10 while the grain size in the equivalent Zr-2.5Nb sheet will be about ASTM 12.

During the certification testing, material is often bent in a guided bend test (described in Section 4.13.5.4) to determine whether the material can be bent to a specified or required minimum bend radius.

The other factor to be concerned about is elastic springback. Springback, for a given material and displacement, increases with a rise in yield strength and the thickness and width of the sheet, and a reduction in Young's modulus and radius of the bend. The common method to overcome springback is to bend the strip or sheet to a tighter bend radius than is desired. This overbending allows some elastic recovery to take place when the bending load is removed.

Springback can also occur during drawing-type forming operations. One method of compensating for springback is to force the punch into the material at the bottom of the die to produce coining (see Section 4.5.1). Excessive coining may lead to cracking in zirconium alloys and this method should be approached very carefully. When precision bending is to be accomplished, the uniformity of the sheet or strip thickness is crucial in controlling the amount of springback. Cold rolled strip can exhibit variations in thickness across the width of the strip and this variability can create a difference in springback of multiple identical features spaced across the strip width.

When cracking occurs during bending, the safest approach is to relax the bend radius. Several other variables can be examined if the design prohibits a larger bend radius. A small amount of heat in the material, about 473 K (200°C), will activate additional slip planes and promote plastic deformation. Since zirconium and its alloys are anisotropic, the texture and

subsequent directionality of properties can be exploited to enhance the bend radius. A tighter bend radius is accomplished when the long axis of the bend is in the rolling direction of the sheet rather than in the transverse direction. Spacer strip with high arches and tight bend radii can be more easily made when the grid straps are blanked out of the width of the sheet rather than along the sheet. In channel boxes, the bend axis runs down the length of the strip, and since this is invariably the rolling direction, the sheets are already set up with the best directionality for executing the bends. Defects in the sheet surface can also control bendability. Small scratches parallel to the bend axis, and especially on the outside of the bend radius, can be initiation points for cracking. Zirconium and its alloys are notch sensitive and care should be taken to keep the surfaces associated with the bend area free from defects.

4.5.5. Sheet metal drawing

Drawing is the process used for shaping flat sheets into cup-shaped articles. In some of the designs of outer grid straps for some BWRs, there are a series of bathtub-shaped indents with the convex side towards the fuel bundle. The convex peaks of these indents bear against the fuel rods and provide support for the outer row of rods. There is an element of drawing (along with bending) that takes place during the raising of arch-type features in spacer grid straps for PWRs.

Drawing operations occur when the sheet is placed between a male punch and a female die. As the punch is moved down into the die the sheet has to slide inwards over the die radius. The metal also has to bend over the die radius and then unbend as it is drawn down into the wall of the die. It also has to bend to follow the nose profile of the punch. In some cases, the metal is squeezed, or ironed, between the side of the punch and die to produce a uniform wall thickness [4.4]. Zirconium does not respond well to trapping material between the punch and the die; sometimes the material cracks from the imposed tensile stress.

As the material is stretched down into the die it is thinned. It is very important with zirconium alloys that minimum bend radii be established for the entry to the die and for the nose of the punch. A hold down is generally used to keep the strip flat as it is being drawn down into the die. The friction and lubrication between the hold down and the strip and between the strip and the die are critical. If there is excessive static friction between the hold down, strip and die the strip will not deform into the die smoothly and it is possible that sufficient tensile stress will build up in the material to create cracks.

If cracking becomes an issue, close inspection of the part is required to determine whether the cracking is a material problem, a die design problem, a manufacturing problem or a combination of these factors. If the same feature on different parts is routinely cracking, then the tooling that is forming that feature is likely at fault. If the material randomly cracks in different locations this may be indicative of a material issue or of a manufacturing problem with how the drawing is being performed. Items to be investigated include:

- Punch to die clearances.
- Smoothness of the punch and die surfaces. Zirconium galls easily and the galling can be transmitted back to the punch or die surfaces creating highly localized strained areas.
- Lubrication.
- Strain rates. If these are excessive they can lead to strain rate hardening.
- Whether surface defects such as scratches on the material are present.
- The anisotropy of the strip (see the discussion under Section 4.5.4 on Bending).

— Whether the temperature of the strip is being increased by any external application of heat.
— Uniformity of the strip thickness. This is needed to ensure uniform stringback and to make certain that thicker material is not being trapped during drawing.
— Whether slight shifts in the positioning of the punch within the die are present that can result in cracking of the strip. The material becomes trapped on one side of the die and large tensile stresses are developed as the punch continues down into the die.

In summary, conventional metal working techniques can be applied to zirconium alloys by paying attention to anisotropy, work hardening and galling. Cold working of zirconium alloys is used to reduce the dimensions of the products from hot working to those required in the finished components and to develop the final crystallographic texture. The main process for tubing is pilgering, which is used to make fuel cladding, pressure tubes and calandria tubes. To minimize defects, care has to be taken with the amount of deformation, the design and maintenance of dies and rolls, and the condition of lubrication.

4.6. HEAT TREATMENT OF ZIRCONIUM ALLOYS

Heat treating is used for many reasons:

— To homogenize chemical composition;
— To refine microstructure;
— To soften zirconium after cold deformation so that additional work can be imparted;
— To alter microstructural features such as dislocation density, second phase particle size and distribution and grain size to tailor the material for the best combination of strength, flaw tolerance, corrosion resistance and creep strength;
— To relieve stresses.

The main variables are time-at-temperature and cooling rate. The temperature controls which zirconium phases are present and whether any second phases exist. The time determines the amounts of phase transformation and growth. Care has to be taken so that oxidation is minimized and unwanted microstructures are avoided. Examples of technological importance are illustrated using mainly Zircaloy (typically 1.4 wt% (1.08 at.%) Sn, 1200 ppm (0.68 at.%) O, plus minor additions of Fe, Cr and Ni) to represent α alloys, and Zr-2.5Nb to represent (α + β) alloys [4.27].

4.6.1. Beta heat treatment

On heating from room temperature, zirconium undergoes a phase change at 1136 K (863°C) from an HCP crystal structure, the α phase, to a body centred cubic crystal structure, the β phase. The crystallographic relationship between the two phases is described by Burgers [4.28] as:

$$(0001)_\alpha // \{011\}_\beta ; < 11\bar{2}0 >_\alpha // < 111 >_\beta \quad (4.7)$$

The relationship between $(0001)_\alpha$ and $\{011\}_\beta$ corresponds to the closest packed planes and that between $< 11\bar{2}0 >_\alpha$ and $<111>_\beta$ corresponds to the nearest neighbour directions. The fit is not exact and results in small strains between the two phases.

With alloying, a region consisting of a mixture of the two phases is produced, the (α + β) phase region. The temperature of the transformation from the α phase to the (α + β) phase region and from the (α + β) phase region to the β phase depends on the alloying elements and their concentration (see Chapter 2, Section 2.4.4). In α alloys, although the β phase cannot be retained to room temperature, a wide range of microstructures is possible during cooling from the β phase. With very rapid cooling, a type of martensite with a distorted hexagonal crystal structure can form by diffusionless transformation, even in pure zirconium [4.29]. By analogy with steels, it is called α′.

4.6.1.1. Zircaloy

In the Zircaloys, the α phase transformation to (α + β) starts in the range 1093–1123 K (800–850°C) with complete transformation to the β phase in the range 1193 to 1281 K (920–1008°C) [4.30–4.37]. The Fe-Cr-Ni intermetallic second phase particles completely dissolve in the (α + β) phase region above about 1118–1153 K (845–880°C) [4.31, 4.32, 4.34]. The wide range of values is caused partly by the variation in composition allowed by the specification and partly by the interpretation of different experimental methods. The transformation temperatures may shift from equilibrium with rapid heating and cooling. For example, the second phase particles (SPPs) may survive to higher temperatures in the (α + β) region than indicated here as the heating rate is increased, and, under industrial conditions, may not dissolve to just before the (α+β)/β transus.

The average size of β grains, G_β, follows a growth behaviour, G_β = constant (time)^n, that may lead to very large grains, > 100 μm. An early study provided a value of 650 μm after 1 h at 1333 K (1060°C) [4.38]. The experiments to determine β grain size are difficult because times at temperature may be short and the heating period above the α/(α + β) boundary may contribute significantly to the total evaluation time. Also, sometimes the boundaries are difficult to discern because they are observed at room temperature and can be obscured by the transformation products on cooling; this problem may lead to an overestimation of β grain size. An interpretation of two studies [4.39, 4.40] indicates that n is between 0.11 and 0.20. Figure 4.42 shows the values at 1323 K (1050°C). A later study suggested that n was 0.435 but this value is based on data pooled from several different temperatures between 1273 and 1473 K (1000 and 1200°C) [4.41]. The β grains increase in size with increase in temperature, but no sensible activation energy has been determined. The variation in β grain size is weakly correlated with the total concentration of (Si+C+P) impurities, being smaller as this concentration increases [4.40].

Several changes happen during cooling to room temperature from the β phase:

— The phase changes from the β phase to the α phase or α′ phase.
— Intermetallic precipitates from the minor alloying elements Fe, Cr and Ni form.
— The α phase supersaturates in Fe, Cr and Ni.

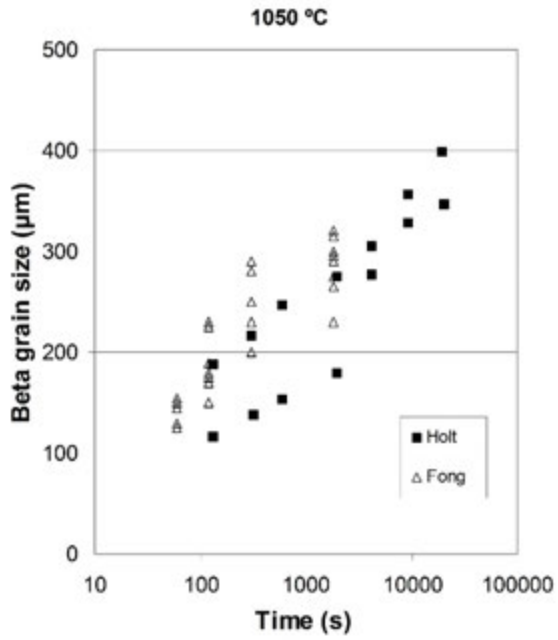

FIG. 4.42. Growth of β grains in Zircaloy-4 at 1050°C [4.39, 4.40].

A time–temperature–transformation diagram describes the various transformation products [4.31, 4.32]; see Fig. 4.43. A cooling rate of 1500°C/s is sufficient to avoid the left hand boundary of the (α + β) region and form the α′ phase. The martensite start temperature, M_s, is about 1073 K (800°C) [4.33]. With moderate cooling rates a Thomson-Widmanstätten structure is formed. The microstructure may consist of lath-shaped α grains in a random, basketweave microstructure, as shown in Fig. 4.44 (a) or the grains may be arranged in groups of parallel plates, as shown in Fig. 4.44 (b) [4.39]. The factors responsible for the latter microstructure have been evaluated; this microstructure is undesirable since it may lead to a poor response to subsequent cold work because the effective α grain size is large. In general, the parallel plate microstructure is nucleated at the prior β phase boundaries whereas when the α phase is nucleated at random precipitates or collections of foreign atoms, the basketweave microstructure is formed. The lamellar plates grow along [0001] [4.42]. With slow cooling, coarse plate-like grains form with irregular boundaries; these grains are called lenticular α grains. Sometimes a few equiaxed α grains form at the prior β grain boundaries, for example, after cooling from 1273 K (1000°C) at about 10°C/s.

Several interacting factors, including cooling rate, chemical composition and β grain size, determine the products of the transformation. In Ref. [4.32], the transformation microstructures on cooling from 1273 K (1000°C) were found to follow the sequence found in Table 4.1.

TABLE 4.1. EFFECT OF COOLING RATE ON β TO α PHASE TRANSFORMATION PRODUCTS [4.32]

Cooling rate (°C/s)	Microstructure
>1500	α′
1500–600	Basketweave and α′
600–10	Basketweave
10–2	Basketweave and parallel plates
2–0.5	Parallel plates
<0.5	Lenticular

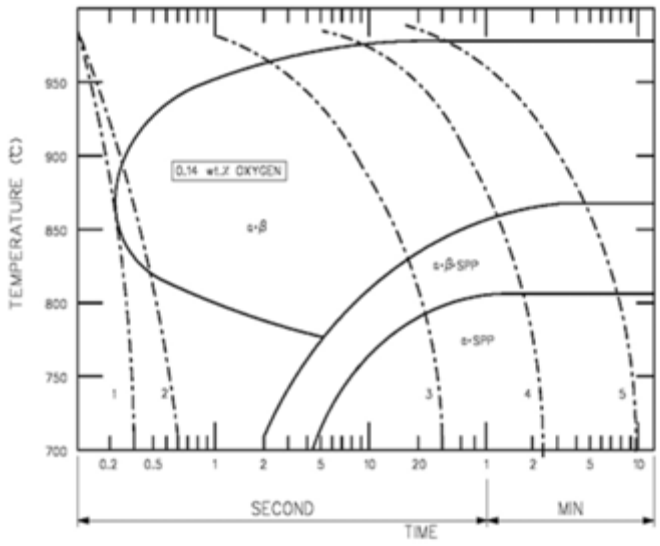

FIG. 4.43. Time-temperature-transformation diagram for Zircaloy-4. Numbers on dashed lines represent cooling rates as follows: 1 — 1500°C/s; 2 — 600°C/s; 3 — 10°C/s; 4 — 2°C/s; 5 — 0.5°C/s [4.32].

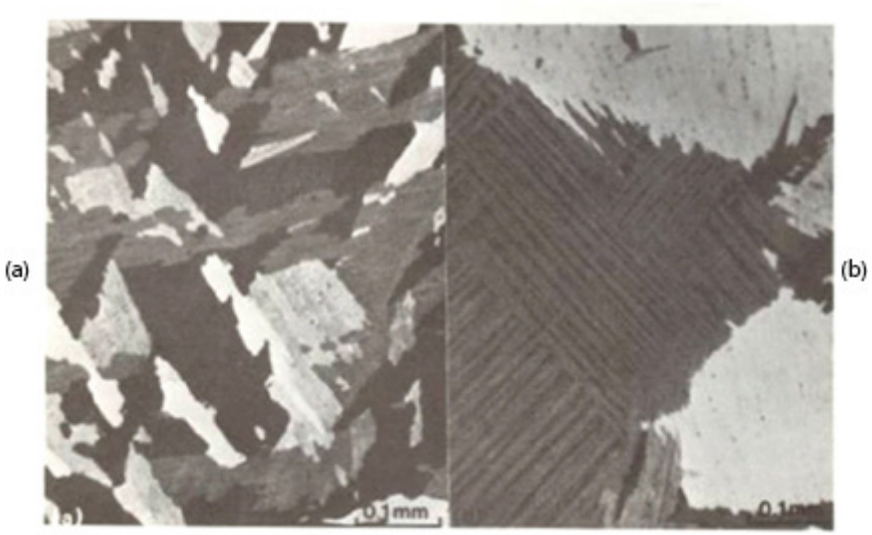

FIG. 4.44. Thomson-Widmanstätten morphologies in Zircaloy-4: (a) Basketweave structure; (b) parallel plate structure [4.39].

This apparently straightforward classification is complicated by both volatile and precipitated impurities, which dominate the selection of transformation products.

Ökvist and Källström [4.43] present convincing evidence that carbon, in the form of carbides, promotes the nucleation of α grains during cooling from the β phase with the subsequent production of a basketweave microstructure. A concentration of C > 100 ppm (0.076 at.%) was sufficient to attain the desired result whereas material containing < 50 ppm (0.038 at.%) C exhibited parallel plates after rapid cooling from the β phase. Holt [4.44] did not observe the cooling rate sequence in Table 4.1; with cooling rates of between 5 and 600°C/s one of his materials, containing 153 ppm (0.116 at.%) C (and 75 ppm (0.024 at.%)

Si), transformed from the β phase with a basketweave microstructure while another material containing 58 ppm (0.044 at.%) C (and 180 ppm (0.058 at.%) Si) transformed with parallel plates, thus corroborating Ref. [4.43]. The significance of the Si concentration is similar to that of C although it seems to operate in an indirect manner, based on the β/(β + Zr_3Si) transus diagram [4.45]. During time in the (β + Zr_3Si) region, the silicides coarsen, and, because their number density decreases, on cooling the nucleation sites for α grains are limited and the parallel plate microstructure is favoured. When cooled from a higher temperature in the single β phase region, many small Zr_3Si precipitates form during passage through the (β + Zr_3Si) region and provide effective nucleation sites for α grains and a subsequent basketweave microstructure. Phosphides also promote the basketweave microstructure but with low efficiency at unusable high P concentrations, for example, 100 ppm (0.029 at.%) [4.46].

Stringers variously containing the volatile elements Mg, Ca, Na and Cl, depending on reduction methods, are frequently found in standard products. Such materials form the basketweave microstructure with rapid cooling from the β phase whereas when the stringers are absent, parallel plates are produced [4.45]. When the metallic elements were added as oxides or hydroxides to stringer-free material with low concentrations of C, Si and P, the parallel plate microstructure was still observed. When the metallic elements were added as chlorides, a mixture of basketweave and parallel plate microstructures was found showing that Cl is a powerful agent for nucleating the α phase during cooling. Additions of C confirmed the earlier results [4.39, 4.43].

The effect of increasing oxygen concentration is to suppress the nucleation of α′ and promote the formation of the parallel plate and lenticular-grain microstructure [4.33]. This behaviour is attributed to the increase in the transformation temperature from the (α + β) region to the β phase and to the increased temperature range of the (α + β) region [4.32, 4.33].

The size of the laths of the α phase depends on their rate of nucleation and time of growth. As the cooling rate is increased, more nucleation sites are activated and the time for growth is short. Consequently, the lath width and length decrease as the cooling rate is increased. An ordered domain growth law can be used to model the relation between the lath width, L, and cooling rate, Ψ [4.41]:

$$\sqrt{\left(\ell^2 + \frac{C}{\Psi}\right)} \tag{4.8}$$

where ℓ is the initial domain diameter, taken as 0.1 μm and C is a constant, representing the grain surface energy density, a diffusivity and the temperature interval over which the cooling rate is measured, taken as 135 $\mu m^2 \cdot K \cdot s^{-1}$.

This correlation describes the data from five studies [4.33, 4.41, 4.44, 4.47, 4.48] over a wide range of cooling rates; see Fig. 4.45.

The strength is increased as the cooling rate from the β phase is increased. For example, starting with α annealed material with a 0.2% yield strength at 573 K (300°C) of 132 MPa, after furnace cooling the strength was slightly increased to 144 MPa, an air cool produced a strength of 173 MPa while water quenching increased the strength to 240 MPa [4.49].

One may expect that a crystallographic texture in the initial material should be much changed by a heating and cooling cycle into the β phase. From the orientation relationship of Eq. (4.7), six equivalent orientations of β grains are possible after the α → β phase transformation. Similarly, because the β phase has six {110} planes and each plane contains two <111> directions, twelve orientations of the α phase are possible during the β → α phase transformation. If all possible orientations were activated during each transformation, then

the crystallographic texture after an α → β → α phase cycle should be almost randomized. The textures are changed by β heat treatment, but the randomization is not as marked as expected from the above analysis, and the texture may even be strengthened. This texture memory is attributed to a biased selection of orientation variants during the transformation. This variant selection has been attributed to elastic anisotropy [4.50] and to some β grain boundaries having optimal properties for the nucleation of α grains with a particular orientation [4.36, 4.51, 4.52].

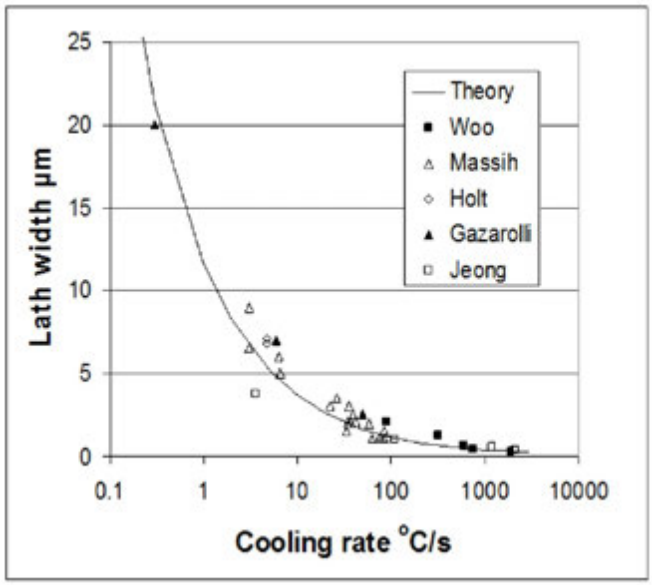

FIG. 4.45. Effect of cooling rate from the β phase on lath width in Zircaloy [4.33, 4.41, 4.44, 4.47, 4.48].

Post-β-heat treatment examination of tubing showed that the strong single or double peaked radial maximum of basal poles was weakened and spread towards the axial direction of the tube [4.53, 4.54] and the $< 11\bar{2}0 >$ directions were also rotated from the axial direction to a series of maxima close to the radial–transverse plane of the tube [4.54]. In a rod with an initial fibre texture and {0002} poles perpendicular to the rod axis and prism plane directions along the rod axis, the inherited texture from a β quench was sharper, as indicated by the texture index [4.55, 4.56] increasing from 2.5 to 4 [4.35]. Some basal poles had rotated towards the axial direction with the consequence that some $< 10\bar{1}0 >$ directions were perpendicular to the rod axis. A tensile stress imposed during the heating part of the temperature cycle led to a reduction in the sharpness of the α texture, which was interpreted as a reduction in variant selection during the β → α phase transformation.

In situ observations of the texture evolution during α → β → α phase cycles using the diffraction of neutron and synchrotron X ray irradiation gave a dramatic insight into the process [4.36, 4.37, 4.57]. The results were in reasonable agreement despite the large difference in heat and cooling rates and hold times; for the neutron diffraction experiments, the heating rate was 0.33°C/s with slower cooling rates and hold times at several temperatures of about one hour whereas during the synchrotron experiments, the heating was continuous at 10°C/s, the hold at 950°C was for 3 s while cooling was faster at 50°C/s. On heating, the initial cold worked texture developed a recrystallized sheet texture, consisting of two split maxima of [0002] close to the normal direction of the sheet with $< 11\bar{2}0 >$ directions parallel with the rolling direction. The texture of the α phase was retained during heating

through the (α + β) phase. The pole figures of the β phase contain a maximum of {111} poles in the rolling direction with the {110} pole figure having four maxima around the normal direction. With time in the β phase these textures intensified, with texture indices between 1.73 and 1.85. On cooling, although some of the texture components of the α phase are spread across the pole figure, some of the features of the texture of the recrystallized material remain, confirming the effect of variant selection. The final texture of the recrystallized microstructure is much weakened with the texture index being reduced from between 2.05 and 2.89 down to 1.82 and 1.65 and the texture factors [4.58], $F_{Normal}^{(0002)}$, being reduced from > 0.6 to 0.33, representing a random texture. If the material is cooled before reaching the β phase, that is, heating is stopped in the (α + β) phase region, the recrystallized texture is retained but a Thomson-Widmanstätten microstructure is produced, demonstrating a texture memory based on the residual α phase but a restructuring of the prior equiaxed α grains. Calculation of the texture of the β phase with no variant selection agreed with the observed texture [4.36, 4.37], but in another analysis variant selection was required [4.57]; this difference needs to be resolved. Similar calculations for the β → α transformation without variant selection disagreed with the observations suggesting that variant selection does occur during the nucleation of the α phase from the β phase. Any modification to the texture of the β phase, for example, by grain growth or deformation, will be inherited by the α phase. In commercial practice, quenching from high temperature can be used if an α phase texture close to random is required. The peak temperature should exceed the β transus but this temperature should be low enough to minimize excessive β grain growth; the recommended temperature range is 1223–1323 K (950–1050°C) [4.37].

The identity, chemistry, crystal structure, distribution, size and number density of the Fe-Cr-Ni intermetallic SPPs and the amounts of these elements retained in solution are important for corrosion resistance, and these features have been the subject of much research (see Chapter 8, Volume 2 of this publication). In some examples, detailed comparisons are difficult because the commercial sensitivity of some of the information means that the exact conditions of heat treatments may be veiled in secrecy. Also, some microstructural information is only provided after a series of fabrication steps, so the consequence of each step can only be inferred; this topic will be covered later (in Sections 4.6.2 and 4.6.3). The resolution of the microscopes, light, scanning electron microscope (SEM) or transmission electron microscope (TEM), and techniques of sample preparation colour the conclusions from some studies. Data on the dimensions of precipitates from TEM are more reliable than those from SEM if preferential dissolution of the zirconium matrix relative to the particles is avoided during specimen preparation [4.59, 4.60], and account is taken of large precipitates that intersect the foil surface. Artefacts from specimen preparation leading to overestimates of particle size using SEM may arise from dissolving very small particles and over-etching around large particles. Consequently, values of particle size from TEM are generally smaller than those measured by SEM. Care has to be taken with quantitative chemical analysis of particles within thin foils since information from the surrounding zirconium matrix can interfere. A summary of the advantages and disadvantages of the common experimental methods for examining SPPs in Zircaloy is provided by Maussner [4.61].

With high cooling rates, Ψ, the minor alloying elements Fe, Cr and Ni can be held in solid solution at room temperature. For example, following line (2) in Fig. 4.43, after holding Zircaloy at 1323 K (1050°C) for 900 s then cooling at a rate of 800°C/s by water quenching, a mixture of coarse and fine Thomson-Widmanstätten needles was produced without any precipitation being produced [4.62]. The interior of the larger grains contained low concentrations of the minor alloying elements while the grain boundaries were enriched with

these elements. The smaller grains contained the alloying elements but again without precipitates. A similar suppression of precipitation was observed in Zircaloy-4 water quenched from 1300 K (1030°C) at 1000°C/s [4.63]. Some magnetic measurements suggest that very small precipitates, < 2 nm in diameter, may be present after quenching, although they are not observable by microscopy [4.64].

With intermediate and low cooling rates (line (3) in Fig. 4.43), precipitates were nucleated on the Thomson-Widmanstätten lath boundaries; these boundaries then define the initial distribution of the precipitates. When cooled at 120–500°C/s after 20 s at 1273 K (1000°C), 30–50 nm platelets formed that were identified as face-centred cubic $Zr_4(Fe_{0.7}, Cr_{0.3})$ [4.42, 4.65]. The precipitates increase in diameter, *d,* and volume fraction, and decrease in number density, *N*, as the cooling rate is decreased [4.48]. Surprisingly, despite the opportunities for measurement, a direct relationship between *d* and *N*, and Ψ is not well founded. The nucleation and growth of SPPs during cooling from the β phase has been calculated based on the diffusivity of the minor alloying elements in a series of isothermal decrements [4.41]. The particle size increased during the time of the quench with the final size being inversely related to Ψ. Despite the assumptions required, especially on the appropriate diffusivities, the agreement with measurement was reasonable: with Ψ of 60°C/s, *d* was calculated to be 100 nm after β quenching compared with 140 nm as measured by SEM, while with Ψ of 6°C/s the same values were about 320 nm. Figure 4.46 depicts a correlation between observed precipitate diameter after quenching and Ψ based on data from the literature, including zero at 800°C/s [4.62].

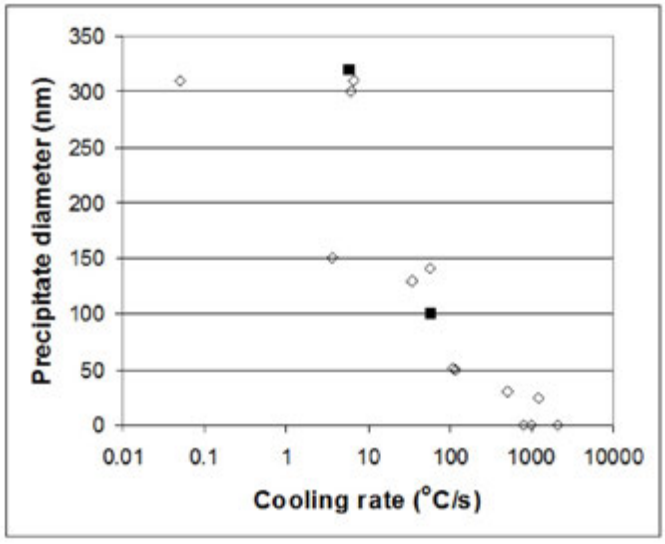

FIG. 4.46. Effect of cooling rate from β phase on size of intermetallic SPPs in Zircaloy-4 [4.41, 4.48, 4.62, 4.63, 4.65]. Solid squares represent calculation [4.41]; diamonds represent measurements.

4.6.1.2. Zr-2.5Nb

The Zr-Nb phase diagram is depicted in Fig. 2.15. An alloy containing nominally 2.5 at.% Nb will be in the β-Zr phase above about 1083 K (820°C), depending on the concentration of Nb, N and O. The initial decrease in the β/(α+β) transformation temperature with Nb concentration is about 12.6°C for each 1% Nb [4.66–4.68], so the usual variation allowed by specifications, for example, ± 0.15%, will change the expected transformation temperature by < 2°C. Concentrations of N are usually very small — < 65 ppm (0.042 at.%)

— so its variation has a limited effect on the transformation temperature. Around 1000 ppm (0.57 at.%) oxygen, the β/(α + β) transformation temperature is increased by about 9°C/100 ppm O, [4.66, 4.67, 4.69–4.74] as shown in Fig. 4.47; in a Zr-2.5Nb alloy containing 100 ppm (0.057 at.%) oxygen, the β/(α + β) transformation is about 1113 K (840°C) [4.66], with 800 ppm (0.45 at.%) oxygen, the β/(α + β) transformation is about 1173 K (900°C) [4.67] while 1440 ppm (0.78 at.%) oxygen raises the β/(α + β) boundary to about 1247 K (974°C). As with Zircaloy, very large grains, >>100 μm, are observed after about one hour in the β phase. They are observed as prior β boundaries in metallographic examinations at room temperature. In an early study, the average size of β grains, G_β, followed a growth behaviour, G_β = constant (time)^n, that was temperature sensitive [4.75], as shown in Fig. 4.48. At 1233 K and 1273 K (960°C and 1000°C), the value of n was about 0.4 but at 1313 K (1040°C) it declined to about 0.2; as the grain size approached 1 mm, the edges of the specimens may have limited grain growth. Later observations suggest that the β grains may grow even faster, possibly because the materials currently used contain fewer impurities than the materials available in the 1960s. As examples, when the alloy was made from very pure zirconium (with oxygen and iron concentrations of 161 ppm (0.092 at.%) and 70 ppm (0.011 at.%), respectively), the β grain size was 800 μm after 900 s at 1248 K (975°C) [4.76]; in the mid-1990s, prior-β grains with diameters of about 9 mm were observed in hollow extrusion billets when they were quenched from the β phase [4.77].

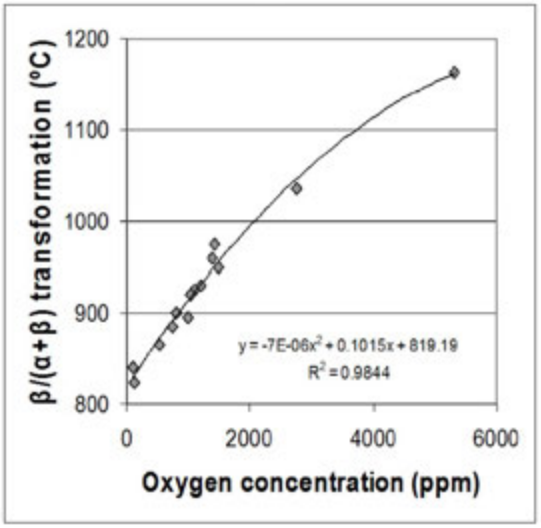

FIG. 4.47. Increase with oxygen concentration of transformation temperature between the β phase and the (α + β) phase region in Zr-2.5Nb [4.66, 4.67, 4.69–4.74].

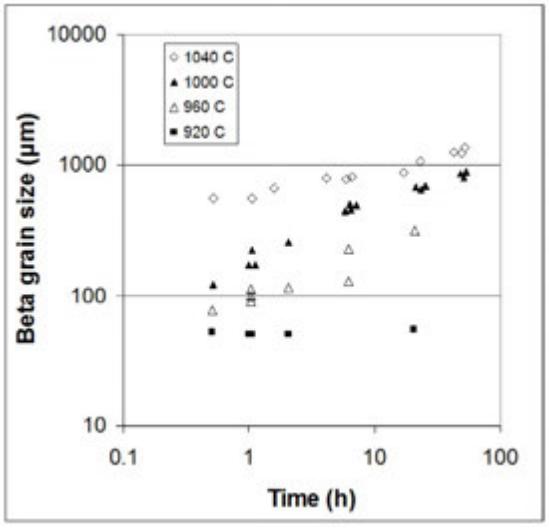

FIG. 4.48. Growth of β grains in Zr-2.5Nb in the β phase and high in the (α + β) phase region [4.75].

On slowly cooling below this transformation temperature, the α phase is formed within the β_{Zr} phase. The growth of the β phase was much curtailed in the (α + β) phase region by the emergent α phase; for example, see data for 1193 K (920°C) in Fig. 4.48 [4.71, 4.75]. On further cooling to below the eutectoid temperature of 893±10 K (610±10°C), some of the β_{Zr} phase transforms by growth on the existing α phase while the remainder, which has been enriched to the eutectoid composition of 17–20% Nb, is metastable to room temperature. The microstructure of slowly cooled Zr-2.5Nb consists of α grains surrounded by β phase. The isothermal transformation of the bulk eutectoid phase is described by a time-temperature-transformation diagram, Fig. 2.16. In the temperature range 800–875 K (525–600°C), this β phase decomposes through [4.78]:

$$\beta \rightarrow \alpha + \beta_{enr} \rightarrow \alpha + \beta_{enr} + \beta_{Nb} \rightarrow \alpha + \beta_{Nb} \quad (4.9)$$

and below 800 K (525°C):

$$\beta \rightarrow \omega + \beta_{enr} \rightarrow \alpha + \omega + \beta_{enr} \rightarrow \alpha + \beta_{enr} \rightarrow \alpha + \beta_{enr} + \beta_{Nb} \rightarrow \alpha + \beta_{Nb} \quad (4.10)$$

The ω phase is an HCP Zr-rich phase; it and the β_{enr} phase impart extra strength to the second phase. These transformations are very slow, even close to the eutectoid temperature.

The time-temperature-transformation diagram for the β phase in Zr-2.5Nb [4.79], as shown in Fig. 4.49, has three main differences from Fig. 2.16:

(a) At temperatures 773 K (>500°C), the rate of formation of the Nb-enriched β phases is faster than in the bulk material.
(b) The upper limit for ω phase formation is lowered to about 748 K (475°C) from 798 K (525°C).
(c) Two metastable β phases, enriched in Nb to different amounts, form between 723 and 873 K (450 and 600°C); one phase is associated with the α/β interface while the other corresponds to the untransformed β phase.

In this alloy, the α phase is the major phase and detection of the small amount of α phase resulting from the decomposition of the β phase is very difficult. After extrusion, the β phase forms in filaments; after long heat treatments or residence in a reactor, the filaments disintegrate to discrete Nb-rich particles. With slow cooling, Nb is retained in supersaturated solid solution in the α phase and is only released by irradiation (see Chapter 6, Section 6.3.3, Volume 2 of this publication) or resolution into the β phase or (α + β) phase regions followed by quenching and tempering.

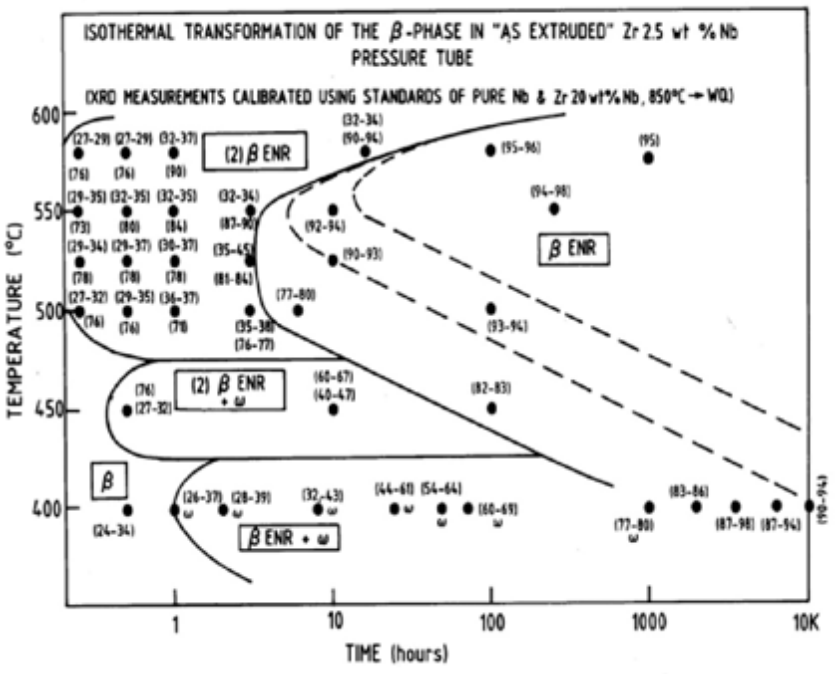

FIG. 4.49. Time–temperature–transformation diagram for Zr-2.5Nb. The numbers in brackets refer to Nb concentration. For two discrete β phase components, there are two bracketed values. Where two numbers are shown in one bracket, the values refer to measurements using the (110) and (200) planes [4.79].

When Zr-2.5Nb is cooled rapidly from the β phase, martensite, or α′ phase, is formed [4.29, 4.69, 4.71, 4.80–4.87]. The start temperature, M_s, is around 943 K (670°C) [4.80]. It is independent of oxygen concentration up to 5320 ppm (2.96 at.%) and cooling rate in the range 100–10000°C/s. Time-at-temperature, and therefore β grain size, had little effect on the transformation temperature. At very high cooling rates, >400°C/s, the α′ phase consists of acicular grains, about 0.5–1.5 μm wide, containing microtwins [4.29, 4.84, 4.85, 4.87]. With slower cooling rates, about 120–300°C/s, no twins are formed. As with Zircaloy, moderate cooling rates, <60°C/s, produce a Thomson-Widmanstätten structure. The reported cooling rates were defined in various ways — for example, the rate was taken at the transformation temperature [4.82] and in other studies it was taken from the time it took to cool down from the quenching temperature to some arbitrary temperature (e.g. 773 K (500°C)) [4.69, 4.85]. Compared with carbon steels, the response to a Jominy test was unusual [4.81] because the highest hardness was not attained with the fastest cooling rate but at some intermediate rate [4.69, 4.81]; see Figs 4.50 and 4.51. These results indicate that some precipitation hardening, possibly from the ω phase, was taking place with the intermediate cooling rates [4.83]. The variation of cooling rate for the peak hardness is attributed to differences in composition and quenching temperature. It should be noted that not all studies show this effect; one example is included in Fig. 4.51.

In Fig. 4.5.1, the line marked ‘Cheadle’ is based on a Jominy test on material containing 2.5 Nb and 1080 ppm (0.61 at.%) oxygen quenched from about 1173 K (900°C) [4.81]; the line marked ‘Winton’ is based on separate specimens containing 2.8 Nb and 1500 ppm (0.85 at.%) oxygen quenched from 1273 K (1000°C) into various media [4.69]; points marked ‘Williams’ are based on separate specimens containing 2.9 Nb and 1125 ppm (0.64 at.%) oxygen quenched from 1273 K (1000°C) into various media [4.85]. The cooling rate also affects the tensile strength in a similar manner. Starting with α annealed material with a 0.2% yield strength at room temperature of 350 MPa, after furnace cooling from the β phase the strength was increased to 520 MPa, while water quenching from the β phase increased the strength to 730 MPa.

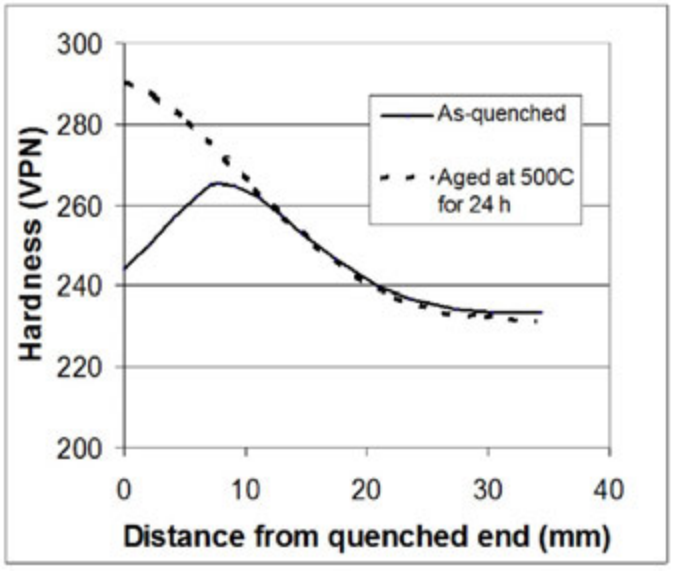

FIG. 4.50. Hardenability curves from Jominy test on Zr-2.5 Nb containing 1080 ppm (0.61 at.%) oxygen quenched from about 1173 K (900°C), as-quenched and after ageing for 24 h at 773 K (500°C) [4.81].

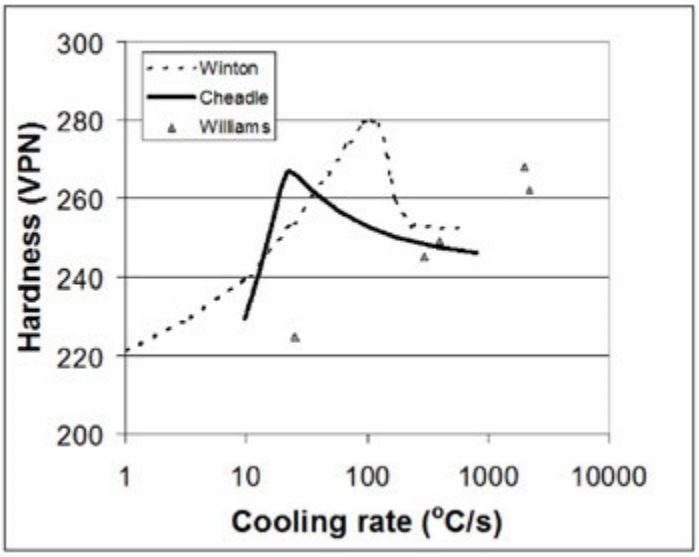

FIG. 4.51. Effect of cooling rate during quenching on hardness of Zr-2.5Nb alloys from the β phase.

When rapidly cooled from high in the (α + β) region, the retained β phase transforms to the α′ phase. The resulting microstructure consists of a mixture of equiaxed α grains and acicular transformed β phase, the proportions depending on the quench temperature. The room temperature tensile strength after quenching from 1123 K (850°C) is 750 MPa, similar to that of β quenched material. The α′ phase is less prominent or absent when quenching from below 1073 K (800°C), leading to lower strength. A steady decline in as-quenched hardness as the quench temperature is reduced is interrupted by a peak in hardness, attributed to a mixture of β phase and ω phase, observed when the quench temperature is around 1033 K (760°C) [4.83].

The texture of Zr-2.5Nb is changed by the β transformation, shown in Fig. 4.52. In these pole figures, the axial direction is vertical, the transverse direction is horizontal and the radial direction is about the centre of the diagram. The pole figures in the starting condition show a strong preferred orientation of basal poles in the transverse direction, shown in Fig. 4.52(a), and a lack of Burgers relation with nearly random orientation of the β phase, shown in Fig. 4.52(b) and (d). After two cycles into the β phase followed by slow cooling, many of the basal poles have rotated into the axial and intermediate directions as shown in Fig. 4.52(e) and are related to the strong texture developed in the β phase, shown in Fig. 4.52(f) and (h), through the Burgers relation. As with Zircaloy, the Burgers relation is involved but the lack of a random texture with slow heating indicates that some variants are being selected. In the experimental studies on pressure tube materials, the starting texture for the basal pole is strong in the transverse radial plane; an example for an high power channel type reactor (RBMK) pressure tube is given in Table 4.2 while Fig. 4.52(a) provides an example for a CANDU pressure tube. Measurements after heat treatment [4.53, 4.88] and in situ [4.74, 4.89, 4.90] show the following general trends:

— Unlike in Zircaloy, no texture change caused by recrystallization is detected in Zr-2.5Nb.
— A single cycle into the β phase is sufficient to greatly modify the texture. After slow heating to the β phase, followed by slow cooling or water quenching, the component of the basal pole texture in the transverse radial plane is much reduced and a strong component is formed in the axial direction; see Table 4.2 and Fig. 4.52(e).

— Heating the same starting material rapidly (>100°C/s) into the β phase (1223 K (950°C)) for a short residence time (about 10 s) followed by a water quench (1000°C/s) produces an isotropic texture, see Table 4.2, and a fine platelet (1–2 μm) microstructure [4.88]. A slower cooling rate from the β phase retains the random texture but creates a coarse Thomson-Widmanstätten microstructure with β_{Nb} particles in the grain boundaries. If the starting material has a strong axial distribution of basal poles, the rapid heating into the β phase has no effect on this texture. Imposition of a tensile stress >2.5 MPa promotes the formation of the isotropic texture in the starting material with basal poles in the transverse radial plane but has no effect on material that has its stable texture.
— With further temperature cycles into the β phase, the new textures are preserved and reinforced, independent of the heating rate; with slow temperature changes, a cubic component symmetry is developed; see Fig. 4.52(e).
— After hot extrusion used to make the tubes, the starting β phase texture does not have a Burgers relation with the α phase; see Fig. 4.52(a)–(d). With heating cycles into the β phase, the initial weak texture of the β phase progresses to one with a strong (110) axial component and a cubic texture with the components about 45° from the principal directions of the tube, as seen in Fig. 4.52(f). This result indicates that the β phase was nucleated from the α phase rather than grown on the initial β phase. In accordance with Eq. (4.7), the subsequent texture of the α phase is strongly reflected as an inheritance from that of the β phase at high temperature — compare Fig. 4.52(e) and (f) and Fig. 4.52(g) and (h).
— As the maximum temperature is reduced through the (α + β) phase, the texture is a mixture of that at low temperature and that produced by the transformation [4.9, 4.53, 4.74]; the retained component of the basal texture in the transverse radial plane is increased but the axial component declines as the amount of β phase is reduced with a decrease in maximum temperature; see Fig. 4.53.

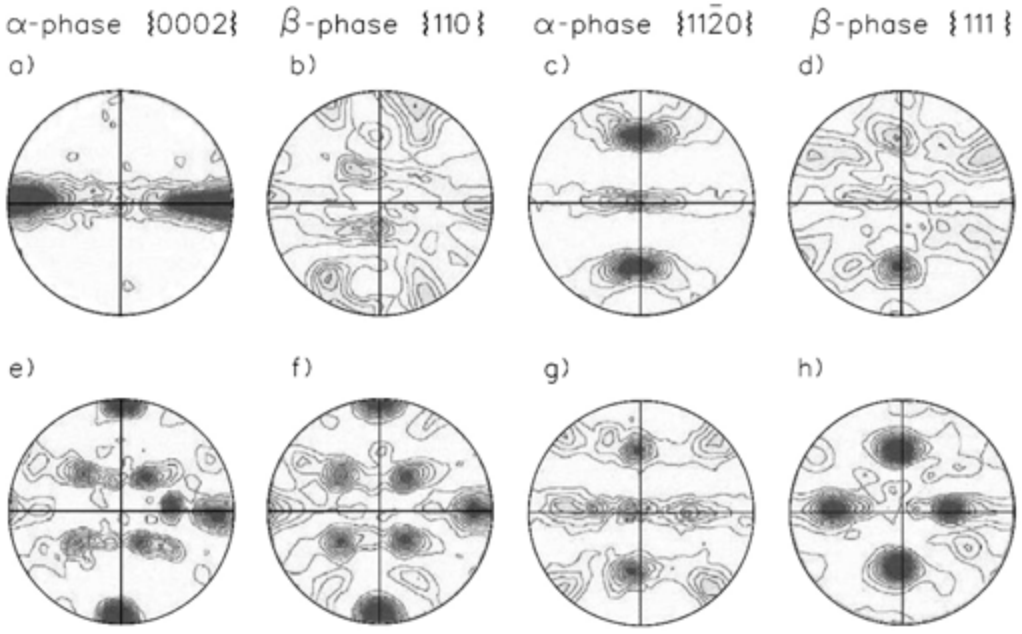

FIG. 4.52. Textures in CANDU Zr-2.5Nb pressure tube, based on Ref. [4.89].

TABLE 4.2. TEXTURE IN ZR-2.5Nb PRESSURE TUBES PRODUCED BY HEATING INTO β PHASE, INDICATED BY KEARNS' FACTORS IN LONGITUDINAL (L), TRANSVERSE (T) AND RADIAL (R) DIRECTIONS [4.88]

Material: Zr-2.5Nb	F_L	F_T	F_R
RBMK pressure tube	0.059	0.466	0.475
Slow heat into β phase, water quench	0.461	0.295	0.244
Fast heat into β phase, water quench	0.334	0.330	0.336

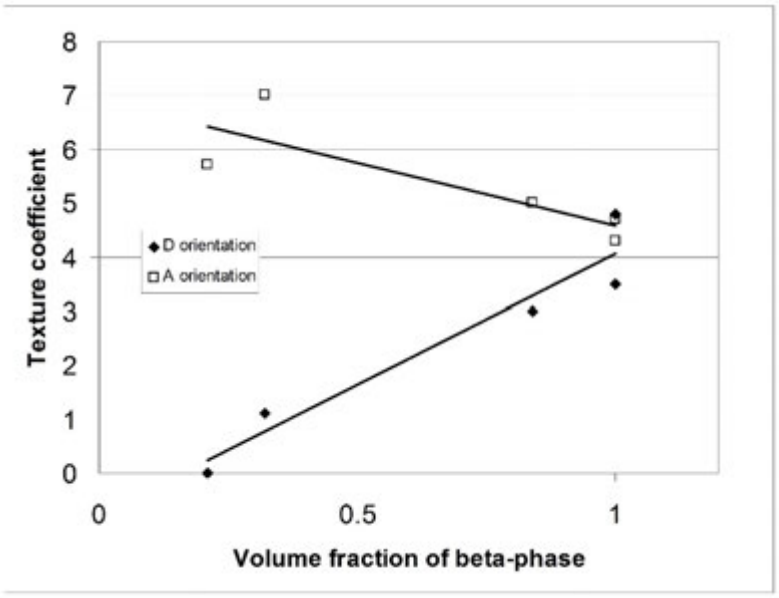

FIG. 4.53. Change in transverse (A) and axial (D) texture coefficients for the basal plane in Zr 2.5Nb with increase in the volume fraction of the β phase during heating into the (α + β) phase (based on data from Refs [4.9, 4.53, 4.74]).

4.6.2. Post β quench heat treatment

4.6.2.1. Zircaloy

Hot and cold working are required to take the material in the form of an ingot to a useful geometry to make a component. In tube manufacturing, the material is usually β quenched just before extrusion or just before the last hot working step. Anneals are used to soften the material between cold reductions to enable succeeding reductions and for the final condition. The two main consequences of the heat treatments are the softening by recovery and recrystallization and modification of the size and distribution of intermetallic SPPs. The latter is important for corrosion resistance (see Chapter 8, Volume 2 of this publication).

(a) Recovery and recrystallization

Recovery consists of the rearrangement of the dislocation structure from cold work by its annihilation or movement into cells. Dislocations can move by cross-slip at low temperatures (for example, 0.2 of the melting temperatures, T_m), provided that enough internal stress is built up by cold working. Dislocation climb requires the movement of vacancies and is characterized by a higher temperature than cross-slip (for example, 0.4 T_m), and less sensitivity to the internal stress from the cold work. The state of recovery can be

detected by changes in electrical resistivity, breadth of X ray diffraction lines, TEM and by softening.

The amount of softening is very large when new grains are nucleated and grown during recrystallization. The line tension of the high density of dislocations from the cold work provides the driving force to form and move high angle grain boundaries. The rate of boundary movement is proportional to the difference in dislocation density between the new grains and the cold worked grains and increases exponentially with temperature, usually following an Arrhenius-type equation. The degree of recrystallization is measured directly from the microstructure and from mechanical testing.

In the laboratory, changes in properties are usually indicated as a function of temperature at constant time or as a function of time at a constant temperature, with the chief metallurgical variable being the amount of cold work. The changes follow an S shaped profile with the rates being low at the start and end of the transformation but relatively rapid in between, as shown in Fig. 4.54.

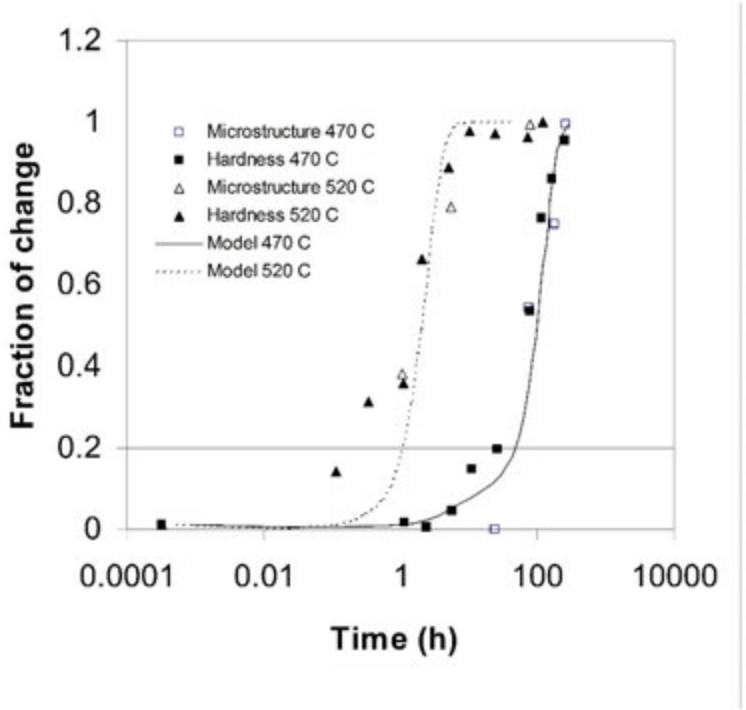

FIG. 4.54. Change with time in hardness and volume of new grains in Zircaloy-4 (cold worked 78%) at 743 K (470°C) and 293 K (520°C) [4.91].

Recovery and recrystallization can be concurrent but operate at different rates, making separation difficult. Recovery at temperatures for times appropriate for fabrication is mostly complete before new grains are detected, as indicated by comparing X ray line sharpening and hardness; see Fig. 4.55 [4.92]. When a cold worked plate of Zircaloy-4 was annealed at 773 K (500°C) for nearly 40 h, X ray line sharpening indicated much of the possible recovery was achieved, about 80%, whereas the hardness only declined by 25% of the possible amount in 40% cold worked material and 50% in 60% cold worked material [4.92]. At 673 K (400°C), the strength is reduced over a very long time without recrystallization; Fig. 4.56 shows the annealing of another Zircaloy-4 plate, cold worked 50%, in which the 0.01% yield stress at 273 K (0°C) was reduced by about 45% of the available softening in 72 days [4.93]. Using TEM, no new grains were observed; rather, the dislocations were rearranged

into cells and subgrains. Similar recovery of strength was observed at 773 K (500°C) up to about 6000 s (point A in Fig. 4.56), at which time heterogeneous nucleation of new grains was observed. The subsequent loss in strength was about 86% of the available amount in 40 h, accompanied by incomplete recrystallization. This softening is greater than that indicated by the previous data [4.92]. At 873 K (600°C), recovery was discerned up to point A, at about 180 s, followed by rapid and complete softening in less than 2 h; see Fig. 4.56.

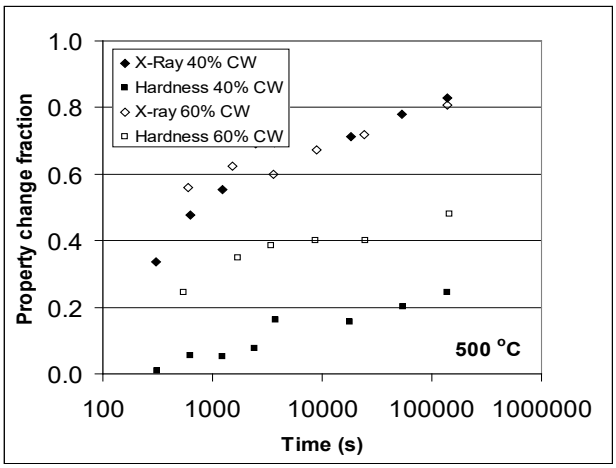

FIG. 4.55. Recovery of cold work in Zircaloy-4 at 773 K (500°C). Based on Ref. [4.92].

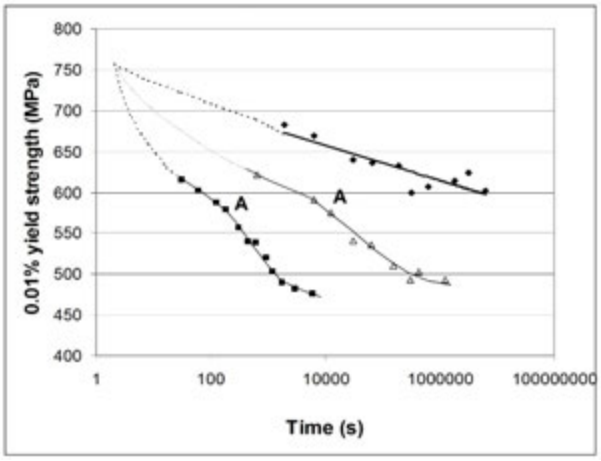

FIG. 4.56. Recovery and recrystallization of Zircaloy-4 plate after 50% cold work. Solid diamonds — 400°C; open triangles — 500°C; solid squares — 600°C. Recrystallization starts at point A [4.93].

In general, the temperature dependence of property changes during recrystallization, as represented by hardness [4.94] and TEM [4.95], again follows an S-shaped curve, as shown in Fig. 4.57. The temperature range between the start and finish of recrystallization can be very narrow. In the example given in Fig. 4.57, the material was cold worked 76–80% and the annealing time was 4–5 h; recrystallization starts at about 773 K (500°C) and is complete at 823 K (550°C). This result indicates that temperature gradients in annealing furnaces have to be minimized to ensure that no large variations in property develop when heat treating in this temperature range. The start and finish temperatures for recrystallization are reduced as the amount of cold work is increased. Data from many studies [4.92, 4.93, 4.95–4.97] are plotted in Fig. 4.58 for an annealing time of 1 h. The data are too scattered to discern whether

the difference between the start and finish temperatures is affected by cold work. At the end of recrystallization, the grain size is usually in the range 3–10 μm.

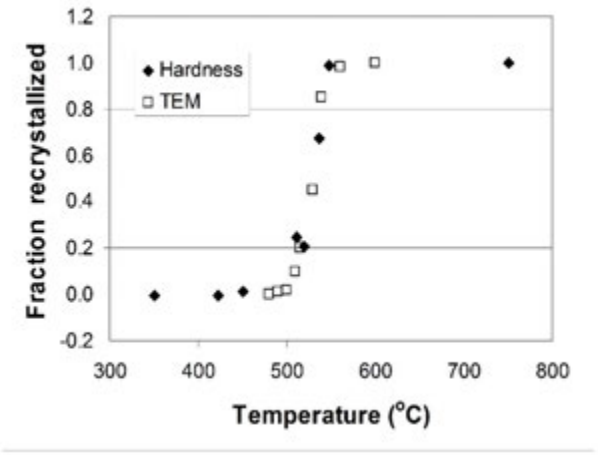

FIG. 4.57. Temperature dependence of recrystallization; Zircaloy cold worked 76–80%, annealed for 4–5 h. Based on Ref. [4.94] (hardness) and Ref. [4.95] (TEM).

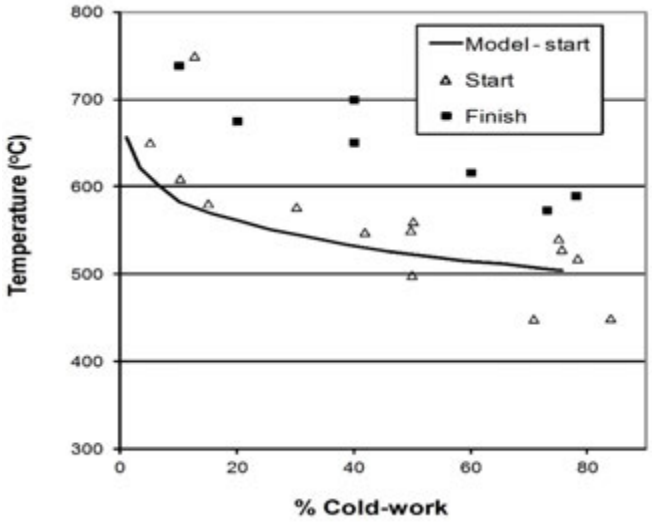

FIG. 4.58. The effect of the amount of cold work on the temperature for the start and completion of recrystallization after an anneal for 1 h. Data from [4.92, 4.93, 4.95–4.97]. Model for start of recrystallization based on Ref. [4.91].

Oxygen concentration can affect the kinetics of recrystallization and the amount of softening [4.98]. In Zircaloy-2 that is cold worked 50% and contains an oxygen concentration of 140 ppm (0.08 at.%), softening started from a Knoop microhardness of 175 at about 748 K (475°C) and finished with a hardness of 105 at about 923 K (650°C); when the oxygen concentration was raised to 1740 ppm (0.98 at.%), softening started from a hardness of 235 at about 803 K (530°C) and finished with a hardness of 195 at about 998 K (625°C). The effect of increasing the oxygen concentration is to postpone the start of recrystallization to a higher temperature but reduce the completion temperature.

Beta quenching Zircaloy-4 before cold working provides a modest hardening, depending on the cooling rate, but much increases the work hardening. For example, starting with α annealed material with a hardness of 198 diamond pyramid hardness, cold working to 40% increased the hardness to 243 diamond pyramid hardness whereas starting with the same

material, 0.38 mm thick quenched into water from 1333 K (1060°C), the hardness was 204 diamond pyramid hardness; after 40% cold work the hardness had increased to 270 diamond pyramid hardness [4.38]. An age hardening was observed after annealing the β quenched and cold worked material at 773 K (500°C) with a peak at about 1 h, but at higher temperatures the softening of the β quenched and cold worked material had similar kinetics to that of the α annealed and cold worked material, as seen in Fig. 4.59 [4.38, 4.92]. Many small equiaxed grains were observed after annealing 20% and 40% cold worked material above 873 K (600°C) indicating recrystallization by nucleation and growth; with material cold worked 10%, the new grains appeared to be formed directly from the α′ phase of the quench.

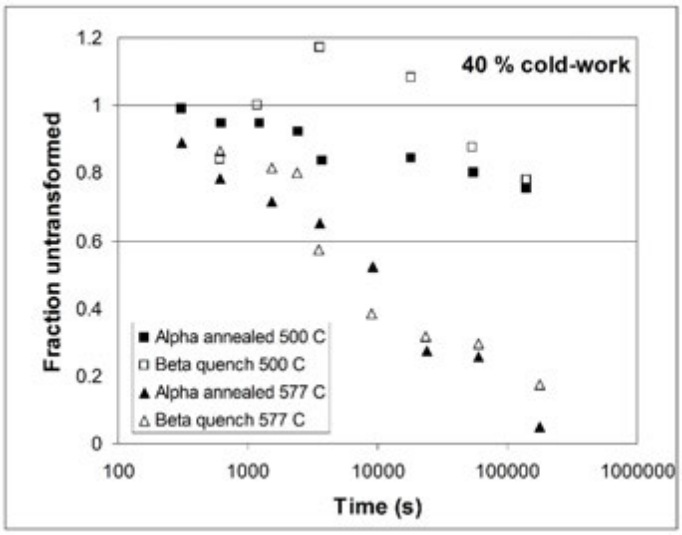

FIG. 4.59. Effect of annealing Zircaloy-4 after 40% cold work; starting material either α annealed or β quenched (based on Refs [4.38, 4.92]).

Care has to be taken not to hold cold worked or quenched and cold worked material at the annealing temperature for too long at too high a temperature; otherwise, secondary recrystallization and runaway grain growth may lead to very large grains. In Zircaloy-4, after one week at 1070 K (800°C) the α grains could be 900 μm in diameter in material cold worked 20–40%. Large grain growth was suppressed in material quenched and cold worked 10%, presumably because of the different mechanism of grain nucleation. In as-quenched material, grain diameters up to 1800 μm were observed [4.38]. This observation was attributed to the lack of precipitates available to slow grain boundary migration. A similar explanation was used for the large grains in Zr-1.25Cr grown after a mixed Thomson-Widmanstätten and martensite structure produced by β quenching was heat treated between 923 and 1073 K (650 and 800°C) [4.99, 4.100]. A low temperature heat treatment, 623–672 K (350–400°C), which produced small precipitates (25–30 nm) without recrystallization, was found to reduce the tendency for massive grain growth during the high temperature anneal. Larger precipitates, about 75 nm, did not suppress massive grain growth when the Thomson-Widmanstätten structure was annealed for 2 h at 1033 K (760°C) after cold working [4.101]. This example shows that below a critical strain, no new grains were nucleated but in a critical strain range, between 11 and 17%, a few new grains formed and grew very large, to about 800 μm, as seen in Fig. 4.60 [4.101]. Such a microstructure should be avoided because of its detrimental effect on mechanical properties, unless the aim is to produce very large or single crystals.

Data from recrystallization experiments can be fitted to a first order chemical rate equation:

$$\frac{\mathrm{d}F}{\mathrm{d}t} = -\lambda_0 \cdot \exp\left[-\frac{Q}{\mathrm{R}\cdot T(t)}\right] \tag{4.11}$$

where

F	is the unrecrystallized fraction;
t	is the annealing time;
λ_0	is a constant;
Q	is the activation energy for the process;
T	is the annealing temperature (in K);

and R is the gas constant.

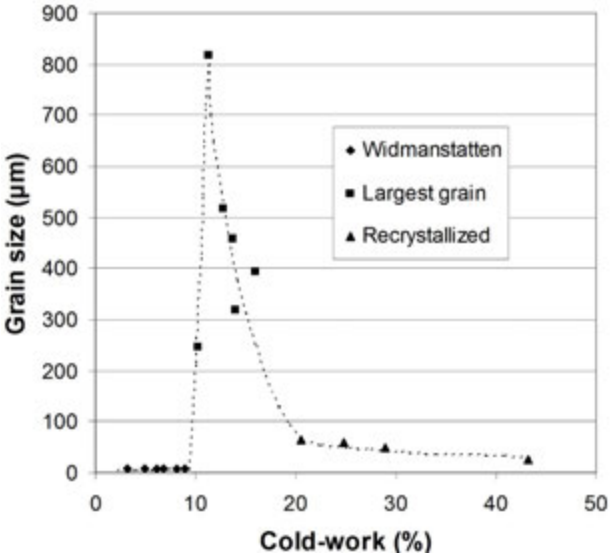

FIG. 4.60. Critical strain for massive grain growth in Zr-1.25 Cr; Thomson-Widmanstätten structure annealed for 2 h at 1033 K (760°C) after various amounts of cold working. Thomson-Widmanstätten plate width plotted as grain size below 10% cold work; above 20% strain, the grains were equiaxed; the largest grain size was plotted between 11 and 20% cold work because of inhomogeneous structure [4.101].

This approach is useful for both isothermal experiments and transient heating experiments [4.102] (care has to be taken to interpret more than an empirical fit since concentration variables are absent). Alternatively, data on recrystallization from isothermal tests are described by:

$$\left(\frac{1}{t}\right) = \mathrm{A}^* \cdot \exp\left[-\frac{Q}{\mathrm{R}\cdot T}\right] \tag{4.12}$$

where

A^*	is a constant;
Q	is the activation energy;

and R is the gas constant.

With either approach the agreement throughout the literature on the value of Q is remarkable. Studies using wide ranges of the amounts of cold work, annealing times and annealing temperatures and different experimental methods varying from hardness and tensile testing, light and electron metallography, X ray diffraction and differential thermal analysis, all provide values of Q/R close to 40 000 K; see Table 4.3.

Often it is useful to normalize t by simply transposing A^* in Eq. (4.10) and taking its reciprocal, A:

$$A = t \cdot \exp\left[-\frac{Q}{R \cdot T}\right] \tag{4.13}$$

This normalized annealing time is called the annealing parameter, A. A measure of recrystallization for any starting metallurgical condition can then be plotted against A for all combinations of annealing time and temperature on a single curve. As an example, Fig. 4.61 depicts the change in the yield strength at 673 K (400°C) of Zircaloy cold worked 63.4% as a function of A [4.95].

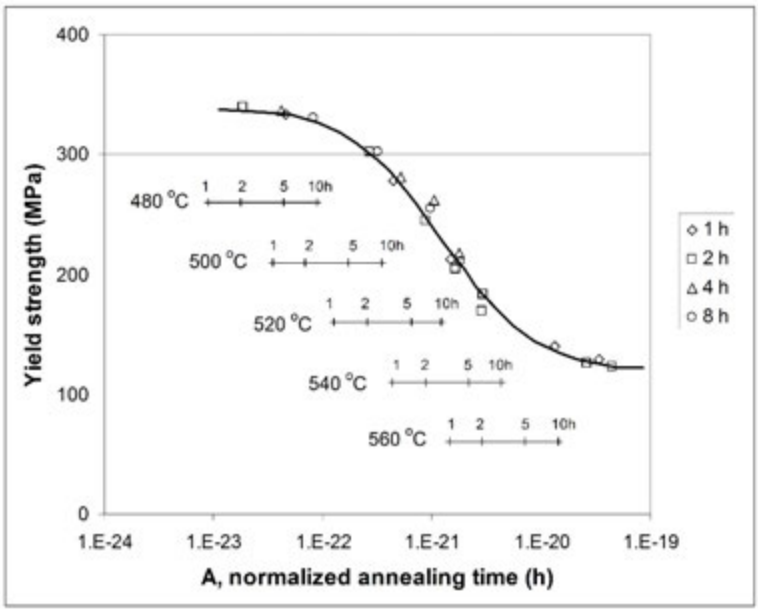

FIG. 4.61. Dependence of the yield strength at 673 K (400°C) of Zircaloy-4, cold worked 63.4%, on the normalized annealing time, A. The value of A at various temperatures for various times is also illustrated (*based on Ref. [4.95]).*

Recovery and recrystallization have been successfully modelled [4.91]. At elevated temperatures, the driving force from the stored energy and the dislocation density induced by cold work decreases with time and leads to recovery. The model compared favourably with the results of a very long recovery experiment at 673 K (400°C); see Fig. 4.62. The initial slow rate of recrystallization is attributed to the time for nuclei of new grains to form; the volume transformed increases rapidly as these grains grow and new ones are nucleated. As the opportunity for new nuclei diminishes and the growing grains impinge on one another, the rate of transformation diminishes. General equations describing nucleation and growth have been developed by Kolmogorov [4.103], Johnson and Mehl [4.104] and Avrami [4.105, 4.106] and can be applied to recrystallization. They have the form:

$$f(t) = 1 - \exp\left[-\frac{\pi}{3N_v G^3 t^4}\right] \quad (4.14)$$

where

$f(t)$ is the fraction transformed in time *t;*
N_v is the nucleation rate;

and N_v is the growth rate.

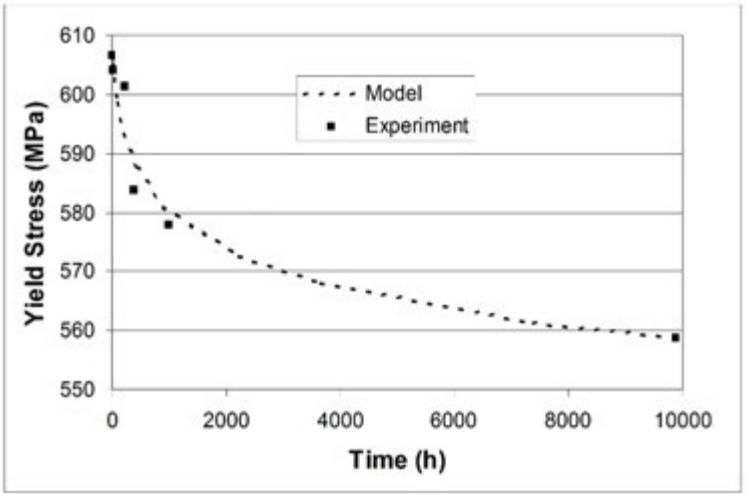

FIG. 4.62. Comparison of model with experiment on softening kinetics of 78% cold worked Zircaloy-4 at 673 K (400°C) [4.91].

Some of the assumptions underpinning this approach, for example, constant nucleation and growth rates, appear to be too simplistic. Because recovery and recrystallization are concurrent, in the new model [4.91], the driving forces for recrystallization lead to a non-constant growth rate. The growth rate of new grains is related to the instability of the underlying subgrains and cell structure through strain induced boundary migration. The model describes the change in strength and degree of recrystallization with time, shown in Fig. 4.54, and the effect of cold work on the starting temperature for recrystallization, shown in Fig. 4.58.

(b) Precipitation

The properties of the SPPs and their surrounding Zr matrix control corrosion and hydrogen pick-up (Chapter 8, Volume 2 of this publication) and this subject has received much attention. The minor alloying elements in Zircaloy — Fe, Cr and Ni — have low solubility limits in the α phase; not greater than 100 ppm (0.016 at.%) at reactor operating temperatures [4.107–4.109] (see also Chapter 2). After rapidly cooling from either the β phase or the (α + β) region, these elements are either in supersaturated solid solution or dispersed as small precipitates with some of the elements still in solution (Section 4.6.1.1). With each subsequent fabrication step of cold working and annealing, recovery and recrystallization have to be repeated but the products of the precipitation processes accumulate.

TABLE 4.3. TEMPERATURE DEPENDENCE OF RECRYSTALLIZATION IN ZIRCALOY EVALUATED BY SEVERAL METHODS

Method	Cold work (%)	Temperature (°C)	Time (s)	Q/R (K)	Comment	Reference
Hardness, light metallography, X ray diffraction	10–60	500–800	300–600 000	40 900–42 400	—	[4.92]
Tensile test at 0°C, hardness, TEM	50	400–700	6–6 000 000	40 620	—	[4.93]
Tensile test at 400°C, TEM	40.2–76.2	480–600	900–18 000	40 000	—	[4.98]
Hardness, light metallography	70	580–850	10–3 600	40 000	—	[4.97]
Differential thermal analysis	50	400–800	Dynamic	36 000	Continuous measurement	[4.110]
Hardness, X ray diffraction, resistivity, TEM	15–78	360–510	7200–14 400 000	30 300	Q based on recovery	[4.111]
Hardness, TEM	Cold worked and stress relieved + 30	540–710	60	41 550	Condition of starting material uncertain	[4.102]
Tensile test at 400°C	70–90	450–750	1 800–72 000	40 000	Cold work amount not stated	[4.112]
Tensile test at 343°C	60+ stress relief	600–800	1–1 000	41 550	Very short heating and cooling times	[4.113]
Hardness	50	400–700	900–14 000	42 940	Oxygen concentrations from 140–1740 ppm (0.08–0.98 at.%)	[4.98]

In Zircaloy-4, the concentration of Ni is specified to be very low, <0.007 wt% (0.011 at.%), so the main precipitates are based on Fe and Cr [4.59]. As indicated in Section 4.6.1.1, during β quenching, precipitates formed that were identified as face-centred cubic $Zr_4(Fe_{0.7}, Cr_{0.3})$ [4.42, 4.65]. On annealing, these first precipitates dissolve as the dislocations are rearranged and new precipitates of $Zr(Fe, Cr)_2$, Laves phase [4.114, 4.115], form. Initially, the metastable C15 cubic structure is observed, but the stable C14 hexagonal form gradually replaces it as ageing proceeds. Which of these three versions of Zr (Fe, Cr) is observed depends on the high temperature from which the material is cooled, the cooling rate from this temperature and the times at annealing temperatures. This variation accounts for the apparent conflicting observations reported in the literature. The results may also be obscured by the presence of precipitates from other almost insoluble solutes. For example, small Si-rich precipitates are often mixed with the Zr (Fe, Cr) precipitates [4.65, 4.116, 4.117].

The composition of the precipitates reflects the proportion of the alloying elements. The amount of Fe is usually about twice that of the Cr in Zircaloy-4 and the precipitates are observed to have a composition ratio of Fe:Cr of close to 2:1. When the concentration of each element is raised to about 3.8 times the specified amount of each element, the 2:1 ratio is maintained; the mean diameter of the particles is unaffected but their number density is proportional to the concentration of the Fe and Cr [4.118]. Up to an Fe:Cr of about 4, the composition of the precipitates is directly proportional to the alloy composition but declines thereafter as other Fe-rich precipitates form; see Fig. 4.63 [4.107, 4.119–4.121].

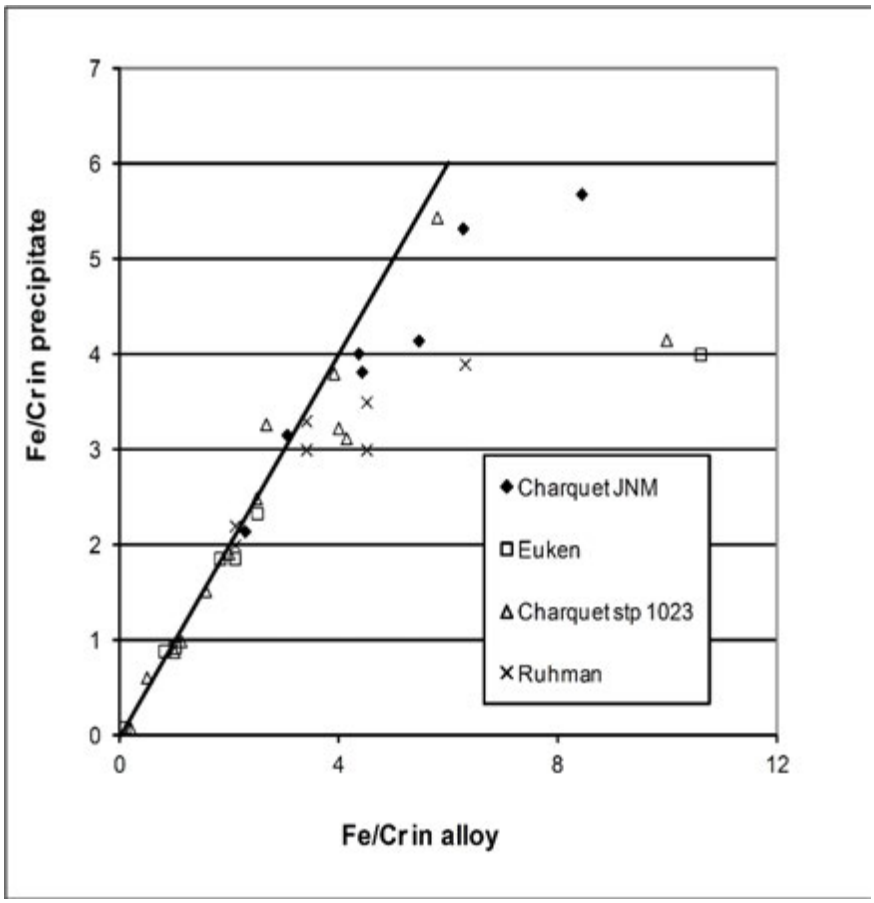

FIG. 4.63. Dependence of composition of Fe/Cr SPPs on the composition of the zirconium alloy [4.103, 4.115–4.117].

A small increase in strength may be attributed to the precipitates. A 5–10% increase in hardness was observed after heating β quenched material for 600–7200 s at temperatures between 773 and 923 K (500 and 650°C) [4.38, 4.42, 4.62]. Quenching from 1073 K (800°C), high in the α phase, produced a hardening that was recovered by annealing for 1 h at 473 to 573 K (200–300°C) [4.98]. Raising the temperature to 673–773 K (400–500°C) produced substantial hardening, which was attributed to strain ageing rather than precipitation hardening.

The temperature range over which the material recrystallizes and precipitates develop is quite varied [4.122]; see Fig. 4.64. An approach for the fabrication of components is to sum Eq. (4.11) for each step of the process after the last β quench, the assumption being that with each subsequent fabrication step of either hot working or cold working and annealing, recovery and recrystallization are reset but precipitation processes are additive. Thus, the cumulative annealing parameter is defined as:

$$\Sigma A = \sum_i \left(t_i \cdot \exp\left[-\frac{Q}{R \cdot T_i} \right] \right), \tag{4.15}$$

which combines the annealing time (t_i) in hours and temperature (T_i) in K of each heat treatment.

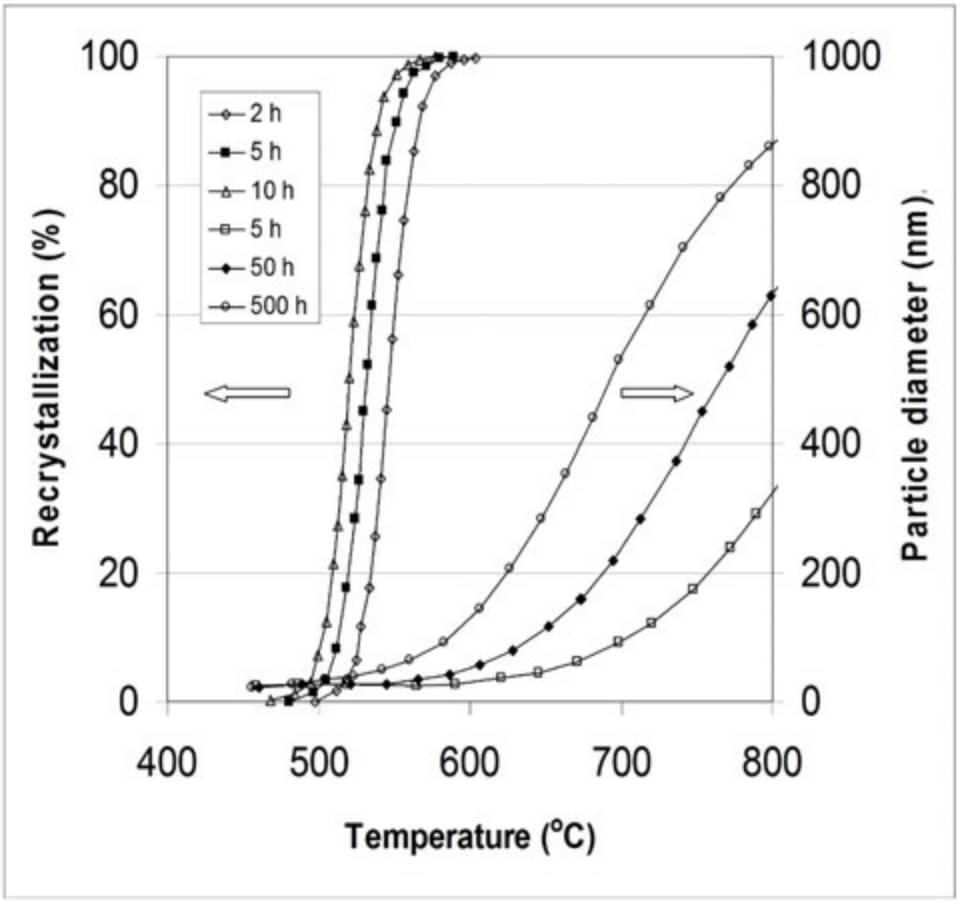

FIG. 4.64. Temperature regimes for recrystallization and precipitation growth in Zircaloy (based on Ref. [4.118]).

Equation (4.13) is sometimes called the cumulative annealing parameter (CAP). Once the SPPs are optimized for the particular application by heat treatment at high temperatures, the mechanical properties are determined by a heat treatment at a lower temperature after the final cold work step. Some fabricators use a Q/R of 40 000 K, even though this value

corresponds to recrystallization. Values of 31 500 K for Q/R, based on corrosion response [4.123] or precipitation kinetics [4.122], have also been suggested, the latter being called the precipitate growth parameter; it is often multiplied by 10^{14} for ease of communication. In Fig. 4.65, the results from eight sets of measurements of particle diameters have been plotted as a function of ΣA; a value of Q/R = 40 000 K was applied to minimize conversion because this value was used in the majority of the studies.

Zircaloy-4 materials were prepared by either annealing or several cold work and annealing steps after β quenching, and examined by TEM [4.124]. The annealing temperatures ranged from 900 to 1070 K (630 to 800°C) with times between 60 s and 1500 h. For an individual heat treatment the precipitate sizes followed a log-normal Gaussian distribution. No difference could be discerned between materials that had received only annealing and those that had been subjected to several fabrication steps, supporting the assumption that precipitation was additive because intermediate cold working had no influence on particle sizes. Q/R was taken as 40 000 K.

A detailed study of the kinetics of precipitation in Zircaloy-4 using thermoelectric power, SEM and TEM techniques indicated that nucleation was complete early during heat treatment and once the volume fraction reached its maximum value of about 0.5%, the particles coarsened [4.125]. Starting with recrystallized Zircaloy-4 containing particles with an initial diameter, d_0, of 120 nm, the material was heated to between 920 and 1050 K (650 and 780°C) for times varying from 5 to 50 h. The increase in the diameter, d, of the precipitates was modelled by a coarsening law:

$$d^3 - d_0^3 = t\left(\frac{constant}{T^2}\right)\exp\left(-\frac{Q}{RT}\right) \tag{4.16}$$

In this analysis Q/R was 18 700 K, although in Fig. 4.65 the data are plotted with a Q/R of 40 000 K. This mechanistically based approach is called the second order CAP. In these experiments, the initial particle diameters were already greater than 100 nm and the immediate application is for late in the fabrication process.

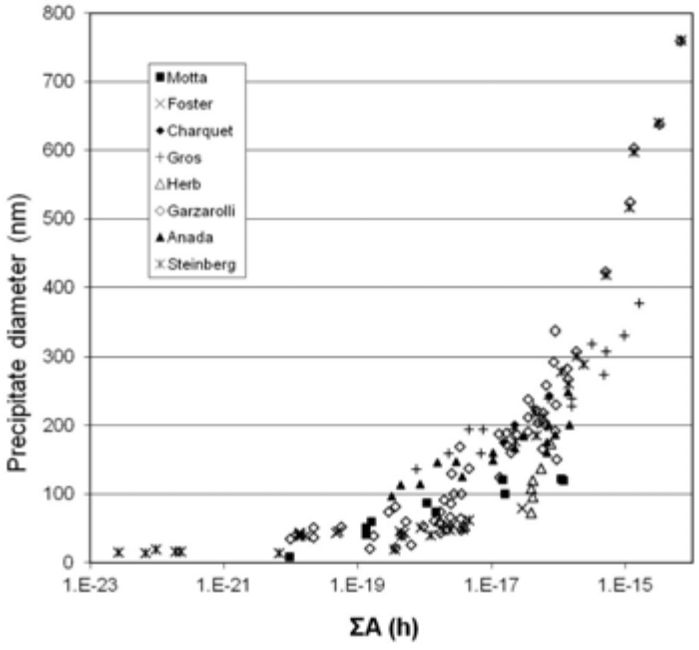

FIG. 4.65. Growth of Zr(Fe, Cr) precipitates as a function of annealing parameter, using Q/R= 40 000 K [4.109, 4.114, 4.118, 4.120–4.124].

Spacer and channel strip made from Zircaloy-4 was processed through several deformation and annealing steps at temperatures of 780–850 K (510–580°C) for 2 h after β quenching into water, then given a final anneal at temperatures between 870 and 1050 K (600 and 775°C) for times varying from 300 s to 2.75 h [4.126]. The precipitates were examined by TEM. Initially, the particles were irregular plates with a cubic crystal structure and a diameter of 22 nm located mainly in the lathe and grain boundaries. After heat treatment, the now almost spherical particles had transformed to the hexagonal version, were uniformly distributed in the alloy matrix and had increased to a maximum mean size of 79 nm. The size of the particles had a skewed distribution with a long tail for large particles, as seen in Fig. 4.66. *Q*/*R* was taken as 40 000 K.

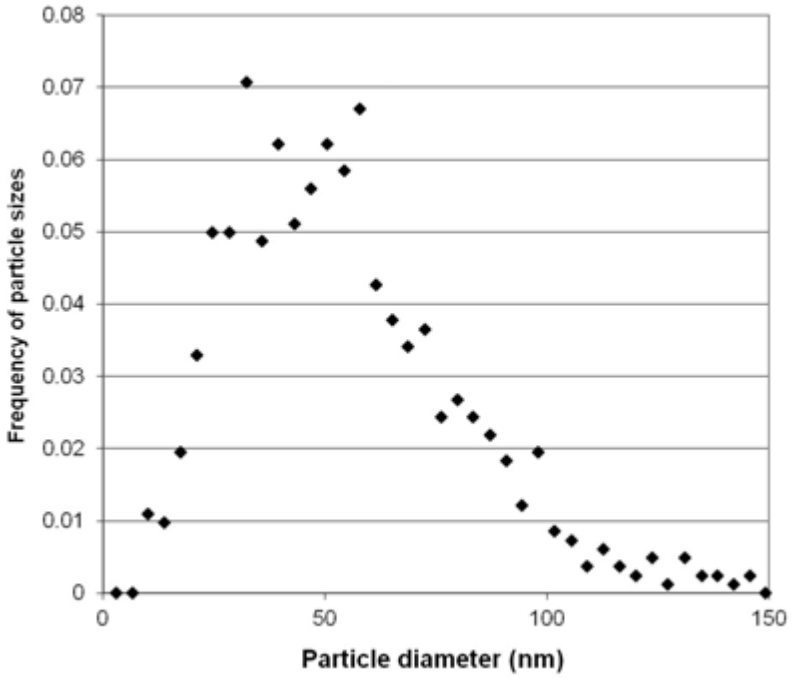

FIG. 4.66. Distribution of second phase particle sizes in Zircaloy-4 after $\Sigma A = 2.62 \times 10^{-18}$ *h [4.122].*

Zircaloy-4 sheets produced by β quenching, followed by various hot rolling, cold reductions and annealing, were evaluated by TEM and SEM [4.127]. All the heat treatments were for 2 h and the temperature range was 673–1053 K (400–780°C). As Σ*A* was increased, coarsening was illustrated by the decrease in the frequency of small particles (<100 nm) and the frequency of intermediate particles (100–200 nm) passing through a maximum. *Q/R* was taken as 40 000 K.

Precipitates were observed by TEM after annealing β quenched material at temperatures between 783 and 1073 K (510 and 800°C) for times between 60 s and 1500 h [4.122]. A log-normal Gaussian distribution of particle sizes was assumed. The initial particle diameter after β quenching was 20 nm. In the study *Q/R* was found to be 32 000 K.

The Zircaloy-4 part of DUPLEX cladding was examined at each stage of fabrication after β quenching and the particle growth measured by SEM and TEM was interpreted in terms of Eq. (4.13), using a *Q/R* of 32 000 K [4.117]. As observed previously, the boundaries of the lamellae formed during quenching were decorated with rod shaped precipitates with dimensions around 60 nm. With subsequent fabrication steps, the precipitates became oval, with a final diameter of up to 276 nm. Log-normal Gaussian distributions used to fit the size

distribution of the particles showed it to be bimodal; Si-rich particles dominated the fraction of smaller precipitates, even though the concentration of Si was only 0.01 wt% (0.032 at.%). These particles grew more slowly than the $Zr(Fe,Cr)_2$ particles, reaching a maximum diameter of about 98 nm.

Zircaloy-4 with a composition of variable sum (Fe+Cr) but constant Fe/Cr of 2 was interpreted using ΣA with a Q/R of 40 000 K after β quenching and a series of cold working and anneals [4.118]. The diameter of the particles was 243 nm after $\Sigma A = 7.3 \times 10^{-17}$ h.

The kinetics of precipitation growth in Zircaloy was followed using synchrotron radiation over the range of ΣA from 10^{-22} to 10^{-16} h, with $Q/R = 40\ 000$ K [4.128]. The specimens were prepared by quenching into water from 1170 K (900°C), which is in the (α + β) region but high enough for all the SPPs to be dissolved. The specimens were subsequently annealed but neither hot nor cold worked. Although a few precipitates were detected by X ray diffraction after quenching, the composition of the quenched matrix was found to be that of the alloy, indicating most of the Fe and Cr was in supersaturated solid solution after quenching. Once the volume fraction had attained its maximum value at ΣA of about 10^{-17} h, and the precipitates started to coarsen, the concentration of alloying elements decreased to around 314 ppm (0.052 at.% Fe, 0.054 at.% Cr). The particle diameters were estimated from line broadening of the diffraction peaks from the particles.

Despite the material histories varying a great deal and the methods used to determine and characterize the particle diameters also varying, these results on Zircaloy-4 are in general agreement on how SPPs grow. The scatter shown in Fig. 4.65 precludes using it directly. Each fabricator must determine the parameters of their own circumstances; for example, variations in cooling rates during quenching and temperature gradients in the material at each stage of fabrication contribute variation in the distributions of composition and size of particles in the intermediate and final product.

In Zircaloy-2, as well as (Fe, Cr)–rich particles, intermetallic particles containing Fe and Ni are also present because the concentration of Ni can be between 0.03 and 0.08 wt% (0.047 and 0.12 at.%) [4.27]. After annealing high in the α phase, these precipitates are large, sometimes over 1000 nm, especially when in grain boundaries, and have been identified as $Zr_2(Fe, Ni)$[1] with Fe/Ni between about 0.8 and 1.5 [4.65, 4.129–4.134]. The crystal structure of these particles is body centred tetragonal [4.65, 4.133, 4.135]. No Zr(Cr, Ni) precipitates are observed. The precipitates can have several configurations — single $Zr(Fe, Cr)_2$ particles (in both cubic and hexagonal versions [4.136]), single $Zr_2(Fe, Ni)$ particles or clusters of both Cr and Ni types in intimate contact, with the Ni-rich particles precipitating first [4.65, 4.130]. In general, the Ni-rich particles are larger than the Cr-rich particles [4.132, 4.133]. As an example, in one fuel cladding the Ni-rich particles had a mean diameter of 310 nm while that of the Cr-rich particles was 175 nm. The Fe concentration is lower in Zircaloy-2 (0.07–0.20 wt% (0.11–0.33 at.%)) than in Zircaloy-4 (0.18–0.24 wt% (0.29–0.39 at.%)), with Fe/Cr in a typical alloy being about 1.3. The Fe partitions between the Cr and Ni particles, and rather than the Fe/Cr being about 1.3 in annealed materials (as expected from Fig. 4.63), the mean value gleaned from several studies is 0.86 [4.65, 4.130, 4.132–4.134, 4.137]. During fabrication, the size of the particles follows a similar time and temperature pattern as indicated for Zircaloy-4 in Fig. 4.65 [4.124].

[1] Sometimes this phase is called a Zintl phase. This nomenclature is inappropriate because Zintl phases form between Group 1 (alkali metals) or Group 2 (alkaline earths) and elements in Groups 13 to 16, not between Group 4 (Zr) and Group 8 (Fe) and Group 10 (Ni) metals.

4.6.2.2. Zr-2.5Nb

During the initial development of Zr-Nb alloys, a reference heat treatment was β quenched followed by a tempering at 773 K (500°C) for 24 h [4.138]. The research then focused on the parameters of this heat treatment. Precipitates formed on the twins and lath boundaries of the α′ phase and in the alloy matrix during tempering [4.76, 4.84, 4.139]. With time at 773 K (500°C), the precipitates increased in size, as shown in Fig. 4.67, and their concentration of Nb gradually increased towards that of β-Nb. The particles started out as being coherent and changed shape from approximately spherical to acicular and became incoherent. Several studies indicated that the hardness increased during this heat treatment and passed through a maximum value after between 10 and 60 h, as shown in Fig. 4.68 [4.73, 4.76, 4.83, 4.84]. In one study the maximum increase was about 14%, but other studies indicated a more modest age hardening. Two maxima in hardness may exist in alloys made from pure materials [4.76]. The hardening and overageing behaviour were attributed to the changes in the structure and coherency of the precipitates rather than their size and spacing. The cause of the discrepancy between the studies is unknown; the chemical compositions, especially oxygen concentration, were similar and the solution temperatures before quenching were all in the β phase although the cooling rates were not stated. Tempering at temperatures lower than 773 K (500°C) increased the amount of hardening [4.83] but slowed the achievement of its maximum value while treatment at a temperature close to the eutectoid temperature produced considerable softening, as seen in Fig. 4.69, due to polygonization and incipient phase transformation [4.76, 4.139].

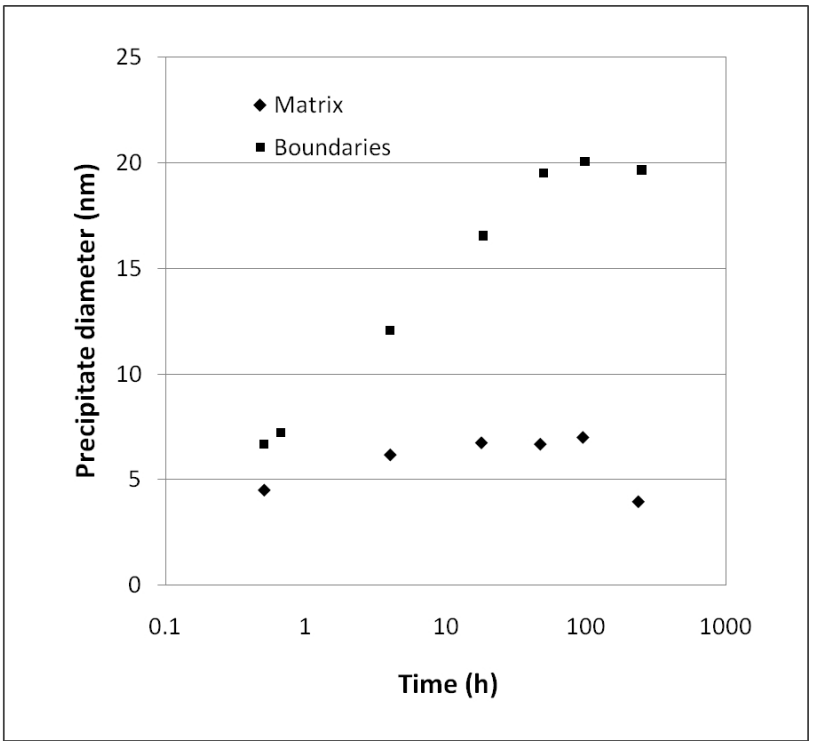

FIG. 4.67. Growth of precipitates in Zr-2.5Nb tempered at 773 K (500°C) after quenching from 1273 K (1000°C); precipitates grow faster and larger in the lath boundaries of the α′ phase than in the alloy matrix [4.76, 4.84, 4.135].

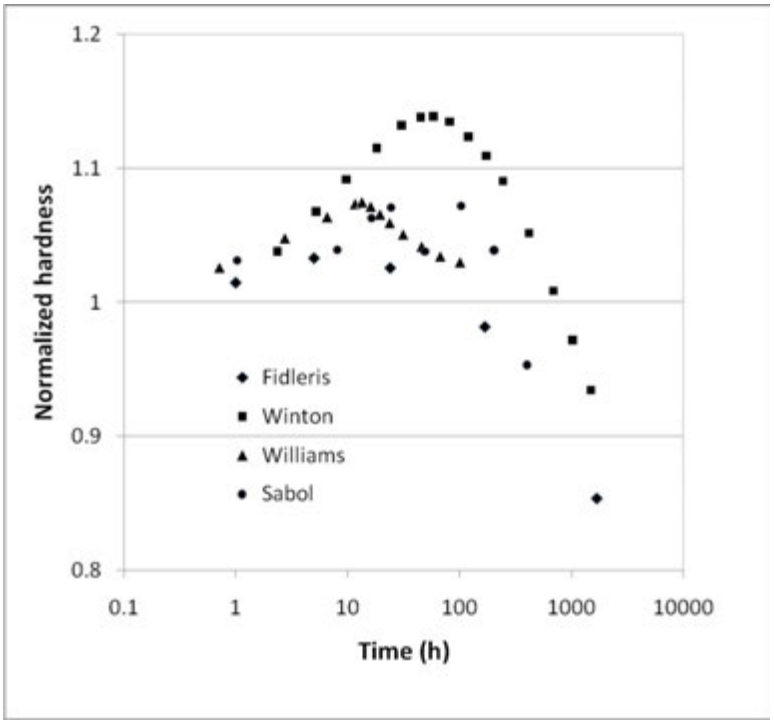

FIG. 4.68. Increase in hardness during tempering at 773 K (500°C) of Zr-2.5Nb quenched from the β phase; hardness values normalized to value of the as-quenched material [4.73]. Fidleris [4.73]: Nb 2.7%, O 1150 ppm (0.65 at.%); quenched from 1273 K (1000 °C); as-quenched hardness: 273 Vickers Pyramid Number (VPN). Winton [4.83]: Nb 2.9%, O 1400 ppm (0.79 at.%); quenched from 1273 K (1000 °C); as-quenched hardness: 254 VPN. Williams [4.84]: Nb 2.5%, O 1300 ppm (0.74 at.%); quenched from 1273 K (1000°C); as-quenched hardness: 267 VPN. Sabol [4.76]: Nb 2.6%, O 800 ppm (0.45 at.%); quenched from 1248 K (975°C); as-quenched hardness: 254 VPN.

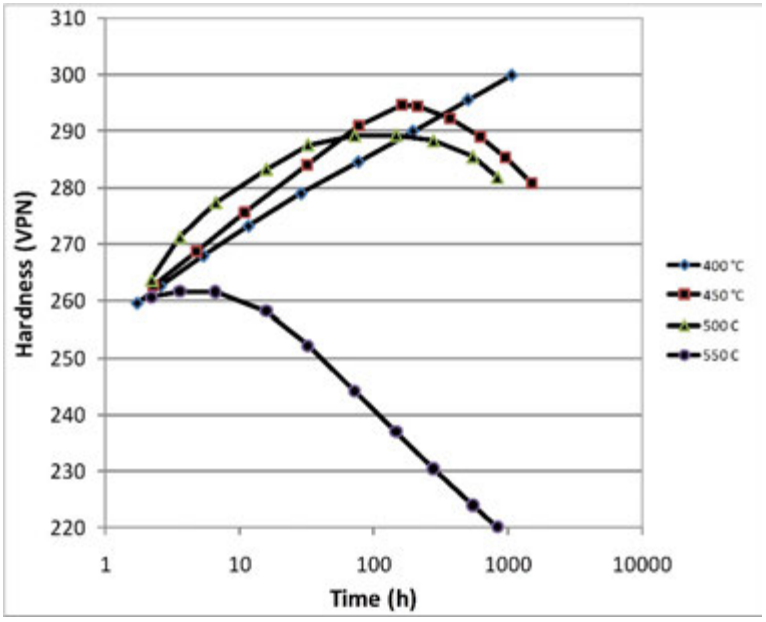

FIG. 4.69. Effect of ageing temperature on Zr-2.5Nb quenched from 1273 K (1000°C) [4.83].

Corrosion can be much reduced by decreasing the supersaturation of the Nb in the as-quenched Zr matrix by precipitation of β Nb [4.140]. For example, the weight gain after 144 days in heavy water at 633 K (360°C) was close to 250 mg/dm^2 for β quenched material but the corrosion was reduced to about 40 mg/dm^2 after ageing at 823 K (550°C) for 10 days. The corrosion can be reduced even further by cold working between the quenching and the tempering. In pure water at 589 K (316°C), 30% cold work between β quenching and annealing at 773 K (500°C) for 24 h reduced the corrosion weight gain by about 20% while corrosion in CO_2 at 573 K (300°C) was reduced by about 45% [4.141].

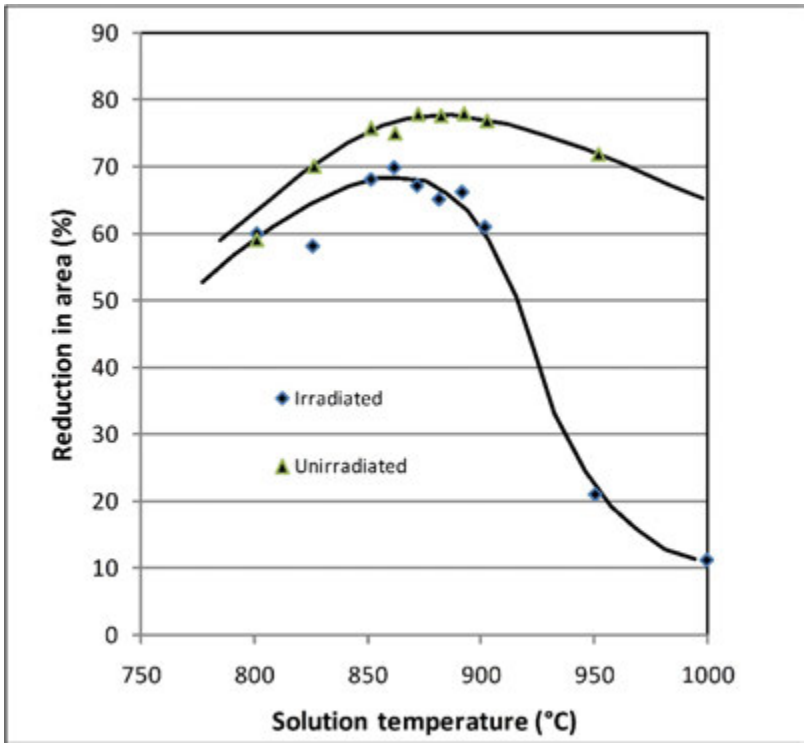

FIG. 4.70. Effect of neutron irradiation and solution temperature before quenching on the tensile ductility of Zr-2.5Nb, showing the large decrease in ductility when β quenched material is irradiated with neutrons [4.71].

Irradiation was found to much reduce the ductility and toughness of β quenched material, as seen in Fig. 4.70 [4.71, 4.142, 4.143]. This embrittlement was attributed to intergranular cracking based on the prior β grain size. During heating in the (α + β) phase region, the α phase inhibits β grain growth from over 100 μm during heating in the β phase to < 10 μm in the (α + β) phase. The focus of development then shifted to quenching from the (α + β) phase field where the reduction in ductility by irradiation was small, but the high strength was maintained, even after ageing at 773 K (500°C) for 24 h — the 0.2% yield strength at 573 K (300°C) for β quenched and aged material was 558 MPa and 586 MPa after quenching from the (α + β) phase and ageing [4.142]. Creep resistance declined as the solution temperature was reduced through the (α + β) region indicating that acceptable creep properties in this metallurgical condition require the quenching temperature to be close to the (α + β)/β phase boundary; see Fig. 4.71 [4.73].

Cold work between (α + β) quenching and tempering also promoted the precipitation of β-Nb and reduced the supersaturation of Nb in the α phase leading to an improved corrosion response [4.144]. Figure 4.72 shows two sets of data for 6 h and 24 h at 773 K (500°C) indicating the lowering of corrosion by 20% intermediate cold work. Other data indicate that

the effect is not as large as indicated here [4.145] but that the intermediate cold work is beneficial.

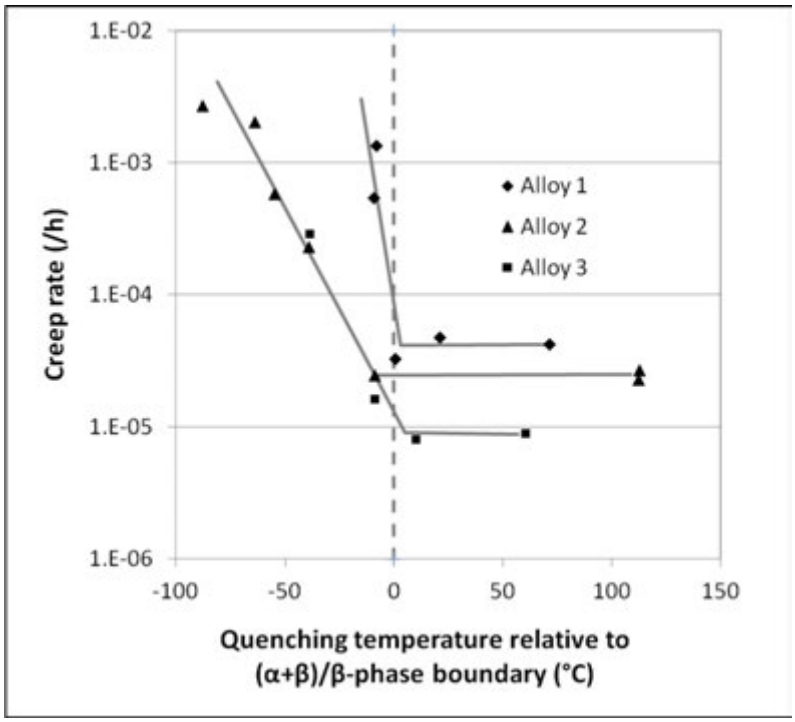

FIG. 4.71. Dependence of creep rate at 723 K (450°C) and 207 MPa on solution temperature of quenched Zr-2.5Nb [4.73]. Alloy 1: Nb: 2.57%; O: 170 ppm (0.097 at.%). Alloy 2: Nb: 2.50%; O: 780 ppm (0.44 at.%). Alloy 3: Nb: 2.70%; O: 1150 ppm (0.65 at.%).

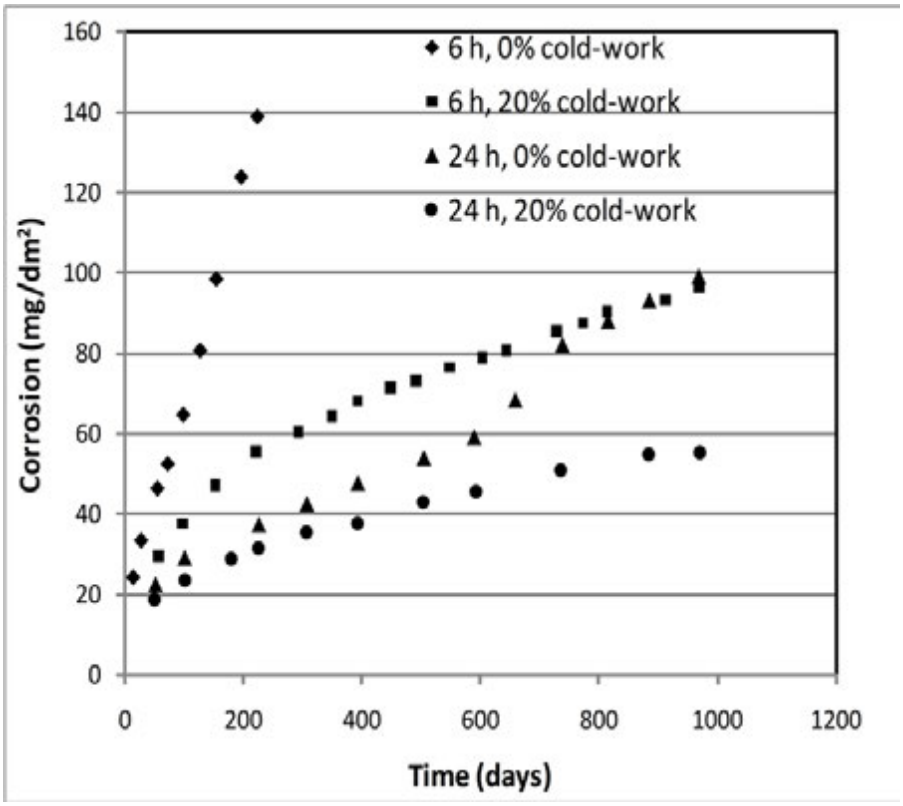

FIG. 4.72. Effect of intermediate cold work and ageing time after quenching from 1153 K (880°C) on the corrosion of Zr-2.5Nb in water at 589 K (316°C) [4.140].

When Zr-2.5Nb is slowly cooled to room temperature from high in the (α + β) phase, the microstructure consists of 2 phases: an area fraction of about 0.93 of α grains containing about 1% Nb and an area fraction of about 0.07 β phase containing about 20% Nb. With material annealed at 1123 K (850°C), the α grains are equiaxed with the β phase concentrated in the grain boundaries and triple points while after extrusion at 1123 K (850°C) the α grains are elongated platelets surrounded by an almost continuous skin of β phase. During ageing, the β phase transforms as described in Section 4.6.1.2. In the equiaxed material, after 24 h at 673 K (400°C), the yield strength at room temperature increased by 16% by age hardening from the ω phase precipitating in the β phase but returned to the original strength after 24 h at 773 K (500°C) as the β phase transformed to α phase and enriched β phase. The competing softening and hardening processes led to a small ageing peak in both temperature (at constant time) and time (at constant temperature). Plate material cold worked 40% after slow cooling from 1033 K (760°C) exhibited a maximum hardening of 4–7% after one hour at about 673 K (400°C) [4.95]. In the longitudinal direction, the yield strength of this material also had a maximum increase of about 4% but in the short transverse direction the total increase in strength was about 23%, indicating a Bauschinger effect in the thickness direction because the cold work deformation was compressive; see Fig. 4.73. The ageing peak at 673 K (400°C) extended over several hours in material cold worked 20% after annealing at 1033 K (760°C) for 1800 s; the hardening at 623 K (350°C) was greater than at 673 K (400°C) but no hardening was observed after tempering at 723 K (450°C); rather, softening started after about 1 h [4.146]; see Fig. 4.74. Recovery and ageing also compete in the extruded material. The result is little change in strength with the heat treatment of 300 h at 673 K (400°C) but a 10% loss in strength after 300 h at 773 K (500°C) [4.147]. When extruded material was annealed at 753 K (480°C) before cold working 58%, it showed no hardening during tempering of the cold worked structure at 673 K (400°C) but softened by about 5% in 32 h [4.148]. The anneal at 753 K (480°C) prevented the transformation and precipitation of ω phase during the tempering so no hardening was observed. As an alternative, after extrusion and cold working, an air cool from the (α + β) region followed by 24 h at 833 K (560°C) also avoided the formation of any ω phase and took the transformation to ($\alpha + \beta_{Nb}$) to completion [4.149].

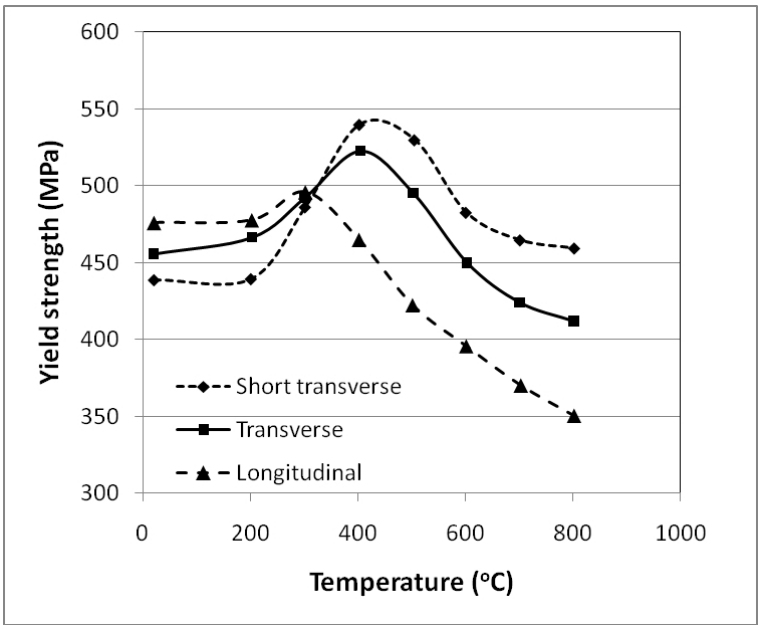

FIG. 4.73. Change in yield strength at room temperature of cold worked Zr-2.5Nb plate after heating for 1 h at various temperatures up to 1073 K (800°C) [4.95].

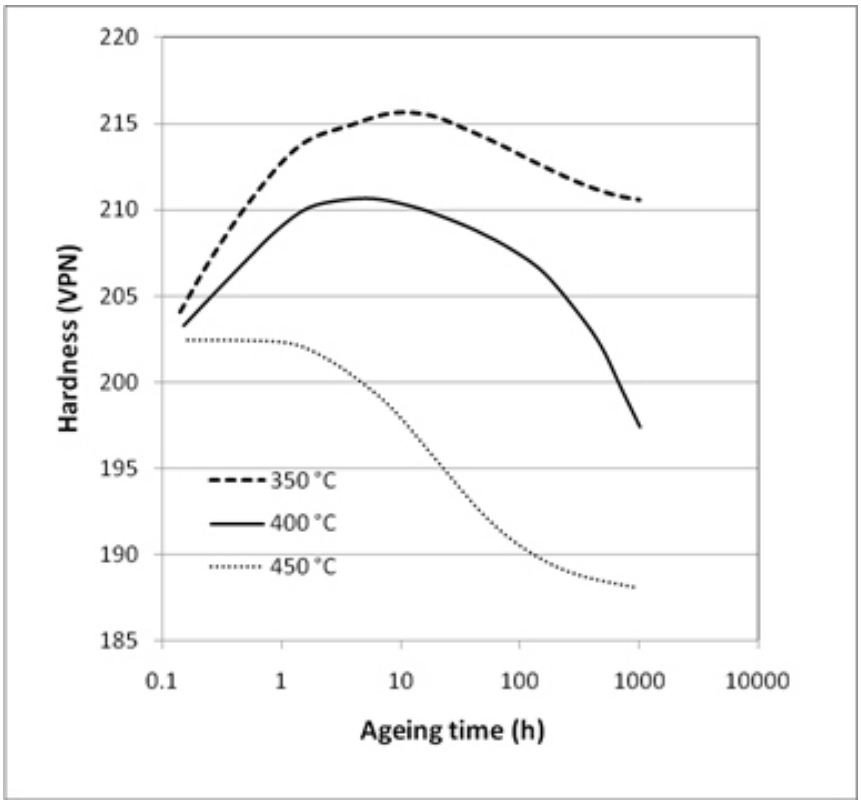

FIG. 4.74. Low temperature ageing of 20% cold worked Zr-2.5Nb pressure tube [4.142].

Although the last working step for fabricating pressure tubes is cold work, in some versions it is the extrusion step that sets the microstructure and texture of the finished product. The cold work further elongates and thins the α phase plates and surrounding β phase skin. The microstructure changes by three processes during heat treatment: the residual stresses recover, the dislocation density declines and subgrains form, and, depending on the time-at-temperature, the β phase transforms and disintegrates:

— Extruded Zr-2.5Nb pressure tube material cold worked either 20% or 40% contained similar lattice strains, 2.2×10^{-3}, which declined when heating was 80–100% removed after 2 h at 923 K (650°C), as seen in Fig. 4.75 [4.150].
— The dislocation density and arrangement observed using X rays and TEM show that recovery proceeds in three stages, as seen in Fig. 4.76. Between 573 and 723 K (300 and 450°C), the initial dislocation density of about 16×10^{-14} m^{-2} decreases linearly with temperature with little change in the arrangement of the dislocations. At higher temperatures, the rate of decline of the number of dislocations slows but clear cells, networks and sub-boundaries form into subgrains that eventually coalesce and contribute to some α grain growth [4.150, 4.151]. At 673 K (400°C) the dislocation density drops rapidly in the first few hours but thereafter changes very little, as seen in Fig. 4.77 [4.150, 4.152, 4.153]. Two caveats should be noted when evaluating dislocation densities from X ray line broadening. If residual stresses are predominant (as they may be in a non-stress relieved material) then the broadening is likely to be affected by intergranular strain distributions that confound analysis — the intergranular strain

distributions cannot be separated from the strain due to dislocations. Also, the lattice strain from dislocations of one Burgers vector will appear as strain on other planes that could be misinterpreted as being due to dislocations of another Burgers vector [4.154, 4.155].

— The β phase transforms according to Fig. 4.49 but in addition the continuity is broken as the temperature and time are increased [4.156–4.159]. The dimensions of the β phase were estimated by SEM on cold worked Zr-2.5Nb before the final autoclave heat treatment. The initial length was in the range 2400–8600 nm and thickness was in the range 160–440 nm. After 1000 h at 673 K (400°C), the length was reduced by a factor of about 3 to 1200–2400 nm, while the thickness was approximately halved, 110–230 nm [4.159]. A consequence of the transformation and disintegration of the β phase is the reduction of diffusivity, D_H, of hydrogen in the alloy, a key parameter for the growth rate of delayed hydride cracks. At 573 K (300°C) in as-extruded Zr-2.5Nb, D_H is 5.8×10^{-10} m^2/s; it is reduced to 1.1×10^{-10} m^2/s after 24 h at 673 K (400°C) and further to 5.8×10^{-11} m^2/s after the complete breakup of the β phase by heating at 24 h at 838 K (565°C) [4.158].

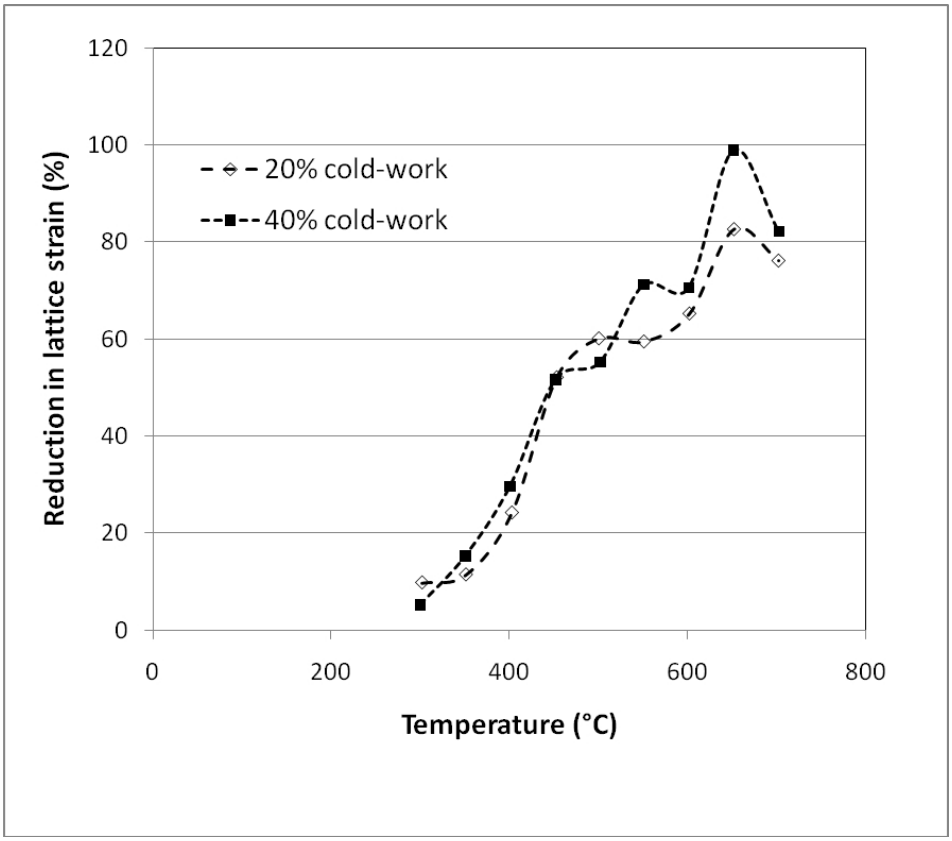

FIG. 4.75. Reduction in lattice strain in cold worked Zr-2.5Nb by heating for 2 h at various temperatures. The lattice strain of as-cold worked material was 2.2×10^{-3} [4.146].

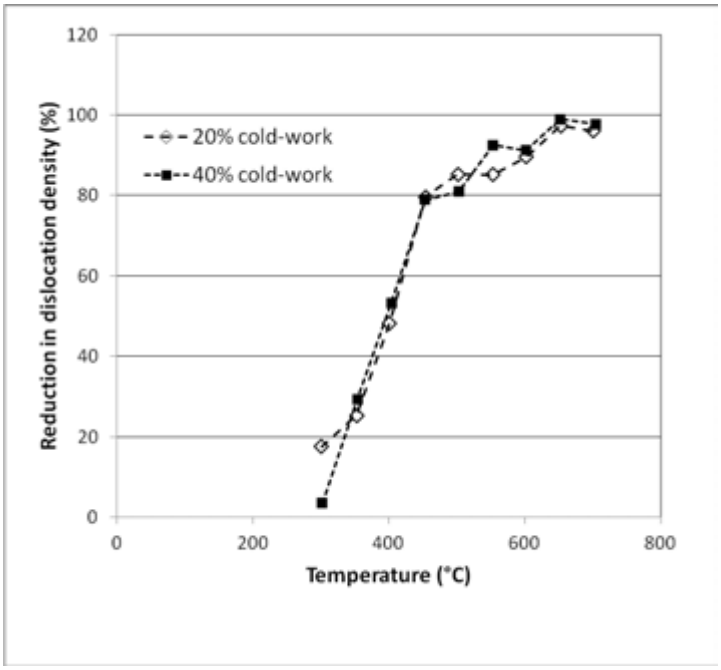

FIG. 4.76. Reduction in dislocation density in cold worked Zr-2.5Nb by heating for 2 h at various temperatures. Initial dislocation density of 20% cold worked material was 15.7×10^{14} m^{-2} and of 40% cold worked material was 17.5×10^{14} m^{-2} [4.146].

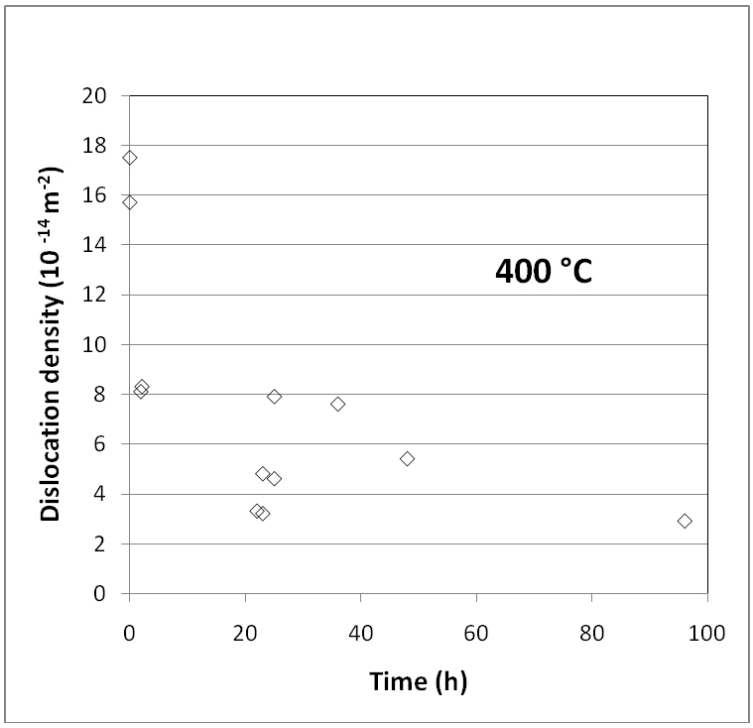

FIG. 4.77. Reduction in dislocation density in Zr-2.5Nb cold worked 20–40% with time at 673 K (400°C) (based on Refs [4.146, 4.148, 4.149]).

After extrusion and cold working, the α phase is supersaturated in Nb; during stress relieving the Nb remains in solution and precipitates as β-Nb only by irradiation (see Chapter 6, Section 6.3.3.1, Volume 2 of this publication).

4.6.3. Heat treatment applications

4.6.3.1. Zircaloy

Beta quenching has been part of the fabrication process since the late 1950s [4.30, 4.160]. The main incentives for its use were to improve corrosion resistance, homogenize minor alloying elements and attempt to produce isotropic material. The position of β quenching in the process flow has varied from the forging stage to the final stage. The minor alloying elements are either taken into solution or their precipitates are much refined by temperatures above the β transus. Rapid cooling retains the refinement. The precipitates grow with time during processing and heat treatment in the α phase. Corrosion resistance is associated with the SPPs and much effort has gone into optimizing their initial distribution. For example, in PWRs, ΣA for Zircaloy-4 was recommended to be between 5×10^{-18} and 2×10^{-17} h to provide good uniform corrosion performance, using Q/R = 40 000 K [4.124]. The development of the appropriate ΣA for Zircaloy-2 used in BWR is described in Chapter 8, Appendix 1 (in Volume 2 of this publication); the current best value is 6×10^{-19} h, with a range from 2×10^{-19} to 1.5×10^{-18} h.

Various versions of the heat treatment parameter, ΣA, are available depending on which mechanism is being modelled — recrystallization, corrosion or precipitation. Fabricators find this parameter useful for process control since it can provide guidance for in-reactor performance. In one study [4.161], each version was compared, using the corrosion of Zircaloy-4 fuel cladding in PWRs. The ΣA was calculated using Q/R of 40 000 K, 31 500 K and 18 700 K in second order CAP for the initial tubing, and a corrosion parameter, E, was evaluated based on oxide thickness, specific fuel rod parameters and power history. Plots of E as a function of ΣA indicated that anneals for longer times at higher temperatures were beneficial, as indicated above. When ΣA was normalized to the maximum value, each version provided similar graphs with the second order CAP having a slightly superior correlation, as shown in Fig. 4.78. A Q/R of 14 200 K has also been proposed [4.162] although it is not frequently used. One caveat to the ΣA scheme is that the basic assumptions made may not be correct; these are that:

— For the same ΣA, a short time anneal at a high temperature produces the same microstructure and properties as a long time at a lower temperature.
— The timing of the anneal during fabrication does not affect the outcome.

For example, with ΣA in the range $(1–6) \times 10^{-18}$ h (based on Q/R = 40 000 K), the mean precipitate sizes were all in the range 160–180 nm [4.163], as expected from Fig. 4.65. When the highest annealing temperature, 1005 K (732°C), was placed after the standard annealing temperature, 933 K (660°C), the nodular corrosion behaviour at 793 K (520°C) was much worse than when the higher temperature anneal was first. These results indicate that one has to be careful on how the ΣA approach is used and that the precipitates themselves are not necessarily responsible for nodular corrosion behaviour.

Early in the development of the Zircaloys, it was recognized that rapid cooling from the β phase, especially through the (α + β) region, was required to avoid severe corrosion in steam [4.164]. Oxide blisters formed in steam at 670 K (400°C) when the particles were formed in clusters or stringers; these blisters nucleated in wide regions of the metal matrix where precipitates were absent. When the precipitates were small and uniformly spaced, the corrosion was minimal [4.165, 4.166]. The development of heat treatments to guard against nodular corrosion in Zircaloy-2 is based on this information. One view is to have a uniform

concentration of minor alloying elements in solution in the zirconium matrix with their concentration as high as possible, with the remainder in small precipitates of the minor elements that can be slowly redistributed during irradiation (see Chapter 6, Volume 2 of this publication), thus maintaining the concentration of minor alloying elements in the zirconium matrix. In practice the recommendations are to:

— Use an alloy with Sn concentration at the low end of the specification and concentration of minor elements Fe, Cr and Ni at the high end of the specification.
— Heat treat so the intermetallic precipitates are small. To achieve this microstructure usually means rapid cooling from a temperature at which most of the minor elements are in solution then annealing at moderate temperatures to form the precipitates. To ensure that the requirement is met may mean that an intermediate β quench is provided late in the fabrication process.

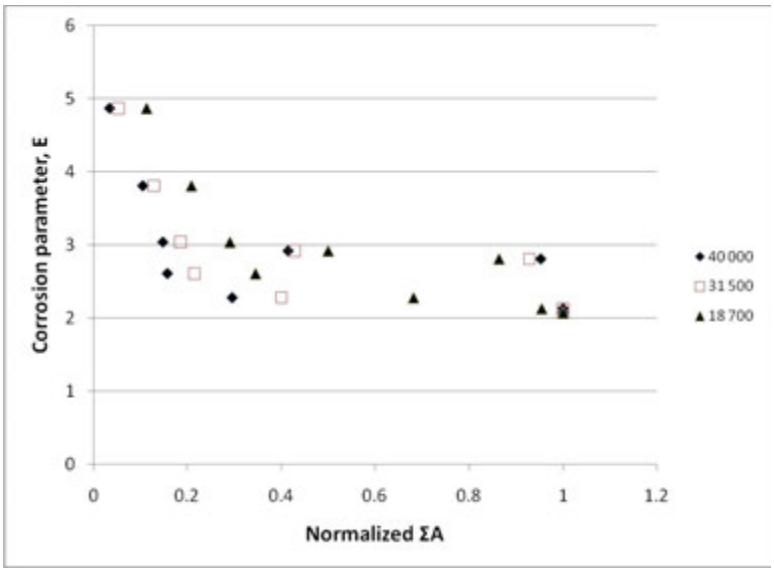

FIG. 4.78. Comparison of corrosion data displayed using different Q/R in the ΣA approach to heat treatment of Zircaloy-4 [4.157].

In Zircaloy-2, Fe is partitioned between the two types of SPPs. If the Fe/Ni in the Zr_2(Fe, Ni) particles is taken as 1.3, and using the low solubility limits of Fe, Cr and Ni in zirconium, the total volume fraction of the precipitates can be estimated through a parameter called *X* [4.167]:

$$X = 4.6Ni + (Fe + Cr - 1.3Ni)/2 \quad (4.17)$$

where Ni, Fe and Cr are the concentrations of each element in wt%.

At the limits of the ASTM Standard Specification, *X* can vary between 0.179 and 0.491.

When Sn is 1.2 wt% (0.92 at.%), nodular corrosion is eliminated when *X* is about 0.4 in quenched and annealed material. As the Sn concentration is increased, *X* has to be increased to suppress nodular corrosion. Similarly, a β quench of 50 K/s requires an *X* of about 0.2 to stop nodular corrosion; this value is increased to about 0.4 when the cooling rate is reduced to 5 K/s, while α annealing requires *X* to be about 0.5. This approach was confirmed by testing material made from an ingot with a gradient in composition varying from low Sn and high Fe,

Cr and Ni concentrations to mid-range values with respect to the ASTM standard [4.168]. When X was 0.44, the nodular corrosion was low and independent of ΣA but when X was about 0.35, nodular corrosion could only be suppressed by low ΣA. To limit a large pick-up of hydrogen at high burnups in BWRs, the concentration of Ni was recommended to be limited to 0.05 wt% (at%) but the Fe and Cr concentrations should be at the upper range of the specification to provide a Ni/Fe ratio between 0.15 and 0.22, to lower the hydrogen pick-up fraction and avoid nodular corrosion [4.169].

Both increasing the number density of precipitates and reducing the size of precipitates and the interparticle distance has been shown to reduce the susceptibility of Zircaloy-2 to nodular corrosion. Quenching from high in the (α + β) phase or from the β phase at > 20 K/s and annealing at $\Sigma A < 10^{-18}$ h (Q/R = 40 000) provided good protection from nodular corrosion. Quenching from low in the (α + β) phase region, cooling at rates < 2 K/s and annealing quenched material high in the α phase to $\Sigma A > 10^{-16}$ h, all promote nodular corrosion [4.47, 4.124]. The need to keep the process under good control and provide a good margin has led to the practice of a second β quench, or a quench from the (α + β) region at intermediate points during fabrication. These heat treatments are very effective in minimizing nodular corrosion. [4.132, 4.170–4.172]. During irradiation, the precipitates are modified (Chapter 6) and initial, very small particles can dissolve. Material containing such particles, as a result of annealing material quenched from the β phase [4.173–4.177] or (α + β) region [4.178–4.180] with a ΣA that is too small, can behave as poorly as material with large particles, thus leading to an optimum particle size and therefore range of recommended heat treatment; see for example Fig. 4.79 [4.173].

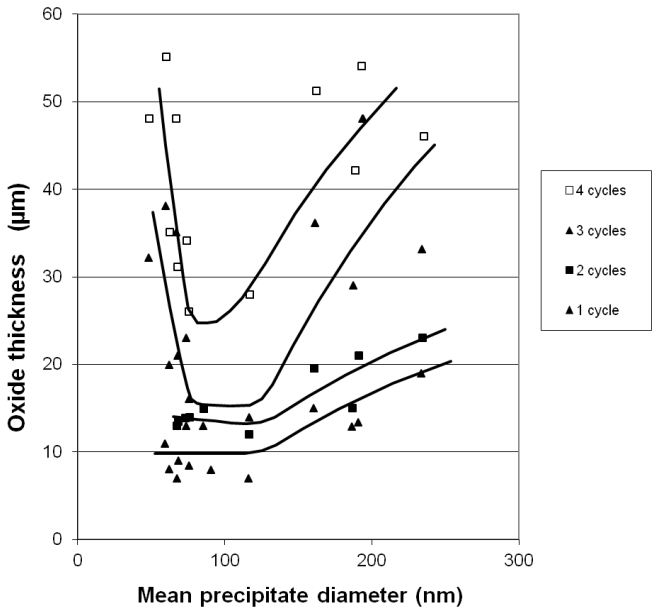

FIG. 4.79. Effect of particle size on corrosion of Zircaloy-2 in BWR showing optimum precipitate size [4.169].

Despite the strong correlation between precipitate geometry and corrosion behaviour, nodules form away from particles, suggesting that the zirconium matrix is the key to the severe corrosion. Increasing the concentration of minor elements in solution reduced susceptibility to nodular corrosion [4.181]. The distribution of the minor alloying elements in the zirconium matrix is important, too. One measure is the variance of the concentration of Fe, Cr and Ni; materials with high variance had regions where the concentration was low, and their frequency

correlated with nodule number density. Quenching from both (α + β) and β phase regions homogenized the concentration of Fe, Cr and Ni and improved nodular corrosion resistance [4.182]. The *X* concentration parameter for the test materials was in the range 0.32–0.38 so they were sensitive to heat treatment. The importance of the distribution of minor alloying elements was confirmed in material with *X* around 0.41 [4.183].

Results from further attempts to separate the effect of the zirconium matrix from that of the precipitates seem to be contradictory. In one study, material with a concentration parameter *X* of 0.31 was heat treated in four ways, the concentrations of Fe, Cr and Ni were measured by atom probe, the median precipitate size was measured by SEM and standard out-reactor corrosion tests were performed [4.184]. The results are summarized in Table 4.4. Material with low concentrations in the matrix and large precipitates corroded badly; material with higher concentrations in the matrix and similar large precipitates corroded modestly; material with intermediate concentrations in the matrix but small precipitates had low corrosion. When similar material was heat treated to provide small particles, its matrix had a low concentration of Fe, Cr and Ni but did not suffer nodular corrosion in-reactor, whereas another similar material had the same small concentrations in the matrix but large particles and many nodules [4.185], as shown in Table 4.4. One source of the discrepancy between the two studies is the difficulty of obtaining good statistics from the atom probe when concentrations are so low.

The efficacy of starting Zircaloy-2 fuel cladding with a small precipitate size was demonstrated with the LK3 cladding used in a BWR. The composition provided an X parameter of 0.34. It has a ΣA of about 6×10^{-19} h and an initial particle diameter of about 42 nm. It performed well for 9 reactor cycles to an average burnup of 78.7 MW d/kg U [4.186].

A variation on conventional induction heating and quenching the whole piece, often early in the process, is to move the tube shell though the induction coil and immediately cool it with a water spray as it exits the coil [4.187]. This process was demonstrated on a Zircaloy-2 tube with an outside diameter of 63.5 mm and wall thickness of 11 mm. The material had a low concentration of Sn, and high concentrations of Fe, Cr and Ni for an X parameter of 0.42. It was heated to 1213 K (940°C) — into the (α + β) region. The whole cycle above 370 K (100°C) took about 30 s. Subsequent heat treatment after two steps of pilgering provided a ΣA of 2.8×10^{-20}. This material was resistant to nodular corrosion in laboratory tests.

Taking about 30% of the wall thickness of a semi-finished tube quickly into the β phase with a laser beam could be a viable alternate to quenching the whole piece [4.188]. As the beam passes over the material, the remaining wall provides self-quenching with a uniform cooling rate. The main advantages of the process are the preservation of dimensions at high temperatures, the ease of protecting from oxidation and control of the microstructure, especially the β grain size. Post-β-quench annealing maintains good corrosion resistance when components are β quenched in their final dimensions. This process was proposed to reduce irradiation growth by randomizing the texture from the usual strong radial texture to one in which the texture components are similar in each direction. Compared with tubes made by the standard route, in the β quenched and annealed condition the growth in Zircaloy-4 guide tubes was halved while the corrosion was similar [4.189].

4.6.3.2. Zr-2.5Nb

Up until 1982, β quenching was not part of the early stages of fabrication of CANDU pressure tubes [4.190]. As with Zircaloy, a more uniform microstructure with smaller grain

size was observed after β quenching into water from about 1288 K (1015°C) [4.191]. This microstructure was confined to the outside surface region after quenching a 255 mm diameter bar. When performed at the log stage before trepanning the hollow for extrusion, the resulting microstructure was more uniform than when the β quenching step was absent. This material produced extruded tubes with a superior surface finish. When quadruple melting was introduced in the mid-90s, extra ultrasonic signals arose during final inspection, presenting the possibility of false indications of cracks and flaws. The purer material contained fewer sites for nucleation of Thomson-Widmanstätten grains during the quench and it was speculated that regions of grains with the same orientation, like parallel plates in Zircaloy, were reflecting the ultrasonic waves. By analogy with Zircaloy, a faster cooling rate, attained by quenching the extrusion hollow rather than the log, solved the problem [4.153].

Two basic fabrication routes for pressure tubes have been established with late stages consisting of:

— Quench, cold work and age, which produce what are often called heat treated tubes;
— Mixtures of cold work and annealing, which produce what are often called cold worked or annealed tubes.

For heat treated tubes, as a result of the development work described in Section 4.6.2.2, after attaining a wall thickness within about 20% of the final value, the tube is heated high into the (α + β) region, 1123–1143 K (850–870°C) and quenched into water. The product is then cold worked to final size and tempered at 773–788 K (500–515°C). The final microstructure consists of a mixture of primary α grains in a matrix of martensite. As indicated in Section 4.6.1.2, the texture contains basal plane normals in the longitudinal direction with a Kearns factor, F_L, of about 0.26, while those in the radial and transverse directions are similar with an F_R of about 0.34 and F_T of about 0.40. A variation on this fabrication route is to quench the tube into inert gas instead of water. The cooling rate is low, and the microstructure consists of a mixture of primary α grains in a matrix of Thomson-Widmanstätten grains [4.192–4.194].

In standard cold worked CANDU pressure tubes, after the last 25–27% cold work, the duration of the final heat treatment at 673 K (400°C) was reduced from 72 h down to 24 h because little further change in dislocation density was gained (see Fig. 4.77), but the elongated grains surrounded by a slightly decomposed β phase (β_{Zr} and ω phase) remained. This heat treatment is performed in an autoclave with the result that the finished surface is coated with a thin, wear resistant black oxide. In these pressure tubes, the α grains have a strong crystallographic orientation with a high concentration in the transverse direction, with an F_T of about 0.61; less in the radial direction, with an F_R of about 0.34; and very low in the longitudinal direction, with an F_L of about 0.05. For the annealed pressure tubes in RBMK-1000 reactors, the stress relief after the last 23% cold work is 813 K (540°C) for 5 h, which produces a microstructure consisting of a mixture of the remnants of elongated cold worked grains; equiaxed, recrystallized grains of about 5 μm in diameter; and discontinuous precipitates of β-Nb within the grains and at grain boundaries. The texture is less intense than in cold worked material, having similar Kearns values in the radial and transverse directions, an F_R in the range of 0.41–0.45, an F_T in the range of 0.42–0.53, and a modest value of F_L in the range of 0.06–0.17 [4.193, 4.194].

TABLE 4.4. EFFECT OF HEAT TREATMENT ON THE DISTRIBUTION OF Fe, Cr, AND Ni IN ZIRCALOY-2 AND CONSEQUENCES FOR NODULAR CORROSION

Metallurgical condition	Log A (Q/R 31 500)	Cr (appm)	Fe (appm)	Ni (appm)	Precipitate diameter (nm)	Weight gain ($mg \cdot dm^{-2}$)	Comment	Reference
Recrystallized — as-received (AR)		84	53	78	210	4000	Two step corrosion test	[4.184]
AR + 800°C,1h, slow cool		194	159	143	230	147		
AR + 800°C,1h, slow cool + 50% cold work 600°C 2 h		146	131	146	230	235		
AR + 1000°C, water quench +50% cold work + 600°C 2 h	−15.4	108	108	133	25	54		
Cladding A	−16	42	62	—	29	No nodules	Irradiated in BWR 35 MWd/kg	[4.185]
Cladding C	−13.9	30	59	30	164	Nodules		

Cold worked CANDU pressure tubes have been made with a reduced transverse texture, dislocation density and grain aspect ratio [4.195] in attempts to reduce irradiation deformation, especially elongation, which is mostly attributed to irradiation growth. To help with the change in texture, the extrusion ratio was reduced from 11 to 7.8. The processing between extrusion and stress relieving was modified from 25% to 27% cold work by three routes:

(1) Cold work 40% and heat to 773 K (500°C) for 6 h to balance the extra strengthening with a higher temperature stress relief to reduce the dislocation density and transform the metastable β_{Zr} to β_{Nb};
(2) Cold work 20%, heat to 923 K (650°C) followed by another 20% cold work to produce less elongated α grains;
(3) Anneal the extruded hollow at 973 K (700°C), cold work 40% and heat to 748 K (475°C) for 6 h to produce a modified grain shape and low dislocation density with the second phase consisting of β-Nb.

The microstructural features of the modified tubes are summarized in Table 4.5 showing that some of the changes thought desirable had been attained by each fabrication route. In each case, the tensile strength met the specification requirements showing that there is flexibility in the manufacturing of pressure tubes. Little difference between the four routes was observed in the fracture or corrosion properties, and only Route 1 showed a difference in irradiation growth from the other routes. After a small positive strain transient, specimens measured in the longitudinal direction shrank whereas with standard tubes and Routes 2 and 3, longitudinal growth was always positive [4.196], as seen in Fig. 4.80. With all routes the transverse growth was negative. This response to irradiation is reflected in the behaviour of pressure tubes in a power reactor. Elongation and diametral strain in standard tubes could not be distinguished from values in tubes made by Routes 2 and 3 whereas, compared with these tubes, tubes made by Route 1 exhibited 40–50% lower elongation but 55–75% higher diametral strain. This behaviour was attributed to the thinner grains and higher radial basal texture [4.197].

TABLE 4.5. SUMMARY OF MICROSTRUCTURE AND STRENGTH OF MODIFIED Zr-2.5NB TUBES [4.195]

Property	Standard tubes	Route 1	Route 2	Route 3
Crystallographic texture F_R/F_T	0.55	0.67	0.58	0.6
Alpha grain width (μm)	0.34	0.25	0.34	0.37
Aspect ratio of alpha grains	15 to >20	15 to >20	5–10	5–10
Relative dislocation density	1	0.3	1	0.5
Second phase	$\beta_{enriched} + \omega$	β_{Nb}	$\beta_{enriched} + \omega$	β_{Nb}
UTS at 573 K (300°C) (MPa)	482–558	534–559	530–548	532–544

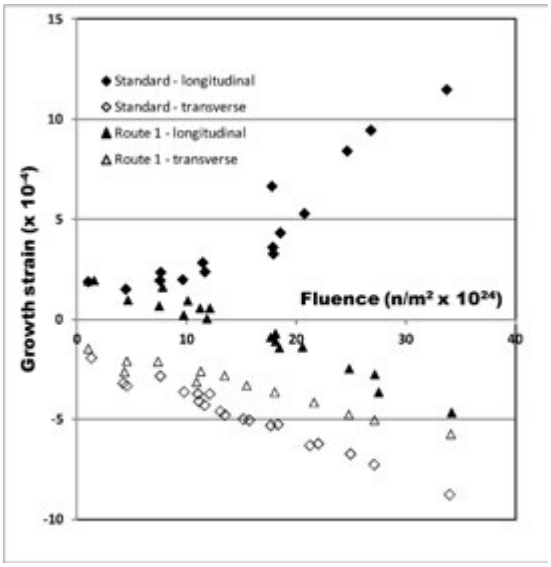

FIG. 4.80. Irradiation growth strain at 553 K (280°C) as a function of fast fluence for longitudinal and transverse specimens machined from Zr-2.5Nb pressure tubes made by the standard route and Route 1 [4.192].

Another variation on the above theme is similar to Route 2 but with the first stage of cold work being about 55% and the intermediate anneal just below the eutectoid temperature — 823 K (550°C) for 6 h [4.151]. The resulting microstructure consisted of elongated α grains surrounded by β phase with an F_R/F_T of about 0.78, larger than for tubes made by the standard fabrication route.

4.6.3.3. Precautions and problems

The preceding sections have described how two types of zirconium alloy respond to heat treatment and how the resulting microstructures affect metallurgical properties. In this section some solutions to typical practical fabrication problems are outlined.

The main causes of variability are gradients in cooling rate, especially during quenching, and temperature gradients in heat treatment furnaces. Time during heat-up and cooldown from annealing temperatures must also be taken into account. If the purpose of the heat treatment is to control precipitation, then one must make sure all the solutes are in solution, for example, by using the phase diagrams. While phase diagrams can be helpful in equilibrium situations, many heat treatment operations are conducted under non-equilibrium conditions, especially β quenching. For example, on cooling, the equilibrium thermal transus can be suppressed by 333 K (60°C) with quench rates on the order of 50 C/s. Likewise, the equilibrium transus can increase during heat-up, and this delay must be taken into account for the very rapid heat-up rates made possible by induction or resistance heating.

By using time–temperature–transformation diagrams and information such as that given in Figs 4.45 and 4.46, the range of grain structure and initial precipitate size can be assessed knowing the range of cooling rates throughout the material. The range of cooling rates will be lower as the cross-section of the product is reduced, consequently the variability from quenching through the thickness will also be reduced. Beta quenching of hollow billets is critical for Zircaloy cladding requiring nodular corrosion resistance. By circulating water through the hole of the billet the effective wall thickness is reduced for a more rapid quench.

The temperature range over which recrystallization takes place in Zircaloy-type alloys is very narrow, as shown in Figs 4.57 and 4.64, so the temperature gradients in annealing

furnaces need to be carefully controlled. The rates and temperature ranges over which precipitates grow and the metal matrix composition changes are much more forgiving than those for grain structure and, although temperature gradients in annealing furnaces will lead to variation, the variation from quenching rates will dominate the overall variation.

As the thickness of the product is reduced during processing, the need for surface protection from oxidation increases. Vacuum annealing is preferred as product thickness decreases and when the surface finish has to be preserved. Alternatively, an inert cover gas can be used. The cover gas should have a dew point of at least 223 K (−50°C) and not more than 10 ppm residual oxygen to provide a bright, shiny surface.

One of the largest problems with vacuum annealing is the resulting gradient of time-at-temperature that can occur without proper care. The heat transfer mechanism is predominantly by radiation and the uniformity of heat-up rates requires line-of-sight to either the wall of the furnace (hot wall furnaces) or to the internal heating elements. Loads should be arranged so that all parts of the load have a direct line-of-sight to the heating source and are not shadowed by other parts of the load. A worst case situation is many thin sheets of metal packed together. The end result is like a multilayer thermos bottle — the outside of the load heats up quickly and the inside of the load can lag behind for 10–20 h before it reaches temperature. Proper load arrangement and introducing a small amount of helium gas during heat-up can minimize this problem. After the load reaches temperature, the gas can be evacuated and the anneal can be performed in a vacuum.

The best method of heat treating thin sheet uses a continuous strip annealing furnace in which a coil is fed from a spool into the furnace that contains an inert gas atmosphere. Fans circulate the gas within the furnace to provide convection to reduce temperature gradients. It is possible to control the temperature on strip products to within 275 K (2°C) by this method.

Very rapid heating can be accomplished by induction heating. This heating can be done with vacuum, inert gas or air atmospheres depending on the allowable surface contamination. In general, the best way to induction heat a part is to scan the part through the induction coil. Heating a part statically in an encircling coil can lead to large thermal gradients while scanning the part minimizes these gradients.

If there is residual strain in α alloys (see discussion on critical grain growth) it is imperative to anneal in the lower α temperature range — certainly no higher than 923 K (650°C) for times of less than one hour. Longer times, higher temperatures or both can lead to blocky α grains (critical grain growth); see Fig. 4.81.

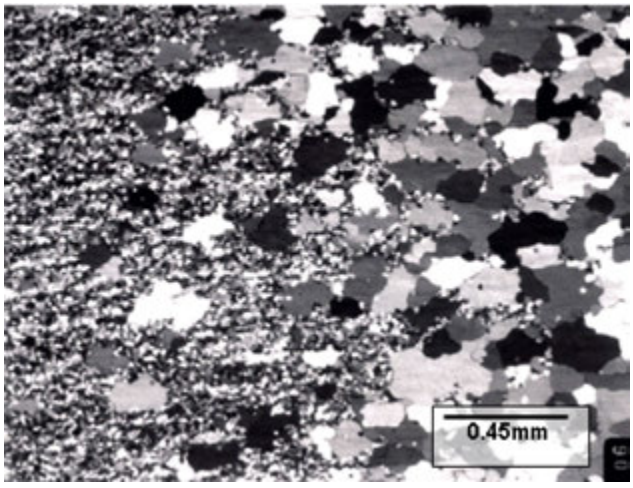

FIG. 4.81. Blocky α grains formed in Zircaloy by cold straining to about 6% and annealing at 1048 K (775°C) for 2 h.

In summary, heat treatment is used to facilitate fabrication and control microstructure to provide good properties in components. A wide range of grain and precipitate distributions is shown to be possible by using Zircaloy, an α alloy, and Zr-2.5Nb, an (α + β) alloy, as examples. Minimizing the sources of variability and ensuring surface protection from oxidation are described.

4.7. JOINING ZIRCONIUM

Zirconium is readily weldable and capable of being brazed by a number of techniques. Fusion welding techniques that are commonly used are gas-tungsten arc welding (GTAW), plasma arc welding (PAW), gas-metal arc welding, electron beam welding (EBW), resistance welding and laser welding. Solid state welding techniques include diffusion bonding, pulse magnetic welding, friction welding and explosion bonding. Brazing is accomplished with special brazing compounds. References of a general nature are found in [4.7, 4.198–4.202].

4.7.1. Metallurgical fundamentals of joining

Zirconium has a high affinity for the light elements such as oxygen, nitrogen, hydrogen and carbon. Since these elements are present in the environment, extreme care has to be exerted to avoid contamination with these metals during heating for welding and brazing.

Zirconium forms a thin, adherent layer of ZrO_2 as a surface oxide film. This film typically has a depth of about 4 nm in ambient air at room temperature. When zirconium is heated in the presence of air, this film thickens, and interference colours can be seen on the surface of the metal. These interference colours are very thin films of transparent oxide. As they thicken, they refract the light within the transparent layer. The interference colours that form typically start with a light straw colour, then turn light blue, and darken into a deeper blue or purple, and finally turn to a deep brown colour. These interference films start to form at temperatures in the 623–673 K (350–400°C) range.

The uptake of oxygen (as evidenced by the formation of the interference colours) creates a hard, potentially brittle surface layer that can result in the loss of ductility, which in turn can lead to cracking problems in fabrication and increased susceptibility to mechanical failures. After exposure at higher temperatures (923 K (650°C)), the oxide film starts to dissolve into the base metal as oxygen diffusion becomes prominent. At even higher temperatures the oxide surface loses its shiny appearance and takes on a dull, matte grey appearance. With increasing temperature and time, the adherent oxide film becomes loose and friable and turns a dull white to buff tan colour. The loose oxide spalls from the surface and re-exposes the underlying tightly adhered oxide.

If the interference films are not removed during subsequent welding (as they are in multilayer welding) their higher oxygen content is then incorporated directly into the weld bead resulting in loss of ductility of the weld joint itself. In the case of gross oxidation, for example, catastrophic oxidation due to loss of shield gas, the entire weld and some of the adjacent parent metal will have to be removed to eliminate the brittle, contaminated layers.

The adverse effects of contaminants require that the weld joint and weld wire (if used) have to be carefully and completely cleaned and remain free of all foreign material during welding processes. Also, the weld surface, the weld root and adjacent hot metal must be protected using inert gas shielding or a vacuum over the temperature range from the melting point (about 2128 K (1855°C)) to below 573 K (300°C).

Along with good thermal conductivity, zirconium also has a low coefficient of thermal expansion; during welding it experiences little distortion. Stress relieving in pure zirconium

is not required as it exhibits low residual stress along with low yield strength. If at a cross-sectional thickness of 25 mm, a stress relief is needed for about 30 minutes; a temperature of 823 K (550°C) is typically used.

Prevention of delayed hydride cracking in Zr-2.5Nb can be achieved using post-weld stress relieving. Stress relief anneal needs to be done on all parts of Zr-705 (non-nuclear Zr-2.5Nb) as required by ASME [4.203] within 14 days of welding at 813–866 K (538–593°C) for a minimum of 1 h for thicknesses up to 25.4 mm.

Residual stresses and crystallographic orientation are responsible for delayed hydride cracking in welds in Zr-2.5 Nb, hence the stress relief requirement [4.204].

Three distinct regions characterize zirconium fusion weld zones of recrystallized, wrought metal:

(1) The weld pool is fully molten. It typically exhibits a β transformed structure upon cooling with a basketweave α platelet morphology.
(2) The adjoining heat affected zone for the Zircaloys is a mixture of (α + β) transformed microstructure. The percentage of alpha ranges from none, adjacent to the weld pool, to 100% at the parent metal. This two phase region is characterized by SPPs decorating the alpha grain boundaries.
(3) The parent metal is characteristic of a recrystallized, wrought structure that has remained completely in the alpha temperature range. Some coarsening of SPPs may be evident, but they remain distributed within the alpha grains.

4.7.2. Fusion welding processes

4.7.2.1. Gas-tungsten arc welding

GTAW is probably the most widely used technique for joining zirconium using fusion welding techniques. It can be used with filler metal or without filler metal (autogenous welding). Millions of end caps are welded onto fuel rods using the autogenous GTAW technique. In one technique, the rods are placed in a sealed chamber. The chamber is evacuated and backfilled, typically with high purity helium. The tungsten electrode tip is aligned over the weld joint (often with a video optical comparator system to align the electrode for the proper application of heat) and the fuel rod is rotated. During rotation, the current is ramped up to steady state, the weld is made by covering more than one full revolution, and then the current is ramped back down to avoid forming a shrinkage cavity at the conclusion of welding. In another technique, the end of the rod is placed in a chamber containing an inert atmosphere, or directly under a GTAW torch equipped with a gas cup and gas lens. After the weld is made, the end plug has a hole in it, and it is evacuated and backfilled with helium. The hole is then autogenously plugged via GTAW.

Joint design is a critical aspect of successful fusion welding. Weld joint preparations are primarily performed to allow access to the root of the joint. The weld joint must be clean, and of uniform geometry. Typical joint designs include single and double V grooves, single and double U grooves, J grooves and butt joints. Butt joints are widely used for autogenous welds where no filler is available to fill the joint. In the case of autogenous welds, careful consideration must be given to the thickness of metal on each side of the joint. The best results are obtained by carefully balancing the thickness so that heat input on either side of the joint is nearly the same. Failing that, careful aiming of the energy of the arc is required so that the thicker side ends up with more heat input than the thinner side of the joint.

A number of subtractive processes — including machining, shearing, abrasive grinding, laser or plasma arc cutting — are used to prepare weld joints. In the case of high temperature cutting techniques, any and all surface contamination that occurs as a result of the cutting must be removed before welding can take place. The weld joint (and filler wire) must be kept completely clean. A wipe down immediately prior to welding with acetone or methyl-ethyl ketone is one way of removing fingerprints, grease and other deleterious substances. In the case of end caps, these are usually pickled in a mixture of nitric acid and hydrofluoric acid, and then thoroughly rinsed in deionized water, and dried.

The tungsten electrode for GTAW welding is typically 2% thoriated tungsten; 2% ceriated, 1% lanthanated or 0.25% zirconated tungsten electrodes are sometimes used for higher current applications. The electrode is ground with a 20–30 degree taper with the end slightly blunted. The electrode must be sized for the electrical current and can range from about 2 mm to about 6 mm in diameter. A ceramic cup with a gas lens may provide shielding gas. Shielding gas may also be applied by supplemental shielding coming from trailing shields or backup shields, or by working within a glove box that has the capability of being evacuated and then backfilled with inert gas. Shielding gas is typically argon; for welding end caps, the shielding gas is usually helium as it is also the internal gas placed within the fuel rod at the time of manufacturing. Mixtures of argon and helium are used, with more helium being desirable for deeper penetration. Helium is often used on the underside of a joint where its buoyant tendency keeps the shield gas up against the joint.

Welding grade shielding gases comprising 99.998% argon or helium are required. Argon provides good arc stability and is less expensive than helium. Its higher density makes it less sensitive to drafts. Gas can be provided from small pressurized cylinders or from large liquid cylinders. The liquid cylinders have the advantage of providing a very pure gas.

Even though pressurized cylinders are certified to contain welding grade or high purity grade gas, the analysis is typically performed at the manifold connecting multiple cylinders. If an individual cylinder has been allowed to ‘go to air’ (reach atmospheric pressure) then the high purity gas is only mixed with air that has been allowed to enter the cylinder. The gas purity is either measured by dew point or with an oxygen analyser. The more common and preferred method is using a dew point analyser. The dew point at the gas supply should not be more than 223 K (−50°C). Small leaks in the delivery lines, valves and regulators can easily aspirate air into the line, even though the line has a pressure higher than atmospheric pressure. Regular monitoring as close to the welding zone as feasible is warranted. In the case of argon, the gas is usually delivered with a guarantee of less than 5 ppm oxygen. The oxygen concentration can reach as high as 50–100 ppm and the weld can still be satisfactory.

When welding in atmospheric conditions, suitable shielding is required. The shield must purge the weld area of air prior to initiating an arc, and the weld site must remain blanketed until the hot metal reaches a temperature of less than 570 K (300°C). Suitable shielding techniques include large gas cups and gas lenses at the torch, backup shields on the root side of the joint, and trailing shields on the torch to allow the weld metal time to cool before air is allowed to come in contact with the completed joint. Gas lenses represent an advance in torch design. They permit laminar flow of the shielding gas at the ceramic cup. This shielding prevents turbulence and mixing with the surrounding air.

Glove boxes must have tight gaskets and must have evacuation and backfill capability. It is often necessary to evacuate and backfill more than once to achieve suitable purity of the cover gas. On-line dew point and oxygen monitoring ensure that adequate purity is maintained within the box. Alternatively, a small coupon of zirconium, niobium, hafnium or

tantalum is kept within the box. An arc is struck on the coupon, after the box has been appropriately evacuated and backfilled with inert gas. This practice serves two purposes:

— The coupon can act as a 'getter' for any residual contaminants in the inert atmosphere.
— The physical appearance of the coupon, where colouration may take place, gives an early warning of any residual contaminants in the box prior to committing the actual weld.

GTAW parameters have to be developed for each joint design. A very rough guide for manual GTAW of zirconium with filler wire of 2 mm diameter is a welding current of 125–175 A at 13–15 V, with a speed of 100–200 mm/min. The welding current is usually DC, electrode negative, which provides 70% of the heat at the work piece, 30% at the electrode. These conditions maximize penetration and minimize current on the electrode. A high frequency starter arc is desirable to preclude touching the weld joint with the tungsten tip. Without the high frequency starter, starting weld tabs can be used to initiate the arc.

Typical defects for GTAW include contamination of the weld and heat affected zone, lack of penetration, over-penetration or 'drop-through', and porosity. Contamination has been dealt with extensively in this section. Lack of penetration is resolved by increasing the power, decreasing the rate of travel of the GTA torch or both. Drop-through on the back surface of the weld is the inverse of lack of penetration and is resolved by less power and a faster rate of travel. Porosity is not common in zirconium welds but can occur if contaminants that can cause out-gassing are present.

Inspection is generally by ultrasonic testing (UT), backed up by dye penetrant examination, or, in some cases, by radiography. For fuel rod end cap joints, a helium leak check is also required.

4.7.2.2. Plasma arc welding

PAW is typically used for heavy sections, usually greater than 10 mm in thickness. PAW, like GTAW, uses a non-consumable electrode. The arc heats the gas fed into a chamber, surrounding the tungsten electrode, to a temperature where it becomes ionized and conducts electricity. Plasma issues from a nozzle orifice at temperatures of about 17 000 K. The orifice constricts the plasma gas, and this design improves directional stability and provides a very high energy concentration. Because the tungsten electrode is well back up inside the nozzle, there is little concern in contaminating the work piece with tungsten, which could then form a high density inclusion. DC electrode negative power is used for most PAW applications.

Advantages of the process include high power density, low current and little distortion, higher arc stability, high penetration and great standoff, which provides room for the introduction of filler metal, if required. All the procedures for cleanliness and inert gas coverage and precautions discussed under GTAW apply to PAW.

Applications for zirconium fabrication include welding ingot electrode assemblies for vacuum arc melting in tanks filled with inert gases and welding heavy plates together. PAW is used to weld sheet and strip up to several millimetres thick in an autogenous fashion without filler metal. These applications typically do not require more than a visual examination for excessive contamination.

4.7.2.3. Gas-metal arc welding

Gas-metal arc welding is typically employed during zirconium fabrication for temporary, low strength welds. The process relies on feeding a wire electrode into the molten pool. The electrode carries the current and serves as the filler metal. Since this technique typically does not employ trailing shields, the weld puddle is uncovered to atmosphere while it is still hot, and some contamination occurs. This technique can be used to weld heavy section ingot electrodes or casting electrodes, where the slight local contamination of the weld joint is mixed with a much larger volume of molten metal during subsequent arc melting. Shielding must be at least adequate to preclude the formation of high melting point nitrides. This technique is also known as wire welding or metal inert gas welding.

4.7.2.4. Electron beam welding

EBW is used to provide high quality, deeply penetrating welds. For zirconium technology, the range of applicable part sizes for EBW is large. It can be used for entire electrodes for vacuum arc remelted melting, while, on a smaller scale, precision components manufactured from thin foils and wires can be welded into various assemblies.

The principle is to generate a focused energetic stream of electrons with an electron gun assembly. The welding is almost always done in a high vacuum chamber with a pressure of 1.33×10^{-1} Pa or less (typically 1.33×10^{-3} to 1.33×10^{-4} Pa), for reactive metals. Maximum weld penetration and minimum weld width can be achieved, thereby minimizing distortion and weld shrinkage. High weld purity is achieved because of the high vacuum. The long gun-to-work distance (which can be at a distance of up to 1 m) permits access to intricate nooks and crannies that would be difficult to get at with other welding techniques.

Joint designs can be either autogenous (most commonly) or with filler metal additions. One of the particular advantages of EBW is precision control of the heat input, which permits adjoining thick and thin sections to be welded to one another. Another advantage is the high penetration of autogenous joint designs, with a very thin molten zone.

A challenge of EBW is developing a proper fixture for the part to be welded. For small traverses, magnetic deflection coils can manipulate the beam. For larger or more complex manipulations, a motion control assembly traverses the part under the beam. Proper joint assembly and retention during welding, and the manipulation of the joint under the beam, can often require very elaborate and precision jigging fixtures and motion control mechanisms.

As a consequence, EBW is mostly used where welds of a repetitive nature are required, or where the geometry is simple. A good example is in the welding of barrier tube extrusion billets for BWR reactor fuels. In this design, the outer, load bearing and corrosion resistant portion of the tube is Zircaloy-2. A thinner, inner barrier layer of pure zirconium is bonded to the outer layer during the extrusion operation. Prior to extrusion, a heavy cylindrical billet of Zr-2 is machined with a central hole. Into this hole is inserted the pure zirconium liner, in the form of a heavy walled tube. The face ends of the billet and liner tube are seal welded together with EBW. The billet is rotated, and the electron beam penetrates the joint between the pure liner and the Zircaloy-2 billet. This weld has to have a high degree of integrity as it has to survive extrusion of the combination billet into a tube.

EBW can produce high quality welds. Base metal recrystallization and grain growth can be minimized. Beam oscillation and travel speed can be used to control heat input and the shape of temperature gradients. Low heat input results in low thermal stresses in the base metal and concomitant low distortion and few cracks from residual stresses. Typical defects

or discontinuities of which the welding engineer must be aware include porosity, shrinkage voids, cracking, undercutting, not filling the joint (underfill), lack of penetration, lack of fusion and missed joints (beam misalignment). Inspection techniques include UT, radiography and dye penetrant examination.

4.7.2.5. Spit and seam resistance welding

Resistance welding is straightforward and can be used to assemble sheet metal components rapidly or to join small cross-sections such as wire-to-wire or wire-to-sheet. Usually no attempt is made to shield the weld nugget. The time-at-temperature is short and the interface between the two sheets is self-shielded to a certain extent. The surrounding mass and the high thermal conductivity of zirconium rapidly quench the molten weld pool.

Spot and seam welding involve a coordinated application of current and mechanical pressure. The welding current must pass through a set of electrodes into the work piece. Sufficient heat must be developed to raise a confined volume of metal to the molten state, and this weld nugget is allowed to cool while the parent metal is constrained with pressure. The heat required for these resistance welding processes is produced by the resistance of the work pieces to the electric current flowing through the material. Because of the short electrical path and limited weld time, high welding currents are required. Variables include, for example, welding current, weld time, welding pressure, electrode composition and shape, and the influence of the surface conditions of the parts to be joined.

Since special tooling is often required to accomplish a resistance weld, it is typically reserved where welds of a repetitive nature are required. It can be a very quick method of welding two thin pieces of sheet metal together over a long length of weld using the wheel technique (seam welding). Alternatively, it can be used to spot weld in a highly localized area. This process is typically reserved for special assemblies.

One application is to resistance spot weld thermocouples so that they are intimately attached to indicate underlying metal temperature during subsequent heating operations. This method is not recommended for Zr-2.5Nb or other high strength alloys because of delayed hydride cracking concerns, unless the local area can be stress relieved or the time between welding and the operation is short.

4.7.2.6. Laser beam welding

Laser beam welding (LBW) is a fusion joining process that employs the heat obtained from a monochromatic, coherent beam of light impinging on the weld joint. LBW is a non-contact process and requires no external pressure to be applied. Industrial lasers utilize neodymium doped, yttrium aluminium garnet crystal rods in the 1–2 kW range, or CO_2 up to 25 kW in energy.

Advantages include minimal heat input, minimal distortion and non-contact fusion welding, which can be performed in an evacuated enclosure. Laser beams can be focused on a small area, permitting the joining of small, intricate parts that are closely spaced. This attribute makes the process ideal for welding the tabs and junctions of fuel grid spacers made from Zircaloy. Grid spacer joint welding has progressed from GTAW to EBW to LBW and this evolution has caused the size of the weld nugget at each grid intersection to decrease. The weld nugget impedes coolant flow and increases pressure drop within the fuel assembly. The process is readily automated, and a high degree of precision can be obtained. As with EBW, the design of the fixture is extremely important as tolerances must be closely held to maintain joint fit-ups without allowing either mismatch or gaps.

4.7.2.7. Inspection techniques for fusion welding

Several non-destructive inspection techniques are appropriate for fusion welds. Visual inspection is required to ascertain freedom from atmospheric contamination or from surface contaminants such as oil. Appearance of a light straw colour in the heat affected zone is acceptable, but any darker discolouration would require reworking the welded area. Surface cracks, incomplete penetration and surface connected shrinkage voids can be detected by die penetrant examination. Radiography can detect internal defects such as voids or porosity. In some instances, ultrasonic testing (UT) techniques can be used, but the welded joint has to be of acceptable geometry and the techniques have to be well standardized.

4.7.3. Solid state welding processes

Solid state welding processes involve no melting of the parent metals. Metallurgical bonding is accomplished by diffusion mechanisms or by extreme pressure.

4.7.3.1. Pulse magnetic welding

Pulse magnetic welding employs a large single turn inductor, typically made from tantalum. The inductor is electrically connected through a rail gap switch to a large capacitor bank. The capacitors are charged, and the energy is discharged by the rail gap switch through the single turn inductor. The rail gap switch consists of two insulated sheets of metal separated by the gap. The gap is filled with the electrically conductive gas, SF_6. The capacitor discharge is initiated when a high frequency starter arc jumps across the insulated terminals of the switch. The conductive gas turns into plasma and the main electrical charge then has a free path to jump the gap. Typically, axisymmetrical work pieces are contained within the bore of the single turn inductor. The collapsing electrical discharge generates a magnetic field that forces the primary work piece with appropriate geometry onto a second work piece. The violent collapse of the electrical discharge and resulting magnetic field accelerates the outer work piece with sufficient velocity to solid state bond onto the inner work piece.

Two requirements are that the metals to be joined must be conductive, and a lap joint configuration is required. The higher the electrical conductivity, the more magnetic force can be generated. Advantages include minimal heat input and the fact that the weld thus produced is a true, solid state metallurgical bond. The cycle time is rapid and typically only limited by how fast parts can be loaded into the coil.

End caps have been attached to fuel rods by pulse magnetic welding. The welding process was developed in the late 1960s and early 1970s for nuclear energy applications. Russian scientists at the Kurchatov Institute of Nuclear Physics invented a technique for the pulsed magnetic welding of end closures of nuclear fuel rods. In one design, the end caps have a tapered section where the weld takes place. The end of the fuel rod rapidly accelerates down the taper and the resulting metallurgical bond at the interface is wavy, similar to the interface obtained from an explosion bonded joint. An appropriately designed joint is inspectable by UT.

4.7.3.2. Diffusion bonding

Diffusion bonding processes permit a solid state weld, often with dissimilar alloys. Necessary conditions include an appropriate temperature, residence time, interfacial pressure and interfacial cleanliness. The advantages are that joints can be produced with properties

very similar to those of the base zirconium, components can be joined with a minimum of distortion, large surface areas can be bonded and defects, such as porosity and shrinkage, normally associated with fusion welding, are not encountered. A further advantage is that sometimes the process can be conducted in conjunction with another operation such as extrusion.

Diffusion bonding of the reactive metals, particularly zirconium, has to be conducted in a vacuum. The two joining surfaces have to be totally evacuated and must stay this way throughout the bonding cycle. Surface preparation is important. Any residual contaminants such as fingerprints, greases and excessive surface oxidation will prevent metallurgical bonding. Chemical cleaning in a standard pickling acid such as 3–5% HF, 30% HNO_3, balance H_2O, followed by rinses in hot deionized water is one method of assuring surface cleanliness.

Diffusion temperatures can range from around 900 K (630°C) up to 1200 K (930°C) depending on the bonding technique being employed. Pressures have to be sufficient to ensure intimate contact during the bonding cycle. Pressure can be applied during a hot working operation, such as during extrusion, or during hot rolling, by vacuum hot pressing or by gas pressure as during hot isostatic pressing.

Dissimilar metal bonding has been cited in Ref. [4.198] with Zircaloy-2 being bonded to 304 stainless steel. Other combinations include zirconium to titanium and zirconium to niobium. A common practice is to produce barrier tubing for BWRs using diffusion bonding. An inner, pure zirconium tube is electron beam welded into an outer Zircaloy-2 extrusion billet. The mating surfaces are cleaned to provide a metallurgical bond. Since the seal welds on either end of the billet are performed using EBW, the interface between the Zircaloy-2 and pure Zr liner is automatically placed under a vacuum. The entire assembly is preheated to about 900 K (630°C) and co-extruded to a tube. The combination of joint cleanliness, vacuum sealing, temperature, dwell time during extrusion and pressure during extrusion are sufficient to metallurgically bond the combinations of the two forms of zirconium together. The integrity of these joints is demonstrated by the fact that the joint is able to survive a cold tube reduction of about 70% RA without fracturing. Testing of the bond interface occurs by rotary head ultrasonic tube inspection machines and by metallographic examination of slices obtained from the tube. A similar process is used to manufacture duplex cladding where a thin layer of more corrosion resistant metal is bonded to a heavier, inner layer of Zircaloy-4.

Diffusion bonding is also used in assembling the RBMK fuel channel where the Zr-2.5Nb pressure tube is joined to stainless steel end fittings.

4.7.3.3. Other solid state processes

Other solid state welding processes have been used to join zirconium to itself and to other alloys. One common process is the explosion bonding of sheets of nominally pure zirconium to other materials such as carbon steel or stainless steel [4.205]. This explosive bonding is usually done where the properties of zirconium such as corrosion resistance are required, but where the strength of steels is also required. An example of using explosion bonded sheets is in pressure vessel construction for shells, heads and tube sheets. Since the technique is unique to individual applications, and requires very specialized facilities, no further discussion of it will be included here.

Zirconium can also be joined to itself and to other alloys by friction welding. This process often serves to join axisymmetric parts such as tubing or bar stock end-to-end. One

end is placed in a lathe-like headstock assembly. The other end is placed in a fixed tailstock. The headstock can be either directly powered or powered by inertia via a flywheel.

Once the headstock has achieved rotational speed, the fixed piece is pushed into the rotating piece. This contact creates local friction at the interface, which heats the joint. The tailstock is then further driven forward, usually by hydraulic means, to upset the joint. The interface metal becomes soft enough that it plastically flows out of the joint, scrubbing the interface clean, and the heated metal is thereby occluded from the atmosphere. This process can be conducted under atmospheric conditions (there is no need for a vacuum or inert atmosphere). Zirconium has been welded to dissimilar metal combinations such as stainless steel, titanium and niobium using friction welding. Inspection techniques include radiography and dye penetrant examination.

4.7.4. Brazing

The brazing of zirconium and its alloys is routinely performed. The brazing process requires a lower melting temperature filler metal that bonds to both surfaces being joined. Key variables include brazing temperature, the gap width of the joint, the cleanliness of the mating surfaces, the composition of the brazing alloy and the exclusion of any atmospheric contamination.

In practice, brazing alloys are mostly zirconium alloys. One composition that has been cited [4.206] is Zr-5%Be, which has a eutectic melting point at 1248 K (975°C). The brazing compound can be a thin foil, a powder suspended in a paste-like binder or a thin film applied by vapour deposition. The parts are preassembled and held together with light pressure. Assembled parts are placed in a vacuum and the heating energy typically comes from a high frequency induction apparatus. The binder paste is volatilized early in the brazing cycle at a low temperature.

One example of brazing is the attachment of the bearing pads and spacers onto CANDU fuel tubes [4.207]. Small pieces of rectangular Zircaloy wire, shaped to the contour of the underlying fuel tube, are held in place with a preapplied brazing compound. Several cladding tubes with their pads are loaded into a fixture and placed in a vacuum bell. The bell is evacuated, and an induction heater applies the necessary energy to melt the brazing compound and fuse the joint. Brazing typically takes place at about 1273 K (1000°C), and the entire heating cycle lasts a few seconds.

In summary, zirconium alloys can be readily joined by a variety of welding techniques. Care has to be taken to maintain cleanliness and determine whether residual stresses are an issue. The choice of technique will depend on the consequences of the extent and severity of the metallurgical changes made by the weld and the economics of the process.

4.8. MACHINING OPERATIONS

There are three basic principles that should be followed when machining zirconium: slow speeds, high feed rates and a flood coolant system using a water soluble oil lubricant. Zirconium tends to gall and work-harden, which requires higher than normal clearance angles on tools to penetrate the work-hardened surface and cut a clean chip.

In most cases, both carbide and high speed steel tools give satisfactory results when machining zirconium; however, carbide usually allows higher productivity and gives a better finish. Performance is greatly enhanced by keeping the tools sharp. It is also important to prevent the accumulation of fine chips, since zirconium can be pyrophoric; small machine chips or turnings with a high surface-area-to-mass ratio are easily ignited and burn at

extremely high temperatures (see Section 4.10). Information for specific operations is given below [4.208].

4.8.1. Turning

There are no special requirements for turning zirconium. It can be done without difficulty using standard equipment, as long as sharp tools and a coolant lubricant are used. Recommended operating parameters are given in Tables 4.6 and 4.7. Lead angles on tools should be between +15 and +60°. Turning is used in myriad applications, including machining of fuel rod end caps, and machining of complex instrumentation assemblies.

TABLE 4.6. SINGLE POINT TURNING OF ZIRCONIUM [4.208]

Depth of cut (mm)	Carbide grade	Speed (m/min)	Feed (mm/rev)	Tool steel grade	Speed (m/min)	Feed (mm/rev)
1	C-2	85–100	0.2	M2, M3	45	0.2
4	C-2	70–80	0.4	M2, M3	30	0.4
8	C-2	50–60	0.5	M2, M3	25	0.5

TABLE 4.7. CUTOFF AND FORM TOOL TURNING OF ZIRCONIUM [4.208]

		Feed, mm/revolution Tool width							
Tool grade	Speed (m/min)	1.5 mm	3 mm	6 mm	12 mm	18 mm	25 mm	35 mm	50 mm
T15, M42 C-2	20	0.5	0.06	0.07	0.08	0.06	0.05	0.05	0.05

4.8.2. Milling

Both vertical face and horizontal slab milling of zirconium give good results. Whenever possible, zirconium should be climb milled to penetrate the work at the maximum approach angle and depth of cut while emerging through the work-hardened area. Climb milling is where the cutter rotates to enter the virgin surface of the work piece. It is important that the milling cutters be kept very sharp and the work area flooded or sprayed with coolant to completely wash away the chips from the tool. Specific operating set points for milling zirconium are given in Tables 4.8–4.12. Lead angles on tools should be between +15 and +30°, with positive axial and positive radial rake angles.

TABLE 4.8. FACE MILLING OF ZIRCONIUM [4.208]

Depth of cut (mm)	Carbide grade	Speed (m/min)	Feed per tooth (mm)	Tool steel grade	Speed (m/min)	Feed (mm/rev)
1	C-2	85–105	0.15	M2, M3	50	0.15
4	C-2	70–90	0.25	M2, M3	35	0.25
8	C-2	55–70	0.35	M2, M3	30	0.35

TABLE 4.9. SLAB MILLING OF ZIRCONIUM [4.208]

Depth of cut (mm)	Tool grade	Speed (m/min)	Feed per tooth (mm)
1	M2, M7	40	0.15
4	M2, M7	24	0.20
8	M2, M7	20	0.25

TABLE 4.10. HOLLOW MILLING OF ZIRCONIUM [4.208]

Tool grade	Speed (m/min)	Feed (mm/rev)
M2, M7	25	0.10
C-2	55	0.20

TABLE 4.11. SIDE AND SLOT MILLING OF ZIRCONIUM [4.208]

Depth of cut (mm)	Carbide grade	Speed (m/min)	Feed per tooth (mm)	Tool steel grade	Speed (m/min)	Feed per tooth (mm)
1	C-2	120–145	0.18	M2, M7	55	0.15
4	C-2	105–135	0.20	M2, M7	50	0.18
4	C-2	75–90	0.23	M2, M7	45	0.20

TABLE 4.12. END MILLING OF ZIRCONIUM [4.208]

Axial depth of cut (mm)	Tool grade	Speed (m/min)	Feed, mm/tooth Width of slot			
			10 mm	12 mm	18 mm	25–50 mm
0.75	T15, M42	40	0.04	0.05	0.06	0.08
3.0	T15, M42	30	0.05	0.06	0.08	0.10
(Dia/2)	T15, M42	22	0.04	0.05	0.06	0.08
(Dia/1)	T15, M42	18	0.02	0.03	0.05	0.06

4.8.3. Hole making operations

Good results for drilling zirconium can be achieved using a standard fresh ground (118°) thin webbed drill and a coolant lubricant. It is important to use a firm backing to prevent burrs at the exit. Ensuring a sufficient amount of stock material is left for reaming can minimize smearing. Tapping zirconium is done best using chip driver or gun type taps; they must be kept sharp. Data for specific hole making operations are given in Tables 4.13–4.16.

TABLE 4.13. DRILLING OF ZIRCONIUM [4.208]

Tool grade	Speed (mm/min)	Feed, mm/rev Nominal hole diameter							
		1.5 mm	3 mm	6 mm	12 mm	18 mm	25 mm	35 mm	50 mm
M1, M7 M10	17	0.05	0.075	0.10	0.15	0.20	0.25	0.30	0.40

TABLE 4.14. BORING OF ZIRCONIUM [4.208]

Depth of cut (mm)	Carbide grade	Speed (m/min)	Feed (mm/rev)	Tool steel grade	Speed (m/min)	Feed (mm/rev)
0.25	C2	70–85	0.075	M2, M3	45	0.075
1.25	C2	60–70	0.13	M2, M3	35	0.13
2.5	C2	45–55	0.30	M2, M3	25	0.30

TABLE 4.15. TAPPING OF ZIRCONIUM [4.208]

Tool steel grade	Speed (m/min) Pitch (mm)			
	> 3	1.5–3	1–1.5	1 or less
M10, M7, M1	14	23	29	30

4.8.4. Grinding

TABLE 4.16. REAMING OF ZIRCONIUM [4.208]

Tool grade	Speed (mm/min)	Feed (mm/rev) Reamer diameter					
		3 mm	6 mm	12 mm	25 mm	35 mm	50 mm
M1, M2, M7	15	0.13	0.20	0.30	0.45	0.50	0.65
C2	50	0.10	0.18	0.25	0.40	0.50	0.65

Both wheel grinding and belt grinding can be used for zirconium. For wheel grinding, conventional speeds and feeds are satisfactory with silicon carbide wheels giving better results than aluminium oxide. The effect of grinding fluid on zirconium is the same as on other metals; grinding oils alone produce higher grinding efficiency than water miscible fluids, which means less wheel breakdown and finer finishes. Recommended operating set points are given in Tables 4.17–4.20.

In belt grinding zirconium, belt speed and contact wheel selection are the key considerations. Contact wheels should be hard and aggressive. Soluble oil coolants used alone, or mixed with water and applied in a flood, are recommended. An abrasive cloth may be used with oil and rubber contact wheels on general polishing operations, while resin bond cloth belts with a skived joint, or a thin Mylar reinforced butt joint, are recommended for use with oil in grinding operations where high grinding pressures are used. Similarly, waterproof cloth silicon carbide for light work and aluminium oxide for heavy work may be effectively employed with soluble oil and water coolants.

TABLE 4.17. SURFACE GRINDING OF ZIRCONIUM [4.208]

Wheel speed (m/sec)	Table speed (m/min)	Downfeed (mm/pass)	Crossfeed (mm/pass)	Wheel identification
15	12	Rough: 0.025 Finish: 0.013	1–10 (max — 1/6 of wheel width)	C46JV

TABLE 4.18. CYLINDRICAL GRINDING OF ZIRCONIUM [4.208]

Wheel speed (m/sec)	Work speed (m/min)	Infeed (mm/pass)	Traverse	Wheel identification
15	15–30	Rough: 0.025 Finish: 0.013	1/6–1/12 of wheel width	C60KV, CA60PB

TABLE 4.19. INTERNAL GRINDING OF ZIRCONIUM [4.208]

Wheel speed (m/sec)	Work speed (m/min)	Infeed (mm/pass)	Traverse	Wheel identification
15	15–45	Rough: 0.013 Finish: 0.005	1/3–1/6 of wheel width	C80KV

TABLE 4.20. CENTRELESS GRINDING OF ZIRCONIUM [4.208]

Wheel speed (m/sec)	Throughfeed of work (m/min)	Infeed (mm/pass)	Wheel identification
15	1.3–1.8	Rough: 0.025 Finish: 0.013	Rough A60TB or CA60RB Finish: CA80PB

4.8.5. Sawing

Band sawing is generally done with a saw with a 1.1 mm raker set and a saw band width of 13 mm, in conjunction with a flood of soluble lubricant or an air stream to wash away the chips from the cut to give satisfactory results. For cold circular sawing, teeth should be alternately levelled and square, with the levelled teeth slightly higher than the square teeth. The cut and the saw blades should be cooled with soluble coolant. Fine chips should be removed from the area frequently to prevent a buildup of flammable solids. Sawing data recommendations are shown in Table 4.21.

TABLE 4.21. BAND SAWING OF ZIRCONIUM [4.208]

Material Thickness (mm)	Tooth form	Threads per inch pitch (mm)	Band speed (m/min)
<12	Precision	2.5–1.8	30
12–25	Precision	3–2.5	27
25–75	Precision	4–3	23
>75	Claw, precision	8.5–6.5	20

4.8.6. Honing

Honing is used to improve the interior surface of tubular items. It is used to provide a smoother surface finish than can be obtained by traditional machining operations. For example, the inside surface of CANDU Zr-2.5Nb pressure tubes are honed after cold drawing [4.190]. Honing can also be used to size the diameter of a bored hole. Honing will follow the original geometry of the hole and will not correct such defects as eccentricity, ovality or axial misalignment of the hole.

In practice, a billet with an axial hole or a tube is fixed to the honing bench. The honing head contains three or four abrasive stones in a typical set-up. The stones are forced against the interior surface of the billet or tube by a spring loaded device or by hydraulic actuation. The head of the hone is on a long shaft that rotates the head and oscillates the head up and down the length of the part being honed.

A mineral oil lubricant is used to lubricate the hone abrasive and to remove swarf. The part can be vertically or horizontally oriented. If the tube is horizontally oriented, it should periodically be rotated to prevent gravity effects from over-honing the bottom of the tube. The parameters of honing (abrasive material, grit size, pressure, rotational and translational velocities) need to be established experimentally on the parts to be honed.

4.9. CHEMICAL AND MECHANICAL CONDITIONING

Zirconium requires a combination of mechanical and chemical conditioning to remove contamination, oxide scales, diffused oxygen (which promotes the formation of α phase), and to provide clean surfaces for cold working, vacuum annealing and to optimize corrosion resistance [4.7, 4.209].

Removal of oxide scales and diffused oxygen-rich layers starts with mechanical descaling methods such as sandblasting, steel shot blasting, glass bead blasting or vapour blasting (a special technique in which a fine abrasive slurry is propelled onto the surface with compressed air). Abrasive media commonly employed include silicon carbide, zircon sand, aluminium oxide, steel shot and glass beads.

The abrasive media are usually propelled onto the surface with compressed air. In the case of steel shot blasting, the shot is generally accelerated towards the surface using a rotary vane or rapidly rotating buckets (i.e. it is mechanically propelled). Sizing of the media must be consistent with the thickness and tenacity of the scale being removed. Heavier media are more effective (carry more energy) for thicker, more tenacious scales. Finer media are appropriate for intermediate scales or to provide final surface finishes.

Abrasive or shot blasting may induce residual compressive stresses into the surface of the work piece. Normally this is not an issue, except on thin sheet items that may warp. Blast cleaning is not intended to eliminate acid pickling. It will not remove an 'α-stabilized case' layer resulting from diffused-in oxygen. Generally, blast cleaning is followed by pickling to ensure the complete removal of surface contamination and a residual cold worked layer, and to produce a smooth, bright finish.

Pickling is used to complete the removal of the diffusion layer of oxygen that occurs during heating in air. Also, imperfect vacuum atmospheres (from residual moisture on work pieces or in the furnace, and diffusion pump oil back streaming) can contaminate the surfaces with a thin diffused layer that requires pickling for removal.

The most common pickle solution for zirconium and the Zircaloys consists of 30–35% nitric acid (of 70% concentration) and 3–5% hydrofluoric acid (of 49% concentration) with the remainder of the bath being water. The acid bath for zirconium-niobium alloys contains 30% sulphuric acid (1.84 specific gravity) and increases the hydrofluoric acid concentration from 5 to 10%. The sulphuric acid prevents smut formation on Zr-Nb alloys.

Pickle bath temperatures should not exceed 340 K (70°C) to prevent pick-up of hydrogen that forms during the pickling reaction. The hydrofluoric acid attacks the zirconium (and alpha-stabilized case layer) while the nitric acid oxidizes the hydrogen and also re-oxidizes the zirconium to stabilize the reaction rate. Except for Zr-Nb alloys, the rate of metal removal is linear with HF acid concentration, and doubles as the bath temperature rises from 318K to 343 K (45°C to 70°C).

A stop bath consisting of 70% nitric acid and 30% water can be used to prevent insoluble fluoride stains (zirconium oxyfluoride) from forming on the surface. The material is pickled in the nitric and hydrofluoric solution and is immediately transferred to the stop bath. Thorough rinsing with cold water follows.

If a stop bath is not used, the material must be transferred from the acid bath to a water rinse bath in the shortest possible time. Often a water rinse is started as the material is being removed from the acid bath. A residual acid film on the metal can rapidly heat up and cause severe surface staining if these precautions are not followed.

Bath compositions need to be monitored for metal accumulation, and HF depletion. Baths can be 'spiked' with HF acid to improve their efficiency, but eventually excessive metal ion loading requires that the bath be discarded. Appropriate treatment of the bath is required to neutralize the spent acid and to capture fluoride-ion species.

4.10. SAFETY PRECAUTIONS

The high energy of combustion of zirconium dictates that it be handled to avoid the hazard this poses. Zirconium metal is not readily ignitable in massive form; it is forged in air while heated to near 1375 K (1100°C). In finely divided forms, where the ratio of surface area to volume is high as in filings, grinding dust, machine-tool swarf and fine powders, friction or sparks can cause ignition, often followed by rapid, even explosive, combustion of the entire mass. Dry chips from a turning or milling operation greater than about 1.5 mm thickness are resistant to burning.

Since zirconium reduces water exothermically, with liberation of hydrogen, water adds to the conflagration or, if the event occurs in a confined space, will almost certainly cause an explosion. Consequently, it is useless to try to control a zirconium fire with water, carbon dioxide or fluorocarbons, all of which support its combustion. Smothering the fire with dry silica sand or with sodium chloride, or the commercially available Ansul Met-L-X dry powder extinguishing agent is the accepted means for controlling small fires. The safe handling of zirconium is described in Ref. [4.7], with more detail in [4.210, 4.211]. The 2006 International Fire Code [4.212] provides limited guidance. Finely divided zirconium is classified as a flammable solid and its shipment is closely regulated. In the United States of America, the pertinent regulations for all transport modes are given in Ref. [4.213]. International shipment by ocean is covered by the International Maritime Association [4.214] and the International Air Traffic Association governs international air shipment [4.215].

Precautions are also necessary when zirconium is mixed with boron, sulphur or carbon powders, or solids containing available carbon, nitrogen, oxygen, sulphur or halogens, since zirconium forms very stable compounds with all these elements, through highly exothermic reactions. Such mixtures can sometimes ignite easily and burn fiercely. As an additional precaution, users should be aware that zirconium forms highly stable, exothermic compounds with palladium, and especially with iridium and platinum.

Fine saw or grinding swarf is often intermingled with an aqueous coolant. Special precautions should be taken to either keep the swarf completely submersed or totally dry. As the swarf dries into the 1–2% moisture range, the zirconium will react with the water molecule, forming gaseous hydrogen. Accumulations of hydrogen gas can be explosive. A small ignition source is sufficient to ignite the hydrogen that can, in turn, ignite the remaining zirconium metal, with the force of the explosion spreading an incendiary-like compound. The best preventative measures are to avoid an accumulation of chips, to use copious quantities of water soluble coolant, and to limit feeds and speeds to prevent heat buildup and a possible ignition source.

An aspect of zirconium's use in corrosion service is the low toxicity of the element and those of its compounds that contain no other toxic moiety (or portion of a molecule). There seems to be no report of either metal or its alloys with non-toxic constituents causing physiological reaction; indeed, zirconium is a constituent of several alloys used in bone and joint prostheses. One of these is described in Ref. [4.216] and comprises Ti-13Nb-13NZr another is Ti-12Mo-6Zr-2Fe. These alloys are covered under ASTM specifications F 1713 [4.217] and F 1813 [4.218], respectively. Certain zirconium compounds are toxic when administered orally or are injected subcutaneously or interperitoneally [4.219, 4.220] and others such as the hydroxy-oxychloride cause granulomas in the lungs; this danger has led to the discontinuance of this compound's use in spray dispensed antiperspirants.

A United States National Institute of Occupational Safety and Health investigation [4.221] found dermatitis and respiratory problems associated with one producer of zirconium, but sound industrial hygiene measures will prevent such problems. At pH values associated with most biological tissues, the zirconium and hafnium moieties of most compounds are hydrolysed to their oxides, the solubility of which is vanishingly small. Thus, toxic doses of most of the compounds are large. In summary, zirconium and its alloys are amenable to standard machining practices and the parameters for satisfactory results are listed. Similarly, the methods for surface preparation are well established to provide clean surfaces for subsequent fabrication steps or for reactor use. Zirconium alloys have low toxicity, the main hazard being from ignition and explosion when the metal is finely divided.

4.11. COMPONENTS — THE BUILDING BLOCKS

Reactor components consist of standard mill products such as TREX, cladding tubes, bar, strip and wire. These items, while they may be complex in terms of their chemical composition, processing routes, metallurgy and heat treatments, have fundamentally simple shapes. Even the most complicated design of component may be broken down into a combination of several basic shapes. The following examples illustrate how rods, sheets and tubes produced by primary manufacturing are used to make several types of nuclear fuel and a reactor control mechanism.

4.11.1. Cladding tube fabrication

Cladding tubes have a number of service requirements. These include good strength, sufficient creep resistance at operating temperatures, good dimensional controls, proper texture and good corrosion resistance. The materials and processes have been fine tuned to the point that cladding tubes are distinct for each of the major reactor types, including PHWRs, PWRs, BWRs, RBMKs and water cooled water moderated power reactors (WWERs). The cladding tube has to perform in a severe external corrosive environment of high temperature water or steam with chemical additives, under intense neutron radiation, with internal fission products — some of which can be highly corrosive and have an embrittling effect on the cladding. The cladding is designed to resist relentless thermohydraulic forces, to hermetically seal internal filler gas and to release fission gas pressures of 2–9 MPa at end-of-life, all the while economizing on neutrons with the least possible volume fraction of zirconium that will perform satisfactorily to design discharge burnups.

As such, the design of the cladding tube starts with the alloy composition, and the fabrication is continued with correct thermal heat treatment cycles (including β quenching, accumulated annealing parameter for Zircaloys and post-β-quench maximum processing temperature limit for zirconium-niobium alloys), the proper degree of hot work to cold work, the correct reduction sequences from stage to stage, and the optimum final heat treatment and final finishing. All of these processes have to be fine tuned to provide the optimum cladding for the intended application.

4.11.1.1. PWR cladding

PWR cladding is a tube of up to 4.4 m in length with an outside diameter of between 9.5 and 11.2 mm with wall thickness in the range 0.6–0.7 mm. It has traditionally been manufactured from Zircaloy-4, containing tin, iron, chromium and oxygen as the major

alloying elements. As end-of-life exposures have been increasing to achieve higher discharge burnups, the life-limiting factor has been recognized as the uniform corrosion resistance. In the 1980s and 1990s, major R&D, followed by intensive in-reactor testing, was accomplished to improve corrosion properties.

Alloy modifications were explored to improve corrosion resistance. In general, it was recognized that the Zircaloy-4 composition was not optimized for corrosion, but even within the ASTM allowable ranges for alloying elements, corrosion resistance could be improved by dropping tin concentration to the lower end of the allowable range and raising iron concentration to the higher end of its range. For example, tin has an ASTM allowable range of 1.2–1.7 wt% (0.92–1.3 at.%); however, many individual fuel vendors now restrict that range to 1.2–1.45 wt% (0.92–1.12 at.%). Likewise, for iron the ASTM allowable range is 1800–2400 ppm (0.29–0.39 at.%), and iron is targeted at the upper end of the range or around 2200 ppm (0.36 at.%). Zircaloy-4 with these compositional variations is often called 'controlled composition Zircaloy'.

Oxygen is an important strengthener at room temperature, but its effects are mitigated somewhat as temperatures increase into the 560–588 K (288–315°C) operating range. A typical specification range for oxygen concentration is 900–1400 ppm (0.51–0.79 at.%) with producers aiming for the 1200–1300 ppm (0.68–0.74 at.%) range. Likewise, carbon and silicon are important grain refiners, although there are indications that lowering carbon concentration improves PWR corrosion properties. Tin was originally added to counteract the adverse effect on corrosion properties induced by nitrogen. In the early manufacturing of zirconium, the nitrogen concentration could be high and variable. It was discovered that tin mitigated this effect. In the process of setting specifications for tin, the amounts required were beyond the optimum amount to offset the effects of nitrogen. From a corrosion standpoint, only about 0.5 wt% (0.38 at.%) tin is required to provide optimal properties. The problem is that tin is also a solid solution strengthener and confers important creep resistance to the cladding. If tin concentration is lowered much below the lower ASTM range of 1.2 wt% (0.92 at.%), other elements have to be added to restore the creep strength, or the design of the cladding itself has to change.

In recognition of this chemistry control issue, alloys such as ZIRLO (1 wt% (0.98 at.%) Nb, 1 wt% (0.77 at.%) Sn, 0.1 wt% (0.16 at.%) Fe and 0.1 wt% (0.57 at.%) O); E635M (0.8 wt% (0.62 at.%) Sn, 0.8 wt% (0.79 at.%) Nb and 0.3 wt% (0.49 at.%) Fe); and E110 or M5 (1 wt% (0.98 at.%) Nb, 150–600 ppm (0.025–0.098 at.%) F, and 900–1800 ppm (0.51–1.02 at.%) O) were developed to enhance long term in-pile corrosion performance.

It is also known that the size distribution of SPPs ($ZrFe,Cr_2$) is important for optimizing the corrosion resistance of Zircaloys. This need for optimization leads to some tightly controlled heat treatments during the manufacturing process. For example, for application in PWRs, the CAP is tracked during manufacturing to provide an optimum value of about 10^{-17} h (Q/R = 40 000 K) [4.124]. The placement of a β annealing and quenching step (β quench) helps determine the overall CAP. The CAP is reset to zero at the time of the quench step. By placing the quench early in the process (for example, during the forging sequence), a higher CAP can be obtained than by a late β quench.

Likewise, the annealing parameter integrates annealing temperatures as a function of time at each incremental temperature and sums all of these to provide the CAP. Thus, the amount of hot working done after beta quenching, and the intermediate and final annealing conditions employed during cold reduction, are all added to provide a final CAP. Final annealing is usually performed to stress relieve the cladding microstructure for Zircaloy-4, while Zr-1Nb cladding is manufactured in the recrystallized state. The oxygen potential of

coolant is low under PWR coolant conditions with a hydrogen overpressure leading to dominant uniform cladding corrosion. For this reason, the PWR cladding microstructure is optimized for uniform corrosion resistance. For niobium containing zirconium alloys, to ensure uniform corrosion resistance, the post-β-quench processing temperatures are controlled below the phase transformation temperature to avoid any β zirconium phase in the microstructure.

Texture in the finished cladding tube is used to control mechanical properties, creep and, most importantly, the orientation of hydrides that form as a result of the corrosion reaction. Since precipitated hydrides are brittle, they must be accommodated. One way to accommodate them is to ensure that the hydride platelet orientation is in the circumferential direction as opposed to the radial direction in the cladding. This orientation is achieved during the final stages of cold reduction of the cladding by having a high Q ratio — that is, a high ratio of wall thinning to diameter reduction taking place during cold pilgering.

To take advantage of high Q ratios, the extruded tube shell has to be made with a heavy wall dimension. Since there is little inner diameter sinking taking place during extrusion, the extrusion billets need to have large outside diameters and small inside diameters. Boring smaller holes in the billets requires higher precision to ensure that the hole remains on centre, is dimensionally accurate and is made without a long bow. Rigid tooling, sharp cutting edges, excellent lubrication and proper feeds and speeds are required during the machining of the billets.

A variation of the PWR zirconium alloy cladding is known as ‘duplex cladding’ as described by Besch et al. [4.222] and Arborelius et al. [4.223]. This concept provides for a high corrosion resistant layer — about 90 μm thick — on the outside of a Zircaloy-4 inner tube. The corrosion resistant layer has a tin concentration of about 0.5 wt% (0.38 at.%) and an iron concentration of about 0.4 wt% (0.65 at.%). The lower tin concentration has superior corrosion resistance but poor thermal creep resistance. To compensate for the higher creep rate of the low tin outer alloy, it is mated to a standard composition Zircaloy-4 inner layer that forms the majority of the total wall thickness of the final cladding.

The manufacturing techniques for duplex cladding were derived from making BWR barrier cladding (see Section 4.11.1.2). The difference is that the outer layer is slightly thicker for PWR duplex cladding than is the inner layer of pure zirconium in BWR barrier cladding. As in BWR barrier cladding, the two layers are assembled at the extrusion billet stage and co-extruded. The duplex tubes are processed conventionally after extrusion using conventional cold pilgering techniques. Care must be taken with the soft low tin outer layer to prevent handling damage and to minimize conditioning losses arising from belt sanding and acid pickling operations.

4.11.1.2. BWR cladding tubes

BWR cladding tubes are up to 4.2 m in length with an outside diameter of between 10.8 and 12.5 mm and a wall thickness in the range 0.6–0.75 mm. Traditionally they are made from Zircaloy-2. For optimum corrosion resistance the tin concentration resides in the lower half of the ASTM allowable range of 1.2–1.7 wt% (0.92–1.3 at.%). If thermal creep is an issue then tin may be targeted at the middle of the allowable ASTM range. Both iron and nickel improve nodular corrosion resistance and thus controlled composition Zircaloy-2 is at the high end of the iron concentration range (0.07–0.20 wt% (0.11–0.33 at.%)) and nickel concentration range (300–800 ppm (0.047–0.12 at.%)). Because there is a total limit for Fe + Cr + Ni of 3800 ppm in the ASTM specifications, the chromium concentration generally

remains near the middle of its range of 500–1500 ppm (0.088–0.26 at.%). BWRs are sensitive to nodular corrosion and thus require different strategies for composition and thermomechanical processing compared with PWRs, where uniform corrosion is the main concern.

From a thermomechanical processing standpoint, BWR cladding requires a distribution of small SPPs ($Zr(Fe,Cr)_2$ and Zr_2Ni being the predominant particles). As such, a late β quench is imparted during the manufacturing of this cladding. Beta quenching can take place on the extrusion billet or even on intermediate TREX to minimize the exposure of subsequent heating operations that would influence the CAP. Quench rates of the order of 20 K/s during the β to α transformation are required to obtain the best nodular corrosion resistance [4.160, 4.168, 4.224]. These cooling rates (or higher) are achievable by controlling the geometry of the billets or TREX. Water coolant needs to flow over the outside surface and through the inside of billets and through the inner surface of the TREX. The quenching water needs to be maintained as close to room temperature as possible to preclude steam jacketing from occurring that would substantially reduce the cooling rates. The CAP for BWR cladding should be about $5–6 \times 10^{-19}$ h.

BWR cladding tubes originally started as a homogeneous Zircaloy-2 tube. However, concerns with pellet–cladding interaction brought about the advent of barrier cladding. In simple terms, this is the inside-out configuration of duplex cladding. An inner liner of nominally pure zirconium is placed within a Zircaloy-2 billet. The liner or barrier is soft, its thickness is limited to about 10% of the wall thickness, and it cannot support mechanical loads. The structural strength must come from the outer Zircaloy-2 layer [4.225–4.227].

In principle, the manufacturing of barrier cladding is much like duplex cladding. Two separate ingot compositions are melted. The ingots are hot worked down to extrusion billets. The pure zirconium billets are extruded (and sometimes tube reduced) to make the liner tubes. The outer Zircaloy-2 billets are match-machined to accept the liner tubes. The assemblies are joined by EBW together, similar to the duplex case. They are preheated and co-extruded, whereby the inner and outer layers metallurgically bond together. Further processing of the tubeshells involves cold pilgering and controlled intermediate anneals to maintain a low annealing parameter that prevents second phase particle growth. Final anneals recrystallize the grains.

One variation on the chemistry for the liner provides small additions of iron or tin to improve corrosion resistance. Tin concentration can be up to 0.5 wt% (0.38 at.%) and iron concentration up to about 1500 ppm (0.26 at.%). One of the failure modes of BWR cladding is external fretting from debris that gets trapped in the spacer grids. The vibration of the cladding within the spacer grids from thermohydraulic forces causes the debris to perforate the cladding and this primary breach permits steam to enter the cladding. The steam can react with the pure zirconium causing it to form locally massive hydrides. Secondary failure follows whereby large axial cracks propagate down the length of the fuel rod. The small additions of tin or iron confer additional corrosion resistance to the pure zirconium barrier layer, thereby mitigating this mechanism.

There is a large yield loss on the ends of each extrusion as the liner comes to a constant thickness along the length of the extrusion — at the lead end the liner tends to be too thick while at the tail end it tends to be too thin and may even disappear. The flow stresses of the inner and outer layers have to be sufficiently matched to permit uniform elongation as the coextrusion billet is forced through the die. Cleanliness of the bond zone area is critical towards achieving a sound metallurgical bond. Temperature has to be adequate to ensure diffusion bonding but has to remain low enough that precipitate growth during the extrusion

preheat is well controlled and grains do not grow too large in the pure zirconium. Finally, thorough UT is necessary to verify both freedom from standard defects such as cracking on the inside surface, and delaminations of the bond zone and uniform (and within specification) liner thickness. UT is used to determine where to crop the non-uniform liner thickness at lead and tail ends.

4.11.1.3. PHWR cladding

Pressurized heavy water reactor cladding has many of the same manufacturing concerns as PWR cladding but also has several major differences. The fuel bundles are 0.5 m in length and the outside diameter depends on the specific design and may vary between 11.5 and 15.2 mm. Another significant difference is in the wall thickness and wall thickness uniformity requirement for PHWR use. Because PHWRs utilize, for the most part, natural uranium, the core designers try to minimize the volume fraction of parasitic absorbers in the core, zirconium being one of these. This requirement necessitates thinner finished cladding, on the order of 0.4 mm thick. The thinner cladding is designed to collapse onto the fuel pellets, where LWR fuel claddings are free standing.

Additionally, wall thickness variation is an issue. There is a minimum wall thickness required (that includes a corrosion allowance) to provide mechanical integrity at end-of-life service. Any additional zirconium resulting from wall thickness variation does nothing to confer additional strength or creep resistance, but merely serves to increase the unwanted volume fraction of zirconium at the expense of moderator volume fraction.

As a result of this restriction, special care is given to ensure that total wall variation is less than 3% of nominal wall. The thin finished cladding requires thin extruded tubeshells. Precision in machining billets is required, as any wall variation in the billet will translate to wall variation in the extruded tubeshell. Additionally, controls must be placed on the uniformity of heating billets prior to extrusion, and on the extrusion tooling to ensure concentricity and alignment are maintained. Eccentric tubeshells can sometimes be corrected for wall thickness variation by selective belt sanding of the outside surfaces.

PHWR cladding operates at lower temperatures than corresponding PWR cladding and to significantly lower burnups, and therefore corrosion wastage is not nearly as much of a concern. Therefore, PHWR cladding has traditionally maintained nominal ASTM compositions for Zircaloy-4.

Another significant difference in practice compared with PWR cladding is that the ingots are double vacuum arc remelted rather than triple melted. PHWR cladding uses bearing pad spacing mechanisms consisting of spot welded or brazed-on pads. These spacers are short lengths of square cross-section wire that bear on each other and maintain spacing between the cladding, allowing efficient heat transfer to the heat transport water, and that provide vibrational damping. The bearing pads maintain spacing between the fuel and the surrounding pressure tube. The brazing operation is conducted at temperatures just above the β transus. This brazing results in a β transformed structure in the heat affected zone.

The transformation structure for triple vacuum arc remelted melted Zircaloy often results in a parallel platelet structure that can result in radially aligned alpha platelets that come close to occupying the entire wall thickness of the cladding. Cladding made from double melted ingots, which contain more impurities than triple melted ingots, tends to form a basketweave Thomson-Widmanstätten structure with high local structural integrity.

4.11.1.4. WWER/RBMK cladding

E110 alloy, Zr-1Nb, is used to make cladding tubes for WWER and RBMK reactors. It was introduced in the former Soviet Union in the 1960s.

The specific features of E110 alloy are discussed in Chapter 2. The processes used to fabricate cladding tubes for the WWER and RBMK fuel rods are similar because the design requirements are similar, although the tubing dimensions are slightly different. In WWERs, the tubing is up to 3.9 m in length with an outside diameter of 9.1 mm and a wall thickness in the range of 0.6–0.7 mm, while in RBMKs the tubing is up to 3.5 m in length with an outside diameter of 13.6 mm and a wall thickness in the range 0.8–0.9 mm.

The process incorporates the following main technological operations: zirconium metal production; melting to produce ingots; fabrication of tube billets by hot working; hot extrusion of thick walled tubes; and cold working to final size with intermediate finishing anneals.

As discussed in Chapter 2, E110 exhibits intolerance to metastable phase formation in the Zr-Nb system. These metastable phases create limitations in corrosion and mechanical property performance. This metallurgy dictates processing where late phase hot working and annealing have to be conducted in the α phase temperature range, not exceeding 873 K (600°C), to remain below the eutectoid temperature.

The tubular structure is close to being fully recrystallized providing high ductility along with high corrosion resistance. Tubes in this state also have high resistance to irradiation induced creep (see Table 2.11).

Tube reducing to the final size is one of the most important technological operations that governs the quality and properties of tubes. The Q value upon pilgering of tubes determines in many respects their resistance to cracking and also the mode of hydride disposition in tubes. In the production of E110 cladding tubes $Q \geq 3$.

E110 alloy cladding tubes are sensitive to variations in final annealing temperature and a temperature range of less than ± 278 K (5°C) is maintained because even small variations in temperature may appreciably affect the properties of tubes. The time of anneal has a less noticeable effect on the properties and structure of E110 tubes.

The final manufacturing operations of E110 cladding tube production are surface treatments to provide optimum corrosion properties. These operations comprise tube etching in an acid solution followed by neutralization (removing fluorides) in alkaline solutions (NaOH, KOH) and mechanical treatment (grinding and polishing).

4.11.2. Zirconium alloy sheet and strip fabrication

The general sequence for sheet and strip fabrication is to start with a vacuum arc remelted ingot and preheat it into the low beta range (about 1320 K (1050°C)) to press forge it to a slab. Forging is conducted through the transus as this regime is the most efficient for dynamic recrystallization (see Section 4.2.3). Slabs are 100–150 mm thick and are usually some multiple of the width of the finished sheet or strip, from 500 mm to about 900 mm in width. If the strip is for PWR grids, the slab is β quenched at 100 mm to 200 mm thickness. The quenching operation eliminates the segregation of alloying components as the slab is forged through the transus, and it resets the second phase particle size to a fine distribution that can be uniformly and intentionally grown to achieve the proper particle size distribution for the end product.

Forged slabs are conditioned by a combination of abrasive grit blasting, surface grinding and chemical etching or pickling. Slabs may be ultrasonically examined at this point. Slabs may then be hot rolled in the 973–1023 K (700–750°C) region for the Zircaloys and <873 K (600°C) for the niobium containing alloys, such as ZIRLO, to a thinner strip or sheet, called hotband. Hot rolling can be either on a continuous basis to make coil or on a reversing hot mill to make flat lengths of hotband. This hotband can range from 4.5 mm thick for channel strips down to 3 mm for thinner spacer strips. For BWR strip that requires a late beta quench, the 100–150 mm slab is hot rolled to an intermediate thickness of 20–25 mm. At this thickness, a β quench is performed. Preheating can be by electric fired air furnace, by salt bath or by fluidized bed furnaces. Quenching is in rapidly recirculating water. After conditioning, the β quenched plate is then heated into the low alpha range (923 K (650°C) or less) and hot rolling to hotband is completed (see Section 4.3.3).

Extruding a round billet into a rectangular sheet bar can make a variation of hotband. This process has the limitation of being able to make only short lengths (e.g. limited by the amount of billet that can fit into the extrusion container).

Hotband has to be conditioned by abrasive blasting, pickling and sometimes edge trimming by slitting. The hotband can either be directly rolled at this point or annealed prior to rolling. In the case of individual lengths of hotband, the anneal can be in air or vacuum, and in the case of continuous hotband, it is annealed in a continuous annealing furnace that is electrically heated with an inert gas atmosphere. The gas atmosphere can be either argon or nitrogen. While nitrogen is not strictly inert, in the temperature range of interest (less than 1073 K (800°C)), the reactivity and diffusivity of nitrogen is low and only a slight staining of the surface results. The stain is easily removed by light abrasion and by chemical etching.

BWR channel strip can be either Zircaloy-4 or Zircaloy-2 and is finished at 2, 2.5, or 3 mm thick. The current method for making this strip is to perform the late β quench at 20–25 mm and hot roll to about 4–6 mm thickness, depending on the final thickness of the strip that is required. The hotband strips (in individual lengths) are annealed and then cold rolled in either one or two multiples of length. The strip is full width so that two matching pairs can be obtained by slitting side-by-side pairs.

To limit the irradiation induced distortion of a BWR channel box, it is necessary to match the texture, material composition, material microstructure, residual cold work and grain size of the two strips forming the four walls of a channel box. This objective is achieved by the use of matching pairs of channel wall obtained by slitting a finished strip. Annealing operations are performed in the low alpha range (898–948 K (625–675°C)). The BWR strip is cold rolled with a total RA of about 25–40% per cold rolling. Lower reductions may lead to critical grain growth, and higher reductions can lead to edge cracking. An intermediate anneal is often performed in vacuum with the strips hanging from a fixture. This procedure keeps the strips flat by creeping them under their own weight. Final anneals can either be performed in vacuum, or preferably by welding the sheets together lengthwise and annealing in an inert gas atmosphere utilizing a continuous strand-type annealing furnace.

Spacer strip for BWR applications also receives a late β quench and processing is similar to channel sheets, except that multiple cold rollings are required to achieve a final thickness of about 0.6 mm. Depending on the thickness of the hotband, it may take as many as four cold rollings with intermediate anneals to achieve final thickness.

PWR spacer strip starts with hotband and requires up to five independent cold rollings to achieve final thickness down to as thin as 0.3 mm. Cold mills are generally four-high mills, although very thin strip requires Sendzimir mills. Intermediate anneals may be employed as either stress relief anneals (748–823 K (475–550°C)) or as full recrystallization anneals

(923–1023 K (650–750°C)). Strip can be either annealed in a vacuum furnace (typically at the lower temperatures cited, but for longer times to permit the heat to soak through the thermally insulating coil) or in continuous furnaces at the higher temperatures, but for just a few minutes' residence time.

Following final annealing, the strip is conditioned by chemical etching to achieve a bright surface and final thickness, and there may be supplemental buffing operations to cosmetically condition the surface. The strip is slit to final width and either packaged as individual pieces or as a coil. It is typical to place some kind of interleaving material such as a thick paper between pieces or between the coil wraps, to cushion the adjacent surfaces from skidding damage during handling that could create localized galling. The strip is gauged for uniformity of width and thickness. Surfaces are visually examined for any defects.

4.11.3. Zirconium alloy bar and wire fabrication

Bars and wires are fabricated with a number of different process flow sheets. Generally, an ingot is hot forged starting at the β temperature to some intermediate size. For PWR end plugs, an intermediate β quench ensures the homogeneity of alloying elements and properly sized SPPs. The forging practice can be by hydraulic press forging alone, or by a combination of press forging and rotary forging. Following β quenching all work is done in the α range to preclude excessive coarsening of SPPs or segregation to the alpha grain boundaries. An alternative is to size the final ingot to fit into the extrusion press and extrude a billet that is then machined and re-extruded to smaller diameter rod.

Forged logs can either be: (1) continuously hot rolled on a multistand hot mill; (2) further reduced by hot rotary swaging or by warm conventional swaging; or (3) individual billets can be parted out of the log, machined and then extruded. The net result is to get to an intermediate bar product of about 12–20 mm in diameter for making end plug bar stock or wire, or to some larger diameter to finish as structural bar components (for making control assemblies, nuts and tie bars). BWR end cap stock requires a late β quench, typically at some intermediate stage, of about 90 mm diameter. This hot working is performed in the alpha temperature range following β quench.

Bars can be cold finished by swaging or by cold drawing. Swaging and drawing impart sufficient cold work in the bars to refine the grain structure and to achieve shape control. These operations are generally limited to 30–40% RA with intermediate anneals in the alpha range. Bars are then straightened and centreless-ground to finished diameter. Owing to the role of end caps (they must hermetically seal the inert filler gas and subsequent fission products inside the fuel rod), they must have high assurance that there are no continuous leak paths down the length of the bar stock. As a result, end cap stock is given a final UT in which the equipment is set up on standards with very small model defects. Diameter variation and ovality are tightly controlled in bar stock for end cap fabrication because the automated machining equipment requires tight dimensional tolerances. The finished bars are machined into finished end caps with swiss lathes or conventional computerized numerical control equipment. In a swiss lathe, the bar is held by a rotating collet and fed through a bushing. The bar is advanced past the tool by sliding through the bushing. The tool moves in and out on a cross-slide positioned where the bar exits the bushing. The length of a turned feature is dictated by how far the bar slides past the bushing. Swiss lathes are able to turn long, spindle sections because the bar is well supported as it exits the bushing; however, tight diameter control of the bar is critical. If the bar is loose in the bushing, eccentric features are possible.

If the bar is too tight, it will not slide through the bushing smoothly (owing to stiction) and the length of various features may not be faithfully reproduced.

Weld wire and bearing pad wire start with an intermediate wire or rod of about 8–15 mm in diameter, which is then cold drawn to the final size. This process requires many cold draw and intermediate anneal steps, as draw steps are typically limited to about 25% RA. Annealing can be by continuous inert gas atmosphere furnace, by vacuum annealing wire that has been coiled up or by salt bath. Wire is used often in the cold drawn finished condition and no supplemental finishing operations are used except for a final chemical etch. For PHWR bearing pads, the round wire is turks-headed into a square or rectangular cross-section suitable for the final bearing pad. The turks head has two pairs of rolls, with one pair arranged vertically and the other pair horizontally. Material is drawn through the turks head to convert it from round to square or rectangular cross-section.

Defects that are particularly important in end cap bar stock are any kind of continuous porosity, pipe or honeycomb through which a leak can occur. These defects often form at the ends of the material being processed. In many operations, such as rotary forging, rotary swaging, hot rolling and cold swaging, ‘end suck’ (Section 4.3.2) may occur. This problem is mitigated by proper removal of these end defects during processing. Additionally, sensitive UT techniques further ensure that any porosity or piping, which inadvertently pass through the process, are removed. Discontinuous porosity can form during cold drawing, but generally not to a level that compromises the bar stock. Parameters that must be controlled during drawing include die angles, lubrication practice and reduction between anneals.

4.12. ZIRCONIUM BASED SUBASSEMBLIES AND ASSEMBLIES

Subassemblies and assemblies are the finished components made from zirconium alloys for reactor core use. Examples include such items as spacer grids, channel boxes, reactivity control mechanisms and the various fuel bundles and assemblies.

4.12.1. Spacer grids

Spacer grids ensure fuel rod to fuel rod interspacing is maintained so that heat transport water flows uniformly all around the fuel rod. In early reactor designs, the spacer grids were manufactured from Inconel. Later grids were introduced made predominantly from the same alloy as the cladding. Thus, PWR grids were made from Zircaloy-4 (with some having spring features still made from Inconel), BWR grids were made from Zircaloy-2, PHWR end plates were made from Zircaloy-4 and RBMK/WWER grids were made from E110. As cladding alloys evolved, so did the grid structures that utilize M5 and ZIRLO, for example.

4.12.1.1. PWR grids

Spacer strip is manufactured by hot rolling long sheets of hotband or by extruding sheet bars. These sheets are reduced by cold rolling to form strips from which spacer grid components are stamped and formed. PWR grid straps can be made either from across the width of the strip, or from along the length. The direction depends on the texture orientation of the cold rolled strip. The texture affects such properties as in-reactor creep and irradiation induced growth and therefore determines how the grid is designed to withstand these strains. Generally, the grid straps are stamped from across the width of the spacer strip. Irradiation induced dimensional changes with respect to the grid envelope (which control the interassembly clearance between neighbouring assemblies in the nuclear reactor core) and

grid to fuel rod support features (which control the development of grid to rod gaps that control the grid to rod fretting) depend on the direction of grid stamping with respect to the strip rolling direction. Some of the intricate PWR features such as arches are also easier to form when the grid strap is obtained across the width of the strip, as texture is optimal for forming in that direction.

PWR grids can have either integral zirconium alloy springs or separate Inconel springs. The latter springs consist of alloys X-718 or X-750. These alloys are age hardenable and they are employed in the solution treated and aged condition.

Similar metallurgical considerations as for cladding are employed in the manufacturing of PWR grids. An early β quench is employed for Zircaloy-4 grid strips to ensure a sufficient CAP and to achieve optimum second phase particle size for best corrosion resistance. Compared with cladding, spacer grids have smaller corrosion limitations because they do not have a significant heat flux across the thickness that can accelerate corrosion. Also, unlike cladding, both surfaces of a grid strip are exposed to the coolant. Spacer strip may be either recrystallized or stress relieved. Stress relief anneals are used where high mechanical strengths are required. Recrystallization anneals are used where forming operations are complex and bend radii are tight.

Attributes that are important to spacer strip are uniformity of gauge thickness and surface finish. As thickness varies, so too does the spring back during stamping and coining operations, leading to a non-uniform height of features such as arches and springs. Surface finish is important because small scratches in the surface can lead to cracking during some of the more extreme forming operations. Zirconium can exhibit notch sensitivity, which means that stresses accumulate in small surface discontinuities during forming and result in failure by cracking. A general rule of thumb for zirconium strip is that it can be formed to a bend radius three times the strip thickness (3T bend radius). Many spacer grid designs call for a much tighter radius, and while grids can be manufactured with tighter radii, during fabrication the loss due to cracking often becomes intolerably high if tooling and tool alignment, lubrication, stamping speeds and thickness tolerances on the strip are not tightly controlled.

Grids are stamped and formed in several operations. Large mechanical stamping presses are used along with precision tooling designed specifically for the blanking and forming operations. The tooling can be single station whereby one set of operations — such as blanking the initial slots to form arches or springs — is done on a single press before the part moves to the next press. Alternatively, tooling can be multistation and progressive, where an integrated tool with several stations is used in a single press to complete all operations.

The slots and interior flow holes in the grid are generally blanked first, followed by the peripheral outline. Next comes a series of forming operations that raise the arches, springs, mixing vanes, integral fins and provide the 3D shape to the grid. There will likely be several different variations of grid straps depending on their placement in the grid (interior grid straps versus the exterior straps), and placement and location of poison and control rods. Tooling must be kept sharp and in good alignment. Misaligned tooling is one of the key reasons for failures in grid forming. Zirconium strip must flow down into the die cavities without being trapped. A misaligned die can prematurely trap the strip close to the entry of the die cavity, and then, as the stroke is completed, the strip has to stretch to continue to be pushed down into the cavity. This ‘coining’ action results in localized thinning in the strip and in failure.

When complex shapes are required with tight bend radii, options to ensure success include slowing down the strain rate of the press, using extra–high-pressure forming lubricants or applying heat to warm the strip up 373–473 K (100–200°C). Zirconium has

additional deformation mechanisms that activate at these low temperatures, and this enhances the deformability. Any burrs on the tooling or burrs left behind on the strip can create pinch points that trap the strip during subsequent forming operations.

After forming, the grid straps are degreased and chemically cleaned. They are generally given a stress relief anneal in a vacuum furnace to preclude warping during subsequent welding operations. The stress relief anneal for Zircaloy is conducted at about 720–770 K (450–500°C) for one to two hours. At this point, some samples of the grids may be examined using penetrant testing.

Following annealing, a chemical etching, water rinsing and drying operation is performed. The finished grid straps are assembled into jigs that hold them in alignment for welding. Welding may be in the form of GTAW, by LBW, by EBW or some combination of the above. For bimetallic grids, the Inconel springs are mechanically fixed during the welding operation.

Welded grids are then functionally tested on go/no-go gauges or by image analysis techniques. It is important that each of the grid cells is dimensionally uniform and located on precise centre-to-centre spacing, otherwise the fuel rods will be distorted during assembly. At this point, some hand rework might be needed to adjust the corresponding cells into conformance.

4.12.1.2. BWR grids

BWR grids undergo many of the same operations as PWR grids. They are simpler in that fewer grid cells are required, and the shapes are simpler, consisting of bathtub-shaped depressions formed into the surface combined with separate Inconel springs. They are generally made from either Zircaloy-4 or Zircaloy-2. A late stage β quench, at about 25 mm thickness, confers nodular corrosion resistance.

A later design of a BWR grid by Global Nuclear Fuel (GNF) utilizes short lengths of tubing, the inside diameter being slightly larger than the outside of the fuel rod. These ferrule tubes are arranged in a two dimensional array and a continuous, thin grid strap is wrapped around the outside of the array of tubes. This ferrule tube assembly is welded together at the intersections of the tube-to-tube and tube–strip contacts.

BWR grids may also need to accommodate water rod tubes, central square water channels or, in the case of the SVEA fuel assemblies, a water cross that is X shaped. These central water channels introduce additional neutron moderation into the centre of the fuel assemblies to provide the best utilization of the available enriched uranium.

4.12.1.3. PHWR end plates

PHWR end plates (in combination with the spacer pads on the fuel cladding) serve the analogous role of spacer grids in LWR fuel assemblies. These components hold the fuel elements (rods) in the fuel bundle (assembly) and provide proper spacing for the flow of heat transport water between the individual elements. End plates are stamped from stress relieved Zircaloy-4 strip approximately 1.3 mm thick. The stamping operation is typically conducted in multiple steps before the finished component is released from the web of the strip. After stamping, the end plates are tumbled with an abrasive medium to clean burrs that may have formed as the result of the stamping operation. The end plates are spot welded to the end caps on each end of the completed fuel element to form the bundle.

4.12.2. Channel boxes

Zircaloy fuel channel boxes with square cross-sections are used in BWRs in a vertical configuration. They are structural components and may be required to operate for multiple reactor cycles. The channel boxes are approximately 135 mm square and are 4.6 m long. The dimensional tolerances are critical, as the fuel assembly has to pass through the channels after being subject to the harsh environment inside the reactor core. Further, maintaining the dimensional tolerances, flatness and squareness in the tubes influences the amount of coolant flow through the fuel channels, which in turn improves the life of the channels. Both seamless and welded routes can be used to fabricate these channels.

Tubes with a square cross-section are produced directly through the process of cold pilgering extrusion hollows, followed by drawing the cylinder to a square channel in a turks head. A typical process flow sheet adopted for the fabrication of seamless square channels is shown in Fig. 4.82.

An alternate route is to cold pilger an intermediate cylindrical tube as a first pass. This intermediate tube is then annealed and a second cold pilgering pass is applied to bring the cylindrical tube to a square channel. The normal turn and feed function used for cylindrical tubing is modified so that only feeding takes place, and turning and indexing do not. The internal mandrel for the pilgering machine must be a tapered, round cornered square and the pilger dies must have a corresponding tapered square profile shape cut into them. Figure 4.83 displays the process flow for this route.

Seam welded BWR channel boxes are fabricated from channel sheets of 2, 2.5 or 3 mm thickness. Two basic schemes are employed to manufacture the welded channel box. The first involves two matching pairs of sheets that are brake press formed into two ‘U’ shaped pieces. The pieces are trimmed so that the legs of the U are equal, and then the ends of the legs are seam welded together either by an automated GTAW set-up or by EBW. The welded boxes are conditioned by etching and are then thermally sized by annealing them in place on a stainless steel mandrel. The mandrel is designed to expand faster than the zirconium sheet and this creep forms the boxes into a dimensionally accurate piece. Thermal sizing is performed in the 898–973 K (625–700°C) range.

An alternate process for making a channel box is to brake form a full width channel sheet into a right circular cylinder. This shaping is done on a press brake with a set of contoured forming dies, as shown in Fig. 4.41. The cylinder is then welded utilizing GTAW along the seam, and a counter weld (to balance metallurgical structure) is made at 180° to the seam weld. The cylinder is then run through a turks head that converts the cylinder to a round cornered square box. The channel boxes are dimensionally perfected and structures such as bracing gussets and entry flow nozzles are welded to them. Figure 4.84 outlines the manufacturing route for this type of channel box.

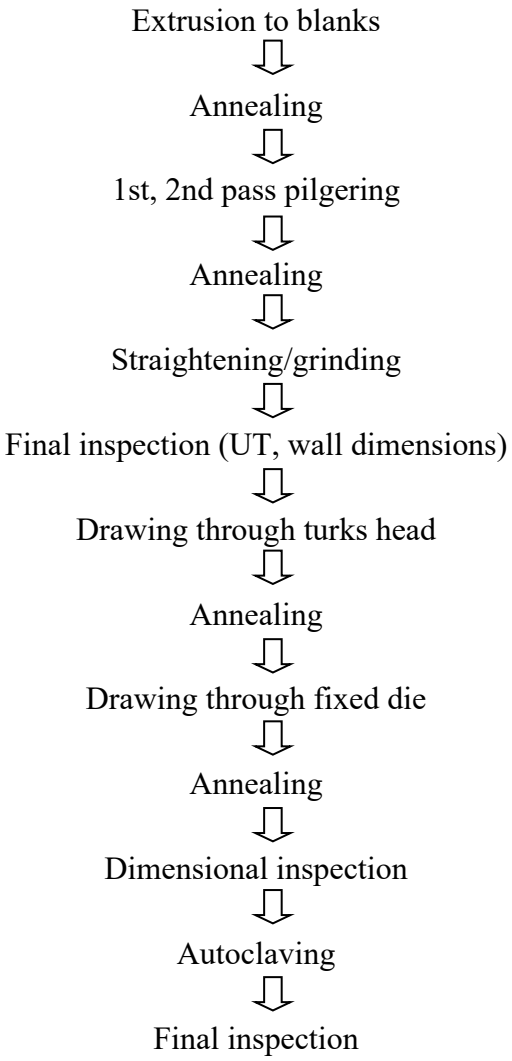

FIG. 4.82. Zircaloy-4 square channels by the seamless drawing route.

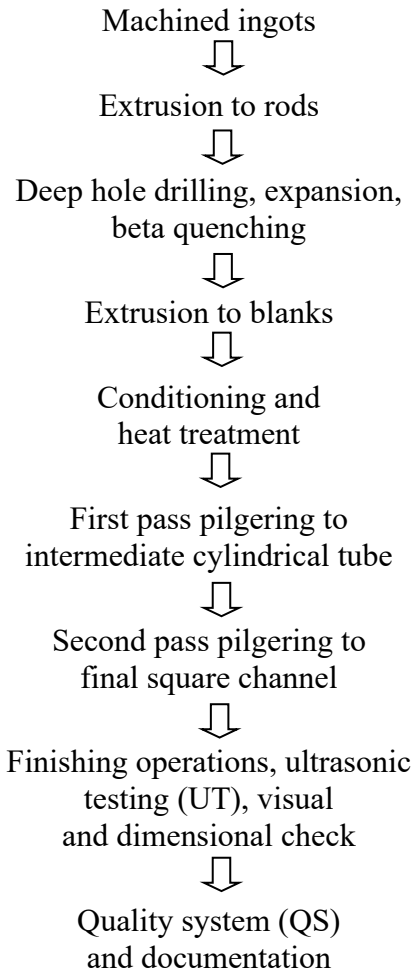

FIG. 4.83. Process flow sheet for seamless square channel by cold pilgering.

Hexagonal channels offer better packing of fuel thus maximizing the available core space in the reactor, particularly around the periphery of the core. These channels can also be produced both by seamless and welded routes. The seamless channels are considered by some to be superior in uniformity, homogeneity and dimensional stability. Cold pilgering channels leads to improved dimensional tolerances. Their processing is very similar to the square channels, outlined below.

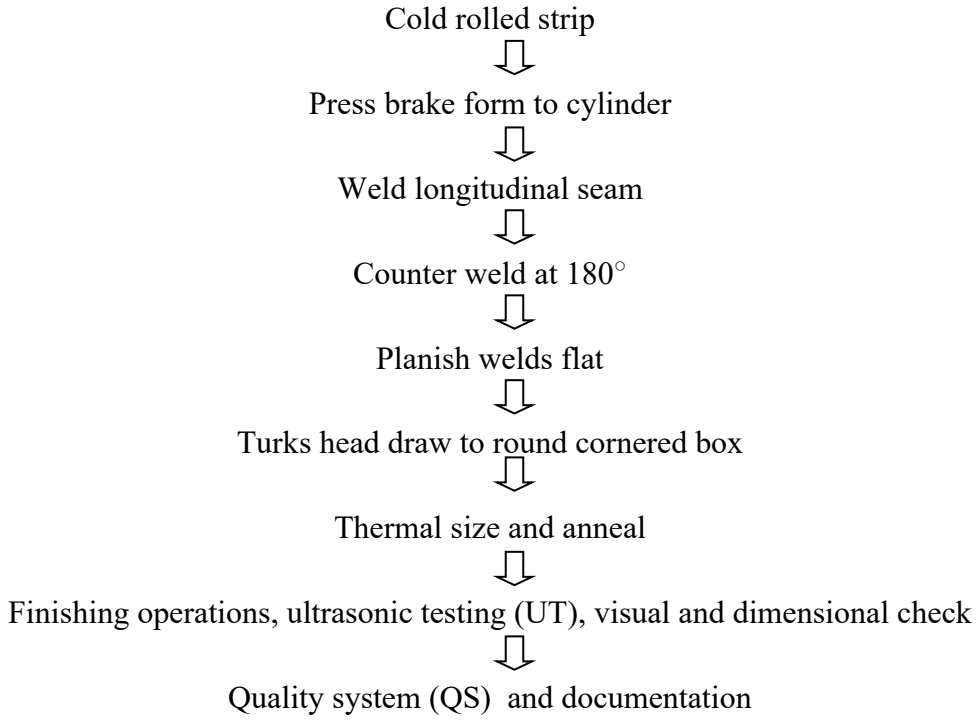

FIG. 4.84. Process flow sheet for seam welded channel by turks head forming.

4.12.3. Pressure tubes

In some reactors, the pressure vessel is a series of tubes that hold the fuel and the heat transport water. These tubes have an inside diameter of 80–110 mm, a wall thickness of 4–5 mm and lengths of up to 8 m. In some early reactors, the tubes were made from Zircaloy–2, for example, the N-reactor, early CANDU reactors in Canada and India, and the Steam Generating Heavy Water Reactor (UK). Currently, Zr-2.5 Nb is used because its extra strength allows the wall thickness to be minimized, thus reducing parasitic material, and because hydrogen pick-up is much reduced with some chemistries of heat transport water.

The basic fabrication steps were developed for the Zircaloy-2 tubes for the N-reactor. Three vendors successfully produced tubes to the desired dimensions and properties using four variations of hot extrusion followed by cold work [4.228]. A wide range of fabrication variables was used, as shown in Table 4.22.

TABLE 4.22. FABRICATION VARIABLES FOR ZIRCALOY-2 PRESSURE TUBES FOR THE N-REACTOR

Tube type	Extrusion temperature (°C)	Extrusion ratio	Cold work (%) reduction
1	700–780	29:1	29–30
1a	700–780	29:1	17–18
2	790	8:1	30–35
3	840	13:1	17–18

These tubes set the example for all future fabrications of pressure tubes. With Zircaloy-2, the main possible variants were crystallographic texture and grain structure; the

former was mostly controlled by the extrusion variables while the latter was mostly controlled by the amount of cold work and subsequent heat treatment. Type 1 and 1a tubes had a larger component of basal plane normals in the transverse direction than Type 2 and 3 tubes; Type 1 and 2 tubes had small elongated grains, Type 1a tubes contained large grains and Type 3 tubes had a mixture of fine irregular grains and highly elongated grains [4.229].

With Zr-2.5 Nb, there is a possibility of much variation in the distribution of the second phases, β-Zr and β-Nb, through variation of extrusion temperature and heat treatment (Section 4.6.2.2).

The current process flow outline for Canadian CANDU reactors is shown in Fig. 4.85. The starting material is Kroll sponge. The main differences between the current fabrication route [4.230] and that used in the 1960s [4.231] and 1980s [4.190] is the adoption of quadruple melting to much reduce chlorine concentration, β quenching before extrusion to refine the microstructure and minimize stray ultrasonic responses during inspection, a reduction of extrusion temperature from 1123 K to 1088 K (850°C to 815°C) and tighter control on the trace elements hydrogen, carbon and phosphorus. The final microstructure, Fig. 4.86, consists of thin platelets of α phase, 0.2–0.5 μm thick, much elongated in the longitudinal direction, less so in the transverse direction, with plate normals generally in the radial direction. The grains are surrounded with a thin skin of partially transformed β-zirconium. The grains tend to be oriented with their basal plane normal in the transverse direction.

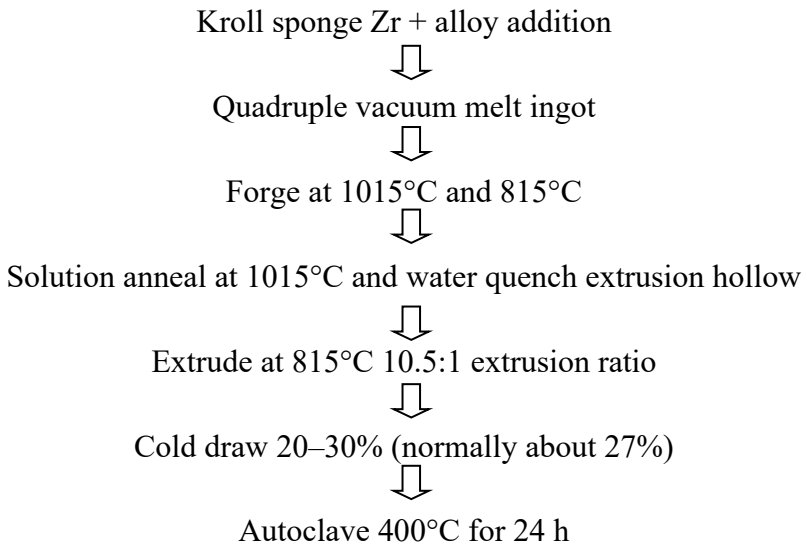

FIG. 4.85. Process flow outline for Zr-2.5 Nb pressure tubes for Canadian CANDU reactors (reproduced from Ref. [4.230] with permission courtesy of AECL, Canada).

In an attempt to reduce in-reactor deformation, the latter part of the fabrication route was modified by reducing the extrusion ratio and temperature and increasing the post–cold-work annealing temperature [4.195] The principle of the second route in this exercise has been adopted for Indian CANDU reactors (see Fig. 4.87) with the main differences being the use of extrusion instead of forging to reduce the ingot [4.151]. The microstructure is similar to that of the cold worked tube, seen in Fig. 4.88, but with a slightly less transverse texture.

Another variation on this theme is to anneal out much of the cold work at a late stage in the fabrication. This route has been adopted for most RBMK reactors [4.193]. The process

flow outline, shown in Fig. 4.89, is based on electrolytic powder and crystal bar zirconium. The microstructure consists of elongated α grains mixed with equiaxed α grains and discontinuous β phase at triple points and within the α grains; see Fig. 4.90. The maximum in the distribution of basal plane normals is about halfway between the radial and transverse directions.

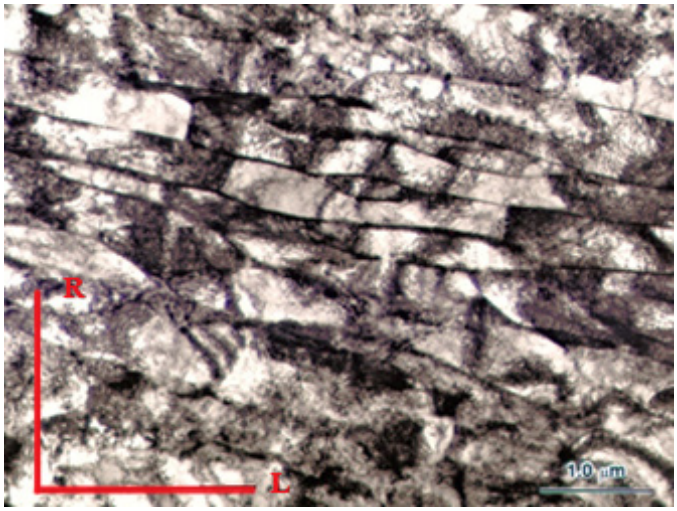

FIG. 4.86. Microstructure of cold worked Zr-2.5 Nb pressure tube for Canadian CANDU reactor showing α and β phases — L is longitudinal direction and R is radial direction (reproduced from [4.190] with permission courtesy of AECL, Canada).

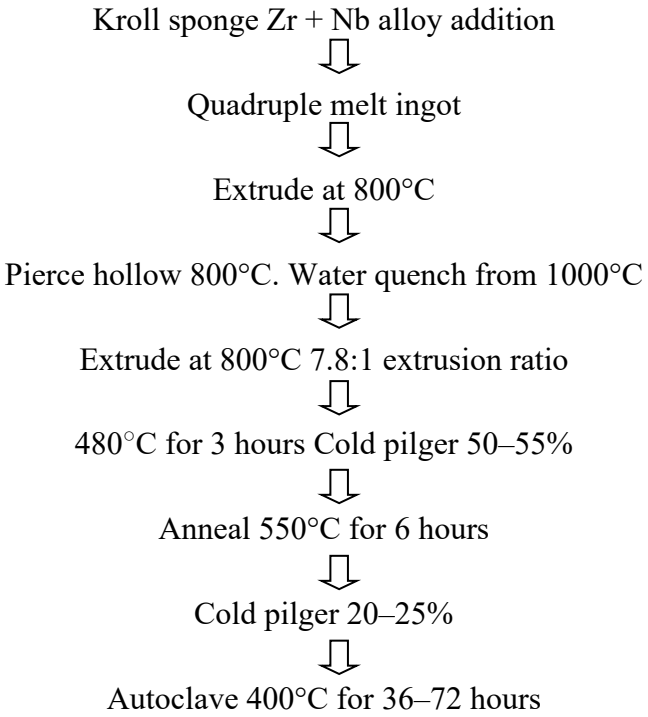

FIG. 4.87. Process flow chart for the fabrication of CANDU pressure tubes in India (this chart was published in Ref. [4.147], copyright Elsevier, 1972).

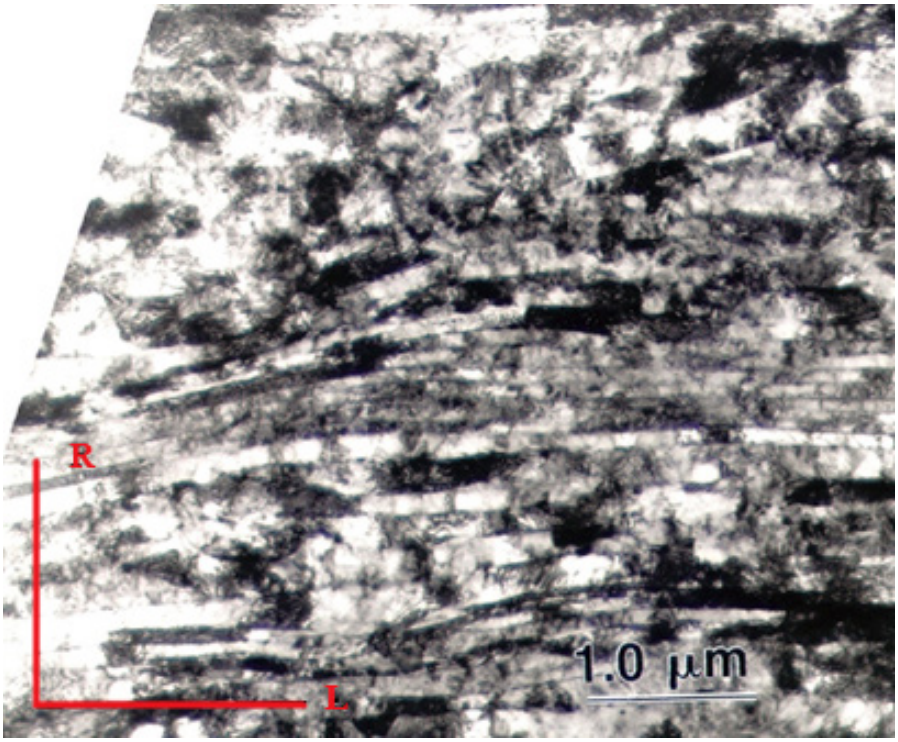

FIG. 4.88. Microstructure of Zr-2.5 Nb pressure tube for Indian CANDU reactor — L is longitudinal direction and R is radial direction [4.151].

Quenching into water from the (α + β) or β phase fields produces an acicular, martensitic type of grain structure. Subsequent tempering precipitates β-Nb on twins, sub-boundaries and grain boundaries [4.84]. Cold working and ageing after a quench from high in the (α + β) phase field (TMT-1 in Fig. 4.89) produces a microstructure comprising α′ phase and 10–20% untransformed α phase, highly dislocated and with β-Nb precipitates; see Fig. 4.91. The texture resulting from this route is much more random than with cold worked tubes, with a much higher concentration of basal plane normals in the longitudinal direction. Pressure tubes with this fabrication route were installed in Ignalina Unit 1, Lithuania. The TMT-2 variation contained Thomson-Widmanstätten structure instead of the α′-phase. This microstructure was produced by cooling from the high (α + β) in a flowing helium and argon mixture. Tubes with this fabrication route were installed in Ignalina Unit 2.

A similar process, called ‘heat treated Zr-2.5 Nb’, was developed for CANDU with tubes being installed in Karachi nuclear power plant and Gentilly Unit 1, France [4.232]. Pressure tubes made in an identical process were used in Fugen, Japan [4.233]. Single tubes in this metallurgical condition were also installed in research reactors in Canada, the Steam Generating Heavy Water Reactor (SGHWR) and the Nuclear Power Demonstration (NPD). After extrusion and quenching into water from high in the (α + β) region, the tubes were cold drawn 15% before tempering at 773 K (500°C) for 24 hours. Cold worked tubes have had wider application than heat treated tubes because, when choices were being made in the 1960s for which fabrication route to use, confidence was greater in the uniformity of their mechanical properties and they could be produced at lower cost.

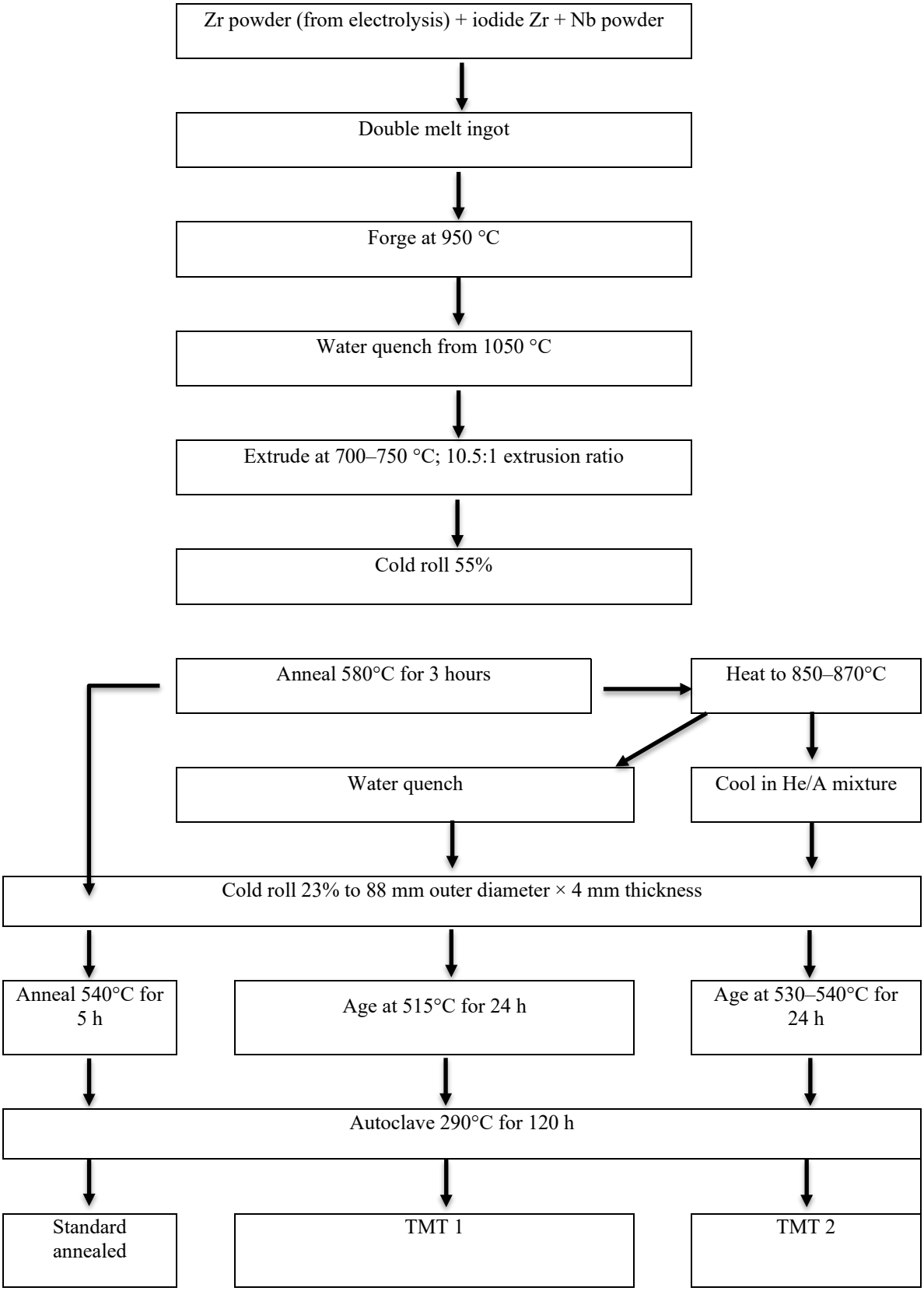

FIG. 4.89. Process flow chart for fabrication of RBMK pressure tubes (reproduced from Refs [4.189, 4.190] with permission courtesy of AECL, Canada).

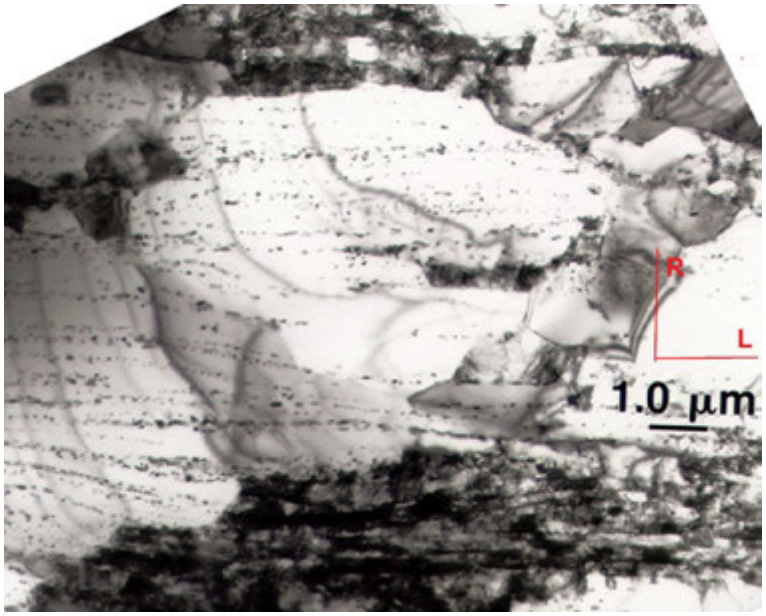

FIG. 4.90. Microstructure of annealed RBMK Zr-2.5 Nb pressure tube — L is longitudinal direction and R is radial direction (reproduced from Refs [4.193, 4.194] with permission courtesy of AECL, Canada).

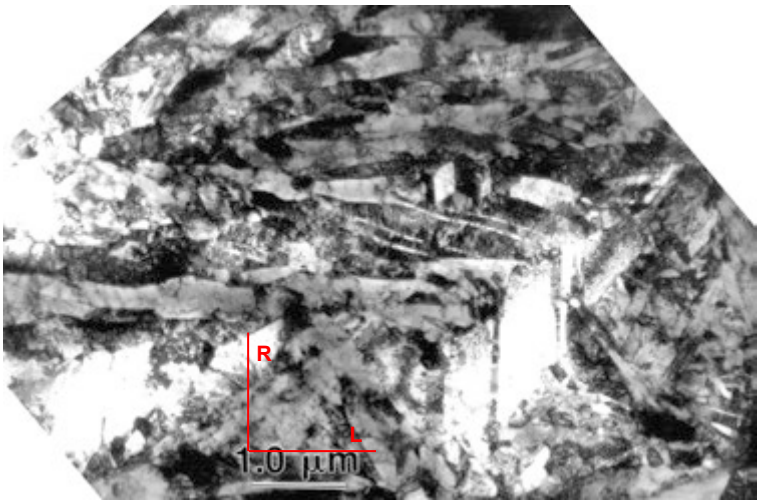

FIG. 4.91. Microstructure of RBMK Zr-2.5 Nb pressure tube with TMT-1 treatment — L is longitudinal direction and R is radial direction (reproduced from Refs [4.193, 4.194] with permission courtesy of AECL, Canada).

4.12.4. Calandria tubes

In PHWRs, the calandria tube isolates the pressure tube from the cool heavy water moderator. Spacers separate the two tubes with the gap being filled with CO_2 close to atmospheric pressure. A calandria tube operates at about 345 K (70°C). It has a large diameter and a thin wall and is made from either Zircaloy-2 or Zircaloy-4. These tubes remain in place during the full life of the reactor.

Initially, calandria tubes were made from sheet material that was brake formed into a tube (Section 4.5.2) then GTAW welded where the two edges met. To date, such tubes have provided exemplary service [4.234]. In the extremely rare event of a pressure tube rupture,

the subsequent pressurization of the calandria tube is well outside the conditions allowed for by the reactor design. Ensured containment of such an event by the calandria tube would be desirable to prevent collateral damage. Thus, an increase in strength could provide additional safety and an economic enhancement.

The appropriate strength is fixed-end biaxial strength; in the reactor, the calandria tubes are firmly held at each end by the reactor structure and when the tube is pressurized its ends cannot move. (The mode of stressing is quite different in a pressure tube where the biaxial stress is closed-end because the tube is free at one end.) In all fixed-end biaxial tests, seam welded tubes broke in the weld region. The reason for this behaviour lies in the difference in texture between the weld and the sheet material [4.204]. The sheet material provided a strong radial texture in the finished tube that in turn induced effective texture strengthening because wall thinning was difficult. The texture in the weld allowed wall thinning and thus the weld was the site of failure. The solution to increasing strength and ductility is to eliminate the weld but retain the strong texture. A further incentive to making seamless tubes is a reduction in processing steps [4.235, 4.236].

In general, tubes are classified into thick walled, thin walled and extremely thin walled categories depending on the diameter to wall thickness ratio. Calandria tubes have an outside diameter of 133 mm and a wall thickness of 1.4 mm. The diameter to wall thickness ratio of 95 mm classifies these tubes as ‘extremely thin walled’ tubes. Several fabrication routes have been used to produce calandria tubes, including roll extrusion [4.19, 4.20] (Section 4.4.5), flow forming [4.21] (Section 4.4.6) and pilgering [4.19, 4.235, 4.236] (Section 4.4.1). To attain a satisfactory product, the tolerances on the initial extrusion blank must be well controlled, the surfaces must be free from flaws and the lubrication must be sufficient. The process flow sheet for the fabrication of seamless calandria tubes by pilgering is given in Fig. 4.92.

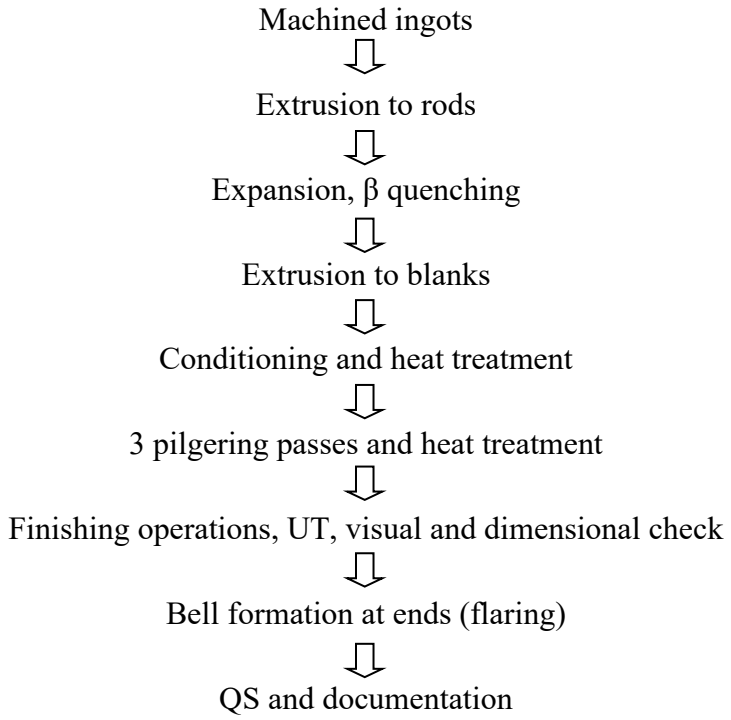

FIG. 4.92. Process flow sheet for the manufacture of seamless calandria tubes (this image was published in Ref. [4.235], copyright Elsevier, 2008).

Some typical problems with pilgering have been mitigated:

— When the pilger mill is stopped for loading a new tube, the mill makes a few idle strokes before the clutch disengages. The result is a local reduction of wall thickness that is seen as a ‘kink’ in the ultrasonic wall thickness chart. Automated loading of the pilger mill reduces this problem [4.235].
— The wall thickness is higher during the initial period after cold starting of the pilger mill than after the mill heats up. Frequent adjustments to the tooling are required until the temperature of the mill stabilizes.
— The thin walled tubes can seize on the mandrel or tear at the tube ends owing to the inadequate structural rigidity of the tube during the final pass of pilgering. Slowing down the stroke rate of the pilger mill and ensuring adequate lubrication can mitigate this problem.

In seam welded calandria tubes, the texture of the sheet material controls the texture (apart from the weld). Typical values of texture factors are listed in Table 4.23. The development of texture in seamless tube is shown for roll extruded tubes and pilgered (tube reduced) tubes; see Fig. 4.93. The maximum in the distribution of basal plane normals tends to shift from about halfway between the radial and transverse directions, in the extrusion, towards the radial direction as cold work is increased [4.19]. This shift is reflected in the texture factors of the finished tubes; see Table 4.23.

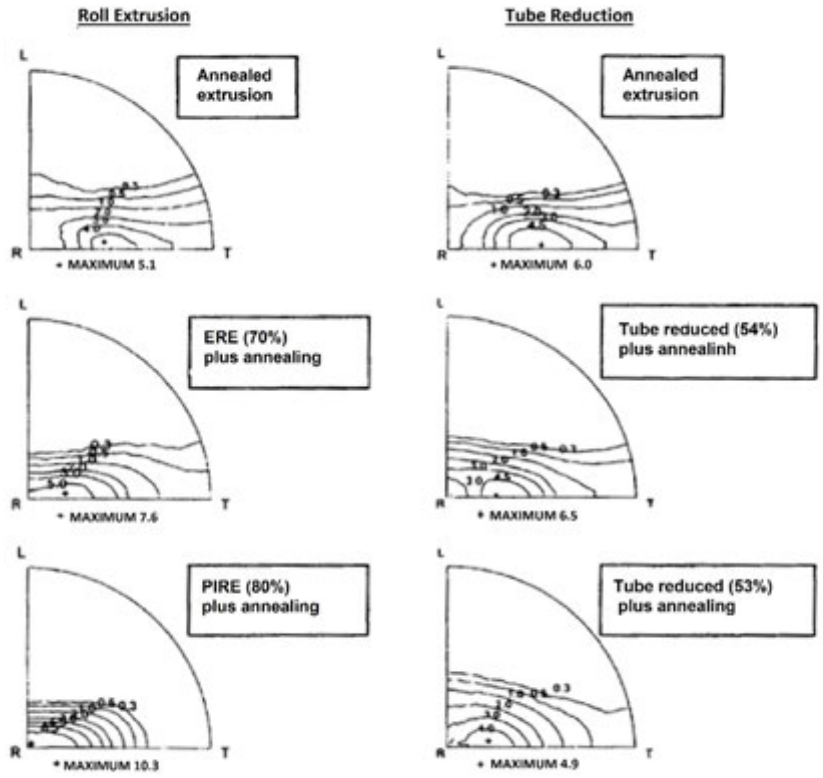

FIG. 4.93. Texture modification in thin walled Zircaloy-2 tubes by two stages of cold work using roll extrusion and tube reduction (pilgering) after hot extrusion (reproduced from Refs [4.19] with permission courtesy of AECL, Canada). ERE — external roll extrusion; PIRE — production internal roll extrusion.

TABLE 4.23. TEXTURE MEASUREMENT IN SEAMLESS AND SEAM WELDED CALANDRIA TUBES

Direction	Seamless tube		Seam welded tube
	Tube reduced	Roll extruded	
Radial direction	0.68	0.78	0.54–0.72
Transverse direction	0.20	0.17	0.18–0.33
Longitudinal direction	0.12	0.05	0.09–0.14

4.12.5. Reactivity control devices

Several devices that help regulate the reactor, monitor the neutron flux and provide pathways for safely shutting down a reactor are contained in zirconium alloy tubes that penetrate through the core of the reactor. The operating conditions for these guide tubes are much less severe than for fuel cladding or pressure tubes. In LWRs, these devices may be subjected to the high temperatures of the reactor heat transport system and must have good corrosion resistance. In PHWRs they operate in the moderator water, which is <370 K (100°C), so corrosion is not an issue. In general, guide tubes are not pressure boundaries, but deformation may be driven by residual stresses and irradiation growth (Chapter 7, Volume 2 of this publication). The tubes may be seamless or fabricated from sheet that is break-formed into a cylinder and welded. The material is usually Zircaloy in PWRs and PHWRs and Zr-2.5Nb or E635 in WWERs or RBMKs. The final metallurgical condition is usually annealed [4.237] although some Zircaloy guide tubes may be used in the β quenched condition [4.189].

Some reactivity devices are complicated. For example, for the liquid zone control system and the flux detectors in a PHWR, the assemblies are over 10 m long; see Fig. 4.94 [4.238]. They consist of many different components, several sizes of tube and over 200 welds.

4.12.6. PWR fuel assembly

PWR fuel bundles are complex assemblies of fuel rods, spacer grids, guide rods, and upper and lower tie plates. As an example, the Framatome-ANP fuel assembly, shown in Fig. 4.95, with a 17 × 17 array consists of 264 fuel rods, 24 control rod guide tubes, one instrumentation tube, a bottom end piece, a top end piece and eight axially arranged spacer grids in the case of an active core height of 3.5 m [4.239]. Optionally, the fuel assemblies are equipped with a debris filter, and for the increase of thermohydraulic margins, with three intermediate flow mixers.

The Framatome-ANP fuel assembly contains a number of features aimed at optimizing performance. Corrosion resistant duplex cladding, capable of high burnup without loss of rod integrity, is used. This cladding tube is proposed for rod burnups over 55 MW d/kg (U). Natural uranium axial blankets are optional. These devices increase neutron economy by an enrichment saving of about 0.06 w/o ^{235}U. A high performance zirconium alloy, M5, is used to fabricate the cladding, spacer grids and control rod guide tubes.

All-Zircaloy high thermal performance spacers with integrated curved flow channels are utilized for all but the bottom spacer position. These spacers increase coolant mixing and enhance the departure from nucleate boiling performance. An Inconel high thermal performance spacer at the lowermost position provides improved fuel rod support throughout

life at the bottom of the fuel rod region and minimizes the possibility of flow induced fretting failures.

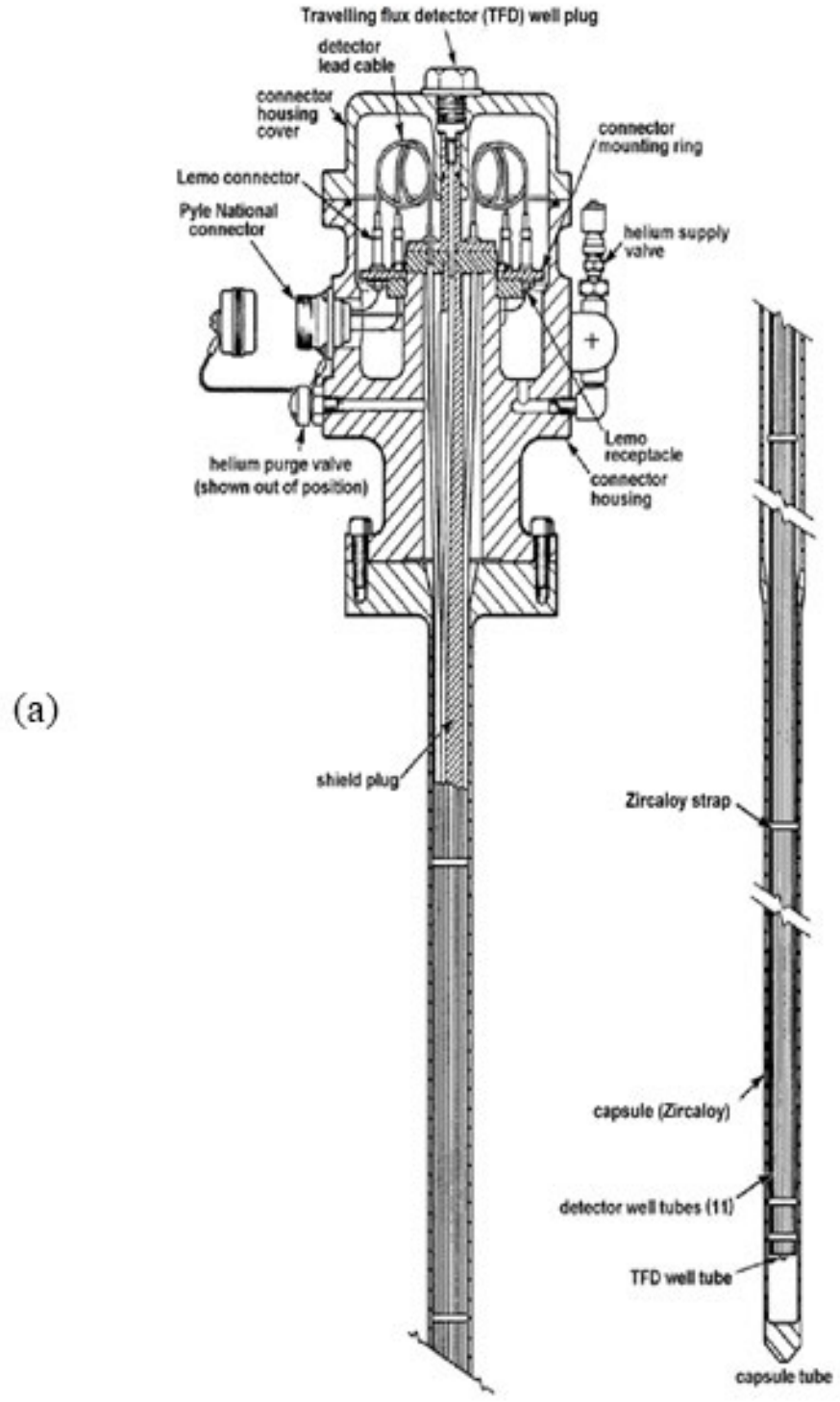

FIG. 4.94(a). Schematic diagram of a vertical flux detector in a PHWR (reproduced from Refs [4.19, 4.238] with permission courtesy of AECL, Canada).

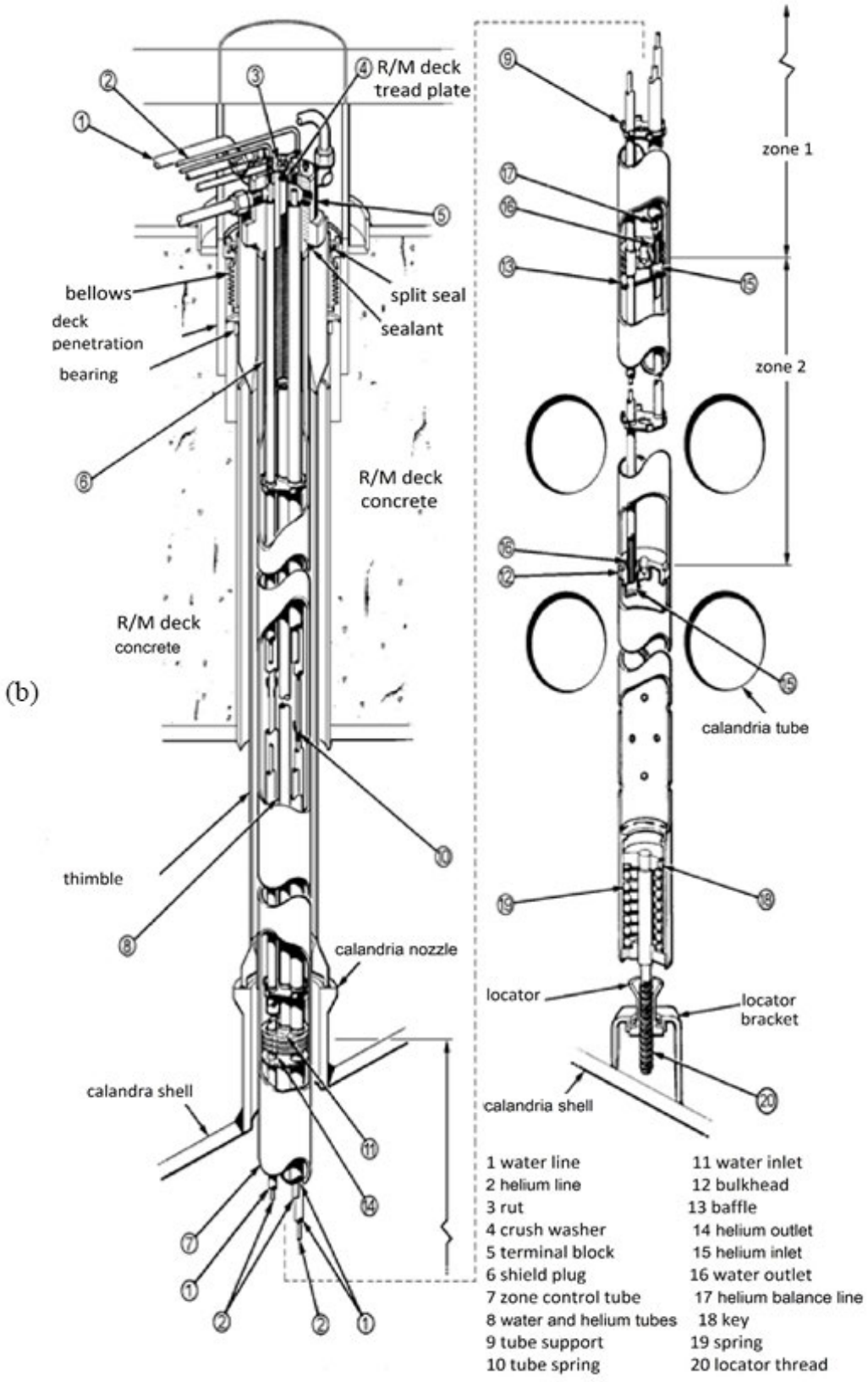

FIG. 4.94(b). Schematic diagram of liquid zone control in PHWR (reproduced from Refs [4.19, 4.238] with permission courtesy of AECL, Canada).

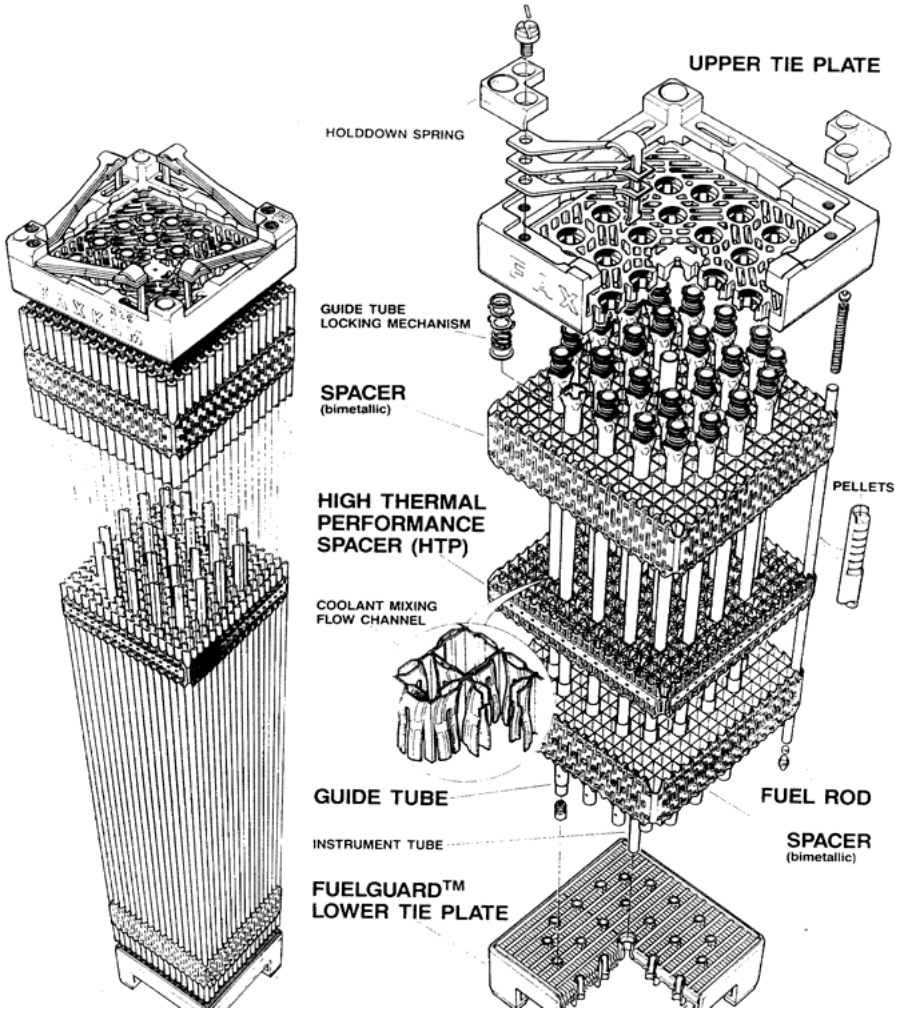

FIG. 4.95. PWR fuel assembly [4.239].

The debris resistant FUELGUARD bottom end piece with curved blades provides almost complete protection against debris induced fretting failures. This bottom end piece is dismountable to allow fuel assembly repair, reconstitution or surveillance from the bottom side, should the need arise. The readily removable top end piece allows quick and easy fuel assembly repair, reconstitution or surveillance from the top side. Other PWR fuel assemblies, such as the Westinghouse design, have similar design features.

4.12.7. BWR fuel assembly

BWR fuel assemblies are substantially smaller in cross-section than PWR fuel assemblies. BWR fuel assemblies consist of 8 × 8, 9 × 9, or 10 × 10 arrays of fuel rods.

Square cross-section channel boxes envelop the fuel assemblies. The channel box provides structural strength to the fuel assembly and guides water in close proximity to the fuel rods. These boxes are 4.25m long, and have a wall thickness of 2, 2.5 or 3mm. The boxes can have features machined into them, including lengthwise grooves on each outer face (to reduce the amount of neutron parasitic zirconium in the core of the reactor) and internal flow trippers that are used to promote mixing of the coolant as it flows up through the channel box. Figure 4.96 provides a schematic view of a BWR fuel assembly [4.240].

FIG. 4.96. BWR fuel assembly [4.240].

In some designs a central portion of the fuel assembly is dedicated to a space where neutron moderating water is present. The SVEA design by Westinghouse uses a water cross — an 'X'-shaped hollow formed from thin Zircaloy-2 strip that is welded to the four sides of the channel box. The Framatome-ANP Atrium design incorporates a small rectangular channel (a channel box within a channel box) through which water flows. The Global Nuclear Fuel design incorporates a cylindrical water rod (tube) that provides additional moderation in the centre of the fuel assembly.

At reactivity control locations, four fuel bundles are located in a square array. A space is maintained between the fuel channels and a cross blade-shaped control element is inserted from the bottom of the reactor core. This arrangement is repeated throughout the core of the reactor. A range of 400–800 individual fuel assemblies makes up a core loading.

The fuel cladding for BWR reactors is composed mostly of Zircaloy-2, sometimes with an internal barrier layer of pure or slightly alloyed zirconium. BWR fuel pins are backfilled with helium to a pressure of 300 kPa.

Lower and upper tie plates hold the fuel rods at either end of the fuel assembly. These tie plates are contained within the channel boxes. The upper tie plate has a handling bail that permits the fuel assembly to be lifted into and out of the core plate assembly that locates each individual fuel assembly into the square array forming the core.

4.12.8. CANFLEX fuel bundle

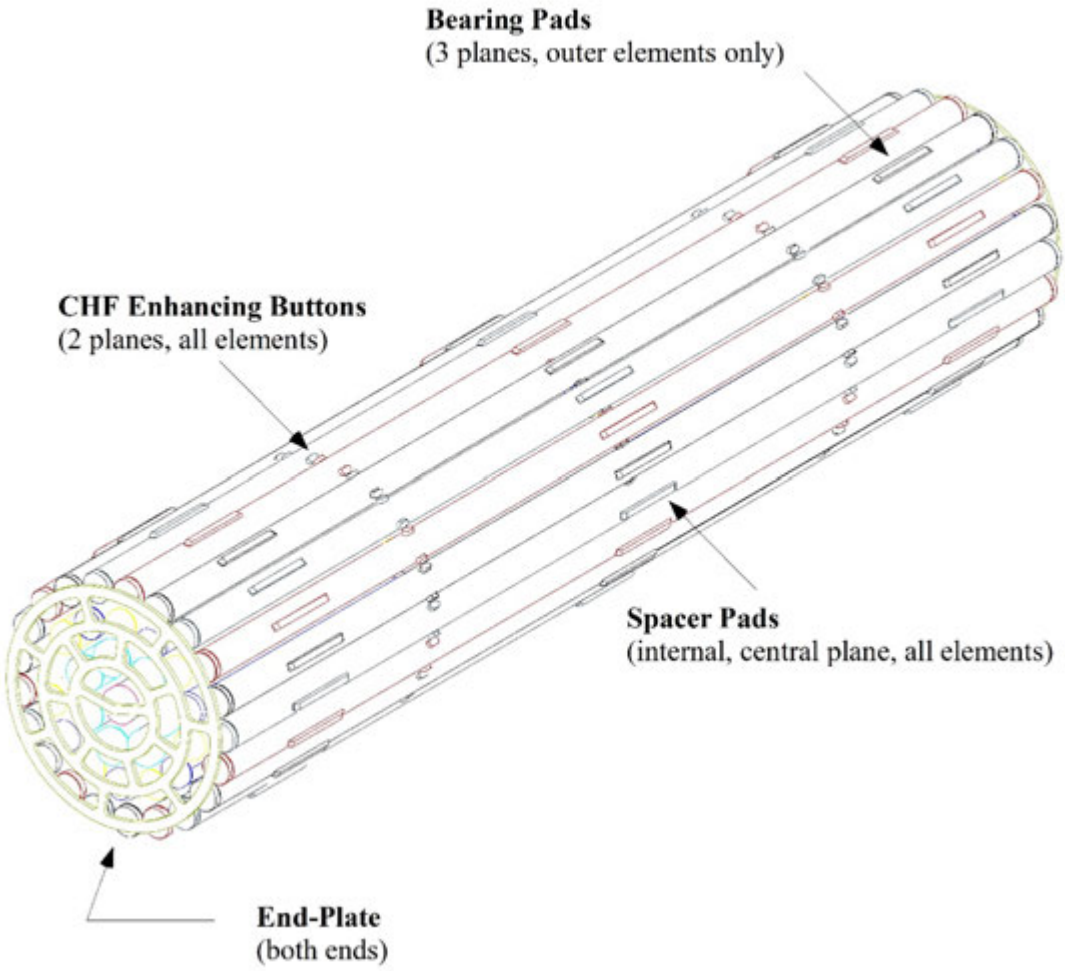

FIG. 4.97. Schematic diagram of CANFLEX fuel bundle (reproduced from Ref. [4.241] with permission courtesy of AECL, Canada). CHF — critical heat flux.

In a CANFLEX fuel bundle (Fig. 4.97) the non-fuel material is Zircaloy-4 in the cold worked and stress relieved condition. The outer two circles of 21 and 14 elements (tubes) have an outside diameter of 11.5 mm while the inner elements, a circle of 7 surrounding a single element, have an outside diameter of 13.5 mm. To maintain separation between elements, spacer pads (rod or sheet) are induction brazed to all elements, while contact with the fuel channel is through bearing pads (rod or sheet) induction brazed to the outer elements.

On two planes in the bundle, small buttons (rod or sheet) are induction brazed on all elements to improve heat transfer. The inside surface of all elements is covered with a CANLUB graphite coating [4.242, 4.243] to minimize cracking from pellet–clad interaction. After the nuclear fuel pellets are loaded, the elements are filled with helium at atmospheric pressure and sealed by resistance welding of end caps (rod) and the whole assembly is held in place by resistance welding the elements to end plates (sheet) at both ends.

In summary, the basic simple shapes resulting from metal working zirconium alloys can be readily combined to produce components of complexity both in their geometry and their production methods.

4.13. INSPECTION AND TESTING

Throughout the manufacturing process a number of inspections, testing and non-destructive testing techniques are used to ensure that intermediate product meets requirements known to produce high quality components. Some of the more common techniques are reviewed here. First it will be instructive to 'walk through' the manufacturing process in sequence to get an overview of the process and what techniques are used.

4.13.1. In-process inspection and testing

Determination of intermediate product chemical composition, particularly impurity elements, dominates the extractive metallurgy processes. There are approximately 25 elements that are either impurity elements or will eventually become controlled elements that are analysed.

The first analytical determination is performed on zircon sand. Impurities that are undesirable, but which naturally occur, include aluminium, phosphorous, uranium, thorium, iron, titanium and lead. These impurities can be difficult to remove or are radioactive and create a waste problem later in the process or can occur at a higher level than the process is designed to remove. In addition, the hafnium concentration is of obvious interest.

A major checkpoint following the separation process is focused on hafnium concentration. The hafnium concentration of zircon sand is about 2 wt% (1.03 at.%) and must be reduced to less than 100 ppm (0.005 at.%) to meet ASTM standards.

The next chemical analysis occurs following reduction to metallic zirconium. Tests can be taken on individual reduction runs, or in the case of semi-continuous electrolytic processing, at some defined frequency. Generally, a full range of impurity elements is measured, including iron, chromium, nickel, aluminium, titanium, silicon, copper, hafnium, magnesium, chlorine, oxygen, carbon and nitrogen.

Individual reduction runs are blended together following crushing to make a master blend. The elemental chemistry values from the individual reduction runs are used to determine which lots to blend to obtain the desired results. Electrolytically produced crystals are blended with Van Arkel iodide produced zirconium to reduce interstitial impurity concentrations. Following this blending, samples are obtained and again analysed for impurity elements as well as eventual alloying elements (e.g. oxygen, silicon, carbon, iron and chromium). This analysis is used to determine the amount of alloying additions that must be added to the sponge or powder during vacuum arc melting to achieve the finished ingot chemical composition.

During the final phases of extractive processing, including reduction, distillation, crushing and blending, there are multiple opportunities for reaction of the intermediate metal

product with the atmosphere. Kroll reduced sponge can be quite flammable because of the large surface area and fine size of some of the particles. If a sponge fire occurs, its consequences must be dealt with by extracting the affected sponge from the lot.

Reactions of sponge with the atmosphere will often discolour the surface of the sponge. The discolouration is generally an interference layer formed by reaction of the underlying zirconium with either oxygen or nitrogen in the air. Sponge is visually inspected, and discoloured particles are removed. Visual standards of acceptable and unacceptable sponge particles are used to determine acceptability. The primary concern at this point is the formation of nitrogen-rich zirconium particles. The nitrogen-rich particles have a very high melting point, about 2700–3300 K (2427–3027°C), and may potentially survive the melting process, becoming incorporated as hard particles in the final metallic product.

Accurate knowledge of the starting chemical composition of all materials used to construct the vacuum arc melt electrode is imperative. This knowledge includes the chemical composition of the sponge or electrolytic powder, that of the recycled materials, and that of the alloying elements (typically carbon, chromium, iron, nickel, niobium, oxygen, silicon and tin) to determine the appropriate additions of alloying and trim additions to meet the desired chemistry requirements.

Once the chemical composition is fixed in the vacuum arc electrode, there generally is no further checking required until a final melt ingot is produced. Exceptions occur if there was an unusual event during melting such as temporary loss of vacuum. In such cases, additional intermediate product analysis may be warranted to ensure that the product would remain within specification for gases such as oxygen, nitrogen and hydrogen.

Once the final ingot has been produced, generally as the result of two or more successive melting operations, the ingot is prepared for additional sampling for chemical analysis. ASTM B350, Standard Specification for Zirconium and Zirconium Alloy Ingots for Nuclear Application [4.27], requires the ingot to be sampled within 125 mm from each end, and at intervening distances not greater than one ingot diameter, along the sidewall of the ingot for alloying elements and elemental impurities; a minimum of three samples per ingot is required. There is segregation of elements such as tin, oxygen and iron at the sidewall of the ingot and care must be taken to get a sample that is representative of the finished product. This requirement generally means sampling deep enough, about 20 mm, that the sidewall segregation is not an issue. During subsequent processing the sidewall material is removed by oxidation from heating processes, and by intermediate and final surface conditioning operations. Alternatively, B350 permits sampling at intermediate steps such as forging, for alloying elements and impurities.

During solidification of the final ingot, a shrinkage cavity occurs near the top. The extent of this shrinkage cavity must be ascertained and that can be accomplished by UT (using a simple handheld probe). The shrinkage cavity can be either removed at this stage or at some later point in the process. A physical examination of the sidewall of the ingot takes place for laps, folds, porosity or any gross oxidation that might indicate vacuum problems. Corrective measures are taken for excessive amounts of these undesirable attributes.

At this point, ingot chemical composition is largely fixed. Only gases such as oxygen, hydrogen and nitrogen can vary during subsequent fabrication processes. As a result, the final product shipped by the zirconium manufacturer is usually analysed only for these gases to ensure that they remain within specification. Furnace heating used for forging, hot rolling and extruding is the typical place for entry of oxygen, nitrogen or hydrogen, as this heating is often conducted in air.

The zirconium manufacturer relies on downstream conditioning and metal removal operations such as machining, sawing, grinding, abrasive grit blasting and chemical pickling to remove outer layers of metal containing undesirable levels of the gases. Oxygen and nitrogen have slow diffusion rates and an increase in these elements is largely limited to the surfaces exposed during heating. While hydrogen can diffuse rapidly in zirconium, the oxide layer that forms during heating serves as a barrier to hydrogen ingress, and the manufacturers are careful to limit sources of hydrogen such as moisture or reducing flames that are hydrogen-rich used to heat furnaces. Additionally, excessive hydrogen can be removed during subsequent vacuum annealing operations.

During fabrication involving hot and cold reduction operations, there are opportunities for internal and external defects such as isolated pores, honeycomb (connected porosity), centre piping and cracks to form. Inspection using UT is required to locate internal defects, and in some cases, surface related cracking. Such non-destructive examination may occur at intermediate size (such as forged slabs for making spacer or channel strip, or TREX for making fuel rod cladding) or at final size (e.g. barstock for making end caps).

4.13.2. Zirconium mill product inspection and testing

At the conclusion of fabrication of zirconium mill products, there is additional inspection to visually examine for surface attributes and to dimensionally inspect the product. In some cases, surface quality is quantitatively measured by surface roughness probes that supplement visual examination. Appropriate samples are obtained to provide material for the destructive testing required for the final certification of attributes. Common destructive tests include steam or water autoclave testing to determine short term corrosion resistance, tensile testing for room temperature or elevated temperature mechanical properties, hardness testing, and metallographic examination for grain size, second phase particle distribution, and inclusion size and distribution. Test requirements are spelled out in the ASTM standards for mill products or in the buyer's purchase specification.

4.13.3. Additional qualification testing for mill products

There may be additional testing required for qualification of new processes or improvements of existing processes. Generally, the zirconium manufacturer works under a fixed practice agreement with the fuel or component manufacturer. Process changes have to be disclosed to the customer and appropriate qualification testing is negotiated between supplier and customer where attributes may vary as a result of the process change.

Examples of qualification requirements include additional intermediate product sampling and examination (by metallography, tensile testing, crystallographic texture analysis, gas analysis and hardness) as well as final product testing for these same attributes. In addition, sampling frequency may be increased for qualification lots or perhaps for some portion of follow-up production lots. In some cases, uniformity of some attributes within a lot is examined to determine the degree of process control established by the manufacturer. Additional, more extensive metallographic or electron microscope procedures to determine size distribution of SPPs, dislocation density, precipitate size and frequency, individual grain orientation and shape can be employed to determine if there is a significant difference between the new and old process methods.

4.13.4. Review of non-destructive examination techniques

A brief review of the techniques for non-destructive examination follows. These techniques include UT, eddy current examination, dye penetrant testing, radiographic testing, pressure testing (hydrostatic and air-under-water) and acoustic emission testing.

4.13.4.1. Ultrasonic testing

Examination by UT utilizes both shear and longitudinal sound waves to interrogate the material. The sound waves are introduced using piezoelectric transducers, which both generate the sound pulse and sense the sound energy reflected from discontinuities in the material, be they gross changes in microstructure, cracks, porosity, corners or other surfaces. This pulse-echo technique, where a pulse is generated, and the echo is detected upon its return, is by far the most common application of the UT method [4.244, 4.245].

The sound energy is introduced into the part (test article) by the transducer using a couplant. The couplant may be water, oil, glycerine or a specifically formulated gel that provides sufficient matching of the acoustic impedances of the search unit and the part being examined to allow transmission. The transmitted pulse traverses the volume of interest, where it may be reflected back to the search unit by a defect such as a crack or lamination, or by a geometric feature of the part such as a corner, a hole or a back surface.

The amplitude of the received signal is typically related to the severity of the defect, since there is a relationship between the reflecting area and the amplitude of the received signal; the orientation, shape and composition of the reflector will also influence the received signal amplitude. The time required for the pulse to travel from the search unit to the discontinuity and back is used to determine the depth and location of the reflector. More refined methods of analysis using the transit time of different wave components can allow very accurate sizing of ultrasound reflectors.

The material being examined can also influence the amplitude of the received signal. Attenuation is the loss of signal amplitude with increasing distance; given the same excitation pulse amplitude, the return signal from a discontinuity 50 mm below the surface will be less than that from a discontinuity that is 25 mm below the surface. The most prominent factors contributing to attenuation are absorption, scattering (seen in large grained materials), beam spreading and refraction. Excitation amplitude, transducer dimensions, test frequency, surface finish and electronic distance-amplitude correction are among the test parameters that can be manipulated to reduce the effects of attenuation.

In practice, reference standards are made from zirconium and typically contain intentionally made reflectors such as sidedrilled holes, flat bottomed holes or machined notches. These standards provide for a consistent set-up of the test system and are used periodically during the test to verify that the set-up, and therefore sensitivity, remains consistent throughout the examination. Acceptability of an indication (the indication of a potential defect resulting from a return signal) is based upon the relationship of the received signal from the examination and the signals received from the standard. Frequently, standards are made so that test indications must have amplitude of some percentage of the standard amplitude, or less, to be accepted.

UT is used for multiple purposes. Not only can suitably oriented subsurface defects be detected, but also the angle beam technique (typically using shear waves) can reliably detect surface discontinuities such as cracks. Since this technique is most sensitive to defects with the broad surface oriented perpendicular to the sound beam axis, examination using angled beams is normally performed in more than one direction.

UT can be performed in either manual or automated modes. The manual techniques are very time consuming, more expensive and less repeatable than the automated techniques, so discussion will be limited to automated testing. Three primary techniques are used for testing zirconium intermediate product. The first of these is the C-scan technique, which is used for flat product such as slab, plate or strip. The material is immersed in water, and an apparatus is used to scan the search unit in X-Y coordinates across the material. This scan is repeated until the entire area of interest has been interrogated. Typically, the longitudinal wave mode is used for this testing, which allows for the detection of discontinuities internal to the material.

The amplitude of the reflection from the back surface is also monitored as a method to verify sound penetration in the part, with electronic gates in the instrumentation used to separate the back surface signal from the material volume testing. If surface defects are of concern, an angle beam test can be performed. The test data are typically displayed in a plan view, which provides the location and size of each detected indication. Depending upon the instrumentation and data acquisition system used, other information such as indication depth, amplitude and area can be determined and displayed. Scanning speed is dependent upon the instrument pulsing rate, beam dimensions and the reference reflector diameter or size.

Cylindrical product such as billets and barstock are also tested in an immersion tank. To complete a scan, the billet or barstock must be rotated relative to the search unit, describing a helical scan path. The pitch of the helix is adjusted to ensure appropriate scan path overlap based upon the pulsing rate of the instrument and the sound beam diameter.

For large billets (150–200 mm diameter), it is most convenient to place the product on rollers that rotate the billet, while a scanning apparatus moves the transducer along the part length. In this way a helical scan path is described, and complete coverage is achieved. For intermediate and small sizes of barstock, the product can be scanned helically past stationary transducers, typically using a stuffing box as the container for the water. Either test set-up may use straight beam or angle beam test techniques. An audible alarm, stop-on-defect circuitry, or electronic or strip chart recording is used to ensure the detection of the defects of interest. The test sensitivity is established using a standard containing the proper reference reflectors, with the acceptability of indications usually based on some percentage of the reference reflector signal amplitude. A typical criterion might be established using a 1.6 mm flat bottom holes reference reflector, with any indication amplitude exceeding 80% of that reflector's amplitude being rejected.

A rotary system is used for tubing and small diameter barstock. A helical scanning path is required for full coverage and is achieved by rotating the transducers about the product as it is fed in a linear manner through the testing apparatus. This rotary head system provides very high throughput rates, as the multiple transducers rotate at speeds over 6000 rpm. The pulsing rate must be set high enough to provide overlap of the individual sound pulses in the material, and the feed rate must be limited to ensure that the helical path overlap is sufficient to ensure defect detection. A system that spins the tubing and feeds it past stationary transducers may be used instead, but throughput rates are not as high, and the higher cost of the rotary head system is usually justified.

Testing of intermediate and final tubing involves multiple channels and transducers to provide a complete interrogation of the tube. At least four shear wave channels will be used for surface defect detection, two in opposing axial directions and two in opposing circumferential directions. Additional transducers may be used for detection of obliquely oriented defects, as well as an additional longitudinal wave test for detection of laminar defects. Dimensional measurement of the outside diameter and wall thickness is

accomplished using longitudinal wave search units; inside diameter values are calculated from the measured outside diameter and wall thickness measurements. Barstock will typically be examined using a longitudinal instrument channel for internal discontinuity detection, and axial and circumferential shear wave search units are used to detect defects on the surface of the tube or barstock.

Bimetallic, co-extruded tubing is a special case that requires additional examination. First, the bonding zone must be examined to determine if there are areas where bonding did not occur between the two layers. This examination is accomplished using a focused longitudinal wave search unit, with a flat-bottomed-holes–type reference standard. Second, the thickness of the liner must be verified. This determination is performed using a focused longitudinal wave transducer and instrumentation capable of performing thickness measurements. Using multiple transducers and instrument channels, these two examinations may be performed in a single pass with the defect and dimensional tests described above. ASTM Standard B811, Standard Specification for Wrought Zirconium Alloy Seamless Tubes for Nuclear Reactor Fuel Cladding, appendix A3, covers detailed procedures for the ultrasonic flaw testing of zirconium alloy nuclear fuel cladding tubes using the immersed pulse-echo technique [4.246].

Typical flaws observed by UT include surface cracks and flaws, centre-pipe or large voids, porosity associated with hard nitrogen-rich particles and high density metallic inclusions with a high melting point, such as tungsten carbide or hafnium metal.

4.13.4.2. Eddy current testing

Eddy current testing (ECT) uses the principles of electromagnetic induction to introduce eddy currents into the material and can detect certain flaws on or near the surface of the material [4.244, 4.247]. An alternating current is passed through the excitation coil, which causes an alternating electromagnetic field to be generated. When the coil is placed near the material, the varying field causes the generation of currents in the material. If a defect is present, the currents are disturbed or interrupted, which in turn disturbs the electromagnetic field. The change in the field results in a change in the coil impedance, and the presence of the defect can be detected. The basic parameters that affect the performance of the test are the material conductivity, material magnetic permeability, geometry, alternating current test frequency and temperature.

Coils may be wound in what is termed a ‘pancake’ configuration and can range from 25 mm in diameter to very small diameters, sometimes referred to as ‘pencil’ coils. Bobbin or probe coils are constructed for the testing of tubing from the inside surface. Encircling coils are wound about an open core, and the product is passed through the coil. Any of these coils may be wound in an absolute or differential configuration, depending on the particular defect of interest.

During testing, a single coil system (absolute mode) or a system of two or more coils that electrically subtract from each other (differential or null mode) may be used to detect defects. When the absolute mode is used, the output of the coil containing acceptable material is fed into the electronic eddy current instrumentation, and variations from this norm are detected indicating a defect. When the coils are connected in the differential mode, they continually test and compare adjacent segments of the material as it passes through the coils. If there is ‘good’ material in both coils, the resulting difference is zero, indicating no defect.

Absolute coils are sensitive to both abrupt and gradual changes in properties and dimensions. They can detect the entire length of defects and provide easily interpreted test

results. Differential coils are more sensitive to localized conditions, are less sensitive to probe movement and are not affected by changes in temperature. Absolute coils have the disadvantage of being susceptible to probe movement or wobble and temperature effects, whereas differential coils are able to detect only the ends of long defects and yield signals that may be difficult to interpret.

Eddy current instrumentation can range in complexity from systems that operate at a fixed frequency and have an analogue meter output, to systems using multiple frequencies that are entirely computer based for set-up and data evaluation and storage. The simpler systems may be limited to conductivity measurement or to rudimentary scanning for gross surface defects, whereas the multiple frequency systems can detect pitting, corrosion and cracking.

The major advantage of ECT is that no direct contact between the exciting or sensing coil and the article being inspected is required. In practice, this technique is infrequently used when testing mill products owing to the thickness of the typical tube shell wall. Eddy currents simply do not penetrate the wall of a tube shell deeply enough, and at a sufficient sensitivity, to provide any truly meaningful information except on the surface of the article being tested. ECT is sometimes used to check intermediate tubes after heat treatment, or after pilgering passes, to check for cracking occurring during that process step.

Most frequently, ECT is used on final and in-service articles, such as with fuel cladding at final testing and on fuel assemblies, and in pressure tubes after a period of operation. ECT can be used to detect wall thickness, liner thickness and surface discontinuities in small diameter, thin walled tubes. On final sized barrier tubes, the test works well for the determination of the pure zirconium liner thickness. In this application, a probe coil is passed down the length of the barrier cladding, on the inside of the cladding tube. The very thin zirconium barrier lining has a sufficiently different conductivity from the Zircaloy-2 tube that the thickness of the lining can be determined.

In some cases, ECT may be performed on end cap barstock as a supplement to UT, again searching for possible surface defects. ECT has sufficient resolution to find a 75 μm wide by 75 μm deep notch in either transverse or longitudinal orientations.

4.13.4.3. Liquid penetrant testing

Liquid penetrant testing (LPT) is the oldest of the modern non-destructive examination methods. Developed in the early twentieth century using oil and chalk powder, the ‘oil and whiting’ method was used to find gross defects in wrought iron and steel products. Today, LPT can be used to locate surface flaws as small as 0.13 mm and can be effectively employed to inspect large amounts of material in a timely and cost effective examination process. The typical surface discontinuities detected using LPT include cracks, laminations, pits, porosity, seams, folds and laps [4.244, 4.248].

The basic principle of the test is that a penetrant is applied to the surface. Either a visible dye, usually red in colour, or a fluorescent dye is used. Capillary action draws the penetrant into surface connected discontinuities. The excess penetrant is then removed by one of several methods, leaving only the penetrant in the discontinuities. The penetrant in the discontinuities then begins to seep back to the surface of the material via capillary action. A developer is used to aid in the detection of the penetrant that has begun moving out of the discontinuity, by providing a contrasting background (visual dye) or by drawing the penetrant into a more visible, larger ‘spot’ (fluorescent dye) or both. Fluorescent dies are detected using ultraviolet or ‘black’ light. In general, the fluorescent technique is more sensitive, owing to

the higher degree of visibility of the fluorescing indication compared with the visible dye on the contrasting background of developer.

LPT is a simple test to perform but has a high labour component. At the same time, there are critical processing parameters that, if not controlled, will result in invalid test results. The part to be examined must be completely clean — this critical step must be performed correctly, or penetrant will not be able to enter the flaws of interest. Smeared metal, for example, generated by grinding out a crack, must also be removed, preferably by pickling or etching. Also critical is the removal of the excess penetrant since zealous removal processing will clean the penetrant from the discontinuities, while insufficient removal will result in a distracting background that will prevent discrimination of the indications from the flaws.

LPT may be used for the verification of defect removal, for instance, when cutting back forging rounds or barstock to remove end defects associated with forging or swaging. In cases where material volume is low, but a detailed surface inspection is required, LPT is useful. An example of this would be in the examination of zirconium alloy sheets for use in end plates, spacers and bearing pads. Finally, the higher sensitivity fluorescent techniques can be used for pinpointing defects found with other non-destructive testing methods, such as a pinhole or weld failure in a fuel rod that was detected by helium leak testing.

4.13.4.4. Pressure testing

Pressure testing falls into two categories. The first is hydrostatic testing and the second is air-underwater testing. Seamless tubing can be tested for through wall discontinuities and complex vessels with welds can be inspected by these methods. ASTM Standard A1047/A1047M-05 provides guidance for hydrostatic testing [4.249].

In hydrostatic testing, the testing media is water that is introduced into a cavity of the part and is pressurized to some predetermined level. In the case of tubing, there are formulas for the minimum allowable test pressure depending on the diameter and wall thickness of the tube. The test article is pressurized and allowed to remain at pressure for a fixed period of time. The pressure is monitored and cannot decline below a fixed amount. The test, in effect, monitors pressure loss. Large leaks are immediately detected during pressurization as a stream of water can be seen issuing from the flawed area.

In air-underwater testing, the article is submerged under water and subjected to a greater than 100 kPa air source. Air leaks through connected flaws and forms bubbles that are monitored during the pressurization period. The test is quick and easy to perform, but it is less sensitive than hydrostatic testing.

A special category of pressure testing is helium leak detection. In this case, a very sensitive leak detector utilizing a mass spectrometer is used to detect the presence of pressurized helium leaking through a flaw. For example, an incomplete fusion of a weld, where the helium can flow through a leak path, is easily detected by this examination. One of the best known applications of this technique is for examining the leaktight integrity of fuel rod end closures [4.250, 4.251]. The rods are filled with high pressure helium. If any of this helium is leaking from a seal weld, it is readily detected by the mass spectrometer, and the fuel rod can be subjected to appropriate rework procedures.

4.13.4.5. Radiographic testing

Radiographic testing is a useful volumetric examination technique that allows the detection of inclusions, voids, cracks and other discontinuities. To be detected, there must be a difference in thickness or physical density from the base material, such as a tungsten

inclusion in weld metal or a crack that is oriented parallel to the radiation beam direction. In most cases, the test technique is established for the given material so that a 1% or 2% difference in material thickness can be detected [4.244, 4.252].

Conventional X ray systems use an X ray tube to generate radiation. The tube consists of a cathode and an anode in a vacuum. When a voltage is placed across the cathode and anode, electrons are emitted from the heated cathode and strike the anode. The high velocity electrons striking the anode target result in the generation of X rays. The voltage, usually measured in kilovolts (kV) will determine the wavelength, and therefore the quality or penetrating ability of the radiation generated. The amperage, usually on the order of milliamps (mA), applied to the cathode, determines the intensity of the radiation. Conventional systems usually operate at up to about 700 kV. Higher energies are generated using systems such as linear accelerators or betatrons and are usually seen only in special applications.

Gamma radiation results from the decay of radioactive isotopes. Most frequently, industrial uses of gamma radiation will utilize ^{192}Iridium or ^{60}Cobalt. Iridium-192, with its energy level of 0.3–0.6 MeV, is often used with portable devices; ^{60}Cobalt is most frequently used in established shooting booths owing to the weight of the device required to provide proper shielding. Gamma sources are simpler to utilize than X ray devices owing to their portability, because they do not need electrical power, and because of the small size of the source itself. A gamma radiation source is constantly emitting radiation, and these systems require much care in operation, storage and security when not being used.

Historically, the most common medium for recording the results of a radiographic test has been specially manufactured photographic film. The electrons released in the interaction with the material under test and the intensifying screens used next to the film cause the formation of an image that is related to the proportion of the radiation passing through the part being tested. This image is made visible by the use of basic photographic processing techniques. Most installations use automatic systems to process the film, providing more consistency and higher quality images than those typically obtained with manual processing. Developments in computed and digital radiography render obsolete many applications using film. The ability of such systems to achieve the image quality formerly only attainable with film have combined with cost savings, shot time reductions and the elimination of processing chemicals to make their use feasible in an ever increasing number of applications.

Radiographic testing has several applications in the manufacturing of zirconium. Due to the high expense of zirconium, scrap is recycled as it is generated. Frequently, the scrap that is used has been generated during various machining operations that utilize tungsten carbide tooling. If a tool breaks or chips, a fragment of tungsten carbide could end up in the recycle material generated at that machine. These particles are generally removed by magnetic sorting; there may be some concern that small particles remain, especially in compacted chips. Since tungsten carbide has a much higher melting point than zirconium, the ingot resulting from re-melting the scrap could contain an inclusion of tungsten. Since the tungsten has a much higher density than the zirconium, it can be detected radiographically before it can cause a material failure in later manufacturing processes. When such inclusions are found, they can be removed from the material by sawing. To allow for the inspection of as much material as possible, ^{60}Cobalt is the source of choice, which will provide sufficient energy for inspection of 150 mm thickness of zirconium using film or digital techniques.

4.13.4.6. Visual inspection

Visual inspection is also an important technique for detecting flaws such as scratches, abrasions, excessive surface roughness, stains and contaminants such as greases or fingerprints. The rule of thumb for visual inspection is that a once-through examination at ×1 is generally 80% effective in spotting defects. Nonetheless, visual examination is a very important final inspection technique.

The personnel doing the inspection should have an annual or biannual examination of their eyes for visual acuity. Additionally, on some periodic basis a measurement of lighting intensity at the surfaces being inspected should be made to ensure there is sufficient illumination. Sometimes a series of acceptable and unacceptable surface standards are used to reduce the chance for interpretation errors between what the manufacturer and the customer believe to be acceptable. These standards should be relevant to the anticipated range of defects, and they should be catalogued and controlled for reference to contractual requirements.

To help automate visual inspection, there are now systems available with cameras that detect defects by feeding the image to a computer with pattern recognition algorithms. The computer software can be trained to either ignore incidental features detected by the camera (such as dust) or to classify the feature into one of several categories of defects.

4.13.5. Destructive testing

Destructive tests consist of testing where a sample is spent or destroyed as a result of the test. Examples include corrosion testing, metallography, tensile testing, microhardness testing and functional testing such as formability testing, bend tests and burst tests. Evaluation of crystallographic texture and fracture properties are not part of the specifications for a successful fabrication of fuel and structural components. Usually, the fuel fabricator does this testing. The techniques are briefly described in Chapters 5 and 9 (in Volumes 2 and 3 of this publication, respectively). In some special circumstances, creep properties may also be measured.

4.13.5.1. Corrosion testing

One of the most important attributes of zirconium in a nuclear reactor environment is its corrosion resistance. The standard test for corrosion is the steam autoclave test, or ASTM G2 test, following the Standard Test Method for Corrosion Testing of Products of Zirconium, Hafnium, and Their Alloys in Water at 633 K (360°C) or in Steam at 673 K (400°C) [4.253]. The steam test is run at 673 K (400°C) for 3 days at a pressure of 10.34 MPa (1500 psig). If the corrosion weight gain is less than 22 mg/dm^2, the sample passes. If it is greater than this limit, the sample can be run for 14 days but must exhibit a weight gain of less than 35 mg/dm^2.

There are many variations of corrosion testing, including the use of long term water tests at temperatures of about 633 K (360°C) where the testing can take months or years to complete. Typically, these kinds of tests are designed to replicate long term in-reactor exposure and are used to prequalify new alloys or different thermomechanical treatments. In some cases, there are additives to the water such as lithium or boron that are designed to replicate the actual water chemistry found in-reactor. The long term tests are usually interrupted at some period (28 days is common) and intermediate weight gains are measured and plotted as a function of accumulated test time. Continuation of the test period is

dependent on a number of factors; for example, if the oxide layer starts spalling, the test is usually terminated. Accelerated weight gains may also be a reason to terminate long term autoclave testing.

Specialized tests are used for BWR conditions and these centre around variations of 783 K (510°C) steam tests in either static or refreshing autoclaves. The refreshing autoclaves are used to maintain an oxidizing environment. In a static autoclave there may be a buildup of hydrogen from the corrosion reaction. With fresh water being supplied to the autoclave in a once-through fashion, any effects from the hydrogen or from an oxygen-depleted environment will be overcome. These tests are typically run at about 10.3–12.3 MPa, and the temperature ramps are customized on agreement with the customer. For example, a 683 K/793 K (410°C for 8 h/510°C for 16 h) two step test [4.254] is specified when sensitivity to nodular corrosion needs to be identified. The criterion for acceptance is to pass a visual standard that has an allowance for a small fraction of nodules. Since this is not an industry standard test, the fuel manufacturers set the visual standards.

The typical ASTM G2 test produces a lustrous, black oxide on the surface. The long term water tests can produce a tan to cream coloured oxide depending on the thickness achieved. The 793 K (520°C) BWR tests will produce a lustrous, black oxide on samples with some small fraction of acceptable nodules, determined by the visual reference cards. The nodules are small, tan coloured, corpuscular protrusions from the surface of the black oxide where the local corrosion rate is much higher. Figure 4.98 displays nodular corrosion.

FIG. 4.98. Nodular corrosion, Zircaloy-2 cladding.

Corrosion coupons (dimensions are about 25 × 37.5 × thickness (in mm^3) for sheet samples and about 50 mm long for both bar and finished cladding samples) are prepared by a thorough cleaning by such means as abrasive grit blasting followed by acid pickling, followed by a thorough rinse in hot, distilled and deionized water. While pickling is not mandatory per ASTM G2 it does provide a thorough cleaning. Alternative cleaning techniques include washing in soapy water, followed by rinsing in hot distilled or deionized water or both, or various wipe downs with acetone or another rapidly drying solvent. Coupons are weighed to the nearest 0.1 mg and the surface area is measured.

Water purity is important for autoclave testing. Small concentrations of impurities such as silicon can dramatically affect test results. Water is typically purified by distillation and deionization. Measuring the electrical resistivity of the water tests purity. ASTM G2 requires that the electrical resistivity be not less than 1.0 MΩ·cm and that the purified water have a pH of 5.0–8.0.

Reference coupons, which have a known weight gain, are run with the ASTM G2 test. These coupons are called sensitivity coupons and ensure that the test variables are under control to produce a minimum specified weight gain.

After autoclaving, the coupons are again weighed to the nearest 0.1 mg. The starting weight is subtracted from the end weight and the surface area is calculated in square decimetres. The weight gain is then recorded in milligrams per square decimetre (mg/dm^2).

4.13.5.2. Metallographic examination

Metallographic examination is used to test for a variety of features. The most common feature is grain size and recrystallization percentage. ASTM Method E112, Standard Test Methods for Determining the Average Grain Size, specifies a common procedure for measuring average grain size [4.255]. The polished and etched samples are placed in a light microscope and are photographed with appropriate magnification. The photographs are compared with reference grain size charts and a grain size to the nearest 1/2 ASTM grain size number is determined.

Alternatively, the grain size can be calculated by either the planar or intercept methods. For example, the intercept method measures the number of grain boundary intercepts per unit test line. This is a measure of grain boundary area per unit volume and is, therefore, related to grain size. An example of the intercept method is the lineal intercept procedure described in Section 11 of ASTM E112:

- On a single field of view at ×100, randomly place one or more straight test lines of known combined total length, L, measured in millimeters.
- Count the total number of intercepts, P, between the test lines and the grain boundaries. Triple points count as 1.5. If the number of intercepts is less than 50, use additional lines.
- Divide the number of intercepts, P, by the total length L to obtain PL.
- Repeat (a–c) for 2–4 additional fields of view.
- Obtain PL as the average result for all fields of view.
- The ASTM grain size number is given as: $n = -3.3 + 6.65 \log 10\,(PL)$.

Grain size distributions can also be calculated by digital image analysis routines using principles of quantitative metallography.

Other items of interest include the observation of features such as porosity, stringers, inclusions and second phase distribution. Normally, zirconium alloys will be free of excessive porosity, high stringer densities and large inclusions, and will have any SPPs (such as $ZrFe_2$ or Zr_2Ni in the Zircaloys) distributed throughout the structure as opposed to accumulating on the grain boundaries.

Specialized metallographic testing can be performed to determine the size and frequency of SPPs and the orientation of hydrides that are intentionally precipitated in the specimens. Second phase particle distributions are generally determined by SEM or TEM or both techniques, as most of the particles have sizes below the limits of light resolution. Hydride orientation is generally performed on cladding to make sure that the cladding contains primarily circumferential hydrides. ASTM Standard B811, appendix A2 [4.256], covers procedures for determination of hydride orientation in zirconium alloy fuel cladding tubes. Section 4.13.6.1 provides more details regarding metallographic sample preparation for light microscopy.

4.13.5.3. Tensile and hardness tests

Tensile testing or mechanical property testing involves machining an appropriately configured test specimen and subjecting it to displacement in a load frame. As the specimen is continuously strained, a load cell records the force required to extend the sample. This force is divided by the cross-sectional area of the gauge section to determine the stress in MPa. An extensometer, clipped to the gauge section of the specimen, measures the

elongation, and also provides information for a feedback loop to the load frame to maintain a constant strain rate up through the yield point. Tensile testing can be done at room temperature, or at some elevated temperature, typically in the range of 561–588 K (288–315°C). Specimen attributes that are generally recorded include the yield strength at 0.2% strain, ultimate strength, reduction of area, uniform elongation (e.g. strain to maximum load) and total elongation [4.247].

ASTM Method E8, Standard Test Methods for Tension Testing of Metallic Materials, governs room temperature testing, and ASTM Method E21, Standard Test Methods for Elevated Temperature Tension Tests of Metallic Materials, is used for elevated temperature testing [4.257, 4.258]. These standard methods govern the specimen geometry and size, the variables used for testing, and the measurement of the various attributes that are reported. For example, the method provides for various standard specimen configurations for round bars, sheet and strip, heavy plate and tubing. Tubing specimens can be either machined from the wall to look like sheet or strip samples, or the tubes can be of full cross-section.

Strain rates are controlled to remain constant in the range of 0.005/minute up until the 0.2% offset yield strength is reached, after which the machine is generally operated at free crosshead speeds of 1.25 mm/min (0.05 inches/minute). ‘Free crosshead’ means that the extension of the machine proceeds at a constant rate without regard to the elongation or strain in the specimen. While E8 relies on the individual material specifications for controlling the strain rates, E21 specifies these rates explicitly.

When testing zirconium alloys two precautions are warranted. First, if the specimen is in the cold worked and stress relieved condition (the condition for many cladding tubes), the determination of the 0.2% offset is complicated by the fact that the apparent elastic modulus is not constant; the slope of the stress–strain curve prior to yield is curved. It becomes difficult to fit a straight line to this curve to determine how to offset to the 0.2% requirement. Second, in the case of thin sheet samples, the test is not conducted under plain strain conditions. Therefore, some properties depend on the gauge thickness of the sheet specimens and are not independent of geometry. For example, total elongation can depend on the gauge width to specimen thickness ratio in sheet that is 1–3 mm thick, as well as gauge length [4.259].

The criterion for acceptability is generally set by either ASTM standards for the various product types or it is spelled out in specific customer specification requirements. Typical values for mechanical properties are provided in Chapter 2.

Several different hardness tests are used depending on the desired attributes. There are two classes of hardness tests — those that determine bulk hardness and those that determine local microhardness. The principle of the test is to push an indenter of a known shape into the material with a given load, and then measure the depth or shape of the penetration. Calculations are made to provide a hardness number.

Examples of bulk hardness tests include the Brinell test (ASTM E10, Standard Test Method for Brinell Hardness of Metallic Materials) [4.260], the Rockwell and Rockwell superficial hardness tests (ASTM E18, Standard Test Methods for Rockwell Hardness and Rockwell Superficial Hardness of Metallic Materials) [4.261] and the Vickers test (ASTM E92, Standard Test Method for Vickers Hardness of Metallic Materials) [4.262]. Examples of microhardness tests include the Vickers test and the Knoop hardness test (ASTM E384, Standard Test Method for Microindentation Hardness of Materials) [4.263]. The Vickers test relies on a pyramidal diamond indenter and the Knoop test uses a rhombohedraldiamond indenter. The Brinell test relies on a spherical ball indenter and Rockwell tests utilize different penetrators, such as a spherical ball or a diamond cone depending on the particular range of hardness being tested.

Hardness requirements are most often provided as customer specifications rather than by ASTM material standards. In the past, Brinell ingot hardness was required by ASTM as an indication of interstitial element control (primarily oxygen and nitrogen). As ingots became larger (from 500 mm up to 750 mm diameter), the anisotropy of individual grains on the sidewalls of the ingots dominated the hardness values and the resulting numbers were not directly correlated to interstitial concentrations.

Microhardness testing is used extensively to back up metallographic observations of hard inclusions such as nitrogen-rich (nitrides) areas, or alpha-case (oxygen-rich) areas on the surface of samples. These tests are generally not required by customers purchasing and using zirconium products but are used to verify microstructural features.

4.13.5.4. Functional tests

Functional tests may be used to determine the suitability of zirconium alloys for an intended purpose. To test for the formability of sheet and strip, one of the most common tests is the semiguided bend test according to ASTM Method E290, Standard Test Methods for Bend Testing of Material for Ductility [4.264]. In one variation of this test, a coupon is subjected to a force through a cylindrical mandrel at the mid-length of the specimen. The specimen is supported by two fixed cylindrical mandrels at a fixed distance to either side and below the moving mandrel. The specimen is bent to either 105° or 180°.

Since zirconium is anisotropic, the test direction (bending parallel or transverse to the rolling direction) is important. With strip that has not been cross-rolled to produce an isotropic structure, the bend radius is usually tighter when the deformation is parallel to the rolling direction than in the transverse direction. Specifications require that some minimum bend radius be achieved with no evidence of cracking. A very common specification is for a $3T$ radius where T is the thickness of the strip. In this case the centre mandrel would be $6T$ in diameter. Bend tests can also be conducted using an upper punch and lower die cavity. However, the punch and die cavity are limited to use on a single thickness of sheet metal.

Another indicator of formability for sheet and strip samples is provided by the ball punch deformation test covered by ASTM Method E643, Standard Test Method for Ball Punch Deformation of Metallic Sheet Material [4.265]. In this test, a sheet sample is clamped between an upper and lower die. A full radius ball punch is then impressed into the sample and the specimen is stretched until failure takes place. The height of the resulting cup is determined and reported as the formability attribute.

Additional functional tests on strip products can be quite specific in design. Spacer grid strips have numerous complicated features, including bathtub-shaped features, cantilever springs and arches. To determine if any given lot of spacer strip is suitable, it may be subjected to testing in a die set specifically designed to replicate the features of the finished spacer grid. These tests are go/no-go tests and are designed to provide an indication of how any given lot of strip will form during production conditions.

Burst tests on tubing are an example of a functional test that would determine failure of a tube subjected to an internal overpressure. Appendix A1 of ASTM B811 is the implementing document for burst testing of zirconium alloy fuel cladding [4.246]. The test requires a minimum length of ten diameters, and a closed-end loading to produce a 2:1 circumferential to axial stress ratio. The use of an internal mandrel is by agreement between the purchaser and the manufacturer. If a mandrel is used, its diameter must be 0.25 mm less than the inside diameter of the cladding. The test is normally performed at room temperature, but if elevated testing is warranted, care has to be taken with the pressurizing

fluids to ensure stability at elevated test temperatures. Reported results include the maximum burst pressure and the resulting ultimate hoop strength, and the percent total circumferential elongation (excluding the opening of the rupture).

A contractile strain ratio test on final sized, wrought, seamless cladding is used to determine whether the crystallographic texture induced by the final sequence of cold tube reducing and annealing procedures is appropriate [4.246, 4.265, 4.266]. In this test, a grid is marked on the surface of the tubing. The grid consists of 3 circumferential marks located 25 mm apart, and 4 longitudinal lines at 90° increments around the tube. The grid intersections are accurately measured before the test and then the specimen is strained in tension to between 3 and 6%. The post-test measurements are made on the strained grid. True circumferential strains, E_c, are calculated as:

$$E_c = \ln\left(\frac{\text{average post-strain diameter}}{\text{average pre-strain diameter}}\right) \tag{4.18}$$

and true axial strains, E_a, are calculated as:

$$E_a = \ln\left(\frac{\text{average post-strain gauge length}}{\text{average pre-strain gauge length}}\right) \tag{4.19}$$

A true radial strain, Er, is calculated, assuming constant volume, as:

$$E_r = -E_a - E_c \tag{4.20}$$

The contractile strain ratio, *CSR*, is calculated as:

$$CSR = \frac{E_c}{E_r} \tag{4.21}$$

The precision with which the grid measurements are made determines the accuracy of the test. Special measuring equipment (such as laser mensuration) is required to assess the very small strains to the degree of required accuracy. *CSR* values of less than 1.0 indicate a circumferential crystal texture, and values greater than 2.0 indicate a high radial texture in which {0002} poles are aligned in the radial direction. In some cases, high contractile strain ratios are desirable, but this is not universal and depends on specific design variables.

X ray diffraction can also be used to measure crystallographic orientation. This technique is not limited to tubular forms and can be used on flat and cylindrical solid forms. Results can be presented in several ways, including direct and inverse pole figures, in terms of the Kearns' factors, and orientation distributions. These measurements are covered in Chapter 5.

Some customers require elevated temperature creep testing be conducted on material in finished geometry — for example, on finished cladding. By necessity, creep testing can require a rather long test period, and performance of this test is conducted according to customer specification requirements. Creep testing variables are highly specific to the end application, including temperature and temperature controls, applied load, atmospheric controls and associated creep rates.

4.13.6. Metallography — light microscopy

Metallographic interpretation of zirconium alloys is paramount in understanding their properties and to help characterize the processing and fabrication activities that result in the underlying microstructure. Throughout this publication, a recurring theme is the importance of microstructure to underlying properties. This chapter deals, in part, with the formation of

microstructures through various fabrication routes. The fabrication–structure–property triad has significant relevance to the performance of zirconium alloys. This section deals with some simple techniques that can be used to prepare and assess metallurgical samples.

4.13.6.1. Metallographic preparation

Metallographic preparation can follow traditional techniques using successively finer grits of diamond polishing compounds and alumina or silica suspensions. Alternatively, the metal sample may be chemical attack polished. This technique is simple to master, and it is sufficiently versatile to allow its use on a wide variety of different metals and alloys. Attack polishing abrades the sample surface and etches it at the same time. Done properly, this technique will result in a true, undisturbed surface. The finished surface shows very little detail in the as-polished condition, since there is no etching relief of topographical features. The important concept is that the sample is etched at the same rate it is being abraded to minimize 'flowed' metal [4.267].

Samples are mounted in a suitable thermoplastic resin, such as diallyl phthalate, or in a room temperature setting epoxy resin. The choice of mounting techniques is dictated by sample volume and features to be observed. The hot mount resins provide superior edge retention. Cold mount epoxy resins are preferred if hydrides are to be observed, as there is some opportunity for the heat from thermosetting resins to alter the distribution and shape of the hydrides. Black thermosetting resins are desirable, especially if polarizing light is used for microscopic observation, because the mounting media remain dark and do not interfere with the interpretation of the object being viewed.

Samples are belt or disc sanded to flatten the surface and remove grossly deformed metal, and rough sanded through 400 grit silicon carbide or 2/0 grit emery. These processes can be accomplished manually or can be mechanized depending on the number of samples to be examined.

Rough polishing follows abrasion on a metallographic wheel using nylon cloth over a thin cotton cloth. An abrasive solution of 10 g of 1 μm alumina diluted with 100 mL of water is applied to a wheel spinning at about 1000 rpm. Following this initial polishing, an acid solution consisting of 250 mL water, 22 mL nitric acid and 3 mL of hydrofluoric acid is applied to the wheel. After an even film is formed on the wheel, the speed is reduced to 500 rpm and the sample is polished with light to moderate pressure. A starting range for hand force is estimated as 10–40 kPa. This can be estimated by pressing one's hand on a weight measuring scale until muscle memory is achieved. As the sample is removed from the wheel, it is immediately rinsed to prevent over-etching or staining.

The technique for final polishing is similar to that for rough polishing. A suspension of two to three grams of 0.05 μm alumina in 150 mL of water is used in the abrasive solution on medium nap synthetic rayon followed by about 10 mL of acid solution added to the slurry. The acid solution consists of 200 mL water, 30 mL nitric acid, 20 mL hydrogen peroxide and 8–10 drops of hydrofluoric acid. Light hand pressure is applied for about 60 s. There will need to be some experimentation to develop the correct proportions of acid, wheel speed and pressure. Too much acid results in over-etching the sample surface. Too much pressure results in flowed metal. The sample should be rotated to prevent the formation of 'comet tails' and other preparation induced artefacts.

An attack polished structure is a good starting point for SEM examination. One scheme starts with an attack polished surface, followed by etching and examination with a light microscope. Suitable features are marked by encircling them with microhardness indents.

The original etch is then eliminated by polishing using the final polishing techniques. Examination of the SEM relies on either secondary electron detectors or back scattered electron detectors to image the polished surface. For guidance on mechanized polishing techniques, see Danielson and Sutherlin [4.267].

Surface enhancement techniques are used to observe various features in the microstructure. These techniques depend, in part, on the illumination employed for light microscope observation. The primary surface enhancement techniques consist of etching, anodization and heat tinting.

Zirconium reacts to etching because the anisotropic crystal structure reacts to acid attack at different rates according to the orientation of the exposed crystal structure. Etching is used to reveal grain boundaries, deformation twins, SPPs and hydrides. Table 4.24 provides some general etching solutions and procedures for enhancement of these features.

TABLE 4.24. ETCHANTS FOR DEVELOPING ZIRCONIUM ALLOY MACRO- AND MICROSTRUCTURES [4.267]

Feature to be resolved	Etchant	Procedure
Macrostructure	4% HF, 35% HNO_3, balance water	Immerse sample for 10–15 min in etchant, rinse and air dry
Microstructure	10 mL HF, 45 mL HNO_3, 45 mL water	Rough polish and swab etch for 5–10 s, rinse in hot water, air dry
SPPs	1 drop HF, 10 mL HNO_3, 10 mL water	Final etch
Hydrides in Zircaloys	8–10 drops HF, 25 mL HNO_3, 25 mL H_2O_2 (30%)	Rough polish and swab etch for 5–10 s, rinse in hot water, air dry
Hydrides in Zr-Nb alloys	8 mL HF, 45 mL HNO_3, 45 mL lactic acid	Rough polish and swab etch for 5–10 s, rinse in hot water, air dry
SPPs for SEM examination	20 mL HF, 5 mL HNO_3, 75 mL glycerol	Immerse sample in solution for 5–15 s, rinse in cold water, heat HNO_3 to 38–43°C and immerse for 2–5 s, rinse in cold water

Note: Nitric acid is 70% concentration. Hydrofluoric acid is 48% concentration.

Zirconium (and hafnium) are amenable to polarized light observation because of their anisotropy. Polarized light observation is particularly valuable to determine grain structure (size, shape and distribution) and crystallographic texturing effects. Proper preparation for grain structure observations is a low voltage anodization to improve the contrast under polarizing illumination.

Colour anodizing is used to improve contrast between intermetallic compounds. Anodizing detects the presence of light element contamination by oxygen or nitrogen. Anodization uses a solution of glycerine, ethanol and acids called Picklesimer's solution [4.268]. This solution consists of 60 mL absolute ethanol, 35 mL water, 20 mL glycerine, 10 mL lactic acid (85%), 5 mL phosphoric acid (85%) and 2 g citric acid.

A 200 V DC power supply is used with a pointed tungsten or tantalum probe. The plastic mounted sample is immersed in Picklesimer's solution in a shallow stainless steel beaker connected to negative polarity. The probe is contacted on the sample, the power supply is turned on and the voltage is ramped at about 5 V/s. Typical anodization voltages for zirconium are 15 V to enhance general grain structure under polarized light observation; 28–30 V to observe zirconium carbides; 108–110 V to observe light element contamination, silicides and phosphides, or coarse SPPs; and 180 V to enhance the contrast of very fine second phase intermetallic compounds consisting of Zr, Fe and Cr [4.267].

Heat tinting is a complementary technique to anodization. While anodizing is relatively insensitive to variations in alloy distribution in the zirconium, heat tinting readily highlights areas that do not have a uniform alloy distribution. Heat tinting relies on variations in the oxidation rate of different areas of the sample. Differences in oxide film thickness result in variations in colour when viewed with bright field illumination as a result of a thin interference film built up on the surface of the sample.

If samples have been mounted in thermosetting resins or cold mount epoxy, they must be broken out of their mounts prior to heat tinting. Samples for heat tinting are attack polished and thoroughly rinsed using distilled water. Heat tinting is performed by forming the oxide layer in a small oven or hot plate set at approximately 575–675 K (300–400°C). The sample is placed on a metal plate that provides thermal mass. Residence times vary between about 2 and 10 minutes.

4.13.6.2. Observation of microstructures

Observation is broken down into the use of light instruments or electron beam instruments, the SEM being the most useful for assessing the effects of fabrication techniques, failures with fractured surface and microchemistry determination of individual phases or particles.

Key features of a bench light microscope include having a smooth stage movement and focusing movements, a turret with several objective lenses for different magnifications, objective lenses with high numerical aperture that are strain-free for observation with polarized light, a good polarizing analyser, access to Nomarski interference contrast lighting, some method of recording images (digital is the preferred method, but film techniques are acceptable), and high intensity mercury vapour lighting. Polarized light observation requires very high illumination, particularly if any film imaging is to be done. Without the very brightest illumination, film exposures become excessively long and deviation from reciprocity (the relationship between the product of time and the intensity of illumination that defines normal exposures) creates unacceptable shifts in colour.

Polarizing illumination is used to display grain orientation effects. Either anodization or heat tinting can be used to enhance the effects of polarized observation. Heat tinting captures more vivid colours but requires more effort than anodization. Features readily observable under polarizing illumination include grain structure, beta transformation structures, deformation twinning, crystallographic orientation effects, weld-heat affected zones, massive hydrides and areas containing critical grain growth or ‘blocky’ α grains.

Bright field illumination is used to image SPPs, inclusions such as carbides and silicides, the presence of light element contamination (nitrides and oxides), hydrides and the presence of internal discontinuities as a result of cracking, laps, folds, porosity, honeycomb and intergranular or transgranular cracking. Bright field illumination also works well in conjunction with anodization and heat tinting. For example, the microstructures of Zr-Nb alloys may have very small alpha grains and distribution of small β phase particles. This structure can be enhanced by heat tinting and bright field illumination.

Differential (or Nomarski) interference contrast illumination is used to determine microstructural features that exhibit surface relief. Therefore, the most satisfactory preparation prior to observation is with an etchant that will reveal differences in surface relief. Features such as grain boundaries, twins and alignment of SPPs are readily observable using differential interference contrast.

Dark field illumination has limited usefulness, but it will vividly image very small inclusions such as second phase precipitates.

4.13.6.3. Interpretation of structures

The interpretation of structures is a key aspect of metallographic examination that is best illustrated and learned from photomicrographs of actual structures.

Figure 4.99 shows fully recrystallized Zircaloy-4 in the cold worked and annealed condition. Preparation is by attack polish and anodization at 15V. Illumination is polarizing light. General grain structure and grain orientation are readily observable under this set of conditions.

Figure 4.100 is a nitrogen-rich defect in Zircaloy-4. The sample was attack polished and anodized at 110 V to reveal a blue-greenish coloured nitrogen-rich area. Illumination is bright field. Notice the nitrogen-rich area is α stabilized and there is no presence of second phase precipitates within this area.

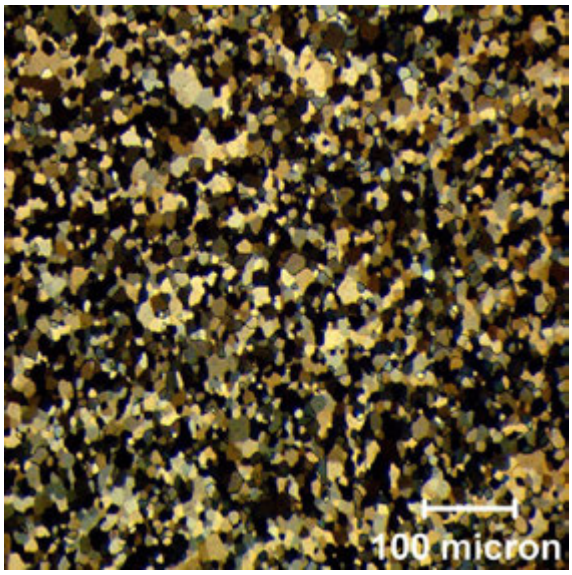

FIG. 4.99. Recrystallized Zircaloy-4.

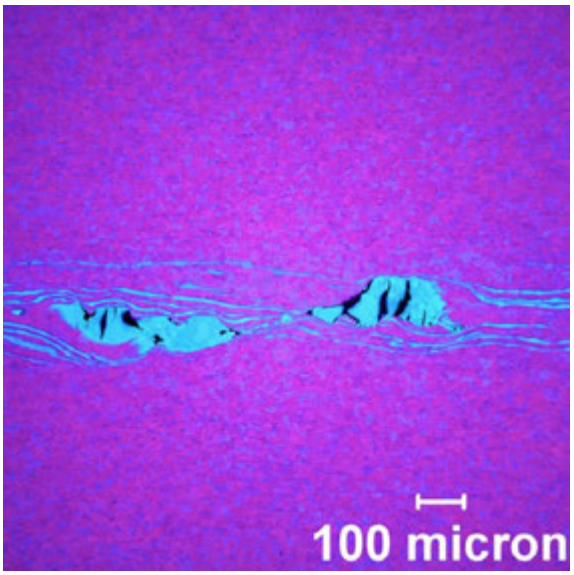

FIG. 4.100. Nitrogen-rich defect in Zircaloy-4.

Figure 4.101 is a zirconium carbide (ZrC) in Zircaloy-4. Preparation is similar to Fig. 4.100 except that anodization was performed at 28 V. Carbides typically exhibit a cuboidal structure and have a very light gold colour. Bright field illumination was used.

Figure 4.102 is a zirconium silicide (Zr_3Si) in Zircaloy-4. An attack polish followed by anodization at 108 V reveals silicide as a slightly darker gold colour than carbides. Silicides have a narrow, rectangular form compared with carbides.

Figure 4.103 is an example of Zr-2.5Nb in the hot worked and annealed condition. In this case, the α grains are roughly equiaxed. Beta-niobium is seen precipitated between the alpha grains as small, elongated globules. This sample was prepared by attack polish and was heat tinted. Bright field illumination was used.

Figure 4.104 shows hydride platelets in a Zircaloy-4 cladding sample. Notice the desired, circumferential orientation of the platelets. The sample was prepared by attack polishing and hydride etched per Table 4.24. The sample was photographed using bright field illumination.

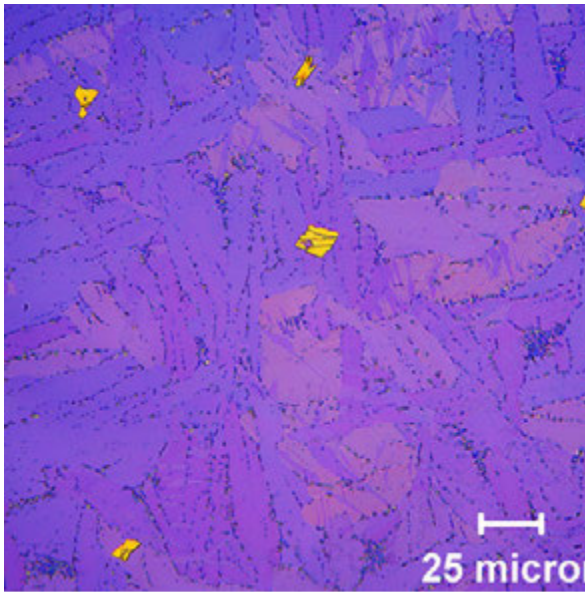

FIG. 4.101. Zirconium carbide in Zircaloy-4.

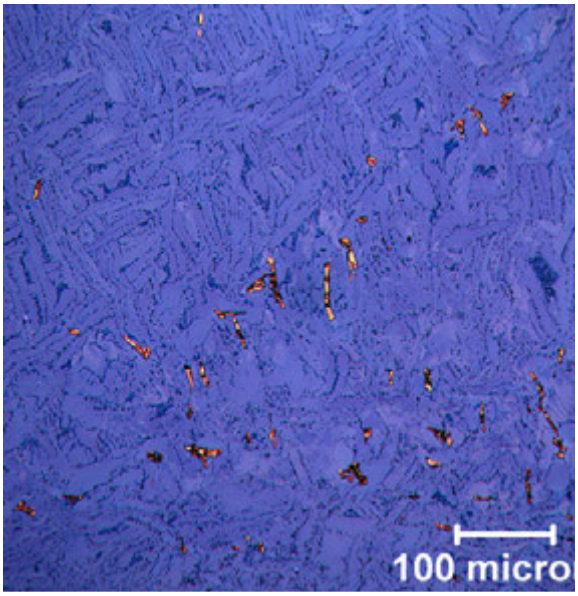

FIG. 4.102. Zirconium silicide in Zircaloy-4.

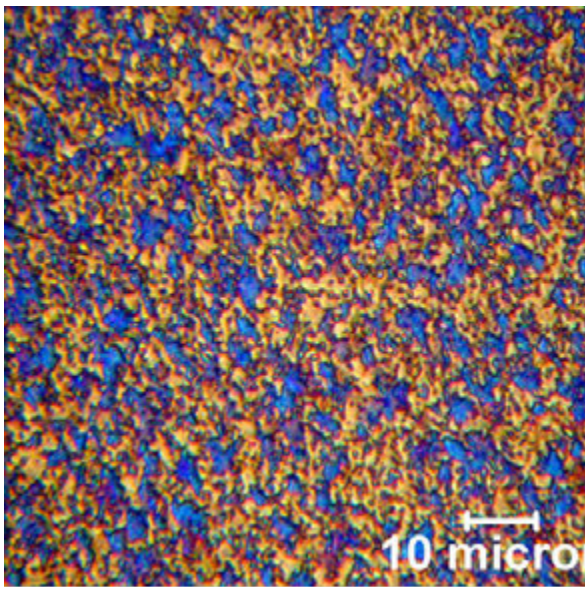

FIG. 4.103. Zr-2.5Nb, hot worked and annealed.

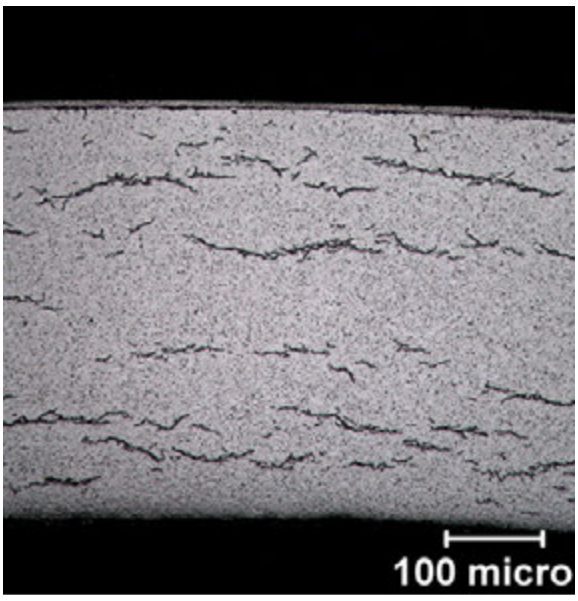

FIG. 4.104. Hydride platelets in Zircaloy-4 fuel cladding.

Figure 4.105 is an SEM micrograph of SPPs in Zircaloy-2. Preparation was by attack polish followed by etching as outlined in Section 4.13.7.4. The SPPs are standing on columns of parent material. The parent material was etched away and slightly undercut to reveal the true diameter of the particles. The larger particles are Zr_2Ni and the smaller particles are $Zr(Fe,Cr)_2$ (Section 4.13.5.2).

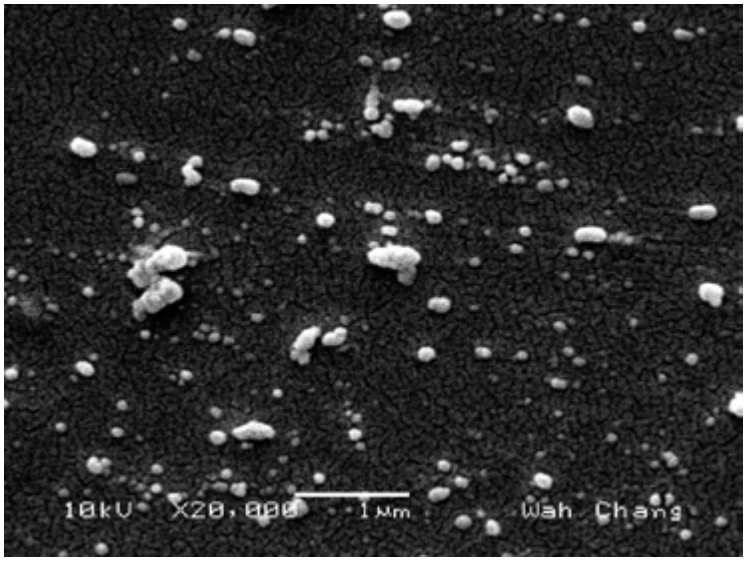

FIG. 4.105. SEM micrograph of SPPs in Zircaloy-2. Large particles are Zr_2Ni and smaller particles are $Zr(Fe,Cr)_2$.

4.13.7. Microanalytical techniques

4.13.7.1. The chemistry of zirconium

Zirconium (Zr) has an atomic mass of 91.224 dalton (unified atomic mass unit, equivalent to grams/mole); this number represents a weighted average of its various isotopes. Naturally occurring zirconium is composed of five isotopes, three of which are stable and two of which are radioisotopes that decay through beta emission [4.269]. The half-lives of naturally occurring radioisotopes of Zr are of sufficient length that they are considered stable for practical purposes. The masses of these isotopes and their relative abundance are given in Table 4.25.

TABLE 4.25. ISOTOPES OF ZIRCONIUM

Isotope	Atomic mass (u)	Abundance (%)	Half-life (years)
Zr-90	89.9043	51.46	Stable
Zr-91	90.9053	11.23	Stable
Zr-92	91.9046	17.11	Stable
Zr-94	93.9061	17.40	1.1×10^{17} (practically stable)
Zr-96	95.9082	2.80	2.4×10^{19} (practically stable)

In its ground state, the electrons in zirconium are expressed by the following configuration: $1s^2 2s^2 2p^6 3s^2 3p^6 3d^{10} 4s^2 4p^6 4d^2 5s^2$ of which $4d^2 5s^2$ are the four valence electrons (the balance belongs to the core). Zirconium has four oxidation states (Zr^+, Zr^{2+}, Zr^{3+} and Zr^{4+}) and four ionization potentials (6.92 V, 13.97 V, 24.00 V and 33.8 V) [4.269].

Zirconium is found below titanium but above hafnium in Group 4 of the periodic table and, as such, shares similar chemical properties. Some common chemical properties of Zr are listed in Table 4.26 [4.270].

TABLE 4.26. CHEMICAL PROPERTIES OF ZIRCONIUM

Property	Value
Atomic radius	0.216 nm
Atomic volume	14.1 cm^3/mol
Thermal neutron capture cross-section	0.184 b
Crystal structure	Hexagonal close packed
Density	6.51 g/cm^3
Electronegativity (Pauling)	1.33
Heat of fusion	16.9 kJ/mol
Melting point	2125 K
Boiling point	4650 K
Specific heat	0.27 J/gK
Electron affinity	41.1 kJ/mol

Although Zr is an extremely reactive metal — when finely divided, it will spontaneously ignite in air — it is highly resistant to corrosion by common acids, alkalis and seawater and is used by the chemical industry where corrosive media are employed. Its corrosion resistance is attributed to the formation (in air or water) of a tenacious, self-healing protective oxide film, ZrO_2 [4.271]. Aside from its oxide, Zr forms several other inorganic compounds such as hydroxides, hydrides, nitrides, nitrates, phosphates, sulphates and halides [4.272].

4.13.7.2. X Ray and electron energy level notation

Given that the following sections discuss various electron and light (including X ray) spectroscopic techniques, this section describes two common nomenclatures used to label spectroscopic emissions. Each electron in an atom is characterized by four quantum numbers, two of which define the specific energy level in which the electron resides: the principle quantum number n, which describes the electron shell and the orbital quantum number l, which describes the type of electron orbital (0 = s, 1 = p, etc.). An interaction between an electron's orbit and spin (m_s) produces a phenomenon known as spin-orbit coupling, which results in a shift of energy levels detectable as a splitting of spectral lines. Spin-orbit coupling is described by the total angular momentum quantum number j, where $j = l \pm m_s$. Depending on the type of spectroscopy, the energy levels that are involved in the excitation and emission processes are described by either X ray notation (common to techniques that detect X rays) or electron orbital notation (common to techniques that detect electrons). The relationships between the various energy level nomenclatures are shown in Table 4.27.

4.13.7.3. Surface analysis using electron properties of zirconium

The analytical techniques described in the following sections are used to examine zirconium alloys, including observations of topography, the distribution and chemical state of alloy and trace elements and the products of operation during service.

TABLE 4.27. COMMON SPECTROSCOPIC NOMENCLATURE FOR DESCRIBING ENERGY LEVELS

Quantum numbers			X ray notation	Electron notation
n	*l*	*j*		
1	0	1/2	K	$1s_{1/2}$
2	0	1/2	L_1	$2s_{1/2}$
2	1	1/2	L_2	$2p_{1/2}$
2	1	3/2	L_3	$2p_{3/2}$
3	0	1/2	M_1	$3s_{1/2}$
3	1	1/2	M_2	$3p_{1/2}$
3	1	3/2	M_3	$3p_{3/2}$
3	2	3/2	M_4	$3d_{3/2}$
3	2	5/2	M_5	$3d_{5/2}$

4.13.7.4. Scanning electron microscopy and associated spectroscopic techniques

Although SEM is primarily used to investigate surface topography, the instrument is often also equipped with multiple detectors to investigate chemical characteristics. SEM is based on principles that are analogous to visible light microscopy. While the resolution of light microscopy is limited by the wavelength, λ, of blue light ($\lambda \approx 450$ nm), SEM attains a greater resolution by probing the surface with a beam of high energy electrons ($\lambda \approx 1$ nm). In addition to high magnification, a key benefit of SEM is its high depth of field (or depth of focus), allowing for sharp images on rough surfaces. In practice, a focused electron beam is rastered across a very small surface area. Electrons that are ejected or backscattered from the sample are detected and a magnified image is produced by simultaneously projecting an electron beam over the pixels of a cathode ray tube. This technique is performed in high vacuum to give both incident and resulting electrons free passage from source to sample and from sample to detector. SEM typically requires the sample of interest to be conductive since electrons that are ejected from the surface must be replenished through an external ground. If samples are not sufficiently conductive, the sample surface will adopt a net positive charge, which deflects both incident and secondary electrons and results in poor image quality. Poorly conductive specimens are often sputter coated with a thin film of gold. Gold not only increases the conductivity of the surface but also increases image quality as it has a high secondary electron yield.

Preparation techniques suitable for light microscopy, including attack polishing, and various etching techniques also serve well for the SEM. Surface enhancement techniques such as anodization and heat tinting are of no value for SEM observations and are even detrimental because the insulating properties of the oxide films thus formed result in the electrical charging effect.

A special technique used to determine the size of SPPs applies only to the SEM. This technique is used to etch the SPPs so that they stand up on a pedestal of the original matrix, allowing a true determination of the diameter of the particle.

To prepare zirconium alloys for second phase precipitate examination in the SEM, the sample is mounted in thermosetting resin. An attack polishing technique is used to attain a smooth, strain-free surface. The sample is etched as outlined in Table 4.24. The images are made under secondary electron imaging mode. A typical set-up uses a 10 keV accelerating

voltage, a 60 μm aperture and a 10mm working distance. See Fig. 4.105 as an example of a properly prepared and imaged surface.

When a sample surface is subjected to a focused beam of electrons, various processes can occur. These processes are shown schematically in Fig. 4.106 [4.273]. By probing the material with an electron beam of small spot size, information is acquired from a pear shaped interaction volume. The sample depth from which a signal is detected is determined by the mean distance the electron or X ray travels in a solid before being inelastically scattered. This property is a function of energy and is referred to as the inelastic mean free path. Typically, X rays are detectable from greater sample depths than electrons since they are not inelastically scattered in the same manner. Often, it is the inelastic mean free path that determines the surface sensitivity[2] of an analytical technique. In some cases, for high energy electrons and very thin specimens, the incident electrons may be transmitted directly through the specimen and yield images of very high magnification. This method, TEM, is discussed below.

Incident electrons can provoke the ejection of low energy secondary electrons, which are valence electrons that arise from only the top few nanometres of the sample surface and are used to study the sample topography in a technique known as secondary electron imaging. Topographical depth contrast in a micrograph is dictated by proximity to the detector. That is, secondary electrons from elevated areas have a greater probability of detection than those from depressed areas and, therefore, appear brighter. The high magnification and depth of focus of secondary electron imaging is shown in Fig. 4.107 [4.274] where it is used to image the fracture surface of a Zircaloy-2 sample following creep testing.

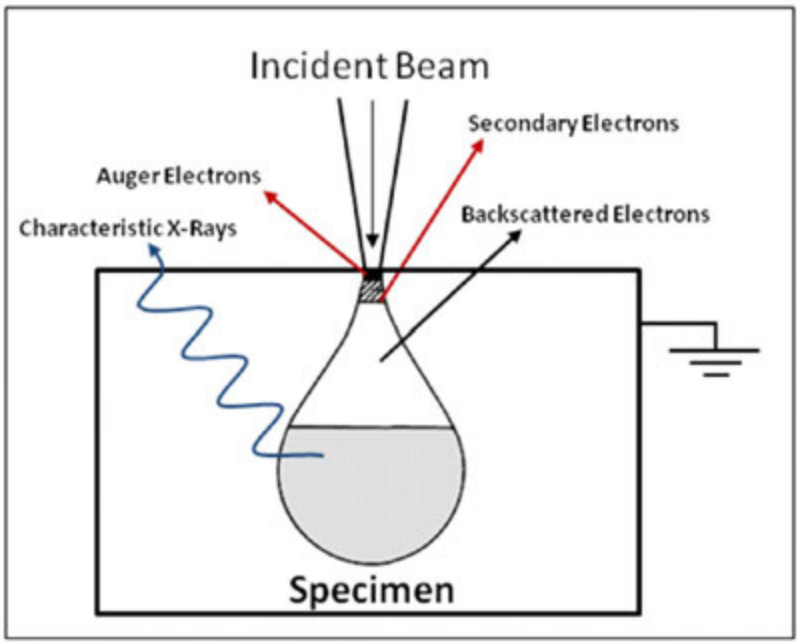

FIG. 4.106. A schematic diagram illustrating the interaction of an incident electron beam with a solid specimen [4.273].

[2] The term ‘surface-sensitive’ is commonly used to describe a technique in which the measured signal arises from the atoms nearest the sample surface and does not necessarily reflect the bulk material.

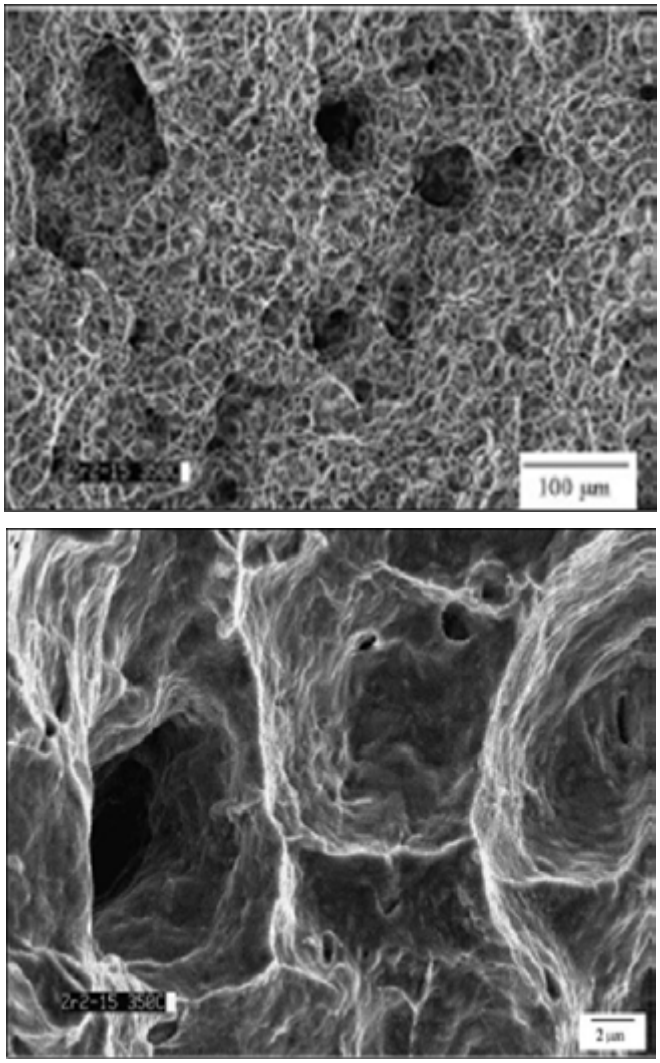

FIG. 4.107. Secondary electron imaging micrographs, showing the ductile fracture surface of a Zircaloy-2 sample following creep testing to failure (this image was published in Ref. [4.274], copyright Elsevier, 2006).

A fraction of incident electrons that have been inelastically scattered (i.e. lost energy due to atomic collisions) escape the solid and are detected as backscattered electrons. A backscattered electron image is useful in discerning near-surface elements of different atomic mass. The larger electron clouds associated with heavier atoms will scatter more incident electrons and appear brighter in the micrograph. This technique is not as surface sensitive as secondary electron imaging since backscattered electrons are of higher energy than secondary electrons and escape from slightly deeper in the sample. As an example, backscattered electron imaging can be used to distinguish hydride phases in zirconium metal by exploiting the mean atomic number contrast between the two [4.275].

Energetic impact between incident electrons and sample atoms can also eject sample electrons from core energy levels. The energy imparted to the sample by the incident electrons can be dissipated by two processes from which spectroscopy can profit.

The first involves the emission of Auger electrons, discussed in Section 4.13.7.5. The second occurs when higher level electrons fill the core level vacancy and, in doing so, emit discrete X rays of an energy that is specific to the excited element. Thus, surface chemical information is obtained by energy dispersive X ray (EDX) spectroscopy. Similar information

can be acquired by a variant of EDX known as wavelength dispersive X ray (WDX) spectroscopy. The WDX excitation process is fundamentally identical to EDX, but the techniques differ in data collection. While an EDX spectrometer directly measures the energy of photons emitted from the sample, a WDX spectrometer uses the principle of diffraction on a crystal or grating to disperse the emitted X rays according to their wavelength. By mechanically moving the spectrometer components, each wavelength in a given range is detected in sequence. Since X rays are diffracted, the detector need not be in the line of sight of the sample and WDX is frequently employed to investigate radioactive specimens (e.g. Zr components removed from nuclear reactors) because shielding can be placed between the sample and detector. Since X rays are not inelastically scattered in the same manner as electrons, typical sampling depths in metals are 2–3 μm, depending on the element and energy of incident electrons. Since EDX and WDX involve the detection of X rays, the spectral lines are labelled by X ray notation. In addition, a subscript α, β or γ is used to describe the energy of the relaxation process, as shown in Fig. 4.108 [4.276].

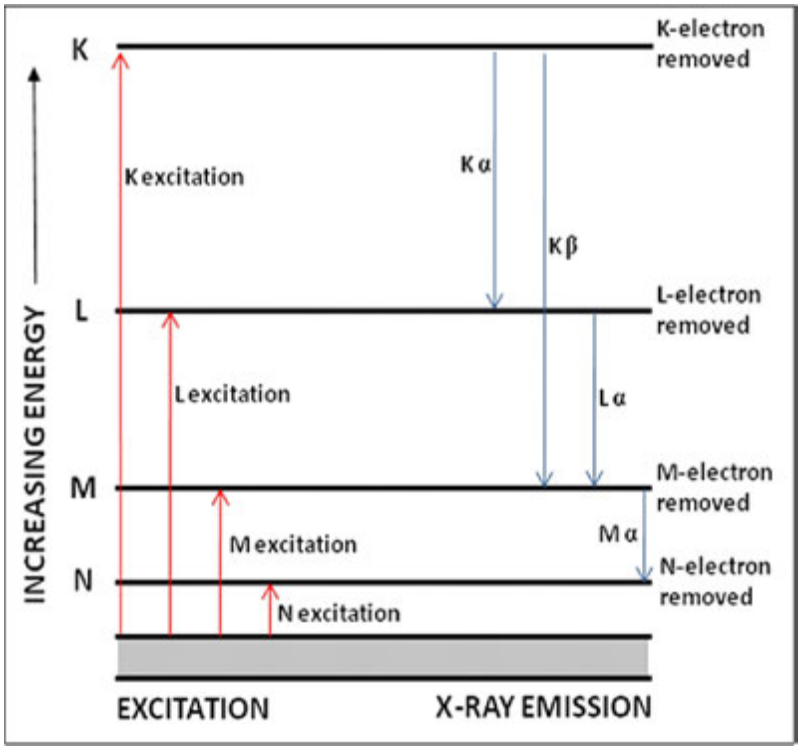

FIG. 4.108. An energy level diagram describing EDX nomenclature (reproduced from Ref. [4.276], with permission of Springer).

Several X ray lines may be apparent for Zr in an EDX spectrum. These lines and their corresponding energies are given in Table 4.28 [4.276]. EDX spectroscopy is typically employed for the characterization of surface films by elemental analysis (either spot analysis or mapping). For example, as shown in Fig. 4.109 [4.277], this technique has been used in corrosion studies of Zr-Nb alloys to distinguish Nb-rich precipitates from a ZrO_2 matrix.

TABLE 4.28. EDX LINES FOR ZIRCONIUM [4.276]

X ray line	Energy (keV)
K_α	15.747
K_β	17.669
L_α	2.0420
L_β	2.1240 2.2190
L_γ	2.3030

On some materials, bombardment with an electron beam can generate radiation with wavelengths in the visible or near-visible region, a phenomenon known as cathodoluminescence. In semiconductors, this phenomenon occurs owing to the recombination of electron-hole pairs brought about by an electron dropping from the conduction band across the band gap to the valence band. This recombination produces a photon that is equal in energy to the band gap of the material. Although not prevalent, cathodoluminescence imaging techniques have shown promise for investigating the distribution of low concentrations of alloying elements in oxides formed on Zr alloys. The exact mechanism of cathodoluminescence from zirconium oxides is still a matter of debate [4.278, 4.279].

4.13.7.5. Auger electron spectroscopy

Although the Auger process can be stimulated by X rays, ion bombardment or gamma irradiation, electron beams are most often used for primary excitation owing to the ease of Auger electron generation at high beam currents (from 0.05–5 μA) and the ability to electrically focus and deflect electrons [4.270]. Auger electron spectroscopy is a technique that provides elemental analysis, complementary to X ray photoelectron spectroscopy (XPS), which is also known as electron spectroscopy for chemical analysis. Typically, owing to their low energy and small inelastic mean free path, detectable Auger electrons originate from the top 2–10 monolayers, making the technique very surface sensitive. A schematic representation of the Auger process is shown in Fig. 4.110. During the Auger process, an atom is initially ionized as a result of the energy imparted by a primary electron, thus losing an electron from a core energy level (e.g. the K level in Fig. 4.110). There are two ways by which the ionized atom can 'relax'. The first is a radiative process via X rays discussed previously in Section 4.13.7.4. In a second independent and competitive process, the core level hole is assumed by a higher level electron (e.g. the L_1 level in Fig. 4.110) and the available energy is dissipated by ejecting an electron from an upper level (e.g. the $L_{2,3}$ level in Fig. 4.110). The ejected Auger electron carries a discrete kinetic energy that is element specific and independent of the energy of the excitation. Typically, several Auger transitions exist for each element and are described by a nomenclature that lists the affected energy levels chronologically. For example, the Auger transition depicted in Fig. 4.110 is labelled $KL_1L_{2,3}$. In general, Auger processes are most readily detected in light elements, while X ray production processes are more detectable for heavy elements. An Auger spectrometer can be used to analyse one particular surface location for a broad range of electron energies (i.e. many elements) or can be tuned to detect a specific energy (i.e. one element) while the incident beam is rastered over the surface to produce a map. When used in the second manner, the instrument is referred to as a scanning auger microprobe (SAM).

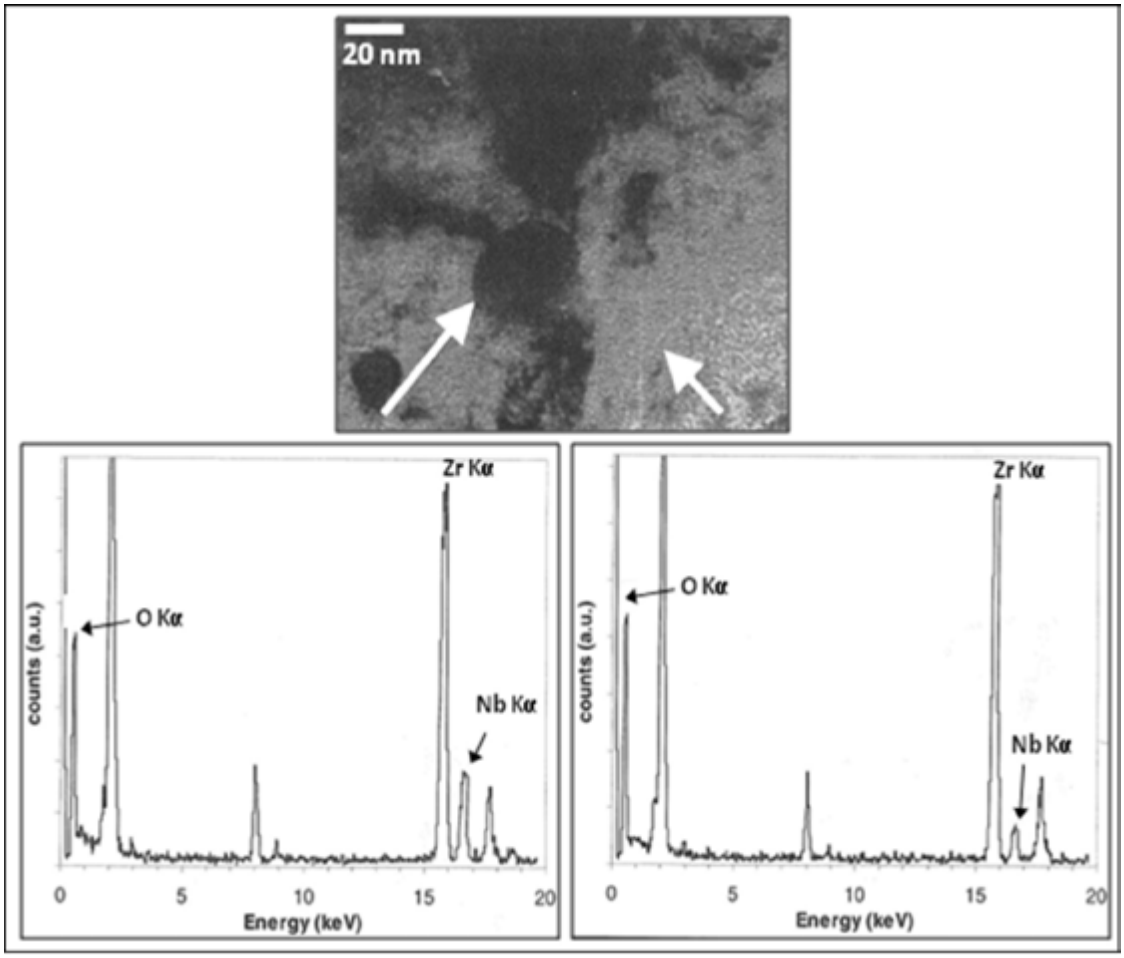

FIG. 4.109. An example of EDX spectroscopy, whereby spot analysis was used to distinguish Nb-rich precipitates from a ZrO_2 corrosion product (reprinted with permission from Ref. [4.277], copyright ASTM International).

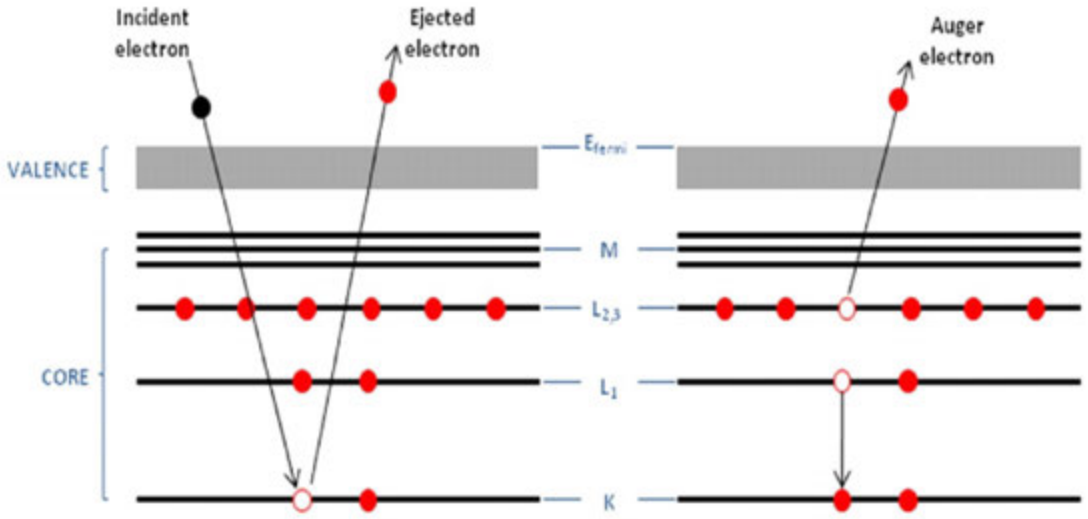

FIG. 4.110. Electron energy level diagrams describing the Auger process [4.280].

Zirconium can be characterized by Auger electron spectroscopy by several spectral lines. These lines and their corresponding energies are given in Table 4.29 [4.280]. SAM and SEM techniques are often combined to take advantage of the high resolution and depth of field of SEM in addition to the elemental and surface sensitivity of SAM. For example, SAM has been used to correlate the presence of Cl with a decrease in the fracture toughness of Zr-2.5Nb [4.281]. As shown in Fig. 4.111, a distinct correlation between areas of brittle fracture and the presence of Cl was observed by mapping the energy of a principal Cl Auger transition.

TABLE 4.29. ELECTRON ENERGIES OF AUGER TRANSITIONS IN ZIRCONIUM [4.280]

Auger transition	Electron energy (eV)
NVV (V = Valence)	24
MNN	90 115 146 173
LMM	1527 1665 1836 1921

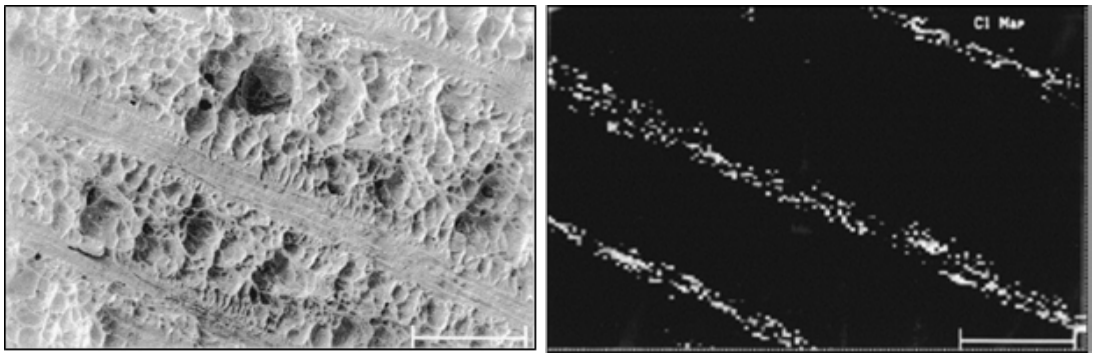

FIG. 4.111. SAM showing the presence of Cl on the fracture surface of Zr 2.5Nb (reproduced from Ref. [4.281] with permission courtesy of AECL, Canada).

4.13.7.6. X ray photoelectron spectroscopy

XPS is a technique that provides elemental and chemical information on the near-surface region of solid materials. The principle of XPS is based on Einstein's photoelectric effect and is shown in Fig. 4.112 [4.282]. Photons from a low energy X ray source (typically AlKα or MgKα), penetrate the sample and excite core and valence electrons. Providing that the energy of irradiation is sufficient, photoelectrons are ejected from the sample. The inherent surface sensitivity of XPS is derived by the same mechanism as previously described for Auger electron spectroscopy, that is, the inelastic mean free path of ejected electrons ensures that only the electrons ejected nearest the surface (i.e. within about 10 nm) escape to the detector without being inelastically scattered. The kinetic energy of the ejected photoelectrons is measured. The equation given in Fig. 4.112 reveals that by knowing the energy of the incident photon (hν) and measuring the kinetic energy of the ejected electron,

the ionization energy (or binding energy) of the electron can be calculated[3]. Signals corresponding to discrete energy levels within the atoms are recorded, which not only provide information on elemental composition but often on the chemical state of the atoms (e.g. ionization state, chemical bonding).

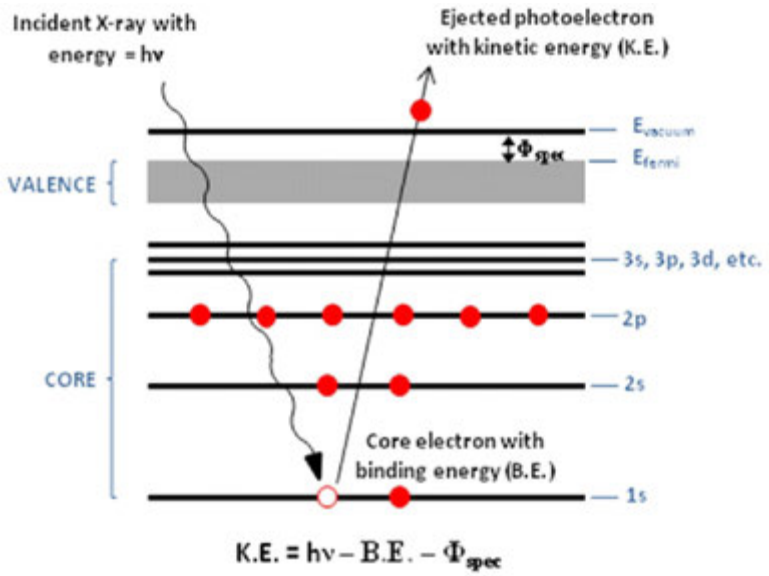

FIG. 4.112. An energy level diagram illustrating the principle of XPS [4.282].

The characteristic binding energies of core electrons in Zr are given in Table 4.30 [4.283, 4.284]. Chemical information can be obtained by observing the binding energy shift of some zirconium spectral peaks. Table 4.31 [4.282] lists the binding energy for the 3d5/2 peak for some Zr compounds.

TABLE 4.30. CORE ELECTRON BINDING ENERGIES FOR ZIRCONIUM

Core orbital	Binding energy (eV)	Reference
1s	17998	[4.283]
2s	2532	[4.283]
$2p_{1/2}$	2307	[4.283]
$2p_{3/2}$	2223	[4.283]
3s	430.3	[4.284]
$3p_{1/2}$	343.5	[4.284]
$3p_{3/2}$	329.8	[4.284]
$3d_{3/2}$	181.1	[4.284]
$3d_{5/2}$	178.8	[4.284]
4s	50.6	[4.284]
$4p_{1/2}$	28.5	[4.284]
$4p_{3/2}$	27.1	[4.284]

[3] It should be noted that a small correction is made for the work function of the spectrometer (Φ_{spec}). This work function is a known constant for a given instrument. Its derivation is beyond the scope of the present publication but is discussed in Ref. [4.281].

TABLE 4.31. ZIRCONIUM BINDING ENERGIES FOR COMPOUNDS

Compound	Binding energy (eV)
Zr	178.8
ZrO_2	182.4
ZrF_5	185.4
K_2ZrF_6	184.4
K_3ZrF_7	183.8
$KZrF_5{\cdot}H_2O$	184.8

XPS is a valuable tool for investigating the chemistry of corrosion products on Zr and its alloys. For example, it has been used to characterize the oxides on Zr-2.5Nb pressure tubes removed from CANDU nuclear reactors. Figure 4.113 [4.285] contains overlaid XPS survey spectra, showing the near-surface oxide constituents in two Zr-2.5Nb pressure tubes.

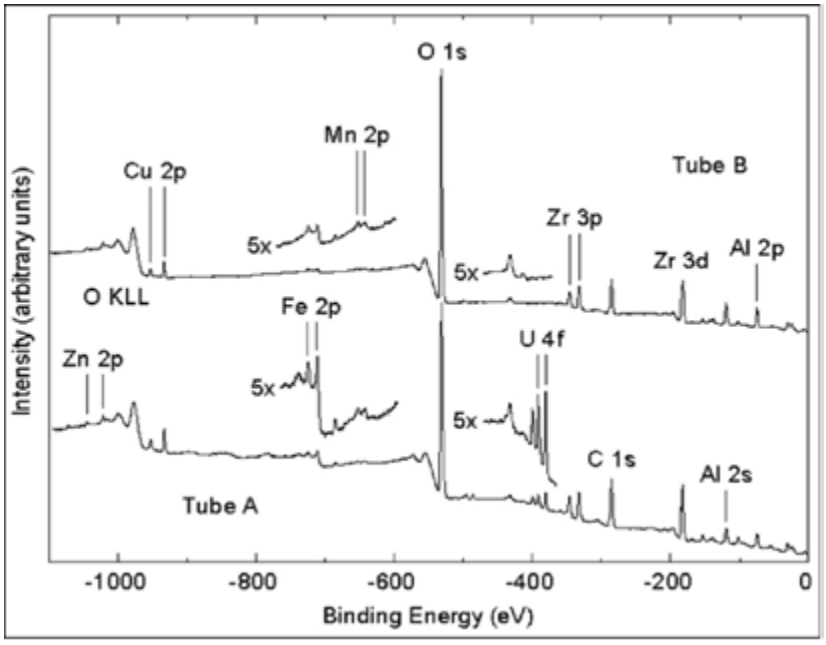

FIG. 4.113. XPS survey spectra, recorded on the outermost surface of the waterside oxide layers of two Zr-2.5Nb CANDU pressure tubes, removed after service (reproduced from Ref. [4.285] with permission courtesy of AECL, Canada).

4.13.7.7. Secondary ion mass spectrometry

Unlike the previously discussed techniques, which employ electron or X ray excitation, secondary ion mass spectrometry (SIMS) involves bombarding the specimen surface with a highly focused beam (spot size < 100 nm) of charged particles. SIMS has high elemental sensitivity and is often useful for three dimensional elemental profiling of surfaces. One benefit of SIMS when compared with most other surface analytical techniques is its ability to detect the complete mass range (i.e. all elements and isotopes from hydrogen to transuranic elements). The principle of SIMS is illustrated in Fig. 4.114 [4.273]. During SIMS analysis, a specimen is bombarded in a vacuum by a primary ion beam with a net impact energy ranging from 0.5 to 25 kV. Examples of primary ions include Ar^+, O^-, O_2^- and Cs^+. The appropriate primary ion is often dictated by the desired information. Some of the primary ions impart a fraction of their energy to the sample atoms via inelastic collisions. Energized

atoms of the solid can collide with neighbouring atoms, producing a collision cascade, which in turn may result in the ejection of secondary ions, neutral atoms or molecular clusters from the surface. While the majority of ejected atoms are neutral, a small fraction (≈5%) are ionized and can be detected through spectrometric analysis, according to their mass-to-charge ratio. This technique can be performed in a manner that is highly surface sensitive (static SIMS) or, alternatively, it can be carried out under sputtering conditions in which quantities of the surface are removed at a greater rate than in static SIMS (dynamic SIMS). For example, the sputter rate for a typical dynamic SIMS experiment on an oxide film can range from 0.5 to 5 nm/s.

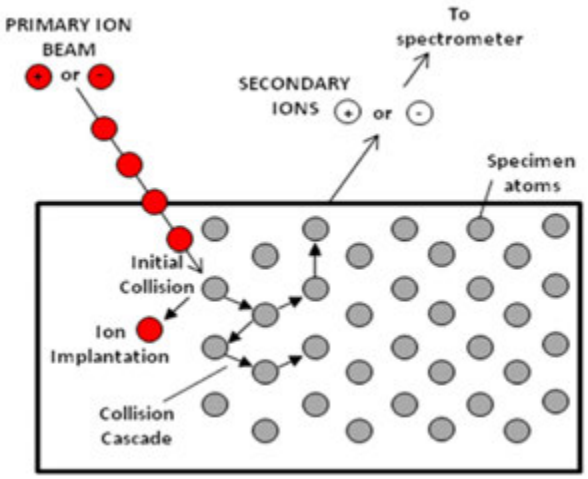

FIG. 4.114. A schematic diagram illustrating the principle of SIMS (reproduced from Ref. [4.273] with permission courtesy of AECL, Canada).

This technique is employed on zirconium to investigate oxide constituents on reactor components. Its high elemental sensitivity is exploited to detect adsorbed surface layers, deposits and corrosion products. In addition, depth profiling may be used to glean information regarding mechanisms or a component's exposure history. For example, as shown in Fig. 4.115 [4.285], SIMS has been used to investigate the deuterium and hydrogen isotope concentration profiles in waterside oxides of Zr-2.5Nb pressure tubes after service in a CANDU nuclear reactor.

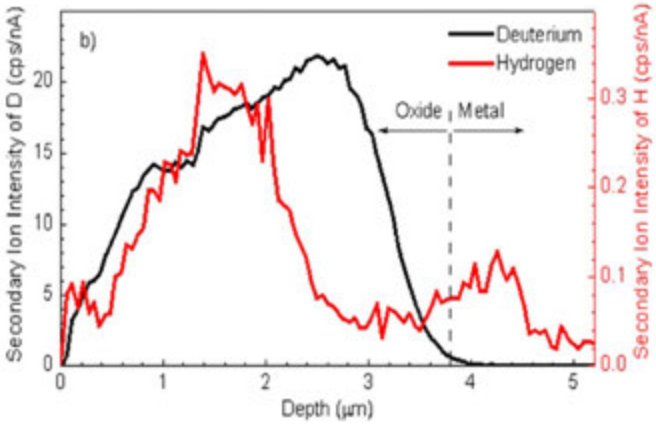

FIG. 4.115. SIMS depth profiles, showing H and D intensity as a function of depth on the waterside oxide of a Zr-2.5Nb CANDU pressure tube after service (reproduced from Ref. [4.285] with permission courtesy of AECL, Canada).

4.13.7.8. Fourier transform infrared spectroscopy

The total energy of a molecule is made up of contributions from translational, rotational, vibrational and electronic energy [4.286]. While many of the analytical techniques described in previous sections involved transitions between electronic energy levels, molecular vibrations give rise to absorption bands in the infrared region of the electromagnetic spectrum. Fourier transform infrared (FTIR) spectroscopy is a technique that exploits the absorption of infrared (IR) radiation in a specimen as a means of material characterization or measuring the thickness of surface layers. As shown in Fig. 4.116, when a material is subjected to IR radiation, the probability of absorbing the radiation is great when the frequency (or energy) of the incident radiation is equal to a vibrational energy level difference in the sample. Therefore, molecules will absorb specific frequencies that are characteristic of their structure. By measuring the intensity of the radiation that is transmitted through a sample as a function of frequency, an absorption spectrum can be inferred. For a particular vibrational mode to be observable by infrared spectroscopy, the vibration must cause a change in the dipole moment[4] of the molecule.

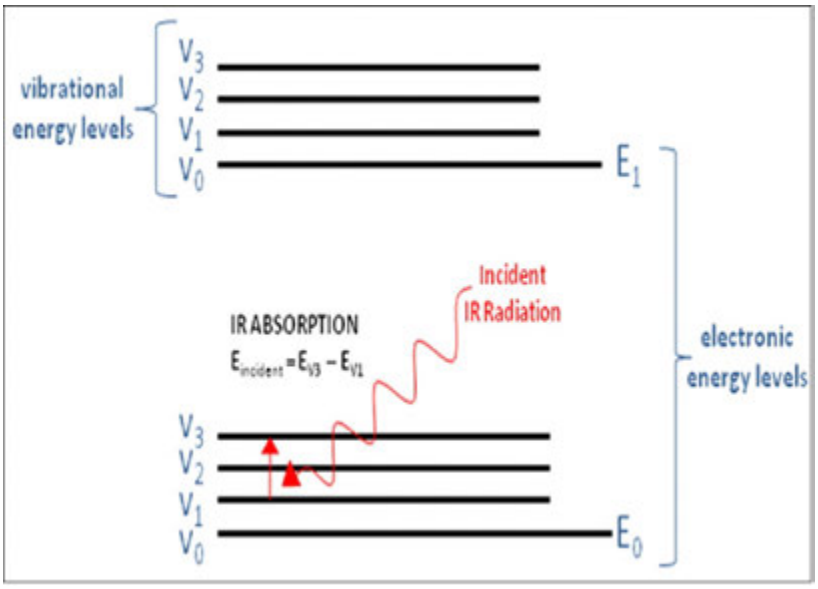

FIG. 4.116. An energy level diagram illustrating the principle of IR absorption (this image was published in Ref. [4.286], copyright Elsevier, 1964).

In FTIR spectroscopy, infrared radiation is directed at the sample through an interferometer. As shown in Fig. 4.117 [4.287], a Michelson interferometer is commonly used. The interferometer splits the radiation into two paths, which differ in length, and then recombines them to generate an interference pattern. The two beams of radiation will undergo either constructive or destructive interference depending on the difference in their path

[4] Even though the total charge on a molecule may be zero, the nature of bonding is such that there is often an asymmetry in the distribution of electrons, producing a net positive and a net negative location. Such a molecule is referred to as a dipole. The magnitude of the dipole, known as a dipole moment, is a function of the magnitude of charges and the separation between them.

length. Since one beam line is reflected off a movable mirror (moving at a constant velocity), the interference pattern generated by the interferometer is a function of time. Following interaction with the sample, the resulting signal is subjected to a mathematical process known as a Fourier transform, which transforms the data from the time domain (i.e. intensity as a function of mirror position) to the frequency domain (i.e. intensity as a function of wavelength) to produce the desired spectrum.

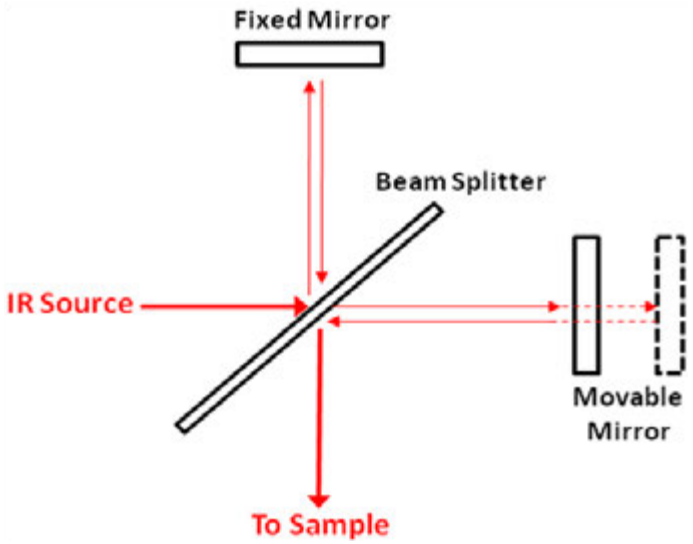

FIG. 4.117. A schematic diagram of a Michelson interferometer (reproduced from Ref. [4.287] with permission of Springer).

An alternative to FTIR is to collect infrared spectra by dispersive methods, which use a scanning monochromator to pass infrared radiation through the sample one wavelength at a time. FTIR spectroscopy holds great advantages over dispersive infrared spectroscopy in that it can collect data from a large wavelength range simultaneously, allowing for fast data acquisition and a large signal-to-noise ratio. FTIR spectra are plotted as intensity versus inverse wavelength, known as wave number, in cm^{-1}.

FTIR can be used to non-destructively characterize corrosion films on Zr alloys. Zirconium oxide absorption bands are observed below 800 cm^{-1} [4.288]. In addition, oxide film thicknesses on zirconium alloys are estimated accurately by FTIR. When FTIR spectra are collected in reflectance mode, secondary interference patterns are generated by the oxide film. By knowing the incident wavelength, the retardation of radiation (observed as a shift between primary and secondary interference patterns) can be used to calculate oxide thickness without destructive examination [4.288].

4.13.7.9. Raman spectroscopy

The Raman effect is a light-scattering effect observed as a change in frequency for a small fraction of monochromatic incident light as a result of interaction with a material. The scattering is a result of coupling between the incident radiation and vibrational energy levels of molecules within the sample; both incident and scattered radiation are within the visible region of the electromagnetic spectrum. An energy level diagram, describing the Raman

scattering process, is shown in Fig. 4.118. When an incident photon interacts with a molecule, the majority of the light is transmitted, refracted, reflected or scattered at the same energy as the incident photon, a process known as Rayleigh scattering. A small portion of the light will undergo inelastic scattering in which the incident and resultant photons are of different energy. This scattering is known as the Raman effect and can occur in two ways. When the incident light promotes an electron from the ground state to a virtual excited state, it can then relax to a vibrationally excited state (v_2 in Fig. 4.118). The result is a scattered photon of lower energy than the incident photon — a process known as Stokes scattering. Interaction with an incident photon may promote an electron from an already excited state (v_2 in Fig. 4.118), which can then relax to the ground state. The result is a scattered photon with greater energy than the incident photon — a process known as anti-Stokes scattering. At room temperature, the initial population of the ground vibrational state is often greater than the excited states and the most intense Raman signal often results from Stokes scattering.

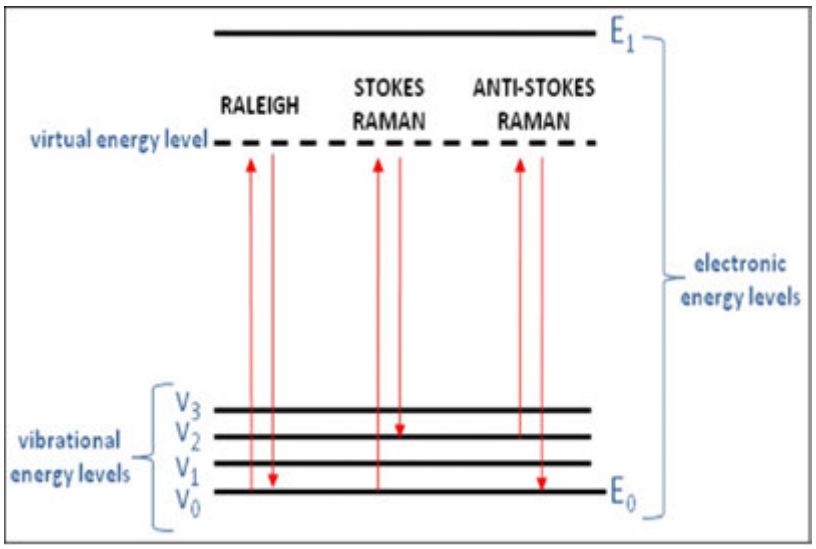

FIG. 4.118. An energy level diagram depicting the definition of Raman scattering.

A large number of molecules are Raman active and exhibit characteristic Raman shifts that can be used as a fingerprint to aid in their identification. For a particular vibrational mode to be observable by Raman spectroscopy, the vibration must cause a change in polarizability of the molecule. This property makes Raman and FTIR spectroscopy complementary techniques. Raman spectra are plotted as intensity versus wave number in cm^{-1}.

Raman spectroscopy has been used in corrosion studies to determine the composition of oxide films on zirconium alloys [4.289]. Furthermore, as shown in Fig. 4.119 [4.290], oxide phase changes have been observed by a change in Raman response following exposure to high temperature aqueous solutions. A phase change from tetragonal to monoclinic has been shown to compromise the corrosion resistance of zirconium alloys. Raman spectroscopy has also been used to measure and map the stress distribution in zirconium oxide films [4.290].

4.13.7.10. X ray absorption spectroscopy

As discussed for XPS in a previous section, if a material is subjected to X rays of sufficient energy, the X ray may be absorbed, causing the ejection of a core level electron (see Fig. 4.112). Since the binding energy of core level electrons is specific to each element, and the absorption of X rays occurs for energies near and above the binding energy, X ray absorption is also an element specific process. In a technique known as X ray absorption fine structure (XAFS) spectroscopy, the incident photon energy is tuned across the absorption threshold of a particular core level of an element in the material of interest. As shown in Fig. 4.120 [4.291], a sharp increase in the X ray absorption spectrum is observed when the energy of the incident X rays reaches and exceeds the binding energy of a core electron. This well defined step is known as an absorption edge. The XAFS spectra can be analysed to provide information regarding the electronic properties and local atomic structure of the sample. Typically, synchrotron radiation is used for XAFS spectroscopy since it can provide a full range of X ray wavelengths and can be tuned in energy [4.291]. The XAFS spectrum is divided into two regimes, which are related but treated separately to yield different information [4.291]. The near edge region of the spectrum from approximately 5 eV below to 50 eV above the absorption edge is known as the X ray absorption near edge structure region. The region of oscillating absorption extending beyond 50 eV above the absorption edge is known as the extended XAFS region. The oscillations in absorption in the extended XAFS region are caused by interference between the outgoing and backscattered photoelectron waves. The X ray absorption near edge structure is strongly sensitive to the formal oxidation state and coordination chemistry of the absorbing atom, while the extended XAFS is used to determine the coordination number, atomic distances and species of the nearest neighbouring atoms [4.291].

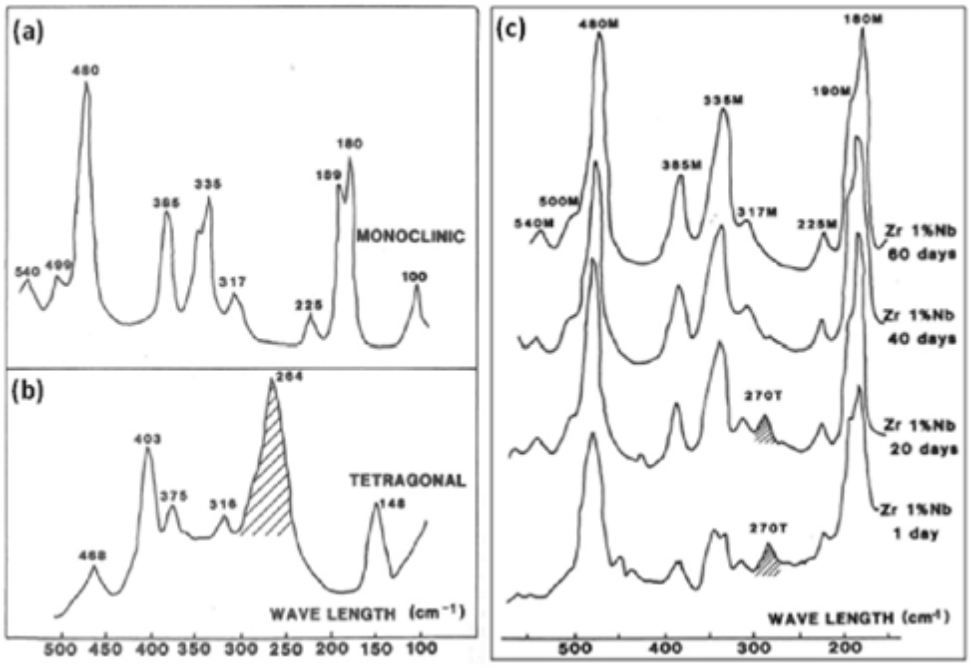

FIG. 4.119. Raman spectra, showing sintered reference material: (a) monoclinic, (b) tetragonal yttria stabilized ZrO_2, (c) the phase evolution of a corrosion film on Zr-1Nb with time (reprinted with permission from Ref. [4.290], copyright ASTM International).

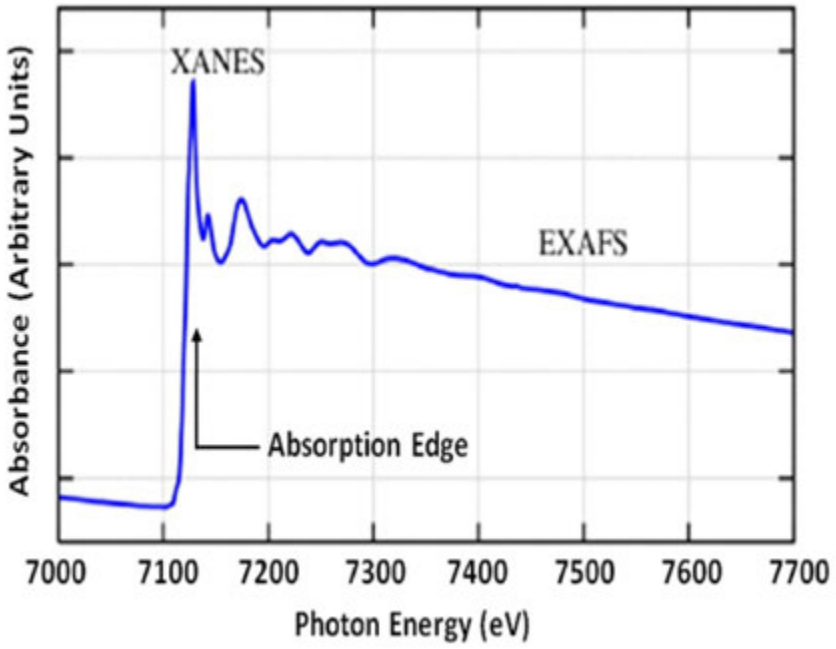

FIG. 4.120. An example XAFS spectrum, showing the absorption edge and the distinction between X ray absorption near edge structure (marked XANES) and extended X ray absorption fine structure (marked EXAFS) [4.291].

X ray absorption spectroscopy has been used to investigate the formal valency and coordination environment of Zr and Nb in the both the metal substrate and oxide film of Zr-2.5Nb alloys after corrosion testing in simulated nuclear reactor environments [4.292]. For example, examination of extended XAFS spectra recorded on various cross-sectional locations of corroded samples showed that Nb within the oxide layer retains some metallic character near the metal–oxide interface but adopts an oxide character at locations further into the oxide from the interface [4.292].

4.13.7.11. Electron backscattered diffraction

Electron backscattered diffraction (EBSD), employed as an additional technique to SEM, has emerged as a valuable tool for characterizing the crystal structure, grain orientations, point-to-point orientation correlations and local texture of polycrystalline materials. Figure 4.121 [4.293] is a schematic diagram outlining the basic principles of EBSD patterns (known as Kikuchi patterns). Incident electrons diffract from the sample surface following Bragg's law of diffraction. Each crystallographic plane forms a Kikuchi band. The band intersections correspond to a prominent zone axis within the crystal. The analysis of these patterns allows for direct measurements of the crystal orientation with respect to the sample surface to be obtained. Modern computers can easily index these Kikuchi patterns for the statistical analysis of large areas of the material. Once the EBSD data have been obtained, the information is available to determine specimen texture (pole figures and orientation distribution functions), grain size and shape, internal plastic strain, grain boundary interactions (e.g. twinning characterization) and phase boundary interactions (i.e. preferential precipitation of SPPs). For a more detailed description of data manipulation and analysis please refer to Ref. [4.294]. The spatial resolution of the EBSD technique is related to the electron beam diameter, and this is dependent on the electron source and the probe current.

Typical SEM conditions of 0.1 nA probe current and 20 kV accelerating voltage will give a beam diameter of 2 nm for a field emission gun source. The resulting spatial resolution greatly depends on sample quality and SEM operating conditions [4.295]. Common issues using EBSD include drift (either beam drift or stage drift), resulting in distorted images, and data 'cleaning' techniques. Being aware of these issues greatly decreases the likelihood of misinterpreting the results. Modern software addresses the issues resulting from drift, a necessary adversary when attempting to characterize fine grained materials such as a Zr-2.5Nb pressure tube. For more information regarding the risks associated with cleaning EBSD data, please refer to Ref. [4.296].

For zirconium alloys, this technique has been employed to measure microtexture in Zr–2.5Nb tubing [4.297], determining the crystallography relationship between α–β phase transformations [4.298] and hydride-α phase boundaries [4.299], microstructure (e.g. grain size) [4.300], twinning morphologies [4.301–4.303], and stress corrosion crack morphologies [4.291].

Figure 4.122 [4.299] is an image collected in a study of preferential hydride precipitation in Zircaloy-4. Utilizing EBSD, the statistics relating the δ-hydride–α-Zr habit planes and precipitation were evaluated. Figure 4.123 shows an EBSD band contrast map (image quality map) of Zr-2.5Nb pressure tube material [4.300]. Here, EBSD was used to obtain statistical data on grain structure in the fine grained Zr-2.5Nb pressure tubes. Using clear images, it was reported that the grain sizes obtained with EBSD were statistically smaller compared with data collected using secondary electron images of the same material, illustrating the power of using EBSD for grain size measurements. The final example shows EBSD results of a stress corrosion crack in Zircaloy-4, Fig. 4.124 [4.293]. Some cracks were not discernible with traditional secondary electron imaging but were observed clearly with EBSD. The texture of the material around the flaw was examined showing the local textures of transgranular cracks. Krishna et al. [4.304] exploited the benefits of EBSD to study the phase transformation kinetics of the β → α transformation in Zr alloys. Using the available data from EBSD, coupled with advanced algorithms, the pretransformation microstructures were successfully reconstructed. Krishna et al. [4.305] also used EBSD to investigate the microstructural and textural developments during the fabrication of Zircaloy-4 fuel cladding. Material taken from different stages of the fabrication process were characterized with EBSD giving new quantitative insights into the development of crystallographic texture and microstructure. Saintoyant et al. [4.306] studied the effect of an applied stress on the mechanisms and kinetics of recrystallization of Zircaloy-4 using EBSD. They showed that when applying stresses during the recrystallization process, the growth stage is slowed and the nucleation rate is dependent on the stress amplitude.

4.13.7.12. Transmission electron microscopy

Current generations of TEM offer imaging of microstructural features with a spatial resolution of ≈ 1 nm. Applications include the qualitative and semiquantitative elemental analyses by EDX spectroscopy, and crystal structure and orientation determination of features and phases using electron microdiffraction [4.307]. Light element detection and quantification is best performed using electron energy loss spectroscopy [4.308]. In Zr alloys, it is possible to distinguish the three hydride phases from one another and from α-Zr by their respective plasmon loss energies [4.309]. The Burgers vectors of the various types of dislocations in Zr alloys can be determined by using selective operating reflections [4.310].

In neutron irradiated Zr alloys, it is important to identify the <c>- and <c+a>-dislocations that contribute to irradiation growth [4.311].

The first step to prepare an electron transparent specimen is to section the bulk material into ≈ 0.12 mm thick wafers using a low speed diamond saw. For preliminary thinning to a thickness of 100–200 μm, mechanical polishing is used first, followed by chemical polishing in a solution of 5% hydrofluoric acid and 40% nitric acid in water at room temperature. Discs, 2.5–3 mm in diameter, are then punched out from the wafers and polished to perforation to attain electron transparency. This final thinning is accomplished by jet electropolishing with a solution of 5% perchloric acid in methanol or ethanol, at a temperature of 223 to 228 K (−45°C to −50°C), to reduce the formation of hydrides. The current used is about 70 mA at a potential of 20–70 V DC [4.312]. The usable foil thickness for Zr alloys is typically ≤ 300 nm at an operating voltage of 300 keV with TEM. Although high quality electron transparent TEM foils can readily be made, as shown in Fig. 4.125, some Zr material, such as Zircaloy, tends to form surface hydrides during electropolishing. Hydride formation is usually exacerbated when thinning is done around room temperatures. Such hydrides can be recognized by imaging with stereoscopic pairs or by the appearance, when viewed under appropriate diffraction conditions, of large strain fields caused by stress relaxation at the foil surfaces. Surface hydrides may precipitate in freshly prepared and apparently clean foils during examination in the TEM. This phenomenon is made worse by focusing the electron beam and is probably stimulated by heating from the beam, although it is also possible that there is a contribution from ballistic electronic interactions with the energetic electron beam.

Ion beam sputtering is also used in the final thinning stage for the preparation of thin foils for TEM, particularly for very coarse (e.g. cast) microstructures or where an interface with a non-conducting phase, such as an oxide, needs to be studied. Unfortunately, serious problems can arise when thinning Zr and its alloys with ion beams. Initial TEM observations [4.313] of Zr that had been thinned in a typical ion milling machine, using Ar ions at an accelerating voltage up to 10 kV, resulted in specimens that appeared to have become severely damaged, containing high densities of dislocations or twins or both. Because mechanical damage on such a scale could be ruled out, it was clear that another mechanism was responsible for these strange microstructures; the cause [4.314] was extensive hydrogen absorption, leading to massive hydride formation. To gain some understanding of the mechanism and hence minimize hydrogen absorption for future applications, several models of ion beam machines were tested under a variety of milling conditions. In addition to examining specimens by TEM, the depth profile of the hydrogen concentration was measured by SIMS. In the most severe cases of hydrogen absorption, macroscopic distortion of a thin specimen into a dome-like shape was found to occur during ion beam thinning; see Fig. 4.126. This shape is caused by the large volume increase [4.315] that accompanies the transformation of Zr into one or more of the three possible ZrH phases, γ, δ and ε. The resulting microstructure, an example of which is shown in Fig. 4.127, is typical of such hydrides.

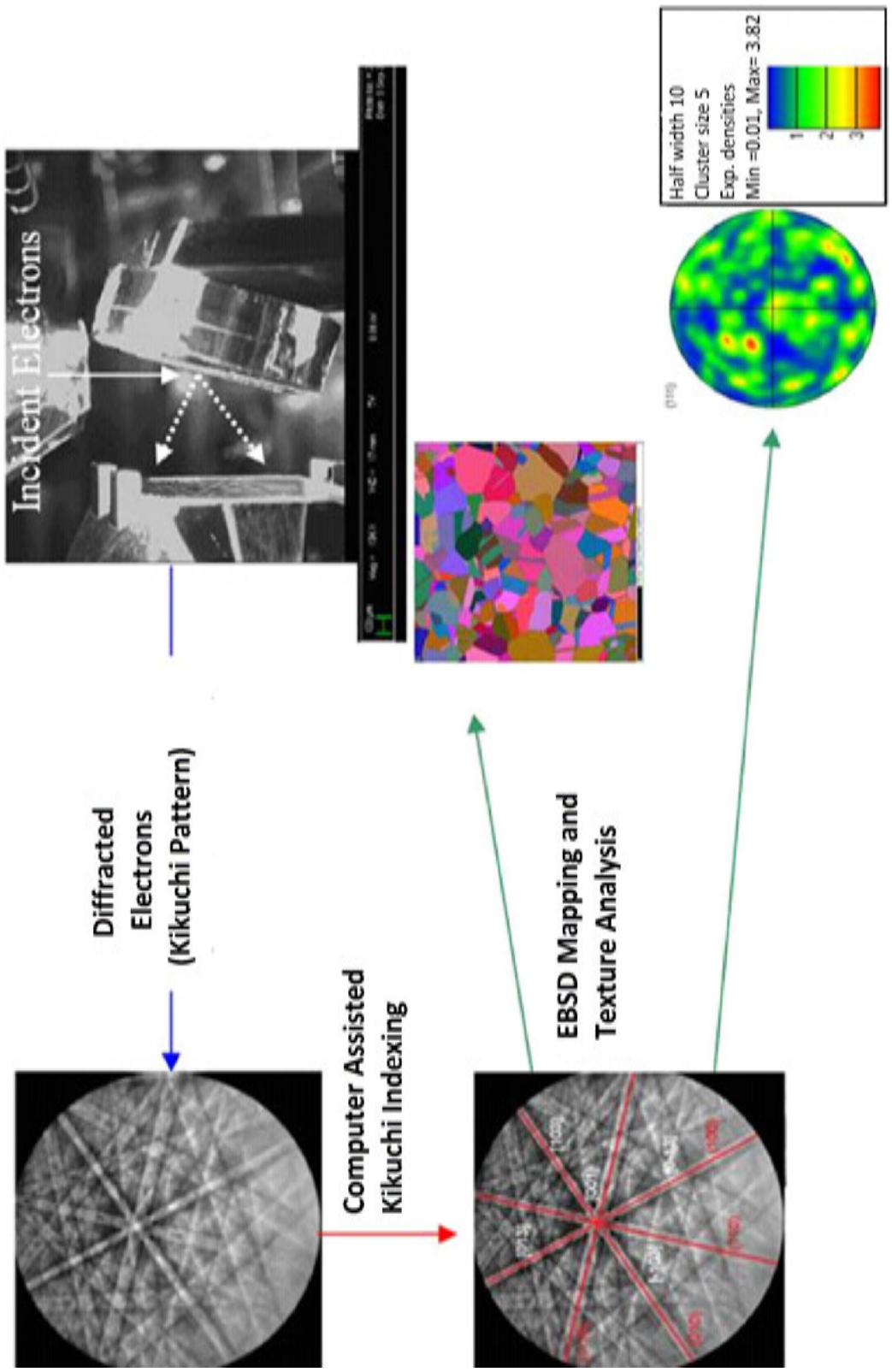

FIG. 4.121. Schematic diagram outlining the principles of electron backscatter diffraction patterns (reproduced from Ref. [4.293] with permission courtesy of AECL, Canada).

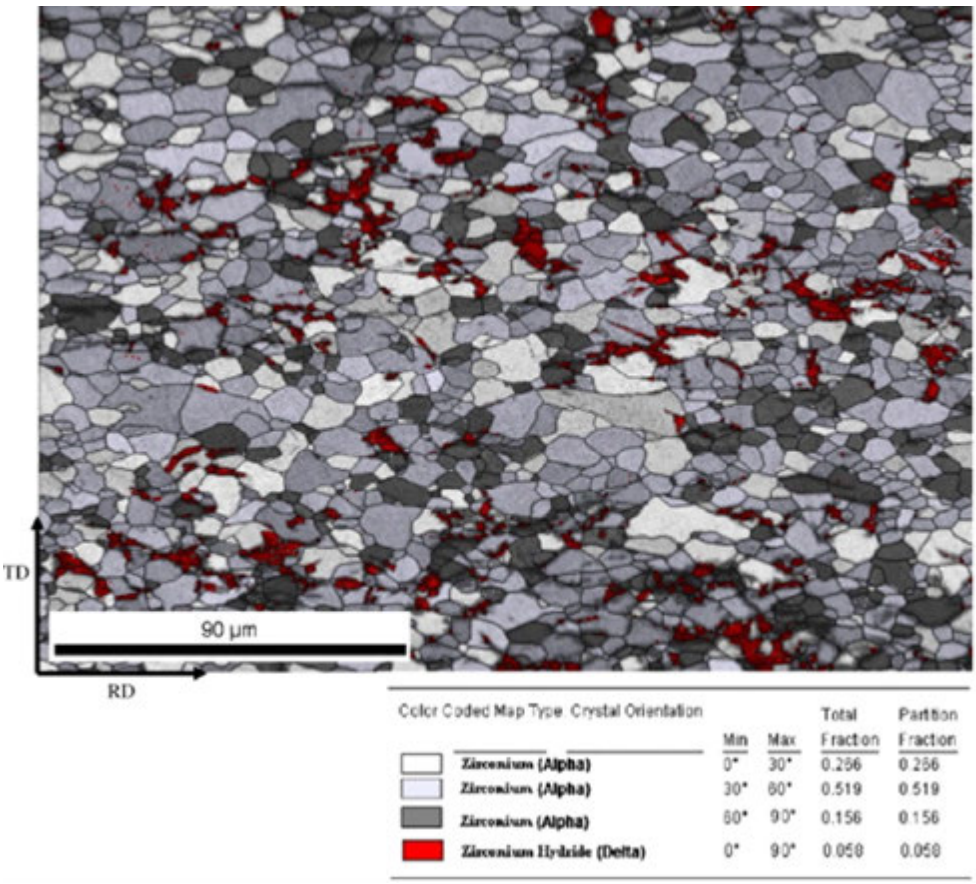

FIG. 4.122. EBSD map showing α-Zr and δ-ZrH (this image was published in Ref. [4.299], copyright Elsevier, 2010).

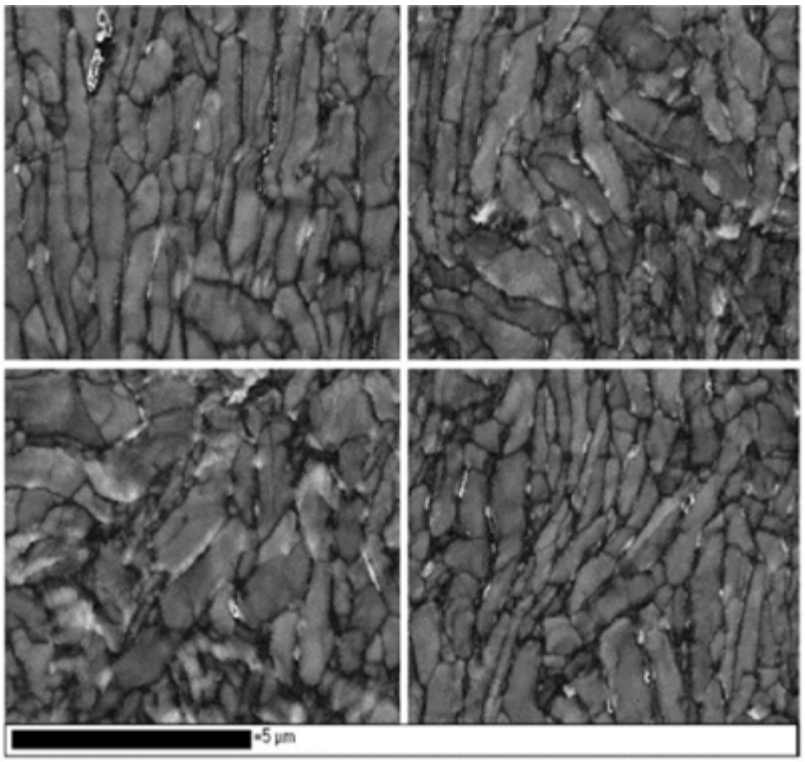

FIG. 4.123. Band contrast images showing the microstructure of Zr-2.5Nb using EBSD (this image was published in Ref. [4.300], copyright Elsevier, 2009).

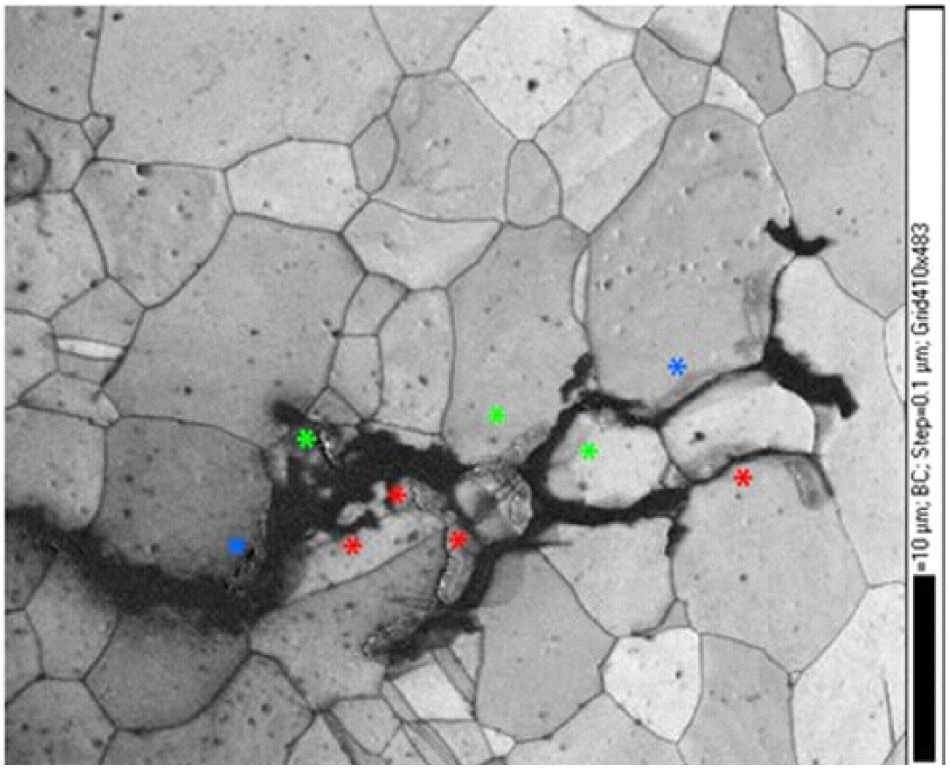

(a)

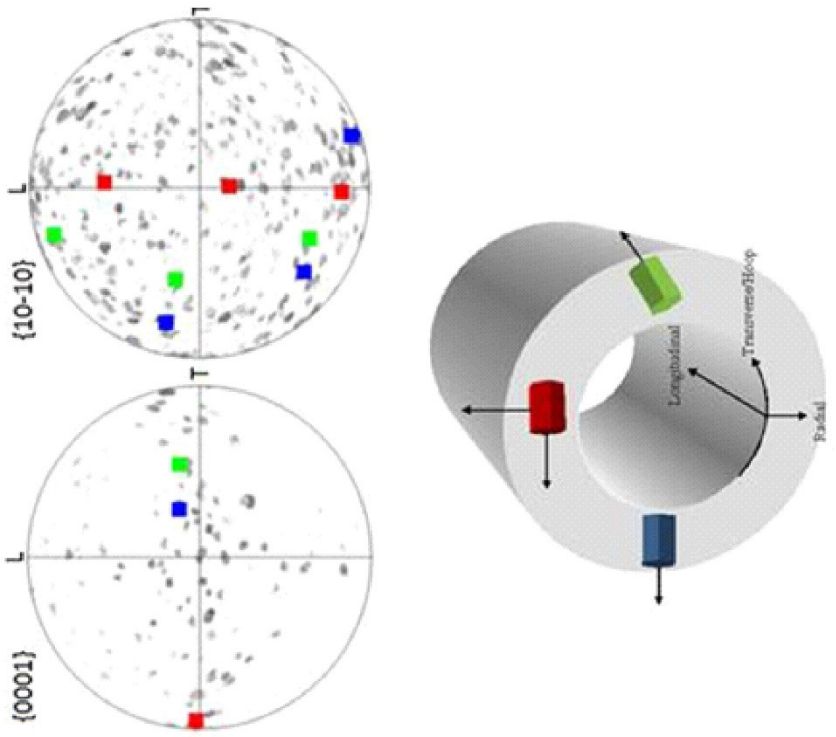

(b)

FIG. 4.124. EBSD band contrast map of stress corrosion cracking in Zircaloy-4 with locations: (a) showing the representative texture in the pole figures (b) (reproduced from [4.293] with permission courtesy of AECL, Canada).

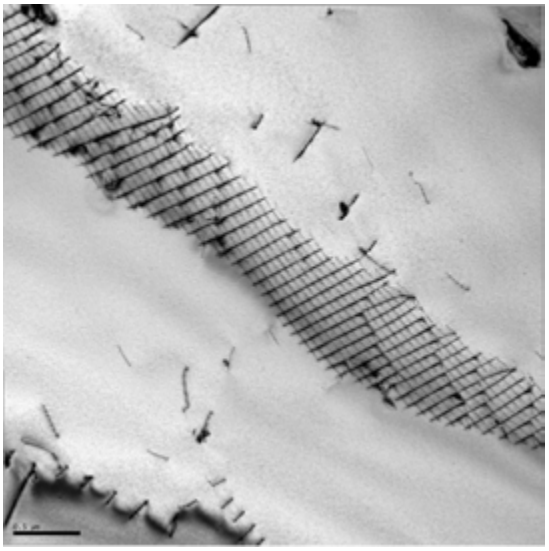

FIG. 4.125. A transmission electron micrograph of a thin foil prepared from annealed Zr-0.75 at. % Fe, showing dislocations in a grain boundary.

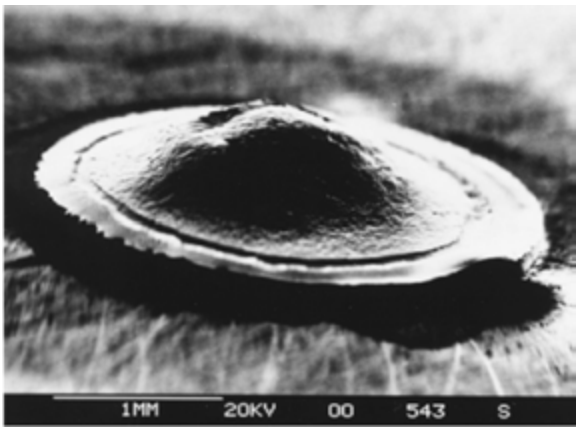

FIG. 4.126. SEM image of a 3 mm disc specimen of Zr, thinned to perforation by ion beam sputtering at room temperature (reproduced from Ref. [4.314] with permission courtesy of Cambridge University Press).

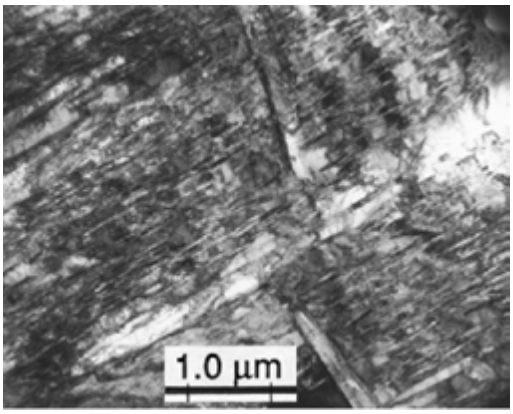

FIG. 4.127. Typical microstructure of a Zr disc specimen, observed by TEM, after conversion to ZrH following ion beam thinning at room temperature (reproduced from Ref. [4.314] with permission courtesy of Cambridge University Press).

The strong chemical affinity of zirconium for hydrogen and the rapid diffusion of H through the Zr lattice, even at room temperature [4.316], guarantee that hydriding will take place in the presence of hydrogen, providing a clean Zr surface is available. The role of the ion beam sputtering is therefore to continually clean the surface of the specimen. Although moisture (H_2O vapour) might be expected to be the most likely source of H in the sputtering chamber, experiments showed that this was not the case. Increasing the partial pressure of H_2O had the effect of reducing the hydrogen uptake; the transient surface absorption of O atoms from any H_2O molecules that had decomposed at the Zr surface had the effect of slowing the absorption of H ions, in common with the general inhibiting effect of oxide films on H absorption. Instead, the presence of hydrocarbon vapours was identified as the most important source of H for the hydrogenation process. Sources of hydrocarbons commonly

present in a sputtering apparatus may include back-streamed oil from the diffusion pump or rotary pump, vacuum grease and human perspiration.

To minimize the ingress of H to a Zr specimen during ion beam thinning, a number of precautions can be taken:

— Pumping the sputtering chamber with an oil-free vacuum system;
— Including a cold trap in the pump system;
— Lowering the diffusion rate for hydrogen by ensuring good heat transfer from the specimen;
— Cooling the specimen with liquid nitrogen;
— Using a high sputtering rate at a low incident angle.

An example of a Zr/ZrO_2 cross-section, thinned successfully using the technique described by Alani and Swann [4.317] in the presence of a cold trap is shown in Ref. [4.314].

Employing a high sputtering rate at a low incident angle is particularly effective when thin specimens are prepared using a focused ion beam (FIB) system, in which an ion beam is employed at glancing incidence to the final specimen plane. Cross-sections of oxidized Zr alloys have been successfully prepared with no significant hydride formation using a FIB machine, the only disadvantage being the presence in images of fine 'black spot' damage caused by the condensation of point defects that form in all Zr specimens during ion sputtering.

Since the FIB microscope was invented in the mid-1980s for semiconductor applications, the FIB technique has evolved into a powerful method for preparing plan view, cross-section and site specific TEM specimens [4.318–4.320]. Innovations such as improved ion guns, gas-assisted milling, a micromanipulator system, the addition of a high resolution SEM and an automated 'lift-out' protocol have substantially reduced the time to prepare TEM specimens to 0.5–2 hours. The in situ lift-out technique is described as follows, in Fig. 4.128.

A dual beam FIB+SEM system uses a focused Ga ion beam, accelerated up to 50 kV, for rapid or slow final milling of a specimen while being observed with the SEM. Once a feature of interest is identified on the surface of a bulk specimen, as shown in Fig. 4.128(a), it is protected by a chemical vapour deposition layer of W, Pt or C in the FIB; see Fig. 4.128(b). Two deep trenches, each 25–30 μm long, 15–20 μm wide and about 12 μm deep are rapidly milled on both sides of the targeted region, creating a 1 or 2μm thick lamella, shown in Fig. 4.128(c), (d). This milling can be done manually or by inserting the proper milling parameters in an automated program. The specimen is tilted 60° and the bottom of the specimen is cut as shown in Fig. 4.128(e). It is then tilted back to the normal position and attached to a micromanipulator by chemical vapour deposition. One side of the specimen is cut, as shown in Fig. 4.128(f), and the other side is also cut, so it can be lifted out of the bulk material, as shown in Fig. 4.128(g). It is then transferred to a copper grid, and attached to it by chemical vapour deposition, as shown in Fig. 4.128(h) and (i). The micromanipulator is then cut free of the specimen, which is now polished with a low voltage and low ion current to create three areas (windows) to electron transparency, shown in Fig. 4. 128(j) and (k) for TEM examination. A low magnification TEM micrograph is shown in Fig. 4.129. Previously thought to be difficult to make, cross-section oxides in Zr-based alloys are now routinely made by FIB for studies on the microstructure and microchemistry of the metal–oxide interface [4.321]; an example is shown in Fig. 4.130.

The in situ lift-out technique is the most versatile FIB technique because it can produce TEM specimens from site specific areas with little or no initial specimen preparation and

with a small amount of material as long as it can fit within the FIB chamber. Also, the resulting TEM specimen has minimal mechanical damage, thus making a FIB system a valuable tool for materials analysis. FIB machines can provide Ga ion currents from about 1 pA to 50 nA at an accelerating voltage range from 1–30 kV. Typically, a 30 kV ion beam from 27–6.5 nA is used for rapid initial milling. This current is lowered to the pA range, from 300–80 pA or lower at 1 kV for final polishing.

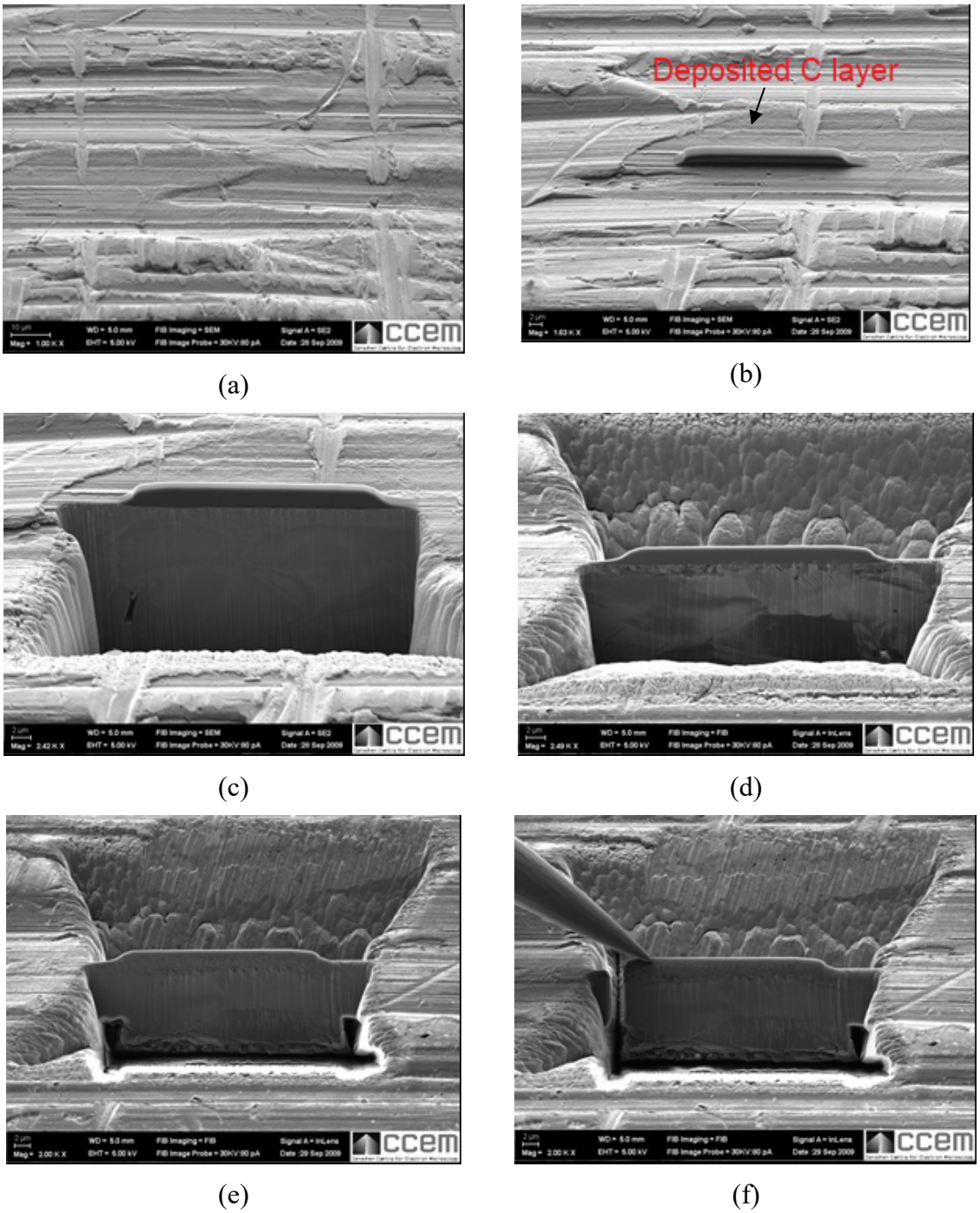

FIG. 4.128. Preparing TEM specimen A using FIB. The images show: (a) the sample; (b) a carbon layer deposited on the surface where the specimen will be made; (c) a trench milled into the material on one side of the specimen; (d) trenches milled into the material on both sides of the specimen; (e) the specimen cut at the bottom of the trench; (f) the manipulator attached to the specimen and one side cut.

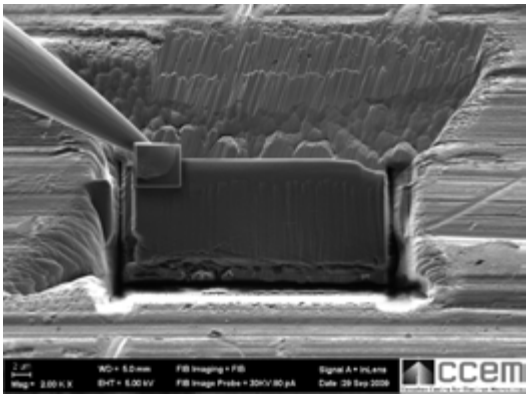

(g)

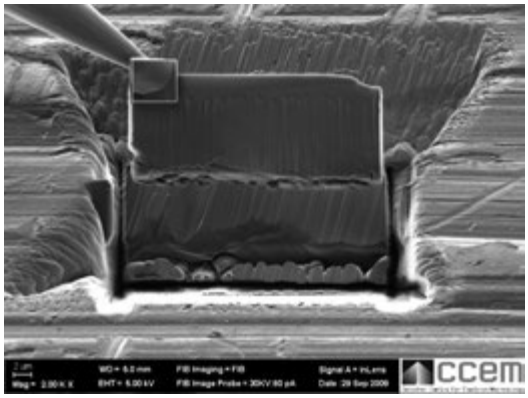

(h)

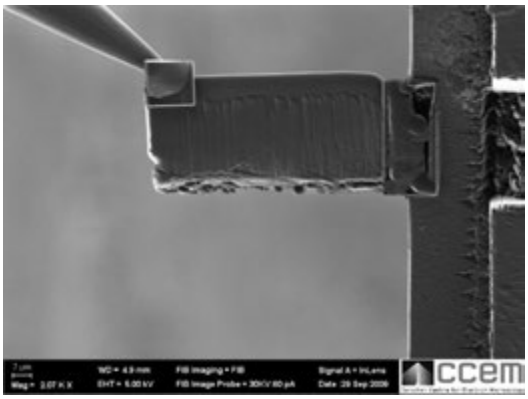

(i)

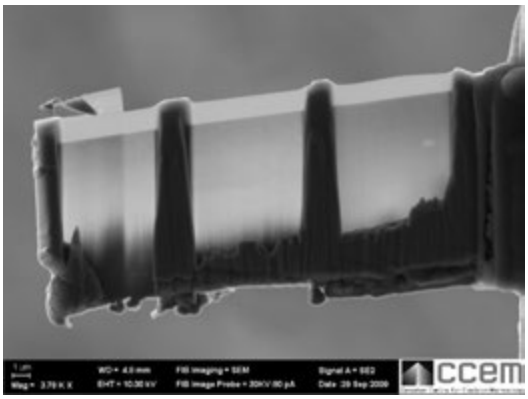

(j)

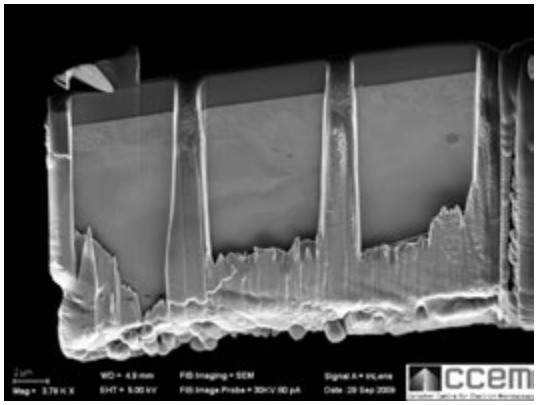

(k)

FIG. 4.128. (cont.) Preparing TEM specimen A using FIB. The images show: (g) other side cut so the specimen is completely free of the bulk material; (h) lifting the TEM specimen out; (i) TEM specimen attached to copper grid; (j) TEM specimen being polished to create three areas that are electron transparent; (k) completed TEM specimen.

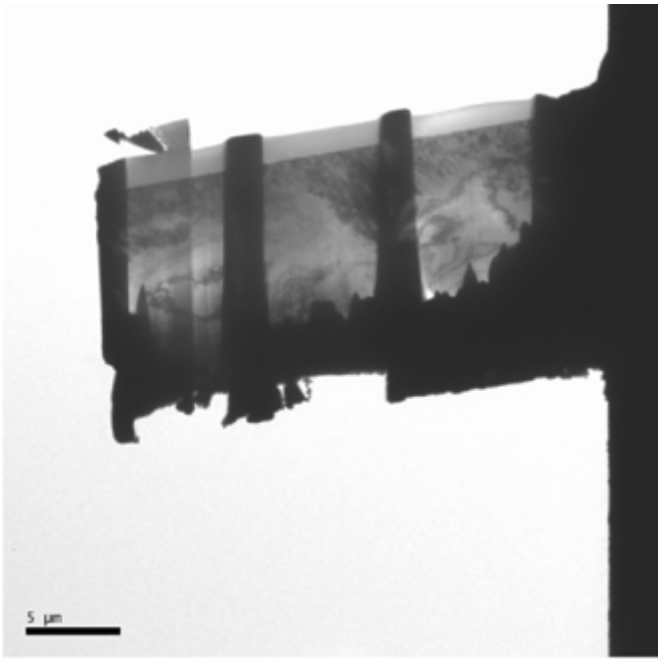

FIG. 4.129. Low magnification electron micrograph showing transparent sample made by FIB.

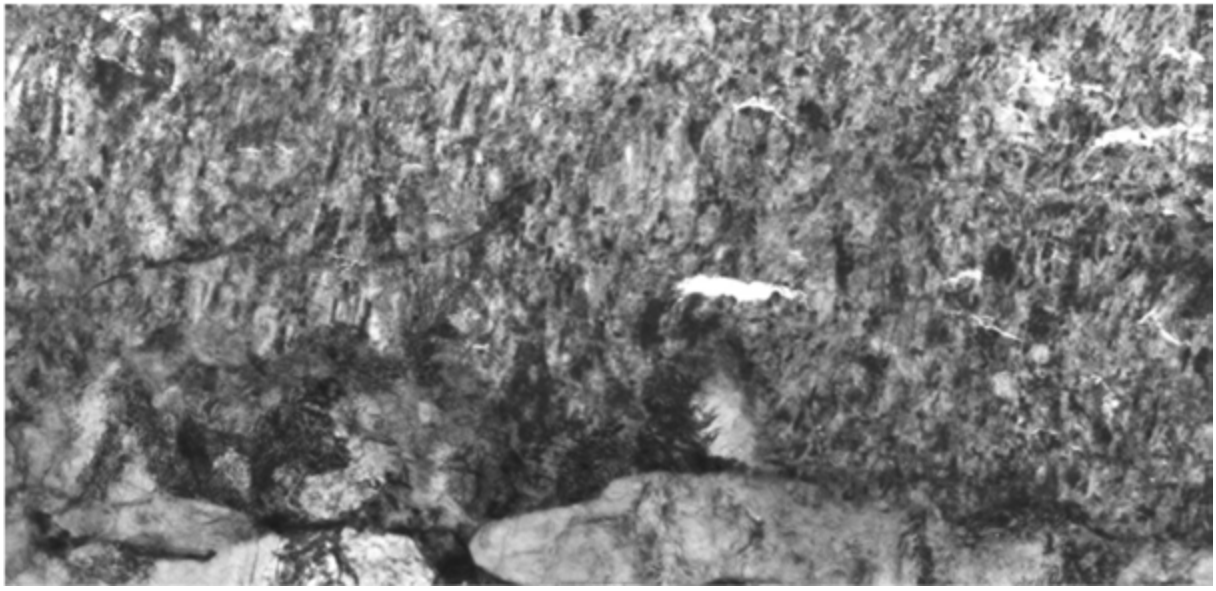

FIG. 4.130. TEM micrograph of an oxide cross-section made by FIB showing an area close to the oxide–metal interface of an oxide grown on Zr-2.5Nb pressure tube material.

Other FIB techniques for preparing TEM specimens are available, described in Ref. [4.322]. Because of the versatility of the FIB technique, it is often important to consider when a FIB technique should be used instead of electropolishing for making TEM specimens. The best jet-disc electropolishing machine costs a hundred times less than a FIB system. If there is sufficient material for specimen preparation, and site specific regions are not required, electropolishing should be the preferred method. Also, an electropolished specimen often reveals more thinned area than a TEM specimen prepared by a FIB technique.

Potential artefacts arising from poor preparation technique using FIB are discussed in Ref. [4.322]. Selection of appropriate beam currents and milling parameters is important to avoid damage caused by the ion beam (e.g. the formation of dislocation loops and curtain effects). Material redeposition can also occur if the milling box is not properly positioned. Many cubic materials exhibit strong orientation contrast that persists for many milling passes. Hexagonal materials such as zirconium, magnesium and zinc have little or no orientation contrast during ion milling. If orientation contrast is required during milling, for three dimensional reconstruction of grain structure, the orientation contrast can be restored by bleeding in a continuous flow of xenon difluoride gas during imaging [4.322].

Particles can be extracted from the metal surface using a replica technique, so they can be analysed without interference from the metal matrix [4.323]. The specimen surface is first prepared by metallographic mounting, polishing and etching to allow the particles to stand proud of the surface. Several drops of methyl acetate or acetone are dropped onto the edge of the etched section, and a piece of cellulose acetate tape is lowered at 20° onto the surface forcing the solvent ahead of the descending tape. The tape may be lightly pressed on the surface to encourage the particles to adhere to the tape, which is allowed to dry for 5 min, and then stripped from the specimen. If air bubbles are trapped between the tape and the specimen surface, replication should be repeated. Two or three replications may be performed for each specimen. The tape is secured onto a glass slide with the replicated surface facing upwards, and uniformly coated with a thin carbon film. The tape is scored and separated into small squares that are then transferred onto 3 mm diameter copper grids with the replicated surface facing upwards. The grids are then placed on a filter paper soaked with methyl acetate or acetone in a Petri dish tilted at about 30°. The bottom of the dish is then filled with acetone, so the cellulose tape is dissolved by capillarity. After the complete dissolution of the tape, the replicas are allowed to dry and they are ready to be examined by TEM.

4.13.8. Chemical analysis

Analytical chemistry techniques roughly break out into determination of the major metallic alloying elements, determination of trace impurities and determination of the interstitial elements (O, H, N and C).

Traditional techniques employed a number of wet analytical procedures for the determination of the major alloying elements such as tin, niobium, iron, chromium and nickel. Nowadays, most of the analytical work is done by spectroscopic techniques using either atomic emission spectroscopy (AES), also known as optical emission spectroscopy, or mass spectroscopy.

As a natural outcome from traditional techniques, results are provided in weights of each element and are reported in either weight per cent or parts per million by weight. In the standards used for zirconium alloy specification, the alloying and trace elements are listed by weight. With spectroscopy, the number of atoms of the target elements is counted yet the results of chemical analysis are still reported as weights. Using a unit describing the number of atoms (e.g. atomic per cent or atom fraction) improves the insight and understanding of many phenomena, simplifies phase diagrams and emphasizes effects from different isotopes. A vivid example of the latter is with the reporting of effects from protium (light hydrogen) and deuterium (heavy hydrogen) where the difference in weight is a factor of two. Counting atoms is especially important when considering nuclear reaction cross-sections. A change to reporting units of composition to reflect the atomic concentration is advocated; the first step

would be to report both weight and atomic concentrations, as has been done throughout this publication.

4.13.8.1. Atomic emission spectroscopy

In AES, the zirconium being analysed is dissolved in an acidic solution (typically a mixture of nitric and hydrofluoric acids) and this solution is aspirated into plasma. Analyte atoms in solution are aspirated into the excitation region where they are desolvated, vaporized and atomized by the plasma, emitting light in the process.

These high temperature atomization sources provide sufficient energy to promote the electrons of atoms into high energy levels. When the electrons decay back to lower energy levels, they emit light. The characteristic wavelengths of light that are emitted from each of the element ion species are broken down into spectral lines by an optical grating, and the intensity of the optical lines that are characteristic of that ion species is read by a photomultiplier tube, or a charge transfer solid state detector. The wavelengths of the light identify an element and the intensity of the light is proportional to the number of atoms of the element in the sample.

Since the transitions are between distinct electron energy levels, the emission lines in the spectra are narrow. The spectra of multielemental samples can be very congested, and spectral separation of nearby atomic transitions requires a high resolution spectrometer. Since all atoms in a sample are excited simultaneously, they can be detected simultaneously, and this is the major advantage of AES compared with atomic absorption spectroscopy (see Section 4.13.8.5).

Elements that can be routinely analysed using atomic (or optical) emission techniques include Al, B, Be, Ca, Cd, Co, Cr, Cu, Fe, Hf, Mg, Mn, Mo, Na, Nb, Ni, Pb, Si, Sn, Ta, Ti, V, W, Y and Zn. Most of these elements can be measured simultaneously with a polychromatic spectrometer.

Because the AES technique uses a liquid solution of the analyte, it is easy to create synthetic standards by dissolving known quantities of elements into solution and diluting them accordingly. The instrumental detection limits for AES are low, ranging from a few hundredths of a part per million up to several parts per million, depending on the element.

AES can further be subdivided into two methods for excitation of the sample solution. The first AES excitation technique is inductively coupled plasma (ICP). An ICP is a very high temperature (7000–8000 K) excitation source that efficiently excites and ionizes the atoms. Molecular interferences are greatly reduced with this excitation source but are not eliminated completely. ICP sources are used to excite atoms for AES and to ionize atoms for mass spectrometry. The sample is broken up into a fine aerosol mist and entrained in the flow of plasma support gas, which is typically argon. The plasma torch consists of concentric quartz tubes. The inner tube contains the sample aerosol and argon support gas and the outer tube contains flowing gas to keep the tubes cool. A radio frequency generator (typically 1–5 kW) produces an oscillating current in an induction coil that wraps around the tubes. The induction coil creates an oscillating magnetic field. The magnetic field in turn sets up an oscillating current in the ions and electrons of the support gas (argon) as the ions and electrons collide with other atoms in the support gas.

The theory and operation of an ICP spectrometer is detailed in ASTM E1479, Standard Practice for Describing and Specifying Inductively-Coupled Plasma Atomic Emission Spectrometers [4.324].

The second is direct current plasma (DCP). In the most common design, two carbon anodes and one tungsten cathode form an inverted 'Y'. Argon flow at each of the electrodes creates a thermal pinch of very high current density sufficient to dissociate and excite refractory oxide-forming elements. The DCP jet is robust and can deal with a wide variety of solution strengths and viscosities. The imperviousness of the jet to hydrofluoric acid from the initial dissolution makes it particularly useful for the analysis of zirconium materials. Detection limits and reproducibility are generally not as good as those possible with ICP-AES or ICP mass spectroscopy techniques.

ASTM procedures offer some guidance. E1552, Standard Test Method for Determining Hafnium in Zirconium and Zirconium Alloys by Direct Current Plasma — Atomic Emission Spectrometry [4.325]; while written only for hafnium, the method can be expanded to include elements such as Al, Cr, Cu, Fe, Nb, Ni, Si, Sn, Ta and Ti. The theory and operation of DCP are detailed in E1832, Standard Practice for Describing and Specifying a Direct Current Plasma Atomic Emission Spectrometer [4.326].

4.13.8.2. Mass spectroscopy

Mass spectrometers use the difference in mass-to-charge ratio (m/e) of ionized atoms or molecules to separate them from each other. Since individual isotopes of the same atom have a different mass, the isotopes can be separated from one another with a high resolution spectrometer.

By using the same liquid sample introduction system found in the ICP method as the ion source, coupled with a mass spectrometer detection system, the technique of ICP mass spectrometry is created.

The general operation of a mass spectrometer is to create gas phase ions, to separate the ions in space or time based on their mass-to-charge ratio and to measure the quantity of ions of each mass-to-charge ratio. The ion separation power of a mass spectrometer is described by the resolution, R, which is defined as:

$$R = \frac{m}{\Delta m}, \tag{4.22}$$

where m is the ion mass and Δm is the difference in mass between two resolvable peaks in a mass spectrum.

A resolution of 1000 or greater is achievable. The most common spectrometer for use in analysis of metals is the quadrapole mass spectrometer. Quadrapole mass spectrometers consist of an ion source, ion optics to accelerate and focus the ions through an aperture into the quadrapole filter, the quadrapole filter itself with control voltage supplies, an exit aperture, ion detector and electronics, and a high vacuum system.

A quadrapole mass filter consists of four parallel metal rods. Ions are admitted through an aperture at one end of the rods. Two opposite rods have an applied potential of $(U + V\cos(wt))$ and the other two rods have a potential of $(-UV\cos(wt))$, where U is a DC voltage and $V\cos(wt)$ is an AC voltage. The applied voltages affect the trajectory of ions travelling down the flight path centred between the four rods. For given DC and AC voltages, only ions of a certain mass-to-charge ratio pass through the quadrapole filter; all other ions are thrown out of their original path. An exit aperture ensures that only the selected ions are passed to the ion detector.

A mass spectrum is obtained by monitoring the ions passing through the quadrapole filter as the voltages on the rods are varied; two methods can be used: varying *w* and holding

U and V constant or varying U and V (U/V fixed) for constant w. The ion detector measures the ion flux, which is proportional to the concentration of analyte in the solution. In general, mass spectrometers have a very high resolving power and they give instrumental detection limits significantly lower than for AES techniques. The elements typically analysed by mass spectroscopy include (but are not limited to) Al, B, Bi, Co, Cr, Cu, Gd, Hf, Mn, Mo, Nb, Ni, Pb, Ru, Sm, Sn, Ta, Th, Ti, total U, ^{235}U, V, W and Zn. In the case of ^{235}U, the analyte has to be concentrated by chemical extraction techniques to improve the sensitivity.

4.13.8.3. Determination of the interstitial gases, O, H, N

Oxygen and nitrogen are analysed by inert gas fusion. A metal specimen held by a graphite crucible is fused in a helium atmosphere by an impulse type fusion furnace. The high fusion temperature releases gases that are then swept through a copper oxide bed where carbon monoxide (evolved from the reaction of oxygen liberated from the sample reacting with the graphite crucible) is converted to carbon dioxide. The specimen gases are then passed through an infrared cell that detects and measures the amount of carbon dioxide. Reagent traps remove the CO_2 and water vapour and the remaining gases are passed through a thermal conductivity cell that detects and measures any nitrogen present. The range of analysis is 10–2000 ppm for oxygen (0.0057–1.23 at.% in Zr) and 5–5000 ppm for nitrogen (0.003 to 3.17 at.% in Zr) for a one gram sample. Analysing specimens smaller than one gram can extend the concentration range to higher values.

While specifically written for titanium materials, ASTM E 1409, Standard Test Method for Determination of Oxygen and Nitrogen in Titanium and Titanium Alloys by the Inert Gas Fusion Technique [4.327], also provides excellent guidance for zirconium materials.

Nitrogen can also be determined by the Kjeldahl method. In this method, the sample is dissolved in acid and the resulting solution is made basic with strong sodium hydroxide solution. Nitrogen is separated as ammonia by steam distillation. Ammonia is determined volumetrically in the distillate by titration with hydrochloric acid. The method is suitable for determination of nitrogen in zirconium in the 1–10 ppm (0.0006–0.006 at.%) concentration range due to the ability to analyse larger sample weights. Samples in the form of solids or fines can be analysed over a large detection range by adjusting sample sizes and the concentration of the standard hydrochloric acid.

Hydrogen determination uses a solid metal sample held in a single use graphite crucible. The sample is fused in an argon atmosphere by an impulse type fusion furnace. The high fusion temperature releases gases that are then swept through Schütze reagent, I_2O_5 on silica, where the oxygen, as carbon monoxide, is converted to carbon dioxide and is absorbed on Ascarite. Nitrogen and hydrogen are chromatographically separated on a molecular sieve.

Hydrogen measurement is by thermal conductivity with a thermistor bridge detector, the output of which is integrated and displayed electronically. The instrumental detection limit for hydrogen, utilizing the thermal conductivity technique, is about 1–2 ppm (0.009-0.018 at.% in Zr). ASTM E1447, Standard Test Method for Determination of Hydrogen in Titanium and Titanium Alloys by the Inert Gas Fusion Thermal Conductivity/Infrared Detection Method [4.328], can be followed for the analysis of hydrogen in zirconium materials even though it was published for titanium and its alloys. An international round-robin exercise of hydrogen analysis in Zr-2.5Nb, conducted in an IAEA programme [4.329], suggested that the use of Ti standards when analysing H in Zr may introduce a bias of about 8%. Zirconium standards were recommended. Care has to be taken with blank errors, which may be as high as 1 ppm (0.009 at.% in Zr).

It should be noted that after a component has operated in a reactor that uses heavy water as a moderator and for heat transport, the hydrogen that is picked up from corrosion is deuterium. A mass spectrometer can be used to distinguish and measure the concentrations of protium (light hydrogen) and deuterium [4.330].

4.13.8.4. Determination of carbon and sulphur

Carbon and sulphur are generally determined simultaneously. The metal sample is ignited in an oxygen atmosphere in a furnace heated inductively. A precisely weighed sample is combusted in a small crucible with oxygen and a small amount of tungsten trioxide. Carbon in the sample is oxidized to carbon dioxide or carbon monoxide. The sulphur is oxidized to sulphur dioxide. These combustion gases are carried by oxygen into an infrared cell where sulphur is detected as sulphur dioxide. Following sulphur analysis, all the carbon is converted to carbon dioxide. The sulphur is converted to sulphur trioxide and removed by filtration.

The carbon dioxide is then measured in a separate infrared cell. The determination of carbon and sulphur is done by non-dispersive (fixed) infrared energy at precise wavelengths as the gases pass through their respective infrared absorption cells. The changes in energy are then observed at the detectors and the concentration determined. Both carbon and sulphur have instrumental detection limits of less than 5 ppm (0.0038 at.% for C in Zr and 0.0014 at.% for S in Zr). ASTM E1941, Standard Test Method for Determination of Carbon in Refractory and Reactive Metals and Their Alloys [4.331], provides a detailed procedure for this test.

4.13.8.5. Atomic absorption spectrometry

Atomic absorption spectrometry is applicable to elements that can be placed in the vapour state as unexcited ground state atoms. Radiation from a hollow cathode light source is passed through vapour containing the element to be analysed, and into a monochromator set for radiation characterization of the element. The degree of absorption is measured and is proportional to the amount of the particular element present. Analysis is made by comparison to reference materials. The initial vapour state is produced in a flame or a furnace.

The instrumentation required has the advantage of being low cost and simple to operate. The disadvantages include inadequate sensitivity for many of the impurity elements of low concentration required for the analysis of zirconium and the fact that, with most instruments, only one element at a time can be determined.

The elements found in Zircaloy with large concentrations (Fe, Cr, Sn) are easily analysed by atomic absorption. Others such as Cu, Pb and Ti can be analysed with careful calibration. ASTM provides three standard methods that can aid the analyst in the fundamentals of the procedure. ASTM E1184, Practice for Electrothermal (Graphite Furnace) Atomic Absorption Analysis [4.332], ASTM E1770 Standard Practice for Optimization of Electrothermal Atomic Absorption Spectrometric Equipment [4.333] and ASTM E1812, Standard Practice for Optimization of Flame Atomic Absorption Spectrometric Equipment [4.334], offer detailed set-up procedures.

4.13.8.6. X ray fluorescence analysis

X ray fluorescence (XRF) analysis employs a primary X ray beam that penetrates the specimen and causes ejection of inner shell electrons from atoms. Outer shell electrons drop down to fill the lower energy electron vacant shell positions. This energy exchange results in

the production of secondary X rays whose energies are defined by the energy differences between the acceptor and donor electron shells. Since each element in the specimen has its own unique set of electron energy levels, it also has its own characteristic fingerprint of secondary X ray energies. These secondary X rays are analysed by either an electronic energy dispersive spectrometer or a crystal wavelength dispersive spectrometer.

Quantitative determination of the elemental concentration of each element in the specimen is obtained by comparing the intensities of the various elements to those of known reference materials. Coverage is usually limited to elements with an atomic number greater than nine, that is the atomic number of fluorine. Detection limits are generally of the order of 0.01 wt%. XRF has been used for Cr, Fe, Ni and Sn in Zircaloy. The cost of the instrumentation is high, and the list of possible elements is short enough that the technique is usually only used by those who have existing instruments and only have the need to check the alloying elements. By making slight revisions specific for a zirconium matrix, ASTM E 536, Standard Test Method for X-Ray Emission Spectrometric Analysis of 6Al-4V Titanium Alloy [4.335], would provide the analyst guidance on performing the analysis.

4.13.8.7. Glow discharge mass spectroscopy

Glow discharge mass spectroscopy (GDMS) can be used to analyse for very low concentrations of elements such as Cl, P, Mg and other trace impurities. A significant difference between GDMS and ICP mass spectroscopy is that the former utilizes a solid metal sample pin or flat surface compared with dissolving the metal sample into solution and aspirating the solution into the plasma. Additionally, the method is reported to be relatively matrix independent because ionization in glow discharge ion sources occurs independently of sample atomization.

A glow discharge is formed when the solid metal sample is the cathode subjected to a 1 kV potential inside an anode cell (typically made from high purity tantalum). There is a negative glow surrounding the sample that atomizes and ionizes the analyte by Penning or electron impact ionization and charge exchange processes. Ions are accelerated through an aperture in the anode. The plasma gas is generally argon, although oxygen can also be used.

In the commercially available GDMS instruments, the double-focusing mass spectrometer is most often found. Commercial GDMS devices are slow and cumbersome to operate, but they have the advantage of low detection limits, uniform element sensitivity and the capability of measuring all elements, and even isotopes. There are certain restrictions on what can be measured as mass/charge ratio interferences occur when the argon plasma combines with ions to form argides. Additionally, the sample cell material (typically tantalum) overwhelms the system so that some elements cannot be analysed. Finally, the sample volume measured is very small. The sample has to be homogeneous as the surface is sputtered away in the glow discharge. To get better, more reproducible results, it is advisable to polish the exposed sample surface (300 grit) and degrease with a suitable organic solvent before sputtering.

Robinson and Hall have employed the GDMS technique for the analysis of Zircaloy [4.336]. The analysis warrants the calculation of relative sensitive factors values for the analytes that are normally generated by using a set of certified reference material of zirconium alloys.

The GDMS technique has also been used for the characterization of Zr-2.5 Nb and Zr-1 Nb alloys [4.337]. Some of the critical constituents, such as chlorine and phosphorus, that reduce the fracture toughness of the alloy, and boron, which is a neutron poison, can be

routinely analysed by this technique [4.338, 4.339]. The concentration of these impurities can also be mapped at various stages of melting. Only by these studies using GDMS was it established that the quadruple melting of ingots was essential for obtaining good homogeneity with regard to alloying elements and at the same time keeping some of the harmful impurities such as chlorine, hydrogen and phosphorous as low as possible [4.230]. Also, the technique has the advantage of being a direct analysis technique without contaminating the sample as in spectrographic techniques.

GDMS can also be used for the analysis of compacted non-conducting powders such as ZrO_2 for trace impurities after prior mixing with a conducting substrate such as Cu powder or alternatively employing the radio frequency glow discharge source to analyse elements directly.

The primary role of GDMS is in detecting very small concentrations of impurity elements without the risk of contamination that comes from other techniques.

4.13.8.8. Chlorine analysis

Chlorine is an important trace element that is recognized for degradation of fracture toughness in Zr-2.5Nb pressure tubes and it can have a positive influence over the morphology of the β–α transformation structure of zirconium and alloys. Samples are either metal turnings, chips or powder that are cleaned to remove surface contamination. The specimen is inserted into an electric furnace and burned to oxide in a moist oxygen atmosphere. The gas that evolves is dried, cleaned and released into a titration cell as HCl. The chloride is titrated coulometrically with silver ions according to:

$$\mathrm{HCL} + \mathrm{Ag}^{+} \rightarrow \mathrm{AgCl} + \mathrm{H}^{+} \tag{4.23}$$

$$\mathrm{Ag} \rightarrow \mathrm{Ag}^{+} + e^{-} \tag{4.24}$$

Coulometric titrations use a constant current system to accurately quantify the concentration of the silver species. The applied current is equivalent to a titrant. Current is applied to the unknown solution until all of the silver is oxidized to the +1 state, at which point the potential of the working electrode shifts dramatically. This potential shift indicates the end point. The magnitude of the current (in amps) and the duration of the current (seconds) can be used to determine the moles of the silver in solution. The method is capable of an instrumental detection limit of less than 0.5 ppm (0.0001 at.%) chlorine.

4.13.9. Analytical reference materials

Any discussion of analytical techniques must include a discussion of reference materials. Analytical techniques are typically comparative, which means that signals generated by an instrument in the measurement of an attribute must be compared with a standard with a known value for that attribute. Reference materials are available for the calibration or verification of every analytical technique from balances and thermocouples to gas chromatographs and plasma spectrometers.

Reference materials can be divided into several categories based on their level of authority. At the highest level are the certified reference materials (CRMs) issued by internationally recognized reference materials organizations, which are generally government agencies or accredited organizations. CRMs would include reference materials from the National Institute of Standards and Technology in the United States or the Institute for Reference Materials and Measurements in Europe. These materials have been carefully

tested for homogeneity and then analysed for specific attributes by a variety of techniques to determine the 'true values' and their uncertainty. Round-robin testing is frequently used as part of the process.

In round-robin testing, a number of cooperating laboratories familiar with the testing of a particular material analyse the material by the techniques employed in their laboratory. The results from the individual laboratories are combined with results determined by the certifying organization and statistically evaluated to establish an agreed upon value.

There are a very limited number of CRMs available for zirconium and zirconium alloys. Some of these are certified for only one or a few elements. It is important for the zirconium industry to work with reference materials organizations to develop new CRMs. Table 4.32 provides a compilation of CRMs and the currently certified concentrations of alloying and trace elements.

Most laboratories in the zirconium industry use reference materials developed in-house for monitoring and setting up their testing procedures. These reference materials are tested for homogeneity and may be compared with CRMs or reference materials (RMs) to establish a value to be used by the laboratory. While they do not have certified values, they are useful for monitoring instrument drift and do not require consumption of expensive CRMs that sometimes have limited availability.

At the lowest level are drift correction or set-up reference materials, which are used for the day to day adjustment of instrumentation that has been previously calibrated using CRMs, RMs and materials developed in-house. These RMs are generally materials that are available in large quantities and have attributes in the normal range of those being tested. These materials are tested for homogeneity but need not have an established value for the attributes. The response for each attribute is measured at the time of initial instrument calibration. Day to day adjustments to the calibration curves are then made based on that day's response for the drift correction standard.

RMs may come in many forms. Balances are calibrated with weight sets that may be certified by a government agency (e.g. National Institute of Standards and Technology) or by a commercial organization that will reference a government certified weight set. Weight sets, because they may change, must be recertified regularly. In the metals industry, for many alloys there are CRMs or RMs available with certified values for one or more attributes. These may come in the form of solids or chips. Because the constituents in most alloys are stable, these RMs do not normally require recertification. RMs may also come in the form of liquid solutions. These solutions will be certified for the concentration of one or more elements or compounds. In most cases, solution RMs will have a defined shelf life and specified storage conditions.

The calibration of instrumentation for analysing solutions can be achieved by dissolving a CRM or RM of the appropriate alloy. Alternatively, a synthetic standard may be prepared by combining solution RMs containing the various elements of interest. These may be a combination of commercially prepared solutions and solutions prepared in-house. Careful matching of the solutions to the matrix being tested can substantially reduce interference problems associated with the testing procedure.

In summary, to ensure the reliable performance of components in power reactors, a strict programme of testing is performed throughout the whole fabrication process of zirconium alloys providing confidence in chemical composition, freedom from defects and maintenance of the appropriate microstructure.

TABLE 4.32. CERTIFIED REFERENCE MATERIALS

	360b	BCR-098	BCR-275	BCR-276
Aluminium (Al)	57	—	—	—
Antimony (Sb)	(1)	—	—	—
Arsenic (As)	(7)	—	—	—
Boron (B)	0.191	—	—	—
Cadmium (Cd)	(<1)	—	—	—
Carbon (C)	109	—	113	108
Chlorine (Cl)	(<1)	—	—	—
Chromium (Cr)	1043	906	—	—
Cobalt (Co)	0.97	—	—	—
Copper (Cu)	12.5	—	—	—
Fluorine (F)	(<10)	—	—	—
Gallium (Ga)	(<1)	—	—	—
Hafnium (Hf)	78.5	77.6	—	—
Hydrogen (H)	43.5	—	—	—
Iron (Fe)	2138	2143	—	—
Lead (Pb)	(<5)	—	—	—
Magnesium (Mg)	(<1)	—	—	—
Manganese (Mn)	9.2	—	—	—
Molybdenum (Mo)	(<25)	—	—	—
Nickel (Ni)	22.5	—	—	—
Niobium (Nb)	(<50)	—	—	—
Nitrogen (N)	45	—	39	41
Oxygen (O)		—	1670	1540
Phosphorus (P)	8.7	—	—	—
Silicon (Si)	80	—	—	—
Sulphur (S)	30	—	—	—
Tantalum (Ta)	(<100)	—	—	—
Tin (Sn)	1.555%	1.460%	—	—
Titanium (Ti)	15.5	—	—	—
Tungsten (W)	(<50)	—	—	—
Uranium (U)	(<2)	—	—	—
Vanadium (V)	(<30)	—	—	—
Zinc (Zn)	(<50)	—	—	—

Note: 360b certified by US National Institute of Standards and Technology. BCR-098, BCR-275, BCR-276 certified by European Commission, Institute for Reference Materials and Measurements. Values in parenthesis are for information only. Concentrations are expressed as ppm mass fraction, unless otherwise designated. Matrix is Zircaloy-4 for all CRMs.

4.14. SUMMARY

This chapter has outlined the technology for reducing an ingot of zirconium alloy into a useful component. The processes include hot working and cold working, heat treatment, joining and machining. Verification of the initial integrity of a component is determined through inspection by both non-destructive and destructive testing and chemical analysis throughout the process.

REFERENCES TO CHAPTER 4

[4.1] LUSTMAN, B., KERZE, F. (Eds), The Metallurgy of Zirconium, McGraw-Hill, New York (1955).

[4.2] MILLER, G.L., Zirconium, Metallurgy of the Rarer Metals No. 2, Butterworths Scientific Publications, London (1957).

[4.3] PRASAD, Y.V.R.K., SESHACHARYULU, T., Modelling for hot deformation for microstructural control, Int. Mater. Rev. **43** (1998) 243–258.

[4.4] DIETER, G.E., Mechanical Metallurgy, McGraw-Hill, New York (1988).

[4.5] PRASAD, Y.V.R.K., RAO, P.N., SASIDHARA, S. (Eds), Hot Working Guide: A Compendium of Processing Maps, ASM International, Material Parks, OH (2015) 545.

[4.6] CHAKRAVARTTY, J.K., PRASAD, Y.V.R.K., ASUNDI, M. K., Processing map for hot working on alpha-zirconium, Metall. Trans. A **22** (1991) 829–836.

[4.7] SCHEMEL, J.H., ASTM Manual on Zirconium and Hafnium, ASTM STP 639, ASTM International, West Conshohocken, PA (1977).

[4.8] BAUSER, M., SAUER, G., SIEGERT, K., Extrusion, 2nd edn, ASM International, Material Parks, OH (2006) 59–113.

[4.9] CHOUBEY, R., ALDRIDGE, S.A., THEAKER, J.R., CANN, C.D., COLEMAN, C.E., "Effect of extrusion-billet preheating on microstructure and properties of Zr-2.5Nb pressure tube materials", Zirconium in the Nuclear Industry: Eleventh International Symposium, Proc. ASTM STP 1295, Garmisch-Partenkirchen, 1995 (BRADLEY, E.R., SABOL, G.P., Eds), ASTM International, West Conshohocken, PA (1996) 657–675.

[4.10] SEMIATIN, S.L., LAMPMAN, S.R., KINSON, J. (Eds), ASM Handbook Volume 14A: Metalworking: Bulk Forming, ASM International, Materials Park, OH (2005).

[4.11] COOK, C.S., SABOL, G.P., SEKERA, K.R., RANDALL, S.N., "Texture control in Zircaloy tubing through processing", Zirconium in the Nuclear Industry: Ninth International Symposium, Proc. ASTM STP 1132, Kobe, 1990 (EUCKEN, C.M., GARDE, A.M., Eds), ASTM International, West Conshohocken, PA (1991) 80–95.

[4.12] VAIBHAW, K., RAO, S.U.R., JHA, S.K., SAIBABA, N., JAYARAJ, R.N., Texture and hydride orientation relationship of Zircaloy-4 fuel clad during its fabrication for pressurized heavy water reactors, J. Nucl. Mater. **383** (2008) 71–77.

[4.13] SCHEMEL, J.H., McKENZIE, R.W., "Pilger tooling design for texture control", Zirconium in Nuclear Applications, ASTM STP 551 (SCHEMEL, J.H., ROSENBAUM, H.S., Eds), ASTM International, West Conshohocken, PA (1974) 169–178.

[4.14] KONISHI, T., HONJI, M., KOJIMA, T., ABE, H., "Effect of cold reduction on anisotropy of Zircaloy tubing", Zirconium in the Nuclear Industry: Seventh International Symposium, Proc. ASTM STP 939, Strasbourg, 1985 (ADAMSON, R.B., VAN SWAM, L.F.P., Eds), ASTM International, West Conshohocken, PA (1987) 653–662.

[4.15] NAGAI, N., KAKUMA, T., FUJITA, K., "Texture control of Zircaloy tubing during tube reduction", Zirconium in the Nuclear Industry: Fifth International Symposium, Proc. ASTM STP 754, Boston, 1980 (FRANKLIN, D.G., Ed.), ASTM International, West Conshohocken, PA (1982) 26–38.

[4.16] NEWNHAM, J.A., "Wire drawing lubrication", Metal Deformation Processes: Friction and Lubrication (SCHEY, J.A., Ed.), Marcel Dekker, New York (1970) 457–535.

[4.17] RAO, P.N., Manufacturing Technology: Foundry, Forming, and Welding, Vol. 1, 4th edn, Tata McGraw-Hill, New Delhi (1999).

[4.18] TORRINGTON FORMING MACHINERY, Rotary Swager (2020), https://torrington-machinery.com/en/machinery-products/swager/rotary-swager/

[4.19] THEAKER, J.R., COLEMAN, C.E., "Development of crystallographic texture in CANDU calandria tubes", Zirconium in the Nuclear Industry: Thirteenth International Symposium, Proc. ASTM STP 1423, Annecy, 2001 (MOAN, G.D., RUDLING, P., Eds), ASTM International, West Conshohocken, PA (2002) 449–467.

[4.20] ERNESTUS, A.W., Method and Apparatus for Roll Extrusion of Small Tubes, U.S. Patent No. 3,411,334, Nov. 1968.

[4.21] PMF INDUSTRIES, Understanding Flowforming (2007), https://www.pmfind.com/about/knowledge-is-power?utm_content=2019-09-30-104009

[4.22] FONTE, V., TOSDALE, J., "Flowforming of Zirconium and Titanium pipe", Proc. Reactive Metals in Corrosive Applications Conf., Sun River, 1999 (HAYGARTH J., TOSDALE, J., Eds), ATI Wah Chang, Albany, OR (1999) 139–144.

[4.23] BLACK, J.T., KOHSER, R.A., "Fundamentals of metal forming", DeGarmo's Materials and Processes in Manufacturing, John Wiley & Sons Chichester (2007) Ch. 15.

[4.24] EFUNDA, Introduction (2009), http://www.efunda.com/processes/metal_processing/coining.cfm

[4.25] SEMIATIN, S.L. (Ed.), ASM Handbook, Volume 14B: Metalworking: Sheet Forming, ASM International, Materials Park, OH (2006).

[4.26] ATI METALS, Zirconium Machining and Forming Operations (2011), https://www.atimetals.com/Products/Documents/datasheets/zirconium/alloy/zirconium-machining-formingoperations.pdf#search=machining%20and%20forming%20operations%20for%20zirconium

[4.27] ASTM INTERNATIONAL, Standard Specification for Zirconium and Zirconium Alloy Ingots for Nuclear Application, ASTM Standard B 350/B 350M-11(2021), ASTM International, West Conshohocken, PA (2021).

[4.28] BURGERS, W.G., On the process of transition of the cubic body-centred modification into the hexagonal close-packed modification of zirconium, Physica **1** (1934) 561–586.

[4.29] BANERJEE, S., KRISHNAN, R., Martensitic transformation in zirconium-niobium alloys, Acta Metall. **19** (1971) 1317–1326.

[4.30] PICKLESIMER, M.L., Method for Annealing and Rolling Zirconium-base Alloys, US Patent 2 894 866, Jul. 1959.

[4.31] ÖSTBERG, G., Metallographic study of isothermal transformation of beta phase in Zircaloy-2, Jernkontorets Ann. **145** (1961) 119–142.

[4.32] CHUNG, H.M., GARDE, A.M., LIN, E.I.H., KASSNER, T.F., Mechanical properties of Zircaloy containing oxygen, Light-Water-Reactor Safety Research Report No. ANL-76–49, Argonne National Laboratory, Argonne, IL (1976) 34–59.

[4.33] WOO, O.T., TANGRI, K., Transformation characteristics of rapidly heated and quenched Zircaloy-4-oxygen alloys, J. Nucl. Mater. **79** (1979) 82–94.

[4.34] MIQUET, A., CHARQUET, D., ALLIBERT, C.H., Solid state phase equilibria of Zircaloy-4 in the temperature range 750–1050°C, J. Nucl. Mater. **105** (1982) 132–141.

[4.35] GEY, N., et al., Study of the α/β phase transformation of Zy-4 in presence of applied stresses at heating: Analysis of the inherited microstructure and textures, J. Nucl. Mater. **302** (2002) 175–184.

[4.36] ROMERO, J., PREUSS, M., QUINTA DA FONSECA, J., Texture memory and variant selection during phase transformation of a zirconium alloy, Acta Mater. **57** (2009) 5501–5511.

[4.37] ROMERO, J., et al., Texture evolution of Zircaloy-2 during beat-quenching: Effect of process variables, J. ASTM International **7** (2010) Paper ID JAI103014.

[4.38] WASHBURN, D.F., Primary and secondary recrystallization of beta-quenched Zircaloy-4, Knolls Atomic Power Laboratory, Niskayuna, NY (1964) KAPL-3103.

[4.39] HOLT, R.A., The beta to alpha phase transformation in Zircaloy-4, J. Nucl. Mater. **35** (1970) 322–334.

[4.40] FONG, W.L., NORTHWOOD, D.O., Microstructure-impurity content relationships in Zircaloy-4 nuclear fuel sheathing, Microstruct. Sci. **10** (1982) 123–130.

[4.41] MASSIH, A.R., ANDERSSON, T., WITT, P., DAHLBÄCK, M., LIMBÄCK, M., Effect of quenching rate on the β-to-α phase transformation structure in zirconium alloy, J. Nucl. Mater. **322** (2003) 138–151.

[4.42] YANG, W.J.S., ADAMSON, R.B., "Beta-quenched Zircaloy-4: Effects of thermal aging and neutron irradiation", Zirconium in the Nuclear Industry: Eighth International Symposium, Proc. ASTM STP 1023, San Diego, 1988 (VAN SWAM, L.F.P., EUCKEN, C.M., Eds), ASTM International, West Conshohocken, PA (1989) 451–477.

[4.43] ÖKVIST, G., KÄLLSTRÖM, K., The effect of zirconium carbide on the β→α transformation structure in Zircaloy, J. Nucl. Mater. **35** (1970) 316–321.

[4.44] HOLT, R.A., Comments on the beta to alpha phase transformation in Zircaloy-4, J. Nucl. Mater. **47** (1973) 262–264.

[4.45] CHARQUET, D., ALHERITIERE, E., "Influence of impurities and temperature on the microstructure of Zircaloy-2 and Zircaloy-4 after the beta → alpha phase transformation", Zirconium in the Nuclear Industry: Seventh International Symposium, Proc. ASTM STP 939, Strasbourg, 1985 (ADAMSON, R.B., VAN SWAM, L.F.P., Eds), ASTM International, West Conshohocken, PA (1987) 284–291.

[4.46] QUACH, V., NORTHWOOD, D.O., Influence of the phosphorus impurity content on the microstructure of Zircaloy-4 air-cooled from the high temperature beta phase region, Metallography **17** (1984) 191–201.

[4.47] GAZAROLLI, F., STEHLE, H., STEINBERG, E., WEIDINGER, H., Progress in the knowledge of nodular corrosion, Zirconium in the Nuclear Industry: Seventh International Symposium, Proc. ASTM STP 939, Strasbourg, 1985 (ADAMSON, R.B., VAN SWAM, L.F.P., Eds), ASTM International, West Conshohocken, PA (1987) 417–430.

[4.48] JEONG, Y.H., RHEEM, K.S., CHOI, C.S., KIM, Y.S., Effect of beta heat treatment on microstructure and nodular corrosion of Zircaloy-4, J. Nucl. Sci. Technol. **30** (1993) 154–163.

[4.49] HOLT, R.A., EVANS, W., CHEADLE, B.A., The Role of Zirconium Alloy Metallurgy in the Fabrication of CANDU Fuel, Atomic Energy of Canada Report No. AECL-5107, AECL, Chalk River, ON (1975).

[4.50] HUMBERT, M., GEY, N., Elasticity-based model of the variant selection observed in the β to α phase transformation of a Zircaloy-4 sample, Acta Mater. **51** (2003) 4783–4790.

[4.51] STANFORD, N., BATE, P.S., Crystallographic variant selection in Ti–6Al–4V, Acta Mater. **52** (2004) 5215–5224.

[4.52] HUTCHINSON, B., KESTENS, L., "Origins of texture memory in steels, applications of texture analysis", Ceramic Transactions (Rollett, A.D., Ed.) (Proc. 15th Int. Conf. on Textures of Materials, ICOTOM), John Wiley & Sons, Hoboken, NJ (2008) 281–290.

[4.53] CHEADLE, B.A., ELLS, C.E., The effect of heat treatment on the texture of fabricated Zr-rich alloys, Electrochem. Technol. **4** (1966) 329–336.
[4.54] CIURCHEA, D., et al., Texture, morphology and deformation mechanisms in β-transformed Zircaloy-4, J. Nucl. Mater. **231** (1996) 83–91.
[4.55] STURKEN, E.F., CROACH, J.W., Predicting physical properties in oriented metals, Trans. AIME **227** (1963) 934–940.
[4.56] BUNGE, H.J., Texture Analysis in Materials Science, Butterworths, London (1982) 88–90.
[4.57] WENK, H.R., LONARDELLI, I., WILLIAMS, D., Texture changes in the hcp→bcc→hcp transformation of zirconium studied in situ by neutron diffraction, Acta Mater. **52** (2004) 1899–1907.
[4.58] KEARNS, J.J., "Thermal expansion and preferred orientation in Zircaloy", Report WAPD-TM-472, Bettis Atomic Power Laboratory, Pittsburgh, PA (1965).
[4.59] VANDER SANDE, J.B., BEMENT, A.L., An investigation of second phase particles in Zircaloy-4 alloys, J. Nucl. Mater. **52** (1974) 115–118.
[4.60] BANGARU, N.V., An investigation of the microstructures of heat-treated Zircaloy-4, J. Nucl. Mater. **131** (1985) 280–290.
[4.61] MAUSSNER, G., "Experimental methods for the examination and the classification of second phase particles in Zircaloy", Proc. Workshop on Second Phase Particles and Matrix Properties of the Zircaloys, Erlangen, 1985, Kerntechnische Gesellschaft, Berlin (1985).
[4.62] MAUSSNER, G., STEINBERG, E., TENCKOFF, E., "Nucleation and growth of intermetallic precipitates in Zircaloy-2 and Zircaloy-4 and correlation to nodular corrosion behavior", Zirconium in the Nuclear Industry: Seventh International Symposium, Proc. ASTM STP 939, Strasbourg, 1985 (ADAMSON, R.B., VAN SWAM, L.F.P., Eds), ASTM International, West Conshohocken, PA (1987) 307–320.
[4.63] LOUCIF, K., BORRELLY, R., MERLE, P., Microstructural evolution of β-quenched Zircaloy-4 during agings between 100 and 750°C, J. Nucl. Mater. **210** (1994) 84–96.
[4.64] MIYAKE, C., TAKAMIYA, T., "Magnetic study of Zircaloy", Zirconium in the Nuclear Industry: Eighth International Symposium, Proc. ASTM STP 1023, San Diego, 1988 (VAN SWAM, L.F.P., EUCKEN, C.M., Eds), ASTM International, West Conshohocken, PA (1989) 487–497.
[4.65] YANG, W.J.S., TUCKER, R.P., CHENG, B., ADAMSON, R.B., Precipitates in Zircaloy: Identification and the effects of irradiation and thermal treatment, J. Nucl. Mater. **138** (1986) 185–195.
[4.66] LUNDIN, C.E., COX, R.H., "A metallographic determination of the Zr-Nb diagram", Proc. USAEC Symp. on Zirconium Alloy Development, Pleasanton, 1962, Vallecitos Atomic Laboratory Report No. GEAP-4089, Vallecitos Atomic Laboratory, Pleasanton, CA (1962) Paper 9.
[4.67] RICHTER, H., WINCIERZ, P., ANDERKO, K., ZWICKER, U., Zur Konstitution von Zirconium-Niob-Legierungen, J. Less-Common Met. **4** (1962) 252–265.
[4.68] ABRIATA, J.P., BOLCICH, J.C., The Nb-Zr (Niobium–Zirconium) system, Bull. Alloy Phase Diagrams **3** 1 (1982) 29–34.
[4.69] WINTON, J., MURGATROYD, R., "The effect of heat treatment on the mechanical properties of the zirconium-2½% niobium alloy", Proc. USAEC Symp. on Zirconium Alloy Development, Pleasanton, 1962, Vallecitos Atomic Laboratory Report No. GEAP-4089, Vallecitos Atomic Laboratory, Pleasanton, CA (1962) Paper 11.
[4.70] KENCH, J.R., FOLEY, J.H., ALDRIDGE, S.A., The Effects of Dissolved Oxygen upon the Mechanical Properties of Zirconium-2.5 wt% Niobium Alloy, Report No. AECL-2623, Atomic Energy of Canada Limited, Chalk River, ON (1966).
[4.71] ELLS, C.E., WILLIAMS, C.D., Beta embrittlement of the Zr-2.5 wt. pct. Nb (Cb) alloy, Trans. Met. Soc. AIME **245** (1969) 1321–1328.
[4.72] HUNT, C.E.L., NIESSEN, P., The effect of oxygen on the equilibrium β/(α+β) transformation temperature of zirconium-niobium alloys, J. Nucl. Mater. **35** (1970) 134–136.
[4.73] FIDLERIS, V., The creep strength of quenched and aged Zr-2.5 wt% Nb alloy, J. Nucl. Mater. **54** (1974) 199–211.
[4.74] FONG, R.W.L., MILLER, R., SAARI, H.J., VOGEL, S.C., "Crystallographic texture and volume fraction of α and β phases in Zr-2.5Nb pressure tube during heating and cooling", Metall. Mater. Trans. A **43** 3 (2011) 806–821.
[4.75] BELL, L.G., DICKS, T.S., The effect of prior beta grain size on the ductility of zirconium-2.5 weight percent niobium alloy, Can. Metall. Q. **4** (1965) 259–268.
[4.76] SABOL, G.P., Precipitation behaviour in Zr/2.5 wt% Nb alloys, J. Nucl. Mater. **34** (1970) 142–150.
[4.77] WOO, O.T., Atomic Energy of Canada, unpublished data.
[4.78] CHEADLE, B.A., ALDRIDGE, S.A., The transformation and age hardening behaviour of Zr-19 wt% Nb, J. Nucl. Mater. **47** (1973) 255–258.
[4.79] GRIFFITHS, M., WINEGAR, J.E., BUYERS, A., The transformation behaviour of the β-phase in Zr-2.5Nb pressure tubes, J. Nucl. Mater. **383** (2008) 28–33.
[4.80] HUNT, C.E.L., NIESSEN, P., The continuous cooling transformation behaviour of zirconium-niobium-oxygen alloys, J. Nucl. Mater. **38** (1971) 17–25.
[4.81] CHEADLE, B.A., The Effect of Cooling Rate on the Hardness of Zirconium-Niobium Alloys, Report No. AECL-2039, Atomic Energy of Canada Limited, Chalk River, ON (1964).

[4.82] SLATTERY, G.F., Some aspects of the beta↔alpha transformation in zirconium-2½ weight per cent niobium alloy with variable cooling rate and soak temperature, Electrochem. Technol. **4** (1966) 336–341.
[4.83] WINTON, J., MURGATROYD, R.A., The effect of variations in composition and heat treatment on the properties of Zr-Nb alloys, Electrochem. Technol. **4** (1966) 336–341.
[4.84] WILLIAMS, C.D., GILBERT, R.W., Tempered structures of a Zr-2.5 wt% Nb alloy, J. Nucl. Mater. **18** (1966) 161–166.
[4.85] WILLIAMS, C.D., GILBERT, R.W., On structural factors influencing the strength of martensite α′ in quenched Zr-2.5%Nb, Trans. Jpn. Inst. Met. **9** (1968) 625–630.
[4.86] STAGNO, E., IENCO, M.G., Metallographic investigation of the phase transformation in Zr-Nb alloys as affected by cooling rate, Radex Rundsch. **3** (1974) 144–153.
[4.87] SHEMYAKIN, V.N., BAYNOVA, G.D., Structure and phase composition of alloy Zr-2.5%Nb rapidly cooled from the β-range, Phys. Met. Metallogr. **60** (1985) 189–191.
[4.88] GRYTSYNA, V., et al., Destruction of crystallographic texture in zirconium alloy tubes, J. ASTM International **2** (2005) JAI12339.
[4.89] DAYMOND, M.R., HOLT, R.A., CAI, S., MOSBRUCKER, P., VOGEL, S.C., Texture inheritance and variant selection through an hcp-bcc-hcp phase transformation, Acta Mater. **58** (2010) 4053–4066.
[4.90] MOSBRUCKER, P., DAYMOND, M.R., HOLT, R.A., In situ studies of variant selection during the α-β-α phase transformation in Zr-2.5Nb, J. ASTM International **8** (2011) JAI 103066.
[4.91] DUNLOP, J.W.C., BRÉCHET, Y.J.M., LEGRAS, L., ZUROB, H.S., Modelling isothermal and non-isothermal recrystallization kinetics: Application to Zircaloy-4, J. Nucl. Mater. **366** (2007) 178–186.
[4.92] WASHBURN, D.F., Primary and Secondary Recrystallization of Alpha Zircaloy-4, No. KAPL-3091, Knolls Atomic Power Laboratory, Schenectady, New York (1964).
[4.93] DEREP, J.L., ROUBY, D., FANTOZZI, G., Restauration et recristallisation de l'alliage Zircaloy-4, Mém. Etud. Sci. Rev. Metall. **78** (1981) 585–600.
[4.94] LEE, D., Recrystallization and mechanical behavior of Zircaloy-2 tubing, J. Nucl. Mater. **37** (1970) 159–170.
[4.95] STEINBERG, E., WEIDINGER, H.G., SCHAA, A., "Analytical approaches and experimental verification to describe the influence of cold work and heat treatment on the mechanical properties of Zircaloy cladding tubes", Zirconium in the Nuclear Industry: Sixth International Symposium, Proc. ASTM STP 824, Vancouver, 1982 (FRANKLIN, D.G., ADAMSON, R.B., Eds), ASTM International, West Conshohocken, PA (1984) 106–122.
[4.96] ELLS, C.E., CHEADLE, B.A., Aging and recovery in cold rolled Zr-2.5 wt% Nb alloy, J. Nucl. Mater. **23** (1967) 257–269.
[4.97] HINDLE, E.D., "38 Annealing studies of Zircaloy-2 cladding at 580–850°C", Dimensional Stability and Mechanical Behaviour of Irradiated Metals and Alloys, Vol. 1, British Nuclear Energy Society, London (1983) Paper 38.
[4.98] SAUBY, M.E., LEE, D., Recovery behavior of cold-worked and quenched Zircaloy with varying oxygen content, J. Nucl. Mater. **50** (1974) 175–182.
[4.99] RUMBALL, W.M., COLEMAN, C.E., Massive grain growth during aging of quenched Zr/1.25 wt% Cr/0.1 wt% Fe, J. Nucl. Mater. **36** (1970) 147–152.
[4.100] NORTHWOOD, D.O., DOSEN, K., A metallographic study of abnormal grain growth during aging of a β-quenched Zr-1.14 wt% Cr-0.08 wt% Fe alloy, Metallography **13** (1980) 249–266.
[4.101] COLEMAN, C.E., RUMBALL, W.M., Inducing a critical strain for grain growth in a duplex zirconium alloy, J. Nucl. Mater. **39** (1971) 345–347.
[4.102] HUNT, C.E.L., SCHULSON, E.M., Recrystallization of Zircaloy-4 during transient heating, J. Nucl. Mater. **92** (1980) 184–190.
[4.103] KOLMOGOROV, A.N., On the statistical theory of the crystallization of metals, Izv. Akad. Nauk. SSSR. Ser. Mat. **1** (1937) 355–359 (in Russian).
[4.104] JOHNSON, W.A., MEHL, R.F., Reaction kinetics in processes of nucleation and growth, Trans. Soc. Min. Eng. AIME **135** (1939) 416–458.
[4.105] AVRAMI, M., Kinetics of phase change. I, General theory, J. Chem. Phys. **7** (1939) 1103–1112.
[4.106] AVRAMI, M., Kinetics of phase change. II, Transformation-time relations for random distribution of nuclei, J. Chem. Phys. **8** (1940) 212–224.
[4.107] CHARQUET, D., HAHN, R., ORTLIEB, E., GROS, J.-P., WADIER, J.-F., "Solubility limits and formation of intermetallic precipitates in ZrSnFeCr alloys", Zirconium in the Nuclear Industry: Eighth International Symposium, Proc. ASTM STP 1023, San Diego, 1988 (VAN SWAM, L.F.P., EUCKEN, C.M., Eds), ASTM International, West Conshohocken, PA (1989) 405–422.
[4.108] WADMAN, B., ANDRÉN, H.-O., "Direct measurement of matrix composition in Zircaloy-4 by atom probe microanalysis", Zirconium in the Nuclear Industry: Eighth International Symposium, Proc. ASTM STP 1023, San Diego, 1988 (VAN SWAM, L.F.P., EUCKEN, C.M., Eds), ASTM International, West Conshohocken, PA (1989) 423–434.
[4.109] BORRELLY, R., MERLE, P., ADAMI, L., Study of the solubility of iron in zirconium by thermoelectric power measurements, J. Nucl. Mater. **170** (1990) 147–156.

[4.110] MUNTASELL, J., NAVARRO, J., CESARI, E., PLANES, A., Recovery and recrystallization of Zircaloy-4, Thermochim. Acta **87** (1985) 169–176.
[4.111] KATZ, O.M., Recovery and Recrystallization Kinetics of Cold-worked Zircaloy-4 Plate and Tubing, No. WAPD-TM-590, Bettis Atomic Power Laboratory Report, Pittsburgh, PA (1968).
[4.112] GARZAROLLI, F., MANZEL, R., SCHÖNFELD, H., STEINBERG, E., "Influence of final annealing on mechanical properties of Zircaloy before and after irradiation", Proc. 6th Int. Conf. Structural Mechanics in Reactor Technology (SMIRT 6), Paris, 1981, North-Holland, Amsterdam (1981) Paper C 2/1.
[4.113] BÄRO, G., WESSJOHANN, H.G., NICOLL, A.R., "On the short-time recrystallization of Zircaloy-4 above 600°C", Zirconium in the Nuclear Industry: Sixth International Symposium, Proc. ASTM STP 824, Vancouver, 1982 (FRANKLIN, D.G., ADAMSON, R.B., Eds), ASTM International, West Conshohocken, PA (1984) 200–209.
[4.114] LAVES, F., WITTE, H., Die Kristallstruktur des MgNi2 und seine Beziehung zu den Typen des $MgCu_2$ und $MgZn_2$, Metallwirtschaft **14** (1935) 645–649.
[4.115] STEIN, F., PALM, M., SAUTHOFF, G., Structure and stability of Laves phases, Part 1. Critical assessment of factors controlling phase stability, Intermetallics **12** (2004) 713–720.
[4.116] THORVALDSSON, T., ANDERSSON, T., WILSON, A., WARDLE, A., "Correlation between 400°C steam corrosion behavior, heat treatment, and microstructure of Zircaloy-4 tubing", Zirconium in the Nuclear Industry: Eighth International Symposium, Proc. ASTM STP 1023, San Diego, 1988 (VAN SWAM, L.F.P., EUCKEN, C.M., Eds), ASTM International, West Conshohocken, PA (1989) 128–140.
[4.117] HERB, B., RUHMANN, H., KÖNIG, A., In-process investigation of precipitate growth in zirconium alloys", Zirconium in the Nuclear Industry: Twelfth International Symposium, Proc. ASTM STP 1354, Toronto, 1998 (SABOL, G.P., MOAN, G.D., Eds), ASTM International, West Conshohocken, PA (2000) 482–504.
[4.118] CHARQUET, D., Influence of precipitate density on the nodular corrosion resistance of Zr-Sn-Fe-Cr alloys at 500°C, J. Nucl. Mater. **288** (2001) 237–240.
[4.119] EUCKEN, C.M., FINDEN, P.T., TRAPP-PRITSCHING, S., WEIDINGER, H.G., "Influence of chemical composition on uniform corrosion of zirconium-base alloys in autoclave tests", Zirconium in the Nuclear Industry: Eighth International Symposium, Proc. ASTM STP 1023, San Diego, 1988 (VAN SWAM, L.F.P., EUCKEN, C.M., Eds), ASTM International, West Conshohocken, PA (1989) 113–127.
[4.120] CHARQUET, D., Influence of precipitates on the corrosion of Zircaloy-4 in 400°C steam, J. Nucl. Mater. **211** (1994) 259–261.
[4.121] RUHMANN, H., MANZEL, R., SELL, H.J., CHARQUET, D., "In-BWR and out-of-pile nodular corrosion behavior of Zry-2/4 type melts with varying Fe, Cr and Ni content and varying process history", Zirconium in the Nuclear Industry: Eleventh International Symposium, Proc. ASTM STP 1295, Garmisch-Partenkirchen, 1995 (BRADLEY, E.R., SABOL, G.P., Eds), ASTM International, West Conshohocken, PA (1996) 865–883.
[4.122] STEINBERG, E., POHLMEYER, I., SCHAA, A., "Annealing parameter for quality control of cladding and structural material", Proc. Conf. TopFuel '97, Manchester, 1997, British Nuclear Energy Society, Manchester, UK (1997) 2.65–2.72.
[4.123] ANDERSSON, T., THORVALDSSON, T., WILSON, A., WARDLE, A.M., "Influence of thermal processing and microstructure on the corrosion behaviour of Zircaloy-4 tubing", Proc. IAEA Symposium IAEA-SM-288/59, Stockholm, 1986, IAEA, Vienna (1987) 435–449.
[4.124] GARZAROLLI, F., STEINBERG, E., WEIDINGER, H.G., "Microstructure and corrosion studies for optimized PWR and BWR Zircaloy cladding", Zirconium in the Nuclear Industry: Eighth International Symposium, Proc. ASTM STP 1023, San Diego, 1988 (VAN SWAM, L.F.P., EUCKEN, C.M., Eds), ASTM International, West Conshohocken, PA (1989) 202–212.
[4.125] GROS, J.F., WADIER, J.F., Precipitate growth kinetics in Zircaloy-4, J. Nucl. Mater. **172** (1990) 85–96.
[4.126] FOSTER, J.P., DOUGHERTY, J., BURKE, M.G., BATES, J.F., WORCESTER, S., Influence of final recrystallization heat treatment on Zircaloy-4 strip corrosion, J. Nucl. Mater. **173** (1990) 164–178.
[4.127] ANADA, H., NOMOTO, K., SHIDA, Y., "Corrosion behavior of Zircaloy-4 sheets produced under various hot-rolling and annealing conditions", Zirconium in the Nuclear Industry: Tenth International Symposium, Proc. ASTM STP 1245, Baltimore, 1993 (GARDE, A.M., BRADLEY, E.R., Eds), ASTM International, West Conshohocken, PA (1994) 307–327.
[4.128] MOTTA, A.T., et al., "Synchrotron radiation study of secondary-phase particles and alloying elements in zirconium alloys", Zirconium in the Nuclear Industry: Thirteenth International Symposium, Proc. ASTM STP 1423, Annecy, 2001 (MOAN, G.D., RUDLING, P., Eds), ASTM International, West Conshohocken, PA (2002) 59–79.
[4.129] ÖSTBERG, G., Determination of the composition of the second phase in Zircaloy, J. Nucl. Mater. **7** (1962) 103–106.
[4.130] CHEMELLE, P., KNORR, D.B., VAN DER SANDE, J.B., PELLOUX, R.M., Morphology and composition of second phase particles in Zircaloy-2, J. Nucl. Mater. **113** (1983) 58–64.
[4.131] ARIAS, D., PALACIOS, T., TURRILLO, C., Composition of precipitates present in Zircaloy-2 and 4, J. Nucl. Mater. **148** (1987) 227–229.

[4.132] RUDLING, P., LUNDBLAD VANNESJÖ, K., VESTERLUND, G., MASSIH, A.R., "Influence of second-phase particles on Zircaloy corrosion in BWR environment", Zirconium in the Nuclear Industry: Seventh International Symposium, Proc. ASTM STP 939, Strasbourg, 1985 (ADAMSON, R.B., VAN SWAM, L.F.P., Eds), ASTM International, West Conshohocken, PA (1987) 292–306.
[4.133] MENG, X., NORTHWOOD, D.O., Second phase particles in Zircaloy-2, J. Nucl. Mater. **168** (1989) 125–136.
[4.134] KURI, G., DEGUELDRE, C., BERTSCH, J., ABOLHASSANI, S., Micro-focussed XAFS spectroscopy to study Ni-bearing precipitates in the metal of corroded Zircaloy-2, Appl. Phys. A **98** (2010) 625–633.
[4.135] VITIKAINEN, E., NENONEN, P., Transmission electron microscopy studies on intermetallics in some zirconium alloys, J. Nucl. Mater. **78** (1978) 362–373.
[4.136] KRAŠEVEC, V., Transmission electron microscopy study of second phase particles in Zircaloy-2, J. Nucl. Mater. **98** (1981) 235–237.
[4.137] VERSACI, R.A., IPOHORSKI, M., Composition of Zr(Cr, Fe)2-type precipitates in Zircaloy-2 and Zircaloy-4, J. Nucl. Mater. **116** (1983) 321–323.
[4.138] IVANOV, O.S., GRIGOROVICH, V.K., "Structure and properties of zirconium alloys", Proc. 2nd Int. Conf. on Peaceful Uses of Atomic Energy, Geneva, 1958, United Nations, New York (1958) Paper 2046, 5: 34–51.
[4.139] BANERJEE, S., VIJAYAKAR, S.J., KRISHNAN, R., Precipitation in zirconium-niobium martensites, J. Nucl. Mater. **62** (1976) 229–239.
[4.140] CHOO, K.N., KANG, Y.H., PYUN, S.I., URBANIC, V.F., Effect of composition and heat treatment on the microstructure and corrosion behaviour of Zr-Nb alloys, J. Nucl. Mater. **209** (1994) 226–235.
[4.141] ELLS, C.E., DALGAARD, S.B., EVANS, W., THOMAS, W.R., "Development of zirconium-niobium alloys", Proc. 3rd Int. Conf. Peaceful Uses of Atomic Energy, Geneva, 1964, United Nations, New York (1965).
[4.142] ELLS, C.E., FIDLERIS, V., Effect of neutron irradiation on tensile properties of the zirconium-2.5 weight per cent niobium alloy, Electrochem. Technol. **4** (1966) 268–274.
[4.143] PICKLES, B.W., Embrittlement of heat-treated Zr-2.5 wt% Nb pressure tubes, Can. Metall. Q. **11** (1972) 139–146.
[4.144] LESURF, J.E., "The corrosion behaviour of 2.5Nb zirconium alloy", Applications-Related Phenomena in Zirconium and its Alloys, No. ASTM STP 458 (E.F. Baroch, Ed.), ASTM International, West Conshohocken, PA (1969) 286–300.
[4.145] COX, B., Long-term Oxidation of Zr-2.5 wt% Nb Alloy, Report No. AECL-5610, Atomic Energy of Canada Limited, Chalk River, ON (1976).
[4.146] WINTON, J., MURGATROYD, R.A., WATKINS, B., NICHOLS, R.W., The strength of Zr-2½%Nb alloy in the annealed and cold worked condition, Trans. Jpn. Inst. Met. **9** (1968) 630–636.
[4.147] ALDRIDGE, S.A., CHEADLE, B.A., Age hardening of Zr-2.5 wt% Nb slowly cooled from the (α+β) phase field, J. Nucl. Mater. **42** (1972) 32–42.
[4.148] HIWARKER, V.D., et al., Annealing of cold worked two-phase Zr-2.5Nb — associated microstructural developments, J. Nucl. Mater. **384** (2009) 30–37.
[4.149] NORTHWOOD, D.O., FONG, W.L., Modification of the structure of cold-worked Zr-2.5 wt% Nb nuclear reactor pressure tube material, Metallography **13** (1980) 97–115.
[4.150] HOLT, R.A., Recovery of cold-work in extruded Zr-2.5 wt% Nb, J. Nucl. Mater. **59** (1976) 234–242.
[4.151] SRIVASTAVA, D., DEY, G.K., BANERJEE, S., Evolution of microstructure during fabrication of Zr-2.5 wt% Nb alloy pressure tubes, Metall. Mater. Trans. A **26** (1995) 2707–2718.
[4.152] CHOUDHURI, G., SRIVASTAVA, D., GURUMURTHY, K.R., SHAH, B.K., Optimization of stress relief heat treatment of PHWR pressure tubes (Zr-2.5Nb alloy), J. Nucl. Mater. **383** (2008) 178–182.
[4.153] COLEMAN, C.E., THEAKER, J.R., KIDD, K.V., Effect of fabrication variables on irradiation response of crack growth resistance of Zr-2.5Nb, J. ASTM International **1** (2004) JAI 12437.
[4.154] GRIFFITHS, M., SAGE, D., GALINDO, D., "Characterisation of dislocation densities in hexagonal close-packed metals by X ray line-broadening analysis", Microscopy and Microanalysis **8** (2002) 1–340.
[4.155] GRIFFITHS, M., X-ray line-broadening analysis of dislocations in single crystal of Zr, Z. Krystallogr. Suppl. **27** (2008) 135–141.
[4.156] SIMPSON, L.A., CANN, C.D., The effect of microstructure on rates of delayed hydride cracking in Zr-2.5% Nb alloy, J. Nucl. Mater. **126** (1984) 70–73.
[4.157] COLEMAN, C.E., SAGAT, S., AMOUZOUVI, K.F., Control of Microstructure to Increase the Tolerance of Zirconium Alloys to Hydride Cracking, Report No. AECL-9524, Atomic Energy of Canada Limited, Chalk River, ON (1987).
[4.158] SKINNER, B.C., DUTTON, R., "Hydrogen diffusivity in α-β zirconium alloys and its role in delayed hydride cracking", Hydrogen Effects on Material Behavior Proc. 4th Int. Conf. on the Effect of Hydrogen on the Behavior of Materials, Moran, 1989 (MOODY, N.R., THOMPSON, A.W., Eds), Minerals, Metals and Materials Society, Pittsburgh, PA (1990) 73–83.
[4.159] JOVANOVIC, M.T., MA, Y., EADIE, R.L., An SEM study of β-phase decomposition during the annealing of Zr-2.5% Nb alloy, J. Nucl. Mater. **244** (1997) 141–146.

[4.160] SCHEMEL, J.H., "Evolution of the beta-quench process", Zirconium Production and Technology: The Kroll Medal Papers 1975–2010 (ADAMSON, R., Ed), ASTM International, West Conshohocken, PA (2010) 353–355.
[4.161] VAN SWAM, L.F.P., SHANN, S.H., "The corrosion of Zircaloy-4 fuel cladding in pressurized water reactors", Zirconium in the Nuclear Industry: Ninth International Symposium, Proc. ASTM STP 1132, Kobe, 1990 (EUCKEN, C.M., GARDE, A.M., Eds), ASTM International, West Conshohocken, PA (1991) 758–781.
[4.162] GARZAROLLI, F., BODMER, R.P., STEHLE, H., TRAPP-PRITSCHING, S., "Progress in understanding PWR fuel rod waterside corrosion", Proc. ANS Top. Mtg on LWR Fuel Performance, Orlando, 1985, American Nuclear Society, La Grange Park, IL (1985) 3–55.
[4.163] BRADLEY, E.R., SCHEMEL, J.H., NYSTRÖM, A.-L., "Influence of alloy composition and processing on the nodular corrosion resistance of Zircaloy-2", Zirconium in the Nuclear Industry: Ninth International Symposium, Proc. ASTM STP 1132, Kobe, 1990 (EUCKEN, C.M., GARDE, A.M., Eds), ASTM International, West Conshohocken, PA (1991) 304–318.
[4.164] KASS, S., "The development of the Zircaloys", Proc. USAEC Symp. on Zirconium Alloy Development, Pleasanton, 1962, No. GEAP-4089, United States Department of Energy, Washington, DC (1962) 1-0–1-44.
[4.165] ARMAND, M., DEMARS, H., GIVARD, J.P., TROLLIET, G., Influence of the structure and the interstitial impurities on the corrosion of Zircaloy-2 by water and steam, Electrochem. Technol. **4** (1966) 104–108.
[4.166] LUNDE, L., VIDEM, K., "Effect of material and environmental variables on localized corrosion of zirconium alloys", Zirconium in the Nuclear Industry: Fourth International Symposium, Proc. ASTM STP 681, Stratford-upon-Avon, 1978 (PAPAZOGLOU, T.P., Ed.), ASTM International, West Conshohocken, PA (1979) 40–59.
[4.167] WEIDINGER, H.G., GARZAROLLI, F., EUCKEN, C.M., BAROCH, E.F., "Effect of chemistry on elevated temperature nodular corrosion", Zirconium in the Nuclear Industry: Seventh International Symposium, Proc. ASTM STP 939, Strasbourg, 1985 (ADAMSON, R.B., VAN SWAM, L.F.P., Eds), ASTM International, West Conshohocken, PA (1987) 364–386.
[4.168] GRAHAM, R.A., TOSDALE, J.P., FINDEN, P.T., "Influence of chemical composition and manufacturing variables on autoclave corrosion of the Zircaloys", Zirconium in the Nuclear Industry: Eighth International Symposium, Proc. ASTM STP 1023, San Diego, 1988 (VAN SWAM, L.F.P., EUCKEN, C.M., Eds), ASTM International, West Conshohocken, PA (1989) 334–345.
[4.169] GARZAROLLI, F., COX, B., RUDLING, P., Optimization of Zry-2 for high burnups, J. ASTM International **7** (2010) JAI102955.
[4.170] ANDERSSON, T., VESTERLUND, G., "Beta-quenching of Zircaloy cladding tubes in intermediate or final size — Methods to improve corrosion and mechanical properties", Zirconium in the Nuclear Industry: Fifth International Symposium, Proc. ASTM STP 754, Boston, 1980 (FRANKLIN, D.G., Ed.), ASTM International, West Conshohocken, PA (1982) 75–95.
[4.171] ANDERSSON, T., THORVALDSSON, T., Nodular corrosion resistance of Zircaloy-2 in relation to second-phase particle distribution", Zirconium in the Nuclear Industry: Seventh International Symposium, Proc. ASTM STP 939, Strasbourg, 1985 (ADAMSON, R.B., VAN SWAM, L.F.P., Eds), ASTM International, West Conshohocken, PA (1987) 321–337.
[4.172] BANGARU, N.V., BUSCH, R.A., SCHEMEL, J.H., "Effect of beta quenching on the microstructure and corrosion of Zircaloys", Zirconium in the Nuclear Industry: Seventh International Symposium, Proc. ASTM STP 939, Strasbourg, 1985 (ADAMSON, R.B., VAN SWAM, L.F.P., Eds), ASTM International, West Conshohocken, PA (1987) 341–363.
[4.173] GARZAROLLI, F., SCHUMANN, R., STEINBERG, E., "Corrosion optimized Zircaloy for boiling water reactor (BWR) fuel elements", Zirconium in the Nuclear Industry: Tenth International Symposium, Proc. ASTM STP 1245, Baltimore, 1993 (GARDE, A.M., BRADLEY, E.R., Eds), ASTM International, West Conshohocken, PA (1994) 709–723.
[4.174] HUANG, P.Y., MAHMOOD, S.T., ADAMSON, R.B., "Effects of thermomechanical processing on in-reactor corrosion and post-irradiation mechanical properties of Zircaloy-2", Zirconium in the Nuclear Industry: Eleventh International Symposium, Proc. ASTM STP 1295, Garmisch-Partenkirchen, 1995 (BRADLEY, E.R., SABOL, G.P., Eds), ASTM International, West Conshohocken, PA (1996) 726–757.
[4.175] RUDLING, P., WIKMARK, G., LEHTINEN, B., PETTERSSON, H., "Impact of second phase particles on BWR Zr-2 corrosion and hydriding performance", Zirconium in the Nuclear Industry: Twelfth International Symposium, Proc. ASTM STP 1354, Toronto, 1998 (SABOL, G.P., MOAN, G.D., Eds), ASTM International, West Conshohocken, PA, (2000) 678–706.
[4.176] GOLL, W., RAY, I., "The behaviour of intermetallic precipitates in highly irradiated BWR LTP cladding", Zirconium in the Nuclear Industry: Thirteenth International Symposium, Proc. ASTM STP 1423, Annecy, 2001 (MOAN, G.D., RUDLING, P., Eds), ASTM International, West Conshohocken, PA (2002) 80–95.
[4.177] TÄGTSTROM, P., LIMBÄCK, M., DAHLBÄCK, M., ANDERSSON, T., PETTERSSON, H., "Effects of hydrogen pickup and second-phase particle dissolution on the in-reactor corrosion performance of BWR claddings", Zirconium in the Nuclear Industry: Thirteenth International Symposium, Proc. ASTM STP 1423, Annecy, 2001 (MOAN, G.D., RUDLING, P., Eds), ASTM International, West Conshohocken, PA (2002) 96–118.

[4.178] SHIMADA, S., ETOH, Y., TOMIDA, K., BWR Zircaloy cladding corrosion behaviour — effect of microstructure, J. Nucl. Mater. **248** (1997) 275–280.
[4.179] ETOH, Y., et al., "The effect of microstructure on the corrosion behaviour of Zircaloy-2 in BWRs", Zirconium in the Nuclear Industry: Twelfth International Symposium, Proc. ASTM STP 1354, Toronto, 1998 (SABOL, G.P., MOAN, G.D., Eds), ASTM International, West Conshohocken, PA (2000) 658–677.
[4.180] TAKAGAWA, Y., et al., The correlation between microstructure and in-BWR corrosion behaviour of highly irradiated Zr-based alloys, J. ASTM International **2** (2004) JAI12357.
[4.181] CHENG, B., ADAMSON, R.B., "Mechanistic studies of Zircaloy nodular corrosion", Zirconium in the Nuclear Industry: Seventh International Symposium, Proc. ASTM STP 939, Strasbourg, 1985 (ADAMSON, R.B., VAN SWAM, L.F.P., Eds), ASTM International, West Conshohocken, PA (1987) 387–416.
[4.182] OGATA, K., "Effects of alloying element distribution on the nodular corrosion of Zircaloy-2", Zirconium in the Nuclear Industry: Eighth International Symposium, Proc. ASTM STP 1023, San Diego, 1988 (VAN SWAM, L.F.P., EUCKEN, C.M., Eds), ASTM International, West Conshohocken, PA (1989) 346–359.
[4.183] WANG, C.T., EUCKEN, C.M., GRAHAM, R.A., "Investigation of nodular corrosion mechanism of Zircaloy products", Zirconium in the Nuclear Industry: Ninth International Symposium, Proc. ASTM STP 1132, Kobe, 1990 (EUCKEN, C.M., GARDE, A.M., Eds), ASTM International, West Conshohocken, PA (1991) 319–345.
[4.184] KRUGER, R.M., ADAMSON, R.B., BRENNER, S.S., Effects of microchemistry and precipitate size on nodular corrosion resistance of Zircaloy-2, J. Nucl. Mater. **189** (1992) 193–200.
[4.185] RUDLING, P., WIKMARK, G., A unified model of Zircaloy BWR corrosion and hydriding mechanism, J. Nucl. Mater. **265** (1999) 44–59.
[4.186] VALIZADEH, S., et al., Effects of secondary phase particle dissolution on the in-reactor performance of BWR cladding, J. ASTM International **8** (2011) JAI103025.
[4.187] ABE, H., MATSUDA, K., HAMA, T., KONISHI, T., FURUGEN, M., "Fabrication process of high nodular corrosion-resistant Zircaloy-2 tubing", Zirconium in the Nuclear Industry: Tenth International Symposium, Proc. ASTM STP 1245, Baltimore, 1993 (GARDE, A.M., BRADLEY, E.R., (Eds), ASTM International, West Conshohocken, PA (1994) 285–306.
[4.188] SABOL, G.P., McDONALD, S.G., NURMINEN, J.I., JACOBSEN, W.A., "Laser beam beta heat treatment of Zircaloy", Zirconium in the Nuclear Industry: Seventh International Symposium, Proc. ASTM STP 939, Strasbourg, 1985 (ADAMSON, R.B., VAN SWAM, L.F.P., Eds), ASTM International, West Conshohocken, PA (1987) 168–186.
[4.189] DAHLBÄCK, M., et al., The effect of beta-quenching in final dimension on the irradiation growth of tubes and channels, J. ASTM International **2** (2005) JAI12337.
[4.190] CHEADLE, B.A., COLEMAN, C.E., LICHT, H., CANDU-PHW pressure tubes: Their manufacture, inspection, and properties, Nucl. Technol. **57** (1982) 413–425.
[4.191] CHEADLE, B.A., "Fabrication of zirconium alloys into components for nuclear reactors", Zirconium in the Nuclear Industry: Third International Symposium, Proc. ASTM STP 633, Quebec City, 1976 (LOWE, A.L., PARRY, G.W., Eds), ASTM International, West Conshohocken, PA (1977) 457–485.
[4.192] NIKULINA, A.V., "Metal science aspects of zirconium-base reactor material production in the Soviet Union", Zirconium Production and Technology: The Kroll Medal Papers 1975–2010 (ADAMSON, R., Ed.), ASTM International, West Conshohocken, PA (2010) 179–194.
[4.193] NIKULINA, A.V., et al., Fabrication technology of RBMK Zr-2.5Nb pressure tubes, Vopr. At. Nauki Tekh., Ser. Materialovedenie i novye materialy **36** (1990) 46–54 (in Russian).
[4.194] COLEMAN, C.E., et al., Mechanical properties of Zr-2.5Nb pressure tubes made from electrolytic powder, J. ASTM International **4** (2007) JAI101111.
[4.195] FLECK, R.G., PRICE, E.G. CHEADLE, B.A., "Pressure tube development for CANDU reactors", Zirconium in the Nuclear Industry: Sixth International Symposium, Proc. ASTM STP 824, Vancouver, 1982 (FRANKLIN, D.G., ADAMSON, R.B., Eds), ASTM International, West Conshohocken, PA (1984) 88–105.
[4.196] PARKER, J.D., PEROVIC, V., LEGER, M., FLECK, R.G., "Microstructural effects on the irradiation growth of Zr-2.5Nb", Zirconium in the Nuclear Industry: Seventh International Symposium, Proc. ASTM STP 939, Strasbourg, 1985 (ADAMSON, R.B., VAN SWAM, L.F.P., Eds), ASTM International, West Conshohocken, PA (1987) 86–100.
[4.197] BICKEL, G.A., GRIFFITHS, M., Manufacturing Variability and deformation for Zr-2.5Nb pressure tubes, J. Nucl. Mater. **383** (2008) 9–13.
[4.198] O'BRIEN, R.L. (Ed.), Welding Handbook, 8th edn, Vol. 2, Welding Processes, American Welding Society, Miami, FL (1991).
[4.199] Zircadyne Zirconium — ATI Technical Data Sheet, https://www.atimetals.com/Products/Documents/datasheets/zirconium/alloy/Zircadyne-702-7052.pdf#search=Zirconium%20Welding%20Technical%20Data%20Sheet
[4.200] SUTHERLIN, R.C., Welding zirconium and zirconium alloys, Part I: Fundamentals for success, The Tube and Pipe Journal **15** (2004) 18–26;

[4.201] WEBSTER, R.T., "Zirconium and hafnium", ASM Metals Handbook, Properties and selection: Nonferrous alloys and special purpose materials, 10th edn, Vol. 2., ASM International, Materials Park, OH (1990) 661–669.
[4.202] WEBSTER, R.T., "Welding zirconium alloys", ASM Metals Handbook, Welding, Brazing and Soldering, 10th edn, Vol. 6, ASM International, Materials Park, OH (1990) 787–788.
[4.203] AMERICA SOCIETY OF MECHANICAL ENGINEERS, ASME Boiler and Pressure Vessel Code, Section II: Materials, Part D: Properties, ASME, New York (2019).
[4.204] COLEMAN, C.E., et al., "Mitigation of harmful effects of welds in zirconium alloy components", Zirconium in the Nuclear Industry: Tenth International Symposium, Proc. ASTM STP 1245, Baltimore, 1993 (GARDE, A.M., BRADLEY, E.R., Eds), ASTM International, West Conshohocken, PA (1994) 264–284.
[4.205] BANKER, J.G., Explosion cladding: An enabling technology for zirconium in the chemical process industry, J. ASTM International **7** (2010) JAI103050.
[4.206] BATISTA, R.I., "Brazing of refractory and reactive metals", ASM Metals Handbook, Welding, Brazing and Soldering, 10th edn, Vol. 6, ASM International, Materials Park, OH (1993) 941–947.
[4.207] BATES, K.T., Brazing of Zircaloy in Nuclear Fuel, Report No. AECL-2813, Atomic Energy of Canada, Chalk River, ON (1966).
[4.208] Zirconium Machining and Forming Operations — ATI Technical Data Sheet, https://www.atimetals.com/Products/Documents/datasheets/zirconium/alloy/zirconium-machining-forming-operations.pdf#search=sawing
[4.209] WEBSTER, R.T., "Surface engineering of zirconium and hafnium", ASM Metals Handbook, Vol. 5: Surface Engineering (REIDENBACH, F., Ed.), ASM International, Materials Park, OH (1994) 854–855.
[4.210] ALLISON, W.W., Zirconium, Zircaloy and Hafnium Safe Practice Guide for Shipping, Storing, Handling and Scrap Disposal, No. WAPD-TM-17, Bettis Atomic Power Laboratory, Pittsburgh, PA (1960).
[4.211] NATIONAL FIRE PROTECTION ASSOCIATION, Standard for the Production, Processing, Handling and Storage of Zirconium, Vol. 13, National Fire Codes NFPA No. 482M, National Fire Protection Association, Boston, MA (1978).
[4.212] INTERNATIONAL CODE COUNCIL, "Chapter 44", 2006 International Fire Code, International Code Council, Country Club Hills, IL (2006) 381–382.
[4.213] BUREAU OF EXPLOSIVES, Tariff No. BOE-6000-P, Hazardous Materials Regulations of the Department of Transportation, Supplement No. 3, 49 CFR 106, 107, 110, 130, 171–180, 209, 397, effective 28 February (1977).
[4.214] INTERNATIONAL MARITIME ASSOCIATION, Dangerous Goods Code, Amendment 29–98, International Maritime Association, London, UK (1998).
[4.215] INTERNATIONAL AIR TRAFFIC ASSOCIATION, Dangerous Goods Regulations, International Air Traffic Association (IATA Resolution 618, Attachment A) 40th edn, Montréal, Canada–Geneva, Switzerland, effective 1 January 1999 through 31 December 1999.
[4.216] DAVIDSON J.A., MISHRA, A.K., KOVACS, P., POGGIE, R.A., New surface-hardened, low-modulus, corrosion-resistant Ti-13Nb-13Zr alloy for total hip arthroplasty, Biomed. Mater. Eng. **4** (1994) 231–243.
[4.217] ASTM INTERNATIONAL, Standard Specification for Wrought Titanium-13Niobium-13Zirconium Alloy for Surgical Implant Applications (UNS R58130), ASTM Standard F1713, ASTM International, West Conshohocken, PA (2013).
[4.218] ASTM INTERNATIONAL, Standard Specification for Wrought Titanium–12 Molybdenum–6 Zirconium–2 Iron Alloy for Surgical Implant (UNS R58120), ASTM Standard F1813, ASTM International, West Conshohocken, PA (2013).
[4.219] BLUMENTHAL, W.B., Zirconium–behaviour in biological systems, J. Sci. Ind. Res. **35** (1976) 485–490.
[4.220] HALEY, T.J., RAYMOND, K., KOMESU, N., UPHAM, H.C., The toxicologic and pharmacologic effects of hafnium salts, Toxicol. Appl. Pharmacol. **4** (1962) 238–246.
[4.221] THOBURN, T.W., STRAUB, W.E., Health-hazard Evaluation Determination, Report No. HHE-74-78-297, Amax Specialty Metals, Niosh, Cincinnati, OH (1976).
[4.222] BESCH, O.A., YAGNIK, S.K., WOODS, K.N., EUCKEN, C.M., BRADLEY, E.R., "Corrosion behavior of duplex and reference cladding in NPP Grohnde", Zirconium in the Nuclear Industry: Eleventh International Symposium, Proc. ASTM STP 1295, Garmisch-Partenkirchen, 1995 (BRADLEY, E.R., SABOL, G.P., Eds), ASTM International, West Conshohocken, PA (1996) 805–824.
[4.223] ARBORELIUS, J., et al., The effect of duplex cladding outer component tin content on corrosion, hydrogen pick-up, and hydride distribution at very high burnup, J. ASTM International **2** (2005) JAI12411.
[4.224] SCHEMEL, J.H., CHARQUET, D., WADIER, J.-F., "Influence of the manufacturing process on the corrosion resistance of Zircaloy-4 cladding", Zirconium in the Nuclear Industry: Eighth International Symposium, Proc. ASTM STP 1023, San Diego, 1988 (VAN SWAM, L.F.P., EUCKEN, C.M., Eds), ASTM International, West Conshohocken, PA (1989) 141–152.
[4.225] ROSENBAUM, H.S., et al., "Zirconium-barrier cladding attributes", Zirconium in the Nuclear Industry: Seventh International Symposium, Proc. ASTM STP 939, Strasbourg, 1985 (ADAMSON, R.B., VAN SWAM, L.F.P., Eds), ASTM International, West Conshohocken, PA (1987) 675–699.
[4.226] ARMIJO, J.S., ROSENBAUM, H.S., WILLIAMS, C.D., Method for Making Fuel Cladding Having Zirconium Barrier Layers and Inner Liners, US Patent 533228, Jan. 1995, filed Jul. 1993, available on-line.

[4.227] ARMIJO, J.S., COFFIN, L.F., ROSENBAUM, H.S., "Development of zirconium-barrier fuel cladding", Zirconium in the Nuclear Industry: Tenth International Symposium, Proc. ASTM STP 1245, Baltimore, 1993 (GARDE, A.M., BRADLEY, E.R., Eds), ASTM International, West Conshohocken, PA (1994) 3–18.
[4.228] AUNGST, R.C., CURTISS, D.H., Procurement of Zircaloy-2 Process Tubes for N-reactor, Report HW-80566, General Electric, Boston, MA (1964).
[4.229] ALEXANDER, W.K., FIDLERIS, V., HOLT, R.A., "Zircaloy-2 pressure tube elongation at the Hanford N reactor", Zirconium in the Nuclear Industry: Third International Symposium, Proc. ASTM STP 633, Quebec City, 1976 (LOWE, A.L., Jr., PARRY G.W., Eds), ASTM International, West Conshohocken, PA (1977) 344–364.
[4.230] THEAKER, J.R., et al., "Fabrication of Zr-2.5 Nb pressure tubes to minimise the harmful effects of trace elements", Zirconium in the Nuclear Industry: Tenth International Symposium, Proc. ASTM STP 1245, Baltimore, 1993 (GARDE, A.M., BRADLEY, E.R., Eds), ASTM International, West Conshohocken, PA (1994) 221–242.
[4.231] CHEADLE, B.A., EVANS, W., The Fabrication and Metallurgical Evaluation of 3¼ in. Diameter Cold-worked Zirconium–2½% Niobium Pressure Tubes, Report No. AECL-2652, Atomic Energy of Canada Limited, Chalk River, ON (1966).
[4.232] EVANS, W., LESURF, J.E., THOMAS, W.R., Heat-treated Zr-2.5 wt% Nb Pressure Tubes for Water-cooled Power Reactors, Report No. AECL-2890, Atomic Energy of Canada Limited, Chalk River, ON (1967).
[4.233] SAWAI, S., HAGA, T., AKEBI, M., KONTANI, K.I., Fugen HWR reaches commercial operation, Nucl. Eng. Int. **24** (1979) 33–39, 47–49.
[4.234] ELLS, C.E., COLEMAN, C.E., CHOW, C.K., Properties of a CANDU calandria tube, Can. Metall. Q. **24** (1985) 215–223.
[4.235] SAIBABA, M., Fabrication of seamless calandria tubes by cold pilgering route using 3-pass and 2-pass, J. Nucl. Mater. **383** (2008) 63–70.
[4.236] KAPOOR, K.P., PADMAPRABU, C., RAMANA RAO, S.V., SANYAL, T., KASHYAP, B.P., Effect of processing on properties of thin walled calandria tubes for pressurised heavy water reactor, J. Nucl. Mater. **312** (2003) 125–133.
[4.237] PRICE, E.G. RICHINSON, P.J., Thin-walled Large-diameter Zirconium Alloy Tubes in CANDU Reactors, Report No. AECL-6345, Atomic Energy of Canada Limited, Chalk River, ON (1978).
[4.238] MENELEY, D.A., RUAN, Y.Q., Introduction to CANDU 6 (1998), http://canteach.candu.org/Content%20Library/19980106.pdf
[4.239] BALEON, J.P., BURTAK, F., PEYRAN, J.C., URBAN, P., "Framatome ANP fuel experience and development", Proc. Top Fuel, Stockholm, 2001, European Nuclear Society, Berne (2001).
[4.240] UNITED STATES NUCLEAR REGULATORY COMMISSION, Boiling Water Reactor (BWR) Systems, Reactor Concepts Manual, Doc. 0400, USNRC Technical Training Center, Chattanooga, TN (2012), 3–5, https://www.nrc.gov/reading-rm/basic-ref/students/for-educators/03.pdf
[4.241] HASTINGS, I.J., LANE, A.D., CANFLEX advanced fuel bundle gives CANDUs more flexibility, Nucl. Eng. Int. **34** (1989) 32–33.
[4.242] COLEMAN, C.E., "Simulation of interaction between cracked UO_2 fuel and Zircaloy cladding", Proc. Int. Conf. on the Physical Metallurgy of Reactor Fuel Elements, Berkeley Nuclear Laboratories, Gloucestershire, 1973, The Metals Society, London (1975) 302–307.
[4.243] ROBERTSON, J.A.L., "Learning from history: A case study in nuclear fuel", Zirconium in the Nuclear Industry: Eleventh International Symposium, Proc. ASTM STP 1295, Garmisch-Partenkirchen, 1995 (BRADLEY, E.R., SABOL, G.P., Eds), ASTM International, West Conshohocken, PA (1996) 3–11.
[4.244] DAVIS, J.R., Nondestructive Evaluation and Quality Control, ASM Metals Handbook, Vol. 17, 9th edn, ASM International, Materials Park, OH (1989).
[4.245] BIRKS, A.S., GREEN, R.E., McINTIRE, P. (Eds), Ultrasonic Testing, Nondestructive Testing Handbook, 2nd edn, Vol. 7, American Society for Nondestructive Testing, Columbus, OH (1991).
[4.246] ASTM INTERNATIONAL, Standard Specification for Wrought Zirconium Alloy Seamless Tubes for Nuclear Reactor Fuel Cladding, ASTM B811-13 (R2017), ASTM INTERNATIONAL, West Conshohocken, PA. (2007).
[4.247] McMASTER, R.C., McINTIRE, P., MESTER, M.L., Nondestructive Testing Handbook, Vol. 4: Electromagnetic Testing: Eddy Current, Flux Leakage and Microwave Nondestructive Testing, 2nd edn, American Society for Nondestructive Testing, Columbus, OH (1986).
[4.248] McMASTER, R.C., Nondestructive Testing Handbook, Vol. 2: Liquid Penetrant Tests, 2nd edn, American Society for Nondestructive Testing, Columbus, OH (1982).
[4.249] ASTM INTERNATIONAL, Standard Test Method for Pneumatic Leak Testing of Tubing, ASTM A1047/A1047M-05(2019), American Society for Testing and Materials, West Conshohocken, PA (2019).
[4.250] AHMED, H.J., Nuclear Fuel Rod Helium Leak Inspection Apparatus and Method, US Patent 5009835, Apr. 1991, filed Jan. 1989, available on-line.
[4.251] LOKTEV, I.I., ROZHKOV, V.V., ALEKSANDROV, A.B., CHAPAEV, I.G., Detection of Gross and Fine Leaks in Nuclear Fuel Elements, Proc. 15th World Conf. on Non-Destructive Testing, Rome, 2000, Italian Society for Nondestructive Testing and Monitoring Diagnostics, Rome (2001).

[4.252] BOSSI, R.H., IDDINGS, F.A., WHEELER, G.C., MOOR, P.O., Nondestructive Testing Handbook, Vol. 4: Radiographic Testing, 3rd edn, American Society for Nondestructive Testing, Columbus, OH (1982).
[4.253] ASTM INTERNATIONAL, Standard Test Method for Corrosion Testing of Products of Zirconium, Hafnium, and their Alloys in Water at 680°F (360°C) or in Steam at 750°F (400°C), ASTM G2/G2M-19, American Society for Testing and Materials, West Conshohocken, PA (2019).
[4.254] CHENG, B., LEVIN, H.A., ADAMSON, R.B., MARLOWE, M.O., MONROE, V.L., "Development of a sensitive and reproducible steam test for Zircaloy nodular corrosion", Zirconium in the Nuclear Industry: Seventh International Symposium, Proc. ASTM STP 939, Strasbourg, 1985 (ADAMSON, R.B., VAN SWAM, L.F.P., Eds), ASTM International, West Conshohocken, PA (1987) 257–283.
[4.255] ASTM INTERNATIONAL, Standard Test Methods for Determining Average Grain Size, ASTM E112–96 (R2004), American Society for Testing and Materials, West Conshohocken, PA (2004).
[4.256] ASTM INTERNATIONAL, Standard Test Methods for Tension Testing of Metallic Materials, ASTM E8/E8M-21, ASTM International, West Conshohocken, PA (2021).
[4.257] ASTM INTERNATIONAL, Standard Test Methods for Elevated Temperature Tension Tests of Metallic Materials, ASTM E21-20, ASTM International, West Conshohocken, PA (2020).
[4.258] ELLS, C.E., CHEADLE, B.A., "The anisotropy of fracture ductility in flat tension-test bars of alpha zirconium alloy", Applications-related Phenomena for Zirconium and Its Alloys, ASTM STP 458, ASTM International, West Conshohocken, PA (1969) 68–91.
[4.259] ASTM INTERNATIONAL, Standard Test Method for Brinell Hardness of Metallic Materials, ASTM E10-18, ASTM International, West Conshohocken, PA (2018).
[4.260] ASTM INTERNATIONAL, Standard Test Methods for Rockwell Hardness and Rockwell Superficial Hardness of Metallic Materials, ASTM E18-20, ASTM International, West Conshohocken, PA (2020).
[4.261] ASTM INTERNATIONAL, Standard Test Method for Vickers Hardness of Metallic Materials, ASTM E92–82 (R2003), ASTM International, West Conshohocken, PA (2003).
[4.262] ASTM INTERNATIONAL, Standard Test Method for Microindentation Hardness of Materials, ASTM E384-17, ASTM International, West Conshohocken, PA (2017).
[4.263] ASTM INTERNATIONAL, Standard Test Methods for Bend Testing of Material for Ductility, ASTM E290-14, ASTM International, West Conshohocken, PA (2014).
[4.264] ASTM INTERNATIONAL, Standard Test Method for Ball Punch Deformation of Metallic Sheet Material, ASTM E643-15, ASTM International West Conshohocken, PA (2015).
[4.265] VAN SWAM, L.F.P., KNORR, D.B., PELLOUX, R.M., SHEWBRIDGE, J.F., Relationship between contractile strain ratio R and texture in zirconium alloy tubing, Metall. Trans. A **10A** (1979) 483–487.
[4.266] SCHEMEL, J.H., Zirconium Alloy Fuel Clad Tubing, Engineering Guide, Sandvik Special Metals, Kennewick, WA (1989).
[4.267] DANIELSON, P.E., SUTHERLIN, R.C., Metallography and Microstructures of Zirconium, Hafnium, and Their Alloys, ASM Handbook, Vol. 9 (VOORT, G.V., Ed.), ASM International, Materials Park, OH (2004) 943–958.
[4.268] PICKLESIMER, M.L., Anodizing for controlled microstructural contrast by colour, Microscope **15** (1967) 472–479.
[4.269] HAYNES. W.M. (Ed.), CRC Handbook of Chemistry and Physics, 91st edn, CRC Press, Boca Raton, FL (2011).
[4.270] ASM INTERNATIONAL, Corrosion: Materials, ASM Handbook, Vol. 13B, ASM International, Materials Park, OH (2007).
[4.271] SHRIER, L.L., JARMIN, R.A., BURSTEIN, G.T. (Eds), Corrosion: Metal/ Environment Reactions, 3rd edn, Butterworth-Heinemann, Oxford (2000).
[4.272] ELINSON, S.V., PETROV, K.I., Analiticheskaya khimiya tsirkoniya i gafniya (Analytical Chemistry of Zirconium and Hafnium), Nauka, Moscow (1965) (in Russian).
[4.273] ASM INTERNATIONAL, Handbook Committee, ASM Handbook, Vol 10: Materials Characterization, ASM International, Materials Park, OH (1998).
[4.274] HAYES, T.A., ROSEN, R.S., KASSNER, M.E., Creep fracture of Zirconium alloys, J. Nucl. Mater. **353** (2006) 109–118.
[4.275] SCHRIRE, D.I., PEARCE, J.H., "Scanning electron microscope techniques for studying Zircaloy corrosion and hydriding", Zirconium in the Nuclear Industry: Tenth International Symposium, Proc. ASTM STP 1245, Baltimore, 1993 (GARDE, A.M., BRADLEY, E.R., Eds), ASTM International, West Conshohocken, PA (1994) 98–115.
[4.276] GOLDSTEIN, J., et al., Scanning Electron Microscopy and X-ray Microanalysis, 3rd edn, Kluwer Academic/Plenum Publishers, New York (2003).
[4.277] BOSSIS, P., THOMAZET, J., LEFEBVRE, F., "Study of the mechanisms controlling the oxide growth under irradiation: Characterization of irradiated Zircaloy-4 and Zr-1Nb-O oxide scales", Zirconium in the Nuclear Industry: Thirteenth International Symposium, Proc. ASTM STP 1423, Annecy, 2001 (MOAN, G.D., RUDLING, P., Eds), ASTM International, West Conshohocken, PA (2002) 190–221.
[4.278] YUEH, K.H., COX, B., Luminescence properties of zirconium oxide films, J. Nucl. Mater. **323** (2003) 57–67.

[4.279] YUEH, K.H., COX, B., Cathodoluminescence imaging of oxidized zirconium alloys, J. Nucl. Mater. **324** (2004) 203–214.
[4.280] HEDBERG, C.L. (Ed.), Handbook of Auger Electron Spectroscopy, 3rd edn, Physical Electronics, Chanhassen, MN (1995).
[4.281] AITCHISON, I., DAVIES, P.H., Role of microsegregation in fracture of cold-worked Zr 2.5Nb pressure tubes, J. Nucl. Mater. **203** (1993) 206–220.
[4.282] MOULDER, J.F., STICKLE, W.F., SOBOL, P.E., BOMBEN, K.D., Handbook of X-ray Photoelectron Spectroscopy (CHASTAIN, J., Ed.), Perkin-Elmer Corporation, Waltham, MA (1992).
[4.283] BEARDEN, J.A., BURR, A.F., Re-evaluation of X ray atomic energy levels, Rev. Mod. Phys. **39** (1967) 125–142.
[4.284] FUGGLE, J.C., MÅRTENSSON, N., Core-level binding energies in metals, J. Electron Spectrosc. Relat. Phenom. **21** (1980) 275–281.
[4.285] DO, T., SAIDY, M., HOCKING, W.H., Chemistry of waterside oxide layers on pressure tubes, J. ASTM Int. **5** (2008) JAI 101292.
[4.286] COLTHUP, N.B., DALY, L.H., WIBERLY, S.E., Introduction to Infrared and Raman Spectroscopy, 3rd edn, Academic Press, New York (1990).
[4.287] THEOPHANIDES, T. (Ed.), Fourier Transform Infrared Spectroscopy, Springer, Dordrecht (1984).
[4.288] RAMASUBRAMANIAN, N., LING, V.C., Fourier transform infrared reflection (FTIR) spectroscopy of corrosion films on irradiated zirconium alloys, J. Nucl. Mater. **175** (1990) 237–243.
[4.289] GODLEWSKI, J., BOUVIER, P., LUCAZEAU, G., FAYETTE, L., "Stress distribution measured by Raman spectroscopy in zirconia films formed by oxidation of Zr-based alloys", Zirconium in the Nuclear Industry: Twelfth International Symposium, Proc. ASTM STP 1354, Toronto, 1998 (SABOL, G.P., MOAN, G.D., Eds), ASTM International, West Conshohocken, PA (2000) 877–900.
[4.290] GODLEWSKI, J., GROS, J.P., LAMBERTIN, M., WADIER, J.F., WEIDINGER, H., "Raman spectroscopy study of the tetragonal-to-monoclinic transition in zirconium oxide scales and determination of overall oxygen diffusion by nuclear microanalysis of O18", Zirconium in the Nuclear Industry: Ninth International Symposium, Proc. ASTM STP 1132, Kobe, 1990 (EUCKEN, C.M., GARDE, A.M., Eds), ASTM International, West Conshohocken, PA (1991) 416–436.
[4.291] NEWVILLE, M., Fundamentals of XAFS, Consortium for Advanced Radiation Sources, Chicago, IL (2004).
[4.292] FROIDEVAL, A., et al., Microprobe analysis of neutron irradiated and autoclaved zirconium-niobium claddings using synchrotron-based x-ray imaging and spectroscopy, J. Nucl. Mater. **385** (2009) 346–350.
[4.293] JUDGE, C.D., "The use of electron backscattered diffraction for material characterization at Chalk River Laboratories", Proc. CNS 31st Annual Conf., Montreal, 2010, Canadian Nuclear Society, Toronto (2010) 24–27.
[4.294] SCHWARTZ, A.J., KUMAR, M., ADAMS, B., FIELD, D.P. (Eds), Electron Backscatter Diffraction in Materials Science, 2nd edn, Springer, New York (2009).
[4.295] OXFORD INSTRUMENTS, Electron Backscatter Diffraction, https://nano.oxinst.com/products/ebsd/
[4.296] BREWER, L.N., MICHAEL, J.R., Risks of "cleaning" electron backscatter diffraction data, Microsc. Today **18** (2010) 10–15.
[4.297] HOLT, R.A., ZHAO, P., Micro-texture of extruded Zr-2.5Nb tubes, J. Nucl. Mater. **335** (2004) 520–528.
[4.298] UNE, K., ISHIMOTO, S., Crystallographic measurement of β to α phase transformation and δ-hydride precipitation in a laser-welded Zircaloy-2 tube by electron backscattering diffraction, J. Nucl. Mater. **389** (2009) 436–442.
[4.299] KIRAN KUMAR, N.A.P., SZPUNAR, J.A., HE, Z., Preferential precipitation of hydrides in textured Zircaloy-4 sheets, J. Nucl. Mater. **403** (2010) 101–107.
[4.300] HOVINGTON, P., et al., Towards a more comprehensive microstructural analysis of Zr-2.5Nb pressure tubing using image analysis and electron backscattered diffraction (EBSD), J. Nucl. Mater. **393** (2009) 162–174.
[4.301] MASON, T.A., BINGERT, J.F., KASCHNER, G.C., WRIGHT, S.I., LARSEN, R.J., Advances in deformation twin characterization using electron backscattered diffraction data, Metall. Mater. Trans. A **33** (2002) 949–954
[4.302] McCABE, R.J., CERRETA, E.K., MISRA, A., KASCHNER, G.C., TOME, C.N., Effects of texture, temperature and strain on the deformation modes of zirconium, Philos. Mag. **86** (2006) 3595–3611.
[4.303] McCABE, R.J., PROUST, G., CERRETA, E.K., MISRA, A., Quantitative analysis of deformation twinning in zirconium, Int. J. Plast. **25** (2009) 454–472.
[4.304] KRISHNA, K.V., et al., Automated reconstruction of pre-transformation microstructures in zirconium, Scripta Mater. **62** (2010) 391–394.
[4.305] KRISHNA, K.V., et al., Microstructural and textural developments during Zircaloy-4 fuel tube fabrication, J. Nucl. Mater. **383** (2008) 78–85.
[4.306] SAINTOYANT, L., LEGRAS, L., BRÉCHET, Y., Effect of an applied stress on the recrystallization mechanisms of a zirconium alloy, Scripta Mater. **64** (2011) 418–421.

[4.307] WILLIAMS, D.B., CARTER, C.B., Transmission Electron Microscopy: A Textbook for Materials Science, Plenum Press, New York (1996).
[4.308] EGERTON, R.F., Electron Energy Loss Spectroscopy in the Electron Microscope, 2nd edn, Plenum Press, New York (1996).
[4.309] WOO, O.T., CARPENTER, G.J.C., EELS characterization of zirconium hydrides, Microsc. Microanal. Microstruct. **3** (1992) 35–44.
[4.310] WOO, O.T., CARPENTER, G.J.C., MacEWEN, S.R., <c>-Component dislocations in zirconium alloys, J. Nucl. Mater. **87** (1979) 70–80.
[4.311] GRIFFITHS, M., GILBERT, R.W., FIDLERIS, V., "Accelerated irradiation growth of Zirconium alloys", Zirconium in the Nuclear Industry: Eighth International Symposium, Proc. ASTM STP 1023, San Diego, 1988 (VAN SWAM, L.F.P., EUCKEN, C.M., Eds), ASTM International, West Conshohocken, PA (1989) 658–677.
[4.312] CARPENTER, G.J.C., WATTERS, J.F., Vacancy precipitation in zirconium alloys, Acta Metall. **21** (1973) 1207–1214.
[4.313] SILVA, E., ROBINSON, J.W., NORTHWOOD, D.O., "Ion beam thinning of a zirconium alloy for TEM", Proc. Ann. Mtg of the Microscopical Society of Canada, Chalk River, 1983 (PARSONS, J.R., Ed.), Imperial Press, Toronto (1983) 56–57.
[4.314] CARPENTER, G.J.C., JACKMAN, J.A., McCAFFREY, J.P., ALANI, R., In-situ hydride formation in zirconium and titanium during ion milling, Microscop. Microanal. **1** 4 (1995) 175–184.
[4.315] CARPENTER, G.J.C., The dilatational misfit of zirconium hydrides precipitated in zirconium, J. Nucl. Mater **48** (1973) 264–266.
[4.316] KEARNS, J.J., Diffusion coefficient of hydrogen in alpha zirconium, Zircaloy-2 and Zircaloy-4, J. Nucl. Mater. **43** (1972) 330–338.
[4.317] ALANI, R., SWANN, P.R., "Precision ion polishing system — A new instrument for TEM specimen preparation of materials", Proc. Symp. on Specimen Preparation for Transmission Electron Microscopy of Materials III (ANDERSON, R., Ed.), Materials Research Society Symposium Proceedings Series 254, Materials Research Society, Pittsburgh, PA (1992) 43–63.
[4.318] LI, J., The focused-ion-beam microscope — more than a precision ion milling machine, J. Met. **58** (2006) 27–31.
[4.319] GIANNUZZI, L.A., et al., "FIB lift-out specimen preparation techniques — Ex-situ and in-situ methods", Introduction to Focused Ion Beams: Instrumentation, Theory, Techniques and Practice (GIANNUZZI, L.A., Ed.), Springer, Boston (2005) 201–228.
[4.320] KAMINO, T., YAGUCHI, T., HASHIMOTO, T., OHNISHI, T., UMEMURA, K., "FIB micro-sampling technique and a site-specific TEM specimen preparation method", Introduction to Focussed Ion Beams: Instrumentation, Theory, Techniques and Practice (GIANNUZZI, L.A., Ed.), Springer, Boston (2005) 229–245.
[4.321] ABOLHASSANI, S., GASSER, P., Preparation of TEM samples of metal-oxide interface by the focused ion beam technique, J. Microscop. **223** (2006) 73–82.
[4.322] PHANEUF, M., "FIB for materials science applications — a review", Introduction to Focused Ion Beams: Instrumentation, Theory, Techniques and Practice (GIANNUZZI, L.A., Ed.), Springer, Boston (2005) 143–172.
[4.323] NG-YELIM, J., WOO, O.T., CARPENTER, G.J.C., A replica technique for extracting precipitates from zirconium alloys for transmission electron microscopy analysis, J. Electron Microscop. Tech. **15** (1990) 400–405.
[4.324] ASTM INTERNATIONAL, Standard Practice for Describing and Specifying Inductively Coupled Plasma Atomic Emission Spectrometers, ASTM International, West Conshohocken, PA (2016).
[4.325] ASTM INTERNATIONAL, Standard Test Method for Determining Hafnium in Zirconium and Zirconium Alloys by Direct Current Plasma — Atomic Emission Spectrometry, ASTM E1552-15, ASTM International, West Conshohocken, PA (2015).
[4.326] ASTM INTERNATIONAL, Standard Practice for Describing and Specifying a Direct Current Plasma Atomic Emission Spectrometer, ASTM E1832-08(2017), ASTM International, West Conshohocken, PA (2017).
[4.327] ASTM INTERNATIONAL, Standard Test Method for Determination of Oxygen and Nitrogen in Titanium and Titanium Alloys by the Inert Gas Fusion Technique, ASTM E1409-13, ASTM International, West Conshohocken, PA (2013).
[4.328] ASTM INTERNATIONAL, Standard Test Method for Determination of Hydrogen in Titanium and Titanium Alloys by the Inert Gas Fusion Thermal Conductivity/Infrared Detection Method, ASTM E1447-09(2016), ASTM International, West Conshohocken, PA (2016).
[4.329] INTERNATIONAL ATOMIC ENERGY AGENCY, Delayed Hydride Cracking in Zirconium Alloys in Pressure Tube Nuclear Reactors, IAEA-TECDOC-1410, IAEA, Vienna (2004).
[4.330] BICKEL, G.A., et al., The determination of hydrogen and deuterium in Zr-2.5Nb material by hot vacuum extraction mass spectrometry, J. Nucl. Mater. **306** (2002) 21–29.
[4.331] ASTM INTERNATIONAL, Standard Test Method for Determination of Carbon in Refractory and Reactive Metals and Their Alloys, ASTM E1941-10(2016), ASTM International, West Conshohocken, PA (2016).

[4.332] ASTM INTERNATIONAL, Standard Practice for Determination of Elements by Graphite Furnace Atomic Absorption Spectometry, ASTM E1184-10(2016), ASTM International, West Conshohocken, PA (2016).
[4.333] ASTM INTERNATIONAL, Standard Practice for Optimization of Electrothermal Atomic Absorption Spectrometric Equipment, ASTM WK55147, ASTM International, West Conshohocken, PA (2016).
[4.334] ASTM INTERNATIONAL, Standard Practice for Optimization of Flame Atomic Absorption Spectrometric Equipment, Historical Standard: ASTM E1812-96(2004)e1, ASTM International, West Conshohocken, PA (1996).
[4.335] ASTM INTERNATIONAL, Standard Test Method for Analysis of Titanium Alloys by Wavelength Dispersive X-Ray Fluorescence Spectrometry, ASTM E539-19, ASTM International, West Conshohocken, PA (2019).
[4.336] ROBINSON, K., HALL, E.F.H., Glow discharge mass spectrometry for nuclear materials, J. Met. **39** (1987) 14–16.
[4.337] SHEKHAR, R., ARUNACHALAM, J., RADHA KRISHNA, G., RAVINDRA, H.R., GOPALAN, B., Determination of elemental composition of Zr-Nb alloys by glow discharge quadrapole mass spectrometry, At. Spectroscop. **25** (2004) 157–164.
[4.338] SHEKHAR, R., ARUNACHALAM, J., RAVINDRA, H.R., GOPALAN, B., Quantitative determination of chlorine by glow discharge quadrapole mass spectrometry in Zr-2.5Nb alloys, J. Anal. At. Spectrom. **18** (2003) 381–384.
[4.339] SHEKHAR, R., ARUNACHALAM, J., RADHA KRISHNA, G., RAVINDRA, H.R., GOPALAN, B., Determination of boron in Zr-Nb alloys by glow discharge quadrapole mass spectrometry, J. Nucl. Mater. **340** (2005) 284-290.

Chapter 5

DEFORMATION AND TEXTURE

E. TENCKHOFF
Kraftwerk Union AG,
Erlangen, Germany

5.1. INTRODUCTION

The element zirconium (Zr) and the Zr based alloys belong to the group of metals with a hexagonal close packed (HCP) crystal structure. This phase is the α phase. Other common metals in this category are titanium, hafnium, zinc, magnesium, beryllium, cadmium and cobalt. At temperatures >1135 K (863°C), Zr undergoes an allotropic transformation from the HCP crystal structure to the body centred cubic (BCC) crystal structure. This phase is the β phase. The α ↔ β phase transformation is also activated in Zr based alloys, with an (α + β) two phase region with different α ↔ α + β and α + β ↔ β solvus temperatures depending on the alloy (see Chapter 2).

The crystal structure of Zr and Zr based alloys and their allotropic transformations cause a strong anisotropy in physical and technological properties. This chapter will:

— Describe the basic crystal structure and deformation modes of Zr and Zr based alloys;
— Discuss the influence of the anisotropic operating deformation systems on the development of crystallographic texture during fabrication;
— Outline the influence of texture on physical and mechanical anisotropy.

These three aspects are mutually interdependent. Understanding these correlations is important, because — within limits — tailoring the properties of structural parts to the requirements of their application becomes possible. The focus of this chapter is the deformation and texture of semifinished products made from Zr based alloys for components in nuclear applications, mainly sheets and tubes of different dimensions and conditions.

5.2. THE CRYSTAL STRUCTURE IN HCP METALS

The crystal structures of HCP metals are more complex than those of face centred cubic (FCC) and BCC metals. The HCP cell consists of three elementary unit cells, which are defined by three coplanar axes $<a_1>$, $<a_2>$ and $<a_3>$ 120° apart in the basal plane. Perpendicular to this plane is the $<c>$ axis (Fig. 5.1). The distance between each *A* plane of atoms is called *c* and the distance between atoms in these planes, along the $<a_n>$ axis, is called *a*. Although the HCP metals normally form what is considered a single class, the individual metals differ in their crystallographic structure. The *c*/*a* axial ratio varies from one metal to another and can attain a value larger or smaller than the ideal packing of spheres, in which $c/a = \sqrt{8/3}$ or 1.633. Irrespective of the *c*/*a* ratio, the stacking sequence in the basal plane is ABAB.

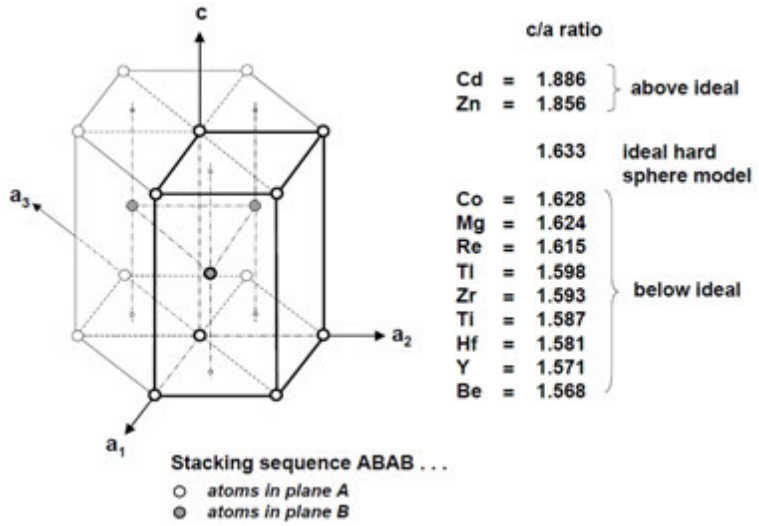

FIG. 5.1. The HCP cell and the c/a axial ratio for various HCP metals. Lines in bold represent the HCP unit cell (reprinted with permission from Ref. [5.1], copyright ASTM International).

To identify the planes and directions in HCP metals, the Miller-Bravais notation is usually used, because it gives similar indices to similar planes and directions [5.2]. This notation is used throughout this publication. Important planes are the basal plane, (0001), and the prism planes of the first and second order, $\{10\bar{1}0\}$ and $\{11\bar{2}0\}$. Basal and prism planes are perpendicular to each other. The planes with an orientation between basal and prism planes are pyramidal planes of various orders (e.g. $\{10\bar{1}1\}$, $\{11\bar{2}1\}$ and $\{11\bar{2}2\}$ (Fig. 5.2)).

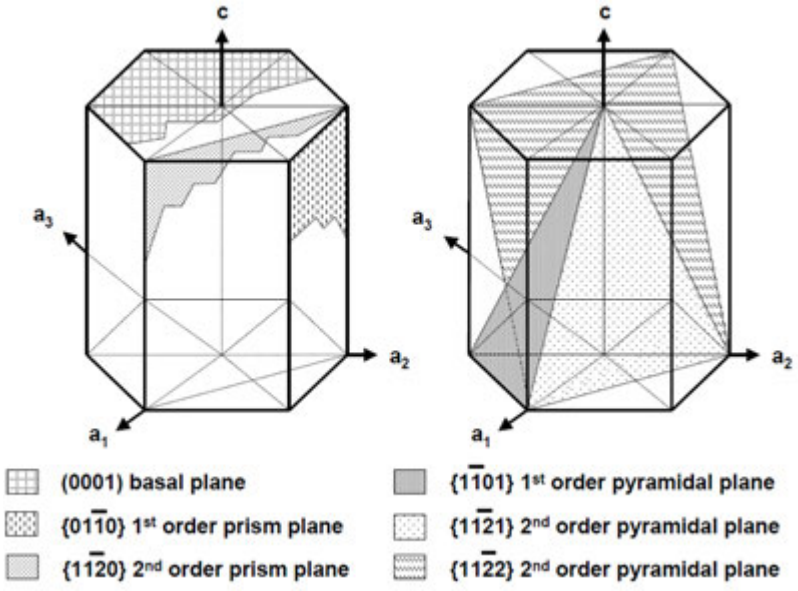

FIG. 5.2. Crystallographic characteristics of the HCP cell: basal plane, different prism and pyramidal planes.

Due to the different *c*/*a* ratios of the HCP metals, the interplanar spacings and angular relationships between the corresponding crystallographic planes are altered, preventing the HCP metals from being considered en bloc. These differences are in contrast to cubic metals, for which the angular relationships between corresponding planes are identical, independent of interplanar spacing.

The hexagonal cell has structural anisotropy, which results in some properties having a pronounced dependency on the orientation of the crystal. A polycrystalline material can inherit these direction dependent properties when its grains have preferred crystallographic orientations; this preferred orientation is called texture. The effect on properties is more pronounced as the texture of the material becomes sharper.

Some anisotropic properties of the hexagonal cell structure, which can affect the behaviour of textured polycrystals in Zr and Zr based alloys in technical, especially nuclear applications, are briefly described below.

Thermal conductivity:

— Parallel to c axis: high thermal conductivity;
— Perpendicular to c axis: low thermal conductivity.

Thermal expansion:

— Parallel to c axis: high thermal expansion;
— Perpendicular to c axis: low thermal expansion.

This anisotropy has to be taken into account when Zr or Zr based alloys are loaded under thermomechanical conditions because it results in the buildup of residual stresses during heat treatment and contributes to creep (see Section 5.7.4 below and Chapter 7 in Volume 2 of this publication).

Optical properties: In the wavelength range of visible light, the optical anisotropy is described by the tensor of the dielectric constant.

In microscopic examinations under polarized light, the colour change of polycrystals, when rotated in the plane perpendicular to the incident light beam is caused by the contribution of free electrons in the electrical field, depending on whether the electrical field is parallel or perpendicular to the c axis.

Chemical reaction properties: Surface corrosion: a crystal with a basal plane orientation parallel to the surface dissolves faster and forms a thicker oxide layer than a crystal with a prism plane parallel to the surface. This anisotropy is exploited in etching techniques for metallographic examinations.

— Localized corrosive attack: the basal plane of a single crystal is less sensitive to localized corrosive attack than its prism plane.

This anisotropy shows up in the behaviour of stress corrosion cracking, where polycrystals with basal planes preferentially oriented parallel to the surface show lower sensitivity to stress corrosion cracking than crystals with basal planes preferentially oriented perpendicular to the surface (see Section 5.7.2 below and Chapter 9 in Volume 3 of this publication).

Mechanical properties:

— Elastic properties (small anisotropy), such as Young’s modulus and Poisson’s ratio.
— Plastic properties (high anisotropy), such as:

- Yield strength (for a single crystal: the critical resolved shear stress (CRSS));
- Ultimate strength;
- Hardness;
- Impact strength;
- Ductility;
- Earing in sheets.

The mechanical properties, especially plastic behaviour, are directly influenced by the anisotropy of the operative deformation systems, which in an HCP crystal structure are not as symmetrically distributed as in FCC or BCC structures. The primary slip systems are not numerous and are limited to deformations in the <a> directions. Therefore, twinning competes with slip in plastic deformation and can, depending on the deformation conditions, play an essential role [5.1–5.7]. The low number of slip systems, their asymmetrical distribution and the strict crystallographic orientation relationships for twinning result in the formation of a strong deformation texture [5.1, 5.8–5.9]. If the material is subsequently heat treated, a pronounced annealing texture develops. For textured materials, the deformation mechanisms are also responsible for the strong anisotropy of the mechanical properties [5.1, 5.10–5.12].

The anisotropy of the deformation systems, the formation of texture and mechanical anisotropy are mutually interdependent. They will be discussed for HCP metals in general and for zirconium and zirconium based alloys in detail in the following sections.

5.3. DEFORMATION MECHANISMS IN HCP METALS

The deformation mechanisms of HCP metals are more complex and less well investigated than those of FCC and BCC metals [5.2, 5.6, 5.13–5.16].

5.3.1. Slip modes

There are three well established laws governing the slip behaviour of metals:

(a) The slip plane with the greatest resolved shear stress acting on it will predominate the slip process. For a given set of slip planes and directions, the crystal slips on the system (plane and direction) for which the difference between the resolved shear stress and the critical resolved shear stress is largest.
(b) The slip plane is normally the plane whose interplanar spacing, that is, whose atomic density, is the largest.
(c) The slip direction is nearly always the one that contains the smallest interatomic spacing. This direction corresponds with the shortest lattice mismatch, called the Burgers vector, in the dislocations causing the slip. The Burgers vector for any given dislocation line is the same all along its length and is defined by the magnitude and direction of the slip movement associated with it [5.2].

Law (a) corresponds to Schmid's law of resolved shear stress [5.17], initially found by experiment, and is discussed in more detail below (Section 5.4.3.1). Laws (b) and (c) are included in the Peierls-Nabarro model of slip [5.18, 5.19]. This model considers the undistorted lattice as a classical elastic continuum; it assumes that the forces for the atomic interactions along the slip plane vary periodically, corresponding to a sine function of the

relative atomic displacements. The model provides estimates of an order of magnitude; exact calculations must take into account the interactions in the distorted crystal lattice and the atomic structure, including the electron structure of the atoms, the bond energies and the geometric arrangement. In spite of its inaccuracy, the Peierls-Nabarro model permits the general trend for metallic bonds to be ascertained, whereby the Peierls-Nabarro forces are small for short Burgers vectors in planes with high atomic density, that is, with large interplanar spacing. Sagel and Zwicker [5.20] have demonstrated that the model is applicable to HCP metals using the example of titanium.

Deformation relationships for FCC metals are considerably simpler than those for HCP metals because 12 possible slip systems belonging to the same primary slip system $\{111\} < 10\bar{1} >$ are symmetrically distributed over the whole reference sphere (Fig. 5.3). Therefore, in FCC metals usually only slip systems of this one family become operative; under uniaxial loading and at low deformation rates, single slip occurs, whereas multiaxial loading, as well as higher deformation rates, leads to duplex or multiple slip of equivalent systems. For BCC structures, such as β-Zr, 24 slip systems become operative: 12 primary slip systems of the type $\{110\} < 1\bar{1}1 >$ and 12 secondary slip systems of the type $\{121\} < \bar{1}1\bar{1} >$. Although both systems have different relevant critical resolved shear stresses, each of the two types of slip systems is again symmetrically distributed over the reference sphere. In FCC and BCC structures, the angular relationships between the different planes are always the same. Consequently, the slip systems can be transferred to the different metals of the same structure, irrespective of their atomic spacing.

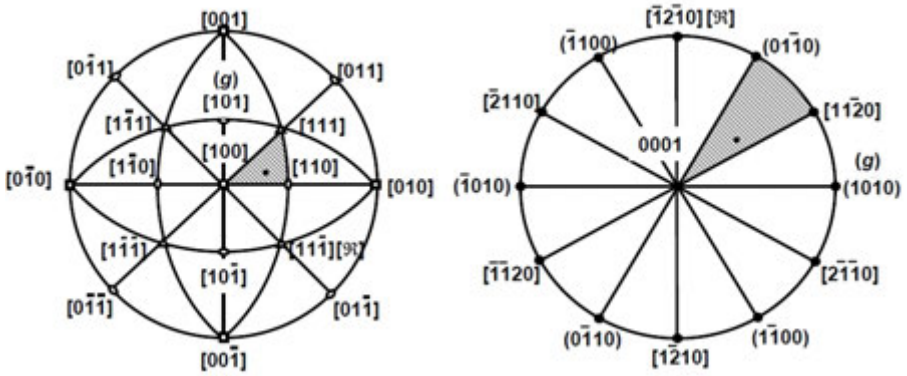

FIG. 5.3. Standard stereographic projections of poles and zone circles for (a) cubic crystals; (001) projection; (b) hexagonal crystals, (0001) projection.

This influence of atomic spacing is not the case for the HCP metals. Within one plane family, there are only a few possible deformation systems. Additionally, they are asymmetrically distributed over the reference sphere (Fig. 5.3). Various primary and secondary slip and twinning systems, which exhibit various critical resolved shear stresses, must operate for compatibility (see Section 5.4.3.7). These slip and twinning systems will now be discussed.

5.3.1.1. Slip plane

Although the interplanar spacing of the basal plane is a constant *c*/2 (referring back to the stacking in Fig. 5.1) for HCP metals, the other types of planes, the prism and pyramidal planes, each have an irregular interplanar spacing for certain planes, as shown in Fig. 5.4 [5.6]. Taking into account the A-B stacking sequence, the clearly visible waviness

of the non-basal planes and their irregular spacing explain why the slip models for prism and pyramidal planes are so complicated.

Influence of the *c*/*a* axial ratio: The interplanar spacing and the packing density vary with the *c*/*a* axial ratio of the hexagonal unit cell. Above, and with ideal axial ratios, the basal plane (0001) is the most densely packed. If the *c*/*a* axial ratio is less than $\sqrt{8/3}$, then the prism plane becomes more densely packed than the basal plane. On the basis of the Peierls-Nabarro model, one would therefore expect that for slip in the *a* direction, a change in slip plane from (0001) to $\{10\bar{1}0\}$ would take place (Fig. 5.5). There are some exceptions, for example, magnesium (Mg), cobalt (Co), and beryllium (Be). Their behaviour is explained by further factors determining the choice of slip plane, for example, the stacking fault energy (SFE) and, if applicable, the α ↔ β phase transformation behaviour.

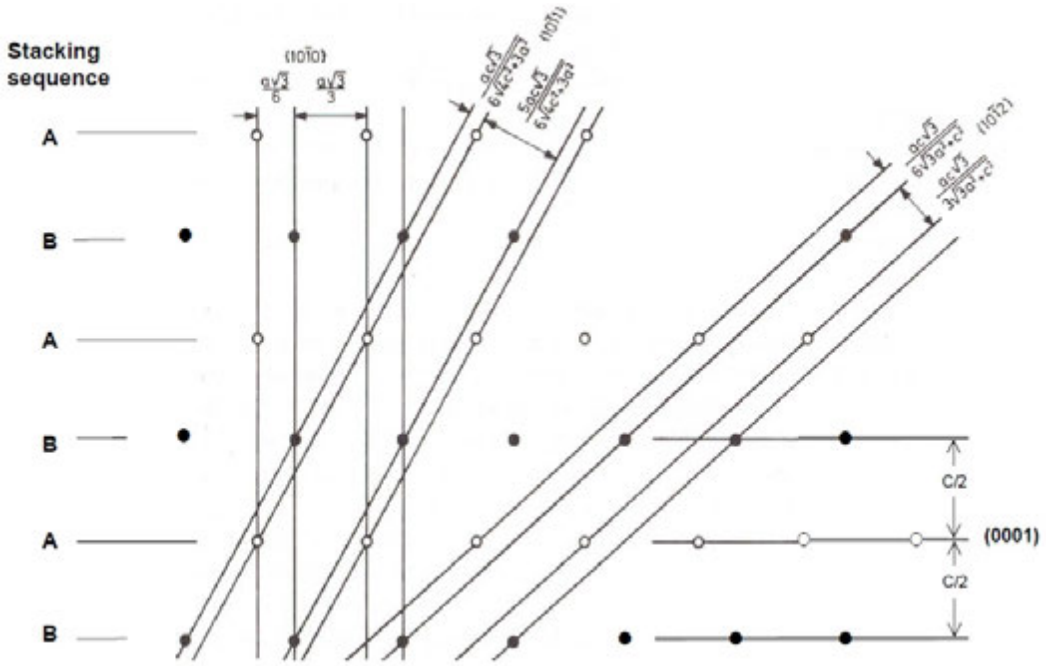

FIG. 5.4. Projections of the atomic layers in the $(1\bar{1}10)$ *plane (○ — atoms in sequence A; ● — atoms in sequence B). The lines show the traces and interplanar spacings of (0001),* $\{10\bar{1}2\}$, $\{10\bar{1}1\}$, *and* $\{10\bar{1}0\}$ *planes for ideal sphere packing (c/a = 1.633) (reprinted with permission from Ref. [5.1], copyright ASTM International).*

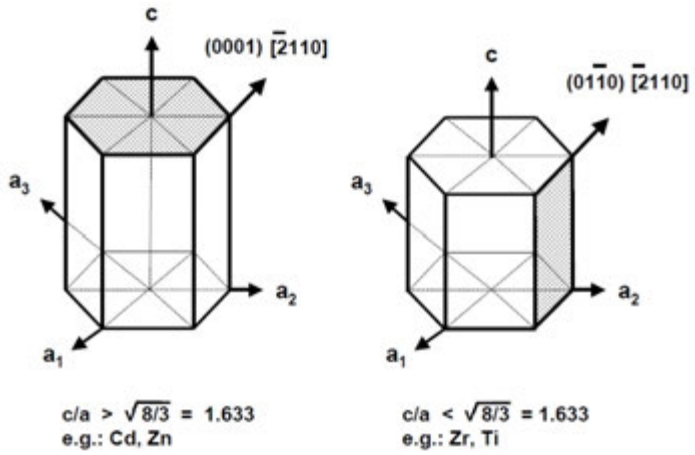

FIG. 5.5. Dependence of the slip plane for 'a' dislocations on the c/a axial ratio (reprinted with permission from Ref. [5.1], copyright ASTM International).

5.3.1.2. Slip direction

The possible Burgers vectors in HCP metals can be represented by means of a double tetrahedron, which is derived correspondingly from the Thompson tetrahedron for FCC metals [5.21, 5.22]. There are thus three possible types of perfect dislocation and three possible types of partial dislocation (Fig. 5.6):

Type I: Six perfect *a* dislocations of the type $1/3 < 11\bar{2}0 >$ AB, BC, CA, AC, CB and BA.

Type II: Two perfect *c* dislocations of the type <0001> with the Burgers vectors ST and TS.

Type III: Twelve perfect ($c + a$) dislocations of the type $1/3 < 11\bar{2}3 >$ with the Burgers vectors SA/TB, SA/TC, SB/TA, SB/TC, SC/TA and SC/TB as well as their negative indices.

Type IV: Six partial *p* dislocations of the type $1/3 < 10\bar{1}0 >$with the Burgers vectors Aσ, Bσ, Cσ, σA, σB, and σC.

Type V: Four partial *c/2* dislocations of the type 1/2 [0001] with the Burgers vectors σS, σT, Sσ and Tσ.

Type VI: Twelve partial ($c/2 + p$) dislocations of the type $1/6 < 20\bar{2}3 >$ with the Burgers vectors AS, BS, CS, AT, BT and CT as well as their negative indices.

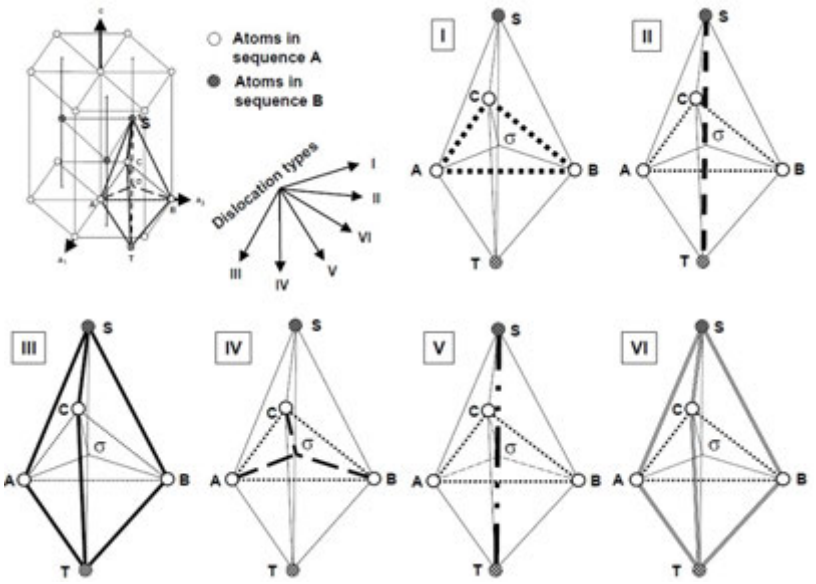

FIG. 5.6. Theoretically possible Burgers vectors in an HCP lattice. Lines in bold represent the traces of the corresponding dislocation type I to VI.

Assuming an ideal packing of spheres (c/a = 1.633), the squares of the vector magnitude are listed in Table 5.1; these values are proportional to a first approximation to the elastic energies of the dislocations. Those dislocations that have the shortest Burgers vector will become active for a given slip direction; within the class of perfect dislocations, *a* dislocations are favoured for slip over *c* dislocations and these, in turn, over ($c + a$) dislocations.

TABLE 5.1. VECTOR ENERGIES FOR POSSIBLE DISLOCATION TYPES IN HCP METALS FOR A C/A AXIAL RATIO OF IDEAL SPHERE PACKING

Dislocation type	Designation	Number of dislocations per type	Burgers vector	Vector energy
I	a	6	$1/3 < 11\bar{2}0 >$	a^2
II	c	2	$< 0001 >$	$c^2 = 8/3\ a^2$
III	$(c + a)$	12	$1/3 < 11\bar{2}3 >$	$11/3\ a^2$
IV	p	6	$1/3 < 10\bar{1}0 >$	$1/3\ a^2$
V	$c/2$	4	$1/2 < 0001 >$	$2/3\ a^2$
VI	$(c/2 + p)$	12	$1/6 < 20\bar{2}3 >$	a^2

Because the Burgers vectors of the *a* and *c* dislocations are perpendicular to one another, they cannot mutually interact. The $(c + a)$ dislocations can interact with *a* or *c* dislocations with an energy gain and form stable dislocation nodes, assuming that the relatively long $<c + a>$ Burgers vectors can exist on the basis of the preceding energy criterion. Corresponding energy considerations can also be made for partial dislocations, which are energetically favourable owing to their short Burgers vectors; if and to what extent dissociation into two dislocation partials is possible also depends on the SFE.

5.3.2. Influence of the SFE, γ

5.3.2.1. Dissociation of 'a' *dislocations in the basal plane*

With a low SFE, *γ,* the a dislocation in the basal plane can be dissociated with energy gain into two Shockley partials, *p,* surrounding an intrinsic stacking fault that violates the two next nearest neighbours in the stacking sequence [5.2, 5.15] (see Fig. 5.6).

$$AB \rightarrow A\sigma + \sigma B \tag{5.1}$$

$$1/3\ [11\bar{2}0] \rightarrow 1/3\ [10\bar{1}0] + 1/3\ [01\bar{1}0] \tag{5.2}$$

For this dislocation reaction in the basal plane, which occurs within a thin intermediate layer in a likewise densely packed FCC stacking sequence, there are two possible slip sequences: Either a B layer slips over an A layer (that is, σB follows σA, as in Fig. 5.7*),* or an A layer slips over a B layer (that is, Aσ follows Bσ, as in Fig. 5.7).

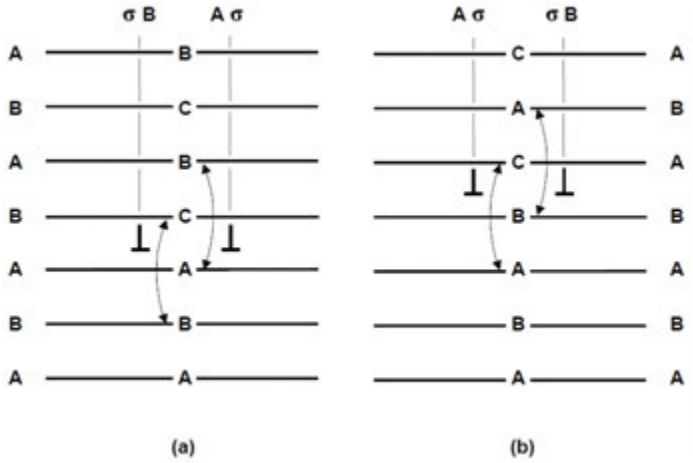

FIG. 5.7. Stacking faults in the basal plane of an HCP lattice (reprinted with permission from Ref. [5.1], copyright ASTM International).

The ribbon width is inversely proportional to the SFE γ. Values of γ, that are measured, calculated, or estimated, are listed for a dislocations in the basal plane and in some prism planes for several HCP metals (Table 5.2). For cobalt, which has low SFE, corresponding dislocation reactions were observed in the basal plane [5.16]. No observations of intrinsic stacking faults could be made of the metals with high SFE, including zirconium, because the dislocations are not dissociated sufficiently.

TABLE 5.2. SFE GAMMA, FOR *a* DISLOCATIONS IN THE BASAL OR PRISM PLANE OF VARIOUS HCP METALS

Material	SFE, γ, ($\times 10^{-3}$ J·m^2)	In plane	Reference
Cd	250–300	Basal	[5.2]
	170	Basal	[5.16]
	150	Basal	[5.23]
Zn	250–300	Basal	[5.2]
	300	Basal	[5.16, 5.23–5.25]
Co	25	Basal	[5.2]
	26	Basal	[5.16, 5.24]
Mg	250–300	Basal	[5.2]
	300	Basal	[5.16, 5.25]
	60	Basal	[5.26]
	10–21	Basal (calculated)	[5.27]
Zr	250–300	Basal	[5.2]
	56	Prism	[5.28]
Ti	250–300	Basal	[5.2]
	300	Basal	[5.16, 5.29]
	145	Prism	[5.30]
Be	250–300	Basal	[5.2]
	~180	Basal	[5.16, 5.29]
	>190	Basal	[5.26]
	279–1147	Basal (calculated)	[5.27]
	$\geq$790	Basal (anticipated)	[5.31]
	$\geq$1190	Prism (anticipated)	[5.31]

The *a* dislocation dissociated into 2*p* partial dislocations is confined solely to slip in the basal plane. The coalescence of screw components can cause cross-slip in the first order prism and pyramidal planes of the $\{10\bar{1}n\}$ type, although each of the given $\{10\bar{1}n\}$ planes can only contain one of the three possible $\pm 1/3 < 11\bar{2}0 >$ Burgers vectors. A dislocation with a first order Burgers vector cannot slip in second order prism and pyramidal planes of the $\{11\bar{2}n\}$ type.

5.3.2.2. Dissociation of 'a' dislocations in the first order prism planes $\{10\bar{1}0\}$

A dissociation of *a* dislocations in the first order prism planes $\{10\bar{1}0\}$ is possible, according to Refs [5.32, 5.33]:

$$1/3\ [1\bar{2}10] \rightarrow 1/18\ [46\bar{2}3] + 1/18\ [2\bar{6}4\bar{3}] \tag{5.3}$$

or according to Ref. [5.34]:

$$1/3\ [1\bar{2}10] \rightarrow 1/6\ [1\bar{2}1\bar{1}] + 1/6\ [1\bar{2}11] \tag{5.4}$$

If the waviness of the prism planes and their irregular spacing from one another are taken into account, the dissociation of the *a* dislocation in the prism plane, according to Eq. (5.3), is energetically more favourable [5.6] compared with Eq. (5.4); both reactions should be energetically less likely compared with the dissociation in the basal plane. This result could explain why even for these metals with a *c*/*a* axial ratio slightly below ideal (for example, cobalt and magnesium), basal slip is favoured over prism slip.

The question as to why beryllium, which constitutes an exception by having the lowest *c*/*a* axial ratio, slips in the *a* direction not only in the prism plane but also in the basal plane, can be answered by the following dissociation proposal [5.35]:

$$1/3\left[1\bar{2}10\right] \rightarrow 1/9[2\bar{1}\bar{1}0] + 2/9[\bar{1}\bar{1}20]. \tag{5.5}$$

This reaction leads to a stacking fault ribbon in which the $(10\bar{1}0)$ plane of the HCP lattice approximates the (112) plane of the BCC lattice. This structural similarity is further improved by the following dissociation [5.31]:

$$1/3\left[11\bar{2}0\right] \rightarrow 1/6\left[12\bar{3}0\right] + 1/6\ \left[10\bar{1}0\right]. \tag{5.6}$$

On the basis of this transformation [5.35], and according to a comparative evaluation [5.36], the formation of a stacking fault on the basal or prism planes is linked with the tendency of the HCP lattice to transform into the BCC or FCC structure. Accordingly, an HCP metal slips primarily in the basal plane if the ratio of the free energies for the lattice transformations $E_{\mathrm{HCP–BCC}}$ and $E_{\mathrm{HCP–FCC}}$ is:

$$\frac{E_{\mathrm{HCP-BCC}}}{E_{\mathrm{HCP-FCC}}} > 1 \tag{5.7}$$

On the basis of this transformation [5.35] and according to a comparative evaluation [5.36], the formation of a stacking fault on the basal or prism planes is linked with the tendency of the HCP lattice to transform into the BCC or FCC structure. Accordingly, an HCP metal slips primarily in the basal plane if the ratio of the free energies for the lattice transformations $E_{\mathrm{HCP–BCC}}$ and $E_{\mathrm{HCP–FCC}}$ is:

$$\frac{E_{HCP-BCC}}{E_{HCP-FCC}} < 1 \tag{5.8}$$

This model of the relative stability of the HCP lattice transformation into the BCC or FCC structure [5.36] leads to a consistent prediction of the slip system for all HCP metals with an <*a*> Burgers vector on a prism or a basal plane, including alloying and temperature dependences [5.31] (see also Sections 5.4.3.3 and 5.4.3.4).

Stacking fault energies for dissociations of *a* dislocations in the prism plane have been measured for titanium, zirconium and beryllium or estimated via the transformation concept and are included in Table 5.2.

5.3.2.3. Dissociation of 'a' dislocations in first order pyramidal planes of various modes

Independent of their *c*/*a* axial ratio, $\{10\bar{1}1\}$ pyramidal planes of the first order and mode represent the most closely packed pyramidal planes. In this planar family, the *a* direction is also included as well as the <*c* + *a*> direction. A dissociation of an *a* dislocation into partial dislocations is improbable for these pyramidal planes, as well as for higher order pyramidal planes, because of the 'nearest-neighbour disturbances', which — based on the hard sphere model of the atom stacking — violate the coordination number of atoms during the movement of the partial dislocations along the corrugated slip planes.

5.3.2.4. Dissociation of < c + a > *dislocations in first order prism planes and pyramidal planes of various orders and modes*

In addition to the first order prism planes $\{10\bar{1}0\}$, the pyramidal planes $\{10\bar{1}1\}$, $\{11\bar{2}1\}$ and $\{11\bar{2}2\}$ also contain <*c* + *a*> Burgers vectors [5.30, 5.37] (Fig. 5.8).

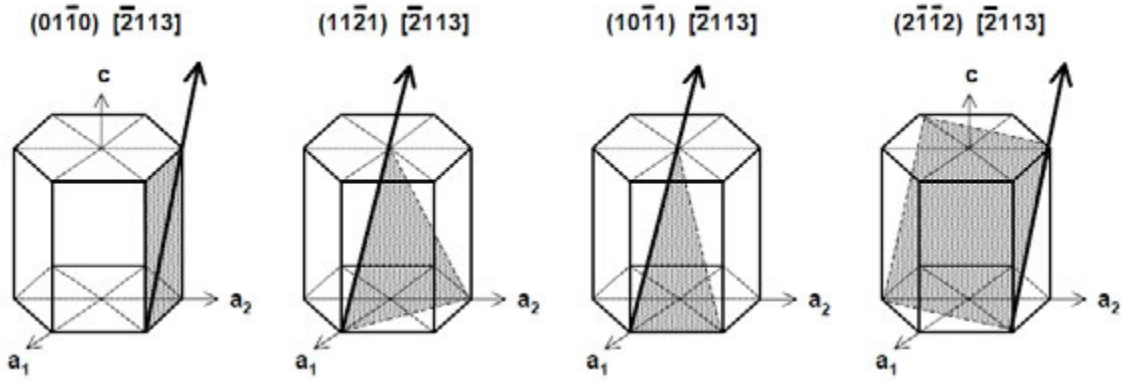

FIG. 5.8. Possible slip systems for <c+a> Burgers vectors in HCP metals (reprinted with permission from Ref. [5.1], copyright ASTM International).

Whereas the dissociation of (*c* + *a*) dislocations in the prism plane is improbable owing to the 'nearest-neighbour-disturbances', this dissociation is possible in pyramidal planes, but with an energy gain.

Investigations of beryllium [5.38] with slip traces in the $(11\bar{2}2)$ plane led to the proposal of a simple dissociation given by:

$$1/3\,[11\bar{2}3] \rightarrow [0001] + 1/3\,[11\bar{2}0] \tag{5.9}$$

A dissociation on the $(11\bar{2}2)$ plane is described by the reactions:

$$(\mathrm{AB} + \mathrm{ST}) \rightarrow \mathrm{SB} + \mathrm{AT} \tag{5.10}$$

$$1/3\,[\bar{1}\bar{1}23] \rightarrow 1/6\,[\bar{2}023] + 1/6\,[0\bar{2}23] \tag{5.11}$$

whereby stacking faults on the basal plane are caused by climb, which requires diffusion (see Fig. 5.6).

Rosenbaum [5.32] discussed the atom movements required for <*c* + *a*> slip in HCP metals, using a hard sphere model for the $(11\bar{2}2)$ pyramidal plane. Based on Kronberg's concept for a zonal split of partial dislocations [5.39, 5.40], Rosenbaum describes a slip mode

on the basis of the formation of a glissile, twin-like stacking fault due to a dissociation into three partial dislocations in three adjacent $\{11\bar{2}2\}$ planes. This model is correspondingly applicable to the $\{10\bar{1}1\}$ and $\{11\bar{2}1\}$ planes. These two plane types can be distinguished from the $\{11\bar{2}2\}$ pyramidal planes because each plane offers two slip directions with a <*c* + *a*> type Burgers vector, while the $\{11\bar{2}2\}$ planes contain only one <*c* + *a*> type Burgers vector (see Fig. 5.8). This observation means that on both $\{10\bar{2}1\}$ and $\{11\bar{2}1\}$ planes, 12 slip systems can operate, whereas on the $\{11\bar{2}2\}$ pyramidal planes, only 6 slip systems are possible. The $\{10\bar{1}1\}$ and $\{11\bar{2}1\}$ planes are thus favoured energetically compared with the $\{11\bar{2}2\}$ planes because of their higher availability of slip systems, their higher atomic density and their less pronounced waviness (see Fig. 5.4).

Pyramidal planes containing <*c* + *a*> type Burgers vectors offer a means of explaining deformations with *c* components by slip, it normally being ascribed to twinning. The critical resolved shear stresses for <*c* + *a*> slip seem to be high, despite the possibility of such deformation configurations.

5.3.2.5. Dissociation of 'c' *dislocations on first and second order prism planes*

The *c* dislocations are to be found in $\{10\bar{1}0\}$ first and $\{11\bar{2}0\}$ second order planes. Dissociation on the $(1\bar{2}10)$ plane can be described [5.6] as follows (see Fig. 5.6):

$$\mathrm{ST} \rightarrow \mathrm{SA} + \mathrm{AT} \tag{5.12}$$

$$[0001] \rightarrow 1/6\,[\bar{2}023] + 1/6\,[20\bar{2}3] \tag{5.13}$$

This reaction may generate stacking faults in the basal plane if diffusion and therefore climb are possible.

In metals with high SFE, prism and pyramidal slip might be favoured at high temperatures, since the split dislocations coalesce due to thermal activation, thus allowing cross-slip [5.2].

5.3.3. Twinning modes

In HCP metals, twinning (on pyramidal planes of different orders and modes) is usually employed to explain deformations with *c* components [5.3–5.6, 5.11].

Most HCP metals form twins of the $\{10\bar{1}2\}$ type, so that the $\{10\bar{1}2\}$ twinning system is often referred to as 'normal' twinning. In those metals with a below ideal axial ratio, 'abnormal' twin systems occur that exploit first and second order pyramidal planes of different modes as twinning planes. A list of the twinning modes observed in various HCP metals is given in Table 5.3 [5.5]. The elements of some systems are completely determined, whereas others are only partly determined or are merely predicted (for the definitions of double twinning and *i* see Section 5.3.3.3).

Depending on the metal, various twinning modes may operate. This variation, as with slip processes, is caused by:

— Variation in the *c*/*a* axial ratio;
— Subsequent variation in packing densities and interplanar spacings;
— Variation in stacking fault energies and corresponding transformation behaviour of the hexagonal structure.

The elements of twinning may be described geometrically by means of the reference sphere (Fig. 5.9) [5.3]. During twinning, the northern half of the reference sphere is deformed into a partial ellipsoid of the same volume. This deformation is accompanied by a homogeneous shear of the crystal lattice parallel to the equatorial plane of the sphere in such a way that the atom layers form mirror images of each other with respect to this plane. The shear associated with twinning leaves two lattice planes undistorted, that is, all distances and angles in these planes remain unchanged. One such plane is K_1 (the equatorial plane in Fig. 5.9), which does not change its position with shear. The other plane is K_2 before twinning, becoming K_2' after twinning. All crystal directions in the upper-left segment between K_1 and K_2 are shortened by the shear.

TABLE 5.3. PREDICTED AND OBSERVED TWINNING MODES AND THEIR ELEMENTS FOR VARIOUS HCP METALS

Experimental observations in	K_1 { }	K_2 { }	η_1 < >	η_2 < >
Mg, Ti, Co, Zr, Zn, Be	$10\bar{1}2$	$\bar{1}012$	$10\bar{1}\bar{1}$	$\bar{1}01\bar{1}$
	$22\bar{4}1$	0001	$1,1,\bar{2},\bar{1}\bar{2}$	$11\bar{2}0$
Mg, Ti	$10\bar{1}1$	$10\bar{1}\bar{3}$	$10\bar{1}\bar{2}$	$30\bar{3}2$
	$10\bar{1}1$	i	i	$41\bar{5}3$
	$20\bar{2}1$	0001	$10\bar{1}\bar{4}$	$10\bar{1}0$
Re, Ti, Zr, Co, graphite	$11\bar{2}1$	0001	$10\bar{2}\bar{6}$	$11\bar{2}0$
	$10\bar{1}3$	$10\bar{1}1$	$30\bar{3}2$	$10\bar{1}2$
Mg	$10\bar{1}3$	i	i	$21\bar{1}\bar{3}$
	i	i	i	i
	$\{10\bar{1}3\}$ double twinning			
	$13\bar{4}0$	$\bar{1}100$	$7\bar{5}\bar{2}0$	$11\bar{2}0$
	$13\bar{4}1$	$\bar{1}101$	i	$11\bar{2}0$
	$13\bar{4}2$	$\bar{1}102$	i	$11\bar{2}0$
	$22\bar{4}3$	0001	$11\bar{2}\bar{4}$	$11\bar{2}0$
	$10\bar{1}4$	$10\bar{1}0$	$20\bar{2}1$	0001
Ti, Zr	$11\bar{2}2$	$11\bar{2}\bar{4}$	$11\bar{2}3$	$22\bar{4}3$
	$11\bar{2}4$	$11\bar{2}2$	$22\bar{4}3$	$11\bar{2}3$
	$30\bar{3}4$	—	—	—
	$11\bar{2}3$	—	—	—

All crystal directions to the right of this segment are extended. The first and second undistorted planes, K_1 and K_2, are normal to the shear plane. The line of intersection of the shear plane with K_1 has the direction η_1, with K_2 the direction η_2, and K_2' the direction η'_1. The shear direction, η_1, is thus parallel to the twinning plane and the magnitude of the homogeneous shear is:

$$S = AA', BB' \tag{5.14}$$

where K_2 is related to the amount of shear, S, by the angle 2Φ, which K_2 and, K'_2 make with K_1 according to:

$$S = 2 \operatorname{ctg} 2\Phi \tag{5.15}$$

The sheer magnitude is determined by the crystallographic relationship between the two undistorted planes. Therefore, the twinning mode can be determined completely by K_1 and η_2 or by K_2 and η_1.

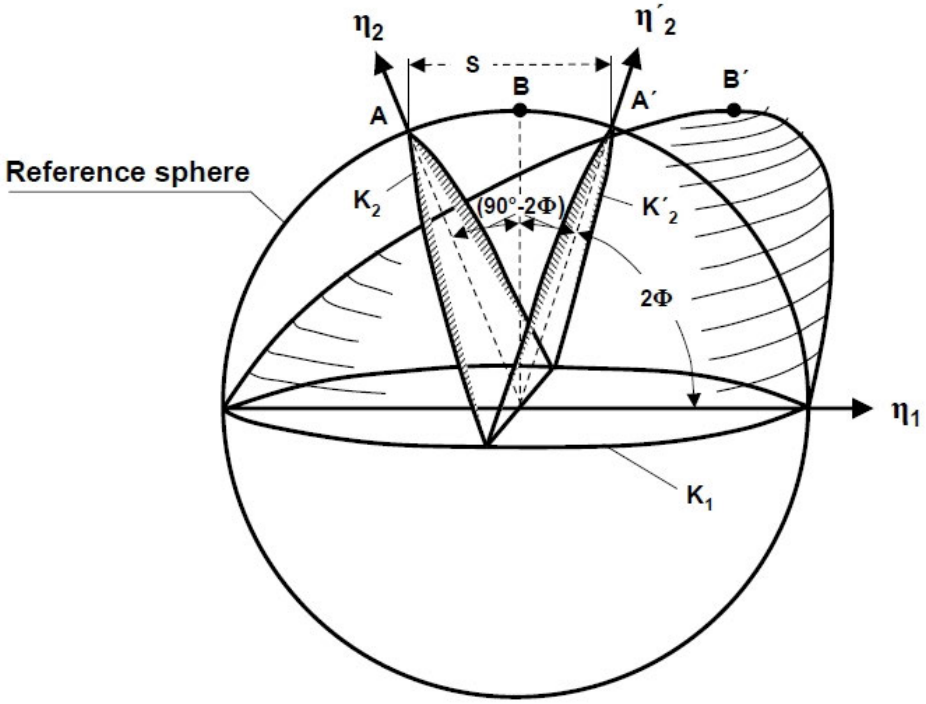

FIG. 5.9. Relationship between reference sphere and twinning ellipsoid (reprinted with permission from Ref. [5.1], copyright ASTM International).

There are important differences between deformation by twinning compared with deformation by slip.

5.3.3.1. Twinning plane

Twinning occurs on planes that are not necessarily slip planes.

5.3.3.2. Orientation change

The crystallographic orientation is changed in a spontaneous transformation by a certain angle, ζ. The rotation pole is normal to the shear plane, where the rotation angle is given by:

$$\zeta = 2\,(90° - 2\Phi) \tag{5.16}$$

The change in orientation depends on the twinning mode and the *c*/*a* axial ratio and may achieve values beyond 90° (for values for zirconium see Section 5.4.2). By contrast during slip, the orientation above and below the slip plane remains unchanged.

5.3.3.3. Shuffles

During twinning, the atomic planes parallel to the twinning plane shift over one another by an amount that is a fraction of the interplanar spacing in the shear direction. In single lattice structures such as BCC and FCC, matrix and twinning are mutually linked by

homogeneous shear. In double lattice structures, such as HCP metals, additional minor atomic movements are necessary along directions other than the shear direction. These movements are called shuffles. They are caused by the varying interplanar spacings and the waviness of the non-basal plane; the corresponding planes and directions are called irrational. Double twinning is the successive or simultaneous application of two twinning shears to a region of crystal, where *i* denotes an irrational plane or direction of the system (see Table 5.3).

These movements, although necessary on an atomic scale, do not change the homogeneous shear at the scale of grains.

By contrast during slip, deformation is restricted to discrete slip planes or to separate slip zones. Amounts of slip are integer multiples of the interplanar spacing in the slip direction.

5.3.3.4. Size of the deformation

The amount of deformation, ε, accompanying twinning depends on the orientation, μ, and the c/a axial ratio of the crystal, that is, on the activated twinning mode, on the size of the connected shear, s, and on the volumetric proportion, V, of the transformed lattice [5.12, 5.41]. For a given twinning system, the relationship is described by

$$\varepsilon = V \cdot s \cdot \mu \tag{5.17}$$

where

ε is compressive or tensile strain;
V is the volumetric proportion of the twin;
s is shear caused by the twin;

and μ is the Schmid factor (see Section 5.4.3.1).

While the orientation change due to twinning may be large, the contribution of twinning to the overall deformation is small compared with that of slip. For example, the complete transformation (V = 100%) of a magnesium single crystal under tension along the c axis into its $\{10\bar{1}2\}$ twin position (s = 0.131) for the most favourable orientation (μ = 0.5) results in an orientation change of 86°18′, but a strain of only about 6.5% (Fig. 5.10; for values for zirconium, see Section 5.4.2). However, twinning is essential to the ductility of HCP metals, since the lattice rotations re-establish orientations that are favourable for slip and thus allow large amounts of deformation; sometimes secondary or further twinning is needed to allow slip.

5.3.3.5. Dependence of deformation on direction

Whereas slip is geometrically reversible under tension or compression, the twinning modes are dependent on the direction of the stress, because of the crystallographic relationship between the extended or compressed orientations. Whether a certain twinning mode leads to an elongation or a shortening in the c direction also depends on the crystallographic orientation relationship and on the c/a axial ratio. This situation is represented by the example of $\{10\bar{1}2\}$ twinning in Fig. 5.10 [5.6]. Twinning under compression parallel to the c axis is favoured for $c/a > \sqrt{8/3}$ leading to shortening in the c

direction, while for $c/a < \sqrt{8/3}$, tensile stress parallel to the c axis results in elongation [5.4]. For $c/a = \sqrt{8/3}$, $\{10\bar{1}2\}$ twinning is impossible [5.42].

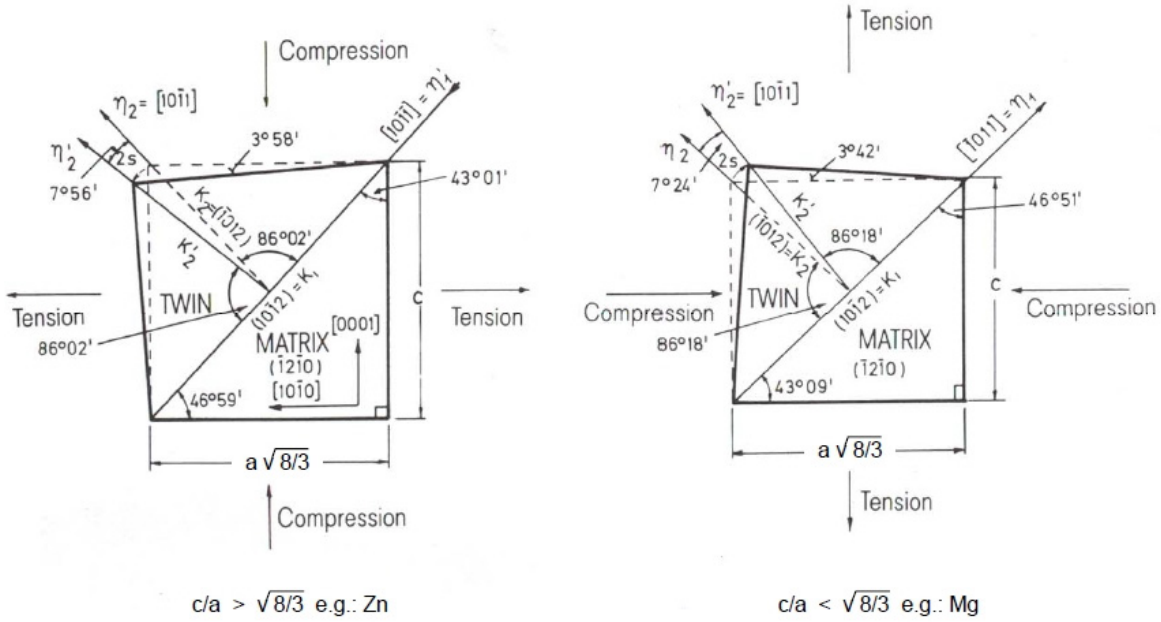

FIG. 5.10. Dependence of deformation direction on c/a axial ratio in the example of $\{10\bar{1}2\}$ *twinning for* $c/a > \sqrt{8/3}$ and for $c/a < \sqrt{8/3}$ *(reprinted with permission from Ref. [5.1], copyright ASTM International).*

5.3.3.6. Dissociation of dislocations

A dislocation mechanism is employed to explain both twinning and slip. During twinning, the dislocations are not perfect and are related to partial dislocations. Possible deformation models for twinning in hexagonal metals have been discussed by Rosenbaum [5.32], Westlake [5.43] and Chyung and Wei [5.44].

5.3.3.7. Critical resolved shear stress

Should it exist [5.5], the critical resolved shear stress for twinning is dependent not only on the line tension of the initial dislocation, as in the case of slip, but also on the surface tension of the twin interfaces. It is usually assumed that the critical resolved shear stress for twinning is higher than that for slip (see also Section 5.4.3.2).

5.3.4. Kink bands

The formation of kink bands is another deformation mechanism that occurs in hexagonal metals [5.45, 5.46] such as magnesium [5.47], zinc [5.14], cadmium [5.48], titanium [5.49–5.51] and zirconium [5.41, 5.52, 5.53]. Similar kink bands are also formed in FCC metals such as aluminium, molybdenum and α uranium [5.54–5.57].

The kink bands in cadmium rods observed by Orowan [5.48] under compressive deformation along the direction of the rod axis are illustrated in Fig. 5.11, together with a corresponding schematic sketch [5.41].

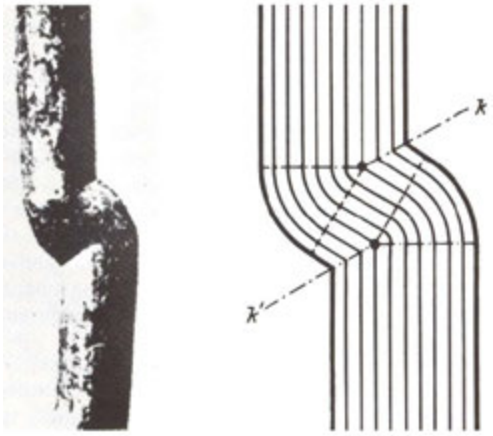

FIG. 5.11. Kink bands in a cadmium single crystal (reprinted with permission from Ref. [5.1], copyright ASTM International).

With the formation of a kink band — as in the case of twinning — part of the crystal lattice is transferred into another crystal orientation. In contrast to twinning, kink bands develop gradually rather than in bursts under increasing deformation. Neither the new orientation nor the plane of the kink band, *kk'*, have a particular relationship with the initial lattice. The kink plane can be a $\{11\bar{2}0\}$ tilt plane [5.53] that contains dislocations with <*a*> type Burgers vectors. Kink planes can be found to contain $\{10\bar{1}0\}$ planes and are often interrelated with twins [5.58–5.60]. These accommodation kink bands contain two different <*a*> type Burgers vectors. Kink bands are not usually mentioned in the context of deformation mechanisms in polycrystals of zirconium and zirconium based alloys; therefore, they will not be discussed further.

In summary, this description of slip and twinning systems in HCP metals indicates that the deformation mechanisms and the resulting textures and mechanical anisotropy have to be dealt with separately for each individual hexagonal metal. Section 5.4 discusses deformation in zirconium and zirconium based alloys.

5.4. DEFORMATION MECHANISMS IN ZIRCONIUM AND ZIRCONIUM BASED ALLOYS

5.4.1. Slip nodes

The primary slip system operating in the α phase of zirconium is slip on the first order prism planes $\{10\bar{1}0\}$ along <$1\bar{2}10$> directions. This slip mode operates at room temperature and higher temperatures, up to about 773 K (500°C) (Fig. 5.12) [5.15, 5.41, 5.61–5.69]. In the same direction, slip has also been observed on the (0001) basal plane, especially at temperatures above 773 K (500°C) [5.41, 5.68–5.70], and slip on $\{10\bar{1}\bar{1}\}$ planes has been observed in regions of high stress concentration, such as grain boundaries [5.63, 5.67, 5.71] (Fig. 5.12). None of these slip planes allow deformation in the *c* direction, which is required to explain the observed ductility in zirconium and other HCP metals. Slip systems with at least a component in the *c* direction as <*c* + *a*> have been observed under constraint and at high deformation temperatures. The corresponding slip mode is slip that occurs on first and second order pyramidal planes $\{10\bar{1}\bar{1}\}$ or $\{1\bar{2}11\}$ in <11 $\bar{2}$ 3> directions (Fig. 5.12) [5.37, 5.72–5.77].

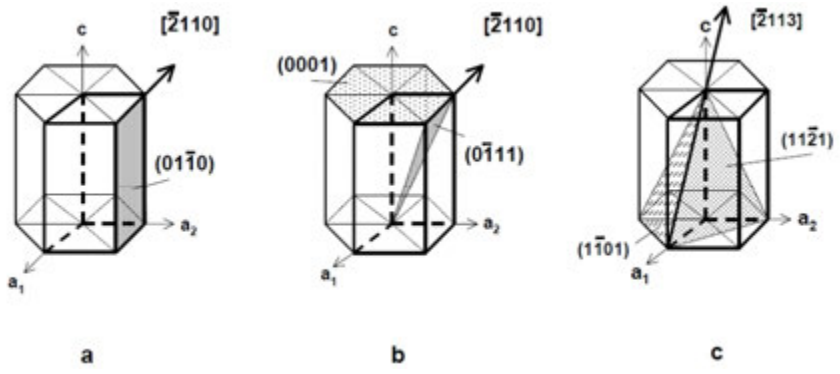

FIG. 5.12. Slip systems in α-zirconium (reprinted with permission from Ref. [5.1], copyright ASTM International).

The existence of these <*c* + *a*> type Burgers vectors on pyramidal slip planes has been verified in experiments with zirconium single crystals sheared in restraint at different temperatures, using trace analysis of distinct dislocation bands under multi- and two-beam conditions in a transmission electron microscope (Fig. 5.13). The $< 11\bar{2}3 >$ type Burgers vectors became operative at temperatures from room temperature to 1023 K (750°C); their occurrence is more likely the higher the temperature. The $\{11\bar{2}1\}$ and $\{10\bar{1}1\}$ pyramidal planes proved to be the slip planes. From a theoretical viewpoint, the $\{11\bar{2}1\}$ pyramidal planes seem to be favoured energetically compared with the $\{10\bar{1}1\}$ planes [5.37].

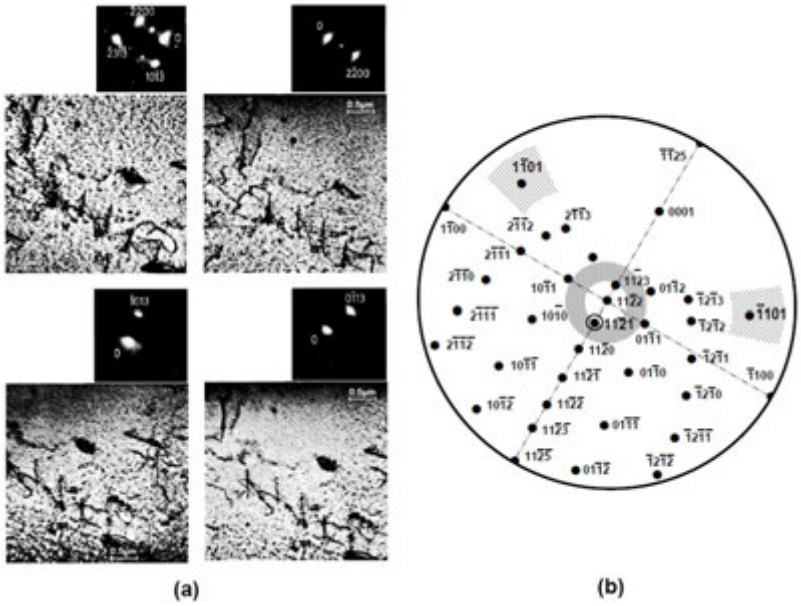

FIG. 5.13. Dislocation band with $< 11\bar{2}3 >$ *type Burgers vector on* $\{11\bar{2}1\}$ *or* $\{10\bar{1}1\}$ *pyramidal planes: (a) contrast images under different diffraction conditions; (b) transformation into the stereographic projection of the corresponding foil plane (reprinted with permission from Ref. [5.1], copyright ASTM International).*

5.4.2. Twinning modes

Apart from pyramidal slip modes, deformation with <*c*> components has been explained primarily by twinning on first and second order pyramidal planes (Fig. 5.14). Under tensile stress along the direction of the c axis, $\{10\bar{1}2\} < \bar{1}011 >$ twins are activated [5.28, 5.41, 5.62–5.64, 5.66, 5.71, 5.78–5.80] and less commonly $\{11\bar{2}1\} < \bar{1}\bar{1}26 >$ twins

[5.28, 5.41, 5.61–5.64, 5.66, 5.67, 5.71, 5.79–5.81]. Under compression in the *c* direction $\{11\bar{2}2\} < \bar{1}\bar{1}23 >$ and at elevated temperatures $\{10\bar{1}1\} < \bar{1}012 >$ twins are observed [5.26, 5.27, 5.30]. For some cases, twinning on the $\{11\bar{2}3\}$ plane is mentioned, although this mode requires confirmation [5.41, 5.61–5.64].

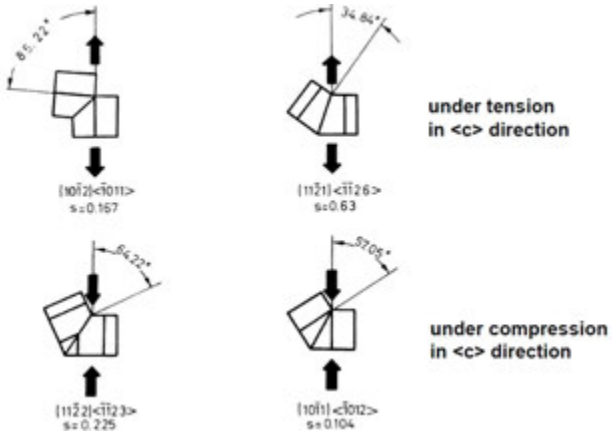

FIG. 5.14. Twinning systems in α-zirconium (reprinted with permission from Ref. [5.1], copyright ASTM International).

As an example, Fig. 5.15 shows a micrograph of the $\{10\bar{1}1\}$ twinning system and its stereographic orientation relationships obtained by trace analysis under multi- and two-beam conditions in a transmission electron microscope.

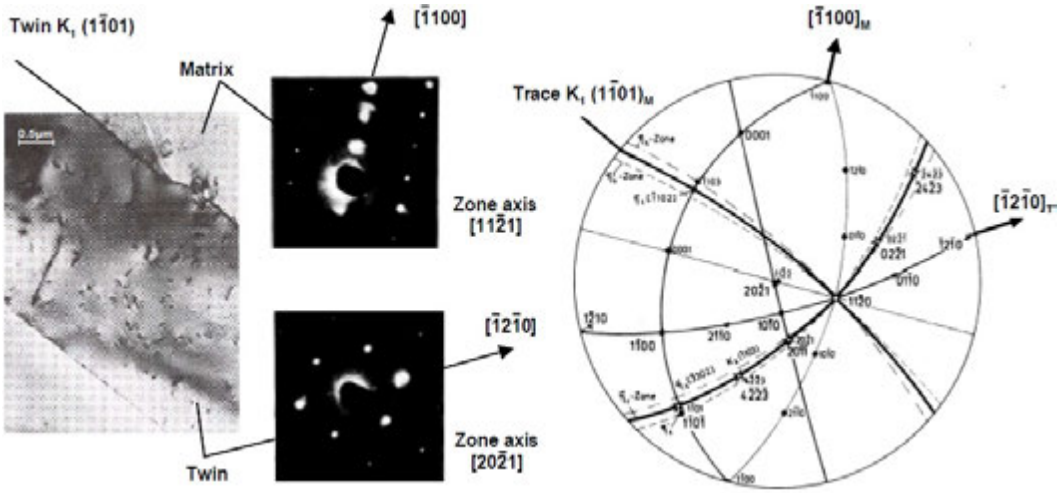

FIG. 5.15. Twinning system: (a) contrast image; (b) diffraction pattern; and (c) correlation to the stereographic orientation relationship (reprinted with permission from Ref. [5.1], copyright ASTM International).

The twinning systems observed in zirconium, the corresponding twin elements, the lattice rotation and the amount of shear, based on Eqs (5.15) and (5.16), are summarized in Table 5.4. Table 5.5 gives a list of the maximum deformation due to twinning for the twinning modes operative in zirconium, according to Eq. (5.17). Although twinning does not allow large amounts of deformation, it plays an important role in deformation, since regions initially unfavourable for slip are reoriented by the lattice rotation caused by twinning. The new orientation allows further strain that either favours slip or causes double twinning. Moreover, twinning activates new slip systems in regions of local stress concentration, such as twin boundaries, or by interactions between dislocations and twinning. This possibility has been discussed, especially for slip systems with <*c*+*a*>-Burgers vectors [5.3, 5.82–5.85].

TABLE 5.4. TWINNING SYSTEMS $\{10\bar{1}2\}, \{11\bar{2}1\}, \{11\bar{2}2\}$ AND $\{10\bar{1}1\}$, AND THEIR CHARACTERISTIC ELEMENTS IN ALPHA-ZIRCONIUM (AXIAL RATIO = 1.593)

Twinning plane (First underformed plane) K_1	Twinning shear direction η_1	Second undistorted plane K_2	Direction of line of intersection between K_2 and the plane of shear η_2	Plane of shear perpendicular to K_1 and K_2	Magnitude of shear s	Lattice rotation ζ	Reference
$\{10\bar{1}2\}$	$< 10\bar{1}\bar{1} >$	$\{\bar{1}012\}$	$< 10\bar{1}1 >$	$\{1\bar{2}10\}$	0.167	94.87°	[5.62–5.64]
$\{11\bar{2}1\}$	$< 11\bar{2}\bar{6} >$	(0001)	$< 11\bar{2}0 >$	$\{\bar{1}100\}$	0.630	34.84°	[5.62–5.64]
$\{11\bar{2}2\}$	$< 11\bar{2}\bar{3} >$	$\{11\bar{2}\bar{4}\}$	$< 22\bar{4}3 >$	$\{\bar{1}100\}$	0.225	64.22°	[5.62–5.64]

TABLE 5.5. ATTAINABLE STRAINS, ε%, (MAXIMUM OR PARALLEL TO C AXIS) FOR ZIRCONIUM TWINNING SYSTEMS, ASSUMING A COMPLETE TRANSFORMATION INTO TWIN POSITION, WITH (+) = TENSION AND (–) = COMPRESSION PARALLEL TO THE C DIRECTION

Twinning mode	Magnitude of shear	Strain, ε (%)			
		loading ∥ c axis			
		for μ_{max}	ε	for μ	ε
$\{10\bar{1}2\}$	0.167	0.5	+8.35	0.497	+8.30
$\{11\bar{2}1\}$	0.63	0.5	+31.50	0.278	+17.50
$\{11\bar{2}2\}$	0.225	0.5	–11.25	0.45	–10.15
$\{10\bar{1}1\}$	0.1044	0.5	–5.22	0.442	–4.62

5.4.3. Factors influencing the deformation mechanisms

To predict whether slip or twinning will occur or, more precisely, which of the deformation modes will be activated, the following factors are recommended to be taken into account.

5.4.3.1. Schmid factor

The Schmid factor [5.17] is a geometrical relationship between the direction of force and the corresponding deformation mode. The relationships between the resolved shear stress operating on the slip plane in the slip direction, the external direction of force and the specimen dimension are given in Fig. 5.16.

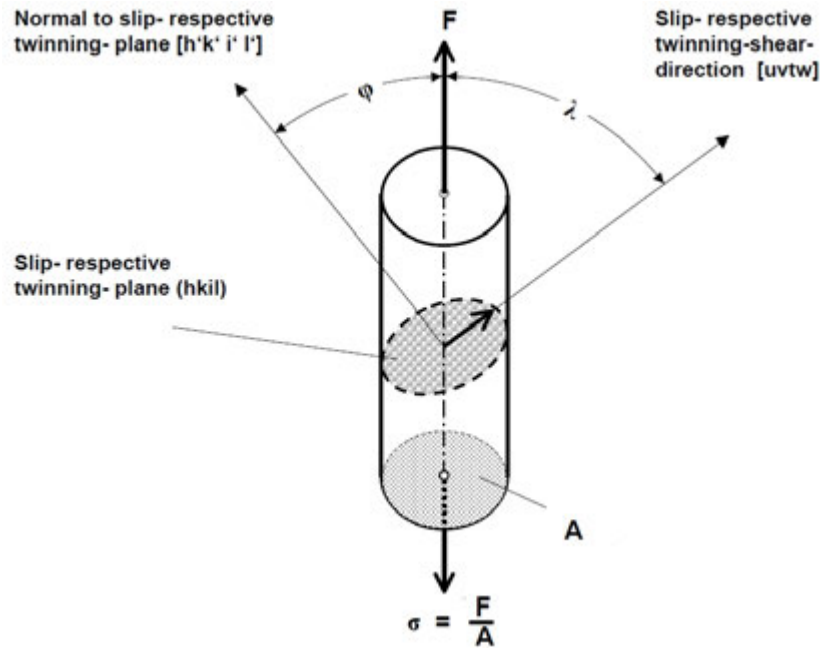

FIG. 5.16. Relationship between the shearing stress acting in the deformation system and the force F, applied externally on the single crystal rod. Note: [h' k' i' l'], because in HCP lattices the planes and directions of the same Miller-Bravais indices are not necessarily normal to each other. This comment is valid for all pyramidal planes; exceptions are basal and prism planes (reprinted with permission from Ref. [5.1], copyright ASTM International).

The resolved shear stress (RSS) τ on the slip plane in the slip direction is:

$$\tau = \{10\bar{1}1\}\,\mu \tag{5.18}$$

$$\mu = \cos\Phi \cos\lambda \tag{5.19}$$

where

μ is the Schmid factor;
F is the externally applied force in the direction of the rod axis;
A is the cross-sectional area of the crystal;
Φ is the angle between the normal to the slip plane and the direction of force of the external reference system;

and λ is the angle between the slip direction and net force of the external reference system.

This relationship also applies to twinning modes with:

τ being the resolved shear stress on the twinning plane in the shear direction;
Φ being the angle between the normal to the twinning plane K_1, and the direction of force of the external reference system;
λ being the angle between the shear direction of twinning;

and η_1 being the direction of force of the external reference system.

In HCP metals, the resolved shear stresses of the various deformation modes are strongly dependent on the direction of force, especially with respect to the c axis. The orientation dependence is illustrated by Fig. 5.17, which shows the Schmid factors of important slip and twinning modes operating in zirconium for the range of angles 0–90° between the basal pole and the direction of force.

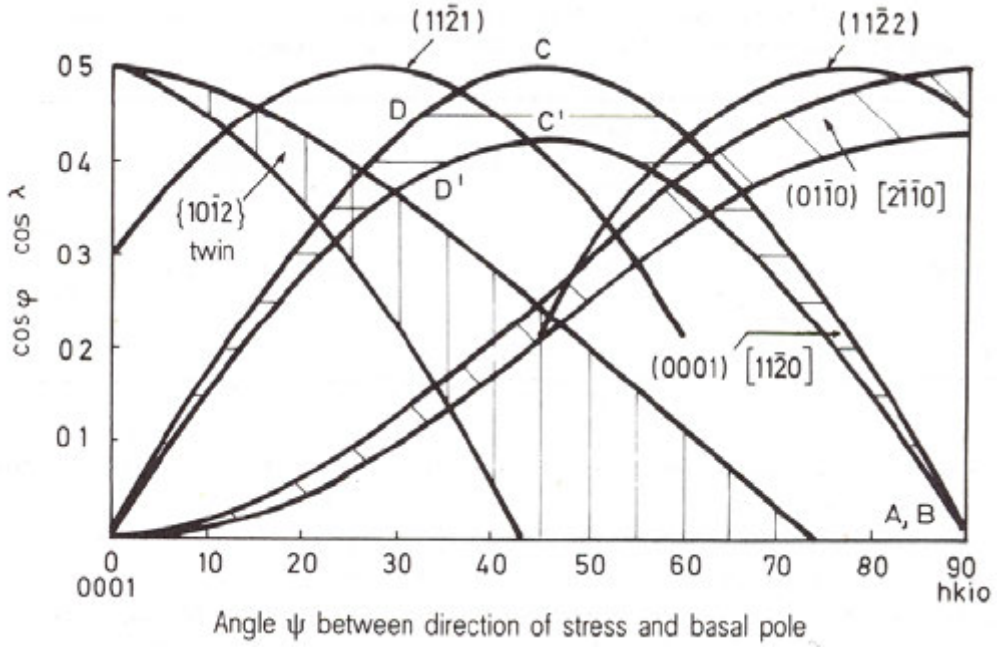

FIG. 5.17. Schmid factor orientation dependence for various slip and twinning systems in zirconium [5.41] (reprinted with permission from Ref. [5.1], copyright ASTM International).

Owing to the low availability of slip systems, the HCP metals with certain orientations show a pronounced tendency to geometrical hardening or softening. This behaviour is caused solely by a change in the Schmid factor, because of lattice rotation during the slip process, and is independent of hardening by dislocation reactions [5.16].

5.4.3.2. Critical resolved shear stress

For a given deformation system, slip takes place if the acting resolved shear stress, $\tau_{(rss)}$, exceeds a critical value. This value is termed the critical resolved shear stress, $\tau_{(crss)}$. It constitutes a material property, which may be influenced by temperature, strain rate and impurities, as well as by mechanical and thermal history. In experiments, the values of $\tau_{(crss)}$ are strongly dependent on the testing method and the accuracy of the measurement. In various HCP metals [5.64, 5.86–5.88], single crystal experiments were performed to obtain critical resolved shear stresses for basal and prism slip on a macroscopic scale, but because of experimental vagaries, the values differ widely.

For zirconium, critical resolved shear stresses have been determined for prism slip systems with <*a*> type Burgers vectors [5.61–5.64]. In Table 5.6, the values for various deformation temperatures are listed for tests under compression or tension. For <*c* + *a*> type Burgers vectors, no precise data on critical resolved shear stresses for pyramidal slip systems are available for zirconium. Akthar [5.73] deduces relative values for pyramidal slip; in Zr single crystals deformed at room temperature, the CRSS for pyramidal slip is between 10 and 20 times higher than for prism slip, and in Zircaloy-2 the CRSS for pyramidal slip is approximately 2 times that required for prism slip.

Values of corresponding critical stresses that initiate the various twinning modes are not available, because the mechanisms governing the generation and the growth of twinning and knowledge on whether slip precedes twinning have still to be resolved [5.5, 5.89, 5.90]. For polycrystalline materials, for which the yield strength or the 0.2% offset yield strength is given in place of the critical resolved shear stress, corresponding values can be derived for slip as well as for twinning by tensile or compressive tests of textured specimens. Table 5.7 gives some of these test results for zirconium and Zircaloy-4. To eliminate material and testing inaccuracies, the respective ratios of the derived critical shear stresses are listed for various deformation modes [5.91]. The critical resolved shear stresses or the corresponding stresses initiating twinning differ for the various twinning modes but are always higher than those for prism slip (Section 5.3.3). Depending on the orientation of the crystal, the deformation system with the lowest critical shear stress need not necessarily operate, since the Schmid factor, which is strongly dependent on the position of the basal pole with respect to the direction of force, determines the acting resolved shear stress (Section 5.4.3.1).

TABLE 5.6. CRITICAL RESOLVED SHEAR STRESSES, $\tau_{(crss)}$, FOR PRISM SLIP IN ZIRCONIUM AT VARIOUS DEFORMATION TEMPERATURES, WHERE (C) IS MEASURED UNDER COMPRESSION AND (T) IS MEASURED UNDER TENSILE STRESS

Deformation temperature (K (°C))	$\tau_{(crss)}$ (MPa)	Reference
76 K (−197 °C)	9.8 (T)	[5.64]
298 K (25 °C)	6.4 (C)	[5.61–5.63]
575 K (302 °C)	2.0 (T)	[5.64]
1075 K (802 °C)	0.2 (C)	[5.64]

TABLE 5.7. RELATIVE RATIOS OF THE DERIVED CRITICAL SHEAR STRESSES FOR VARIOUS DEFORMATION SYSTEMS IN ZIRCONIUM AND ZIRCALOY-4 AFTER DEFORMATION AT ROOM TEMPERATURE [5.91]

Material	Form	Loading condition at room temperature	$\frac{\text{crss}\{10\bar{1}2\}\text{ twin}}{\text{crss}\{10\bar{1}0\}\text{ slip}}$	Ratio of $\frac{\text{crss}\{11\bar{2}1\}\text{ twin}}{\text{crss}\{10\bar{1}0\}\text{ slip}}$	$\frac{\text{crss}\{11\bar{2}2\}\text{ twin}}{\text{crss}\{10\bar{1}0\}\text{ slip}}$	Reference
HCP (Zr)			1.5	—	2.0	[5.92]
Zircaloy-4	Sheet	Uniaxial	1.55	—	2.03	Calculated with data from Ref. [5.93]
Zircaloy-4	Tube	Biaxial	1.25	1.35	1.45	[5.94]

5.4.3.3.Alloying elements and impurities

The effects of alloying elements and impurities are discussed in detail in Chapter 2. Here some effects of alloying elements and impurities on the operation of the deformation systems in Zr and Zr based alloys will be pointed out.

The critical resolved shear stress required to initiate the corresponding deformation mode may be influenced by impurities and alloying elements in the form of substitutional and interstitial solid solutions as well as in the form of decomposed and precipitated phases. The decisive factors are: changes in interplanar spacing and atomic packing density, changes in stress field due to lattice distortions and changes in SFE accompanied by the possible coalescence of dissociated screw components of dislocations (cross-slip at high SFE).

The dependencies often are examined together with other parameter studies as side effects. The influence of impurities and alloying elements such as the interstitial atoms O, N and C are discussed in Refs [5.28, 5.32, 5.95, 5.96]; correspondingly, the effects of substitutional alloying elements, such as Sn, Nb and Mo, are covered in Refs [5.97–5.99].

Conrad et al. [5.100] showed by experiments on the deformation kinetics of α-titanium that the strengthening effects of substitutional solid solutions on single crystals and textured polycrystals is caused by the fact that the critical resolved shear stress is increased due to differences in atom sizes and changes in bond energies, although the slip system is retained. Conrad [5.101] assumes that this result, confirmed for prism slip, also applies to the other deformation modes possible in HCP metals.

Mills and Craig [5.102] strained Zr single crystals (containing oxygen in the range 740–6800 atom ppm) in the easy glide direction over the temperature range 77–756 K (–196–483°C). They found that with increasing concentration of the interstitials, the CRSS of prism slip in the *a* direction was raised and concluded that the rate controlling deformation mechanism in the low temperature range 77–560 K (–196–287°C) was the overcoming of oxygen atoms by moving dislocations. For the high temperature experiments, they concluded that the drop in flow stress was due to the arrival of vacancies at jogs in the dislocations.

Comparing pure Zr and Zircaloy-4, the ratios between the stresses initiating the various twinning modes and the critical resolved shear stress for prism slip are maintained, as shown in Table 5.7, although the absolute values of critical resolved shear stress can be increased by alloying and deformation.

By taking into account these relationships, the knowledge gained about the deformation mechanisms from Zr may also be applied to Zr based alloys. Therefore, it is possible to explain with the same mechanisms the data on deformation textures and mechanical anisotropy in the alloys.

5.4.3.4. Deformation temperature

The above results mainly apply to temperatures around room temperature. In regions above and below room temperature, certain deformation modes may not operate or new ones may be activated.

Generally, twinning is preferred to slip at low deformation temperatures and high deformation rates; slip is favoured at high temperatures and low deformation rates (for example, creep). The decisive factors may be thermally activated processes, such as the surmounting of stress fields caused by the impurity atoms and the coalescence of screw components for cross-slip. These processes may act differently depending on the concentration of impurities and deformation.

5.4.3.5. Deformation direction

Twinning mechanisms are dependent on the c axis orientation with respect to the direction of deformation (see Sections 5.3.3.5 and 5.4.2). Therefore, the dependence of the various twinning systems on the macroscopic change in shape must be taken into account.

For a single crystal under uniaxial loading, the Schmid factor, the CRSS and the effect of impurities and alloying (see Sections 5.4.3.1–5.4.3.3) would be sufficient to predict quantitatively the operating deformation system. If twinning was activated at certain orientations, it should be possible to predict qualitatively the corresponding operating deformation systems on the basis of the critical stress to initiate twinning (Table 5.7).

For materials of technological interest (i.e. polycrystalline alloys employed in components under reactor operating conditions) the predictions are much more complicated, because the factors described in Sections 5.4.3.6–5.4.3.8 must be taken into account.

5.4.3.6. Multiaxial stress conditions

Components are normally subjected to multiaxial loadings during their fabrication and operation. Only in some cases is it possible to quantify the loading conditions accurately. For example, for the simple process of sheet rolling, the forces acting during deformation cannot be given precisely [5.103, 5.104]. For deformation processes such as tube drawing and rocking, the interaction of forces is even more complicated. Even simple components such as pressure tubes are subject to complicated stress fields during service.

Apart from the problem of exactly determining multiaxial forces, there is the difficulty of the anisotropic deformation behaviour. The yield strength measured under uniaxial loading can only be applied to predict the yield point under multiaxial loading for homogeneous, isotropic materials. In isotropic plasticity, it is possible, knowing the three principal stresses (σ_1, σ_2, σ_3), to compute the onset of plastic deformation, if the yield criterion of Von Mises [5.105] is fulfilled by Eq. (5.20); this equation applies to a cylinder of infinite length with the axes passing through the coordinate origin and at an equal angle to all three axes:

$$(\sigma_1 - \sigma_2)^2 + (\sigma_2 - \sigma_3)^2 + (\sigma_3 - \sigma_1)^2 = 2K_f^2 \quad (5.20)$$

For K_f, the design stress, normally the 0.2% offset yield strength, determined in a uniaxial tension test, is used.

For the anisotropic yield behaviour of metallic materials, Hill [5.106] extended the maximum distortion energy criterion of Von Mises by introducing anisotropy parameters, without going into the reasons for the anisotropy itself. Propositions to establish the mechanical anisotropy by crystallographic means using criteria for operating deformation mechanisms have been made. On the basis of the state of deformation, Taylor [5.107] calculated the combination of five deformation systems, which resulted in the smallest sum for glide and shear (principle of minimum work performed in deformation). Bishop and Hill [5.108] used an equivalent approach, but they based their calculations on the state of stress and calculated the combination of five deformation systems that provided the largest deformation energy (principle of maximum-work-performed in deformation). A precise prediction of the operating deformation mechanism under triaxial tensile loading has yet to be formulated. Initial steps towards computing the mechanical anisotropy under the simplified conditions of uniaxial or biaxial loadings in textured FCC and BCC metals were successfully carried out by Piehler and Backofen [5.109], Backofen et al. [5.110], Hosford and Backofen [5.111], and by Althof et al. [5.112].

For HCP metals, the theory was presented by Chin and Mammel [5.113] and by Thornburg and Piehler [5.114] according to the principle of maximum-work-performed in deformation. Here, the factors mentioned in Sections 5.4.3.1–5.4.3.5 complicate both the prediction of the texture development and the prediction of the mechanical anisotropy. Hosford [5.115] and Dressler at al. [5.94, 5.116] reported good agreement between theoretically and experimentally derived yield loci, especially for zirconium and Zircaloy.

5.4.3.7. Compatibility conditions

Assuming the volume remains constant during plastic deformation, according to the Von Mises criterion [5.105, 5.111], at least five mutually independent deformation modes are required in a single grain embedded in a polycrystal to ensure homogeneous deformation of the grain on a macroscopic scale without cracking along grain boundaries. These compatibility conditions result in a superposition of internal stresses and externally applied stresses. This effect, which is more pronounced the smaller the grain size and the higher the difference in orientation between grains, makes it difficult to estimate the stresses needed to initiate deformation in a single grain. A quantitative determination has not yet been made.

For deformation in polycrystalline materials, Ashby [5.117] illustrated the highly complicated interactions along grain boundaries (Fig. 5.18) by arranging the dislocations in such a way that potential overlaps or cavities are accommodated during deformation. The interactions are even more complex if twinning is included in the accommodation process, as with HCP metals.

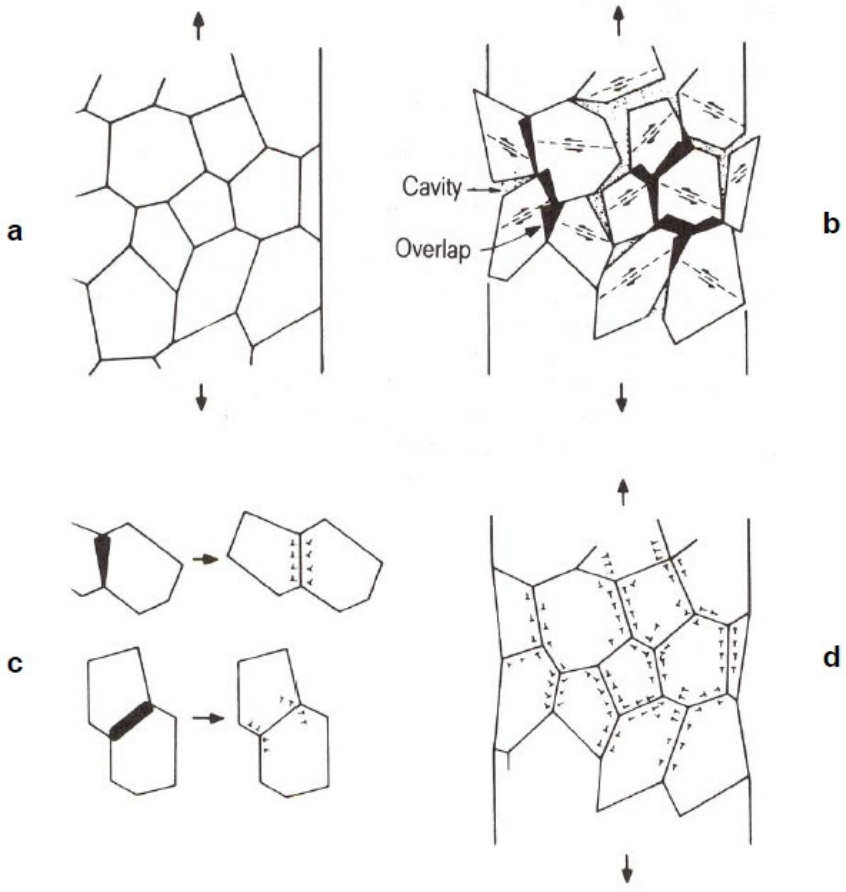

FIG. 5.18. Deformation model of a polycrystalline material, shown in (a). If each grain of a polycrystal deforms equally, overlaps and cavities would develop, as shown in (b). These incompatabilities can be offset by the introduction of dislocations, as shown in (c) and (d) [5.117] (reprinted with permission from Ref. [5.1], copyright ASTM International).

5.4.3.8. Preferred crystallographic orientation

When predicting the deformation mechanisms of polycrystalline materials, any preferred orientation of the crystals or crystallographic texture must be taken into account. If the crystals were randomly oriented, the anisotropy of each grain would be largely balanced by the random distribution. If the grains have a preferred crystallographic orientation, then the properties of the polycrystal approximate those of a single crystal. This behaviour is more pronounced the stronger and sharper the texture and the coarser the grains.

In summary, the deformation of zirconium is qualitatively understood but, as yet, there have only been initial attempts at quantitatively evaluating the complicating factors such as the role of alloying elements and multiaxial loading, described in Sections 5.4.3.6–5.4.3.8 (see also Section 5.7).

5.5. TEXTURE

The term ‘texture’ describes the orientation of crystals. It is a statistical quantity that describes a distribution of frequencies, which depends on three orientation parameters. It does not describe the form and arrangement of the crystals.

To determine the texture, procedures that measure the crystallographic orientations of the grains in a specimen or component with respect to its outer dimensions are used. One can distinguish between direct measurements and indirect methods.

5.5.1. Direct determination of texture (diffraction methods)

The structure of crystallites can be directly examined using rays (X ray photons, electrons or neutrons) if their wavelengths are similar to the distances of the atomic lattice (between 0.01 and 1 nm). The decisive effect is that the atomic lattice diffracts the rays and the resulting interference can be used to analyse the grain orientations of a polycrystal. The energy dependences to produce the appropriate wavelengths of X ray photons, electrons and neutrons are given in Fig. 5.19 [5.118].

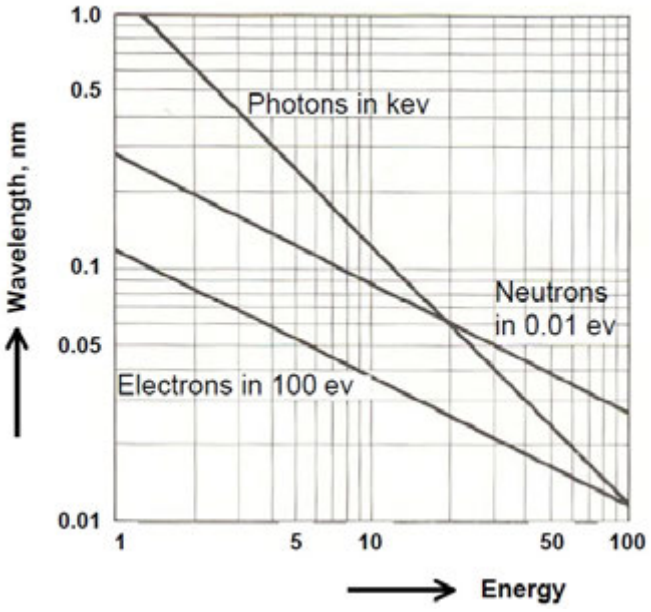

FIG. 5.19. Wavelength versus particle energy for photons, neutrons and electrons [5.118].

When an incident ray with characteristic wavelength λ impinges on a series of parallel lattice planes spaced equal distances d apart at an angle θ, then the rays interfere constructively, if the difference of the path length is a multiple n of the wavelength (Fig. 5.20). This relation is defined in Bragg's law of interference:

$$n\,\lambda = 2\,d\,\sin\theta \tag{5.21}$$

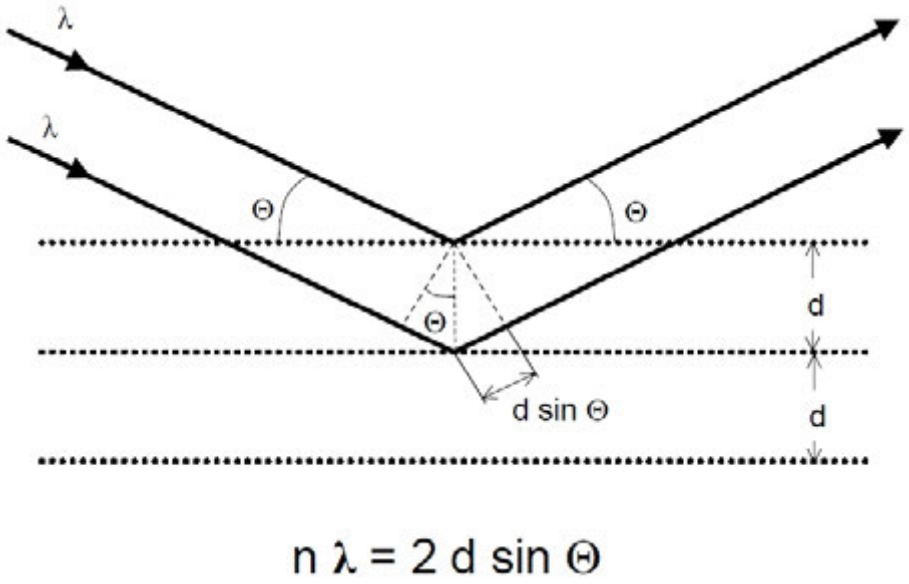

FIG. 5.20. Constructive interference of rays when the difference of path length fulfils Bragg's law.

The physical phenomenon of constructive interference of the diffracted beam as defined in Bragg's law is the basic principle for the application of X ray photons, electrons or neutrons for structural analysis and for determining preferred crystallographic orientations and texture. X ray, electron and neutron diffraction measurements complement one another, each one giving a particular kind of information that the others cannot or, if they can, they give it less conveniently. Each of these technologies is briefly compared to show the ranges of their special applications.

5.5.1.1. X ray photons

The most widely applied technology is the use of X rays, because the cost of the apparatus is low relative to that for electrons or neutrons. Furthermore, X rays contain a share of continuous as well as characteristic wavelength distributions, which can be used alternatively depending on the diffraction test applied. X ray microbeam technology allows texture analysis with a geometrical resolution of about 1 μm. Because of their medium depth of penetration, X rays can be used in transmission and reflection modes. The geometric conditions for diffraction are commonly achieved by a eucentric (meaning 'well-centred') goniometer arrangement fulfilling the focusing requirement within the Seemann-Bohlin and Bragg-Brentano circles [5.14]. Using a characteristic wavelength, this geometry is applied to texture measurements, as shown by the schematic diagrams for the Schulz [5.119] reflection and transmission modes (Fig. 5.21).

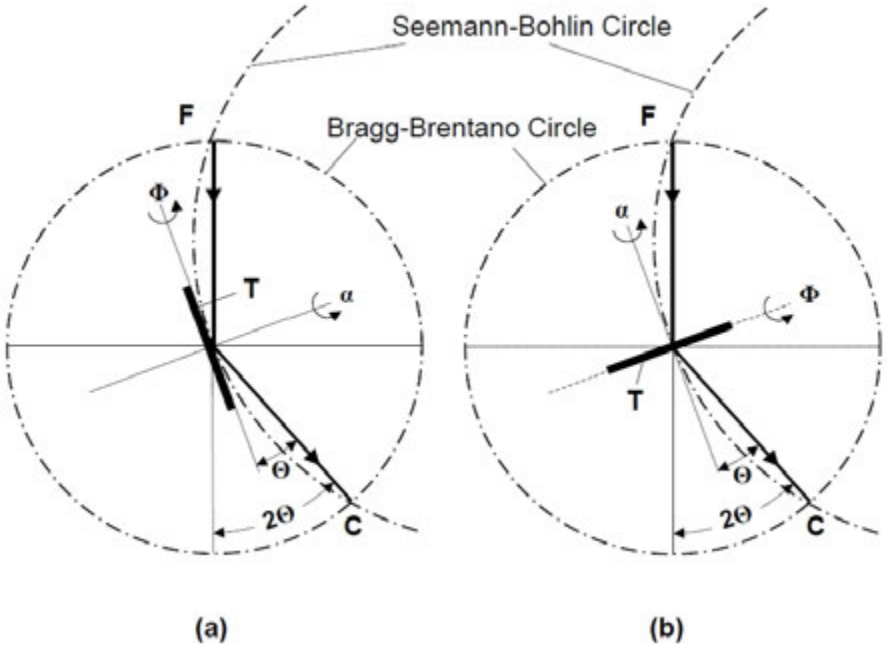

FIG. 5.21. Geometry of Schulz's (a) reflection and (b) transmission methods for texture measurement with focusing requirements of Bragg-Brentano and Seeman-Bohlin circles in the projection of the plane of the goniometer. T is the textured specimen, F is the focal point of the incident X ray beam, C is the counter, Θ is the Bragg angle derived from $n\lambda = 2d \cdot \sin\Theta$, where Φ is the tilt angle of the normal to the sample surface and the normal to the diffracting net plane.

5.5.1.2. Electrons

Electrons are charged and interact strongly with matter; they penetrate a short distance into a crystal, a few tens of nm, but give good diffraction patterns. Reflection patterns are representative of a thin surface layer of the specimen, while transmission patterns can be made only of specimens classified as thin foils or films. Diffraction by electrons is used to study the structure of surface layers, metal foils, oxide films or any layers that are produced by chemical or physical vapour deposition. The high geometrical resolution of electron microscopes ($<0.2-0.5$ μm) allows the analysis of single grain orientations, grain boundaries and interaction between neighbouring grains, even for bulk material after thin foil preparation. Because of the high absorption of electrons by air, the measurements (electron source, specimen and detector) have to be performed in an evacuated apparatus such as a transmission, scanning or scanning-transmission electron microscope.

5.5.1.3. Neutrons

A diffraction experiment with a neutron beam is not a standard method. A prerequisite is access to a source of high intensity thermal neutrons through a slot in the wall of a fission reactor or from spallation of a proton accelerator. The monochromatic beam is obtained by diffraction from a single crystal. The chief advantage of neutrons for zirconium is their low mass absorption and therefore their high depth of penetration (for example, a neutron beam is attenuated by 30% on traversing a thickness of 12 mm). Thus, neutrons can also be used for the non-destructive examination of actual components. There is no regular variation between the scattering power for neutrons and the atomic number of the material. Neutrons are scattered with the same intensity at all scattering angles, irrespective of the atomic number of the material.

5.5.1.4. Measurement procedures

Various devices collect the data from the diffracted beam, the intensity of which is measured qualitatively by film or quantitatively by counters. The detailed technologies, including geometry of the assembly, production of a characteristic beam (filters, monochromators), correcting factors (defocusing, absorption, fluorescence, extinction), specimen preparation and measuring procedure are described in handbooks [5.14, 5.120].

Function of the goniometer: As indicated in Fig. 5.21, there are several geometric conditions and variants of rotations that must be realized to cover the collection of data over all possible orientations in the specimen. The common approach is that the required movements of the specimen and the counter are performed by a spectrometer with a eucentric goniometer positioned in the centre of the Bragg-Brentano circle (Fig. 5.22).

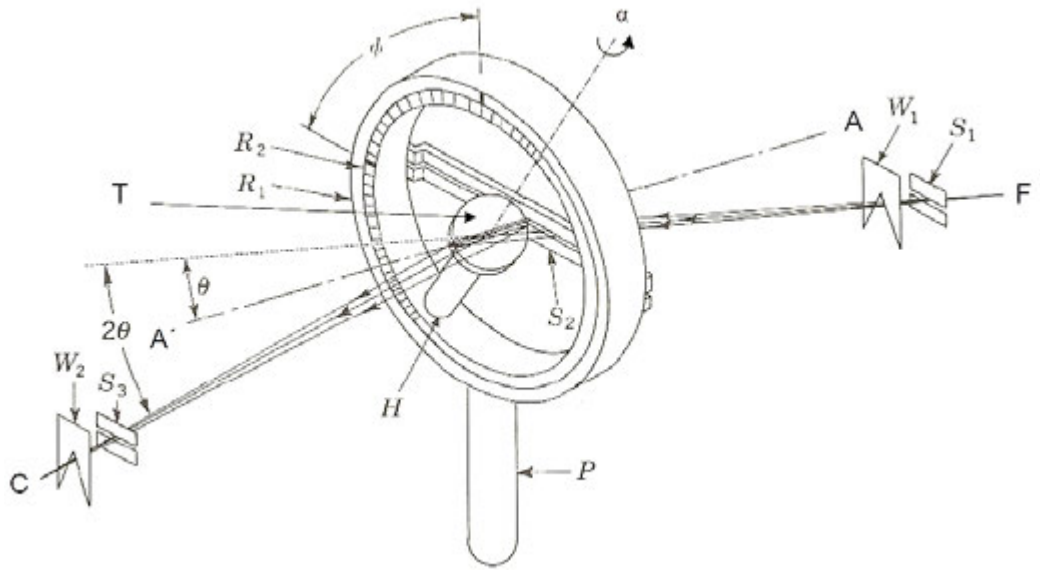

FIG. 5.22. Goniometer head for Schulz's reflection method. On the axis of the spectrometer is mounted the post P of the goniometer. This post supports a ring R_1 in which rests a smaller ring R_2 that can be turned through angles Φ. A second post H supports the specimen holder. H is adjustable so that the surface of the specimen T coincides with the ring axis AA`. The specimen itself rotates in its own plane around its face normal through angles α. Simultaneously the specimen T oscillates in its own surface plane to average over more crystallites. The collimating system is composed of slits S_1, S_2, S_3 and wedges W_1, W_2, which control the divergence of the incoming and diffracted beam in vertical and horizontal directions, respectively [5.14]. (By turning the specimen through 90°, the goniometer can also be used for the transmission mode, see Fig. 5.21).

With such devices and scanning with a time-synchronized counter, it is possible to collect automatically the intensities of the diffracted beam for orientations in Φ and α within the specimen.

Depending on the technique used to determine the texture, various factors can cause a loss in intensity of the diffracted beam and therefore have to be taken into account. The various techniques and necessary corrections are given in Refs [5.1, 5.14, 5.120, 5.121].

Correction for defocusing effects: The defocusing effect, caused by the tilt of the specimen in the angle Φ, is also a function of the Bragg diffraction angle Θ [5.122–5.126]. Owing to the movement and geometry of the specimen and the diffractometer, for the reflection method, defocusing, and for the transmission method, absorption plus defocusing, have to be taken into account. Owing to the defocusing effect, the Schulz reflection and transmission technique is limited with respect to the tilt angle Φ, because larger tilts in Φ will broaden

increasingly the 'illuminated' area on the specimen. Thus, not all of the diffracted beam can be captured by the receiving slit and the measured intensity will be lower than the actual intensity (Fig. 5.23). With an accurate alignment of the diffractometer, with a narrow setting of the slits, and with a proper correction of the defocusing geometry, the Schulz reflection technique applies to Φ angles of 70–80°.

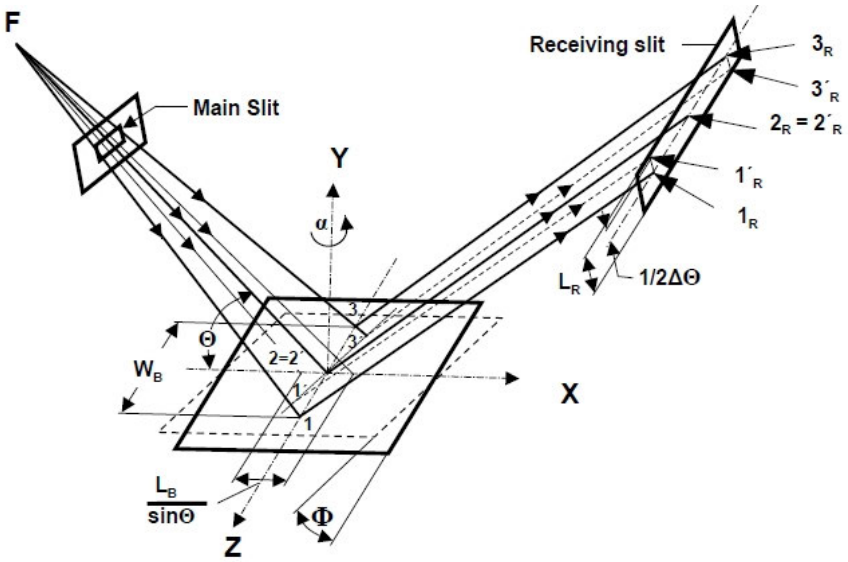

FIG. 5.23. Schematic diagram of the spectrometer geometry used for Schulz's reflection technique of determining preferred crystallographic orientation [5.125]. F is the focal point of the incident X ray beam; Θ is the Bragg angle derived from nλ = 2d sinΘ; Φ is the tilt angle between the normal to the sample surface and the normal to the diffracting net plane; a is the angle of rotation of the specimen in its own plane around the face normal; WB is the width of the incident X ray beam at the centre of the goniometer, given by the slit width of the aperture; LB is length of the incident X ray beam at the centre of the goniometer as a function of Θ; LR is the width of the receiving slit at the X ray counter; Δ2Θ is the width of the Bragg diffraction peak at the receiving slit.

The physical configuration of the diffracting arrangement, including the slit conditions, as well as the geometrical movements of the specimen and the goniometer, can be described by a mathematical function. The corresponding integral to correct the intensity loss, *y*, is given in Eq. (5.22). By means of this convolution integral, or rather by a simplified numerical version of the equation solved by computer, a correction of the defocusing effect and hence a quantitative determination of the intensity is possible [5.125]:

$$\frac{I_A(\Phi,\theta,W_B,L_R)}{I_A(\Phi=0,\theta,W_B,L_R)} = 1 - \frac{2}{(2\pi)^{\frac{1}{2}}}\int_{-\infty}^{-L_R/\mathrm{P}(W_B\cdot\tan\Phi\cdot\sin2\theta)/\sin\theta)} e^{-\frac{y^2}{2}}dy \qquad (5.22)$$

Where

I_A is the measured X ray intensity above background level;
P is a constant factor that is determined empirically for the individual equipment to account for effects such as the flatness of the sample, misalignment of the goniometer or the sample, the intensity profile and the wavelength distribution of the X ray source (values of the order of 1);
F is the focal point of the incident X ray beam;
θ is the Bragg angle derived from $n\lambda = 2d\sin\theta$;

Φ is the tilt angle of the normal to the sample surface and the normal to the diffracting net plane;
α is the angle of rotation of the specimen in its own plane around the face normal;
W_B is the width of the incident X ray beam at the centre of the goniometer, given by the slit width of the aperture;
L_B is the length of the incident X ray beam at the centre of the goniometer as a function of θ;
L_R is the width of the receiving slit at the X ray counter;

and $\Delta 2\theta$ is the width of the Bragg diffraction peak at the receiving slit.

Measurement procedures for complete pole figures: To avoid the defocusing, or at least to keep it constant over the tilt angle Φ, there are several methods to collect the intensity data over the whole reference sphere [5.8, 5.14]:

— The reflection method on three orthogonal surfaces, usually perpendicular to the principal directions in a component, for example, the axial, radial and tangential directions in a tube. The resulting overlap in regions of higher tilting angles is used to match the overlapping diffracted intensities.
— A combination of the reflection and transmission methods: two measurements are necessary with a certain overlap of the exposed regions to match the diffracted intensities of both methods.
— Reflection method on a specimen with a 45° cut through its cross-section: Owing to the 45° cut, the goniometer has to scan over Φ from −45° to +45°. This scan allows coverage of the whole 0–90° range in a single measurement without major defocusing effects. (The specimen has to be sufficiently thick or else thin walled specimens must be stacked together before the 45° cut, so inhomogeneities over the wall thickness of the specimen become averaged.)

Reflection method on a spherical specimen: There is a large preparative expense for machining the sphere with a small shaft to attach the specimen to the rotational devices of the goniometer in Φ and Θ. There is an additional defocusing effect that remains constant over the whole 90° Φ scan. The specimen has to be sufficiently thick or else must be stacked, so inhomogeneities over the wall thickness of the specimen become averaged.

Accounting for background intensities: To achieve quantitative texture measurements requires comparative intensity values of the diffracted beam. Therefore, the intensity of the diffracted beam from a textured specimen must be related to that from a randomly oriented specimen. These correlations have to be performed for each individual lattice plane and simultaneously the respective background intensity must be subtracted (5.23):

$$\mathrm{I}_{\mathrm{Quant}} = \frac{\mathrm{I}_{\mathrm{Text}} - \mathrm{I}_{\mathrm{BGText}}}{\mathrm{I}_{\mathrm{Rand}} - \mathrm{I}_{\mathrm{BGRand}}} \tag{5.23}$$

where

$\mathrm{I}_{\mathrm{Quant}}$ is the quantified comparative intensity value;
$\mathrm{I}_{\mathrm{Text}}$ is the intensity of the textured sample;
$\mathrm{I}_{\mathrm{BGText}}$ is the background intensity of the textured sample;
$\mathrm{I}_{\mathrm{Rand}}$ is the intensity of the random sample (usually Zr powder);
and $\mathrm{I}_{\mathrm{BGRand}}$ is the background intensity of the random sample.

Another approach to account for a random sample is to collect the intensity data of a specific plane over the complete reference sphere, to average the intensity as an equal distribution and to gain a virtual value for a random distribution. This method does not rely on a randomly oriented powder sample, with its disadvantage of differences in density. Additional effort is needed to collect the intensity values reliably over the whole reference sphere.

5.5.2. Indirect determination of texture

Besides the direct determination of texture by diffracting methods, there are several other methods that measure the anisotropy of properties; for example, optical properties, acoustic and ultrasonic properties, mechanical properties such as Young's modulus, yield strength, hardness indentation, bending and earing in sheets, thermal expansion, and electrical and magnetic properties. Knowing the anisotropic properties of the single crystal (Section 5.2) or knowing the influence of the preferred crystallographic orientation on these properties, one can indirectly deduce the underlying texture. The sharper the texture, the more pronounced is the anisotropy of the property. These rather coarse but cheap and quick methods are often used for quality control for specific fabrication processes and fulfil the requirements for the specific application.

5.5.3. Description of texture

The basis for depicting texture is the stereographic projection, which reduces the three dimensional angle relations of the reference sphere to the two dimensions of a circle, similar to the projection of geographical maps, with great circles, small circles, longitudes and latitudes, as shown in Fig. 5.24. This depiction is required for the classical presentation of textures by pole figures.

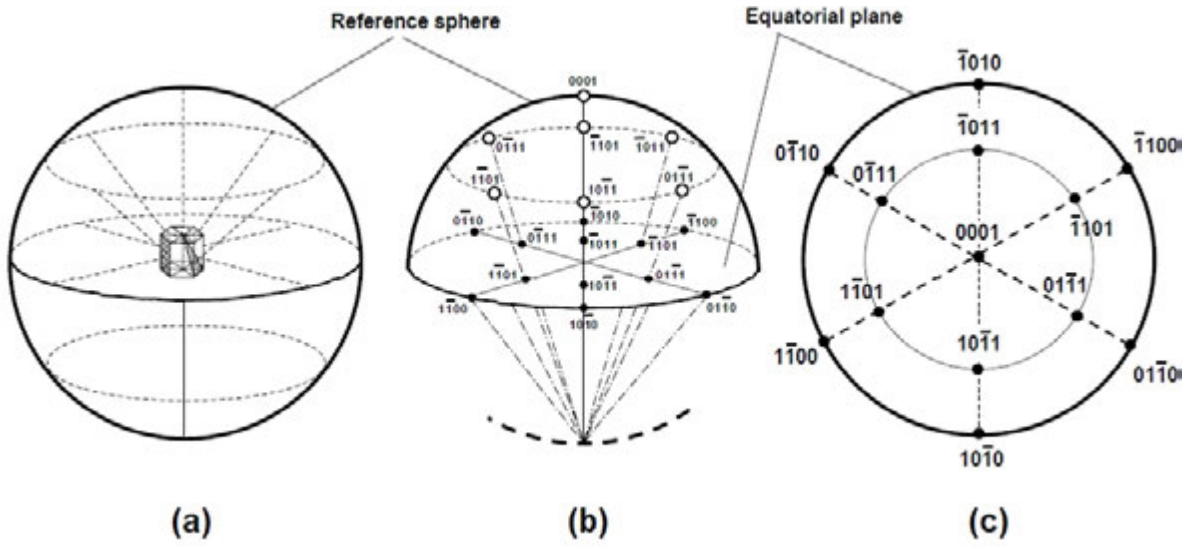

FIG. 5.24. Derivation of the stereographic projection: (a) poles of basal, prism and first order pyramidal planes; (b) stereographic projection of plane poles from the reference sphere to the equatorial plane; (c) stereographic projection of basal-, prism- and first-order pyramidal plane poles.

The drawback to this two dimensional plot is that many orientations come together at one point in the pole figure. To reduce this ambiguity, several pole figures of various crystallographic planes are plotted, although two can usually provide enough information for most purposes. For the calculation of crystallographic orientation distribution functions (ODFs) at least three pole figures are needed (see Section 5.5.3.4).

5.5.3.1. Standard (direct) pole figure

Direct pole figures are stereographic projections showing the density of crystallographic poles of selected crystal planes as a function of orientation with respect to the principal directions of a specimen or of a product; for example, the normal direction (ND), rolling direction (RD) or transverse direction (TD) of a sheet; see Fig. 5.25.

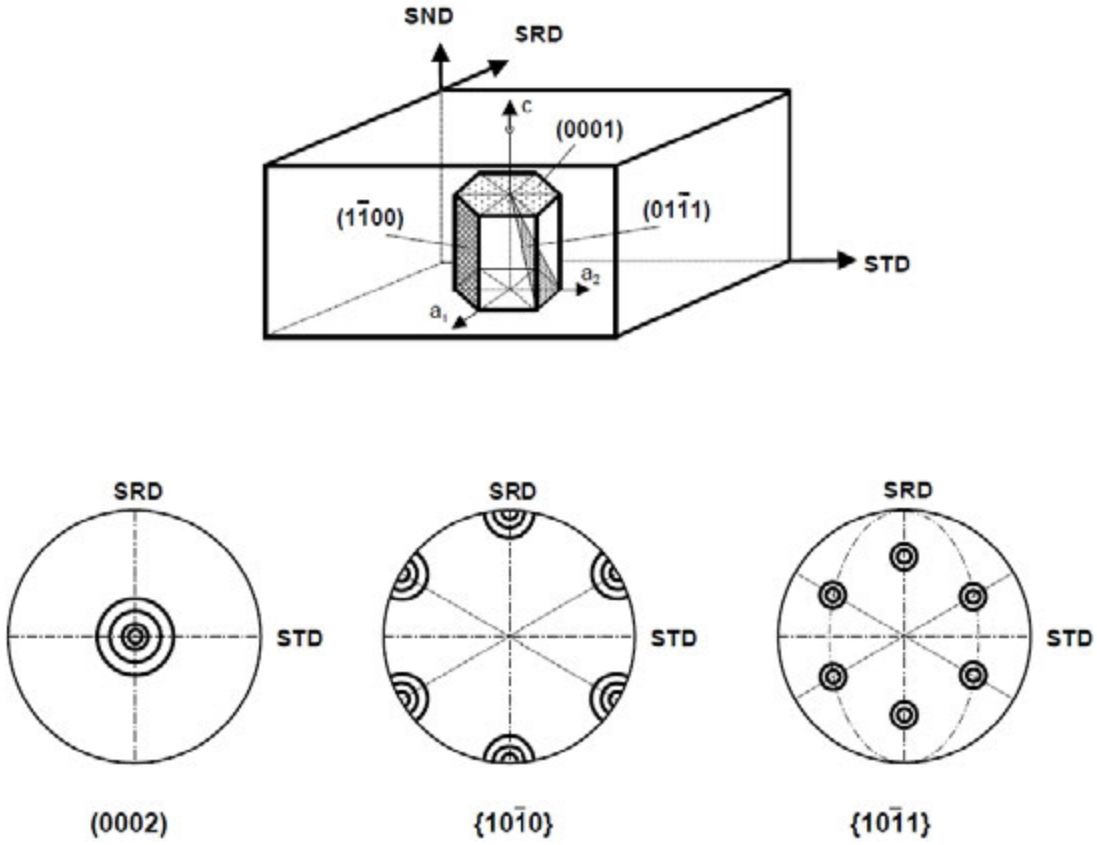

FIG. 5.25. Pole figures for the (0002)-, $\{10\bar{1}0\}$-, $\{10\bar{1}1\}$- planes, derived from the ideal single crystal orientation in a sheet. SND — sheet normal direction; SRD) — sheet rolling direction; STD — sheet transverse direction.

5.5.3.2. Inverse (indirect) pole figure

Inverse pole figures are stereographic projections of a principal direction in a sample or component on a standard projection of the crystal lattice, as shown in Fig. 5.26.

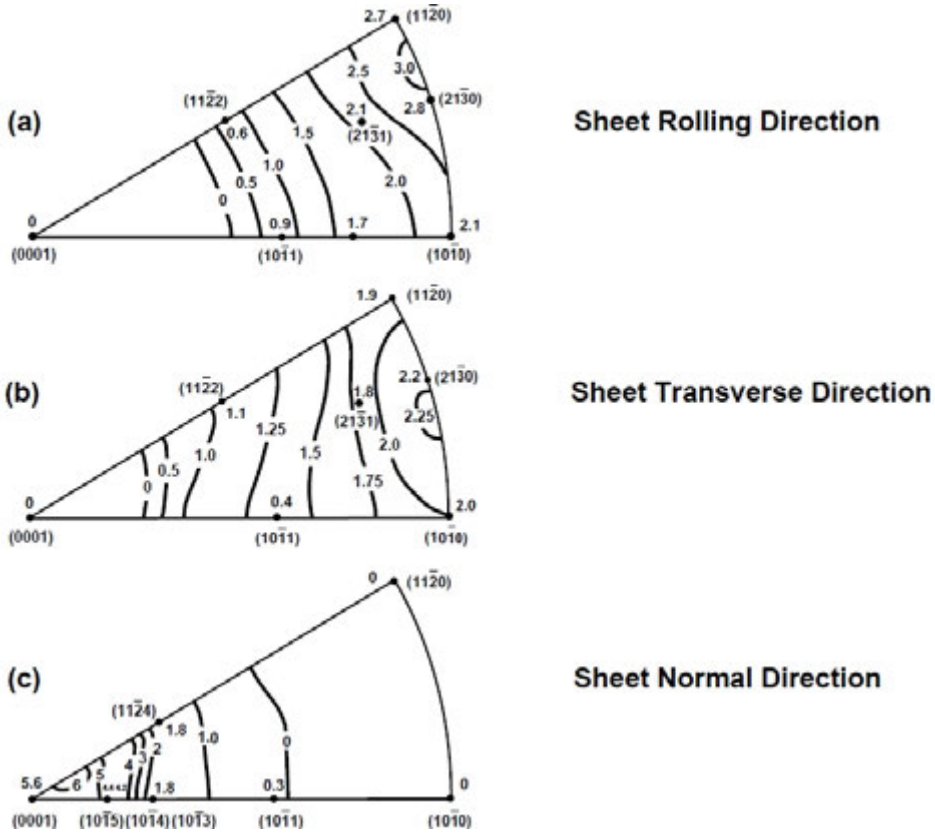

FIG. 5.26. Inverse pole figures showing the intensity distributions of the preferred crystallographic orientations plotted in standard orientation projections of the hexagonal structure [5.127]. For each outer dimension of the Zircaloy-2 plate, an inverse pole figure is plotted: (a) SRD, (b) STD, (c) SND.

5.5.3.3. Texture coefficients

For a quantitative analysis of texture, it is important to know how often the crystallites are oriented in any predetermined orientation of the sample. The pole figure is a two dimensional projection of a three dimensional structure. Looking only at one pole figure, for example, the basal pole figure (0002) of Fig. 5.25, the description of the orientation of the crystals is not definite, because the rays are diffracted independently from the rotation of the diffracting plane around its normal.

Additional information must be gained, for example, from the $\{10\bar{1}0\}$ pole figure, which now defines the rotation of the c axis around the basal plane with respect to the reference directions. To eliminate ambiguity and for a more accurate description of the texture, at least three pole figures must be taken; for example, the $\{10\bar{1}1\}$ pole figure could be added. Statistical distribution functions are used for a quantitative description of the preferred crystallographic orientations.

The f parameter: Kearns [5.128] and Tempest [5.129] deduced quantitative expressions, which relate the texture to bulk physical properties. Individual crystallites of specific orientation are assumed to contribute to the bulk property in proportion to their volume fraction (Fig. 5.27). The derived *f* parameters are based on the numerical description of the pole density distribution over the reference sphere. For any angle, Φ_i and Ψ_i, the pole density is divided into their vector parts with reference to the principal directions of the specimen or component, for example, the axial, radial and tangential directions in a tube. To derive quantitative values, the vector density distributions are referred to the overall density distribution of the reference sphere.

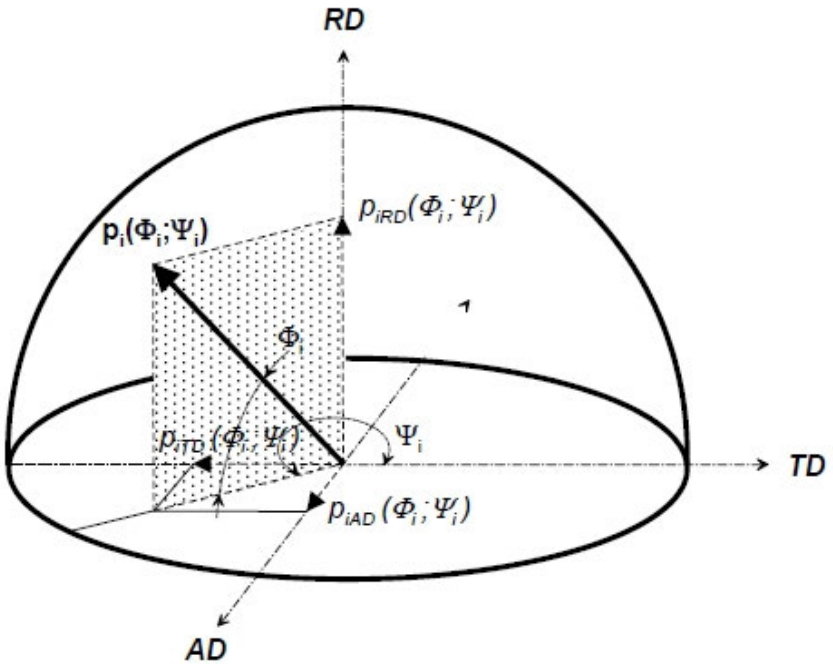

FIG. 5.27. Definition of the spherical coordinates for pole density determination.

Texture factors, *f*, derived from the (0002) pole densities of a Zircaloy-4 tube, are given in Eqs (5.24–5.26) for the RD (rolling direction), axial direction (AD) and TD (transverse direction):

$$f_{\mathrm{RD}} = \frac{\sum p_{i\mathrm{RD}}(\Phi_i;\Psi_i)}{\sum p_i(\Phi_i;\Psi_i)} = \frac{\sum p_i(\varphi_i;\Psi_i)\cos\varphi_i \sin^2\varphi_i}{\sum p_i(\varphi_i;\Psi_i)\cos\varphi_i} \tag{5.24}$$

$$f_{\mathrm{AD}} = \frac{\sum p_{i\mathrm{AD}}(\Phi_i;\Psi_i)}{\sum p_i(\Phi_i;\Psi_i)} = \frac{\sum p_i(\varphi_i;\Psi_i)\cos^3\varphi_i \cos^2\Psi_i}{\sum p_i(\varphi_i;\Psi_i)\cos\varphi_i} \tag{5.25}$$

$$f_{\mathrm{TD}} = \frac{\sum p_{i\mathrm{TD}}(\Phi_i;\Psi_i)}{\sum p_i(\Phi_i;\Psi_i)} = \frac{\sum p_i(\varphi_i;\Psi_i)\cos^3\varphi_i \cos^2(90+\Psi_i)}{\sum p_i(\varphi_i;\Psi_i)\cos\varphi_i} \tag{5.26}$$

In practice, the texture factors in any direction fiD are:

$$f_{\mathrm{iD}} < 1.0 \tag{5.27}$$

and the sum of fiD in the three principal directions adds up to:

$$\mathrm{S}\, f_{\mathrm{iD}} = 1.0 \tag{5.28}$$

5.5.3.4. Orientation distribution function

The orientation distribution function is a density of probability that a crystal lattice is oriented in a certain way. The reference orientation is the axis of the sample. The orientations of the crystals are expressed by the Euler angles Φ_1, Φ, and Φ_2. This orientation is called *g*. Thus, if *f* is the ODF, the volume d*V* of crystals with orientation in $[g; g + \mathrm{d}\, g]$ (i.e. $[\Phi_1; \Phi_1+\mathrm{d}\Phi_1]$, $[\Phi; \Phi+\mathrm{d}\Phi]$, $[\Phi_2; \Phi_2+\mathrm{d}\Phi_2]$), is:

$$\mathrm{d}V/V = f(g)\mathrm{d}g \tag{5.29}$$

where V is the total diffracting volume of the sample.

Mathematical methods have been developed to compute three dimensional ODF with the help of intensity values derived from direct or inverse pole figures [5.121, 5.130–5.133]. Figure 5.28 shows the derivation of an ODF figure, which by averaging gives the extent to which crystals of a given orientation are present in a polycrystalline sample. It thereby represents a quantification of the texture.

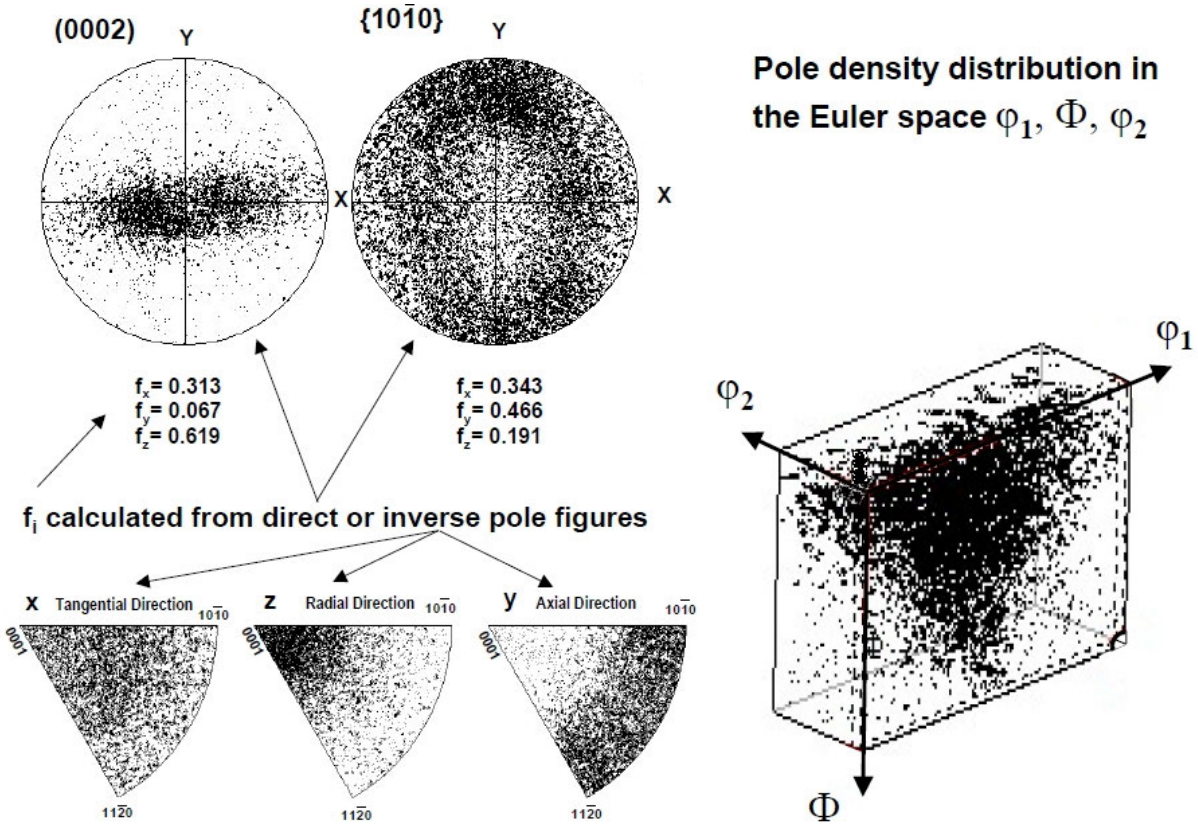

FIG. 5.28. ODF derived from orientation measurements of a Zircaloy-4 tube.

In summary, the measurement and description of crystallographic texture are well founded for components made from zirconium alloys and are used to evaluate the formation of the preferred orientation.

5.6. TEXTURE DEVELOPMENT IN ZIRCONIUM AND ZIRCONIUM BASED ALLOYS

5.6.1. Interaction between deformation mechanisms and the change of preferred crystallographic orientation during deformation in the α phase

To understand the development of deformation textures and to predict ideal preferred orientations, the deformation mechanisms comprising systems with set crystallographic slip or twinning planes and the corresponding slip or shear directions (see Section 5.3) need to be considered.

The various theories referred to in the literature that explain texture development differ in the combination of five slip systems chosen out of the overall possible combinations, according to the yield criterion of Von Mises [5.105]. The operative deformation mechanisms chosen by Taylor [5.107] were based on the principle of internal least-work-performed in

deformation, while Bishop and Hill [5.108] chose the equivalent principle of external maximum-work-performed in deformation (see Section 5.4.3.6).

The theories concerning the development of deformation textures have been applied successfully to cubic metals, in particular for deducing deformation textures of FCC metals [5.134–5.136]. In comparison, the theory regarding the development of deformation textures in HCP metals is not as extensive and complete. There are several reasons for this shortfall (see Sections 5.2 and 5.3):

- The slip systems are neither as numerous nor as symmetrically distributed in hexagonal metals as in cubic metals. Therefore, twinning competes with slip and, depending on the conditions of deformation, can play a significant role.
- The lattice rotations caused by the unipolar twinning modes depend on stringent crystallographic orientation relationships and are inhomogeneous. The theories of deformation texture available so far are based on homogeneous deformations.
- Compared with cubic metals, the larger number of deformation systems (different slip and twinning modes) in HCP metals results in significantly more combinations of five mutually independent deformation systems.
- The interaction between slip and twinning is complicated and makes the formulation of the theory for texture development even more difficult.
- In HCP metals the critical resolved shear stresses (CRSSs) are different for the various deformation systems and are not entirely known; for the twinning systems, it is not certain whether CRSSs exist. As a substitute for these stresses, shear stress ratios have been used, derived from yield strengths of textured polycrystalline materials.
- In HCP metals, the operating deformation systems vary from metal to metal and are not entirely known. Therefore, the theory of the development of deformation textures must be altered or tailored for each HCP metal.

Approaches to explain the development of deformation textures in HCP metals have been made by Calnan and Clews [5.137] for zinc and magnesium, by Williams and Eppelsheimer for titanium [5.138] and by Hobson for zirconium [5.139].

On a theoretical basis, Calnan and Clews [5.137] predicted the main rotations of the crystal lattice by averaging the rotation tendencies of the grains for all possible orientations. They assumed that the deformation systems with a maximum shear stress ratio, RSS/CRRS, became effective. Whether slip or twinning occurred also depended, among other factors, on this ratio. In addition, taking into account the deformation accommodations at grain boundaries due to the compatibility conditions (Section 5.4.3.7), they differentiate between the stress applied to the component and the stress effective in the specific glide or shear plane of the grain.

Williams and Eppelsheimer [5.138] relied on this theoretically derived prediction. Taking into account the interactions of those deformation mechanisms known for titanium, they traced the texture development in polycrystalline sheet material by means of the (0002) and $\{10\bar{1}0\}$ pole figures. These integral methods cannot predict in detail which deformation mechanisms become effective in the individual grains after subsequent deformation steps.

Hobson [5.139] deformed zirconium single crystals of different orientations by rolling and drawing procedures starting with deformations higher than 20% and traced the lattice rotations caused by the observed deformation systems in shear stress contour diagrams. Under the simplifying assumption that the critical resolved shear stresses are equal for the different deformation systems, it was concluded that twinning is more important in the initial stages and that slip is more important in the final stages of texture development.

The main difficulty in applying these results is that the critical resolved shear stresses for the different deformation modes are needed, but they are only partly known for the slip and twinning systems in HCP metals.

After cold deformation, a polycrystalline zirconium specimen was recrystallization annealed to coarsen the grain structure. The crystal orientation of each individual grain was determined by microfocus Laue back reflection technique (Fig. 5.29) [5.140]. The orientation change of each individual grain was followed in consecutive rolling steps by two methods, (a) and (b) (see below).

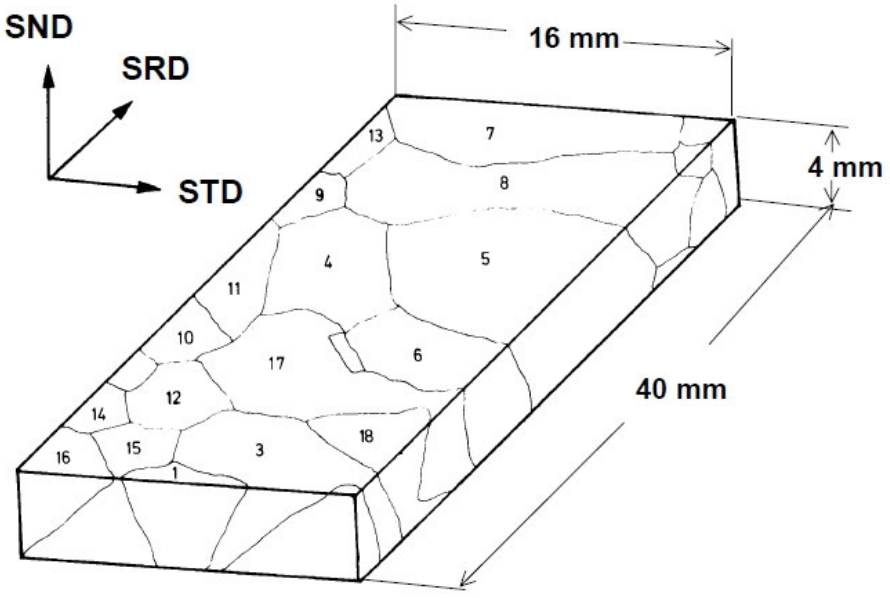

FIG. 5.29. Polycrystalline zirconium sample with identification of each individual grain [5.140]. SND — sheet normal direction; SRD — sheet rolling direction; STD — sheet transverse direction.

Method (a): Starting from the single crystal orientation of the undeformed grain, the slip and twinning traces and corresponding lattice rotations were followed for each of the grain orientations after each consecutive deformation step. As an example, the changes of basal pole orientation of two extreme grain orientations are discussed in more detail:

— At low deformation and a suitable starting grain orientation, preferential traces of the main slip system on prism planes in the <*a*> direction are found (Fig. 5.30). Slip causes the lattice to rotate continuously but effects only small orientation changes, although the strain achieved can be high (Fig. 5.31).
— Simultaneously with slip, twinning is activated even at low amounts of deformation, for example, 0.5%. Twinning causes discontinuous, spontaneous lattice rotations. The angle of rotation and the shear strain of these inhomogeneous deformation processes depend on which twinning system is activated. Twinning causes large lattice rotations, although the strain achieved is small (Sections 5.3.3 and 5.4.2). With increasing deformation, the volume affected by the initial twinning system increases, and additional second- and even third-order twinning systems are activated within the primary twins (Fig. 5.32).

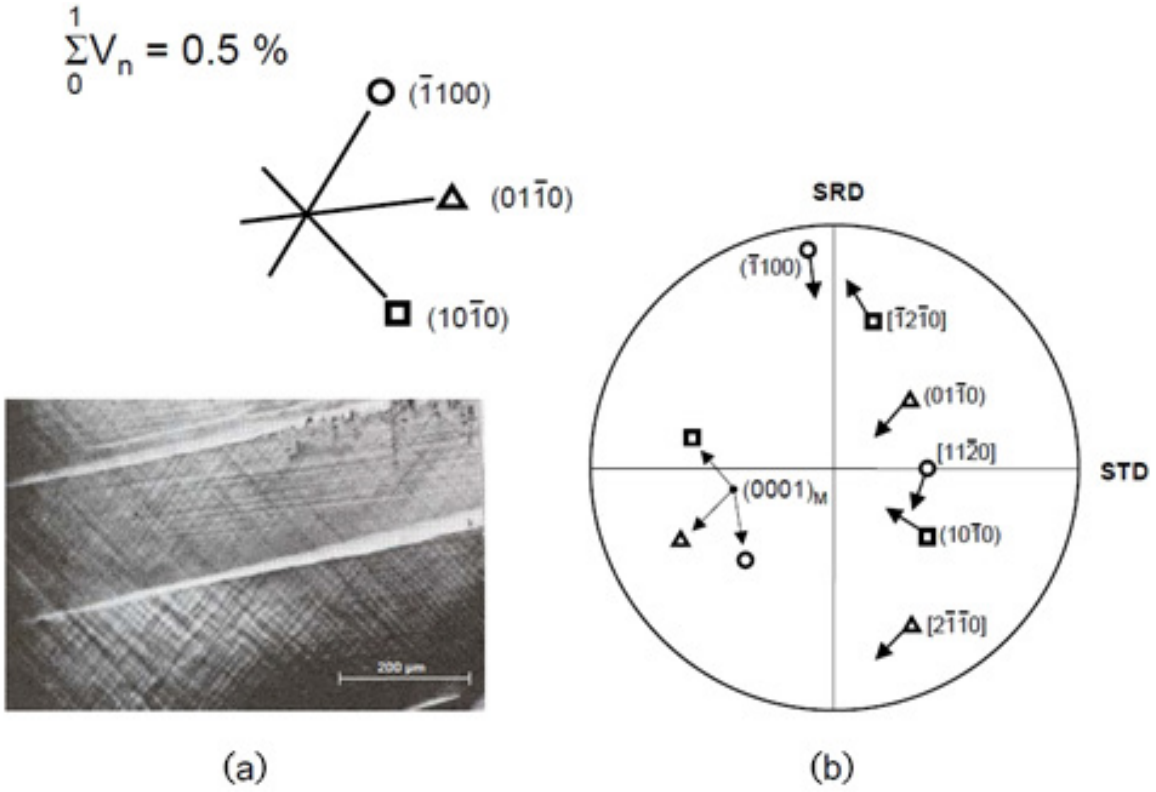

FIG. 5.30. Grain 9 with its starting orientation $(0001)_M$ is favourably oriented for slip on prism planes in <a> directions [5.140]. (a): After 0.5% rolling deformation, predominant traces of these slip systems appear; (b): Their potential activation is depicted as lattice rotations with respect to the SRD and STD. SRD — sheet rolling direction; STD — sheet transverse direction (reprinted with permission from Ref. [5.1], copyright ASTM International).

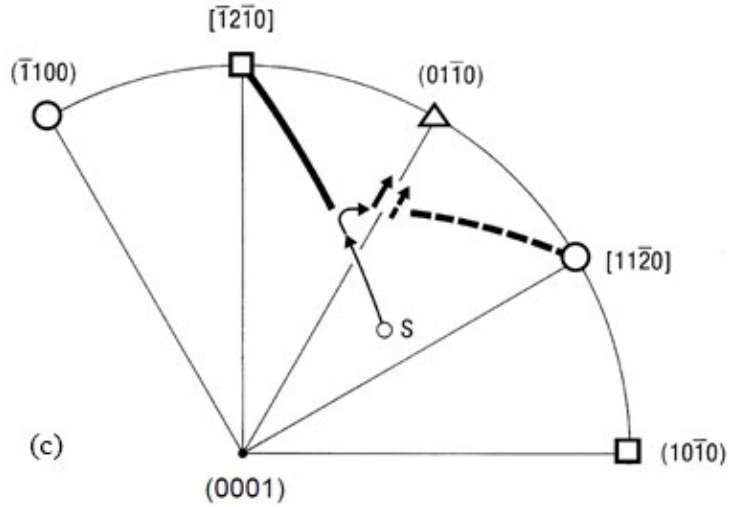

FIG. 5.31. Continuous lattice rotation due to slip on prism planes in <a> directions, first by slip on $(10\bar{1}0)$ $[\bar{1}2\bar{1}0]$ *and then double slip by additional activation of* $(\bar{1}100)[11\bar{2}0]$. *The lattice rotation is shown schematically with respect to the axis of the main compressive force S [5.140].*

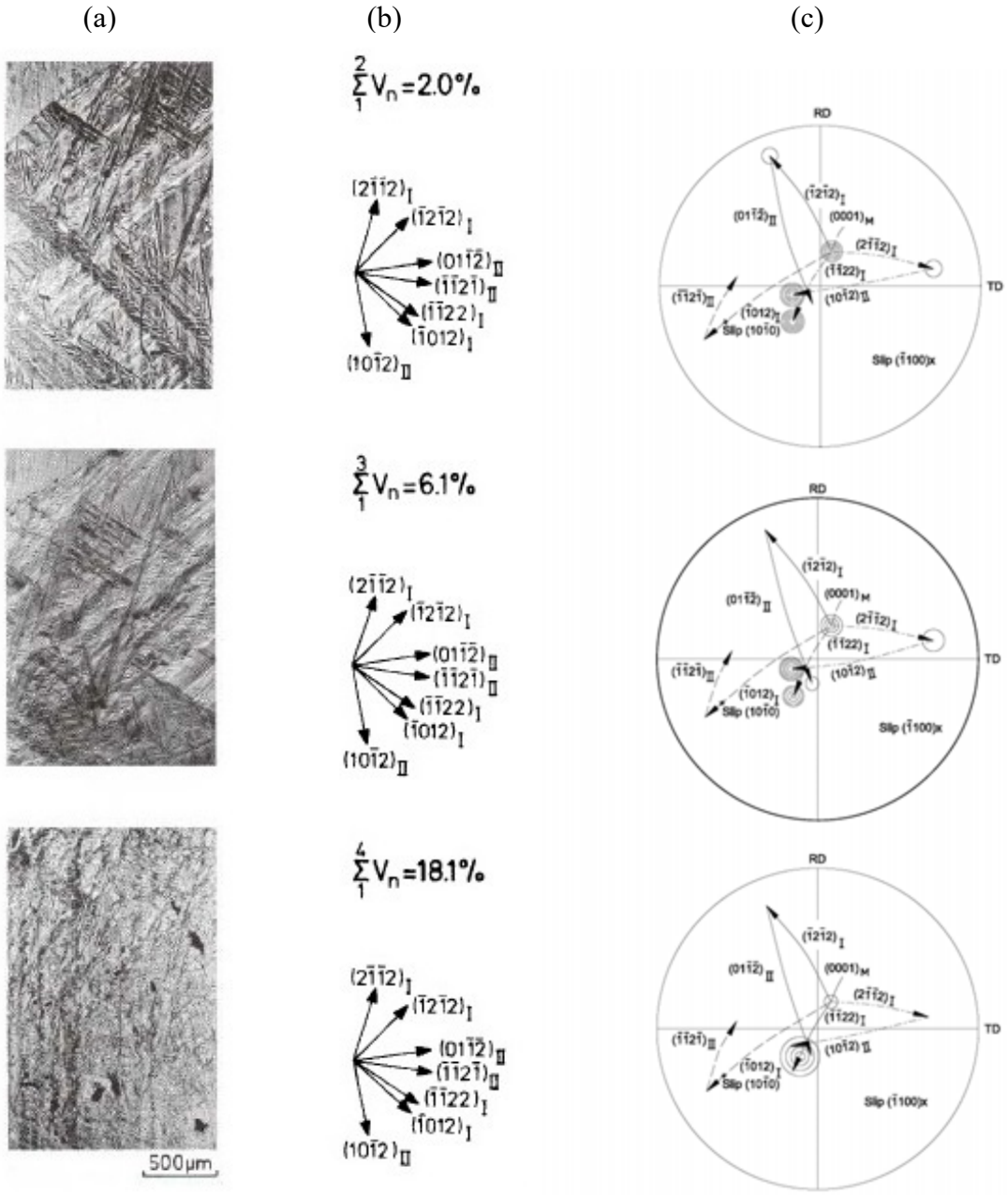

FIG. 5.32. Spontaneous lattice rotation of the basal pole due to twinning in grain 18 [5.140] (reprinted with permission from Ref. [5.1], copyright ASTM International).

Figure 5.32 shows the following:

(a) The microstructure with traces of the deformation systems (for the different degrees of deformation $\sum_1^i V_n$ a photograph was taken of the same microsection).
(b) The associated degree of deformation and the indexed traces of the activated deformation systems.
(c) The stereographic projection with the correspondingly attributed lattice rotations for the basal pole, derived from the different deformation systems. The measured texture intensities for the (0002) planes are also included, as indicated by the number and size of the circles.

Following up the orientation changes of all grains, three different areas for the activation of twinning systems and their corresponding lattice rotations can be deduced, as shown in Fig. 5.33.

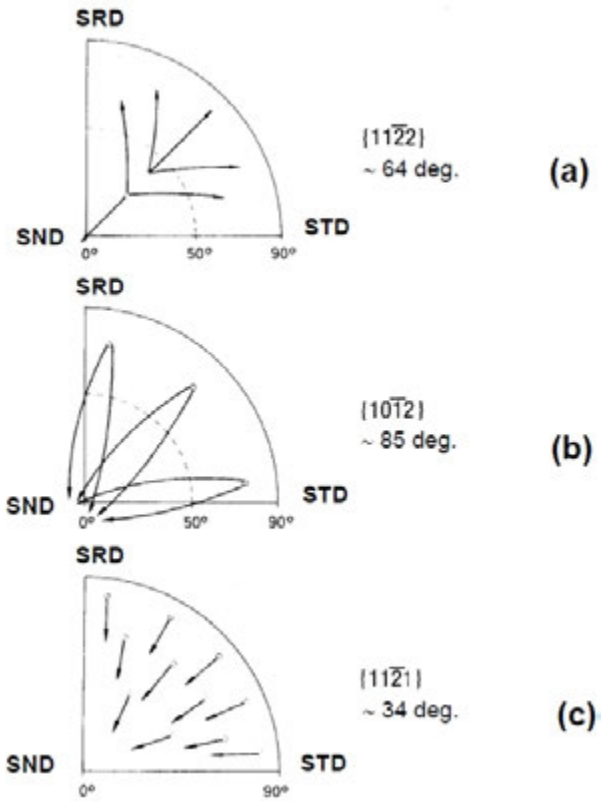

FIG. 5.33. Lattice rotations of the basal pole due to twinning (schematically). SND — sheet normal direction; SRD — sheet rolling direction; STD — sheet transverse direction (reprinted with permission from Ref. [5.1], copyright ASTM International).

In Fig. 5.33, depending on the starting orientation of the matrix, different twin systems are activated [5.140]: (a) Basal pole orientation 0–50° tilted from normal direction (ND); lattice rotation by $\{11\bar{2}2\}$ twinning. (b) Basal pole orientation 50–90° tilted from ND; lattice rotation by $\{10\bar{1}2\}$ twinning. (c) Basal pole orientation 0–90° tilted to ND; accommodation lattice rotation by $\{11\bar{2}1\}$ twinning.

For basal pole orientations 0–50° from the ND, irrespective of the azimuthal position of the basal pole, $\{10\bar{2}2\}$ twinning dominates. Under a compressive strain parallel to the c axis, this twinning system rotates the basal pole by approximately 64° away from the centre of the pole figure (Fig. 5.33). By means of this rotation in the twinned structure, an orientation is usually achieved that is tilted 50–90° away from the ND. In some grains, the lattice could be rotated across the ND from +50° towards −15°, or vice versa.

For basal pole orientations 50–90° from the ND, again irrespective of the azimuthal position of the basal pole, $\{10\bar{1}2\}$ twinning becomes preferentially operative. Under a tensile strain parallel to the c axis, this twinning system rotates the basal pole by approximately 85° towards the centre of the pole figure, also across the ND (Fig. 5.33). This process is often activated as secondary twinning in orientations that were brought into this area (50–90° away from the ND) by $\{11\bar{2}2\}$ primary twinning.

Additionally, $\{11\bar{2}1\}$ twinning can be activated over the entire reference sphere. Under a tensile strain parallel to the c axis, this twinning system rotates the basal pole by

approximately 34° preferentially towards the centre of the pole figure (Fig. 5.33). This twinning system operates less often than the first two systems [5.4, 5.11, 5.12]. Furthermore, the twins act only as a complementary system to accommodate large lattice strains at grain boundaries or at twin interactions and therefore are restricted to a small volume.

These twinning processes, although described separately, in reality interact simultaneously with one another, and, at large amounts of deformation, often act as secondary or higher order twins. In addition, the glide processes must be taken into account, which result in a variety of complicated interactions of different deformation systems (compare Figs 5.30 and 5.32).

Method (b): In parallel with these microscopic examinations, a macroscopic follow up of the basal pole rotations gives further insight into the texture development. After each deformation step, a basal pole figure obtained by X ray diffraction (Schulz reflection technique) revealed the orientation change of the basal poles, starting from the undeformed grains and ending with the final sheet texture, as shown in Fig. 5.34 [5.140].

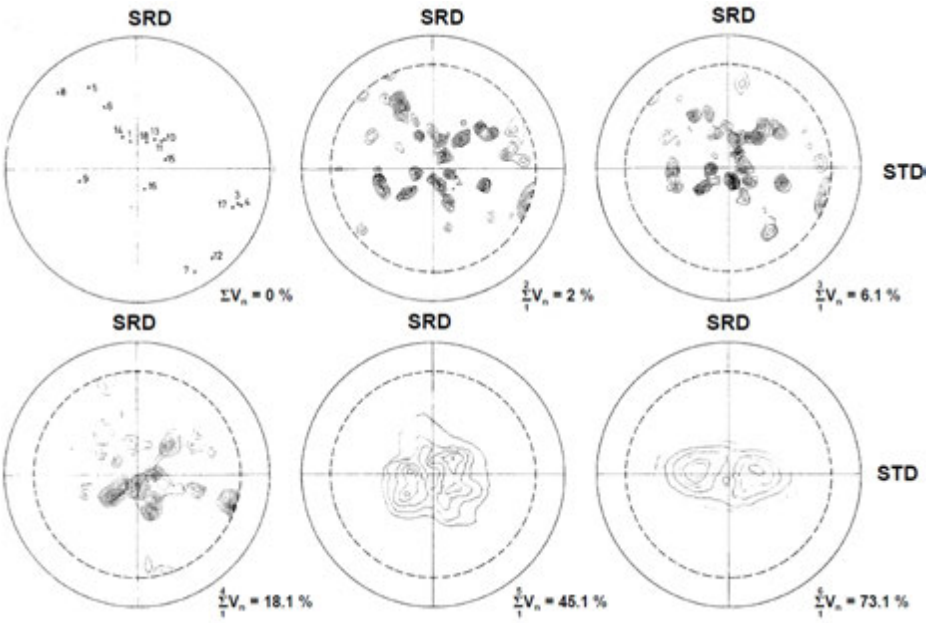

FIG. 5.34. Development of the preferred orientation of the basal poles, starting from the (0002) position of the undeformed individual grains, as shown in FIG. 5.29, up to the final sheet texture [5.140]. SND — sheet normal direction; SRD — sheet rolling direction; STD — sheet transverse direction (reprinted with permission from Ref. [5.1], copyright ASTM International).

Even at low deformations, the results show that twinning causes the basal poles to orient towards the SND (i.e. parallel to the compressive force). At 20% total deformation, this process has already made great progress. From 20 to 40% deformation, the basal poles align further towards the SND. At this point, the microstructure is completely twinned by first and higher order twinning. For deformations of more than 40%, the alignment of the basal poles towards its final stable position (0002) ±20–40° in the STD can be explained by means of pyramidal slip under constraint with a <c+a> type Burgers vector on $\{10\bar{1}1\}$ or $\{11\bar{2}1\}$ planes [5.37].

A prism pole figure taken after the last rolling step showed that a $\{10\bar{1}0\}$ direction was aligned parallel to the SRD.

This micro and macroanalytical follow-up of the evolution of the deformation texture by rolling [5.140] is confirmed and supplemented by additional experimental and modelling approaches performed for HCP metals in general, and for Zr and Zr based alloys in particular, deformed by rolling, tension and compression, to explain and predict texture development [5.141–5.152].

5.6.2. General characteristics of deformation textures in HCP metals

As an introduction, a general review of the texture characteristics in HCP metals with different *c*/*a* ratios will be given. Particular and detailed differences, possibly due to less accurate measurements, are described at full length by Wassermann and Grewen [5.8], Dillamore and Roberts [5.9] and Grewen [5.153].

Most of the texture measurements are related to the basal pole distribution, which plays an important role with respect to the anisotropy of HCP metals. Less is known about the distribution of prism or pyramidal plane poles. These poles are not as decisive as the basal poles for mechanical behaviour, but strongly indicate the state of annealing. They are also needed to perform quantitative determinations of textures by analysing texture coefficients such as Kearns or Tempest factors and the ODF (Section 5.5.3.3).

In all HCP metals, for cold deformed semifinished products (for example, wire, sheet or tubing), the final orientation of the basal plane (0002) is parallel to the direction of elongation of the respective semifinished product. Deviations from this preferred orientation, comprising tilts of the basal plane and their rotation around its pole, exhibit characteristic differences, depending on the specific metal parameters [5.1, 5.8, 5.9, 5.11, 5.153, 5.154]. The textures of the HCP structures can be categorized into three groups, according to the *c*/*a* axial ratio and their resulting operating deformation systems. Figure 5.35 shows these three types of texture in cold-rolled sheet schematically:

— For metals or alloys with a *c*/*a* ratio >1.633 (for example, zinc and cadmium) the position of the basal poles is tilted by ±15–25° from the ND towards the RD. A $< 11\bar{2}0 >$ direction is aligned parallel to the RD (Fig. 5.35(a)).
— For metals or alloys with a *c*/*a* ratio approximately equal to the ideal ratio, 1.633 (for example, magnesium and cobalt), the basal poles concentrate in symmetrical rotation around the ND. The $< 10\bar{1}0 >$ and $< 11\bar{2}0 >$ directions are randomly distributed around the basal pole $< 0001 >$ fibre texture (Fig. 5.35).
— For metals or alloys with a *c*/*a* ratio <1.633 (for example, zirconium, titanium and hafnium), the position of the basal poles is tilted by ±20–40° from the ND towards the TD. A $< 10\bar{1}0 >$ direction is aligned parallel to the RD (Fig. 5.35).

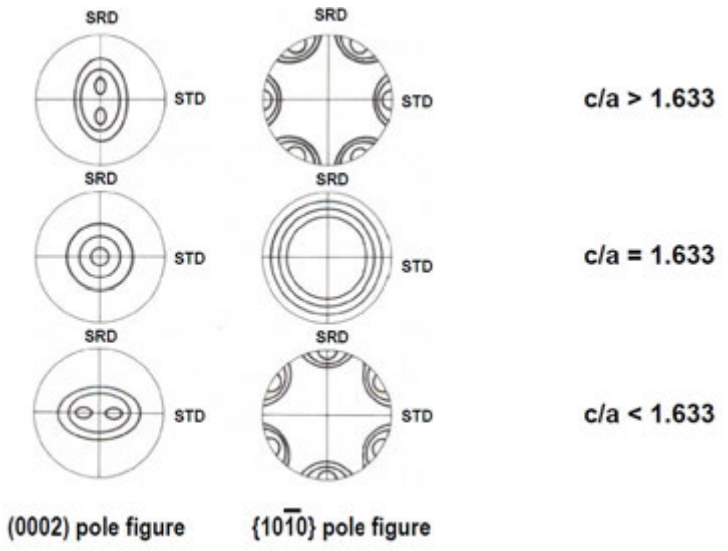

FIG. 5.35. Sheet textures in HCP metals with different c/a ratios (schematically). (a) c/a >1.633; (b) c/a = 1.633; (c) c/a <1.633. SRD — sheet rolling direction; STD — sheet transverse direction (reprinted with permission from Ref. [5.1], copyright ASTM International).

5.6.3. Texture in zirconium and zirconium based alloys from deformation in the α phase

In many texture analyses of the most common cold deformation processes, such as wire drawing, sheet rolling and tube reducing, it has been found that the basal planes always align parallel to the direction of the main deformation. The poles of the basal plane orient themselves differently depending on the deformation conditions:

— For wire drawing: random distribution of the basal poles in the radial-tangential plane (fibre texture) [5.20, 5.155, 5.156].
— For sheet rolling: alignment of the basal poles predominantly in the ND, with a tendency to split towards the TD by ±20–50° [5.8, 5.93, 5.157, 5.158].
— For tube reducing: alignment of the basal poles in the radial-tangential plane. Depending on the reduction parameters, the alignment may occur predominantly in the radial direction, in the tangential direction, in intermediate positions or be randomly distributed in the radial-tangential plane [5.8, 5.159–5.172].

For all cold deformed semifinished products, a $[10\bar{1}0]$ direction is parallel to the direction of deformation.

In comparison to sheet rolling or wire drawing, the symmetry of the deformation process for tube reducing is lowest (i.e. the degree of freedom in varying the deformation parameters is highest in tube reducing processes). The material flow caused by the reduction in area (R_A) is strictly constrained by the deformations in the radial and the tangential directions, resulting in an extension of the tube in the AD. Consequently, the conclusions about the operating forces, about the material flow and about the resulting textures are defined best in tube reduction processes. Therefore, the textures developed during tube reduction will be discussed first.

5.6.3.1. Deformation textures in tubing

The reduction of tubing is a complicated deformation process with a triaxial stress-strain condition that can vary according to different fabrication routes. A characteristic of the tube deformation process is that reduction in cross-section, R_A, can be achieved by reduction in wall thickness, R_W, by reduction in diameter, R_D, or by any combination of R_W and R_D. The main deformations are the changes in wall thickness and in diameter that result in the axial extension of the tubing.

As described in Ref. [5.154], "Systematic investigations on the influence of the reduction parameters (R_A, R_W and R_D) on the resulting preferred crystallographic orientation in Zircaloy tubing have shown that the determining factor controlling the texture is the ratio of R_W/R_D" [5.169, 5.170]; see Fig. 5.36.

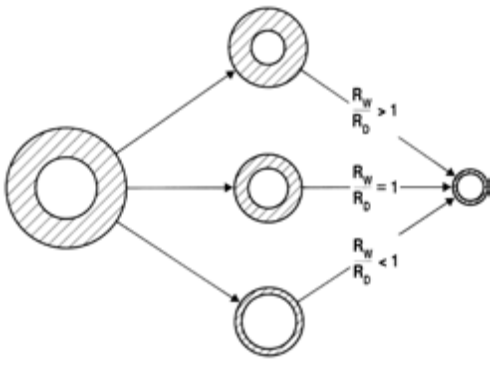

FIG. 5.36. Change of tube dimensions by the same reduction in area (R_A), but different deformation paths of reductions in wall thickness (R_W) and diameter (R_D) ending with the same final tube dimension [5.169].

The plastic deformations are primarily caused by compressive forces [5.140, 5.169, 5.170, 5.173]. During tube reduction (Chapter 4), for instance, the material will be compressed in the radial direction between the rolls and the mandrel and tangentially by the tapered sections of the rolls. The radial and tangential compressive forces can vary according to the reductions in wall thickness and diameter. If the wall thickness reduction prevails, the compressive forces in the radial direction dominate. If the diameter reduction prevails, the compressive forces in the tangential direction dominate. Figure 5.37 illustrates three extreme examples of reduction ratios R_W/R_D in the context of the primary compressive deformations and the corresponding strain ellipse, which describes the effective strains in the plane perpendicular to the elongation of the tube. A very thin layer, δ_w, within the tube wall will be considered first.

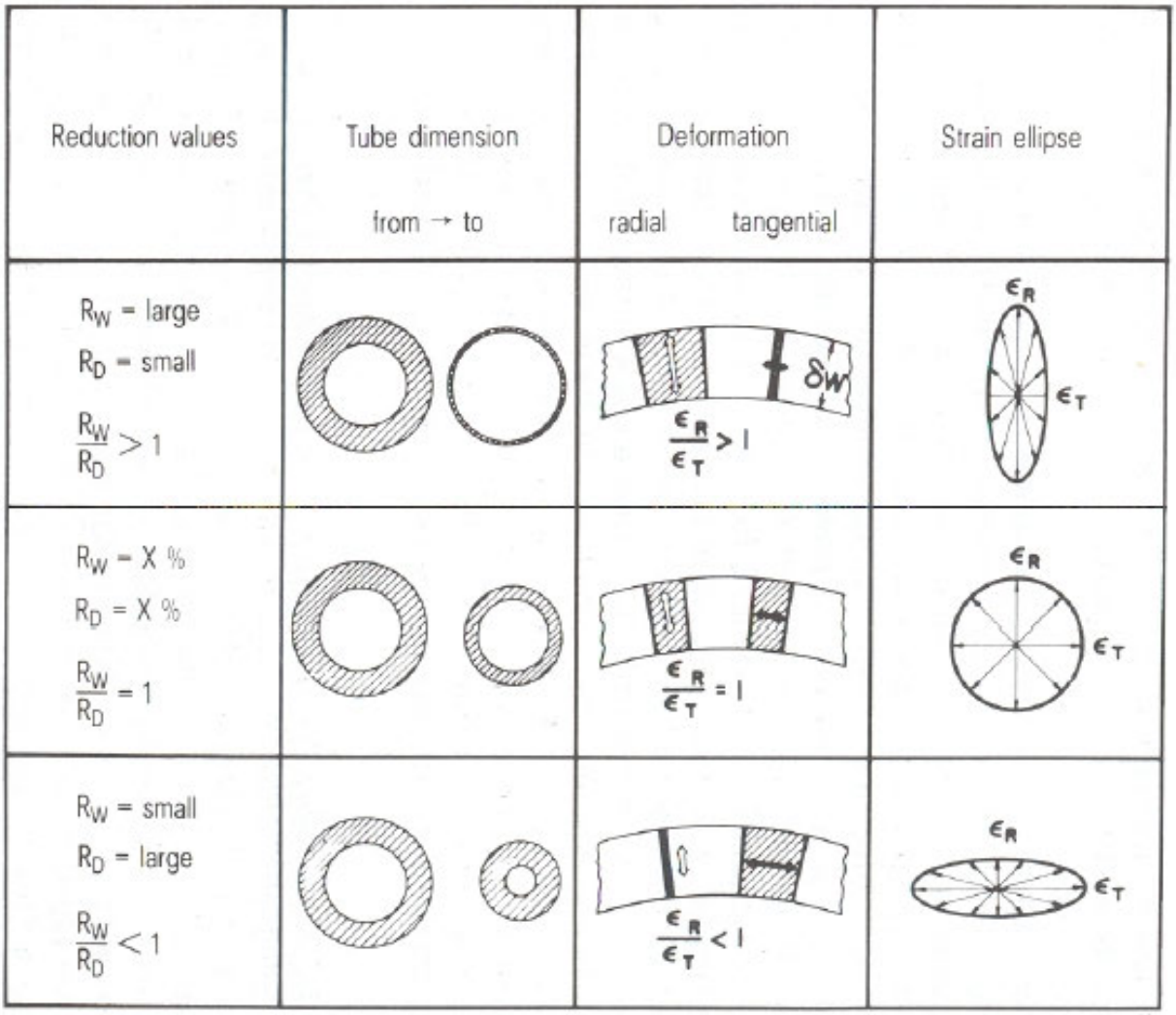

FIG. 5.37. Reduction values, tube dimensions, deformation and resulting strain ellipse [5.169] (reprinted with permission from Ref. [5.1], copyright ASTM International).

Figure 5.38 depicts the resulting textures for the three theoretical cases of R_W/R_D. It is assumed that the material had a random orientation distribution before the deformation processes.

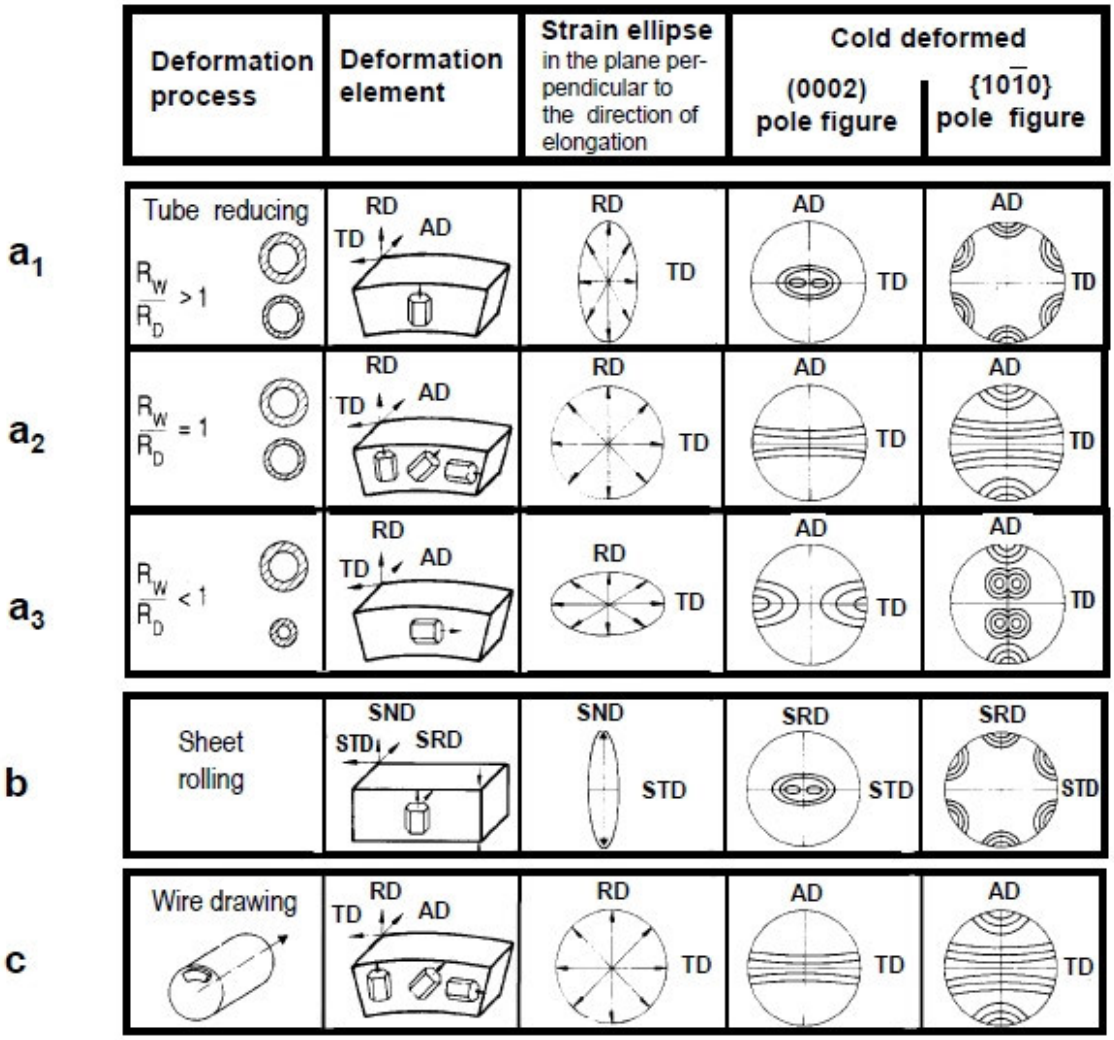

FIG. 5.38. Application of the stress-strain concept to texture development for zirconium and zirconium based alloys: deformation process, deformation element, strain ellipse and resulting basal and prism pole figures (schematically) [5.154]. (a) Tube reduction (for the last pass of the 3 tube reduction routes of Fig. 5.26 (a_1) $R_W/R_D > 1$, (a_2) $R_W/R_D = 1$, (a_3) $R_W/R_D < 1$); (b) sheet rolling; (c) wire drawing (reprinted with permission from Ref. [5.1], copyright ASTM International).

Tubing deformed by a high wall thickness and a low diameter reduction ($R_W/R_D > 1$) is mainly compressed in the radial direction, whereas the compressive forces in the tangential direction are comparatively small. Since the basal poles primarily align parallel to the direction of the effective compressive force (see Section 5.6.1), the resulting strain ellipse leads to a (0002) figure with the basal poles preferentially parallel to the radial direction. In parallel, the basal pole maxima have a characteristic split of ±20–40° tilted from the radial towards the tangential direction (Fig. 5.38).

If the wall thickness reduction is approximately equal to the diameter reduction ($R_W/R_D = 1$), the deforming compressive forces operate with equal strength in the radial and the tangential directions. Then the strain ellipse converts into a circle. The result is a fibre texture with a random distribution of basal poles in the radial-tangential plane (Fig. 5.38).

Tubing deformed by a small wall thickness and a large diameter reduction ($R_W/R_D < 1$) is mainly compressed in the tangential direction. Compared with the first case, the main deformation direction and consequently the resulting strain ellipse are tilted by 90°. Accordingly, in the (0002) figure, the basal poles align in the tangential direction with a split of the basal pole maxima of ±20–40° now tilted from the tangential towards the radial direction (Fig. 5.38).

To compare tube reducing processes, the strains are sometimes defined by a Q value:

$$Q = \frac{\ln\left(\frac{W_1}{W_2}\right)}{\ln\left(\frac{\mathrm{midD_1}}{\mathrm{midD_2}}\right)} \tag{5.30}$$

$$\frac{W_1}{W_2} = \mathrm{R_W} \tag{5.31}$$

and

$$\frac{\mathrm{midD_1}}{\mathrm{midD_2}} = \mathrm{R}_D \text{ (measured in mid-wall)} \tag{5.32}$$

A tube fabrication process with a large Q tends to produce a strong radial texture while a process with a small Q tends to produce a strong transverse texture.

As is characteristic for cold deformation textures in zirconium and zirconium based alloys, the prism pole figures tend to align with a $< 10\bar{1}0 >$ direction parallel to the direction of elongation (i.e. the AD) (see Fig. 5.35).

The stress-strain concept for the texture formation, derived from the deformation process of tube reducing (see Fig. 5.38), applies also for textures developed during sheet rolling or wire drawing [5.1, 5.154].

5.6.3.2. Deformation textures in sheet

During the rolling process, the sheet is compressed in the SND, a process by which the sheet is lengthened in the SRD and barely changes dimension in the STD. (This observation applies for a ratio of sheet width/thickness > 6.) In the plane normal to the RD, the strain ellipse is characterized by a compressive deformation in the ND and a small compressive deformation in the TD. Since in cold deformed sheet, the basal poles always tend to align parallel to the deforming compressive force, the basal poles are preferentially parallel to the ND with a tendency to spread by ±20–40° towards the TD (Fig. 5.38). The texture shown is identical to the texture in tubing for $R_W/R_D > 1$ (Fig. 5.38); this result is to be expected, since the stress-strain conditions are similar.

5.6.3.3. Deformation textures in wire

During the drawing process of wire, the material is compressed concentrically, resulting in a diameter decrease and an axial extension of the wire. In the plane normal to the AD, the strain ellipse converts into a circle (Fig. 5.38). Consequently, because of the dependence on the compressive direction (Section 5.6.1), the basal poles become randomly distributed in the radial-tangential plane. This fibre texture is identical to tubing texture if the tubes are deformed with $R_W/R_D = 1$ (Fig. 5.38). This result is to be expected since the stress-strain conditions are similar. In wire drawing, these deformation conditions are valid for each volume element of the cross-section. One can visualize the wire as consisting of concentric tubes of different diameters. Under the assumption that the volume stays constant during the deformation process, the visualized tubes of different diameters must all be deformed with $R_W/R_D = 1$, otherwise they will separate or overlap.

5.6.3.4. Features of texture formation in tubing

The existence of intensity maxima between the extreme positions in the radial and tangential directions is explained by considering the texture existing in the material before the

deformation process. The shift of the basal pole maxima and their intensity depend on the degree of deformation, that is, on the reduction in cross-section, R_A, and on the ratio, R_W/R_D [5.169, 5.170].

To explain texture gradients through the wall of a tube, the operating forces, the resulting plastic deformations and the derived texture development (see Fig. 5.38) must be applied to each layer in the tube wall. Experimental tubing with extreme reduction ratios of wall thickness-to-diameter showed characteristic texture gradients through the tube wall [5.169]. The intensity distributions of (0002) poles in the radial-tangential plane were measured in 15 equal layers, δ_W, through the 0.7 mm wall thickness. From the outer to the inner surfaces, the spread of basal pole maxima either increased (Fig. 5.39(a1)), decreased (Fig. 5.39(a2)) or the position of the basal poles remained constant (Fig. 5.39(a3)). The texture gradients can be explained by correlating the R_W/R_D reductions in each layer, δ_W, in the tube wall (Fig. 5.39(b)). In the example, a starting texture with a 45° split of basal poles towards the tangential direction was assumed, and for simplicity was considered to be constant through the tube wall. Similar, but less extreme gradients across the wall thickness were measured for tube reductions with less extreme deformations [5.168–5.170].

Manufacturing of seamless tubing is performed in several steps (typically 2–4) by tube reduction processes such as pilgering, mandrel drawing, planetary ball swaging or hammer swaging. Neither fabrication method nor a change of the deformation in AD causes significantly different textures when the processes are carried out with the same reductions in wall thickness, diameter and area [5.169, 5.170].

For tubes fabricated in sequential passes, the dependence of texture development on the ratios of wall-to-diameter reduction can be followed continuously. The texture of the material before the deformation step in question and other metallurgical conditions, such as microstructure from previous cold deformation, annealing, or β quenching, must be taken into account.

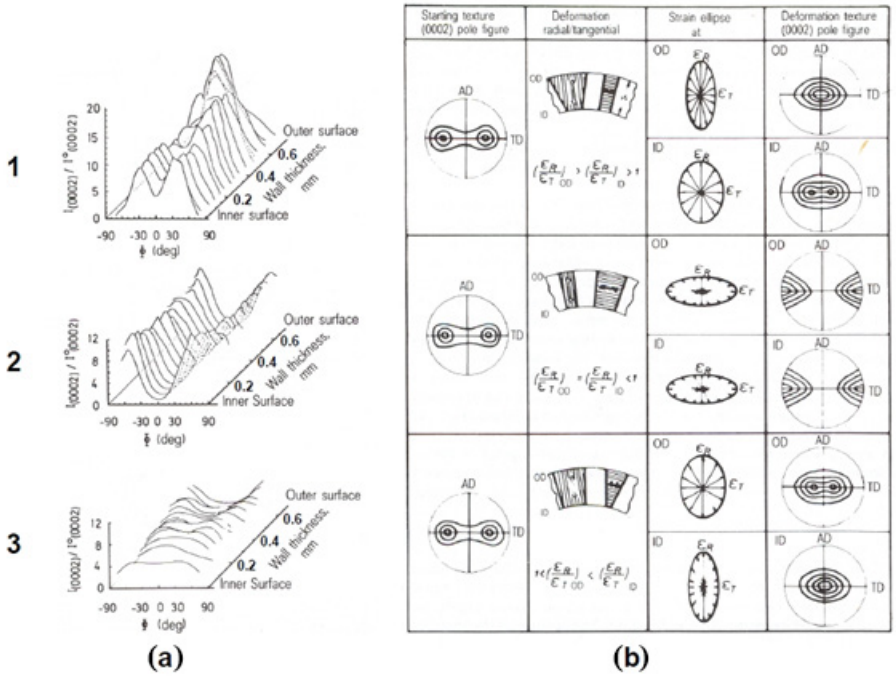

FIG. 5.39. Explanation of the texture gradients through the tube wall [5.169]. (a) Measured intensity distributions of basal poles in the radial-tangential plane through the wall thickness of tubes (Φ is the angle between the normal to the sample surface and the normal to the diffracting plane); ((a1) spread of basal pole maxima decreases from inner to outer diameter; (a2) spread of basal pole maxima stays constant from inner to outer diameter; (a3) spread of basal pole maxima increases from inner to outer diameter); (b) application of the R_W/R_D–stress-strain concept to each successive layer in the tube wall (reprinted with permission from Ref. [5.1], copyright ASTM International).

One of the decisive influences on the final texture is the last cold deformation step. If the basal poles are to be aligned preferentially in the radial direction, an initial preponderance in diameter reduction is required so that the final dimensions of the tube can be achieved by a preponderance of reduction in wall thickness. If the tangential position of the basal poles is desired, then the order of the wall thickness and diameter reductions has to be reversed. Once the final texture has been attained, a further reduction with the same R_W/R_D ratio influences only the intensity and the sharpness of the texture but not the position of the maximum basal pole maxima [5.168, 5.170, 5.174]. Figure 5.40 gives an example of the texture evolution for each step of four manufacturing sequences.

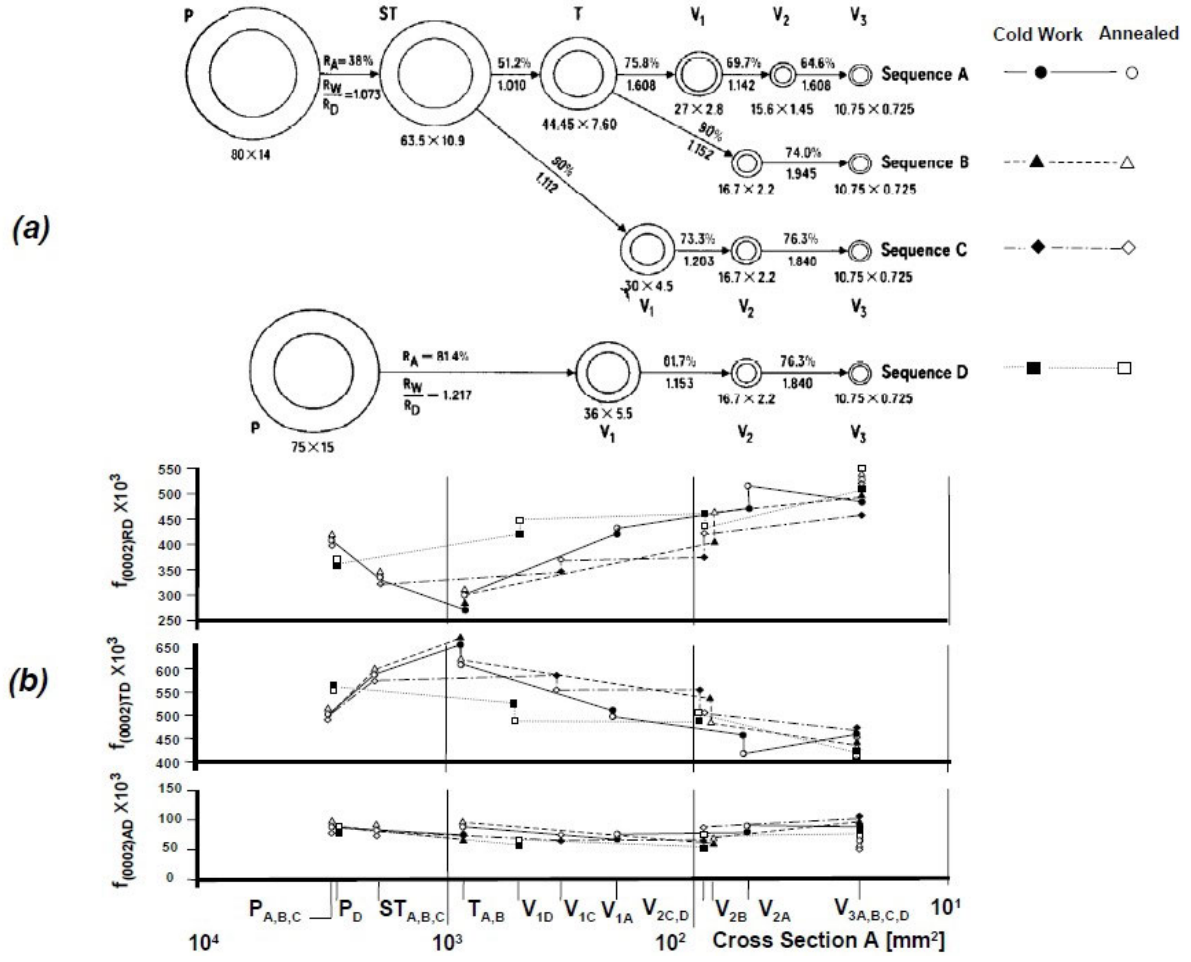

FIG. 5.40. Texture development in sequential passes [5.174]: (a) Reduction sequences A, B, C, D. All reductions steps P-ST-T-V_1-V_2-V_3 are cold reduced (CW). Heat treatment (AN) after: P, ST, T = 700°C/1h; V_1 = 750°C/2h; V_2 = 750°C/3h; V_3 = 510°C/5h. (b) Texture factors $f_{(0002)i}$ in radial, tangential and AD.

The above results of the final cold deformation reductions for thin walled tubing, mainly deduced on Zircaloys, apply also to other Zr based alloys. Since most of the Zr based alloys used for cladding are essentially α phase during cold working, with small amounts of β phase or intermetallic compounds, the discussed effect of the fabrication parameters have been confirmed in experimental, pathfinder and commercial manufacturing processes for Zr based Sn alloys in Refs [5.169–5.175], for Zr based Nb alloys in Refs [5.176–5.179] and for ZIRLO in Refs [5.152, 5.180].

Calandria tubes: Similar texture evolutions can be followed during the cold work reduction processes of seamless thin walled, large diameter tubes. Calandria tubes used for pressurized heavy water reactors (PHWRs) [5.181, 5.182] are made from Zircaloy-2. These

tubes have an outside diameter, D, of 132 mm and a wall thickness, t, of 1.4 mm giving a D/t of 94. Fuel cladding usually has D/t values of < 30. The texture of seamless calandria tubes is strongly radial because the manufacturing process consists of mostly wall thinning. Seam-welded calandria tubes are made from sheet material with basal poles strongly oriented in the thickness direction. When the sheet is folded into a tube, the corresponding tube texture is strongly radial.

Pressure tubes: Thick walled Zr-2.5Nb pressure tubes for PHWRs commonly receive only two small steps of cold deformation after extrusion. The texture of the preceding hot deformation process (see Section 5.6.4) dominates the final texture. It consists of basal poles in the radial-tangential plane biased to the TD, but with a few basal poles in the AD [5.183–5.185]. Despite the cold deformation having an R_W/R_D of about 1.3, the 27% cold work is insufficient to change the transverse texture. The tubes for high-power channel-type reactor (RBMK) 1000 reactors are in the CW and annealed condition after being deformed in three cold work and annealing steps. The over 70% total cold working, with much wall thinning, is sufficient to shift the strong transverse texture after extrusion to one where the basal poles are concentrated about halfway between the radial and transverse directions.

In summary, the textures arising from cold deformation as the final manufacturing step for tubes, sheets and wires are well characterized and understood. Other parts of the fabrication process are considered below.

5.6.4. Textures from deformation in the (α + β) and β phases (usually extrusion) in zirconium and zirconium based alloys

Prior to the cold reduction processes, various hot reduction stages are performed with intermediate and final thermal treatments (Fig. 5.41). Therefore, not only the texture of the material before the deformation step in question must be taken into account, but also other metallurgical conditions producing changes in microstructure such as grain size, recovery, recrystallization and α ↔ β phase transformations.

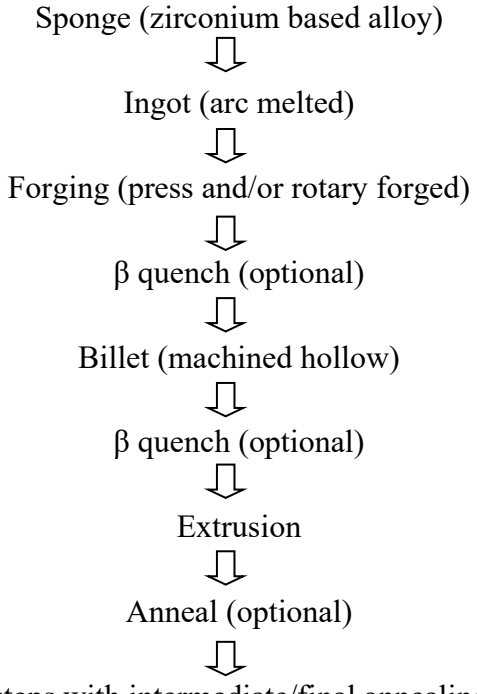

FIG. 5.41. Manufacturing process flow outline (from ingot via hollow billet to extrusion) [5.184].

The manufacturing route for seamless tubing of Zr based alloys starts from forged or extruded ingots of multi-melted Zr based alloys, which are formed into hollow billets as feedstock for the extrusion [5.182, 5.184–5.189] (see Chapter 4).

The majority of the forging is carried out in the β phase field (i.e. at temperatures >1073 K (800°C) for Zr with Nb additions and >1136 K (863°C) for Zr with Sn additions). Extrusion is normally carried out in the (α + β) phase field (i.e. in the temperature range 998–1123 K (725–850°C) [5.184, 5.186]).

For deformations at elevated temperatures in the α phase field, thermally activated processes such as slip, cross-slip, dislocation climb and grain boundary sliding are preferably activated compared with spontaneous twinning-like processes. Additional to the primary slip system $\{10\bar{1}0\} < 1\bar{2}10 >$, slip on basal planes and even on pyramidal planes in this direction may become activated. In addition, slip in $< 11\bar{2}3 >$ directions on different pyramidal planes can be activated (see Section 5.4).

For deformations in the (α + β) or β phase field, besides the above mentioned dependencies for the α structure, an additional 18 independent slip modes for the BCC β structure, being more or less homogenously distributed over the reference sphere, come into play (6 independent primary slip systems on $\{110\} < 1\bar{1}1 >$ and 12 independent secondary slip systems on $\{121\} < \bar{1}1\bar{1} >$). In addition, during heating and cooling, the α ↔ β phase transformations with its Burgers relationships are activated, which can also influence the texture development (Section 5.6.5.2). Also, effects of quenching can have an influence, if the cooling rate from the extrusion temperature is fast enough (see Section 5.6.5.3).

The temperature and cooling rate control the microstructure during and after extrusion. The major factor for texture formation is the way the metal flows, which is controlled by the shape of the extruded shell, the extrusion die, the extrusion ratio and the lubricant. Figure 5.42 gives two examples of basal and prism pole figures of extrusion shells after different wall-to-diameter reductions R_W/R_D [5.168]. There are additional influences, such as extrusion temperature and time, the proportion of prior β and α grains and the corresponding grain sizes, which lead to basal pole distributions in the radial-tangential plane. Often, some fraction of a typical BCC texture from the β phase results in some portion of the α phase basal pole orientating in the rolling (for sheet) or axial (for tubing) direction [5.167, 5.184–5.191].

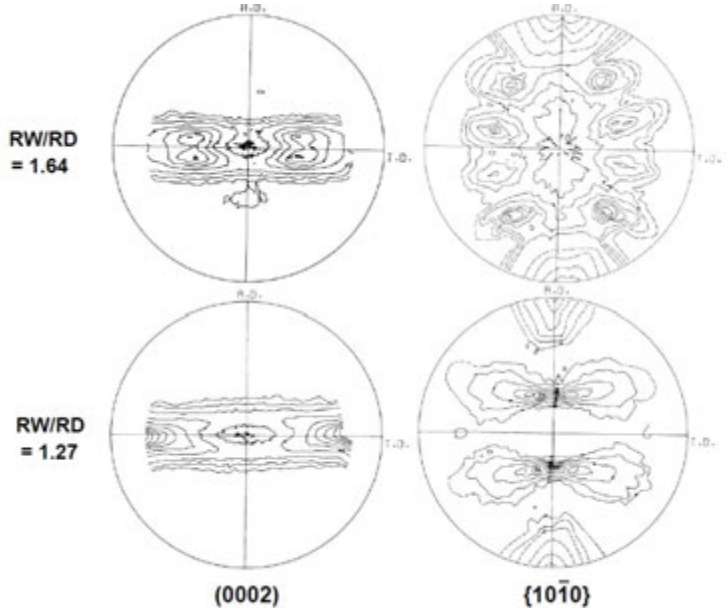

FIG. 5.42. Basal and prism pole figures of extrusion stage with different wall-to-diameter reductions (relative R_W/R_D values) [5.168].

5.6.5. Textures from thermal treatment in zirconium and zirconium based alloys

5.6.5.1. Textures from α annealing

The annealing textures in zirconium and zirconium based alloys can be summarized as follows [5.8, 5.9, 5.192–5.195]. For Zr and Zircaloy, the basal pole figures do not change significantly during annealing. In part, the basal poles tend to concentrate more towards the radial direction for tubing or the ND for sheet, respectively, while the pole density is slightly decreased. In contrast, the prism $\{10\bar{1}0\}$ pole figures reveal a marked change. During recrystallization, with increasing annealing temperature, the basal planes rotate continuously up to ±30° around their pole, so that in the final stable position a $< 11\bar{2}0 >$ direction becomes parallel to the AD or RD instead of a $< 10\bar{1}0 >$ direction. This simultaneous clockwise and anti-clockwise rotation of the prism poles around their basal poles is described in Fig. 5.43 on a sample of a Zr sheet [5.194]. For Ti, the development of the α annealing textures is very similar [5.196]. For Zr-2.5Nb, the rotation of basal planes by ±30° around their pole is not observed or is retarded, requiring longer annealing times than in Zircaloy [5.193].

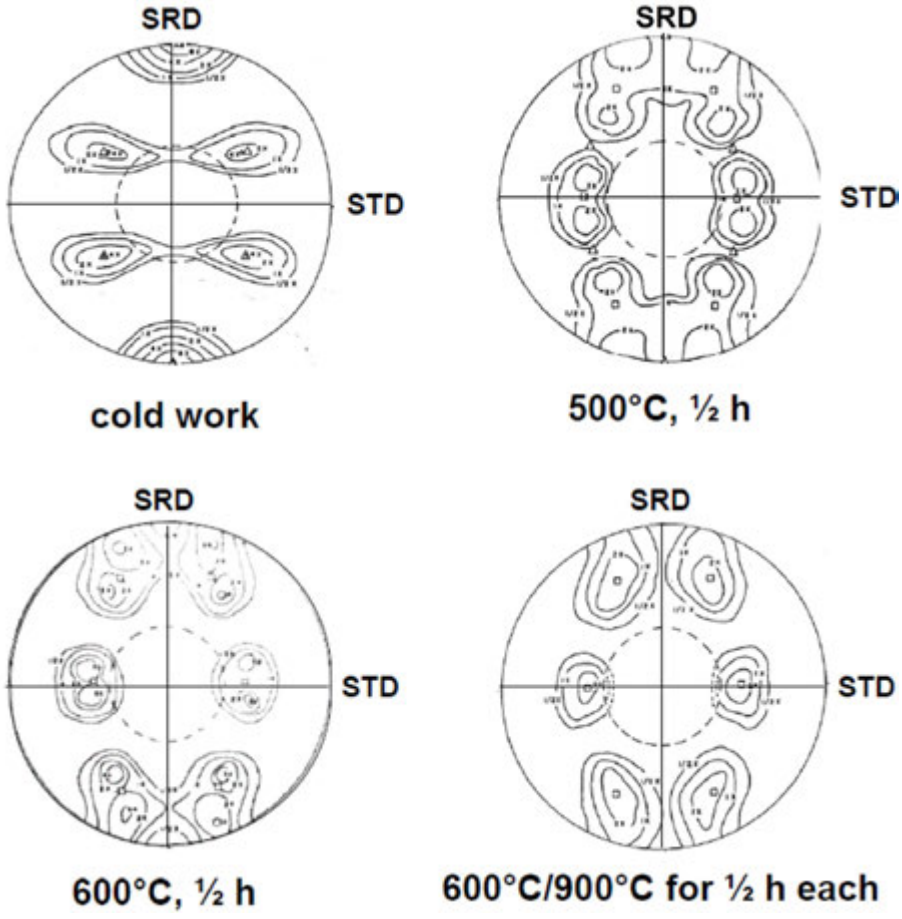

FIG. 5.43. Lattice rotations of prism poles after annealing a cold deformed Zr sheet (basal poles tilted ±40° from the SND to the STD) for 30 min at temperatures between 673 K and 1173 K (400°C and 900°C)[5.194]. SRD — sheet rolling direction; STD — sheet transverse direction.

This process is not completed before the annealing temperature is raised above the α ↔ β transus temperature (see Section 5.6.5.2). The theory of these rotations and their retarding effect need further clarification.

5.6.5.2. Textures from (α + β) or β phase annealing

Zr undergoes a phase transformation when a certain temperature, the transformation temperature, is exceeded. The α ↔ β phase transformation is also activated in Zr based alloys, with an (α + β) two phase region with different α ↔ α + β and α + β ↔ β solvus temperatures depending on the alloy. This transformation from the HCP α crystal structure to the BCC β crystal structure is reversible and has the following relationship between crystallographic planes and directions — the Burgers transformation [5.10, 5.16]:

$$(0001)_\alpha \text{ parallel to } \{110\}_\beta \tag{5.33}$$

$$< 11\bar{2}0 >_\alpha \text{ parallel to } < 111 >_\beta \tag{5.34}$$

For one α orientation, one α–β–α transformation and retransformation theoretically results in 72 different orientations. Experiments show that some but not all of these transformation relationships are used [5.193, 5.197–5.201]. The crystallographic transformations have consequences for the development of annealing textures when the annealing temperature surpasses the transformation temperature. Figure 5.44 shows both basal and prism pole figures after annealing in the (α + β) and β temperature field. Annealing at 900–1173–1373 K (1100°C) (i.e. in the temperature range 323–523 K (50–250°C) above the transformation temperature) results in the completion of the rotation of the basal planes around their pole, so that in the prism pole figure the $< 11\bar{2}0 >$ direction becomes parallel to the SRD (compare Fig. 5.43). The basal pole figure shows typical {110} <001> components of the BCC β phase, which partly retransform on cooling, to produce a multiplicity of (0002) poles in the α phase. For annealing at 1473 K (1400°C), both pole figures show that, because of the transformation, the original α poles divided up into several β poles, leading to a diffuse pole distribution on cooling back to the α phase [5.193–5.195, 5.201]. In situ tracking of the change in texture during the phase transformation in both Zircaloy and Zr-2.5Nb is discussed further in Chapter 4, Section 4.6.1.

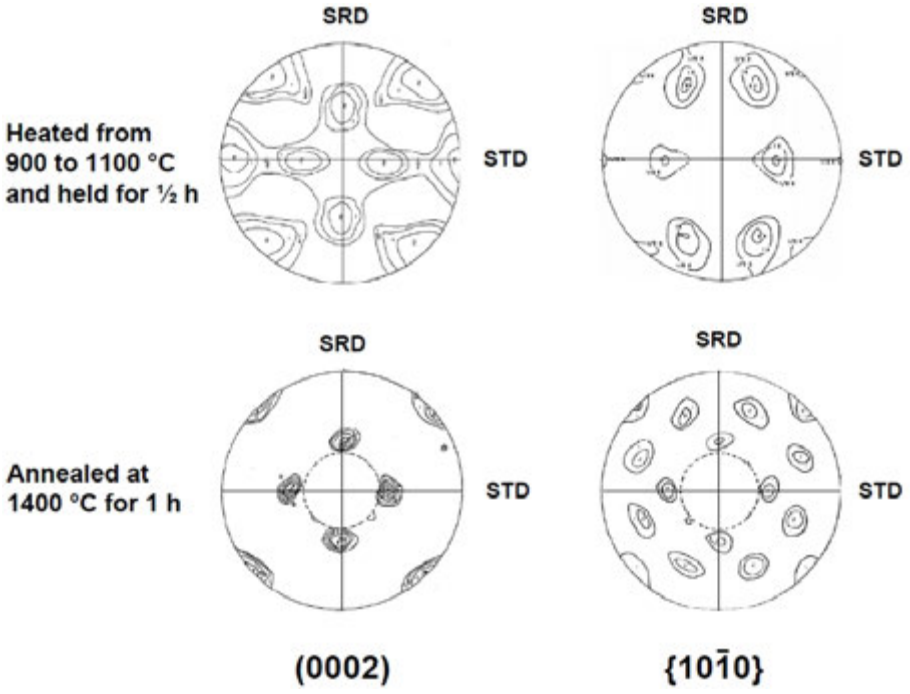

FIG. 5.44. (0002) and $\{10\bar{1}0\}$ *pole figures after annealing a cold deformed Zr sheet (basal poles tilted ±40° in the sheet normal-transverse direction) in the* (α + β) *or β temperature field [5.194]. SND — sheet normal direction; SRD — sheet rolling direction; STD — sheet transverse direction.*

5.6.5.3. Textures from β quenching

When α stabilized Zr based alloys, such as Zr-Sn (i.e. Zircaloy) are quenched with a high enough cooling rate from the β or (α + β) phase to the α phase, a Thomson-Widmanstätten structure with a plate- or needle-like microstructure can be formed [5.193, 5.202, 5.203]. This structure exhibits a split of the basal and prism poles over the reference sphere (Fig. 5.45). This treatment is chosen in applications where the material needs a high strength, provided by the Thomson-Widmanstätten structure, and a low mechanical anisotropy, resulting from a close to random, more homogeneous distribution of pole densities over the reference sphere [5.204].

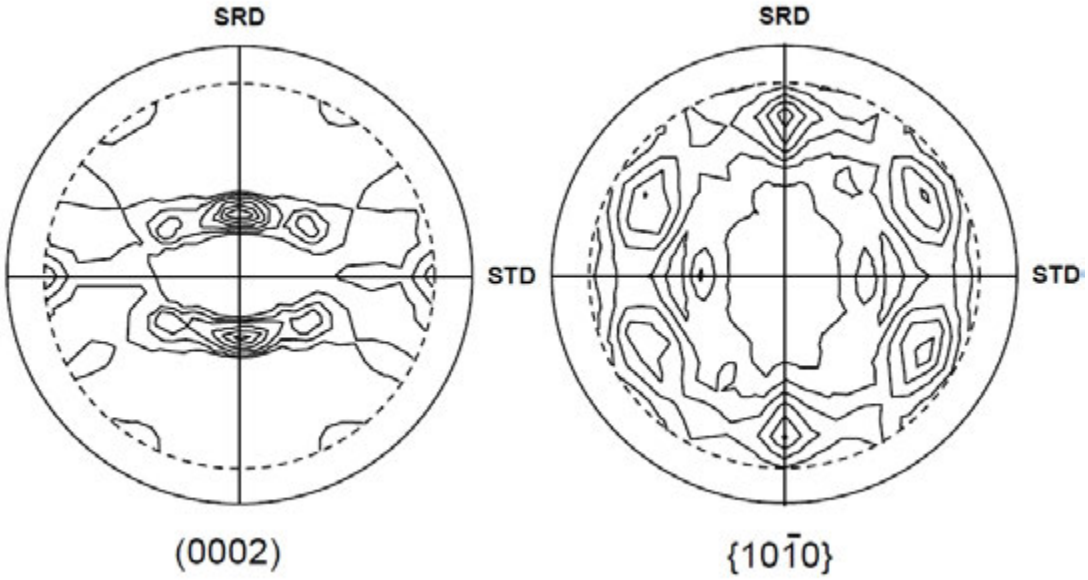

FIG. 5.45. Basal and prism pole figures after β quench of a Zircaloy sheet [5.203]. SRD — sheet rolling direction; STD — sheet transverse direction.

When β stabilized Zr based alloys, such as Zr-Nb (i.e. Zr-2.5Nb) are cooled slowly from a hot working process in the β or (α + β) region, the α phase separates from the β phase; with intermediate cooling rates again a Thomson-Widmanstätten structure is formed and with a rapid quench a martensite type α' microstructure can be formed. Despite the different metallographic structures obtained by either slow or fast cooling from the β or (α + β) phase, the Burgers relationship is obeyed during the transformation. In the martensitic type BCC ↔ HCP transformation, a new crystalline phase grows out of the parent phase by the propagation of a semicoherent interphase, where an ordered, cooperative and rapid transfer of atoms from one structure to another crosses the interface as it moves. Such an interface must be composed of dislocations whose movement permits the martensite to form rapidly [5.2]. As well as the fabrication routes of Zr-2.5Nb pressure tubes that are cold worked or cold worked and annealed (as described in Section 5.6.3.4), there is another fabrication version for pressure tubes, where the almost finished tube is water quenched from the (α + β) region, followed by a small amount of cold work (15–23%) and a temper at about 773 K (500°C) for 24 h. In these experimentally and commercially produced pressure tubes, the quench from (α + β) seems to dominate the texture evolution, which is characterized by similar basal pole intensities in the radial and the tangential directions, plus a relatively large intensity in the AD, with an f_a of about 0.25 [5.185, 5.193, 5.205].

5.6.6. Textures from welding and casting in zirconium and zirconium based alloys

Semifinished products such as bar, sheet, rod and tubing sometimes must be welded to form nuclear components of zirconium or zirconium based alloys. Welding produces local internal stresses and changes in microstructure and texture. These features have to be taken into account if welded components are used, because welds affect properties and thus behaviour [5.182, 5.206–5.208].

With respect to texture formation in welds of zirconium or zirconium based alloys, four material zones have to be considered.

The base material: Depending on the heat treatment applied to the component during or after welding, the starting texture of the semifinished product to be welded has to be taken into account. Figure 5.46(a) gives an example of basal and prism pole distributions, in this case of two plates of Zr-2.5Nb, which were welded with gas-tungsten arc welding along their RD [5.208]. The texture in pressure tubes is similar to this base plate [5.206].

The heat affected zone (HAZ) with temperatures in the α phase field: In an area distant from the fusion plane the base material experiences different temperatures following the isothermal waves of the various peak temperatures. In this part of the HAZ, the positioning of the weld with respect to the outer dimensions of the components to be welded has to be considered (for sheet: weld in rolling or TD; for tubing: weld in longitudinal or circumferential direction). Here the texture changes correspond to the α annealing textures of the base material (i.e. the basal pole figure does not change significantly). But the prism pole figure is characterized by a ±30° rotation of the basal planes around their pole resulting in a continuous change from $< 10\bar{1}0 >$ to $< 11\bar{2}0 >$ directions with respect to the direction of elongation of the semifinished component; with increasing annealing temperature and sufficient time this is a continuous change (see Section 5.6.5.1).

The HAZ, subjected to the α ↔ β phase transformation: The closer the HAZ is to the fusion plane, the higher the peak temperatures are. This zone is characterized by the α ↔ β transformation and is limited by the solidus–liquidus border of the fusion plane. As in the α phase field, the positioning of the weld with respect to the outer dimensions of the components to be welded has to be considered.

The evolution of texture is caused by the α ↔ β transformation according to the Burgers relationship (5.6.5.2). Figure 5.46(b) shows the texture of the coarse grain HAZ of the sheet with the starting texture given in Fig. 5.46(a). The pole figures show dominant (110) [001] texture components of the BCC β phase, which partly retransforms on cooling, to produce a high multiplicity of (0002) poles in the α phase. The pronounced maximum in density of basal poles in the RD is explained by a rotation of the $\{11\bar{2}0\}$ planes around their poles such that the (0002) plane normals — originally aligned tangentially — become aligned in the longitudinal direction [5.206].

The weld itself: The fusion zone of a weld consists of molten base material and additional feed material. The fusion line limits this zone and this line is the border of the liquid-to-solid phase (in three dimensions corresponding to the fusion plane). This plane is the indicator for the dominant heat flow (i.e. the cooling after the weld process takes place predominantly perpendicular to this plane).

The fusion zone itself has no memory of the original plate texture. The texture evolution depends on the geometry of the component (size of the fusion zone, heating during welding and cooling flow after welding) and on the welding conditions (heat input during welding, welding speed), and whether the fusion zone after welding is cooled down slowly or rapidly (quenched) from the liquid phase via the β, (β + α) to the α phase. Also, there are several isothermal waves with different peak temperatures that run over each segment of the fusion zone. Correspondingly, the microstructure and the crystallographic orientation develop. The

texture evolution is determined by the cooling from the melt and is superimposed by corresponding transformations via the β to the α phase. Figure 5.46(c) shows the texture of the fusion zone in the as-welded condition for the two Zr-2.5 Nb sheets. The resulting texture indicates that the high temperature β phase was composed of two dominant BCC orientation components: (001) [100] and (110) [001]. The first component (001) [100] conforms to the expectation that the texture arises from solidification with the easy <001> crystallographic growth direction perpendicular to the solid–liquid interface (characterized by columnar grain growth in the direction of the dominant heat flow, i.e. perpendicular to the fusion plane). The second component (110) [001] is the same as that observed in the HAZ subjected to the α ↔ β phase transformation.

In general, the same crystallographic texture formation is true for castings, where the wall of the casting mould functions as the plane of dominant heat flow.

An α anneal for an hour at 923 K (650°C) effected a qualitative change in the texture of the fusion zone (Fig. 5.46(d)); it had no effect on textures of the HAZ and the base material. An α anneal at 803 K (530°C) was sufficient to relieve macroscopic residual stresses, but the grain interaction stresses in the HAZ could not be relaxed [5.208].

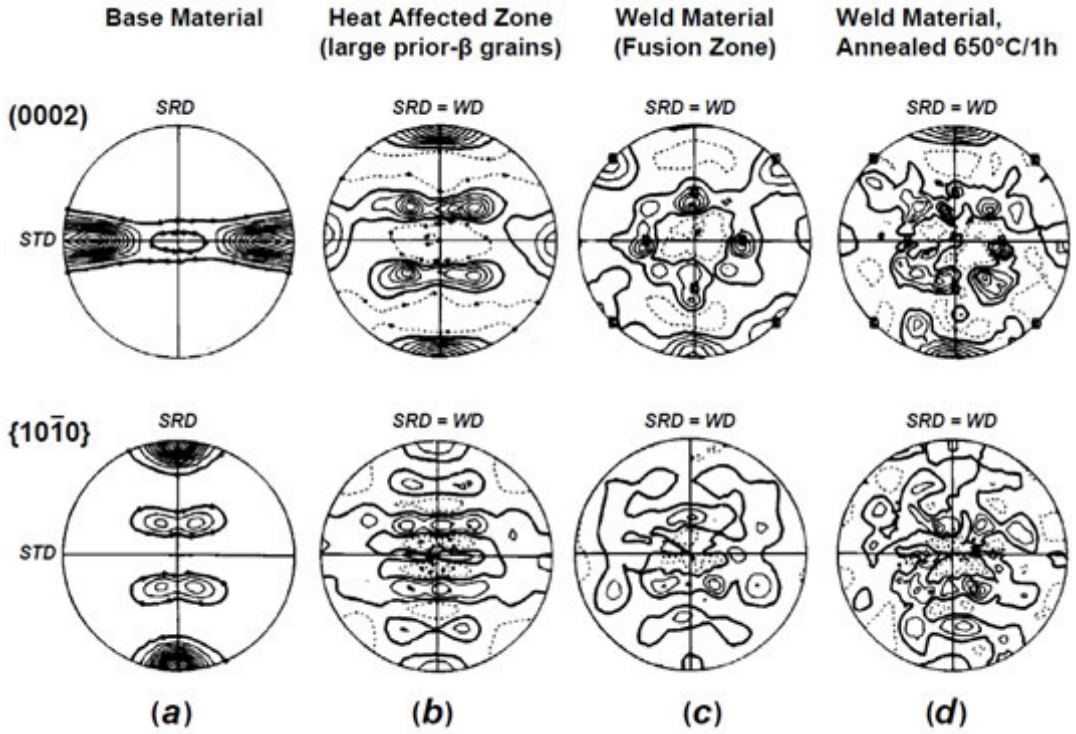

FIG. 5.46. Basal and prism pole figures of welds made with GTAW between Zr-2.5Nb plates is in SRD) [5.208]. (a) Base material; (b) HAZ; (c) fusion zone (the weld itself); (d) fusion zone after 650°C/1 h anneal. SRD — sheet rolling direction; WD — weld direction.

5.6.7. Listing of the most common deformation and annealing textures in zirconium and zirconium based alloys

Figure 5.47 sums up Section 5.6 with a schematic depiction of cold deformation and α → β annealing textures for the most common semifinished products (tubing, sheet and wire) in zirconium and zirconium based alloys [5.9, 5.154]. Knowing these interrelations and dependences, it is possible to tailor the texture of Zircaloy and zirconium based alloys tubing within limits.

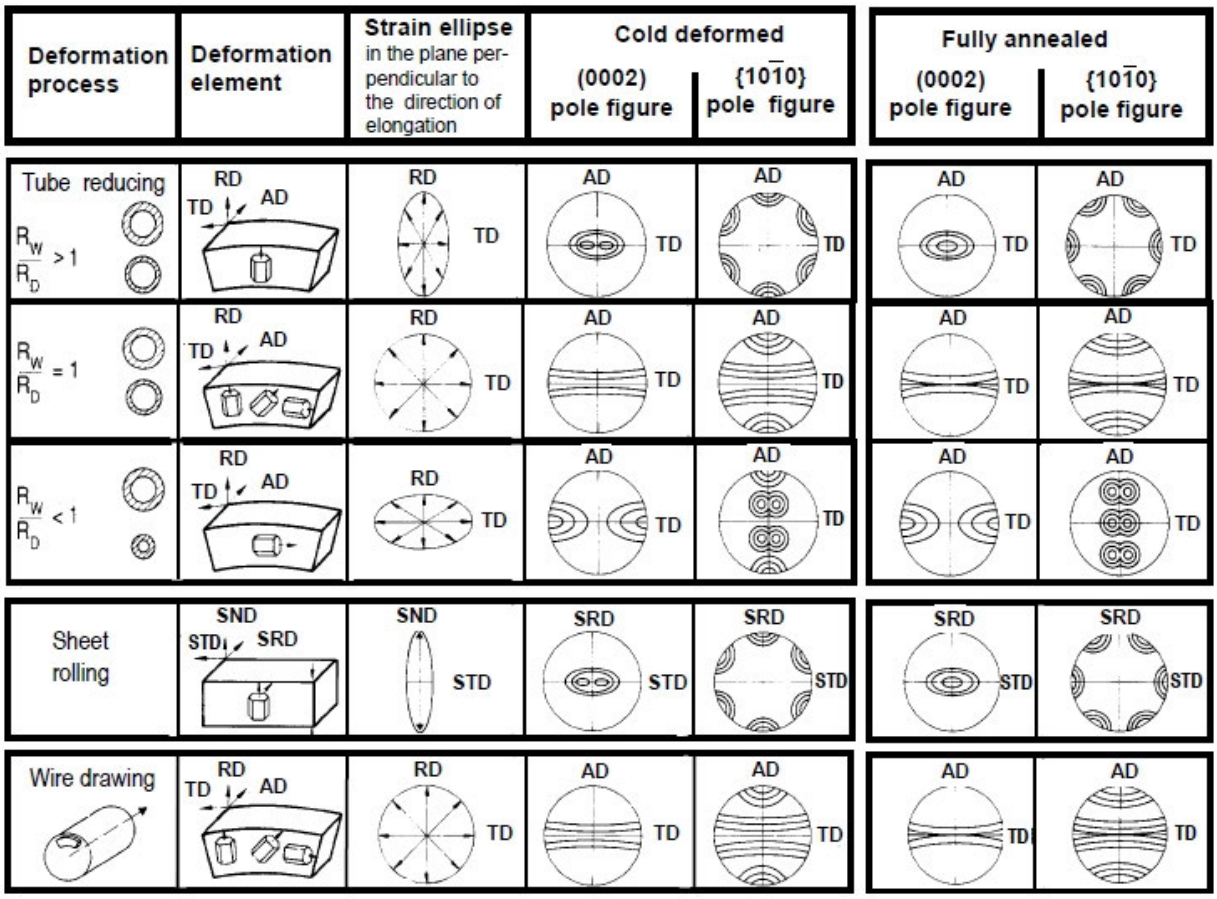

FIG. 5.47. Schematic depiction of deformation and α → β annealing textures for Zr and Zr base tubing, sheet and wire (reprinted with permission from Ref. [5.154], copyright ASTM International). AD — axial direction; RD — rolling direction; SND — sheet normal direction; SRD — sheet rolling direction; STD — sheet transverse direction; TD — transverse direction.

The final output in the fabrication process of Zr base tubing or sheet is limited by the specified dimensional tolerances as well as by the desired technological and metallurgical properties (see Chapters 4, 7–9). Besides the texture, microstructural properties such as grain size, the degree of recrystallization and β quench status have an influence on macroscopic mechanical, chemical and technological properties and must be taken into account [5.209–5.211].

5.7. MECHANICAL ANISOTROPY IN ZIRCONIUM AND ZIRCONIUM BASED ALLOYS

The objective of a metallurgical texture investigation is not only to elucidate the interactions between deformation mechanisms and texture development (Section 5.6) but also to explain the mechanical anisotropy of textured polycrystals. If one knows the interactions between deformation mechanisms and texture development, it should then be possible to explain and predict the mechanical anisotropy of a component with a given texture by means of the deformation mechanisms.

5.7.1. Mechanical anisotropy of textured sheet

The anisotropy of strength in a Zircaloy-4 plate with a typical sheet rolling texture (0002) tilted ±30° from the sheet normal towards the STD, $< 10\bar{1}0 >$ in the RD is given in Fig. 5.48.

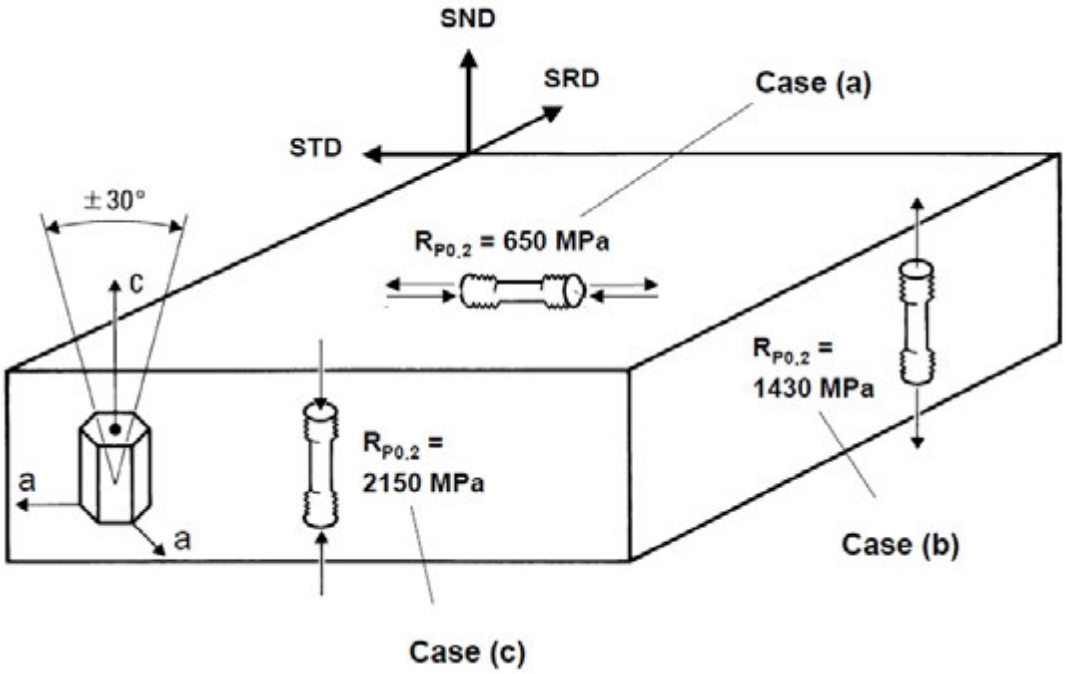

FIG. 5.48. Yield stresses in different directions and orientations of textured Zircaloy-4 plate at room temperature. (a) Tensile or compressive stress ⊥ c axis, yield strength $R_{P0.2}$ 650 MPa; (b) Tensile stress || c axis, yield strength $R_{P0.2}$ 1430 MPa; (c) Compressive stress || c axis, yield strength $R_{P0.2}$ 2150 MPa. SND — sheet normal direction; SRD — sheet rolling direction; STD — sheet transverse direction.

Tensile and compressive samples were taken in the SND and STD of the plate in such a way that in case (a) the basal poles are preferentially aligned perpendicular to the direction of the applied force and in cases (b) and (c) preferentially parallel to the applied force. Depending on the orientation and the direction of force (tensile or compressive), the yield strengths at room temperature are significantly different [5.93, 5.212]. The ratio of the yield strengths is approximately 1:2:3, qualitatively confirming the corresponding ratios of the deduced critical resolved shear stresses for the operative twinning systems relative to prism slip (Section 5.4.3.2, Table 5.7).

On the basis of these correlations and on the anisotropic single crystal behaviour (Section 5.4), the difference in strengths can be explained by the corresponding critical shear stresses of the active deformation systems. For deformation at room temperature, in case (a) primarily $\{10\bar{1}0\}$ <$11\bar{2}0$ > prism slip is active, in case (b) primarily $\{10\bar{1}2\}$ and $\{11\bar{2}1\}$ twins are generated, and in case (c) primarily $\{11\bar{2}2\}$ twinning becomes activated.

5.7.2. Mechanical anisotropy of Zircaloy tubing

The influence of texture on mechanical anisotropy as well as the causal interactions with the deformation mechanisms was demonstrated with a specially prepared Zircaloy tube shown in Fig. 5.49(a). This experimental tube was machined out of a thick Zircaloy plate with a pronounced rolling texture; the tube axis corresponded with the RD. By this procedure, continuously changing preferred orientations of the basal poles are obtained around the circumference of the tube, with the extreme orientations possible in Zircaloy tubing at positions I and II, and the following is true for the texture:

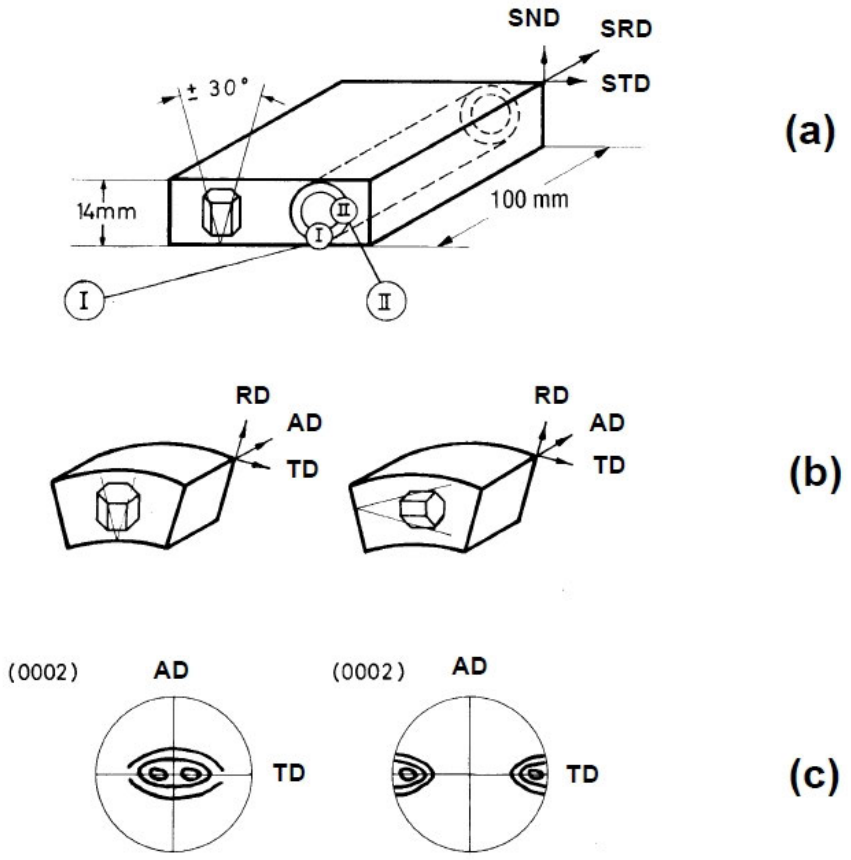

FIG. 5.49.(a) Zircaloy tube machined out of textured plate, (b) single crystal analogue, and (c) (0002) pole figures in the experimental tube at positions I and II (reprinted with permission from Ref. [5.91], copyright ASTM International). AD — axial direction; RD — rolling direction; SND — sheet normal direction; SRD — sheet rolling direction; STD — sheet transverse direction; TD — transverse direction.

— The texture at position I corresponds to the tube texture with preferential position of the basal poles in the radial direction shown in Fig. 5.49 (b).
— The texture at position II is rotated through 90° compared with that of position I (i.e. the basal poles lie preferentially in the tangential direction shown in Fig. 5.49 (b)).

Thus, it is possible to measure the purely textural influence on the mechanical anisotropy of Zircaloy tubing, since other parameters such as microstructure (for example, the distribution of particles), the degree of cold deformation and state of recrystallization are constant [5.91].

Zircaloy tube under uniaxial tension: If an element of this experimental tube is stressed axially (indicated by solid arrows in Fig. 5.50) then contractile strains result in the radial and tangential directions (outlined arrows). Therefore, for a tube with basal poles preferentially aligned in the radial direction (case I), the stress-strain conditions would activate the following deformation mechanisms:

— $\{1\bar{1}00\} < 11\bar{2}0 >$ prism slip from tension in the AD;
— $\{1\bar{1}00\} < 11\bar{2}0 >$ prism slip by transverse contraction in the tangential direction;
— $\{11\bar{2}2\}$ twinning by transverse contraction in the radial direction.

Since the critical resolved shear stress for prism slip is lower than the corresponding stress to initiate $\{11\bar{2}2\}$ twinning, the tube will elongate primarily by reduction of the diameter with little change in wall thickness (Fig. 5.50, case I).

For a tube element with preferred basal pole positions in the tangential direction (case II), the stress-strain conditions would cause:

— $\{1\bar{1}00\} < 11\bar{2}0 >$ prism slip by tension in the AD;
— $\{11\bar{2}2\}$ twinning by transverse contraction in the tangential direction;
— $\{1\bar{1}00\} < 11\bar{2}0 >$ prism slip by transverse contraction in the radial direction.

Because of the differences in critical resolved shear stresses, the tube in this case would be expected to elongate by decreasing its wall thickness with little change in diameter (Fig. 5.50, case II). The strength (for example, the axial yield stress) would be equally low for either type of texture, because prism slip is operative in the AD in both cases.

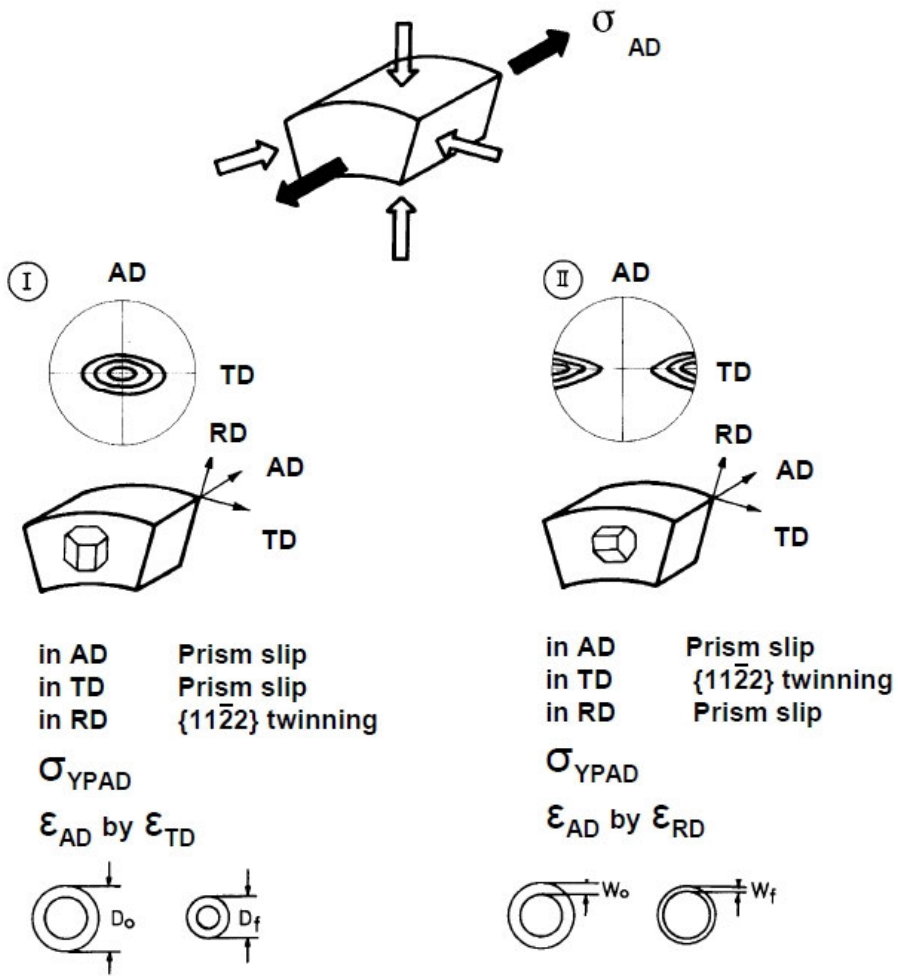

FIG. 5.50. Zircaloy tube under tension in the AD (prediction of deformation behaviour) (reprinted with permission from Ref. [5.91], copyright ASTM International). AD — axial direction; RD — rolling direction; TD — transverse direction.

The deformations predicted for the two types of texture can be followed by a single tensile test on the tube machined out of the sheet (Fig. 5.51). During the tension test, the tube became elliptical; at position I the curvature decreased while the wall thickness stayed nearly

constant and at position II the tube wall decreased in thickness while the curvature stayed nearly constant. The difference in reductions in wall thickness can be seen in the axial microsections of positions I and II. Additionally, position I exhibited a 90° fracture while position II had a 45° fracture. The two types of fractures also differed in the fractographic microstructure, with position I exhibiting pure tensile dimples and position II showing shear dimples. These results were obtained in tests at room temperature and at 673 K (400°C), indicating that the deformation mechanisms did not change in this temperature range.

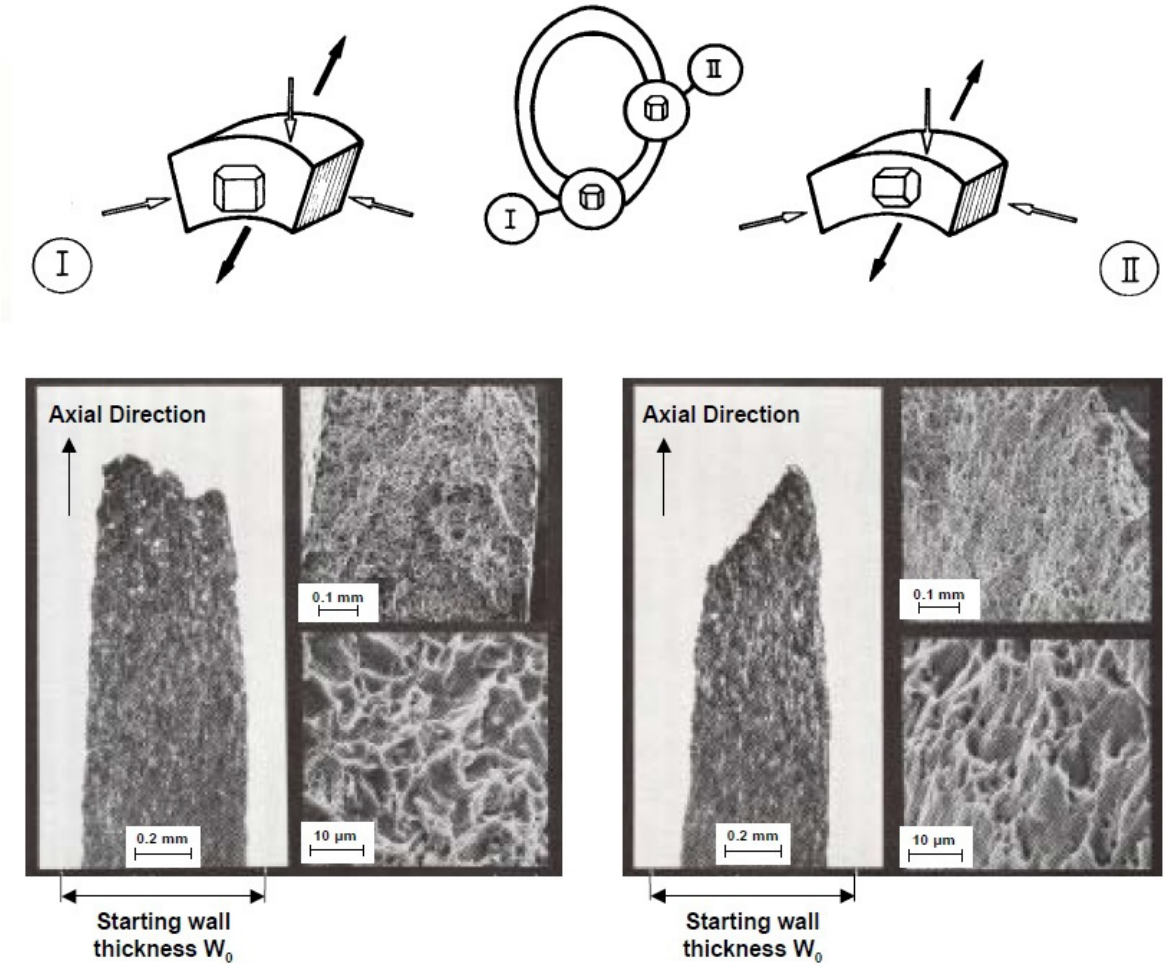

FIG. 5.51. Zircaloy tube under tension in the AD (verification of deformation behaviour) (reprinted with permission from Ref. [5.91], copyright ASTM International).

Zircaloy tube under internal pressure (burst test): According to Fig. 5.52, a similar tube element, stressed bi-axially under internal pressure (with $\sigma_{AD}/\sigma_{TD} = 0.5$, shown by solid arrows), would deform by contractile strain in the radial direction (shown by outlined arrows). The stresses applied would result in buckling of the tube, primarily through reduction of the wall thickness. The wall thickness can be realized in case I by $\{11\bar{2}2\}$ twinning, which requires a higher initiating force than the prism slip that would operate in case II. Consequently, a tube with preferred radial position of the basal poles possesses a higher hoop resistance than a tube with a preferred tangential basal pole orientation.

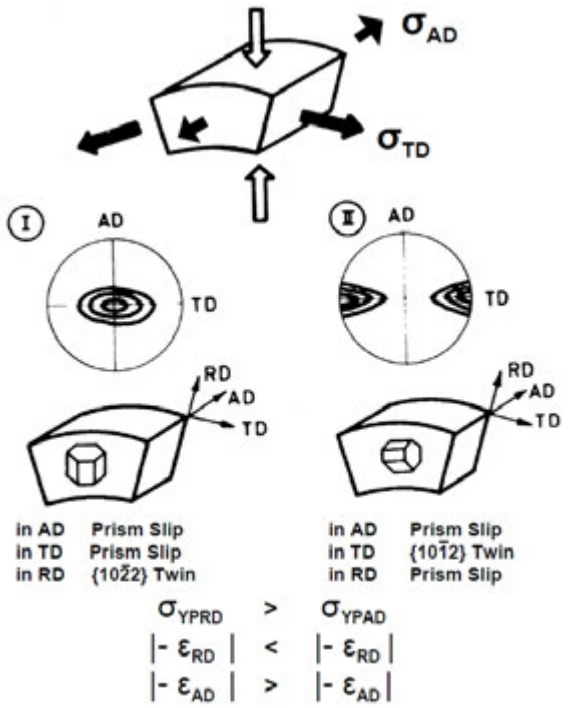

FIG. 5.52. Zircaloy tube under internal pressure (burst test) with σ_{AD}/σ_{TD} = 0.5 (prediction of deformation behaviour) (reprinted with permission from Ref. [5.91], copyright ASTM International). AD — axial direction; RD — rolling direction; TD — transverse direction.

The stress-strain behaviour is confirmed by burst tests of the experimental tube at room temperature and at 673 K (400°C) (Fig. 5.53). The fracture occurs where the basal poles are preferentially aligned along their tangential direction (position II).

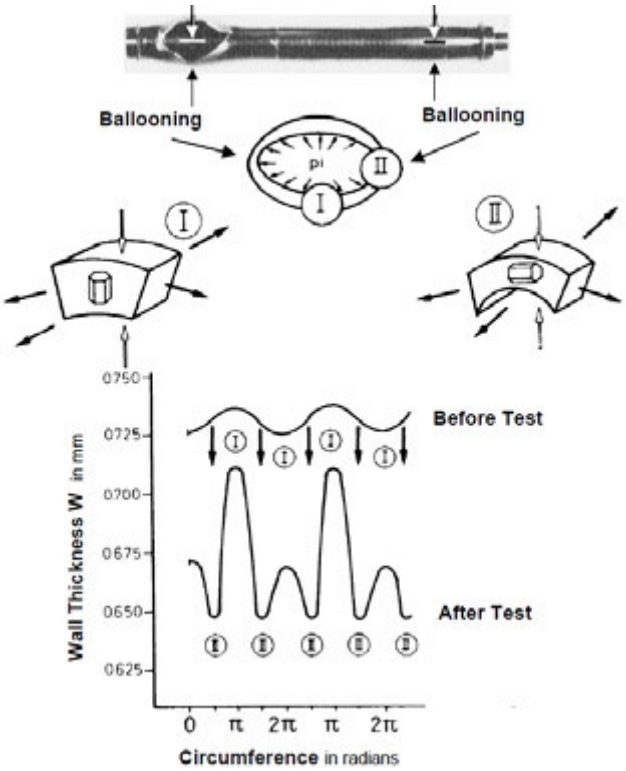

FIG. 5.53. Zircaloy tube under internal pressure (burst test) with σ_{AD}/σ_{TD} = 0.5 (verification of deformation behaviour) [5.91].

These types of loading show that the analysis of operative deformation mechanisms allows a qualitative estimation of the mechanical anisotropy of textured components. Further derivations of the mechanical anisotropy and their experimental verification have been performed for similar tubes under axial bending, axial torsion and superposed bending moment, and external pressure (collapse) [5.91]. In all cases, the experimental results from the tubes taken out of the textured Zircaloy plate agree with the theoretically derived behaviour. Results described in the literature corroborate this analysis [5.213–5.216].

This approach also allows the examination of the influence of basal pole positions in the radial-tangential plane on other properties. For example, stress corrosion behaviour with an iodine inner pressure at 673 K (400°C) [5.217] is shown in Fig. 5.54. The inner surface cracks preferentially in regions where the basal poles are aligned parallel to the tangential directions. To maximize resistance against iodine-induced stress corrosion cracking, tubing with radial basal pole orientations is preferred [5.218].

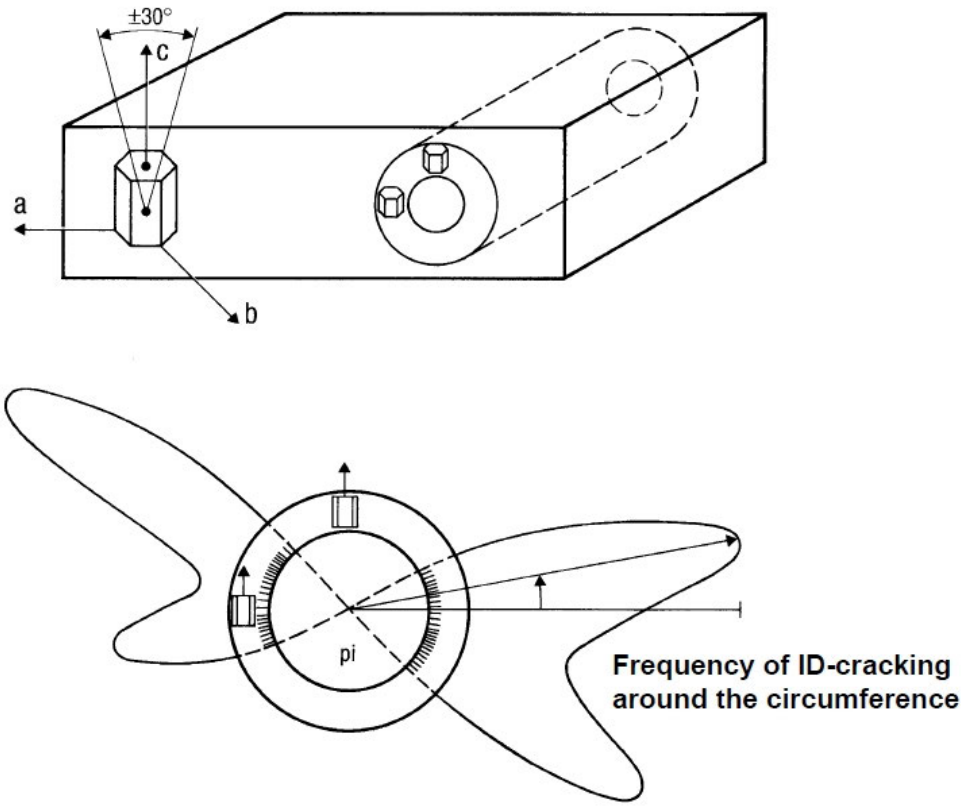

FIG. 5.54. Influence of preferred basal pole orientations on iodine stress corrosion behaviour of Zircaloy tubing [5.217].

5.7.3. Multiaxial stress strain conditions

The behaviour of an anisotropic material under multiaxial stress conditions uses the correlation between the properties of single crystals and the behaviour of textured polycrystalline materials as interpreted with deformation theories. To solve the complicated relationships encountered, one usually starts with two dimensional stress conditions. In many of the load conditions found in technological applications, one of the three stress components is zero or negligibly small; for example, in the radial direction in thin walled tubing used for fuel cladding. Then the general Von Mises criterion can be reduced from the equation of an ellipsoid to the equation of an ellipse [5.105].

5.7.3.1. Yield loci

This elliptical equation provides a two dimensional representation of the stress conditions required for yielding. It is therefore termed the yield locus. Figure 5.55 shows a comparison of the Von Mises yield locus [5.105] with a yield locus described by Tresca [5.219]. The maximum distortion criterion of Von Mises accounts for the total stress conditions, whereas the maximum shearing stress criterion of Tresca allows for only parts of the stress components present in the material (i.e. the smallest and largest principal stress corresponding to Mohr's circle for plane stress). This difference explains the discrepancy (0 to about 12%) from the Von Mises boundary curve.

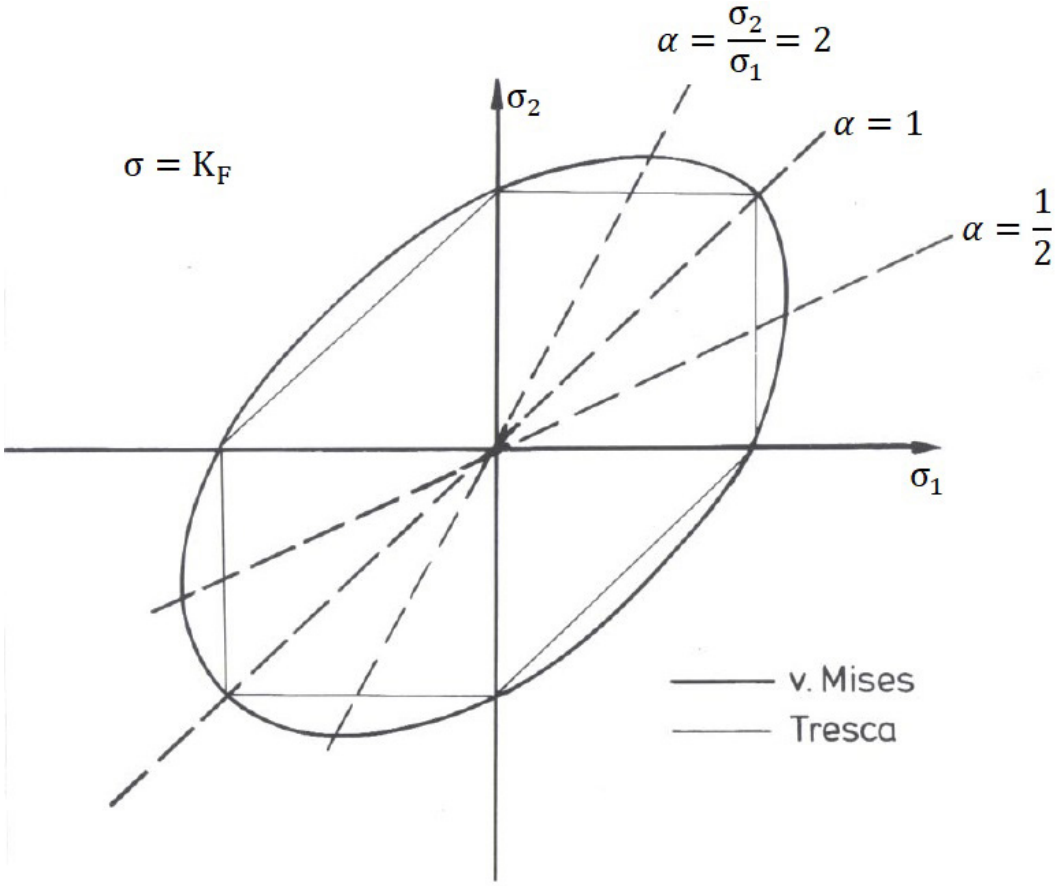

FIG. 5.55. Von Mises yield criterion (ellipse) and Tresca yield criterion (hexagon) (reprinted with permission from Ref. [5.1], copyright ASTM International).

The inherent anisotropy of textured metals is not allowed for in these initial considerations. Correspondingly, there are differences between real, measured yield loci and those given by Von Mises and Tresca. To render these deviations amenable to mathematical analysis, Hill [5.106] proposed anisotropic factors based solely on computational, rather than crystallographic grounds. Taking into account the different active deformation systems, the procedure to calculate the yield surface of HCP metals in general, and of Zr and Zr based alloys in detail, is described by Tomé and Kocks [5.220].

For two dimensional conditions, the distortion behaviour in an indicated direction is described by the *r* coefficient. The *r* coefficient is defined as the ratio of the logarithmic distortions in the width and thickness directions of a uniaxial sample subjected to tensile stress. For example, to evaluate anisotropy in a metal sheet, *r* is measured with specimens taken from

various directions. Based on these propositions, Zircaloy-4 cladding tubes with different preferred basal pole positions were examined with regard to their yield behaviour under two dimensional stress conditions (tensile and inner pressure) and compared with those predicted from the textures (Fig. 5.56). Allowing for the various slip and twinning systems, as well as the adapted critical shear stress conditions, the yield loci theoretically derived for basal pole tilts of γ = 0–30° and γ = 70° towards the tangential direction were compared with yield loci determined from Von Mises and showed good agreement [5.116, 5.221–5.224].

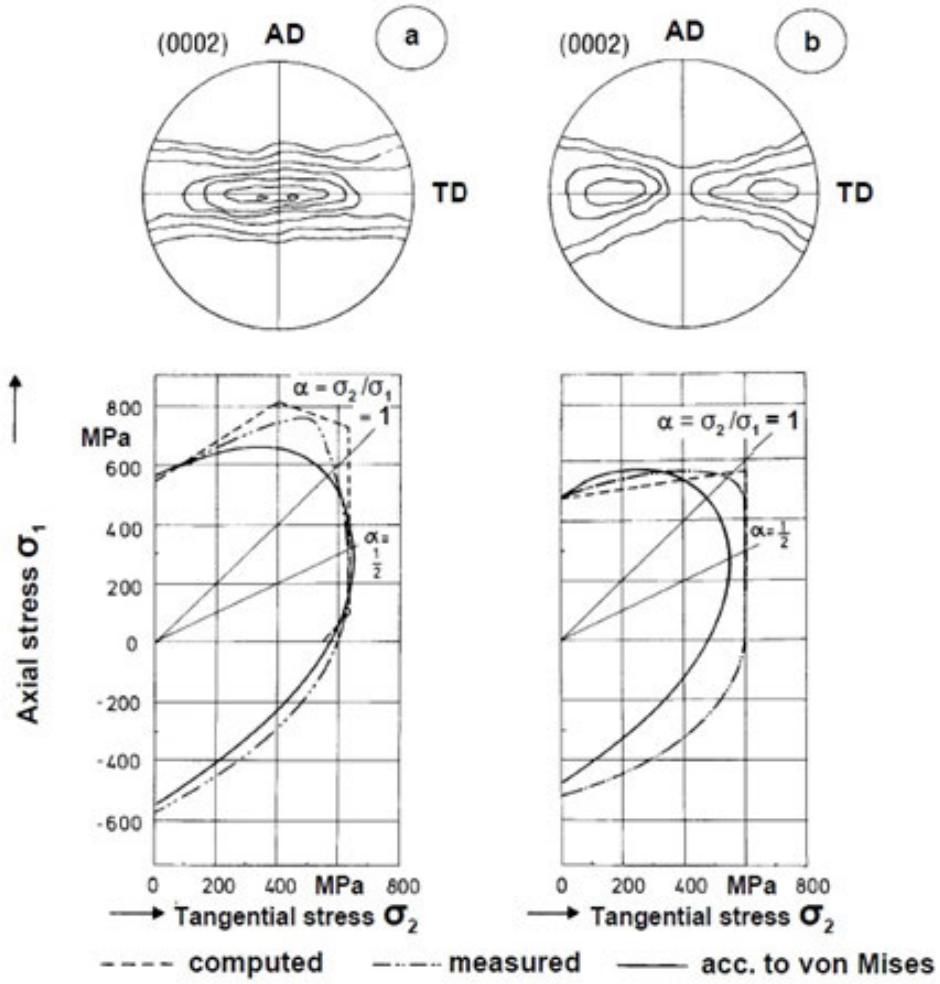

FIG. 5.56. Basal pole textures (a_I and a_{II}) and yield loci (b_I and b_{II}) of Zircaloy-4 cladding tubes [5.116]. (a) Basal pole inclination in TD approximately ±0–30°; (b) basal pole inclination in TD approximately ±70° (reprinted with permission from Ref. [5.1], copyright ASTM International). AD — axial direction; TD — transverse direction.

5.7.3.2. Creep loci

Equivalent to the approach of deriving yield loci for short term loading, creep loci can be determined for long time loading up to 673 K (400°C). The creep loci represent locus diagrams of constant comparative creep rate [5.225]. Figure 5.57 shows such creep loci for four differently textured Zircaloy tubes. The locus was derived by obtaining pairs of stress values in axial and tangential directions for which a constant creep rate occurred. To determine the locus experimentally under these conditions, the creep rates were measured for various stress ratios and stresses. The work W performed in deformation can be calculated and interpolation can be made between these values. Additionally, creep in pressure tubes was evaluated using

Hill's anisotropy factors [5.226]. Assigning anisotropy factors calculated from crystallography to experimentally determined anisotropy factors, based on short time deformation mechanisms, is not satisfactory for predicting long term behaviour [5.95, 5.225, 5.227].

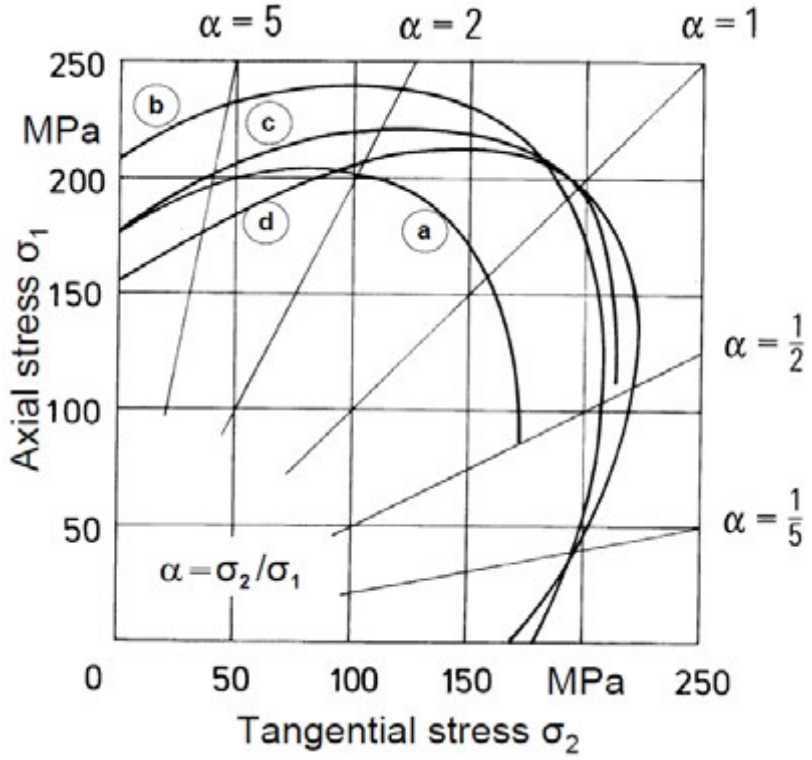

FIG. 5.57. Creep loci for various Zircaloy tube textures, obtained at 673 K (400°C) and a constant deformation efficiency of $W = 3 \times 10^{-2}$ MPa·h^{-1} [5.225] (reprinted with permission from Ref. [5.1], copyright ASTM International).

For Fig. 5.57, the traces (a), (b), (c) and (d) belong to tubing taken out of commercial production processes after cold deformation and different recovery or recrystallization annealings. The corresponding texture coefficients for basal poles in the radial direction F_r are for (a) 0.760, for (b) 0.751, for (c) 0.796, and for (d) 0.754.

5.7.3.3. Burst loci

In analogy to the yield loci, a further method of assessing the plastic behaviour of metallic materials is to use burst loci [5.220, 5.224, 5.227]. The burst locus is the two dimensional representation of the stress conditions that lead to burst (Fig. 5.58). The elliptical shape of these curves is less marked than that of the yield loci. In addition, they cannot be described using the propositions made by Hill [5.106]. Duncombe [5.228] attempted to link yield loci to mechanical processes in the metal; a satisfactory explanation has yet to be provided.

Zirconium hydrides can embrittle a component. Texture is important because hydrides usually precipitate as platelets on a plane close to the basal plane (in Zr and Zr based alloys $\{10\bar{1}7\}$). They also tend to align perpendicular to a tensile stress [5.218, 5.229–5.231]. If the basal plane normal is parallel with the tensile stress, then preferred alignment may result. This observation provides another reason for preferring a radial basal pole texture in fuel cladding.

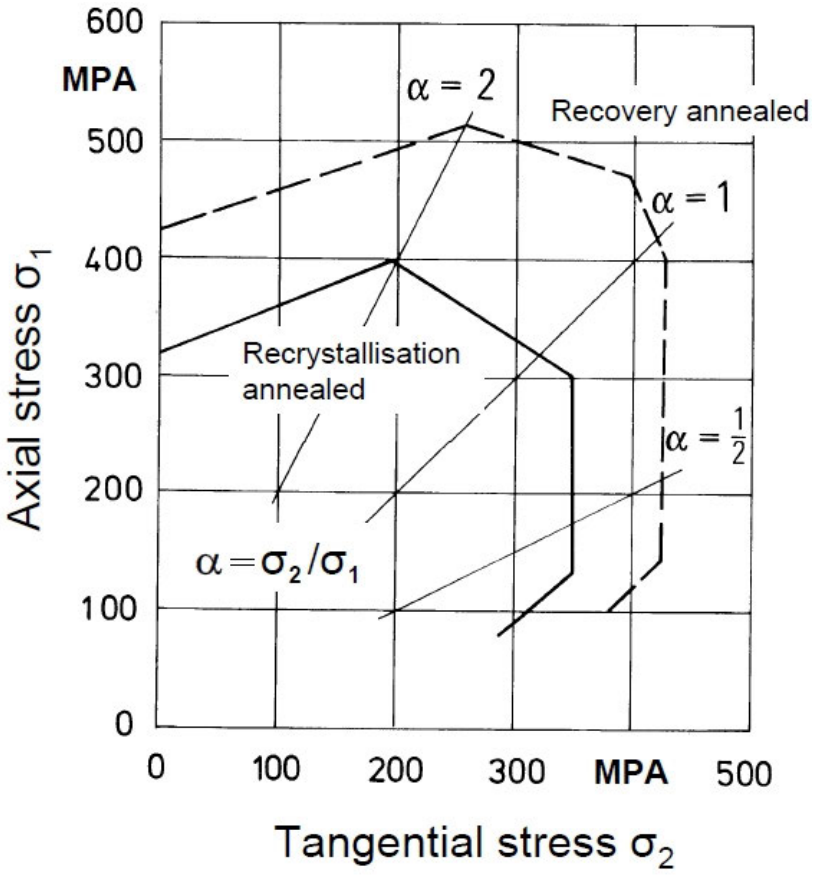

FIG. 5.58. Burst loci at 673 K (400°C) for Zircaloy tubes after recovery and recrystallization annealing [5.225]. Rate of stress increase 200–400 MPa·min^{-1} (reprinted with permission from Ref. [5.1], copyright ASTM International).

5.7.4. Combined loads under reactor operation — effects on irradiation induced creep and growth

The loading conditions for Zr based alloy tubing during reactor service are complex. Various types of stresses can be applied simultaneously and can alter in size, direction and rate of change with time and temperature of operational conditions. In addition to short term deformation, long term deformation (creep), cyclical deformation and irradiation induced creep and growth play important roles.

Irradiation damage and irradiation induced creep and growth phenomena [5.232–5.234] are discussed in detail in Chapters 6 and 7, Volume 2 of this publication. In this section, some effects of neutron irradiation on the operation of the deformation systems in Zr and Zr based alloys are pointed out.

At low loading rates and with increasing temperature appropriate for plastic deformation by creep, dislocation reactions and diffusion controlled processes such as slip are favoured over twinning type deformations [5.13, 5.235–5.238]. Neutron irradiation produces point defects that can cluster, segregate to dislocations and create forest obstacles. Irradiation influences slip behaviour through dislocation climb and thermal cutting processes; twinning should not be affected [5.13, 5.239]. For short time deformations, an increase in strength and a decrease in ductility are observed [5.13, 5.240–5.242]. For long time deformations, the effect of neutron irradiation is a pronounced increase in creep rate, stress relaxation and rupture ductility [5.13, 5.225, 5.239, 5.243–5.246]. In the temperature range from 573 to 673 K (300 to 400°C),

recovery of the irradiation damage occurs; at some limit, irradiation damage is annealed out as fast as it occurs [5.247–5.249].

Although the detailed mechanisms for creep [5.235–5.238] and creep during irradiation [5.250–5.252] are different, in both cases deformations with a c component may be accomplished by slip with a (c + a) type Burgers vector, which has been shown to become operative at elevated temperatures under restraint [5.37]. For creep under reactor service conditions, pyramidal slip may also become operative in Zr based alloy tubing. Wavy slip lines observed on creep specimens after irradiation testing can be interpreted as cross-slip on pyramidal planes [5.74].

The different CRSS on the newly activated slip systems may lead to anisotropic behaviour that is characteristic of creep, or of creep under neutron irradiation, and is different from short term mechanical behaviour.

5.8. SUMMARY — TAILORING TEXTURE TO OPTIMIZE PROPERTIES

The deformation systems in HCP metals are not as symmetrically distributed nor as numerous as in cubic metals. Primary slip systems are limited to deformation in the <*a*> direction and twinning competes with slip in plastic deformation to play an essential role, depending on the deformation conditions.

The low number of slip systems, their asymmetrical distribution and the strict crystallographic orientation relationships of first and second order pyramidal twinning result in the formation of a strong deformation texture. Even small amounts of deformation by twinning lead to large lattice rotations, which change the orientation of the crystallites so that basal poles align preferentially in the direction of the compressive force.

For deformations in the α phase, the decisive factors in texture development are the material deformation and the degrees of freedom of the forming process. The degrees of freedom are lower for tube reduction than for sheet rolling and wire drawing. According to Ref. [5.154], the reduction of the tube is characterized by a decrease in the cross-section R_A, wall thickness R_W and diameter R_D, making it possible to accurately predict the acting forces and the resulting deformation mechanisms. The factor controlling the development of texture is the R_W/R_D ratio. In tubes with $R_W/R_D > 1$, the basal poles are oriented predominantly in the radial direction, with $R_W/R_D = 1$, the basal poles are randomly distributed in the radial-tangential plane and with $R_W/R_D < 1$, basal poles are predominantly oriented tangentially. The sheet texture is identical to the pipe texture with $R_W/R_D > 1$, since the material flow is characterized by the predominance of wall thickness reduction in both processes. The texture of the wire fibre is identical to the texture of the pipe with $R_W/R_D = 1$. It can be seen that the deformation of the wire corresponds to the deformation of concentric tubes of different diameters, which corresponds to a decrease in the pipe with $R_W/R_D = 1$ at a constant volume. During any cold working, first order prism poles align parallel to the direction of elongation.

During recrystallization, the basal poles do not change significantly. The basal planes rotate continuously up to ±30° with increasing annealing temperature so that in the final stable position, a second order prism pole becomes parallel to the elongation.

For textured materials, the deformation mechanisms are also responsible for the strong anisotropy of the mechanical properties. This behaviour was demonstrated with specially prepared tubes machined out of a thick Zircaloy plate with pronounced sheet texture. The preferred orientations of the basal poles changed continuously around the circumference of the tubing. Theoretical predictions of the mechanical behaviour agreed with experimental results for different applied uni- and multiaxial loadings.

This anisotropic behaviour does not restrict the range of industrial applications. Anisotropy may even be an advantage, for instance, if the direction of highest stress coincides with the direction of highest strength as result of mechanical anisotropy. Similarly, it is possible to select the direction in which the material can be deformed easily for deformation procedures, such as rolling and bending, where high ductility is required. Knowing these dependencies, it is possible to tailor the texture of zirconium alloy tubing, within limits, to the requirements of nuclear applications.

In nuclear applications, the anisotropic behaviour of biaxial loading conditions in tubes is represented by yield loci, creep loci or burst loci according to the respective criteria of yield stress, creep rate or fracture stress. An attempt is made to correlate the shape of the loci to the operative deformation mechanism. A prerequisite for a realistic analysis is knowledge of the complex loading conditions acting on the component. It then may be possible to find selection criteria for the desirable texture of the zirconium alloy semifinished shape to ensure the highest performance of the final component.

REFERENCES TO CHAPTER 5

[5.1] TENCKHOFF, E., Deformation Mechanisms, Texture, and Anisotropy in Zirconium and Zircaloy, ASTM STP 966, ASTM International, West Conshohocken, PA (1988).

[5.2] SMALLMAN, R.E., Modern Physical Metallurgy, Butterworths, London (1970).

[5.3] HALL, E.O., Twinning and Diffusionless Transformations in Metals, Butterworths, London (1954).

[5.4] REED-HILL, R.E., HIRTH, J.P., ROGERS, H.C. (Eds), Deformation Twinning, Metallurgical Society Conferences Vol. 25, Gordon and Breach Science Publishers, New York (1964).

[5.5] CHRISTIAN, J.W., The Theory of Transformations in Metals and Alloys, Pergamon Press, Oxford (2002).

[5.6] PARTRIDGE, P.G., The crystallography and deformation modes of hexagonal close-packed metals, Metall. Rev. **12** (1967) 169–194.

[5.7] BACON, D.J., VITEC, V., Atomic-scale modeling of dislocations and related properties in the hexagonal-close-packed metals, Metall. Mat. Trans. A **33** (2002) 721–733.

[5.8] WASSERMANN, G., GREWEN, J., Texturen Metallischer Werkstoffe, Springer Verlag, Berlin (1962).

[5.9] DILLAMORE, I.L, ROBERTS, W.T., Preferred orientation in wrought and annealed metals, Metall. Rev. **10** (1965) 271–380.

[5.10] BUNGE, H.-J., Entstehung von Verformungstexturen in metallischen Werkstoffen, Krist. Tech. **6** (1971) 667–728.

[5.11] PICKLESIMER, M.L., Deformation, creep, and fracture in alpha-zirconium alloys, Electrochem. Technol. **4** (1966) 289–300.

[5.12] REED-HILL, R.E., Tensile properties of alpha-zirconium, Rev. High Temp. Mats. **1** (1972) 97–154.

[5.13] INTERNATIONAL ATOMIC ENERGY AGENCY, Atomic Energy Review Supplement 1971: The Metallurgy of Zirconium, D.I. Douglass, Atomic Energy Review, IAEA, Vienna (1971).

[5.14] BARRETT, C.S., MASSALSKI, T.B., Structure of Metals, McGraw-Hill, New York (1966).

[5.15] WEERTMAN, J., WEERTMAN, J.R., Elementary Dislocation Theory, Collier-Macmillan, London (1964).

[5.16] SEEGER, A., Moderne Probleme der Metallphysik, Springer, Berlin (1965).

[5.17] SCHMID, E., BOAS, W., Kristallplastizität, Springer, Berlin (1935.

[5.18] PEIERLS, R., The size of a dislocation, Proc. Phys. Soc. **52** (1940) 34–37.

[5.19] NABARRO, F.R.N., The mechanical properties of metallic solid solutions, Proc. Phys. Soc. **58** (1946 669–676.

[5.20] SAGEL, K., ZWICKER, U., Verformungs- und Rekristallisationstexturen von Titan und Titanlegierungen, Z. Metallkd. **46** (1955) 835–842.

[5.21] THOMPSON, N., Dislocation nodes in face-centred cubic lattices, Proc. Phys. Soc. B **66** (1953) 481–492.

[5.22] BERGHEZAN, A., FOURDEUX, A., AMELINCKX, S., Transmission electron microscopy studies of dislocations and stacking faults in a hexagonal metal: Zinc, Acta Metall. **9** (1961) 464–490.

[5.23] SCHOTTKY, G., SEEGER, A., SPEIDEL, V., Thermisch aktivierte Quergleitung in Zink und Cadmium, Phys. Status Solidi B **9** (1965) 231–242.

[5.24] THORNTON, P.R., HIRSCH, P.B., The effect of stacking fault energy on low temperature creep in pure metals, Philos. Mag. **3** (1958) 738–761.

[5.25] HARRIS, J.E., MASTERS, B.C., The annealing of faulted loops in magnesium and zinc, Proc. R. Soc. Sect. A **292** (1966) 240–263.

[5.26] CONRAD, H., PERLMUTTER, I., Beryllium as a Technological Material, Report No. AFML-TR-65–310, Air Force Materials Laboratory, Wright-Patterson AFB, OH (1965).

[5.27] DEVLIN, J.F., Stacking fault energies of Be, Mg, Al, Cu, Ag, and Au, J. Phys. F Met. Phys. **4** (1974) 1865–1882.
[5.28] THOMAS, G., WASHBURN, J., Electron Microscopy and Strength of Crystals, Interscience, New York and London (1963).
[5.29] AKHTAR, A., TEGHTSOONIAN, A., Prismatic slip in α-titanium single crystals, Metall. Mater. Trans. A **6** (1975) 2201–2208.
[5.30] AKHTAR, A., TEGHTSOONIAN, A., Plastic deformation of zirconium single crystals, Acta Metall. **19** (1971) 655–663.
[5.31] ALDINGER, F., JOENSSON, S., "Stacking faults in beryllium and dilute beryllium-copper alloys", Proc. Beryllium 1977, 4th Int. Conf. on Beryllium, Royal Society, London, 1977, Metals Society, London (1977) 4/1–10.
[5.32] ROSENBAUM, H.S., "Non-basal slip in HCP metals and its relation to mechanical twinning", Deformation Twinning, Metallurgical Society Conferences Vol. 25 (REED-HILL, R.E., HIRTH, J.P., ROGERS, H.C., Eds), Gordon and Breach Science Publishers, New York (1964) 43–76.
[5.33] TYSON, W., Basal and prismatic slip in h.c.p. crystals, Acta Metall. **15** (1967) 574–577.
[5.34] FRANK, F.C., THOMPSON, N., On deformation by twinning, Acta Metall. **3** (1955) 30–33.
[5.35] REGNIER, P., DUPOUY, J.M., Prismatic slip in beryllium and the relative ease of glide in H.C.P. metals, Phys. Status. Solidi B **39** (1970) 79–93.
[5.36] ALDINGER, E., PETZOW, G., Gefüge und Bruch, Materialkundliche Technische Reihe No. 3, Gebrüder Bornträger Berlin, Stuttgart (1977).
[5.37] TENCKHOFF, E., Operation of dislocations with (c+a)-type Burgers vector during the deformation of zirconium single crystals, Z. Metallkd. **63** (1972) 192–197.
[5.38] DAMIANO, V.V., LONDON, G.J., CONRAD, H., Microstrain compression of beryllium and beryllium alloy single crystals parallel to the [0001]: Part II slip trace analysis and transmission electron microscopy, Trans. Metall. Soc. AIME **242** (1968) 987–994.
[5.39] KRONBERG, M.L., Atom movements and dislocation structures in some common crystals, Acta Metall. **9** (1961) 970–972.
[5.40] KRONBERG, M.L., Atom movements and dislocation structures for plastic slip in single crystals of β-uranium, J. Nucl. Mater. **1** (1959) 85–95.
[5.41] REED-HILL, R.E., "Role of deformation twinning in the plastic deformation of a polycrystalline anisotropic metal", Deformation Twinning, Metallurgical Society Conferences Vol. 25 (REED-HILL, R.E., HIRTH, J.P., ROGERS, H.C., Eds), Gordon and Breach Science Publishers, New York (1964) 295–320.
[5.42] STOLOFF, N.S., GENSAMER, M., Deformation and fracture of polycrystalline cadmium, Trans. Metall. Soc. AIME **227** (1963) 70–80.
[5.43] WESTLAKE, D.G., Some dislocation models of twinning modes, Deformation Twinning, Metallurgical Society Conferences Vol. 25 (REED-HILL, R.E., HIRTH, J.P., ROGERS, H.C., Eds), Gordon and Breach Science Publishers, New York (1964) 29–42.
[5.44] CHYUNG, C.K., WEI, C.T., Nucleation of deformation twins in zinc bicrystals, Philos. Mag. **15** (1967) 161–175.
[5.45] BLASDALE, K.C.A., KING, R., Tensile kinking in single crystals of cadmium, Phys. Status. Solidi **10** (1965) 175–184.
[5.46] BLASDALE, K.C.A., KING, R., PUTTICK, K.E., The microstructure of tensile kinks in cadmium crystals, Phys. Status. Solidi **18** (1966) 491–503.
[5.47] HAUSER, F.E., LANDON, P.R., DORN, J.E., Deformation and fracture mechanisms of polycrystalline magnesium at low temperatures, ASM Trans. **48** (1956) 986–1002.
[5.48] OROWAN, E., A type of plastic deformation new in metals, Nature **149** (1942) 643–644.
[5.49] ROSI, F.D., Mechanism of plastic flow in titanium: Manifestations and dynamic of glide, JOM **6** (1954) 58–69.
[5.50] ROSI, F.D., PERKINS, F.C., SEIGLE, L.L., Mechanism of plastic flow in titanium at low and high temperatures, JOM **8** (1956) 115–122.
[5.51] CHURCHMAN, A.T., The yield phenomena, kink bands and geometric softening in titanium crystals, Acta Metall. **3** (1955) 22–29.
[5.52] REED-HILL, R.E., MARTIN, J.L., Fifth Quarterly Progress Report, AEC Contract No. AT(38–1)-252, Atomic Energy Commission, Washington, DC (1963).
[5.53] REED-HILL, R.E., MARTIN, J.L., Sixth Quarterly Progress Report, AEC Contract No. AT(38–1)-252, Atomic Energy Commission, Washington, DC (1963).
[5.54] CAHN, R.W., Slip and polygonization in aluminium, J. Inst. Met. **79** (1951) 129–158.
[5.55] HONEYCOMBE, R.W.K., Inhomogeneities in the plastic deformation of metal crystals — Part I: Occurrence of X ray asterisms, Part II: X ray and optical micrography of aluminium, J. Inst. Met. **80** (1952) 45–56.
[5.56] CAHN, R.W., Plastic deformation of alpha-Uranium: Twinning and slip, Acta Metall. **1** (1953) 49–70.
[5.57] CHEN, N.K., MADDIN, R., Observations on cleavage and polygonization of molybdenum single crystals, Trans. Metall. Soc. AIME **191** (1951) 531–532.
[5.58] ROSENBAUM, H.S., Non-basal slip and twin accommodation in zinc crystals, Acta Metall. **9** (1961) 742–748.
[5.59] PARTRIDGE, P.G., ROBERTS, E., The formation and behaviour of incoherent twin boundaries in hexagonal metals, Acta Metall. **12** (1964) 1205–1210.
[5.60] ROBERTS, E., PARTRIDGE, P.G., The accommodation around $\{10\bar{1}2\} < \bar{1}011 >$ twins in magnesium, Acta Metall. **14** (1966) 513–527.

[5.61] RAPPERPORT, E.J., Room temperature deformation processes in zirconium, Acta Metall. **7** (1959) 254–260.
[5.62] RAPPERPORT, E.J., Room Temperature Deformation Processes in Zirconium", Atomic Energy Commission, Oak Ridge, TN (1958).
[5.63] SOKURSKII, U.N., PROTSENKO, L.N., Deformation systems of alpha-zirconium, Sov. J. At. Energy **4** (1958) 579–582 (in Russian).
[5.64] RAPPERPORT, E.J., HARTLEY, C.S., Deformation Modes of Zirconium at 77 K, 300 K, 575 K and 1075 K, Nuclear Metals, Concord, MA (1959).
[5.65] HOWE, L.M., WHITTON, J.L., McGURN, J.F., Observation of dislocation movement and interaction in zirconium by transmission electron microscopy, Acta Metall. **10** (1962) 773–787.
[5.66] POLLARD, J., RZEPSKI, M., LEHR, P., "Observation de lames minces de zirconium au microscope électronique en transmission", Proc. 9th Conf. on Métallurgie, Etude sur la Corrosion et la Protection du Zirconium et de des Alliages (SALESE, M., CHAUDRON, M., Eds), Press Universitaires de France, Paris (1966) 123–133.
[5.67] BALDWIN, D.H., REED-HILL, R.E., Some observations of the deformation modes of polycrystalline hafnium and zirconium, Trans. Metall. Soc. AIME **233** (1965) 248–249.
[5.68] BAILEY, J.E., Electron microscope studies of dislocations in deformed zirconium, J. Nucl. Mater. **7** (1962) 300–310.
[5.69] AKHTAR, A., Basal slip in zirconium, Acta Metall. **21** (1973) 1–11.
[5.70] MARTIN, J.L., REED-HILL, R.E., A study of basal slip kink bands in polycrystalline zirconium, Trans. Metall. Soc. AIME **230** (1964) 780–785.
[5.71] ROSI, F.D., personal communication to A.R. Kaufman, cited in: Roberts, E., Partridge, P.G., The accommodation around $\{10\bar{1}2\} < \bar{1}011 >$ twins in magnesium, Acta Metall. **14** (1966) 513–527.
[5.72] JENSEN, J.A., BACKOFEN, W.A., Deformation and fracture of alpha zirconium alloys, Can. Metall. Q. **11** (1972) 39–51.
[5.73] AKHTAR, A., Compression of zirconium single crystals parallel to the c-axis, J. Nucl. Mater. **47** (1973) 79–86.
[5.74] BELL, W.L., "Discussion on textured Zircaloy tubing", Zirconium in Nuclear Applications, ASTM STP 551 (SCHEMEL, J.H., ROSENBAUM, H.S., Eds), ASTM International, West Conshohocken, PA (1974) 199–200.
[5.75] PETTERSON, K., Evidence for basal or near-basal slip in irradiated Zircaloy, J. Nucl. Mater. **105** (1982) 341–344.
[5.76] NUMAKURA, H., MINONISHI, Y., KOIWA, M., $\{10\bar{1}1\} < \bar{1}\bar{1}23 >$slip in zirconium, Philos. Mag. A **63** (1991) 1077–1084.
[5.77] ROVIGLIONE, A., HERMIDA, J.D., Pyramidal slip in the orientation distribution function analysis of Zry-4 tubes, Scr. Metall. Mater. **34** (1996) 1615–1620.
[5.78] REED-HILL, R.E., "An evaluation of the role of deformation twinning in the plastic deformation of zirconium", Ninth Quarterly Report, AEC Contract No. AT(38–1) 252, Atomic Energy Commission, Washington, DC (1963).
[5.79] WARREN, M.R., BEEVERS, C.J., Fatigue life and twinning in alpha zirconium, Metall. Trans. **1** (1970) 1657–1661.
[5.80] TENCKHOFF, E., Zwillingsbildung in Zirkonium-Einkristallen bei erhöhten Verformungstemperaturen, Z. Metallkd. **63** (1972) 729–734.
[5.81] WESTLAKE, D.G., Twinning in zirconium, Acta Metall. **9** (1961) 327–331.
[5.82] PARTRIDGE, P.G., ROBERTS, E., "Slip and deformation twinning in magnesium", Proc. 3rd European Regional Conference on Electron Microscopy, Prague, 1964, Czechoslovak Academy of Sciences, Prague (1964) 213–214.
[5.83] PARTRIDGE, P.G., Slip band extrusion in fatigued close packed hexagonal metals, Acta Metall. **13** (1965) 517–525.
[5.84] CONRAD, H., PERLMUTTER I., "Effect of structural factors on the yield strength of beryllium", Proc. Int. Conf. Metallurgie du Beryllium, Grenoble, 1965, Presses Universitaires de France, Paris (1966) 319–326.
[5.85] KOCKS, U.F., WESTLAKE, D.G., The importance of twinning for the ductility of HCP polycrystals, Trans. Metall. Soc. AIME **239** (1967) 1107–1109.
[5.86] DORN, J.E., MITCHELL, J.B., "Slip mechanisms in single crystals of hexagonal close-packed phases", High Strength Materials, Proc. 2nd Berkeley Int. Materials Conf., Berkeley, 1964 (ZACKAY, V.F., Ed.), Wiley, New York (1965) 510-577.
[5.87] TEGART, W.J.McG., Elements of Mechanical Metallurgy, Macmillan, London (1966).
[5.88] LEVINE, E.D., Deformation mechanisms in titanium at low temperatures, Trans. Metall. Soc. AIME **236** (1966) 1558–1565.
[5.89] ALTSHULER, T.L., CHRISTIAN, J.W., Low temperature twinning in pure iron, Acta Metall. **14** (1966) 903–908.
[5.90] BOLLING, G.F., RICHMAN, R.H., Remarks on the nucleation of mechanical twins, Acta Metall. **15** (1967) 678–680.
[5.91] TENCKHOFF, E., "Operable deformation systems and mechanical behaviour of textured Zircaloy tubing", Zirconium in Nuclear Applications, ASTM STP 551 (SCHEMEL, J.H., ROSENBAUM, H.S., Eds), ASTM International, West Conshohocken, PA (1974) 179–198.
[5.92] HOSFORD, W.F., Texture strengthening, Met. Eng. Q. **6** (1966) 13–19.
[5.93] RITTENHOUSE, P.L., PICKLESIMER, M.L., Research on the mechanical anisotropy of Zircaloy-2, Electrochem. Technol. **4** (1966) 322–329.

[5.94] DRESSLER, G., MATUCHA, K.-H., WINCIERZ, P., Yield loci of Zircaloy with different textures, Can. Metall. Q. **11** (1972) 177–184.
[5.95] BRENNER, R., BÉCHADE, J.L., CASTELNAU, O., BACROIX, B., Thermal creep of Zr–Nb1%–O alloys: Experimental analysis and micromechanical modelling, J. Nucl. Mater. **305** (2002) 175–186.
[5.96] KASCHNER, G.C., GRAY G.T., The influence of crystallographic texture and interstitial impurities on the mechanical behaviour of zirconium, Metall. Mat. Trans. A **31** (2000) 1997–2003.
[5.97] FUNDENBERGER, J.J., PHILIPPE, M.J., ESLING, C., Mechanical twinning at high temperatures in some hexagonal alloys, Scr. Metall. Mater. **24** (1990) 1215–1220.
[5.98] MURTY, K.L., JALLEPALLI, R., MAHMOOD, S.T., Effects of recrystallization and Nb additions on texture and mechanical anisotropy of Zircaloy, Nucl. Eng. Des. **148** (1994) 1–15.
[5.99] CHUN, Y.B., HWANG, S.K., KIM, M.H., KWUN, S.I., CHAE, S.W., Effect of Mo addition on the crystal texture and deformation twin formation in Zr-based alloys, J. Nucl. Mater. **295** (2001) 31–41.
[5.100] CONRAD, H., DE MEESTER, B., DÖNER, M., OKAZAKI, K., "Strengthening of alpha titanium by the interstitial solutes C, N, and O", Proc. Symp. on the Physics of Solid Solution Strengthening in Alloys, Chicago, 1973, Plenum Press, New York (1975) 1–45.
[5.101] CONRAD, H., Kraftwerk Union AG, Erlangen, personal communication, 1973.
[5.102] MILLS, D., CRAIG, G.B., Plastic deformation of zirconium-oxygen alloy single crystals in the range 77–950 K, Trans. Metall. Soc. AIME **242** (1968) 1881–1890.
[5.103] BACKOFEN, W.A., Deformation processing, Metall. Trans. **4** (1973) 2679–2699.
[5.104] TARNOVSKII, I.Ya., et al., Deformation of Metals During Rolling, Pergamon Press, New York (1965).
[5.105] VON MISES, R., Mechanik der plastischen Formänderung von Kristallen, Z. Angew. Math. Mech. **8** (1928) 161–185.
[5.106] HILL, R., A theory of the yielding and plastic flow of anisotropic metals, Proc. R. Soc. Sect. A, **193** 1033 (1948) 281–297.
[5.107] TAYLOR, G.I., Plastic strain in metals, J. Inst. Met. **62** (1938) 307–324.
[5.108] BISHOP, J.F.W., HILL, R., A theory of the plastic distortion of a polycrystalline aggregate under combined stresses, Philos. Mag. **42** (1951) 414–427.
[5.109] PIEHLER, H.R., BACKOFEN, W.A., "Prediction of anisotropic yield for textured sheet," Texturen in Forschung und Praxis, Proc. Int. Symp. Clausthal-Zellerfield, 1968 (GREWEN, J., WASSERMANN, G., Eds), Springer, Berlin (1969) 436–443.
[5.110] BACKOFEN, W.A., HOSFORD, W.F., BURKE, J.J., Texture hardening, ASM Trans. **55** (1962) 264–267.
[5.111] HOSFORD, W.F., BACKOFEN, W.A., "Strength and plasticity of textured metals", Fundamentals of Deformation Processing, Proc. 9th Sagamore Army Materials Research Conference, Raquette Lake, 1962 (BACKOFEN, W.A., BURKE, J.J., COFFIN L.F., Jr., REED, N.L., WEISS, V., Eds), Syracuse University Press, New York (1964) 259–298.
[5.112] ALTHOFF, J., DREFAHL, K., WINCIERZ, P., Charakterisierung der mechanischen Anisotropie stranggepreßter aushärtbarer Aluminiumlegierungen (Preßeffekt) durch Kurven des Fließbeginns und r-Werte, Z. Metallkd. **62** (1971) 765–771.
[5.113] CHIN, G.Y., MAMMEL, W.L., Competition among basal, prism and pyramidal slip modes in HCP metals, Metall. Trans. **1** (1970) 357–361.
[5.114] THORNBURG, D.R., PIEHLER, H.R., Analysis of constrained deformation by slip and twinning in hexagonal close packed metals and alloys, Metall. Trans. A **6** (1975) 1511–1523.
[5.115] HOSFORD, W.F., "Texture hardening", Texturen in Forschung und Praxis (GREWEN, J., WASSERMANN, G., Eds), Springer, Berlin (1969) 414–435.
[5.116] DRESSLER, G., MATUCHA, K.-H., WINCIERZ, P., "Experimental and theoretical analysis of anisotropic mechanical properties of Zircaloy fuel element claddings", Proc. 2nd Int. Conf. on Structural Mechanics in Reactor Technology, Berlin, 1973, Vol. 1, Commission of the European Communities, Brussels (1973) 1–12.
[5.117] ASHBY, M.F., The deformation of plastically non-homogeneous materials, Philos. Mag. **21** (1970) 399–424.
[5.118] KITTEL, C., Introduction to Solid State Physics, 3rd edn, John Wiley, New York (1968).
[5.119] SCHULZ, L.G., A direct method of determining preferred orientation of a flat reflection sample using a Geiger counter X ray spectrometer, J. Appl. Phys. **20** (1949) 1030–1033.
[5.120] CULLITY, B.D., Elements of X-Ray Diffraction, 3rd print., Addison-Wesley, Reading, MA (1967).
[5.121] KOCKS, U.F., TOMÉ, C.N., WENK, H.-R., Texture and Anisotropy, Cambridge University Press, Cambridge (1998).
[5.122] CHERNOCK, W.P., BECK, P.A., Analysis of certain errors in the x-ray reflection method for the quantitative determination of preferred orientations, J. Appl. Phys. **23** (1952) 341–345.
[5.123] CHERNOCK, W.P., Diskussion zur Anwendung des Zählrohres für die Texturbestimmung von Bunk, W., Lücke, K. und Masing, G., Z. Metallkd. **46** (1955) 311.
[5.124] WILSON, A.J.C., Geiger-counter x-ray spectrometer — Influence of size and absorption coefficient of specimen on position and shape of powder diffraction maxima, J. Sci. Instr. **27** (1950) 321–325.
[5.125] TENCKHOFF, E., Defocusing for the Schulz technique of determining preferred orientation, J. Appl. Phys. **41** (1970) 3944–3948.
[5.126] HERMIDA, J.D., Influence of the sample radius and irradiated zone width on the defocusing phenomenon in the Schulz technique, Mater. Sci. Eng. **56** (1982) 135–141.
[5.127] RITTENHOUSE, P.L., PICKLESIMER, M.L., Metallurgy of Zircaloy-2, Part II, Report No. ORNL-2948, Oak Ridge National Laboratory, Oak Ridge, TN (1961).

[5.128] KEARNS, J.J., Thermal Expansion and Preferred Orientation in Zircaloy, Report No. WAPD-TM-472, Bettis Atomic Power Lab., Pittsburgh, PA (1965).
[5.129] TEMPEST, P.A., Preferred orientation and its effect on bulk physical properties of hexagonal polycrystalline materials, J. Nucl. Mater. **92** (1980) 191–200.
[5.130] WILLIAMS, R.O., The representation of the textures of rolled copper, brass, and aluminium by biaxial pole figures, Trans. Metall. Soc. AIME **242** (1968) 105–115.
[5.131] BUNGE, H.J., Mathematische Methoden der Texturanalyse, Akademie Verlag, Berlin (1969).
[5.132] BUNGE, H.J., Texture Analysis in Materials Science, Butterworth, London (1983).
[5.133] BUNGE, H.J., ESLING, C., Advances and Applications of Quantitative Texture Analysis, DGM Metallurgy Information, Oberursel, NY (1991).
[5.134] CHIN, G.Y., MAMMEL, W.L., DOLAN, M.T., Taylor's theory of texture for axisymmetric flow in body-centred cubic metals, Trans. Metall. Soc. AIME **239** (1967) 1854–1855.
[5.135] BUNGE, H.J., Some applications of the Taylor theory of polycrystal plasticity, Krist. Tech. **5** (1970) 145–175.
[5.136] SIEMES, H., Die Endlagen bei der Stauch- und Zugverformung von polykristallinen Metallen, Z. Metallkd. **58** (1967) 228–230.
[5.137] CALNAN, E.A., CLEWS, C.J.B., The development of deformation textures in metals, Part III: Hexagonal structures **42** (1951) 919–931.
[5.138] WILLIAMS, D.N., EPPELSHEIMER, D.S., A theoretical investigation of the deformation textures of titanium, J. Inst. Met. **81** (1953) 553–562.
[5.139] HOBSON, D.O., Textures in deformed zirconium single crystals, Trans. Metall. Soc. AIME **242** (1968) 1105–1110.
[5.140] TENCKHOFF, E., The development of the deformation texture in zirconium during rolling in sequential passes, Metall. Trans. A **9** (1978) 1401–1412.
[5.141] MacEWEN, S.R., et al., "The evolution of texture and residual stress in Zircaloy-2", Proc. Eighth Int. Conf. on Textures of Materials (ICOTOM 8), Santa Fe, 1987, The Metallurgical Society, Warrendale, PA (1988) 825–836.
[5.142] TOMÉ, C.N., LEBENSOHN, R.A., KOCKS, U.F., Model for texture development dominated by deformation twinning: Application to zirconium alloys, Acta Metall. Mat. **39** (1991) 2667–2680.
[5.143] CHIRKIN, A.V., AL-NAKOW, A.S., The formation of twin structures in an industrial Zr-2.5% Nb alloy, J. Nucl. Mater. **183** (1991) 62–69.
[5.144] LEBENSOHN, R.A. TOMÉ, C.N., A self-consistent anisotropic approach for the simulation of plastic deformation and texture development of polycrystals: Application to zirconium alloys, Acta Metall. Mat. **41** (1993) 2611–2624.
[5.145] LEBENSOHN, R.A., TOMÉ, C.N., Self-consistent viscoplastic model: Prediction of rolling textures of anisotropic polycrystals, Mater. Sci. Eng. **A175** (1994) 71–82.
[5.146] BÉCHADE, J.L., BACROIX, B., GUILLEN, R., The effects of the cold rolling process on the texture of Zircaloy-4 sheets, Mater. Sci. Forum **157**–**162** (1994) 617–626.
[5.147] PHILIPPE, M.J., SERGHAT, M., VAN HOUTTE, P., ESLING, C., Modelling of texture evolution for materials of hexagonal symmetry — II. Application to Zirconium and Titanium α or near α Alloys, Acta Metall. Mater. **43** (1995) 1619–1630.
[5.148] SALINAS-RODRIGUEZ, A., Grain size effects on the texture evolution of α-Zr, Acta Metall. Mater. **43** (1995) 485–498.
[5.149] FRANCILLETTE, H., BACROIX, B., GASPÉRINI, M., BÉCHADE, J.L., Effect of initial textures on deformation mechanisms and texture evolutions of α-Zr polycrystals deformed by channel-die compression tests, Mater. Sci. Eng. A **234**–**236** (1997) 974–977.
[5.150] FRANCILLETTE, H., BACROIX, B., GASPERINI, M., BÉCHADE, J.L., Grain orientation effects in Zr702α polycrystalline samples deformed in channel die compression at room temperature, Acta Metall. Mater. **46** (1998) 4131–4142.
[5.151] SANCHEZ, P., POCHETTINO, A., CHAUVEAU, T., BACROIX, B., Torsion texture development of zirconium alloys, J. Nucl. Mater. **298** (2001) 329–339.
[5.152] ALLEN, V.M., et al., Determination and interpretation of texture evolution during deformation of a zirconium alloy, J. ASTM International 5 (2008), Paper ID: JAI 101255.
[5.153] GREWEN, J., "Textures of hexagonal metals and alloys and their influence on industrial application", Proc. 3rd European Conf. on textures de déformation et de recristallisation des métaux et les application industrielles, Pont-a-Mousson (PENELLE, R., Ed.), Société Française de Métallurgie, Nancy (1973) 195–216.
[5.154] TENCKHOFF, E., "Review of deformation mechanisms, texture, and mechanical anisotropy in zirconium and zirconium base alloys", Zirconium in the Nuclear Industry: Fourteenth International Symposium, ASTM STP 1467, Stockholm, 2004 (RUDLING, P., KAMMENZIND, B., Eds), ASTM International, West Conshohocken, PA (2006) 25–50.
[5.155] BURGERS, W.G., FAST, J.D., JACOBS, F.M., Drawing and recrystallization textures in zirconium wire, Z. Metallkd. **29** (1937) 410–412.
[5.156] McHARGUE, C.J., HAMMOND, J.P., Preferred orientations in iodide titanium, Trans. Metall. Soc. AIME **197** (1953) 57–61.
[5.157] CHARQUET, D., ALHERITIERE, E., BLANC, G., Cold-rolled and annealed textures of Zircaloy-4 thin strips", Zirconium in the Nuclear Industry: Seventh International Symposium, ASTM STP 939, Strasbourg, 1985 (ADAMSON, R.B., VAN SWAM, L.F.P., Eds), ASTM International, West Conshohocken, PA (1987) 663–672.

[5.158] TOMÉ, C.N., MAUDLIN, P.J., LEBENSOHN, R.A., KASCHNER, G.C., Mechanical response of zirconium — I. Derivation of a polycrystal constitutive law and finite element analysis, Acta Mater. **49** (2001) 3085–3096.
[5.159] NERSES, V., Texture of Extruded Zirconium and Zircaloy-2 Tubing, Report No. NMI-1222, Atomic Energy Commission, Washington, DC (1960).
[5.160] TUXWORTH, R.H., A Study of Preferred Orientation in Extruded Zircaloy-2 Pressure Tubes, Report No. CRMet-901, Atomic Energy of Canada Limited, Chalk River, ON (1960).
[5.161] LAIDLER, J.J., Preferred Orientations in Extruded Zircaloy-2 Tubing, Report No. HW-64815, Atomic Energy Commission, Washington, DC (1960).
[5.162] WOOD, D.S., WINTON, J., WATKINS, B., Effect of irradiation on the impact properties of hydrided Zircaloy-2 and zirconium-niobium alloy, Electrochem. Technol. **4** (1966) 250–258.
[5.163] OKADA, T., HIRANO, H., KUNIMOTO, N., Texture and microstructure of thin-walled Zircaloy-2 tubes, Electrochem. Technol. **4** (1966) 365–374.
[5.164] STURCKEN, E.F., DUKE, W.G., Measurement of Preferred Orientation of Thin-Walled Zircaloy-2 Tubes, Report No. DP-607, Atomic Energy Commission, Washington, DC (1961).
[5.165] HINDLE, E.D., SLATTERY, G.F., Preferred orientations in Zircaloy-2 tubing manufactured by various routes, J. Inst. Met. **93** (1964) 565–570.
[5.166] CHEADLE, B.A., ELLS, C.E., Effect of crystallographic orientation on the fracture ductility of Zr-2.5 Wt Pct Nb(Cb) and Zircaloy-2 tubular products, Trans. Metall. Soc. AIME **233** (1965) 1044–1052.
[5.167] CHEADLE, B.A., ELLS, C.E., EVANS, W., The development of texture in zirconium alloy tubes, J. Nucl. Mater. **23** (1967) 199–208.
[5.168] TENCKHOFF, E., RITTENHOUSE, P.L., "Texture development and texture gradients in Zircaloy tubing", Applications-Related Phenomena in Zirconium and Its Alloys, ASTM STP 458 (BAROCH, E.F., Ed.), ASTM International, West Conshohocken PA (1970) 50–67.
[5.169] TENCKHOFF, E., The influence of reduction ratio on the development of textures and texture gradients in Zircaloy tubes, Z. Metallkd. **61** (1970) 64–71.
[5.170] TENCKHOFF, E., RITTENHOUSE, P.L., Influence of the reduction values on texture formation in Zircaloy tubing produced with low deformations, Z. Metallkd. **63** (1972) 83–88.
[5.171] KÄLLSTRÖM, K., Texture and anisotropy of zirconium in relation to plastic deformation, Can. Metall. Q. **11** (1972) 185–198.
[5.172] LEBENSOHN, R.A., GONZÁLEZ, M.I., TOMÉ, C.N., POCHETTINO, A.A., Measurement and prediction of texture development during a rolling sequence of Zircaloy-4 tubes, J. Nucl. Mater. **229** (1996) 57–64.
[5.173] PICKLESIMER, M.L., A Preliminary Examination of the Formation and Utilization of Texture and Anisotropy in Zircaloy-2, Report No. ORNL-TM-460, Oak Ridge National Laboratory, Oak Ridge, TN (1963).
[5.174] MOULIN, L., RESCHKE, S., TENCKHOFF, E., "Correlation between fabrication parameters, microstructure, and texture in Zircaloy tubing", Zirconium in the Nuclear Industry: Sixth International Symposium, ASTM STP 824, Vancouver, 1982 (FRANKLIN, D.G., ADAMSON, R.B., Eds), ASTM International, West Conshohocken, PA (1984) 225–243.
[5.175] GIRARD, E., GUILLÉN, R., WEISBECKER, P., FRANÇOIS, M., Effect of plastic shearing on damage and texture on Zircaloy-4 cladding tubes: Experimental and numerical study, J. Nucl. Mater. **294** (2001) 330–338.
[5.176] NIKULINA, A.V., et al., "Zirconium alloy E635 as a material for fuel rod cladding and other components of VVER and RBMK cores", Zirconium in the Nuclear Industry: Eleventh International Symposium, ASTM STP 1295, Garmisch-Partenkirchen, 1995 (BRADLEY, E.R., SABOL, G.P., Eds), ASTM International, West Conshohocken, PA (1996) 785–804.
[5.177] ZAVODTCHIKOV, S.Y., ZUEV, L.B., BELOV, V.I., LOSITSKIY, A.F., SHEVNIN, Y.P., "Plastic deformation and fracture during the Zr1%Nb tube production", Zirconium in the Nuclear Industry: Thirteenth International Symposium, ASTM STP 1423, Annecy, 2001 (MOAN, G.D., RUDLING, P., Eds), ASTM International, West Conshohocken, PA (2002) 427–448.
[5.178] SHISHOV, V.N., et al., "Influence of structure-phase state of Nb containing Zr alloys on irradiation-induced growth", Zirconium in the Nuclear Industry: Fourteenth International Symposium, ASTM STP 1467, Stockholm, 2004 (RUDLING, P., KAMMENZIND, B., Eds), ASTM International, West Conshohocken, PA (2006) 666–685.
[5.179] GLOAGUEN, D., BERCHI, T., GIRARD, E., GUILLEN, R., Examination of residual stresses and texture in zirconium alloy cladding tubes after a large plastic deformation: Experimental and numerical study, J. Nucl. Mater. **374** (2008) 138–146.
[5.180] SABOL, G.P., et al., "In-reactor corrosion performance of ZIRLO™ and Zircaloy-4", Zirconium in the Nuclear Industry: Tenth International Symposium, ASTM STP 1245, Baltimore, 1993 (GARDE, A.M., BRADLEY, E.R., Eds), ASTM International, West Conshohocken, PA (1994) 724–744.
[5.181] THEAKER, J.R., COLEMAN, C.E., "Development of crystallographic texture in CANDU calandria tubes", Zirconium in the Nuclear Industry: Thirteenth International Symposium, ASTM STP 1423, Annecy, France, 2001 (MOAN, G.D., RUDLING, P., Eds), ASTM International, West Conshohocken, PA (2002) 449–467.
[5.182] KAPOOR, K., PADMAPRABU, C., RAMANA RAO, S.V., SANYAL, T., KASHYAP, B.P., Effect of processing on properties of thin walled calandria tubes for pressurized heavy water reactors, J. Nucl. Mater. **312** (2003) 125–133.
[5.183] SRIVASTAVA, D., DEY, G.K., BANERJEE, S., Evolution of microstructure during fabrication of Zr-2.5 wt pct Nb alloy pressure tubes, Metall. Mat. Trans. A **26** (1995) 2707–2718.
[5.184] CHOUBEY, R., ALDRIDGE, S.A., THEAKER, J.R., CANN, C.D., COLEMAN, C.E., "Effects of extrusion billet preheating and properties of Zr-2.5Nb pressure tube materials", Zirconium in the Nuclear Industry:

Eleventh International Symposium, ASTM STP 1295, Garmisch-Partenkirchen, 1995 (BRADLEY, E.R., SABOL, G.P., Eds), ASTM International, West Conshohocken, PA (1996) 657–675.
[5.185] COLEMAN, C.E., et al., Mechanical properties of Zr-2.5Nb pressure tubes made from electrolytic powder, J. ASTM International **4** 10 (2007), Paper ID: JAI 101111.
[5.186] HOLT, R.A., ALDRIDGE, S.A., Effect of extrusion variables on crystallographic texture of Zr-2.5 wt% Nb, J. Nucl. Mater. **135** (1985) 246–259.
[5.187] CHEADLE, B.A., ALDRIDGE, S.A., ELLS, C.E., The Effect of Temperature during Deformation on the Development of Texture in Zirconium Alloy Rolled Sheet and Extruded Tubes, Report No. AECL–3372, Atomic Energy of Canada Limited, Chalk River, ON (1969).
[5.188] CHEADLE, B.A., ALDRIDGE, S.A., ELLS, C.E., The effect of temperature during deformation on the development of texture in zirconium alloy rolled sheet, J. Nucl. Mater. **34** (1970) 119–124.
[5.189] CHEADLE, B.A., ALDRIDGE, S.A., ELLS, C.E., Development of texture and structure in Zr-2.5wt%Nb extruded tubes, Can. Metall. Q. **11** (1972) 121–127.
[5.190] SALINAS-RODRIGUEZ, A., JONAS, J.J., Evolution of textures in zirconium alloys deformed uniaxially at elevated temperatures, Metall. Trans. A **23** (1992) 271–293.
[5.191] LOGE, R.E., SIGNORELLI, J.W., CHASTEL, Y.B., PERRIN, M.Y., LEBENSOHN, R.A., Sensitivity of α-ZY4 high-temperature deformation textures to the β-quenched precipitate structure and to recrystallization: Application to hot extrusion, Acta Metall. **48** (2000) 3917–3930.
[5.192] TENCKHOFF, E., RITTENHOUSE, P.L., Annealing textures in Zircaloy tubing, J. Nucl. Mater. **35** (1970) 1–23.
[5.193] CHEADLE, B.A., ELLS, C.E., The effect of heat treatment on the texture of fabricated Zr-rich alloys, Electrochem. Technol. **4** (1966) 329–336.
[5.194] KEELER, J.H., GEISLER, A.H., Preferred orientation in beta-annealed zirconium, Trans. Metall. Soc. AIME **203** (1955) 395–400.
[5.195] CHAUBET, D., BACROIX, B., BÉCHADE, J.L., An EBSD study of static recrystallization of cold-rolled Zircaloy-4 sheets, Mater. Sci. Forum **408**–**412** (2002) 797–802.
[5.196] KEELER, J.H., GEISLER, A.H., Preferred orientations in rolled and annealed titanium, Trans. Metall. Soc. AIME **206** (1956) 80–90.
[5.197] CIURCHEA, D., et al., Texture, morphology and deformation mechanisms in β-transformed Zircaloy-4, J. Nucl. Mater. **231** (1996) 83–91.
[5.198] GEY, N., et al., Study of the α/β phase transformation of Zircaloy-4 in presence of applied stresses at heating: Analysis of the inherited microstructures and textures, J. Nucl. Mater. **302** (2002) 175–184.
[5.199] GEY, N., HUMBERT, M., GAUTIER, E., BÉCHADE, J.L., Analysis of the β→α variant selection in a Zircaloy-4 rod by means of specific crystal orientation maps, Mater. Sci. Forum **408**–**412** (2002) 1759–1764.
[5.200] GEY, N., HUMBERT, M., GAUTIER, E., BÉCHADE, J.L., Study of the β→α variant selection for a Zircaloy-4 rod heated to the β transus in presence or not of an axial tensile stress, J. Nucl. Mater. **328** (2004) 137–145.
[5.201] WENK, H.R., LONARDELLI, I., WILLIAMS, D., Texture changes in the HCP → BCC → HCP transformation of zirconium studied in-situ by neutron diffraction, Acta Metall. Mater. **52** (2004) 1899–1907.
[5.202] RUCH, M., ARIAS, D., β/α transformation in dilute titanium and zirconium base alloys, Scr. Metall. Mater. **24** (1990) 1577–1582.
[5.203] MAUSSNER, G., AREVA-ANP, Erlangen, private communication, 2006.
[5.204] DAHLBÄCK, M., et al., "The effect of beta-quenching in final dimensions on the irradiation growth of tubes and channels", Zirconium in the Nuclear Industry: Fourteenth International Symposium, ASTM STP 1467, Stockholm, 2004 (RUDLING, P., KAMMENZIND, B., Eds), ASTM International, West Conshohocken, PA (2006) 276–304.
[5.205] KOIKE, M., ASADA, T., Irradiation creep and growth of pressure tubes in HWR Fugen, J. Nucl. Mater. **159** (1988) 62–74.
[5.206] HOSBONS, R.R., IBRAHIM, E.F., HOLDEN, T.M., ROOT, J.H., "The use of neutron diffraction to determine non-destructively the residual strain and textures in welds", Proc. 2nd Int. Conf. on Trends in Welding Research, Gatlinburg, 1989, American Society for Metals, Materials Park, OH (1989) 103–106.
[5.207] ROOT, J.H., SALINAS-RODRIGUEZ, A., Neutron diffraction measurement of texture variations near a weld in a Zr-2.5%Nb plate, Texture, Stress, and Microstructures **14**–**18** (1991) 989–994.
[5.208] COLEMAN, C.E., et al., "Mitigation of harmful effects of welds in zirconium alloy components", Zirconium in the Nuclear Industry: Tenth International Symposium, ASTM STP 1245, Baltimore, 1993 (GARDE, A.M., BRADLEY, E.R., Eds), ASTM International, West Conshohocken, PA (1994) 264–284.
[5.209] JUNG, S.-H., Effect of β-heat treatment of microstructure and mechanical anisotropy of Zircaloy-4 fuel cladding, J. Nucl. Sci. Technol. **26** (1989) 516–524.
[5.210] HWANG, S.K., RYOO, H.S., MORRIS, J.W., Jr., Effects of transformation on texture and iodine stress corrosion cracking resistance of Zircaloy sheet, Metall. Trans. A **22** (1991) 2247–2256.
[5.211] YOO, J.S., KIM, I.S., Texture transformation and its role on the yield strength of (α+β) heat-treated Zircaloy-4, J. Korean Nucl. Soc. **24** (1992) 75–85.
[5.212] ISAENKOVA, M.G., KONOPLENKO, V.P., NOVIKOY, V.V., PERLOVICH, Y.A., PRASOLOV, P.F., Influence of texture on plastic tensile strain of rolled Zr-1% Nb alloy, At. Ehnerg. **52** (1982) 299–303 (in Russian).
[5.213] HOBSON, D.O., RITTENHOUSE, P.L., Nonhomogeneous deformation in Zircaloy tubing, Trans. Metall. Soc. AIME **245** (1969) 797–800.

[5.214] STEWARD, K.P., CHEADLE, B.A., The effect of preferred orientation on the mechanical properties and deformation behaviour of Zircaloy-4 fuel sheathing, Trans. Metall. Soc. AIME **239** (1967) 504–513.
[5.215] PICKMAN, D.O., Properties of Zircaloy cladding, Nucl. Eng. Des. **21** (1972) 212–236.
[5.216] RITTENHOUSE, P.L., "The effect of texture on the torsional yielding of Zircaloy tubing", Applications-Related Phenomena in Zirconium and its Alloys, ASTM STP 458 (BAROCH, E.F., Ed.), ASTM International, West Conshohocken, PA (1969) 241–251.
[5.217] PEEHS, M., STEHLE, H., STEINBERG, E., "Out-of-pile testing of iodine stress corrosion cracking in Zircaloy tubing in relation to the pellet-cladding interaction phenomenon", Zirconium in the Nuclear Industry: Fourth International Symposium, Proc. ASTM STP 681, Stratford-upon-Avon, 1978 (PAPAZOGLOU, T.P., Ed.), ASTM International, West Conshohocken, PA (1979) 244–260.
[5.218] FREGONESE, M., et al., "Failure mechanisms of irradiated Zr alloys related to PCI: activated slip systems, localized strains, and iodine-induced stress corrosion cracking", Zirconium in the Nuclear Industry: Twelfth International Symposium, Proc. ASTM STP 1354, Toronto, 1998 (SABOL, G.P., MOAN, G.D., Eds), ASTM International, West Conshohocken, PA (2000) 377–398.
[5.219] TRESCA, M.H., Mécanique Appliquée — Mémoire sur l'écoulement des corps solides soumis à de fortes pressions, c.r. hebd. des seances Acad. Sci. **59** (1864) 754–758.
[5.220] TOMÉ, C., KOCKS, U.F., The yield surface of H.C.P. crystals, Acta Metall. **33** (1985) 603–621.
[5.221] DRESSLER, G., MATUCHA, K.-H., "Yield and fracture of biaxially stressed Zircaloy-4 cladding tubes at room temperature and at 400°C", Zirconium in the Nuclear Industry: Third International Conference, Proc. ASTM STP 633, Quebec City, 1976 (LOWE, A.L., PARRY, G.W., Eds), ASTM International, West Conshohocken, PA (1977) 508–522.
[5.222] EISENBERG, M.A., HARTLEY, C.S., LEE, H.-C., YEN, C.F., Influence of texture on the analysis of thermoelastic/plastic anisotropy and the initial yielding of Zircaloy tubes, J. Nucl. Mater. **88** (1980) 138–152.
[5.223] BALLINGER, R.G., PELLOUX, R.M., The effect of anisotropy on the mechanical behaviour of Zircaloy-2, J. Nucl. Mater. **97** (1981) 231–253.
[5.224] FUNDENBERGER, J.J., PHILIPPE, M.J., WAGNER, F., ESLING, C., Modelling and prediction of mechanical properties for materials with hexagonal symmetry (zinc, titanium and zirconium alloys), Acta Mater. **45** (1997) 4041–4055.
[5.225] STEHLE, H., STEINBERG, E., TENCKHOFF, E., "Mechanical properties, anisotropy, and microstructure of Zircaloy canning tubes", Zirconium in the Nuclear Industry: Third International Conference, Proc. ASTM STP 633, Quebec City, 1976 (LOWE, A.L., Jr., PARRY, G.W., Eds), ASTM International, West Conshohocken, PA (1977) 486–507.
[5.226] ROSS-ROSS, P.A., FIDLERIS, V., FRASER, D.E., Anisotropic creep behaviour of zirconium alloys in a fast neutron flux, Can. Metall. Q. **11** (1972) 101–111.
[5.227] EARTHMAN, J.C., MURTY, K.L., TANIKELLA, B.V., BRITT, J.C., Effects of grain-shape anisotropy and texture on balanced-biaxial creep of Ti and Zr alloys, JOM **46** (1994) 48–54.
[5.228] DUNCOMBE, E., Improved First Order Analysis of the Plastic Stability of Diffuse Patches in Tubes and Sheets, Report No. WAPD-TM-984, Bettis Atomic Power Laboratory, Pittsburgh, PA (1973).
[5.229] VELEVA, M., ARSENE, S., RECORD, M.C., BÉCHADE, J.L., BAI, J.B., Hydride embrittlement and irradiation effects on the hoop mechanical properties of pressurised water reactor (PWR) and boiling water reactor (BWR) zircaloy cladding tubes: Part II. Morphology of hydrides investigated at different magnifications and their interaction with the processes of plastic deformation, Metall. Mat. Trans. A **34** (2003) 567–578.
[5.230] ARSENE, S., BAI, J.B., BOMPARD, P., Hydride embrittlement and irradiation effects on the hoop mechanical properties of pressurised water reactor (PWR) and boiling water reactor (BWR) zircaloy cladding tubes: Part I. Hydride embrittlement in stress-relieved, annealed, and recrystallized Zircaloy at 20°C and 300°C, Metall. Mat. Trans. A **34** (2003) 553–566.
[5.231] ARSENE, S., BAI, J.B., BOMPARD, P., Hydride embrittlement and irradiation effects on the hoop mechanical properties of pressurised water reactor (PWR) and boiling water reactor (BWR) zircaloy cladding tubes: Part III. Mechanical behaviour of hydride in stress-relieved annealed and recrystallized zircaloys at 20°C and 300°C, Metall. Mat. Trans. A **34** (2003) 579–588.
[5.232] FIDLERIS, V., Irradiation Growth in Zirconium Alloys: A Review, Report No. AECL-7053, Atomic Energy of Canada Limited, Chalk River, ON (1980).
[5.233] ADAMSON, R.B., TUCKER, R.P., FIDLERIS, V., "High-temperature irradiation growth in Zircaloy", Zirconium in the Nuclear Industry: Fifth International Symposium, Proc. ASTM STP 754, Boston, 1980 (FRANKLIN, D.G., Ed.), ASTM International, West Conshohocken, PA (1982) 208–234.
[5.234] FIDLERIS, V., Irradiation creep and growth phenomena, J. Nucl. Mater. **159** (1988) 22–42.
[5.235] ARDELL, A.J., SHERBY, O.D., Steady-state creep of polycrystalline alpha zirconium at elevated temperatures, Trans. Metall. Soc. AIME **239** (1967) 1547–1556.
[5.236] FIDLERIS, V., "The effect of texture and strain aging on creep of Zircaloy-2", Applications-Related Phenomena in Zirconium and Its Alloys, ASTM STP 458 (BAROCH, E.F., Ed.), ASTM International, West Conshohocken, PA (1969) 1–17.
[5.237] HOLMES, J.J., The activation energies for creep of Zircaloy-2, J. Nucl. Mater. **13** (1964) 137–141.
[5.238] BERNSTEIN, I.M., Diffusion creep in zirconium and certain zirconium alloys, Trans. Metall. Soc. AIME **239** (1967) 1518–1522.
[5.239] ONIMUS, F., MONNET, I., BÉCHADE, J.L., PRIOUL, C., PILVIN, P., A statistical TEM investigation of dislocation channeling mechanism in neutron irradiated zirconium alloys, J. Nucl. Mater. **328** (2004) 165–179.

[5.240] IRVIN, J.E., Effects of irradiation and environment on the mechanical properties and hydrogen pick-up of Zircaloy, Electrochem. Technol. **4** (1966) 240–249.
[5.241] AZZARTO, F.J., BALDWIN, E.E., WIESINGER, F.W., LEWIS, D.M., Unirradiated, in-pile and post-irradiation low strain rate tensile properties of Zircaloy-4, J. Nucl. Mater. **30** (1969) 208–218.
[5.242] VEEVERS, K., ROTSEY, W.B., Effect of irradiation on strain ageing in annealed Zircaloy-2, J. Nucl. Mater. **27** (1968) 108–111.
[5.243] GILBERT, E.R., In-reactor creep of Zr-2.5 at % Nb, J. Nucl. Mater. **26** (1968) 105–111.
[5.244] IBRAHIM, E.F., "In-reactor creep of zirconium alloy tubes and its correlation with uniaxial data", Applications-Related Phenomena in Zirconium and Its Alloys, ASTM STP 458 (BAROCH, E.F., Ed.), ASTM International, West Conshohocken, PA (1969) 18–36.
[5.245] COLEMAN, C.E., CAUSEY, A.R., FIDLERIS, V., In-reactor creep of zirconium-2.5 wt% niobium at 570 K, J. Nucl. Mater. **60** (1976) 185–194.
[5.246] CHRISTODOULOU, N., TURNER, P.A., TOMÉ, C.N., CHOW, C.K., KLASSEN, R.J., Analysis of steady-state thermal creep of Zr-2.5Nb pressure tube material, Metall. Mat. Trans. A **33** (2002) 1103–1115.
[5.247] HOWE, M.L., The Annealing of Irradiation Damage in Zircaloy-2 and the Effect of High Temperature Radiation on the Tensile Properties of Zircaloy-2, Report No. AECL-1024, Atomic Energy of Canada Limited, Chalk River, ON (1960).
[5.248] HOWE, M.L., Radiation Damage in Zirconium, Zircaloy-2, and 410 Stainless Steel, Report No. AECL-1484, Atomic Energy of Canada Limited, Chalk River, ON (1962).
[5.249] ELLS, C.E., COLEMAN, C.E., WILLIAMS, C.D., The Temperature Dependence of Irradiation Damage in Zirconium Alloys, Report No. AECL-5470, Atomic Energy of Canada Limited, Chalk River, ON (1974).
[5.250] HESKETH, R.V., Application of the generalized theory of yielding creep to irradiation creep in zirconium alloys, J. Nucl. Mater. **26** (1968) 77–86.
[5.251] PIERCY, G.R., Mechanisms for the in-reactor creep of zirconium alloys, J. Nucl. Mater. **26** (1968) 18–50.
[5.252] NICHOLS, F.A., Theory of the creep of Zircaloy during neutron irradiation, J. Nucl. Mater. **30** (1969) 249–270.

ABBREVIATIONS

AC	alternating current
AD	axial direction
AES	auger electron spectroscopy
BCC	body centred cubic
BWR	boiling water reactor
CALPHAD	computer coupling of phase diagrams and thermochemistry
CANDU	Canada deuterium uranium reactor
CAP	cumulative annealing parameter
CRM	certified reference materials
CRSS	critical resolved shear stress
CW	cold worked
DC	direct current
DRX	dynamic recrystallization
EB	electron beam
EBSD	electron backscattered diffraction
EBW	electron beam welding
ECT	eddy current testing
EDX	energy dispersive X ray
FCC	face centred cubic
FIB	focused ion beam
FTIR	Fourier transform infrared
GDMS	glow discharge mass spectroscopy
GTAW	gas-tungsten arc welding
HANA	high temperature alloys for nuclear applications
HAZ	heat affected zone
HCP	hexagonal close packed
HPU	hydrogen pick-up
ICP	inductively coupled plasma
LPT	liquid penetrant testing
MDA	Mitsubishi developed alloy
MIBK	methyl isobutyl ketone-thiocyanate
MOX	mixed oxide
ND	normal direction
NDA	new developed alloy
ODF	orientation distribution function
PAW	plasma arc welding
PHWR	pressurized heavy water reactor
PWR	pressurized water reactor
RA	reduction in area
RBMK	high-power channel-type reactor
RD	rolling direction
SAM	scanning auger microprobe

SEM	scanning electron microscopes
SFE	stacking fault energy
SIMS	secondary-ion mass spectrometry
SND	sheet normal direction
SOS	state of stress
SRD	sheet rolling direction
STD	sheet transverse direction
TBP	tributyl phosphate
TD	transverse direction
TEM	transmission electron microscope
TMT	thermomechanically treated
TREX	tube reduced extrusions
UT	ultrasonic testing
UTS	ultimate tensile strength
VAR	vacuum arc remelting
VPN	vickers pyramid number
WDX	wavelength dispersive X ray
WWER	water cooled water moderated power reactor
XAFS	X ray absorption fine structure
XPS	X ray photoelectron spectroscopy

Since the last publication on zirconium by the IAEA in 1971 there has been a need to gather and update relevant information. In an effort to bridge the years-long gap on zirconium, its development and use in industry, and to provide comprehensive information on the material the IAEA initiated a comprehensive project on the metallurgy of zirconium, which resulted in this publication. These volumes cover a wide range of the applications, properties and irradiation behaviour of zirconium.

INTERNATIONAL ATOMIC ENERGY AGENCY
VIENNA